Springer Proceedings in Physics 228

Mohamed Belhaq *Editor*

Topics in Nonlinear Mechanics and Physics

Selected Papers from CSNDD 2018

Springer

Springer Proceedings in Physics

Volume 228

Indexed by Scopus

The series Springer Proceedings in Physics, founded in 1984, is devoted to timely reports of state-of-the-art developments in physics and related sciences. Typically based on material presented at conferences, workshops and similar scientific meetings, volumes published in this series will constitute a comprehensive up-to-date source of reference on a field or subfield of relevance in contemporary physics. Proposals must include the following:

- name, place and date of the scientific meeting
- a link to the committees (local organization, international advisors etc.)
- scientific description of the meeting
- list of invited/plenary speakers
- an estimate of the planned proceedings book parameters (number of pages/articles, requested number of bulk copies, submission deadline).

More information about this series at http://www.springer.com/series/361

Mohamed Belhaq
Editor

Topics in Nonlinear Mechanics and Physics

Selected Papers from CSNDD 2018

Springer

Editor
Mohamed Belhaq
Faculty of Sciences Ain Chock
University Hassan II - Casablanca
Casablanca, Morocco

ISSN 0930-8989 ISSN 1867-4941 (electronic)
Springer Proceedings in Physics
ISBN 978-981-13-9462-1 ISBN 978-981-13-9463-8 (eBook)
https://doi.org/10.1007/978-981-13-9463-8

This Springer imprint is published by the registered company Springer Nature Singapore Pte Ltd.
The registered company address is: 152 Beach Road, #21-01/04 Gateway East, Singapore 189721, Singapore

Contents

Contributors

Karam Allali Faculty of Sciences and Technologies, University Hassan II Casablanca, Mohammedia, Morocco

Gioacchino Alotta Department of Engineering, University of Palermo, Palermo, Italy

B. Ambrożkiewicz Faculty of Mechanical Engineering, Department of Automation, Lublin University of Technology, Lublin, Poland

Krzysztof Augustynek University of Bielsko-Biala, Bielsko-Biala, Poland

Jan Awrejcewicz Department of Automatics and Biomechanics, Technical University of Łódź, Łódź, Poland

Jose M. Balthazar Federal University of Technology—Paraná, Ponta Grossa, PR, Brazil

Jabrane Belabid Faculty of Sciences and Technologies, University Hassan II Casablanca, Mohammedia, Morocco

Mohamed Belhaq Faculty of Sciences Ain Chock, University Hassan II Casablanca, Casablanca, Morocco

Yaroslav M. Blanter Kavli Institute of Nanoscience, Delft University of Technology, Delft, The Netherlands

Americo Cunha Jr Universidade do Estado do Rio de Janeiro, Rio de Janeiro, Brazil

Antonio Fernandez-Barbero Departamento de Quimica y Fisica, Universidad de Almeria, Almeria, Spain

Pawel Fritzkowski Institute of Applied Mechanics, Poznan University of Technology, Poznań, Poland

Zakaria Ghouli Faculty of Sciences Ain Chock, University Hassan II Casablanca, Casablanca, Morocco

Y. Guo Faculty of Mechanical and Electrical Engineering, Kunming University of Science and Technology, Kunming City, Yunnan Province, China

Eduardo Guzman Instituto Pluridisciplinar, UCM, Madrid, Spain;
Departamento de Quimica Fisica, UCM, Madrid, Spain

Giuseppe Habib Department of Applied Mechanics, MTA-BME Lendület Human Balancing Research Group, Budapest University of Technology and Economics, Budapest, Hungary

T. Haj Mohamad Villanova Center for Analytics of Dynamic Systems (VCADS), Villanova University, Villanova, PA, USA

Mustapha Hamdi University Mohammed I Oujda, FST-Al Hoceima, Al-Hoceima, Morocco

Daiki Hatanaka NTT Basic Research Laboratories, NTT Corporation, Kanagawa, Japan

Samer Houri NTT Basic Research Laboratories, NTT Corporation, Kanagawa, Japan

Raouf A. Ibrahim Department of Mechanical Engineering, Wayne State University, Detroit, MI, USA

Elżbieta Jarzębowska Warsaw University of Technology, Warsaw, Poland

C. A. Kitio Kwuimy Department of Engineering Education, College of Engineering and Applied Science, University of Cincinnati, Cincinnati, OH, USA

Wagner B. Lenz Federal University of Technology—Paraná, Ponta Grossa, PR, Brazil

G. Litak Faculty of Mechanical Engineering, Department of Automation, Lublin University of Technology, Lublin, Poland

Vinicius G. Lopes Universidade do Estado do Rio de Janeiro, Rio de Janeiro, Brazil

Thiago C. L. Marsola Federal University of Technology—Paraná, Ponta Grossa, PR, Brazil

Alberto Di Matteo Department of Engineering, University of Palermo, Palermo, Italy

Peter A. Meleshenko Communication Department, Zhukovsky–Gagarin Air Force Academy, Voronezh, Russia

C. Nataraj Villanova Center for Analytics of Dynamic Systems (VCADS), Villanova University, Villanova, PA, USA

Francisco Ortega Instituto Pluridisciplinar, UCM, Madrid, Spain;
Departamento de Quimica Fisica, UCM, Madrid, Spain

Mario Di Paola Department of Engineering, University of Palermo, Palermo, Italy

Mateus F. V. Pereira Federal University of Technology—Paraná, Ponta Grossa, PR, Brazil

João Victor L. L. Peterson Universidade do Estado do Rio de Janeiro, Rio de Janeiro, Brazil

Francesco Paolo Pinnola Department of Structures for Engineering and Architecture (DIST), University of Naples "Federico II", Naples, Italy

Antonina Pirrotta Department of Engineering, University of Palermo, Palermo, Italy

Olga O. Reshetova Digital Technologies Department, Voronezh State University, Voronezh, Russia

Mauricio A. Ribeiro Federal University of Technology—Paraná, Ponta Grossa, PR, Brazil

Ramon G. Rubio Instituto Pluridisciplinar, UCM, Madrid, Spain;
Departamento de Quimica Fisica, UCM, Madrid, Spain

Yuri S. Ryazantsev Instituto Pluridisciplinar, UCM, Madrid, Spain

Waldemar Samociuk Faculty of Production Engineering, University of Life Sciences in Lublin, Lublin, Poland

Mikhail E. Semenov Geophysical Survey of Russia Academy of Sciences, Obninsk, Russia;
Meteorology Department, Zhukovsky–Gagarin Air Force Academy, Voronezh, Russia;
Digital Technologies Department, Voronezh State University, Voronezh, Russia;
Mathematics Department, Voronezh State University of Architecture and Civil Engineering, Voronezh, Russia

Andrey M. Solovyov Digital Technologies Department, Voronezh State University, Voronezh, Russia

Roman Starosta Institute of Applied Mechanics, Poznan University of Technology, Poznań, Poland

Akim V. Tolkachev Zhukovsky–Gagarin Air Force Academy, Voronezh, Russia

Angelo M. Tusset Federal University of Technology—Paraná, Ponta Grossa, PR, Brazil

Andrzej Urbaś University of Bielsko-Biala, Bielsko-Biala, Poland

Manuel G. Velarde Instituto Pluridisciplinar, UCM, Madrid, Spain

Piotr Wolszczak Faculty of Mechanical Engineering, Department of Automation, Lublin University of Technology, Lublin, Poland

Hiroshi Yamaguchi NTT Basic Research Laboratories, NTT Corporation, Kanagawa, Japan

Chapter 1
Parametric and Autoparametric Dynamics of Ships with Liquid Sloshing Interaction

Raouf A. Ibrahim

Abstract Two mechanisms of parametric roll resonance of navigating ships together with roll-pitch autoparametric interaction of ship dynamics are outlined. Deterministic and stochastic parametric roll ship's stability are outlined. Sloshing flow in liquid ship cargo adds additional problem in the vessel stability and dynamics. A liquid cargo tank is excited by the ship motion and the subsequent liquid sloshing flow itself affects the ship dynamics. The problem of ship interaction with liquefied natural gas (LNG) sloshing dynamics is discussed. Ship designers have been motivated to develop passive and active controls of ships roll instability. This includes free surface anti-roll tanks and U-tube anti-roll tanks. The basic principle of the two anti-roll tank types is to transfer the liquid from starboard to port side and vice versa, with a certain phase lag with respect to the ship's rolling motion. This provides a counteracting moment to stabilize the ship roll oscillations. This article is dedicated in memory of two outstanding leaders in the field of nonlinear dynamics: the late Professor Ali H. Nayfeh and the late Professor Allan D. S. Barr.

1.1 Introduction

Extreme loadings acting on the ship structure have many sources including impact with stationary structures, slamming loading, sloshing impact loading, grounding accidents, etc. Under extreme loadings, structural reliability will be a major issue in the design stage of ocean structures [84]. There has been great progress made by engineers and designers to secure the stability of ships and particularly reducing ships' capsizing. The estimation of liquid sloshing loads in tanks of ships is important in the design of ship vessels such as liquefied natural gas (LNG) carriers and double-hull tankers. Sloshing in a real LNG tank involves many complicated physical phenomena such as wave breaking [83], phase transition between liquid and gas during the impact, gas entrapment, cushioning effect due to corrugation, etc. Fluid-structure interaction plays an important role in the structural analysis of the containment sys-

R. A. Ibrahim (✉)
Department of Mechanical Engineering, Wayne State University, Detroit, MI 48202, USA
e-mail: ibrahim@eng.wayne.edu

M. Belhaq (ed.), *Topics in Nonlinear Mechanics and Physics*,
Springer Proceedings in Physics 228, https://doi.org/10.1007/978-981-13-9463-8_1

tem under sloshing load. The structural analysis of the containment system considers fluid-structure interaction between liquid cargo and the LNG containment system. Analytical techniques and numerical algorithms of liquid sloshing impact dynamics in moving liquid containers are well documented by Ibrahim [82]. Specific applications of liquid sloshing problems to marine systems are well addressed by Faltinsen and Timokha [49].

The main objectives of this Chapter are to provide an assessment of the main results of parametric and autoparametric dynamics of ships including their interaction with liquid sloshing. Section 1.2 presents two mechanisms of ships parametric resonances. The first is due to the fact that the righting arm may exhibit time variation (*parametric excitation*) under certain conditions of the sea waves. The second is that it may implicitly exhibit time variation when the ship roll is coupled with its pitching oscillations (known as *autoparametric coupling*). The deterministic ships parametric stabilities are discussed. Ocean waves are generally not harmonic but irregular and random. In an attempt to facilitate the analysis under irregular wave, Grim [66] introduced the concept of effective waves, which constitutes of replacing an irregular wave is replaced by a regular wave of length equivalent to the ship length and its crest or trough situated at the center of gravity. The ship stochastic roll stability conditions are outlined in terms of stochastic modes of convergence [81]. Section 1.3 deals with the ship autoparametric roll-pitching interaction. The concept of autoparametric interaction is first introduced and demonstrated using the example of autoparametric vibration absorber developed originally by Haxton and Barr [74]. The Autoparametric vibration absorber concept is similar to a great extent to the nonlinear pitch-roll coupling of the forced response of a ship sailing in longitudinal waves. The interaction of ships with its liquid cargo is introduced in Sect. 1.4. This section is closely related to Sect. 1.5, which deals with the passive control of ship roll instability using the free surface liquid anti-roll tanks and the U-tube anti-roll tanks. Section 1.6 provides the main conclusions and recommendations for future research.

1.2 Ships Parametric Roll Resonance

1.2.1 Preliminary

It is known that the ship parametric roll resonance may cause a significant amplification of roll motions of containerships and cargo ships in longitudinal (head and following) waves. It is believed that Froude [57, 58] was the first to observe and report ships parametric resonance when the ship's frequency of oscillation in heave/pitch is twice its natural frequency in roll, exhibiting undesirable seakeeping characteristics that can lead to the possibility of exciting large roll oscillations. Other early studies of ships parametric roll oscillations were considered by Watanabe [195], Kempf

[90], Graff and Heckscher [63]. Later, the problem of ships large roll oscillations in longitudinal seas was addressed by Kerwin [93] and Paulling and Rosenberg [153].

In order to understand the parametric roll instability of ships, it is mandatory to begin with the mechanics of a ship motion. Figure 1.1 shows a schematic diagram of a ship indicating body axes and rotational motions. A floating ship displaces a volume of water whose weight equal to the weight of the ship. The ship will be buoyed up by a force equal to the weight of the displaced water.

The *metacenter M* shown in Fig. 1.2a is the point through which the *buoyant* force acts at small angles of roll (*list*). At these small angles the center of buoyancy tends to follow an arc subtended by the *metacentric* radius $\overline{BM}$, which is the distance between the *metacenter* and the *center of buoyancy B*. As the vessels' *draft* changes so does the *metacenter* moving up with the center of *buoyancy* when the draft increases

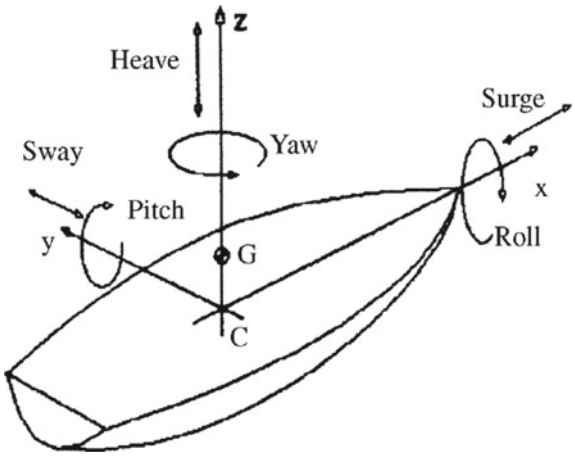

Fig. 1.1 Ship schematic diagrams showing hydrostatic forces in a displaced position

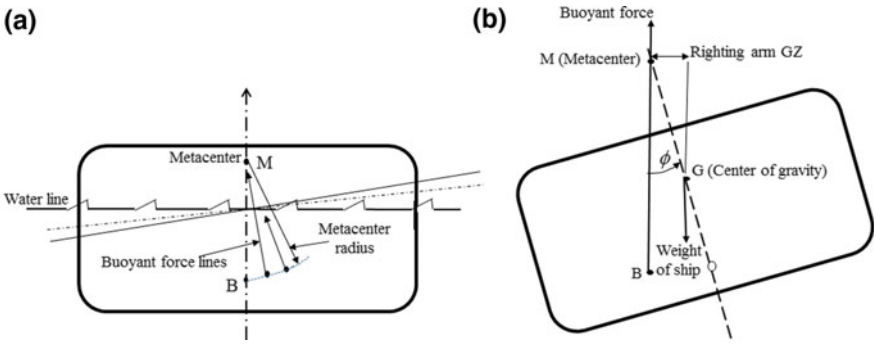

Fig. 1.2 Schematic diagrams showing **a** possible locations of the metacenter and **b** the righting arm and roll angle

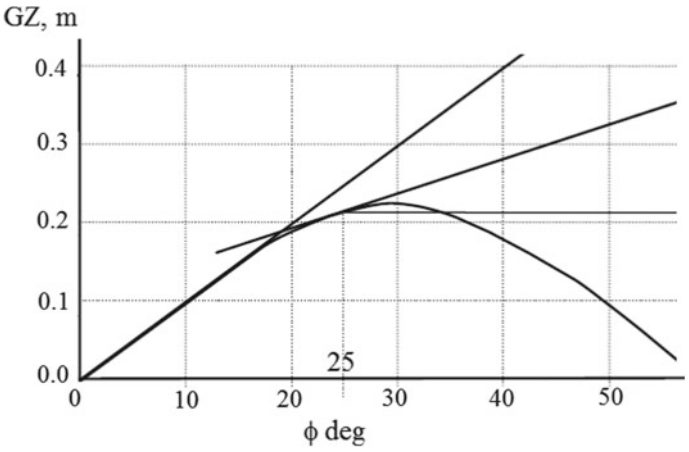

Fig. 1.3 Dependence of righting arm on the roll angle [3]

and vice versa when the draft decreases. For a small angle it is assumed that the *metacenter* does not move. The *center of Buoyancy B* is the point through which the buoyant forces act on the wetted surface of the *hull*. The position of the *center of buoyancy* changes depending on the attitude of the vessel in the water. As the vessel increases or reduces its *draft* (drawing or pulling), its *center of buoyancy* moves up or down respectively caused by a change in the water displaced. As the vessel roll the *center of buoyancy* moves in a direction governed by the changing shape of the submerged part of the *hull* as demonstrated in Fig. 1.2b. For small angles, the *center of buoyancy* moves towards the side of the ship that is becoming more submerged. This is true for small angle stability and for vessels with sufficient *freeboard*.[1] When the water line reaches and moves above the main deck level a relatively smaller volume of the *hull* is submerged on the lower side for every centimeter movement as the water moves up the deck. The *center buoyancy* will now begin to move back towards the centerline.

As a vessel rolls its *center of buoyancy* moves off the centerline. The center of gravity, however, remains on the centerline. For small roll angles up to $\phi = 10°$, depending on *hull* geometry, the *righting arm* $\overline{GZ}$ is

$$\overline{GZ} = \overline{GM} \sin \phi \tag{1.1}$$

The instantaneous value of $\overline{GM}$ is generally dependent of roll angle. It is also known that the natural roll frequency depends on $\overline{GM}$ value. Figure 1.3 shows the dependence of the instantaneous righting arm $\overline{GZ}$ on the roll angle ϕ. It is seen that the $\overline{GZ}$ curve is practically linear for small values of roll angle, over which the $\overline{GM}$ does not change. Thus the natural roll frequency remains constant for small values

[1]The height of a ship's hull (excluding superstructure) above the waterline. The vertical distance from the current waterline to the lowest point on the highest continuous watertight deck.

of roll angle. Once the roll angle increases beyond the linear portion of the GZ curve, the instantaneous $\overline{GM}$ value changes as the $\overline{GZ}$ curve bends as shown in Fig. 1.3.

It is interesting to note that the righting arms can experience explicit or implicit time variation. If the ship experiences roll oscillations, the righting arm may exhibit time variation (*parametric excitation*) under certain conditions of the sea waves. It also may implicitly exhibit time variation when the ship roll is coupled with its pitching oscillations (known as *autoparametric coupling*). The mechanisms of these two classes of time variations will be described in the next two subsections.

1.2.2 Mechanism of Roll Parametric Resonance

France et al. [53] and Shin et al. [169] provided nice description of all scenarios of the mechanism of time variation of the restoring roll moment of ships in head seas based on experimental and numerical studies of Paulling [152]. The danger of capsizing by parametric resonance in following regular waves was first shown theoretically and experimentally by Grim [64, 65]. Arndt and Roden [6] and Paulling [152] demonstrated the variation of the righting moment in following seas using model measurements. It was found that the stability variations are most pronounced in waves of length nearly equal to the ship length associated with an increase in the righting arm when a wave is near amid-ship. On the other hand, the stability is reduced when a wave crest occurs is near amidships. The main reason why the restoring arm changes with time is that the water plane area and the underwater hull volume change as the waves pass along the ship. The variation of the righting arm curve with the roll angle for the C11 container ship in waves of length equal to the ship length L and height of $L/20$ is illustrated in Fig. 1.4. When the forward and after sections are in successive wave crests with a trough amidships, the water-plane is, on average, wider than it is when in still water as a result of the flared section shape. This results in increasing the metacentric height and roll righting moments compared to still water. When the crest is amidships the mean waterline width, therefore the metacentric height and righting moments, are generally less because of the narrowing waterline at the ends and the stability is diminished compared to its value in still water. In other words, when a wave trough is amidships the intercepted water-plane area is greater than that of the still water-plane area causing a larger restoring moment and increasing roll stability. On the other hand, when a wave crest is amidships then the intercepted water-plane area is less than that of the still water-plane area causing a smaller restoring moment, i.e., reduced roll stability.

Note that full-formed parts of the bow and stern are more deeply immersed than in calm water and the wall-sided midship is less deep. This makes the mean instantaneous water-plane wider with the result that the GM is increased over the calm water value as depicted by Shin et al. [169] in Fig. 1.5a. On the other hand, when the ship is located with the wave crest amidships, the immersed portion the bow and stern sections are narrower than in calm water and the GM is correspondingly decreased in comparison to calm water as shown in Fig. 1.5b. This will cause the roll restoring

moment of the ship to change as a function of the ship's longitudinal position relative to the waves. The waterlines in both waves and calm water are schematically described in Fig. 1.6.

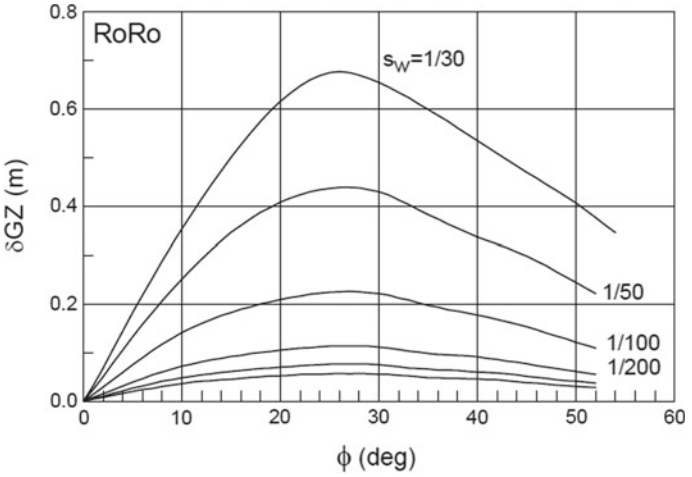

Fig. 1.4 Dependence of the difference between the righting arm corresponding to wave trough amidships and wave crest amidships on the roll angle for different values of wave steepness sw = 1/30, 1/50, 1/100, 1/200, 1/300 [21]

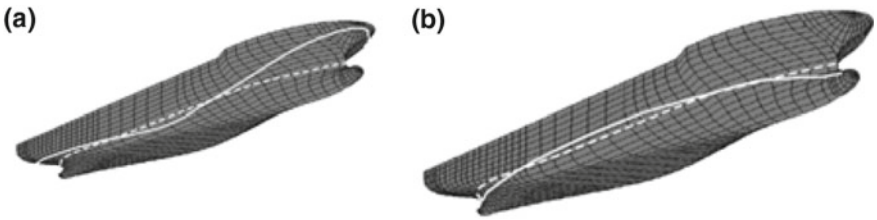

Fig. 1.5 Form of waterline in **a** wave trough versus in calm water, **b** wave crest versus in calm water [169]

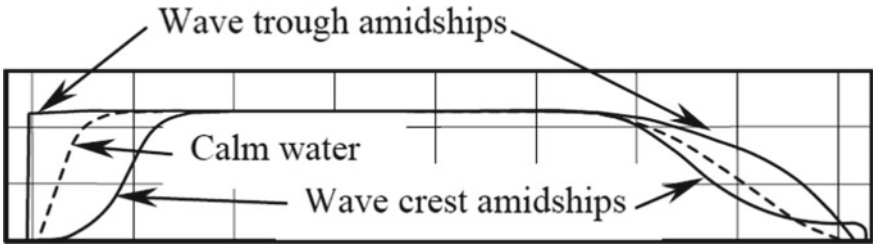

Fig. 1.6 Waterlines in wave crest and wave trough as compared in calm water [169]

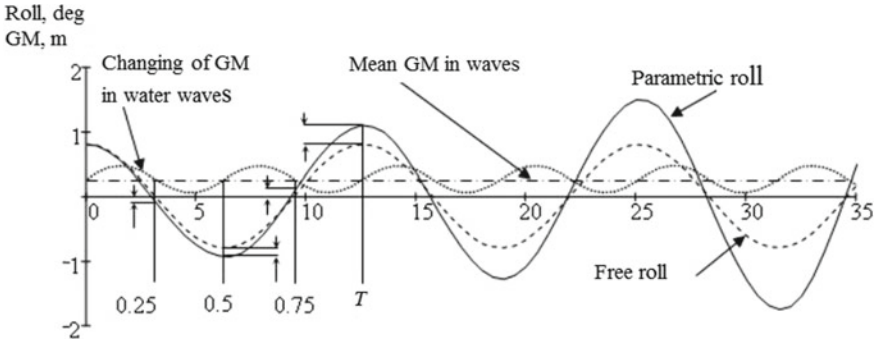

Fig. 1.7 Time evolution of ship parametric roll resonance [169]

By definition, principal parametric resonance occurs when the ship encounters the waves at a frequency near twice its roll natural frequency. The roll disturbance occurs in the time interval between the wave crest and trough amidships position, and the restoring moment, tending to return the ship to its equilibrium position, is greater than the calm water moment. As a result, after the first quarter period, the roll angle will be slightly larger than it would have been in calm water as indicated in Fig. 1.7. At the end of the first quarter of the period, the ship rolls back to the initial position and continues to roll to the other side. During the second quarter of the period, the ship encounters a wave crest and the restoring moment becomes less than that of the still water value. As a result, the ship rolls to a larger angle than it normally would in calm water with the same roll disturbance, and after the second quarter, the roll angle is increased to a larger value than that at the end of the first quarter as shown in Fig. 1.7. In the third quarter, the ship enters the wave trough and a restoring moment greater than the still water value now opposes the motion. The situation is analogous to that observed during the first quarter, and the observations in the fourth quarter are similar to those in the second quarter as well.

Righting arm curves vary between the wave trough and crest amid-ship values shown in Fig. 1.4 as the waves move past the ship. In regular waves the righting moment will vary approximately sinusoidally with time between the extreme values. It was indicated by Hashimoto et al. [73] that due to the exaggerated bow flare and transom stern of recent large containerships have, this change can be significant in longitudinal waves.

1.2.3 Ships Roll Parametric Stability

Ships navigating in longitudinal or oblique seas may experience time variation in their metacenter height GM due waves passing along the hull. The time variation of GM can be considered as sinusoidal,

$$GM(t) = \overline{GM} + GM_a \cos \Omega_e t \tag{1.2}$$

where $\overline{GM}$ is the mean value of the metacentric height, GM_a is the amplitude of the variations of the metacentric height in waves, Ω_e is the wave encounter frequency. This time variation may result in the onset and build-up of parametric roll resonance. This can be realized by deriving the ship equation of motion in roll in the absence of external excitation as

$$I_x \frac{d^2\varphi}{dt^2} + \rho g \Delta \left(\overline{GM} + GM_a \cos \Omega_e t\right) \sin \phi = 0 \tag{1.3}$$

where I_x is the ship's mass moment of inertia about the roll axis-x, including the added mass, ϕ is the roll angle, ρ is the density of see water, g is the gravitation acceleration and Δ is the ship displament volume. For small roll angle, $\sin\phi \approx \phi$, (1.3) is reduced to the well known Mathieu-Hill equation whose stability conditions are well documented [117] in which the ship will experience parametric roll resonance occurs if the waves encounter frequency is very close to twice the roll natural frequency ($\Omega_e \approx 2\omega_n$), where $\omega_n = \left(\frac{\rho g \Delta \overline{GM}}{I_x}\right)$. Other conditions of parametric roll resonance include the wave length λ_w to be close to the ship length L_{PP}, and the wave height h_w is greater than a ship-dependent threshold $\bar{h}_s$. The resulting roll angle amplitude can reach 30°– 40°, which may bring the vessel into dangerous conditions. Note that the equilibrium position $\phi = 0$ of (1.3) is not stable and will, under the slightest initiation, pass into a diverging oscillation.

The safety risk of parametric resonance for a given ship geometry and loading condition is of great concern to the maritime transport industry. In the literature (see, e.g., [46, 47, 106]) this risk is usually measured by the roll damping coefficient. A critical value for the roll damping coefficient is derived based on a comparison between roll damping from the hull and the one that occurs in an unstable situation. The influence of damping sources (see, e.g., [85]) upon the stability-instability boundaries is to shrink the instability region and also results in a critical value of the *righting arm*, $GM(t)\sin\varphi$, or the metacenter height. If the damping moment is included, (1.3) may take the form after dividing by the ship's mass moment of inertia [21]

$$\ddot{\phi} + d\left(\phi, \dot{\phi}\right) + \omega_n^2 \frac{\overline{GZ}(\phi, t)}{\overline{GM}} = 0 \tag{1.4}$$

where $d\left(\phi, \dot{\phi}\right)$ is the damping moment, which is generally nonlinear, $\overline{GM}$ is the metacentric height in still water, and $\overline{GZ}(\phi, t)$ is the righting arm. The fluctuation of the righting arm around the still water value may be split into its mean value plus the incremental time fluctuation.

$$\overline{GZ}(\phi, t) = \overline{GZ}_{SW}(\phi) + \delta\overline{GZ}(\phi, t) \tag{1.5}$$

where $\delta\overline{GZ}(\phi, t)$ is the time variation of the righting arm measured from its value in still water $\overline{GZ}_{SW}(\phi)$. The nonlinear nature of the righting arm has been analytically described by Bulian [20] by the two expressions:

$$\overline{GZ}_{SW}(\phi) = \sum_{j=0}^{N} Q_{j0}.\phi^j \tag{1.6a}$$

$$\delta\overline{GZ}(\phi, t) = \sum_{j=0}^{N}\left\{\sum_{n=1}^{M} Q_{jn}^{c}\cos\left(n\frac{\Omega_e t}{\cos\chi}\right) + Q_{jn}^{s}\sin\left(n\frac{\Omega_e t}{\cos\chi}\right)\right\}\phi^j \tag{1.6b}$$

For symmetric ships and symmetrically loaded, the coefficients of even powers in the polynomial expansion are set to zero. The number of harmonic components M is uniquely determined (by the Nyquist-Shannon sampling theorem) from the number of wave crest positions for which $\overline{GZ}$ is evaluated, in the polynomial fitting two parameters can be freely chosen. These are the degree of the polynomial N and the maximum fitting roll angle up to which polynomial fitting is performed. The maximum fitting roll angle must be larger than the maximum steady state roll amplitude. Furthermore, the number of harmonics N should be sufficiently high to allow a good fitting of the shape of the righting arm $\overline{GZ}$. Figure 1.4 shows a typical example of the dependence of calculated variation of $\delta\overline{GZ}(\varphi, t)$ on the roll angle for different values of wave steepness (ratio of wave height to wavelength) as calculated by Bulian et al. [21] of RoRo pax TR2 body plan.

When the roll angle increases beyond the linear portion of the $\overline{GZ}$ curve, the instantaneous $\overline{GM}$ value changes as the $\overline{GZ}$ curve bends as shown in Fig. 1.3. This causes the natural roll frequency to changes as well. Since the wave encounter frequency remains the same, the roll natural frequency may no longer be close to twice the encounter frequency. As a result, parametric resonance conditions no longer exist and roll motions no longer receive additional energy at each cycle. This nonlinear characteristics of the righting arm brings amplitude of roll angle to a bounded value. Note that the nonlinearity of the righting arm curve and roll damping play an important role in the intensity of parametric roll response. Nonlinearity can magnify small variations in excitation to the point where the restoring force contributes to capsizing. The nonlinearity is due to the nature of restoring moment and damping. The environmental loadings are nonlinear and beyond the control of the designer. The nonlinearity of the restoring moment depends on the shape of the righting-arm diagram. Time-domain simulations can be used to evaluate the risk of damage to a containership and its cargo caused by parametric roll resonance.

Umeda et al. [186] conducted experimental study and showed that a container ship could suffer severe parametric rolling even in short-crested irregular following waves and could capsize in long-crested irregular following waves. Dallinga et al. [40] and Luth and Dallinga [113] considered the phenomenon of roll parametric excitation in head seas when testing a model of a cruise vessel. Neves et al. [139] reported on tests with two models of typical fishing vessels in head seas. They demonstrated that very large roll angles may be reached at some specific conditions for a transom stern

hull of a fishing vessel. Another example of parametric resonance in head seas was reported by Palmquist and Nygren [150], as it was recorded at sea on a vessel, the PCTC M/V Aida.

In analyzing the 1998 post-Panamax, C11 class containership, France et al. [53] indicated that parametric rolling in head seas introduces loads into on-deck container stacks and their securing systems well in excess of design limits. Similar incident of head-sea parametric rolling was reported for destroyers [54]; RoRo paxes [56]; and a pure car and truck carriers (PCTC) in the Azores Islands waters [80, 150]. Parametric roll resonance was found to be the main cause of ships rolling over 47° and resulted in the loss of 133 containers in January 2003 [30]. Because of the particular hull shape, container carriers, are the most prone to parametric roll resonance. These cargo ships have large bow flare and stern overhang, and thus experience abrupt variation in the intercepted water-plane area when a wave crest or trough is amidships. A simple approach to identify whether a ship is susceptible to extreme parametric rolling (susceptibility criteria) was outlined by Silva et al. [172]. The calculations for particular vessels were performed for a given wave and forward speed, which would lead to the development of parametric roll. Non-linear numerical simulations of ship in six degrees-of-freedom for regular head waves were conducted for a C11 class containership in the time domain.

Simulations for polar diagrams were carried out by Belenky et al. [14] who used potential codes calibrated for roll damping with roll decay tests. The polar diagram is based on the maximum roll angle observed during a one-hour simulation. Criteria for polar diagrams are based on lashing strength and engine conditions. The choice of loading conditions should be determined by sufficient coverage of the range of natural frequency. Parametric roll resonance, pure loss of stability, and broaching-to are among the primary modes of stability failures, which were addressed by Belenky et al. [16].

Ocean waves are generally not harmonic or regular but irregular and random. In an attempt to facilitate the analysis under irregular wave, Grim [66] introduced the concept of effective waves, which is described in the next section

1.2.4 Grim Effective Wave Concept

It is known that the largest GZ fluctuations in regular longitudinal waves occur when the wave has a length close to the ship length. Crest amid-ship and trough amid-ship are the two nominal critical conditions used to characterize the ship righting arm fluctuations. However, the largest and the smallest value for the metacentric height are found for wave positions different from the critical two condition. The effective wave concept introduced by Grim [66], and extended later by Belenky and Sevastianov [11], is demonstrated in Fig. 1.8. The idea is that an irregular wave should be replaced, using a least square fitting, by a regular wave of length L_{pp} (equivalent to the ship length) and height h_{eff} (its crest or trough situated at the center of gravity). By introducing the effective wave, the relationship between the

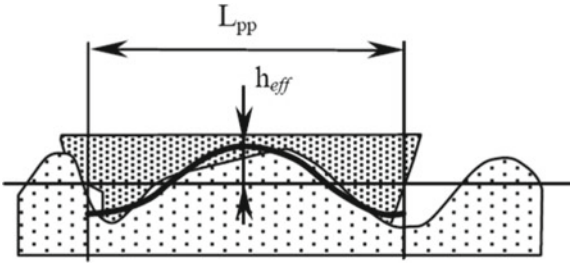

Fig. 1.8 Concept of effective wave, thick curve is one complete effective wave of length L_{pp} and wave height h_{eff} [66], after [169]

ocean wave and the effective wave amplitude becomes linear so that the restoring variation can be calculated by a linear superposition with nonlinear but non-memory relationship between the roll restoring moment and the effective wave amplitude. The effective wave concept was used by Umeda [184], Umeda and Yamakoshi [185] and Umeda et al. [187] for calculating probability of ship capsizing due to pure loss of stability in quartering seas. The reduction of restoring moment due to wave profile was considered using Grim's effective wave concept. A comparison between effective wave concept and direct stability calculations has validated such an approach.

Grim [66] expressed the actual wave profile by an "equivalent" wave having the following expression:

$$z_{eq}(x,t) = a(t) + h_{eff}(t)\cos\left(\frac{2\pi}{L_{pp}}x\right) \tag{1.7a,b}$$

where $a(t)$ a is the mean instantaneous value and an instantaneous height amplitude $h_{eff}(t)$. The equivalent wave always has a crest, for $h_{eff}(t) > 0$, or a trough, for $h_{eff}(t) < 0$, at miship, $x = 0$.

Hashimoto et al. [73] adopted the Grim's effective wave concept for the prediction of parametric rolling in irregular waves. Figure 1.9 shows the dependence of the maximum roll angle of parametric rolling of a post-Panamax containership on

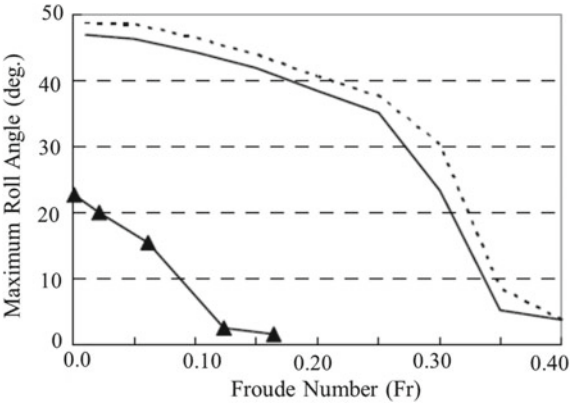

Fig. 1.9 Comparison of maximum roll angle of parametric rolling in long-crested irregular head waves with $H_{1/3} = 0.221$ m and $T_{01} = 1.32$ s. - - - - Froude-Krylov, —— numerical simulation of Hashimoto et al. [72], ▲ experimental results [72, 73]

Froude number as predicted numerically and experimentally by Hashimoto et al. [72, 73]. It is seen that both numerical estimates excessively overestimate the maximum roll angle of parametric rolling. The roll restoring variation in irregular waves was estimated as the sum of nonlinear Froude-Krylov force[2] with heave and pitch obtained by hydrostatic balance for an instantaneous effective wave, radiation and diffraction components calculated under the assumption that it has a linear relation with wave steepness and roll angle. The uncoupled roll model was applied to parametric rolling prediction. The roll damping was estimated from a roll decay test without forward velocity, and long-crested irregular wave was assumed to follow the ITTC spectrum[3] expressed as the sum of 1000 components of sinusoidal waves with their random phases. Bulian et al. [23] modified Grim's effective wave concept to improve the approximation accuracy of random wave surface by adjusting its wave crest position as an additional random variable. This modification (named Improved Grim Effective Wave, IGEW) improves the prediction of the pitch moment and/or static pitch equilibrium angle, while the roll moment prediction itself is sufficient even with the original concept.

1.2.5 Ships Stochastic Roll Stability

Under random sea waves one must deal with probabilistic approaches when studying stochastic stability, response, and reliability of ships roll motion. The probabilistic theory of ship dynamics is well documented by Price and Bishop [160] and Lloyd [111]. If the nonlinear effect of roll is neglected, the pitch equation of motion is reduced to a linear differential equation, which is free from roll motion terms. The probabilistic description of ships roll parametric resonance was studied numerically by Belenky et al. [12]. The large amplitude of the roll response encountered in a parametric resonance regime might significantly influence the probabilistic characteristics of rolling. The conventional models of ship behavior in irregular seas assumed ergodicity (i.e., using one long realization) and a normal distribution of rolling. However, these assumptions do not always have a solid background. Observations and records have validated the assumption of normal distribution and ergodicity of sea waves. Numerical simulations and experimental tests conducted by Belenky et al. [9, 10] and Belenky [8] revealed that large amplitude roll cannot be considered ergodic. Roll distribution, however, might be assumed normal for low-built ships. On the other hand, if a ship has high free-board and *GZ* possesses S-shape, roll distribution might not be Gaussian.

If the nonlinear effect of roll is neglected, the pitch equation of motion is reduced to a linear differential equation, which is free from roll motion terms. When the pitch

[2]The Froude–Krylov force is the force introduced by the unsteady pressure field generated by undisturbed waves.

[3]International Towing Tank Conference (ITTC) spectrum for fully developed sea is a modified Pierson-Moskowitz spectrum.

equation is solved, its response appears as a coefficient to the restoring moment of the roll motion, and the roll equation of motion is reduced to the Mathieu equation

$$I_x \frac{d^2\varphi}{dt^2} + 2\bar{\zeta}\omega_n \frac{d\phi}{dt} + \omega_n^2[1 + \varepsilon\Theta(t)]\phi = \varepsilon M(t) \tag{1.8}$$

where $\Theta(t)$ represents the pitch angle which is assumed to be a random stationary process, $M(t)$ represents the wave random excitation, $\bar{\zeta}$ is a linear damping factor, ω_n is the natural frequency of the ship roll oscillation, and ε is a small parameter.

Bulian et al. [21] experimentally investigated the applicability of the Markov process approach for a Ro-Pax, and confirmed the agreement is good for a narrow band spectrum. Levadou and van't Veer [106] also showed that the Markov process approach can well predict the critical wave height of parametric rolling in irregular waves. Bulian and Francescutto [22] proposed a fully analytical approach for the determination of the stochastic stability threshold of parametric rolling, and it overestimates roll motion without a tuning factor. Themelis and Spyrou [181] proposed a probabilistic assessment of parametric rolling by assuming probability of occurrence of instability is represented by that of encountering the critical or worse wave groups.

Belenky et al. [12, 13] simulated parametric rolling in irregular waves with 50 realizations and numerically confirmed that roll motion is practically non-ergodic while heave and pitch motions are not. The distribution of the roll response from wave realizations of head seas was found to be quite far from Gaussian [15] since the peak of the distribution is significantly sharp. The reason why rolling does not follow Gaussian distribution is attributed to the inherent roll nonlinearity expressed in damping and the righting arm curve. A similar shape of roll distribution was observed in beam seas [9, 10]. Belenky et al. [16] proposed a method based on the group structure of waves and envelope of parametric excitation might be very promising and deserve special attention [18, 56, 182].

Under random wave forces on a ship hull in following or head seas, Dostal and Kreuzer [44] studied parametric excitation of the roll motion. The transient evolution of the joint probability density function of roll angle ϕ and roll velocity $\dot{\phi}$ was computed for a significant wave height of 15 m, starting from an initial probability density at $t = 0$ shown in Fig. 1.10a. The joint probability densities were computed numerically at different times. Samples of the results are shown in Fig. 1.10b–d for $t = 200$ s, 1000 s between (3300 s and 3700 s), 1000 s between, respectively.

The probability density function of Fig. 1.10d was averaged over one roll oscillation period (1000 s to 1012.4 s). The bi-modality of the densities shown in Fig. 1.10c and d has dynamic reasons. Sample trajectories move counterclockwise in the coordinate, $(\varphi, \dot{\phi})$ used in Fig. 1.10a–d. Starting a sample trajectory at $\dot{\phi} = 0$ and positive ϕ, the trajectory is slow in the first quadrant of the coordinate system. Due to the parametric excitation and the restoring forces, the roll velocity increases and the time spent in the fourth quadrant decreases, leading to lower probability density values. Because of symmetry, the same arguments hold for a sample trajectory starting at negative ϕ and $\dot{\phi} = 0$. Since there is no significant difference between the densities in Fig. 1.10c and d, the transient evolution of probability density already converged

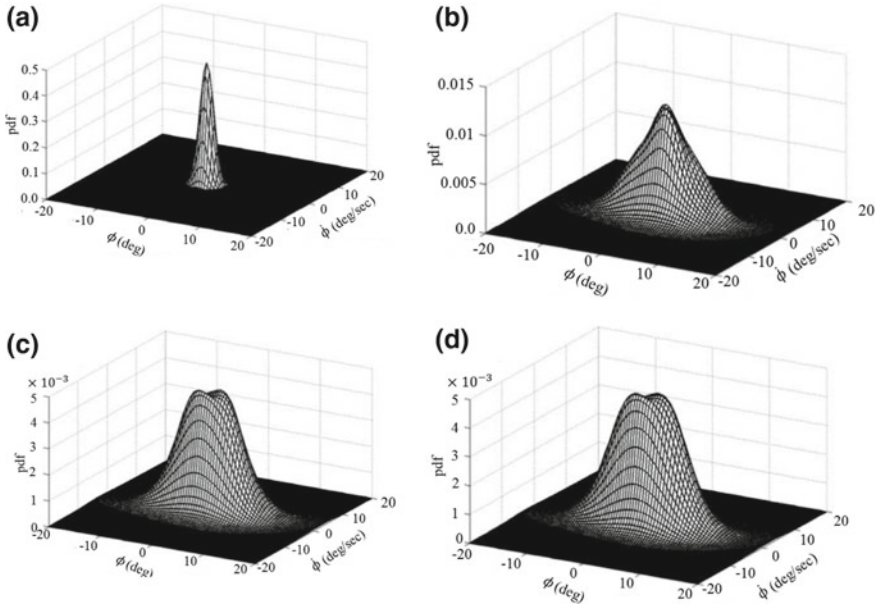

Fig. 1.10 Ship roll response joint probability density function (pdf): **a** Initial pdf at $t = 0$, **b** pdf at $t = 200$ s, **c** pdf at $t = 1000$ s, and **d** averaged pdf from $t = 1000$ s to $t = 1012.4$ s [44]

to a stationary distribution in state space at this time. However, as can be seen from Fig. 1.10b and c, the probability of stable roll motions gets lower with time, because some Gaussian densities leave the safe basin at the critical roll angle, which corresponds to zero righting arm. This is the condition for the occurrence of ship capsizing. Dostal and Kreuzer [45] examined the problem of parametric roll in random seas, where the random wave excitation is modeled by a non-white stationary stochastic process using the method of stochastic averaging. The fast oscillatory dynamics of roll was averaged over the roll period. This procedure yields equations for the drift and diffusion of the roll energy. The non-stationary probability density of roll energy was estimated by solving the corresponding Fokker-Planck equation using a finite difference approach.

Van Daalen et al. [191] considered the full Pierson–Moskowitz [158] spectrum discretized in a number of frequencies covering the spectrum and performed Monte Carlo simulation to study the roll dynamic behavior of ships in large amplitude head waves. They also considered the evolution of the roll amplitude when starting with a probable state of the vessel in a given sea. The total energy in the roll motion was taken as a measure to distinguish between safe and unsafe states. The risk that the ship will reach a critical state was characterized by the time of arrival at this state, starting from an arbitrary pattern of the waves and the dynamic state of the vessel in the stationary situation. The percentiles of the arrival time distribution were taken as a measure of the risk of significant rolling to which the vessel is exposed.

1.3 Autoparametric Roll-Pitching Coupling

The concept of autoparametric interaction can be demonstrated using the example of autoparametric vibration absorber developed by Haxton and Barr [74] and shown in Fig. 1.11. This system consists essentially of a cantilever beam (of length ℓ, stiffness k_2 and inherent damping c_2) attached to a primary vibratory system of mass M, stiffness k_1 and dashpot of damping coefficient c_1. Under external excitation $F(t)$, the response of the primary system, x, imposes an axial motion on the cantilever, thus generating a parametric excitation term in the equation of transverse motion of the coupled cantilever. The transverse motion, y, in turn induces a reaction force on the primary system. The system is analytically described by the equations of motion:

For the main mass:

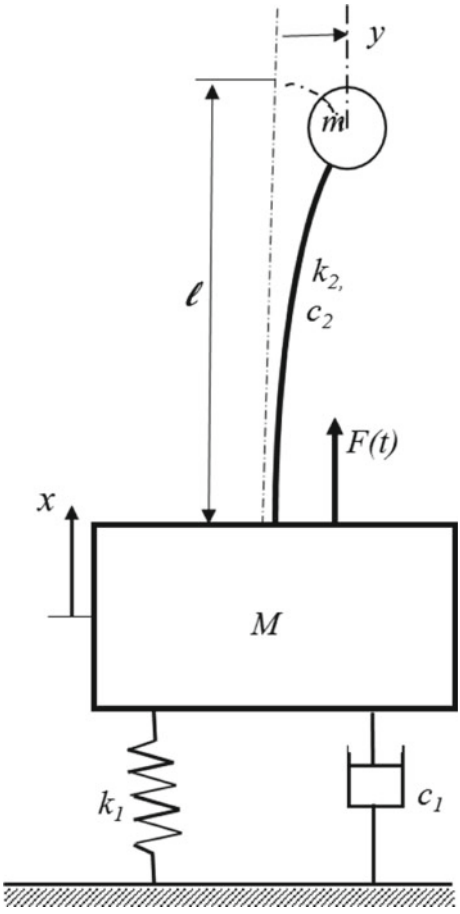

Fig. 1.11 Schematic diagram of an autoparametric vibration absorber [74]

$$(M+m)\ddot{x}+c_1\dot{x}+k_1xx-\frac{6}{5\ell}m\left(\dot{y}^2+y\ddot{y}\right)=F(t) \tag{1.9}$$

For the coupled cantilever with mass m

$$m\ddot{y}+c_2\dot{y}+\left(k_2-\frac{6}{5\ell}m\ddot{x}\right)y+\frac{36}{25\ell^2}my\left(\dot{y}^2+y\ddot{y}\right)=0 \tag{1.10}$$

The form of autoparametric coupling action is clear from (1.9) and (1.10). In (1.10) the x motion appears as an implicit time dependent modification of the cantilever stiffness, i.e. a parametric excitation. For a lightly damped primary system the additional term will have a negligibly small effect on the interaction between the two systems under internal resonance conditions. Under harmonic excitation $F(t)=F_0\sin(\Omega t)$, Haxton and Barr [74] showed that large transverse motions of the coupled system could be induced by harmonic forcing of the main system under conditions of internal resonance $\omega_1=2\omega_2$, where $\omega_1=\sqrt{k_1/m_1}$, and $\omega_2=\sqrt{k_2/m_2}$. Under this condition, the response of the primary system is modified by the reaction of the coupled system in the manner of a vibration absorber.

Figure 1.12 presents the amplitude-frequency response curves of the main mass,

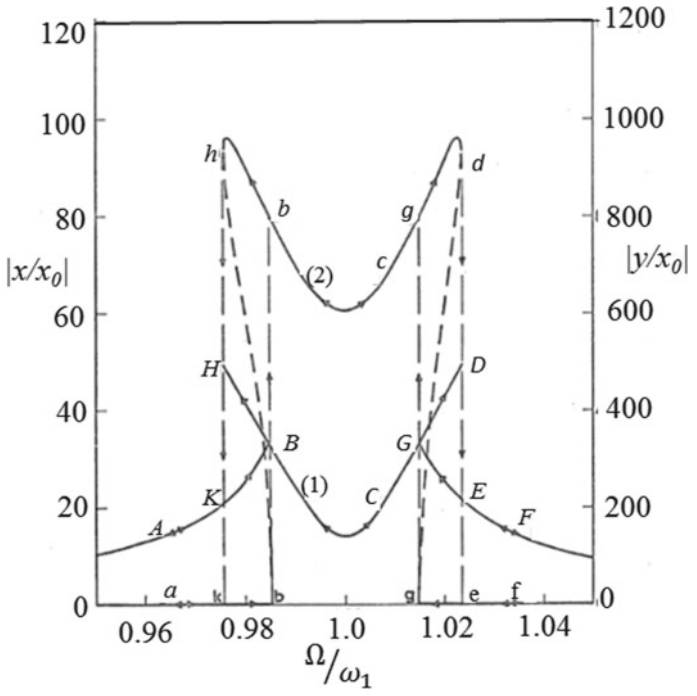

Fig. 1.12 Amplitude-frequency response curves of the main mass (1) and cantilever absorber mass (2) [74]

"1", together with the corresponding absorber response mass "2". It should be noted that the lower branches of the absorber response curves are unstable as indicated by the broken curves and that the amplitudes of the absorber mass are approximately ten times greater than those experienced by the main mass.

The absorber action occurs for a limited range of excitation frequency Ω is in the neighborhood of the main mass natural frequency ω_1 when the damping is not too large. The points of vertical tangency on the absorber response curves are important as they define the boundaries of the region of parametric instability of the absorber. They coincide with the jumps observed in the main mass displacements. It is seen that following the path of increasing frequency (indicated by arrows) the system behaves as a normal one-degree of freedom system (region A) until it reaches the cross-over point (point B). This corresponds to a point of vertical tangency in the absorber solution and so absorber action begins. The main mass system then follows the two-degree of freedom solution (region c), its amplitude reaching a minimum value at $\Omega/\omega_1 = 1$. It then climbs steadily until the collapse amplitude is reached (point D). This corresponds to a vertical tangency in the absorber solution, which defines the collapse frequency and marks the bound of absorber action. The result is that absorber action ceases and the main mass amplitude drops to its one-degree of freedom level (point E). Following a path of decreasing frequency (again arrowed) the main system behaves in a similar fashion tracing the path F, G (absorber entry point), C, H (collapse amplitude), K and A. The corresponding regions and points on the absorber response curve are similarly illustrated using lower case letters, the jumps bb and gg coinciding with the entry points B and G on the main mass response.

The nonlinear coupling may give rise to the occurrence of internal resonance conditions among the interacting modes. Internal resonance implies the presence of a linear relationship between the normal mode frequencies of the interacting mode (i.e., $\sum_{j=1}^{n} K_j \omega_j = 0$, where K are integers, and ω_j are the natural frequencies of the coupled modes, the number $K = \sum_{j=1}^{n} |K_j| = 0$ is known as the order of internal resonance). This type of coupling is referred to as *autoparametric interaction* when an externally excited mode can act as a parametric excitation to other modes. The problem of internal resonances in nonlinearly coupled oscillators is of interest in connection with redistribution of energy among the various natural modes. This energy sharing is usually brought about by resonant interactions among the natural modes of the system. The coupling among these modes plays a crucial role in such interactions. In a straightforward perturbation theory, internal resonances lead to the problem of small divisors. Note that autoparametric interaction takes place when both the internal resonance, $\omega_1 = 2\omega_2$, and external resonance, $\Omega = \omega_1$, conditions exist.

The equations of motion for a ship pitching and rolling in a calm sea considered by Kinney [98] are coupled by means of a second order term in the rolling equation of motion. When the pitching motion is simple harmonic the equation of motion in roll is of the Mathieu type, the two independent parameters being pitching amplitude

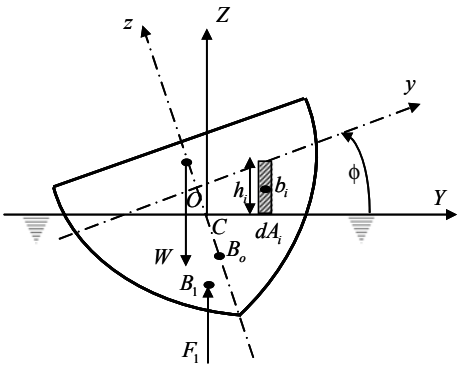

Fig. 1.13 Ship schematic diagrams showing weight and hydrostatic forces in a displaced position

and frequency. It was concluded that unstable rolling motions are possible for very small pitching amplitudes. Furthermore, when the natural frequency of pitch is twice that of roll the amplitude required to produce unstable motion is a minimum.

With reference to Fig. 1.13 and within the framework of the nonlinear coupling of the forced response of a ship whose motion is restricted to pitch and roll for longitudinal waves can be modeled by the following equations after keeping only nonlinearity up to quadratic terms [140–145]:

$$\left(J_{yy} + K_{\ddot{\theta}}\right)\ddot{\theta} + M_{\dot{\theta}}\dot{\theta} + M_{\theta}\theta + M_{\theta\theta}\theta^2 + M_{\phi\phi}\phi^2 = M_w(t) \tag{1.11}$$

$$\left(J_{xx} + K_{\ddot{\phi}}\right)\ddot{\phi} + K_{\dot{\phi}}\dot{\phi} + K_{\phi}\phi + K_{\theta\phi}\theta\phi + K_{\phi\phi}\phi^2 = 0 \tag{1.12}$$

where J_{xx} and J_{yy} are the ship mass moment of inertia about roll and pitch axes. $K_{\ddot{\phi}}$ and $K_{\ddot{\theta}}$ are the hydrodynamic added polar mass moment of inertia about the ship roll and pitch axes, respectively. $M_{\dot{\theta}}$ and $K_{\dot{\phi}}$ are the pitch and roll damping coefficients, respectively. In particular, $K_{\dot{\phi}}$ is nonlinear (see, e.g., [85]). M_{θ} and K_{ϕ} are hydrostatic coefficients of linear restoring moments in pitch and roll, respectively. $M_{\theta\theta}$ and $K_{\phi\phi}$ are second-order hydrostatic coefficients of linear restoring moments in pitch and roll, respectively. The other second-order coupling coefficients of pitch and roll restoring moments are $M_{\phi\phi}$, $K_{\theta\phi}$ and $K_{\phi\phi}$. In particular, the quadratic nonlinear coupling terms $K_{\theta\phi}\theta\phi$ is the main source of autoparametric interaction, in which the pitch oscillation, θ, acts as an implicit parametric excitation to the roll motion. $M_w(t)$ is the wave external excitation, usually referred to in the literature as the Froude-Krylov plus diffraction wave forcing terms, dependent on wave heading, encounter frequency Ω_e. It is observed that for longitudinal waves, there is no roll external excitation.

Generally, the coupling between pitch and roll of ships was described by Nayfeh et al. [137] in the simplified form

$$\ddot{\theta} + \omega_1^2\theta = -c_1\dot{\theta} + \kappa_1\phi^2 + M_1\cos(\Omega_e t + \beta_1) \tag{1.13}$$

$$\ddot{\phi} + \omega_2^2 \phi = -c_2 \dot{\phi} + \kappa_2 \phi\theta + M_2 \cos(\Omega_e t + \beta_2) \tag{1.14}$$

where ω_1^2 and ω_2^2 are the undamped natural frequencies of pitch and roll, respectively. c_1 and c_2 are the damping coefficients in pitch and roll, respectively. Generally, the roll damping is more complicated than this linear representation. κ_1 and κ_2 are coefficients of nonlinear terms. M_1 and M_2 are the amplitudes of pitch and roll moments after dividing by the inertia of each, i.e., $\left(J_{yy} + K_{\ddot{\theta}}\right)$ and $\left(J_{xx} + K_{\ddot{\phi}}\right)$, respectively, Ω_e is the encounter forcing frequency, and β_1 and β_2 are phase angles. The coefficients of (1.3) and (1.4) are dependent on the ship speed and other sea wave characteristics. Nayfeh et al. [137] considered the response of (1.11) and (1.12) for using the method of multiple scales. Three cases were considered: (i) when the encounter frequency is zero, i.e., $\Omega_e = 0$ (ii) when $\Omega_e = \omega_1$, and (iii) when $\Omega_e = \omega_2$. These cases are studied in the neighborhood of internal resonance, $\omega_1 = 2\omega_2$, i.e. when the pitching frequency is twice the rolling frequency. In the analysis two detuning parameters were introduced to measure the nearness of the internal resonance and external resonance from the exact values. These are

$$2\omega_2 = \omega_1 + \varepsilon\sigma_1, \text{and} \Omega = \omega_1 + \varepsilon\sigma_2 \tag{1.15}$$

Another control parameter, γ were found to govern the characteristics of the roll response

$$\gamma = 4\omega_1\omega_2[2\sigma_2(\sigma_1 - \sigma_2) + c_1c_2] \tag{1.16}$$

It is known in linear single degree-of-freedom systems that the response amplitude is linearly proportional to excitation amplitude for a given excitation frequency. This is true for the main mass of Fig. 1.11 and for the ship roll response of (1.12) as long as the absorber mass (1.10) or the ship roll (1.12) remains undisturbed up to a critical forcing amplitude F_{0st} above which the main mass amplitude or the ship pitch response does not increase with the forcing amplitude and reaches a saturation value. At F_{0st} the absorber mass or the ship roll begins to bifurcate from its equilibrium position and its response increases nonlinearly with the forcing amplitude. Above that level the pitch amplitude does not change from the critical value (i.e., the pitch mode is saturated), and all of the extra energy is transferred to the roll mode. Thus, for large excitation amplitudes, the amplitude of the roll mode is very much larger than that of the pitch mode. For large excitation amplitudes, the response is a combined role and pitch motion, with the amplitude of the roll mode being very much larger than that of the pitch mode. This *saturation phenomenon* was originally reported by Nayfeh et al. [137, 138] and Haddow et al. [68]. This saturation phenomenon takes place only with coupled systems with quadratic nonlinearity (such as $y\ddot{x}$). If the coupling is cubic this phenomenon disappears. For the case $\Omega_e = \omega_1 + 0.025$, $\omega_1 = 2\omega_2$, and $\gamma > 0$, Fig. 1.14 shows the dependence of the pitch, $2\vartheta_0$, and roll, $2\varphi_0$ response amplitudes on the excitation amplitude parameter $\mu_1 = \left(\frac{\kappa_2}{\varepsilon^2}\right)M_1$. Two values of the excitation amplitude are indicated by vertical arrows at which the response

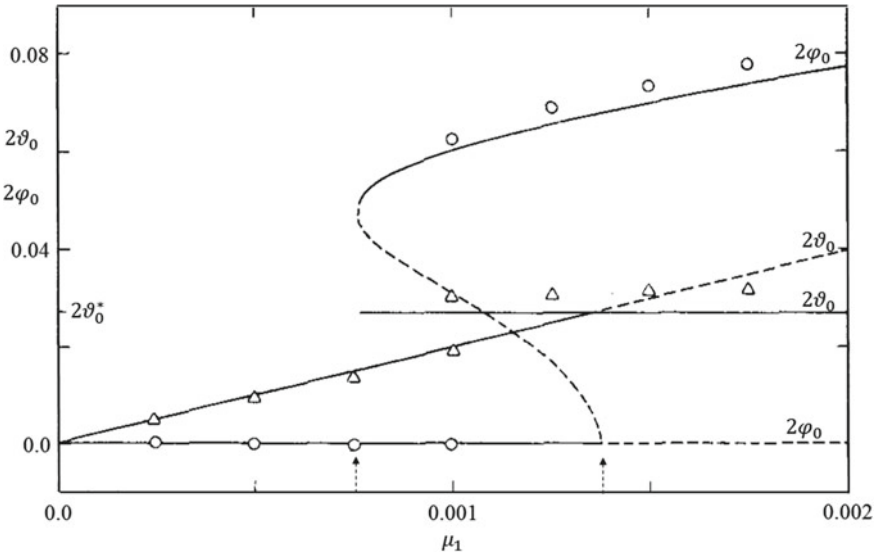

Fig. 1.14 Dependence of pitch and roll response amplitudes ϑ_0 and φ_0 of the excitation amplitude $\mu_1 = \left(\frac{\kappa_2}{\varepsilon^2}\right) M_1$ for a fixed encounter frequency close to the pitch frequency, where $\omega_1 = 1$ rad/s, $\omega_1 = 2\omega_2$, $\Omega_e = \omega_1 + 0.025$ and $\gamma > 0$: —— Stable solution, - - - Unstable solution, ○, Δ numerical simulation [137]

amplitudes bifurcate, where the pitch amplitude assumes the value $2\vartheta_0^*$ while the roll jumps from its zero equilibrium to a non-zero value. All dashed curves are belonging to unstable solutions. Figure 1.14 reveals the saturation phenomenon. As the excitation amplitude increases from zero, the pitch amplitude increases linearly until it reaches the value ϑ_0^*, while the roll amplitude remains zero. This corresponds to the linear solution of a linear single-degree-of-freedom system. Figure 1.15 shows the bifurcation and saturation phenomenon for the case $\gamma < 0$.

The nonlinear coupling of the pitch (heave) and roll modes of ship motions in regular seas when their frequencies are in the ratio of two-to-one was studied by Nayfeh et al. [137], Mook et al. [128] and Nayfeh [136]. A significant observation was that the nonlinear theory predicts instabilities in regions where the linear theory predicts stability. Moreover, the nonlinear theory predicts conditions for the nonexistence of steady-state periodic responses. Instead, the responses can be amplitude-and phase-modulated roll and pitch motions or even chaotic. When the excitation frequency is near the roll frequency, there is no saturation phenomenon and at close to perfect resonance, there is no steady state response in some cases. In the absence of two-to-one frequency ratio between pitch and roll natural frequencies Mook et al. [128] found that there are five resonant situations and, depending on the value of the parameters, three can involve large motions.

A perturbation analysis of the nonlinear coupling between the pitch and roll modes was employed by Nayfeh et al. [138] who demonstrated that an energy approach can

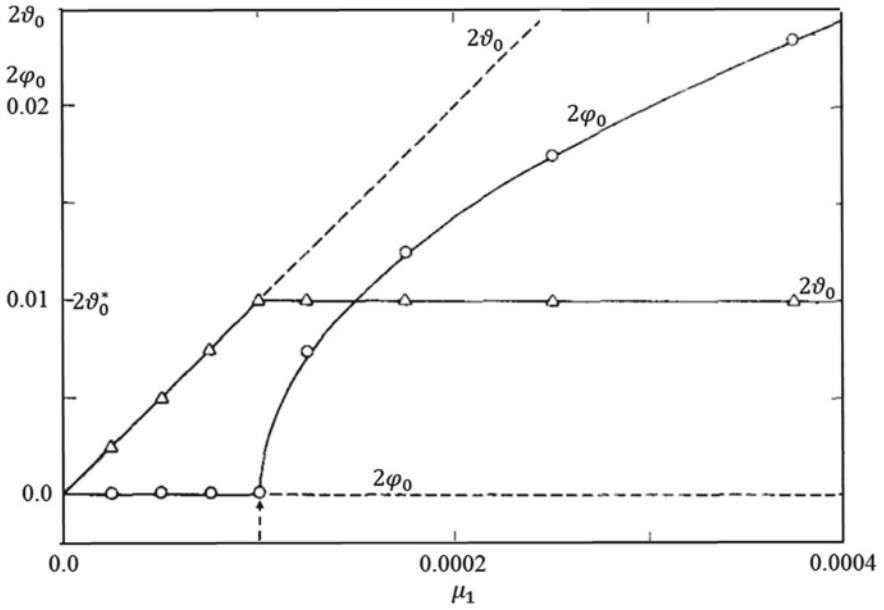

Fig. 1.15 Dependence of pitch and roll response amplitudes ϑ_0 and φ_0 of the excitation amplitude $\mu_1 = \left(\frac{\kappa_2}{\varepsilon^2}\right) M_1$ for a fixed encounter frequency close to the pitch frequency, where $\omega_1 = 1$ rad/s, $\omega_1 = 1$ rad/sec, $\omega_1 = 2\omega_2$, $\Omega_e = \omega_1 + 0.025$ and $\gamma < 0$: —— Stable solution, - - - Unstable solution, ○, Δ numerical simulation [137]

be used to advantage in developing the nonlinear equations governing the motion of ships. They also indicated that employing Taylor series expansions to determine the loads on the hull of a ship can lead to the physically unrealistic prediction of self-sustained oscillations, unless certain relationships among the nonlinear coefficients are satisfied. It was shown that the simplified equations of motion which result after imposing these relationships can be found directly from an energy formulation of the problem. The energy approach is used to develop the nonlinear equations governing the roll and pitch modes to third order and the equations governing motions having six degrees-of-freedom to second order. The nonstationary responses of a ship model with nonlinearly coupled pitch and roll modes were studied under modulated or nonstationary excitation by Pan and Davies [151]. The nonstationary excitation is a sinusoidal excitation with either a slowly varying amplitude or frequency. The loss of dynamic stability and the resulting large-amplitude roll of a vessel in a head or following sea were studied theoretically and experimentally by Oh et al. [148, 149]. The ship dynamics was described in terms of roll, pitch, and heave oscillations. The governing equations for the heave and pitch modes were linearized and their harmonic solutions were coupled with the roll mode. The principal parametric resonance was considered in which the excitation frequency is twice the natural frequency in roll. Force- response phenomena and multiple stable solutions for the case of subcritical instability was observed in the experiments.

1.4 Coupling with Liquid Sloshing

Liquid sloshing dynamics in ships' cargo adds additional problem to the vessel stability and safety. A liquid cargo tank is excited by ship motion and the subsequent liquid sloshing flow itself affects the ship motion in return. The simultaneous existence of liquid free surfaces outside and inside a liquid cargo tank results in different hydrodynamic loads on the ship. Ships with large ballast tanks and liquid bulk cargo carriers often have to deal with significant sloshing loads during their operations. The interaction between sloshing and ship motion becomes significant as the ratio of volume of the containers to that of the ship exceeds a critical value. Recent experimental and numerical studies have shown that the coupling effect between liquid cargo sloshing and LNG (Liquefied Natural Gas) ship motion can be significant at certain partial filling levels. This effect is of great concern to the LNG FPSO/FSRU operation in the production site and offloading operation of LNG-carriers close to LNG terminal. The coupling effects are expected to become more important as the size of LNG-carriers significantly increases with greater market demand.

When the tank motion is large, a hydraulic jump hits the bulkhead before breaking, a large impact can occur. Sloshing impact occurs when there is a sudden change in the wetted surface due to liquid motion in the tank. In a partially filled compartment, a wider area on the tank wall is vulnerable to the sloshing impact of the cargo. The local pressure due to sloshing hydrodynamic loads can cause a critical damage in the insulation box of liquefied natural gas[4] (LNG) carriers. Most ships with liquid cargo experience impulsive local loads on the cargo ceiling depending on the state of the sea. The ocean/sea state is characterized by statistics, including the wave height, period, and power spectrum. The state of the sea waves varies with time, as the wind conditions or swell conditions change. Several studies have been conducted to examine the influence of liquid sloshing impact in LNG carriers [2, 38, 48, 51, 119].

Sloshing of liquefied natural gas (LNG) cargo can cause high impact loads on the supporting and containing structures. This is particularly critical for membrane-type tanks possessing flat surfaces and corner regions, which can lead to increase peak impact pressures. Determination of the sloshing load inside LNG cargo tanks and subsequent strength assessment of membrane-type containment systems are documented in the ABS [4, 5]. Inside the membrane-type tank hull structure, there are two major structural systems—LNG containment system and pump tower structure. The membrane-type LNG containment system consists of three components. These are thin metal membranes to prevent cargo leakage, foam or powdery insulation material to maintain the low temperature to keep the LNG cargo in a liquid state; and an associated structure to retain the membrane and insulation material in order to secure them with the hull structure.

Ship motions of liquid vessels tend to be relatively large in comparison with those of large vessels (see, e.g., [27, 170, 171, 178, 202]). A numerical analysis of sloshing impact pressure induced on a middle-sized double hull tanker was carried out by

[4]LNG is a natural gas (predominantly methane, with some mixture of ethane) that has been cooled down to liquid form for ease and safety of non-pressurized storage or transport.

Shinkai and Tamia [171] using the SOLA-SURF scheme. Numerical simulations were carried out for the cargo oil tanks in order to examine the characteristics of sloshing impact pressure. Takemoto et al. [178] carried out an experimental study on sloshing loads acting on middle-sized tankers with double hull structures. Sloshing impact pressures were measured at inner surfaces of the models and on the inner structural members. Peak values of impact pressures were detected, processed statistically and evaluated by 1/10 highest mean values. As a result, basic aspects of sloshing loads were shown through experimental studies such as effects of fill rates on resonance frequencies, effects of inner structural members on sloshing impact pressures and effects of swash bulkhead to reduce sloshing.

Extensive studies were devoted to the new-generation large LNG vessels of 200,000 to 250,000 m^3 cargo capacity (see, e.g., [24, 25]). Zalar [205] considered the safe operation of 138,000 m^3 membrane type LNG carrier with intermediate fillings during the transient phase of LNG transfer. Later, Zalar et al. [206, 207] developed sloshing assessment based on hydrodynamic analysis, model tests, numerical simulation, finite element method, and drop tests. Particular attention was given to different types and nature of sloshing liquid flows and to dynamic effects of large liquid free surfaces on global sea-keeping behavior. An efficient numerical model of hydrodynamic-structural coupling was developed to simulate linear and nonlinear hydro-elastic responses. The hydrodynamic analysis of second-order wave interaction with the floating system was presented by Chen [35, 36] who evaluated the drift loads and the low-frequency wave loads. The problems of sloshing-induced fatigue damage of ship tankers are well documented by Ibrahim [84].

Floating liquefied natural gas (FLNG) consists of a ship-shaped floating hull equipped with liquefaction plants and LNG storage tanks. The ocean wave-induced motions of the vessel would result in violent liquid sloshing inside liquid tanks in the vessel. The liquid sloshing in return results in highly localized impact pressures on the tank walls, which may cause structural damages and may even induce sufficient moment to capsize the vessel that carries the tank. This coupled phenomenon is one of the design concerns and is essential for FLNG systems in production or offloading operations in real sea states. Vessels carrying crude oil possess few number of lard tanks and thus the natural period of free surface waves becomes close to the period of ocean waves. This causes substantial ship motions and imposed on the contained liquid. It is known that liquid sloshing in partially filled cargo and ballast tanks can cause severe damage to ship structures. For ships that operate with partially filled tanks of relatively large size, Hamlin [70] reported some experimental results for measuring hydrodynamic forces and pressures acted on model structural elements during forced pitching, rolling and surging. By using the Laplace transformation technique, the dynamic coupling of a liquid tank system under transient excitation was numerically examined by Lui and Lou [112]. Numerical results for various types of external excitations and the resultant motions of the fluid-tank system are presented and compared with the equivalent non-shifting cargo system. The results of the comparison indicate that the discrepancy of responses in the two systems can obviously be observed when the ratio of the natural frequency of the fluid and the natural frequency of the tank is close to unity.

The coupling between the roll motion of a ship in a regular beam sea and the sloshing of a free surface liquid in a compartment was studied experimentally by Francescutto and Contento [55]. The amount of the water in the compartment was been kept constant during any single test but four different degrees of filling were considered. To emphasize the effect of the free surface of the liquid in the container, the frozen liquid condition was tested as well.

By using the Laplace transformation technique, the dynamic coupling of a liquid tank system under transient excitation was numerically examined by Lui and Lou [112]. Numerical results for various types of external excitations and the resultant motions of the fluid-tank system are presented and compared with the equivalent non-shifting cargo system. The results of the comparison indicate that the discrepancy of responses in the two systems can obviously be observed when the ratio of the natural frequency of the fluid and the natural frequency of the tank is close to unity.

Experimental measurements of the ship roll amplitude and its dependence on the encounter wave frequency for both frozen and free surface liquid condition were obtained by Francescutto and Contento [55] for different tank fillings. Sample of the results are shown in Fig. 1.16a and b for two different liquid fillings 0.1 m and 0.16 m, respectively It is seen that the principal natural rolling period is increased and the main resonance is shifted to a lower frequency than for the frozen liquid case. The sloshing of liquid was found to cause a stabilizing effect as compared to the case of the ship with or without frozen liquid. Figure 1.16a and b show another resonance peak in rolling oscillations at a frequency higher than the principal natural frequency of the ship with or without frozen liquids. This resonance was associated with violent sloshing with formation of liquid jets.

The early work dealing with sloshing interaction with ship dynamics was largely carried out within the framework of the linear solution of ship dynamics and linear sloshing dynamics. The linear potential theory was employed for external wave action and internal sloshing flow. In addition, a considerable number of these studies considered a two-dimensional case. For example, Mikelis and Journée [119] presented a two-dimensional finite difference transient solution for the prediction of

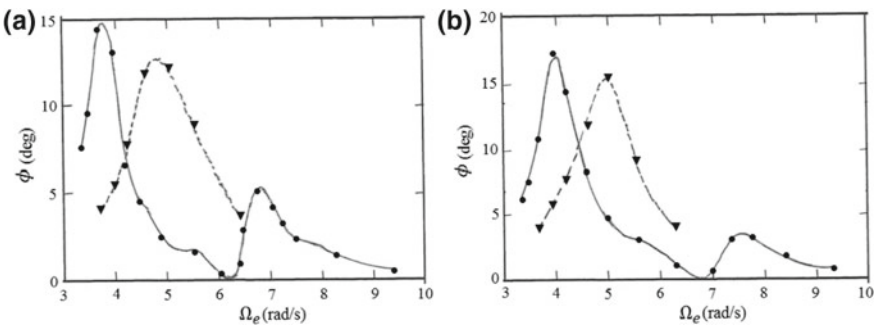

Fig. 1.16 Dependence of measured roll response amplitudes on the wave encounter frequency for (▼) frozen and (●) free surface liquid tanks: **a** filling depth is 0.1 m, **b** filling depth is 0.16 m [55]

liquid motions and induced pressures in partially filled containers on ships. Experiments were also conducted on scaled tanks and the measured pressures and bending moments were compared with numerical predictions. Journée [89] analyzed a ship model with liquid cargo tanks and the model was tested in beam waves at zero forward speed for a wide range of filling levels. The measured roll data of the model were compared with the results obtained from strip theory calculations. Lee and Choi [101] conducted experiments and numerical study on the sloshing problem in cargo tanks. The fluid motion was predicted using a high order boundary element method. In cases of low filling depths, hydraulic jumps were formed when the excitation frequency is close to the resonance frequency whereas in the case of high filling depths, a large impact pressure was obtained. Molin et al. [127], Malenica et al. [114] and Newman [146] performed numerical simulations on the coupled problem between ship motions and internal sloshing based on the assumption of linear sloshing flows inside the tanks. Two-dimensional experiments of a hull section containing tanks filled with different levels of water excited in sway by regular waves were conducted by Rognebakke and Faltinsen [164]. The steady-state motion of the ship was found almost linear and sinusoidal with the frequency of the linear incident waves although the liquid sloshing in the tanks was violent. This implies that higher-order harmonics of the sloshing force are filtered out by the system. The calculated coupled motion was found sensitive to the damping of the sloshing motion in a certain frequency range where the coupled sloshing and ship motions caused resonant ship motions.

Nam and Kim [129] carried out a series of model tests to investigate the effects of sloshing on the motion responses of FLNG. They found that the coupling effects do not always result in the increase of sloshing-induced pressure and that the increase or decrease of pressure is dependent on resonant condition. Nasar et al. [131–135] conducted an experiment to study the phenomenon of liquid sloshing in partially filled tanks mounted on a LNG carrier exposed to regular beam waves. Three ballasting conditions of the vessel with different filling levels, drafts, and center of gravities have been considered.

Kim et al. [96] considered linear ship motion using an impulse-response function method, while the nonlinear sloshing flow was simulated using a finite-difference method. The sloshing-induced forces and moments were added to wave-excitation forces and moments, to determine the corresponding body motion. The developed schemes were applied for the sway motion of a box-type barge with rectangular tanks and the roll motion of a modified S175 hull with rectangular anti-rolling tank. It is found that the nonlinearity of sloshing flow is very important in coupling analysis. Due to the nonlinearity of sloshing flow, the ship motion was found to exhibit a strong sensitivity to wave slope. The interaction of nonlinear sloshing flows inside ship tanks with ship dynamics was simulated in time domain based on computational fluid dynamics by Lee et al. [104] and Lee and Kim [105]. Lee et al. [103] considered rectangular LNG tanks subjected to external loadings using a computational fluid dynamics simulation, which were verified experimentally. It was found that the effects of viscosity and density ratio of fluid on impact pressures are insignificant, while the compressibility of fluid plays an appreciable role. In another study, Lee

et al. [104] analyzed the coupling and interaction between ship motion and inner-tank sloshing using a time-domain simulation scheme.

Mitra et al. [121, 122] employed the finite element method for the simulation of nonlinear sloshing coupled with nonlinear ship motion in time domain. Taking into account the strong nonlinear characteristics, such as overturning and breaking waves, Peric et al. [154] carried out a numerical simulations of coupling between translational ship motions and internal sloshing. Depending on the filling level, Clauss et al. [37] found that the vessel's response amplitude of roll motion was found to be affected by the wave incident angle as well as the phase shift of tank sloshing and body motions. This was attributed to the coupling between the moving liquid and the hull motions. 138,000 m3 LNG carrier with four membrane tanks was numerically analyzed for different filling levels and wave incident angles in frequency domain. Instead of one single resonance peak as for the solid filling case, the roll response amplitude of the dual-mass system features two peaks, whose magnitudes and positions were found to depend on the filling level of the cargo tanks. But coupling effects due to resonant sloshing also affect longitudinal body motions.

The sloshing effect on the motions of a two-dimensional rectangular cylinder was studied experimentally and numerically by Kim et al. [97]. Their results revealed that the sway response is considerably affected by the motion of the fluid, particularly near the sloshing natural frequency, while the roll response changes comparatively small. The coupling effect between ship motion response and internal sloshing flow was studied by Jiang et al. [87] who considered a viscous two-phase flow model with the Volume of Fluid (FOM) interface technique based for solving the internal liquid sloshing problem, while the impulse-response-function method was employed for the external ship response. Numerical simulations for a three-dimensional simplified LNG-FPSO ship with two partially-filled prismatic tanks were carried out, including the global ship response and sloshing impact loading. The ship motion response was found to reveal strong sensitivity to incident wave steepness for low-filling conditions in the neighborhood of the ship natural frequency and sloshing natural frequency. If the incident wave frequency is close to the sloshing natural frequency, the impact loading was observed in global sloshing moment signal. However, the steady-state ship motion is still of sinusoidal characteristics with incident wave frequency. It implies that the impact loading of sloshing-induced moment has no important coupling effect on global ship response. The occurrence of impulsive signal can be observed in local pressure evolution on structure, indicating that the local impact action of sloshing flow is significant around sloshing motion natural frequency.

Numerical simulations of the coupling cases were carried out by Jiang et al. [87] for the three-degree-of-freedom ship carrying two liquid tanks. The dependence of the roll motion response amplitude operators[5] (RAOs), ϕ_0 B/2A, (where ϕ_0 is the roll angle amplitude, B the length of the liquid tank, and A is the wave amplitude) in beam-sea on incident wave frequency parameter, $\omega\sqrt{L/g}$ (where ω is the wave frequency,

[5]Response amplitude operators (RAOs) are statistic parameters that are used to determine the likely behavior of a ship when operating at sea.

and L is the ship length) for four different ratios of tanks filling: (20%, 20%), (30%, 30%), (57.5, 43.3%), and (82.6%, 82.6%) (where the first filling percentage is for the fore peak tank, while the second percentage is for aft peak tank) are shown in Fig. 1.17a–d, respectively. These figures include other results obtained by Nam et al. [130] and Gou et al. [62]. The comparison reveals agreement with the numerical and experimental results of Nam et al. [130]. However, the numerical results in Gou et al. [62] have evident discrepancy with others, especially for (20%, 20%) and (30%, 30%) filling conditions. It was implied that the nonlinear effect of internal liquid sloshing is important for ship roll motion, especially for low-filling conditions. The linear potential sloshing model cannot predict this phenomenon.

In addition, it should be noted that the numerical models in Nam et al. [130] and Gou et al. [62] are not capable of simulating the (82.6%, 23.5%) filling condition as shown in Fig. 1.17d. In the fore peak tank, the still water level is at the upper slope of the tank for 82.6% filling condition. The numerical model by Nam et al. [130] adopted a single-valued function to track the free surface motion. It fails to simulate the non-orthogonal still water level and adjacent wall.

Scaled model tests of an FLNG section considering the sloshing flows inside the tank were carried out by Zhao et al. [209]. It was reported that the natural period of roll motion shifts towards higher periods due to the effects of the internal liquid

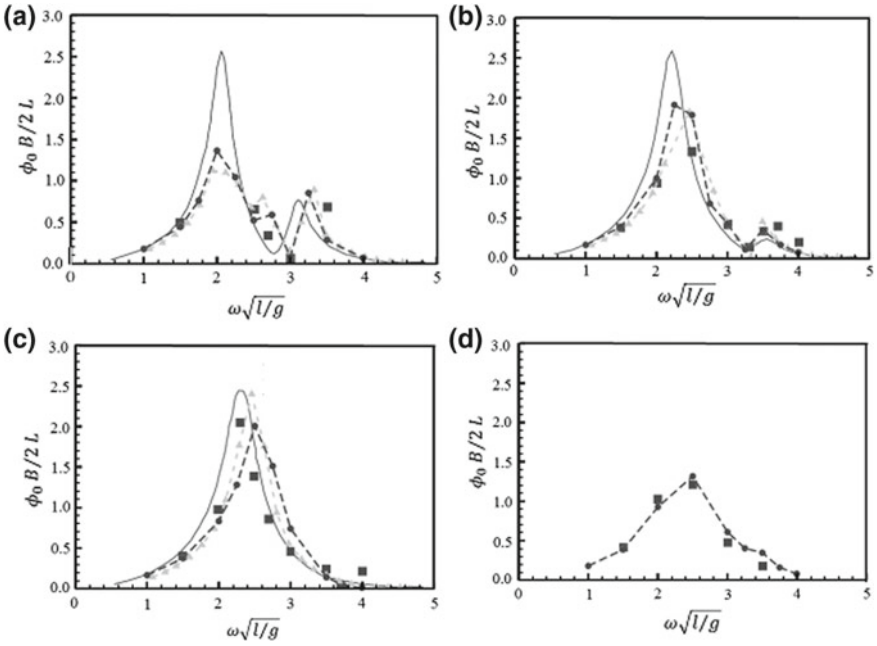

Fig. 1.17 Dependence of roll response amplitude operators on incident wave frequency of LNG ship for four different tanks fillings (fore peak, aft peak) in beam-sea: **a** 20%, 20%, **b** 30%, 30%, **c** 57.5%, 43.3%, and **d** 82.6%, 82.6%. ■ experiment, —— [62], - - ▲- - [130], and - -● - - [87]

sloshing. The internal liquid flows would serve as a damper in free decay motions of an FLNG vessel in still water.

Under band limited random excitation of the wave maker with a spectral density of about 0.45 m^2s/rad that covers a frequency band 0.2–1.6 rad/s, Zhao et al. [209] measured the response spectra of the roll motions ballasted with fresh water and then equivalent solid weights shown in Fig. 1.18. The peak value of the response spectra in the liquid case is much larger than that in the steel ballasting case. The response spectrum of liquid sloshing is shown in Fig. 1.19 and it reveals two peaks closely related to the vessel motions, while the other peaks correspond to the natural periods of the internal sloshing in different surface modes. This is a clear demonstration that there is a certain degree of coupling between the roll motions and the first mode internal sloshing, while little coupling lies in between those in higher modes.

The response peak of the vessel motions shifts towards higher periods due to liquid sloshing as shown in Fig. 1.20. The roll response amplitude operators of the FLNG section in the liquid case is observed to be smaller than that in the solid loaded case near the first mode periods of the liquid sloshing. This indicates that the internal sloshing would either amplify or reduce the global roll motions of the vessel. A similar phenomenon has also been observed in the numerical simulations by Kim et al. [96]. A possible explanation for this interesting phenomenon may be related

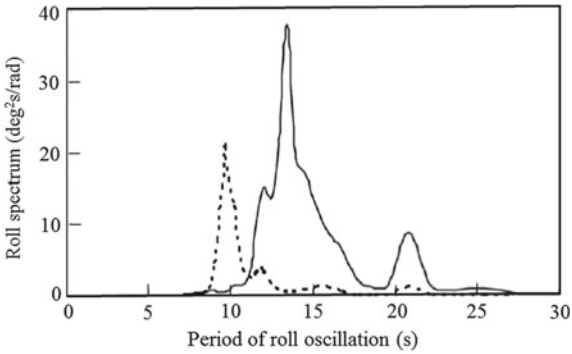

Fig. 1.18 Comparison of roll response spectrums of the FLNG section: —— with sloshing, - - - without sloshing [209]

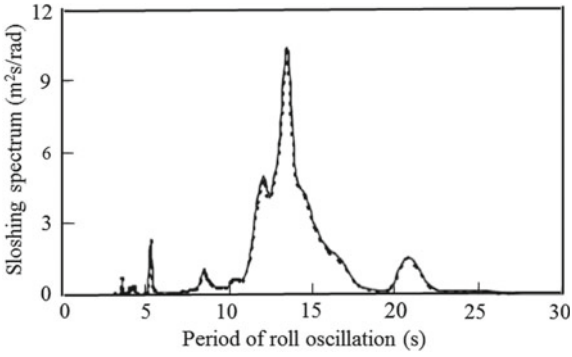

Fig. 1.19 Comparison of the response spectrums for the internal sloshing oscillations at ———— Head side of the tank, and at - - - - Following side of the tank [209]

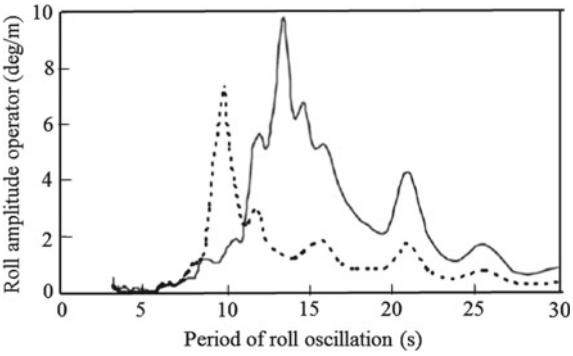

Fig. 1.20 Comparison of the response amplitude operators for the roll motions of the FLNG section: —— with sloshing, - - - without sloshing [209]

to the phase difference between the internal and external forces of the FLNG vessel. As reported in the numerical simulations of Kim et al. [96], the phases near the first mode sloshing period show almost 180° difference between internal sloshing forces and external excitation forces, in which case the sloshing can effectively reduce the global motions. On the other hand, as the excitation periods move away from the first mode sloshing period, the phase differences tend to approach the value 0°, in which case the sloshing would amplify the global motions.

Cercos-Pita et al. [31] considered the nonlinear dynamics of a vessel interacting with a free surface tank onboard using nonlinear ship motion simulation program with six degrees of freedom and a computational fluid dynamics approach. Numerical results were presented for the nonlinear roll motion of a vessel with and without a free surface tank in regular beam waves with different values of wave steepness. The behavior of the roll response with the tank partially filled with fluid was that the tank acted as an anti-rolling device for the case of the lowest two values wave steepness (1/80 and 1/67). In such cases the roll response shows the double-peak shape. However, the roll motion has a totally different behavior for the largest forcing steepness (1/50). In such case, the maximum roll amplitude with tank was found to be much closer to the maximum roll amplitude without tank, and the effectiveness of the tank, as an anti-rolling device, is very significantly reduced. The interaction between vessel motions and internal tank sloshing for Floating Liquefied Natural Gas (FLNG) was extended by Zhao et al. [208]. They developed a numerical code based on potential flow to investigate the coupling interaction between 6 degrees of freedom vessel motions and internal nonlinear sloshing. The impulsive response function method was adopted in the resolution for the 6 DOF vessel motions, and internal liquid sloshing was numerically solved with the boundary element method. Their study mainly dealt with the effects of sloshing on the global motion responses of a vessel, which are slightly affected by the impact of sloshing loads as indicated by Jiang et al. [87]. The sloshing effects on a vessel's motions are closely related to the phase shift between the sloshing and vessel's motions, and coupling properties differ for different motion modes. It was found that significant coupling effects can be induced in beam sea conditions between sway and roll motions and internal sloshing; heave motion is slightly affected by internal sloshing. The sloshing responses are

mainly excited when the natural roll motion and natural sloshing frequencies are close to each other. Coupling effects will increase rapidly when the natural sloshing frequency is close to the main response frequency region of the ship. The phase shift between wave loads and sloshing loads shows rapid change near the natural roll motion and natural sloshing frequencies.

Saripilli and Sen [165–167] and Sen and Saripilli [168] developed a ship motion algorithm coupled with slosh loads and studied the effect of the coupling on both slosh loads and ship motions for different conditions. A hybrid approach by combining a potential flow based solution scheme for the external fluid flow and a viscous flow solver for the internal sloshing flow was adopted. The potential flow solution for the ship motion problem was obtained by using boundary element method (BEM), while the viscous flow solution for the sloshing problem was determined using finite volume method (FVM) based on viscous multiphase interface capturing volume of fluid (VoF) technique. The influence of filling on coupled motion responses was studied and coupling was observed to be more severe at low filling conditions which is expected. For three-dimensional cases of LNG FPSO equipped with large prismatic tanks [130, 166, 168], it was reported that at lower fill levels roll motion is more significantly damped and the magnitude of roll response amplitude operator is less for lower fill levels when compared to higher fill levels. However, But the cases of FLNG, Saripilli and Sen [167] found that the magnitude of roll response amplitude operator may increase as the fill level decreases. Similar trend was reported in the experiments of Zhao et al. [210].

1.5 Passive Control of Ship Roll

1.5.1 Early Developments

Stabilization of ship tankers roll dynamics has been the focus of several studies over many years. According to McMullen [118], the types of tank systems may be classified as undamped free surface tanks [196, 197], damped free surface tanks, U-tube tanks, active tanks, and controlled tanks. Passive water tanks have two basically different structures. One is the free surface anti-rolling tank (ART) and the other one is the U-tube tank (ART). The anti-roll tanks basically act as mechanical absorbers to attenuate the ship roll motion. They can be classified as passive [32, 33, 39, 52, 69, 108, 159, 174, 192, 194], controlled-passive [17] and active [41, 120, 198, 212]. The reduction of rolling of ships by using auxiliary wing tanks connected by pipes was realized long time ago. The basic principle the two anti-roll tank types is to transfer the liquid from starboard to port side and vice versa, with a certain phase lag with respect to the ship's rolling motion. This provides a counteracting moment to stabilize the ship roll oscillations. The use of anti-rolling tanks in the German luxury liners *Bremen* and *Europa* reduced the maximum roll from 15° to 5° [162]. The motion of the ship causes appropriate masses of fluid, water or reserve

fuel, to flow side-to-side between tanks that are mounted at specific heights and distances from the ship's center line. The resistance in the connection between the tanks is tuned so that the fluid motion is out-of-phase with the ship roll motion; thus, generating opposing moments that will minimize the adverse effects of wave-induced excitations. Burger and Corbet [26] explored the means of resisting rolling, including bilge keels, oscillating weights, anti-rolling tanks, gyroscopic stabilizers, and tilting fin systems. In particular, the anti-rolling tanks that are divided into three types, including diversified tanks, free surface tanks, and U-tube tanks. Kula [99] presented an overview of different methods of roll motion compensation including passive and active control.

Frahm [52] introduced an anti-roll tank in the form of a U-tube. This is shown in Fig. 1.21 (taken from [43]). In this system, a moment opposing the roll motion of the ship is generated by the oscillating fluid. Figure 1.21a depicts the old version of Frahm's anti-roll system, which consists of two half-full tanks that are connected at the bottom by a water pipe and at the top through an air pipe fitted by a V-valve. Figure 1.21b shows a newer version of Frahm's anti-roll system in which the lower pipe connecting the tanks is omitted and replaced by the open ocean. The "blisters" are extended along two-thirds of the length of the ship and are subdivided into three or more compartments by vertical partitions. Stigter [174] derived the equations of motion of the fluid in a passive U-tube anti-roll tank and determined the coupling terms between the ship and the tank. Stigter [174] employed an equivalent double pendulum in which the mass of the tank fluid can be regarded as a second pendulum attached to the pendulum representing the ship, over most of the roll frequency range. Lewison [108] proposed a scheme to optimize the design of free-surface passive tanks.

Bell and Walker [17] examined two differently controlled anti-roll tanks. The first is controlled by valves mounted in the water channel. The second is controlled by valves in the air channel. In active anti-roll tanks, either air pressure or a pump is used to move the fluid between tanks. Webster [198] examined the control of pump-activated U-tube tanks. He demonstrated the superiority of active anti-roll tanks over passive ones in reducing the ship roll motion. It should be emphasized that both anti-roll tanks and moving weights are independent of the vessel forward speed. As

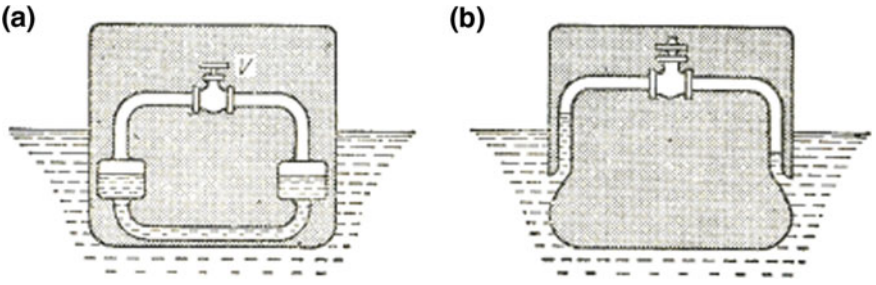

Fig. 1.21 Frahm's anti-roll ship tanks: **a** Two tanks each half filled with water (old type), **b** Modern "blister" construction of Frahm's anti-rolling tanks [43]

a consequence, both systems have the advantage of being effective when the ship is not underway or moving at low-speeds. However, the drawback of these systems stem from the fact that they require a significant amount of hull space.

1.5.2 Anti-roll Tank

Ships with free surface anti-rolling tanks (ARTs) involve nonlinear coupling between the ship dynamics and liquid sloshing dynamics. The major concern related to the sloshing flow is the slosh-induced loads such as local impulsive pressure. The slosh-induced forces and moments affect the ship motion. Accordingly, the ship dynamics and sloshing problems should be solved simultaneously. The key of ART design is to tune the natural periods of the ship roll motion with the sloshing flow. The main advantages of such an ART are the large damping moment at small roll amplitudes and the ease to adapt the response by changing the water level. The performance prediction of ART is not a simple task because the sloshing flow is a strongly nonlinear phenomenon and the slosh-induced moment is not linear with respect to the excitation amplitude. Moreover, the phase difference is hard to predict when the sloshing flow is coupled with the ship motion. It is believed that the free surface ART concept was tested for the first time by Watts [196]. Later, extensive bench tests were carried out to provide datasets necessary for the design of such devices (see, e.g., [79, 100]). Several attempts were made to predict the response of the (see, e.g., [7, 193]). The experimental studies showed that the response of an ART to roll motion is highly frequency and amplitude dependent [29].

Bosch and Vugts [19] conducted an experimental investigation on a free-surface anti-roll rectangular tank, partially filled with water (shown in Fig. 1.22a) subjected to sinusoidal oscillations about a fixed axis. The moment amplitude, A_M, due to water sloshing and phase angle, ϑ_M with respect to the forced tank rolling motion were estimated. Systematic measurements were done for a wide range of tank parameters (tank width and mean water depth) and motion parameters (roll amplitude and frequency). The complete series of experiments was simulated with the program ComFlo by Van Daalen et al. [189]. Taguchi et al. [177] experimentally and numerically studied the nonlinear roll motion of a ship with a Frahm anti-rolling tank (ART) onboard for two

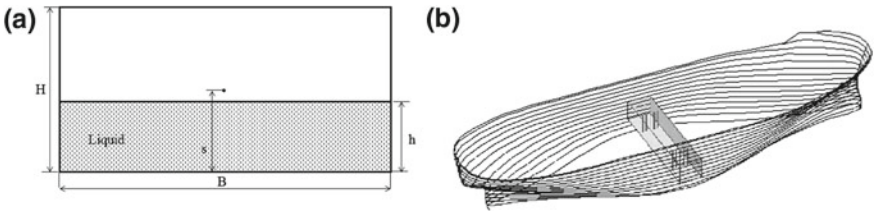

Fig. 1.22 **a** Geometry of an anti-roll tank [190] and **b** Modified S175 hull with an anti-roll tank [95]

loading conditions, namely normal stability condition and poor stability condition, in regular beam waves. It was found that the model ship with the ART in poor stability condition can exhibit irregular and complicated roll motion even in regular waves. Numerical investigation with equations of the coupled motions of rolling of a ship and fluid in an anti-rolling tank showed that roll motion in poor stability condition could exhibit complicated response in a wide range of control parameters (namely Ω the wave frequency and the wave steepness), in relatively low frequency region. The numerical simulation of passive roll-damper tanks for fishing vessels using smoothed particle hydrodynamics was presented by Iglesias et al. [86]. The results of the simulations were validated with experimental tests. Large amplitude waves and breaking waves appear were reproduced.

The variation of the restoring moment in the process of sloshing motion for the anti-rolling tank was studied by Gao et al. [59] who considered the effect of the change of the tank angle of the anti-rolling tank in the process of sloshing motion. The damping coefficient was regarded as a time-varying function. The restoring moment provided by the tank at different frequencies of the harmonic motion was calculated. A three-dimensional numerical simulation of the liquid sloshing dynamics was estimated using a computational fluid dynamics simulation, which was found in agreement with the predicted theoretical values for the calculation of the restoring moment. The shape of the interior geometry, e.g. additional struts, plates or other flow obstructions, has an effect on the response, which makes it difficult to predict the response by analytical models. The response of a two-dimensional and three-dimensional model scale free surface ART using the computational fluid dynamics code ReFRESCO (www.refresco.org) was studied by Kerkvliet et al. [92]. The computational fluid dynamics results were validated experimentally using model-scale test results of Carette [28]. At the off-resonance frequencies, the two-dimensional simulations showed very accurate results. Around the resonance frequencies, three-dimensional simulations provided better agreement, since air enclosure during wave breaking is better captured. If air enclosure occurs in two dimensional simulation, the enclosed air was found to damp the impact on the side wall, but more importantly it reduced the transversal transport of water and, as a result, less water is concentrated at the side corner. This will reduce the overall roll opposing moment and damping response. Monitoring of the change in total water volume during the simulation was found to be important for a free surface ART since the response strongly depends on the filling height. By optimizing the numerical settings, e.g. increase the iterative convergence, the conservation of water volume could be improved.

Van Daalen et al. [190] studied the performance the ART and the corresponding forces and moments using computer simulations and experimental tests for a prescribed rolling motion. They provided a systematic demonstration of the water free surface motion and the resulting hydrodynamic moment as the excitation frequency is increasing. For shallow water, i.e., $h/B < 0.1$, and at low excitation frequencies a long standing wave takes place, but with increasing frequency very short progressive waves appear. In the transition regime the short waves interfere with the long wave. After these small disturbances the bore rises rather suddenly, while the phase lag between the water transfer and the imposed motion increases as shown

in Fig. 1.23b; and the quadrature component of the moment, $A_M \sin \vartheta_M$, increases rapidly as shown Fig. 1.23c. Over a large frequency range the phenomenon does not change significantly, although the water motion becomes more violent and large vortices appear when the direction of wave propagation is reversed. This is followed by a solitary wave, which is a single steep wave running from one side of the tank to the other. After the bore has disappeared, the moment exerted by the water falls down rapidly as shown in Fig. 1.23a. With a small further increase in frequency the water approximates the "frozen" state if the tank bottom is situated below the axis of rotation. When the tank is mounted above this axis, the water motion becomes rather chaotic. In this high frequency range there is hardly any water transfer. When the tank was mounted below the axis of rotation, the centrifugal force adds to the gravity force. When the tank was mounted above the rotation axis, the centrifugal force subtracts from the gravity force and the transverse acceleration is reversed as well. When the tank was placed at a higher level, the moment amplitude was found to increase considerably, whereas the phase angle decreases but slightly. As a result, the quadrature component becomes larger and covers a wider frequency range.

Kim [95] numerically studied the coupling problem in sloshing flow and ship dynamics using the Large-Amplitude Motion Program (LAMP) for the ship motion. For analysis of the sloshing flow, a finite-difference method was applied. The slosh-induced forces and moments was combined with the wave-induced excitations at each time step. A modified S175 hull was adopted and Fig. 1.22b shows the hull profile and the location of a typical ART. Figure 1.24 shows the amplitude of roll moment

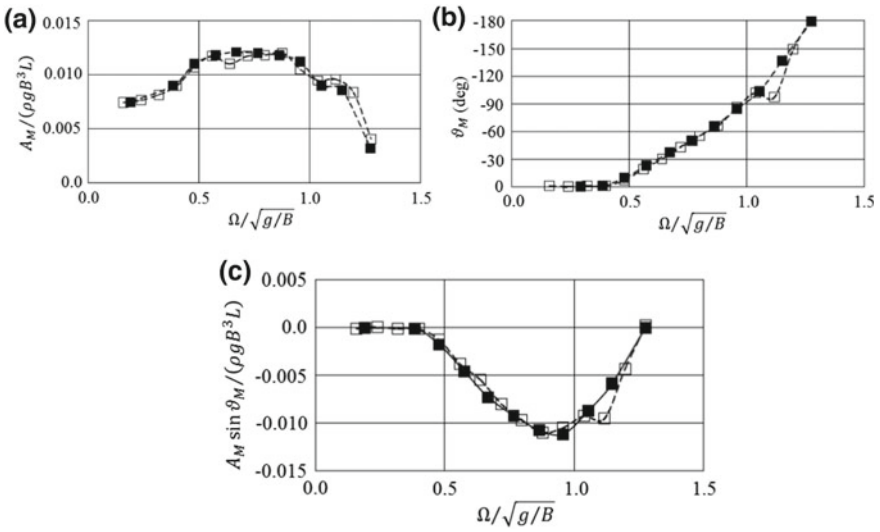

Fig. 1.23 Dependence of free-surface hydrodynamic moment on tank in regular roll motion on roll excitation frequency parameter: **a** Non-dimensional moment amplitude, **b** Phase angle, and **c** quadrature component. $s/B = 0.2, h/B$, roll excitation amplitude angle $\phi = 3.8°$. ■ experimental measurement, and □ computer simulation (ComFlo) [190]

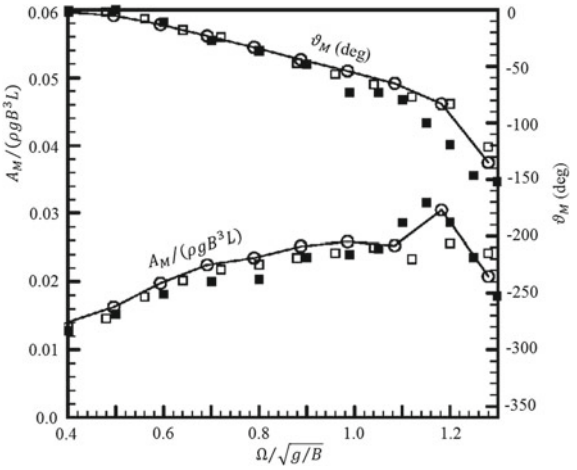

Fig. 1.24 Dependence of free-surface hydrodynamic moment and phase on roll excitation frequency and comparison with experimental measurement by Van Daalen et al. [189]. ○ measured results, □ Van Daalen et al. for smoothed tank model, ■ computer simulation results [95]

including a comparison of the measured results for the smooth tank model tested by Daalen et al. [189]. This figure shows the first harmonic component of excitation frequency and the corresponding phase difference with the forced frequency. It is seen that the peak moment with the phase difference of $\pi/2$ occurs at excitation frequency $\Omega/\sqrt{g/B} \approx 1.2$. Figure 1.25 shows time history records of the ship roll amplitude response operator without and with a smooth tank and with a tank with vertical tubes for the purpose of sloshing damping. It is seen that three-tube tank with tank/ship mass ratio of 2.1% has the best performance.

Figure 1.26 shows the dependence of the roll response amplitude operator (RAO) of the modified S175 hull ship on the wave excitation frequency parameter. It is seen that the roll motion with ARTs shows a dramatic reduction near the roll resonance, but

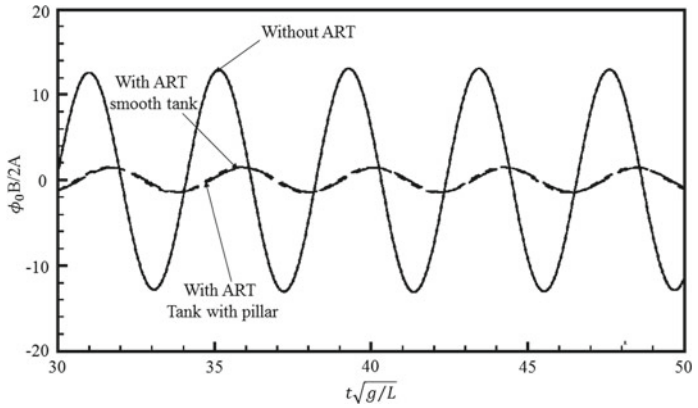

Fig. 1.25 Time history records of roll amplitude response operator showing the influence of the ART, for tank/ship mass ratio of 2.1% [95]

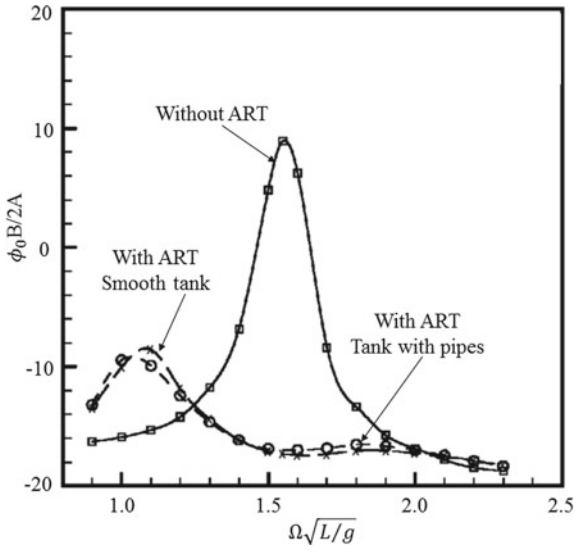

Fig. 1.26 Dependence of the ship roll amplitude response operator on the excitation frequency for tank/ship mass ratio of 2.1% [95]

the motion becomes larger at out of- resonance frequency. At the out-of-resonance frequency, the phase of slosh-induced moment is not close to 180°. Thus the slosh-induced moment can increase the total excitation moment, resulting in larger roll motion. Another important observation is that at a resonance frequency the difference between two cases with and without internal pipes is not significant. However, at the low frequencies, some reduction of motion can be expected with the internal pipes. The internal members delay the fluid motion, therefore they can be effective in damping the slowly moving flows at low frequencies.

Further studies dealing with the ARTs on floating vessels were performed by Kim et al. [94] who employed a boundary element method-based for the ship motion coupled a computational fluid dynamics program for the inner sloshing effects. The two programs allowed real time coupling effects of inner sloshing on vessel motion and the response amplitude operators of the vessel with and without anti-rolling tank were obtained. The results revealed that the effects of ART changed and shift RAOs as reported previously in other studies (see, e.g. Lee et al. [102]). An analytical model was developed by Nielsen and Nielsen [147] for evaluating the performance of a passive free surface tank. The analysis includes the coupling of a roll ship model to a fluid flow model. The effects of the passive free surface tank were evaluated and a significant damping effect was achieved particularly in cases with resonant roll. A numerical model based on Volume of Fluid was introduced to simulate the liquid sloshing inside a free surface tank by Li [109] and Li et al. [110]. The performance of the free surface tank was studied when the tank is excited by different excitation amplitudes and frequencies. It was found that roll damping increases nonlinearly with increasing roll amplitude at resonance frequency region. Smaller excitation amplitude was found to result in higher damping moment. However, the damping moment has liner increase when the excitation period away from the damping domi-

nated region. A method determining ship motion with anti-roll tanks in time domain was presented by Zou and Xu [213] who used potential and viscous flow theories to the simulation of the ship motion coupled with fluid motion in the anti-roll tank. The six degree-of-freedom motions of the ship were input to the anti-roll tank while the induced force/moment by anti-roll tank was added to the ship equations of motion. The coupled equations were solved in the time domain. The ship roll motion of an offshore supply vessel (OSV) equipped with an anti-roll tank was computed and compared with model test results.

1.5.3 U-Tube Tanks

The advantages of passive U-tube anti-roll tanks stem from the fact that they do not have moving parts and require little maintenance. However, they occupy a very significant portion of the ship's hull. Lloyd [111] used one-dimensional Euler's equation to derive the equation of fluid motion in the U-tube tank. Zhong et al. [211] presented results of two-dimensional simulations of a U-tube tank using computational fluid mechanics to solve the discretized Navier-Stokes equations. Based on the equation of Lloyd [111], Gawad et al. [60] studied the effect of U-tube tank parameters to the ship roll motion. A limitation of the passive tank is its inability to effectively reduce ship roll at frequencies encountered at sea. It can, however, reduce ship roll motion near the ship roll natural frequency. Gawad et al. [60] aimed at optimizing the performance of passive U-tube tanks over a wide range of excitation frequencies. They focused in their study on optimal values for tank damping and mass along with its location with respect to the ship's center of gravity. Moreover, their study demonstrated a 67% reduction in the ship roll motion for a well-tuned and well-designed U-tube tank. Furthermore, Vugts [194] designed and compared the performances of four passive tanks in reducing the roll motion of the same ship.

The implementation of a U-tube tank model for the ShipMo3D ship motion library was described by Taggart [175, 176] in terms of the frequency and time domains. The relative effectiveness of a U-tube tank was found to be achieved when a ship has small roll damping, such as a vessel with small or no bilge keels. Example computations indicated that ship motions are not very sensitive to variation of the damping coefficient within a realistic range of values. Example computations showed that a U-tube tank is most effective when its natural frequency is near the ship natural roll frequency. Experimental tests were carried out by Ramana Reddy et al. [161] to quantify the influence of the U-tube tank alone. Forced oscillation tests were conducted for the U-type tank on a moving platform for different frequencies and also for different amplitudes of the pure roll forced motions by Silva et al. [173]. The most important aspect was to obtain a large set of roll restoring moments, for this passive configuration, which gives a discrete distribution of the roll restoring moments along the entire range of wave frequencies of interest. It was demonstrated that non-linear effects associated with large amplitudes of 10° to 15° would result in a reduction of the moment exerted, which would degrade the performance characteristics of this

anti-roll passive device. Gong [61] adopted the meshless particle method to study the liquid sloshing dynamics in anti-roll tanks and for an offshore supply vessel (OSV). The fluid movement between anti-roll tanks lags ship rolling movement. The tanks were found to generate maximum counter-moment against ship rolling and give optimal anti-rolling effect at the phase lag of 90°.

The position of the tank above the center of gravity was seen as positive for the performance of the tank, supposedly with an optimal distance (see, e.g., [19]). Two passive U-tube anti-roll tanks with distinct natural frequencies to provide ship roll reduction over a wide range of metacentric heights of ships were proposed by Jin et al. [88]. A practical dual-tank system was designed for a special RoRo ship. Simulations were performed for both the passive dual-tank system and the passive single-tank system to compare the responses of ship rolling. The results showed that the dual-tank anti-roll system has better anti-rolling performance than the single-tank system. Xiaoyong et al. [199, 200] presented some studies for measuring the natural period of U-shape anti-roll tank and the optimal control condition of a tank model of anti-roll tank based on oscillation platform.

The influence of a U-tube passive anti-roll tank on parametric roll motion together with the role of initial conditions of a coupled roll motion and fluid motion on the performance of an anti-roll tank were investigated by Peşman et al. [155]. Parametrically exited roll motion was modeled as a single degree of freedom system incorporating heave and pitch effects by means of a time varying restoring moment. Gunsing et al. [67] reported experimental results of the internal damping inside U-tube anti-roll tanks to reduce the water motions at resonance and to increase the frequency range over which the tank works efficiently. The sensitivity and validation of the anti-roll performances of passive U-tank were reported by Kerkvliet et al. [91]. The sensitivity on the results for the U-tank was analyzed by varying the grid resolution and the numerical time step of computational fluid dynamics code. The two-dimensional full-scale and Froude based model-scale ReFRESCO (www.refresco.org) results were compared to two-dimensional and three-dimensional full-scale computational fluid dynamics results of Delaunay [42] and Thanyamanta and Molyneux [180] and validated with model-scale experimental results of Field and Martin [50] and experimental results by Gunsing et al. [67]. Taskar et al. [179] developed the fluid governing equation of motion inside ART and proposed a computational fluid dynamics algorithm to determine the damping coefficient for five different designs of ARTs, and validated the results through both transient computational fluid dynamics simulations and experimental measurements.

Neves et al. [145] presented a mathematical model, which describes the fluid motion inside a U-tank nonlinearly coupled with the heave, roll and pitch motions of the ship. With the purpose of controlling the roll motion in the case of parametric resonance in longitudinal waves. It was reported that when the tank is above the origin (ship center of mass) the ship roll amplitudes are significantly reduced less than 10° for low range excitation frequency. However, in the range of higher excitation frequencies, a higher tank is worse than a lower one. This was explained by the positive effect of the roll induced sway: which is in phase above the rotating axis while being at an opposite phase for positions under the axis. This roll induced

sway motion can be related to the concept of effective gravity angle. The effective gravity angle is the angle to the vertical of the acceleration in the transverse plane at a given location. Carette [28] extended the study of the effect of the effective gravity angle on the response of the tank, with the hypothesis that an ART does not respond differently to the roll angle than to the effective gravity angle. The effects of sway in the response of anti-roll tanks were experimentally examined by Carette [28] under arbitrary combinations of roll and sway motions. Harmonic and irregular excitation tests were performed in roll, heave and sway, both independently and combined using a six degrees of freedom hexapod table. Abeil [1] conducted experimental tests on a model of the ART mounted on a six component force transducer frame installed in the ship model. The analysis of the measured moment revealed that the amplitude and phase of the ART moment depends on the amplitude of the roll motion, and the natural frequency of the ART increases with increasing roll amplitude. After translating the ART moment into damping and restoring components, it was observed that when the ship rolling increases, the magnitude of the damping generated by the ART decreases. Repeat tests in waves conducted for a variation of filling levels have shown that increasing the filling level past a certain threshold does not affect the damping property of the ART, but influences negatively the stability of the vessel.

The performance of the passive tanks is limited by their ability of moving the water from one ship's side to the other. This motivated researcher to consider active tanks for generating larger stabilizing moments from the same tank volumes. The ability to pump large volumes of water in a short time requires sufficiently large powers for the actuators. Improvement in warship roll stabilization was achieved by the application of active controlled anti-roll tanks [163]. The sensitivity of ship's roll motion and anti-roll tank controller design to the ship's metacentric height was highlighted. Further studies included the selection of suitable control valves and blower for the active control scheme and an analysis of their contribution to the stabilization effect. The effects of damping plates in the duct of U-tube tank on the oscillating period of the moving fluid and of swash plates on roll damping moment of the tank were studied experimentally by Lew et al. [107]. Their study presented development of active U-tube tanks using air blower to control the flow in the tank by simple control algorithm. U-shape anti-roll tanks were analytically modelled by Moaleji [123], Moaleji and Greig [124–126] using an Euler equation and the Lagrange energy method. An adaptive control strategy was used to control the actuating pumps of an active U-tank based on predicting the waves reaching the ship according to the pre-history of the waves over few minutes. The pumps therefore move the water in a manner to counteract the wave moments by the time they arrive. Alternatively, a blower, instead of a pump, was proposed to further improve the roll stabilization effect of the anti-roll tanks. A strategy in controlling the actuating pumps of an active U-tank with an adaptive inverse controller using filtered-x least mean square algorithm was outlined. Umeda et al. [188] evaluated experimentally two approaches for reducing parametric roll (large roll motion that might occur when a ship is moving in head or follower seas). The first is a sponson (floats attached to the side of a ship) and the other is a passive single U-tube ART with rectangular cross-section. The experiments were conducted using a free-running model of a 6600-TEU post-Panamax container

ship in regular head waves. The sponson was found to reduce the roll by decreasing the frequency of the roll-restoring moment. It reduced the roll from 20° to 15°. This is a modest reduction compared to that of the ART, which reduces the roll to about 1°. The ART lost its effectiveness beyond a wave amplitude of 0.148 m (corresponding to 14.8 m for the full-scale ship).

The U-tube tank can also be used for active ship roll mitigation. Yamaguchi and Shinkai [201] showed U-tube anti-roll tanks that had an impeller in the center of the cross tube. The system was found to effectively decrease the rolling angle over a wide frequency range and can cope with changes in motion characteristics by application of the adaptive control theory to the control of an activated anti-rolling tank device. Treakle [183] designed a PID controller for an on-board moving weight to mimic the motion of the fluid in an active anti-roll-tank system. The simulation results demonstrate that the moving weight system is very effective in reducing the ship roll motion. Chen et al. [34] also used the U-tube anti-roll tank with robust control. Adaptive ship roll mitigation by using a U-tube tank was considered by Phairoh and Huang [156, 157]. The active control of ship roll motion with proportional and derivative controller, linear quadratic regulator, generalized predictive control (GPC), and deadbeat predictive control, was adopted. For the predictive control, system identification was applied to update the parameters of linear ship roll model with U-tube tank when the ship dynamics changes. Numerical simulations demonstrated that the generalized predictive control has the best performance and the U-tube tank is effective in ship roll mitigation. Marzouk and Nayfeh [115, 116] studied the control of ships' roll dynamic behavior using passive and active anti-roll tanks in rough sea state 5 for multiple heading angles. Each the three U-tube tanks has a pump in the horizontal duct. The pumps were switched on for active ARTs but switched off for passive ones. It was found the active ARTs outperform the passive ones and their performance was found to be insensitive to their natural frequencies.

Holden et al. [75] considered an active tank and design the controller using Lyapunov theory. A nonlinear back-stepping controller was developed to provide global exponential stability of roll. U-tank models were considered to account for large roll angles, and the control design was evaluated using simulation on the high-fidelity model of a vessel under roll parametric resonance. Using a Lagrangian approach Holden et al. [76] developed five models of U-shaped anti-roll tanks (three nonlinear models and their linearized counter-parts (two of which are identical). The proposed models satisfy physical energy-related properties and are validated using data from 44 different experiments performed on a small-scale rig. It was found that the nonlinear terms in the models have a profound effect on the model performance, even at medium roll amplitudes. The Lagrangian approach was employed by Holden and Fossen [78] to develop a two degree-of-freedom (roll and tank fluid) model for a U-tank-equipped ship. A controller giving global exponential stability of the equilibrium position was developed for ships in parametric roll resonance. Using Hamiltonian mechanics Holden and Fossen [77] developed a nonlinear seven degrees of freedom model for ships equipped with a U-tank of arbitrary shape. The model can describe high-amplitude motions due to its nonlinearity and the coupling to all degrees of freedom. The active control of a ship roll angle of in still waters based on the utiliza-

tion of anti-roll tanks operated by pressurized air was considered by Haro et al. [71] who designed a nonlinear adaptive controller as a means of counteracting the parameter inaccuracies that are involved in the nonlinear model. The design is based on the back-stepping procedure. The controller provided a robust control system under parametric uncertainties and state variable errors. The designed control provided an improvement on the actual systems based on the proportional–integral–derivative (PID) control implemented under programmable logic controllers.

A section of a U-tube passive tank is shown in Fig. 1.27 which consists of two side reservoirs and a connecting duct of constant rectangular cross-section. The coordinate system shown is used to determine the motion of the liquid in the tank caused by the motion of the ship. The origin 0 is at the midpoint of the connecting duct and the axis y runs along the duct and up the reservoirs of the U-tube. The fluid velocity along the positive y direction (up the port reservoir) is v. Three additional axes are defined y_d has its origin at 0 and runs parallel to the duct, positive to port; y_{rp} and y_{rs} have their origins on the duct centerline and run parallel to the reservoir walls. For the case of pure ship roll motion, ϕ, in beam seas, around the CG of the ship, the equation of the tank angle τ, and the equation of motion of the ship roll oscillation, ϕ, take the form, (see, [60, 111])

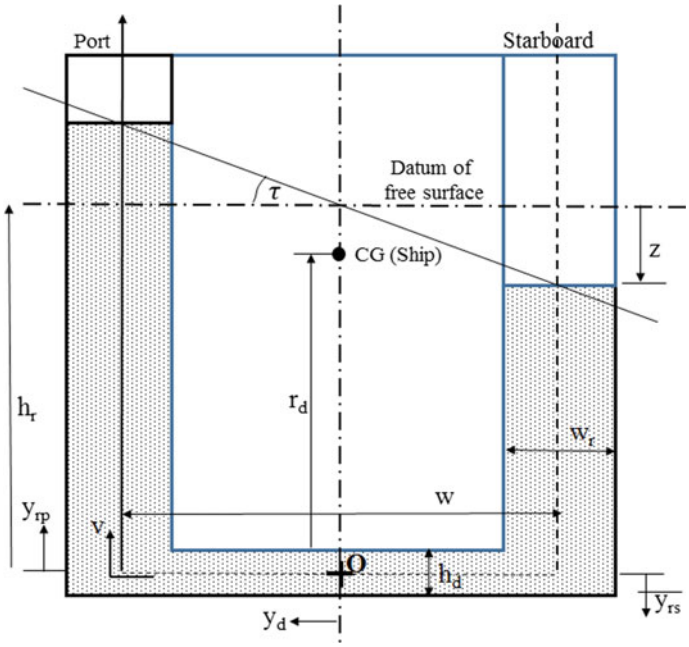

Fig. 1.27 Schematic diagram of U-tube tank considered by Gawad et al. [60]

$$\begin{bmatrix} a_{\tau\tau} & a_{\tau 4} \\ a_{4\tau} & A_{44} \end{bmatrix} \begin{Bmatrix} \ddot{\tau} \\ \ddot{\phi} \end{Bmatrix} + \begin{bmatrix} b_{\tau\tau} & 0 \\ 0 & b_{44} \end{bmatrix} \begin{Bmatrix} \dot{\tau} \\ \dot{\phi} \end{Bmatrix} + \begin{bmatrix} c_{\tau\tau} & c_{\tau 4} \\ c_{4\tau} & c_{44} \end{bmatrix} \begin{Bmatrix} \tau \\ \phi \end{Bmatrix} = \begin{Bmatrix} 0 \\ F\sin(\omega_e t) \end{Bmatrix} \tag{1.17a, b}$$

where subscript τ denotes tank, $a_{\tau 4} = Q_t(r_d + h_r)$, $c_{\tau 4} = Q_t g$, $a_{\tau\tau} = Q_t w_r\left(\frac{w}{2h} + \frac{h_r}{w_r}\right)$, $b_{\tau\tau} = Q_t q_v w_r\left(\frac{w}{2h_d^2} + \frac{h_r}{w_r^2}\right)$, $c_{\tau\tau} = Q_t g = c_{\tau 4}$, $Q_t = \frac{1}{2}\rho_t w_t w^2 x_t$, x_t is the length of the tank in the fore/aft direction), q_v is the coefficient of linear damping in the tank, A_{44} is the ship roll inertia, b_{44} is the ship roll damping coefficient, c_{44} is the ship roll restoring moment, $a_{4\tau} = a_{\tau 4}$, $c_{4\tau} = c_{\tau 4}$, F is the amplitude of the excitation roll moment acting on the ship, ω_e is the sea wave encounter frequency, and all other notations are indicated in Fig. 1.27. These equations are linearly differential equations with dynamic and static coupling, where the off-diagonal terms represent the influence of the ship motion on the liquid tank and vice versa. Since the excitation roll moment acting on the ship, the liquid in the U-tank will act as a linear vibration absorber (see, e.g., [43]).

The uncoupled natural frequency of the tank is

$$\omega_t = \sqrt{\frac{c_{\tau\tau}}{a_{\tau\tau}}} = \sqrt{\frac{2gh_d}{w_r w + 2h_r h_d}} \tag{1.18}$$

The ship roll natural frequency is

$$\omega_s = \sqrt{\frac{c_{44}}{a_{44}}} \tag{1.19}$$

Figure 1.28 shows the dependence of the ship roll response amplitude operator, $\phi/(h/\lambda)$, where h is the sea wave height and λ is the sea wave length, on the wave encounter frequency ratio, ω_e/ω_s, for different values of tank damping ratio parameter, $b_{\tau\tau}/(2a_{\tau\tau}\omega_s) = 0, 0.08, 0.17$, and 0.26, as well as the case of no tank. It is seen that optimal performance is achieved when the corresponding damping parameter is 0.17, which results in a reduction of the roll ship amplitude to about 1/3 of the non-stabilized case.

Youssef et al. [203, 204] developed design procedures for passive U-tube tanks for roll reduction in rough seas. The tank-liquid equation of motion was integrated simultaneously with the six-degree-of-freedom equations of the ship motion. The nonlinear coupled set of equations was solved by using the Large Amplitude Motion Program (LAMP), which is a three-dimensional time-domain simulation of the motion of ships in waves. For high-amplitude waves, the roll angle was found to exhibit typical nonlinear phenomena such as a shift in the resonance frequency, multi-valued responses, and jumps. The performance of a S60-70 ship with a passive tank was investigated in various sea states with different encounter wave directions. It was found that passive anti-roll tanks tuned in the linear or nonlinear ranges are very effective in reducing the roll motion in the nonlinear range. Their study revealed that passive anti-roll tanks are very effective in reducing the roll motion for ships having

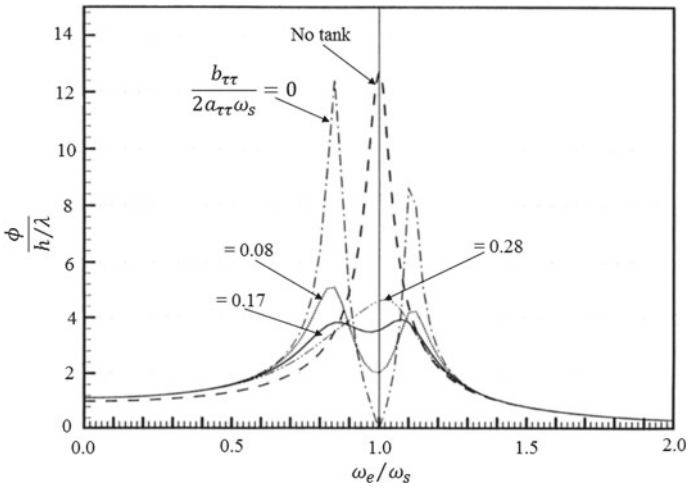

Fig. 1.28 Dependence of the ship roll response amplitude operator, $\phi/(h/\lambda)$, (h is the sea wave height, and λ is sea wave length) on the encounter frequency ratio, $\frac{\omega_e}{\omega_s}$, ($\omega_s$ is the ship roll natural frequency) for the tank mass ratio of 2.0% of the ship mass and for different values of tank damping coefficient parameter $\frac{b_{\tau\tau}}{2a_{\tau\tau}\omega_s}$ [60]

a pitch frequency that is nearly twice the roll frequency in sea states 5 (rough) and 6 (very rough).

Without the U-tube tanks, Fig. 1.29 shows the dependence of the roll amplitude of a S60-70 ship on the encounter frequency ratio, ω_e/ω_s, where ω_s is the ship roll natural frequency in beam waves for different values of wave amplitude ratio (wave

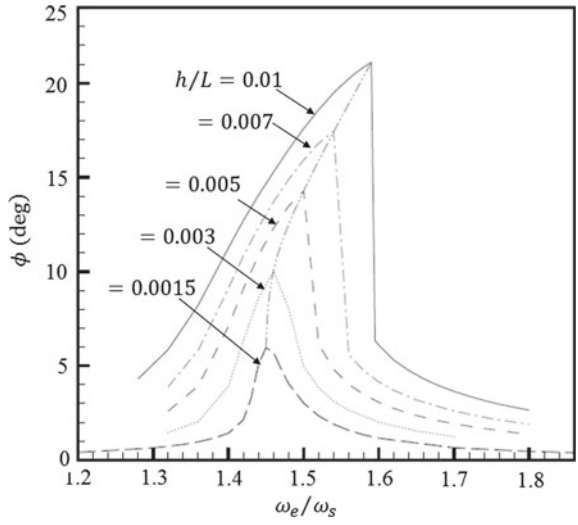

Fig. 1.29 Dependence of ship roll amplitude on the wave encounter frequency for different wave amplitude ratios for the case of a ship without U-tanks [204]

amplitude to ship length) $h/L = 0.01, 0.007, 0.005, 0.003,$ and 0.0015. It is seen that for low wave amplitude ratio 0.0015, the response is single-valued and linear. The response curves bend to the right as the wave amplitude increases, indicating a hardening type nonlinearity. The peak amplitude increases with increasing wave amplitude. The backbone curve indicates that the nonlinearity shifts the resonance frequency to higher values. The influence of the mass of the liquid in the tank on the performance of the tank/ship system was studied in the nonlinear range in a beam wave with an amplitude equal to 0.01. Youssef et al. [204] considered a tank system with three tubes for three different values of the tank/ship mass ratio (0.7, 1.4, and 2.1%). Figure 1.30 shows the dependence of the ship roll angle on the encounter wave frequency ratio. This figure reveals that the best performance is obtained for a tank/ship mass ratio = 2.1%.

The performance of the three-tube passive tank for the 6DOF ship motion was studied for the case sea state five. The incoming wave was represented as the linear superposition of sinusoids, which is an approximation to the nonlinear free surface problem in the absence of the ship, and hence it does not capture the influence of the ship on the incoming wave. The natural frequency of the tank was taken to be 1.59 to match the frequency at which the maximum roll amplitude occurs for the unstable ship at a wave amplitude ratio of 0.01.

The ship roll time history responses for beam and head seas are shown in Fig. 1.31 and Fig. 1.32, respectively. It is seen that a tuned passive tank significantly damps the roll motion in beam and head seas. One can notice from Fig. 1.32 that the unstable roll angle increases significantly for head waves in sea state five. This is because the head waves excite the pitch mode in primary resonance, and in turn the pitch mode excites the roll mode via a two-to-one internal or autoparametric resonance (the natural frequencies of pitch and roll are in the ratio of two-to-one). Inspecting the time

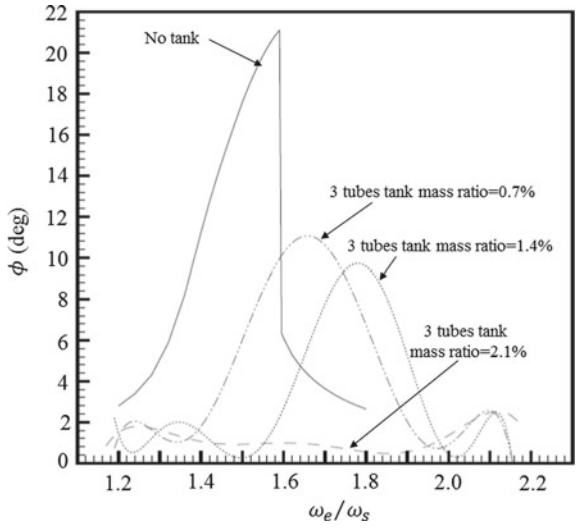

Fig. 1.30 Dependence of ship roll amplitude on the wave encounter frequency for different values of U-tank mass ratio in the nonlinear range in a beam sea wave amplitude ratio of 0.01 [204]

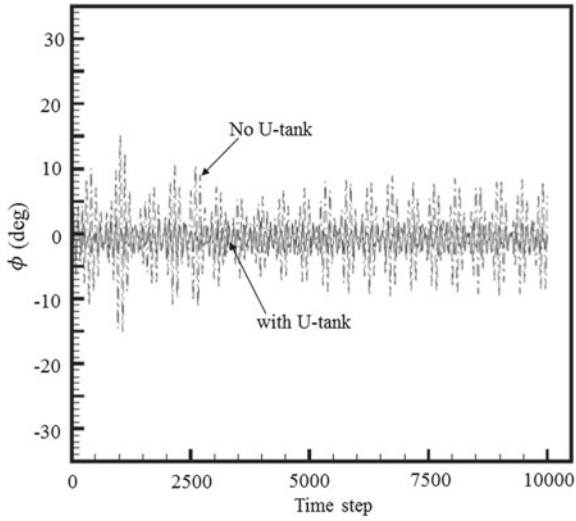

Fig. 1.31 Ship roll time history response records in an irregular beam sea state 5, with and without U-tank [204]

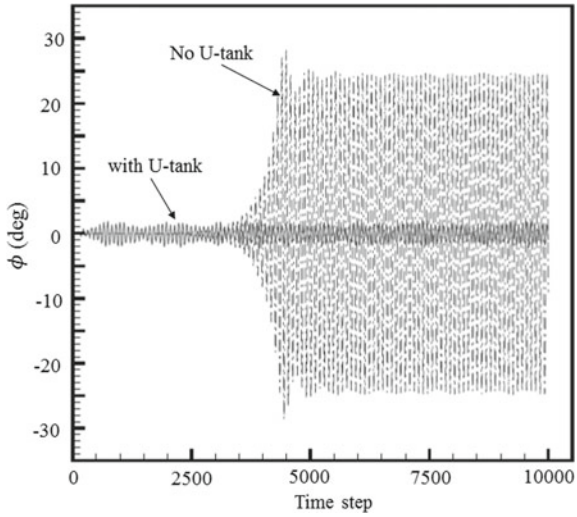

Fig. 1.32 Ship roll time history response records in an irregular head sea state 5, with and without U-tank [204]

histories of the unstable roll and pitch motions for sea state five in Figs. 1.32 and 1.33, one can identify the two-to-one resonance: the pitch response is synchronized to the wave frequency and the roll response is synchronized to one-half the wave frequency. The high roll amplitude of the unstable S60-70 ship is significantly damped by using the tuned passive tank, as shown in Fig. 1.32.

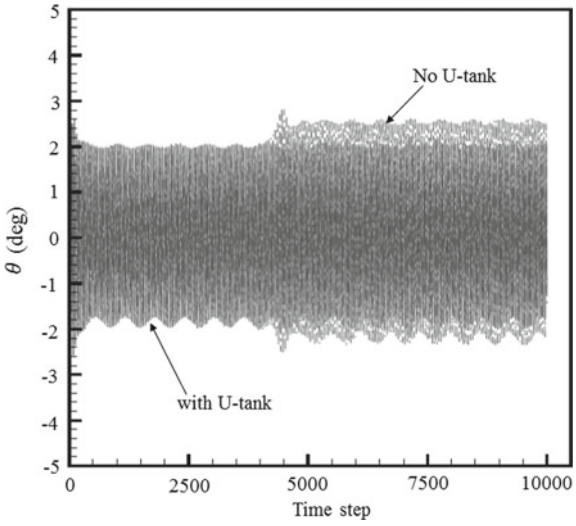

Fig. 1.33 Ship pitch time history response records in an irregular head sea state 5, with and without U-tank [204]

1.6 Conclusions

Parametric roll resonance and autoparametric of ship roll-pitch interaction together with ship interaction with liquid sloshing of LNG carriers have been described. The mechanism of parametric roll resonance were mainly of two sources. The first is due to the time variation of the ship righting arm in waves of length nearly equal to the ship length associated with an increase in the righting arm when a wave is near amid-ship. On the other hand, the stability is reduced when a wave crest occurs is near amidships. The second is due to the fact the ship roll motion is coupled with its pitching motion. This can create either parametric resonance or autoparametric interaction due to internal resonance. Under random sea waves the different approaches were introduced such as Grim's effective eave concept and stochastic dynamic schemes. The interaction between liquid sloshing in ship tanks and ship motion is significant as the ratio of volume of the tanks to that of the ship exceeds a critical value. The coupling effect between liquid cargo sloshing and LNG ship motion can be significant at certain partial filling levels. Depending on the phase angle between the liquid sloshing and the ship roll motion, the liquid sloshing can be beneficial to the ship roll stability or can cause ship capsizing. The beneficial effect was the realized by ship builders and designers long time ago and motivated them to introduce the anti-roll tanks in the form of either free surface ART or U-tube ART.

References

1. B. Abeil, Experimental prediction of anti-roll tanks on the rolling of ships, in *Proceedings of 13th International Symposium on PRActical Design of Ships and Other Floating Structures (PRADS 2016)* (Copenhagen, Denmark, 2016), Paper ID 146
2. H.N. Abramson, R.L. Bass, O. Faltinsen, H.A. Olsen, Liquid slosh in LNG carriers, in *10th Symposium on Naval Hydrodynamics* (Boston, 1974), pp. 371–388
3. ABS, Assessment, *of Parametric Roll Resonance in the Design of Container Carriers (American Bureau of Shipping* (, Houston, Texas, USA, 2004)
4. ABS, *Strength Assessment of Membrane-type LNG Containment Systems under Sloshing Loads* (Amer Bureau of Shipping, Houston, Texas, 2006)
5. ABS, *Guidance Notes on Strength Assessment of Membrane-Type LNG Containment Systems Under Sloshing Loads* (Amer Bureau of Shipping, Houston, Texas, 2009), p. 90
6. B. Arndt, S. Roden, Stabilitiit bei vor- und achterlichem Seegang (Stability in fore and aft seas). Schiffstechnik **5**(29), 192–199 (1958)
7. D.W. Bass, Roll stabilization for small fishing vessels using paravanes and anti-roll tanks. Mar. Technol. **35**(2), 74–84 (1998)
8. V.L. Belenky, Probabilistic approach for intact stability standards: State of the art review and related problems. Trans. Soc. Nav. Archit. Mar. Eng. **108**, 123–146 (2000)
9. V.L. Belenky, A.B. Degtyarev, A.V. Boukhanovsky, Probabilistic qualities of severe ship motions, in *Proceedings of 6th International Conference on Stability of Ships and Ocean Vehicles*, vol. 1 (Varna, Bulgaria, 1997), pp. 163
10. V.L. Belenky, A.B. Degtyarev, A.V. Boukhanovsky, Probabilistic qualities of nonlinear stochastic rolling. Ocean Eng. **25**(1), 1–25 (1998)
11. V.L. Belenky, N.B. Sevastianov, *Stability and Safety of Ships: Risk of Capsizing*, vol. 2 (Elseveir, Amsterdam, 2003)
12. V.L. Belenky, K.M. Weems, W.M. Lin, J.R. Paulling, Probabilistic analysis of roll parametric resonance in head sea, in *Proceedings of 8th International Conference on Stability of Ships and Ocean Vehicles*, Escuela Técnica Superior de Ingenieros Navales (Madrid, 2003), pp. 337–339
13. V.L. Belenky, H.C. Yu, K. Weems, Numerical Procedures and practical experience of assessment of parametric roll of container carriers, in *Proceedings of 9th International Conference on Stability of Ships and Ocean Vehicle*, vol. 1 (Rio de Janiro, Brazil, 2006), pp. 119–130
14. V. Belenky, H.C. Yu, K. Weems, Numerical procedures and practical experience of assessment of parametric roll of container carriers, in *Contemporary Ideas on Ship Stability and Capsizing in Waves* (Springer, Berlin, 2011), pp. 295–305
15. V.L. Belenky, K.M. Weems, Probabilistic analysis of roll parametric resonance in head seas, *Parametric Resonance in Dynamical Systems* (Springer, Berlin, 2011), pp. 555–569
16. V. Belenky, C.G. Bassler, K.J. Spyrou, Development of second generation intact stability criteria, Naval Surface Warfare Center Carderock Div., Bethesda, MD. Hydromechanics Directorate, Report: NSWCCD-50-TR-2011/065 (2011), p. 175
17. J. Bell, W.P. Walker, Activated and passive controlled fluid tank system for ship stabilization. SNAME Trans. **74**, 150–193 (1966)
18. W. Blocki, Ship safety in connection with parametric resonance of the roll. Int. Shipbuild. Prog. **27**(306), 36–53 (1980)
19. J.J. van den Bosch, J.H. Vugts, Roll damping by free surface tanks, Report No 83S (Shipbuilding Laboratory of the Technical University of Delft, 1966)
20. G. Bulian, Development of analytical nonlinear models for parametric roll and hydrostatic restoring variations in regular and irregular waves. Ph.D. Thesis, University of Trieste, Trieste, Italy, 2006
21. G. Bulian, A. Francescutto, C. Lugni, On the nonlinear modeling of parametric rolling in regular and irregular waves, in *Proceedings of 8th International Stability of Ships and Ocean Vehicles*, Escuela Técnica Superior de Ingenieros Navales (2003), pp. 305–323
22. G. Bulian, A. Francescutto, On the effect of stochastic variations of restoring moment in long-crested irregular longitudinal sea. Int. Shipbuid. Prog. **54**(4), 227–248 (2007)

23. G. Bulian, A. Francescutto, C. Lugni, Theoretical, numerical and experimental study on the problem of ergodicity and 'practical ergodicity' with an application to parametric roll in longitudinal long crested irregular sea. Ocean Eng. **33**(8–9), 1007–1043 (2006)
24. Bureau Veritas, Sloshing on Board Ship-Partial filling Study, Guidance Note N.I. 171 ARD.1 (Paris, France, 1984)
25. Bureau Veritas, Sloshing Assessment–Partial Fillings of Membrane Type LNG Carriers and Offshore Floating Units, Preliminary Guidelines, Rev. 1, (Paris, France, 2005)
26. W. Burger, A.G. Corbet, *Ship Stabilizers: A Handbook for Merchant Navy Officers* (Pergamon Press/Elsevier, New York, 1966)
27. Z.H. Cai, D.Y. Wang, Z. Li, Numerical simulation and experimental study of sloshing in a liquefied natural gas tank (in Chinese). J. Shanghai Jiaotong Univ. **43**(10), 1559–1563 (2009)
28. N. Carette, A study of the response to sway motions of free surface anti-roll tanks, in *Proceedings of World Maritime Conference (WMTC)* (Providence, Rohde Island, 2015), Paper #133
29. N. Carette, R.P. Dallinga, G.K. Kapsenberg, On the design of anti-roll tanks, in *Proceedings of 13th International Symposium on PRActical Design of Ships and Other Floating Structures (PRADS 2016)* (Copenhagen, Denmark, 2016), Paper ID030
30. S.M. Carmel, Study of parametric rolling event on a panamax container vessel. J. Transp. Res. Board **1963**, 56–63 (2006)
31. J.L. Cercos-Pita, G. Bulian, L. Pérex-Rojas, A. Francescutto, Coupled simulation of nonlinear ship motions and free surface tanks, in *Proceedings of 12th International Conference on Stability of Ships and Ocean Vehicles* (Glasgow, U.K., 2015), pp. 1050–1061. Also, Ocean Eng. **120**, 281–288 (2016)
32. J.H. Chadwick, Anti-roll stabilization of ships by means of activated tanks. Part C. Synthesis of high performance systems, Report TR-15 (Div of Engineering Mechanics, Stanford University, CA, 1951), p. 90
33. J.H. Chadwick, K. Klotter, On the dynamics of anti-roll tanks. Schiffstechnik **2**, 23–45 (1954)
34. S.L. Chen, S.W. Shaw, H.K. Khalil, A.W. Troesch, Robust stabilization of large amplitude ship rolling in beam seas. ASME J. Dyn. Syst. Meas. Control **122**(1), 108–113 (2000)
35. X.B. Chen, Hydrodynamics in offshore and naval applications, in *Proceedings of 6th International Conference on Hydrodynamics* (Perth, Australia, 2004)
36. X.B. Chen, Hydrodynamic analysis for offshore LNG terminals, in *Proceedings of 2nd International Workshop on Applied Offshore Hydrodynamics* (Rio de Janeiro, Brazil, 2005)
37. G.F. Clauss, D. Testa, F. Sprenger, Coupling effects between tank sloshing and motions of a LNG carrier, in *Proceedings of 29th ASME International Conference on Offshore Mechanics and Arctic Engineering (OMAE)*, vol. 1 (Shanghai, China, 2010), pp. 75–82
38. P.A. Cox, E.B. Bowles, R.L. Bass, *Evaluation of Liquid Dynamic Loads in Slack LNG Cargo Tanks*, Ship Structure Committee SSC-297 (Southwest Research Institute, San Antonio, Texas, 1980)
39. C.R. Crockett, Passive anti-roll tanks, Report: DDS-9290-4; DDS-565-1 (Bureau of Ships, Washington, DC, 1962), p. 21
40. R.P. Dallinga, J.J. Blok, H.R. Luth, Excessive rolling of cruise ships in head and following waves, in *Proceedings of RINA International Conference on Ship Motions and Manoeuvrability* (Royal Institute of Naval Architects, London, UK, 1998)
41. J.F. Dalzell, W.H. Chu, J.E. Modisette, Studies of ship roll stabilization tanks, SWRI, Technical Report 1 (San Antonio, Texas, 1964)
42. J. Delaunay, Numerical simulation of motion stabilization by U-tube anti-roll tanks using CFD. Master's thesis, Universite de Bretagne Occidentale, Brest, Brittany, France, 2012
43. J.P. Den Hartog, *Mechanical Vibrations* (Dover Publications Inc, New York, 1985)
44. L. Dostal, E. Kreuzer, Probabilistic approach to large amplitude ship rolling in random seas. Proc. Inst. Mech. Eng. C J. Mech. Eng. Sci. **225**(C10), 2464–2476 (2011)
45. L. Dostal, E. Kreuzer, Non-stationary probability of parametric roll of ships in random seas, in *Proceedings of 5th International Conference on Computational Methods in Marine Engineering* (Hamburg, Germany, 2013), pp. 772–780

46. A.B. Dunwoody, Roll of a ship in Astern Seas—Metacentric height spectra. J. Ship Res. **33**, 221–228 (1989)
47. A.B. Dunwoody, Roll of a ship in Astern Seas—Response to GM fluctuations. J. Ship Res. **33**, 284–290 (1989)
48. O.M. Faltinsen, H.A. Olsen, H.N. Abramson, R.L. Bass, *Liquid Slosh in LNG Carriers* (Det Norske Veritas, Norway, 1974). Publication No 85
49. O.M. Faltinsen, A.N. Timokha, *Sloshing* (Cambridge University Press, Cambridge, U.K., 2009)
50. S.B. Field, J.P. Martin, Comparative effects of U-tube and free surface type passive roll stabilization systems. R. Inst. Nav. Arch. **2**, 73–92 (1976)
51. C.G. Filstead Jr., The design and operation of LNG ships with regard to safety. Shipp. World Shipbuild. **165**(3866), 259–262 (1972)
52. H. Frahm, Results of trials of the anti-rolling tanks at sea. Transact. Inst. Nav. Archit. **53**, 183–197 (1911)
53. W.N. France, M. Levadou, T.W. Treakle, J.R. Paulling, R.K. Michel, C. Moore, An investigation of head-sea parametric rolling and its influence on container lashing systems, in *Proceedings of SNAME Annual Meeting* (Orlando, FL, 2003), p. 24. Also Mar. Technol. **40**(1), 1–19 (2003)
54. A. Francescutto, An experimental investigation of parametric rolling in head waves. ASME J. Offshore Mech. Arct. Eng. **123**(2), 65–69 (2001)
55. A. Francescutto, G. Contento, An experimental study of the coupling between roll motion and sloshing in a compartment, in *Proceedings of International Society of Offshore and Polar Engineers Conference*, vol. 3 (Osaka, Japan, 1994), pp. 283–288
56. A. Francescutto, G. Bulian, C. Lugni, Nonlinear and stochastic aspects of parametric rolling modeling. Mar. Technol. **41**(2), 74–81 (2004)
57. W. Froude, On the rolling of ships. Trans. Inst. Nav. Arch. **2**, 180–227 (1861)
58. W. Froude, Remarks on Mr. Scott Russel's paper on rolling. Trans. Inst. Nav. Archit. **4**, 232–275 (1862)
59. D.D. Gao, T.L. Li, J.M. Hu, D. Guo, Research on numerical simulation of sloshing motions for anti-rolling tank (in Chinese). J. Dalian Univ. Technol. **54**(5), 537–542 (2014)
60. A.F. Gawad, S. Ragab, A.H. Nayfeh, D.T. Mook, Roll stabilization by anti-roll passive tanks. Ocean Eng. **28**, 457–469 (2001)
61. S.J. Gong, Design of anti-roll tanks and study of sloshing phenomenon by meshes method. Navig. China **36**(4), 147–151 (2013)
62. Y. Gou, Y. Kim, T.Y. Kim, A numerical study on coupling between ship motions and sloshing in frequency and time domains, in *Proceedings of 21st International Ocean and Polar Engineering (ISOPE) Conference*, vol. 8 (Maui, Hawaii, 2011), pp. 158–164
63. W. Graff, E. Heckscher, Widerstand und Stabilität Versuche mit Drei Fischdampfer Modellen (Resistance and Stability Tests with Three Fish Steamer Models). Werft Reederei Hafen **22**, 115–120 (1941)
64. O. Grim, Das Schiff in von achtern mitlaufender Sea (The ship in astern of the lake), Hamburg. Trans. STG **45**, 264–287 (1951)
65. O. Grim, Rollschwingungen, Stabilitiit und Sicherheit im Seegang (Roll vibration, stability and safety in the sea) Schiffahrts-Verlag Hansa, *Schiffstechnik* **1**(1), 10–21 (1952)
66. O. Grim, Beitrag zu dem Problem der Sicherheit des Schiffes im Seegang (Contribution to the problem of the safety of the ship in the sea). Schiff und Hafen, Helft **6**, 490–491 (1961)
67. M. Gunsing, N. Carette, G. Kapsenberg, Experimental data on the systematic variation of the internal damping inside a U-shaped anti-roll tank, in *Proceedings of 33rd International Conference on Offshore Mechanical and Arctic Engineering*, vol. 7 (San Francisco, California, 2014), p. 10
68. A.G. Haddow, A.D.S. Barr, D.T. Mook, Theoretical and experimental study of modal interaction in a two-degree-of-freedom structure. J. Sound Vibr. **97**, 451–473 (1984)
69. P.A. Hamill, *A note on the rolling of ships and stabilizing systems, particularly anti-roll tanks*, Ship Section, Division of Mechanical Engineering, Technical University of Delft (1965), p. 9. http://mararchief.tudelft.nl/file/22534

70. N.A. Hamlin, *Liquid Slosh Loading in Slack Ship Tanks: Forces on Internal Structure & Pressures*, Ship Structure Committee SSC-336, 1990: *Liquid Sloshing in Cargo Tanks* (Washington, D.C, 1986), p. 123
71. M. Haro, R. Ferreiro, F.J. Velasco, Ship's roll stabilization by anti-roll active tanks, in *Proceedings of OCEANS 2011 Conference* (Santander, Spain, 2011), p. 10
72. H. Hashimoto, N. Umeda, A. Matsuda, S. Nakamura, Experimental and numerical study on parametric roll of a post-panamax containership in irregular waves, in *Proceedings of 9th International Stability of Ships and Ocean Vehicles*, vol. 1 (2006), pp. 181–190
73. H. Hashimoto, N. Umeda, Y. Ogawa, H. Taguchi, T. Iseki, G. Bulian, N. Toki, S. Ishida, A. Matsuda, Prediction methods for parametric rolling with forward velocity and their validation: final report of SCAPE Committee (Part 2), in *Proceedings of 6th Osaka Colloquium on Seakeeping and Stability of Ships* (2008), pp. 265–275
74. R.S. Haxton, A.D.S. Barr, Autoparametric vibration absorber. ASME J. Eng. Indust. Ser. B **94**, 119–125 (1972)
75. C. Holden, R. Galeazzi, T. Perez, T.I. Fossen, Stabilization of parametric roll resonance with active U-tanks via lyapunov control design, in *Proceedings of the 10th European Control Conference* (Budapest, Hungary, 2009)
76. C. Holden, T. Perez, T.I. Fossen, A lagrangian approach to nonlinear modeling of anti-roll tanks. Ocean Eng. **38**(2–3), 341–359 (2011)
77. C. Holden, T.I. Fossen, A nonlinear 7-DOF model for U-tanks of arbitrary shape. Ocean Eng. **45**, 22–37 (2012)
78. C. Holden, T.L. Fossen, A U-tank control system for ships in parametric roll resonance, *Parametric Resonance in Dynamical Systems* (Springer, Berlin, 2012), pp. 239–263
79. M. Honkanen, Tests and design data of tank stabilizers of the free-surface type. Technical Report 6 (Helsinki University of Technology, Helsinki, Finland, 1971)
80. J. Hua, M. Palmquist, G. Lindgren, An analysis of the parametric roll events measured onboard the PCTC AIDA, in *Proceedings of 9th International Stability of Ships and Ocean Vehicles* (2006), pp. 109–118
81. R.A. Ibrahim, *Parametric Random Vibration* (Wiley, New York, 1985)
82. R.A. Ibrahim, *Liquid Sloshing Dynamics: Theory and Applications* (Cambridge University Press, Cambridge, U.K., 2005)
83. R.A. Ibrahim, Recent advances in physics of fluid parametric sloshing and related problems. ASME J. Fluids Eng. **137**(9), 090801, 52 (2015)
84. R.A. Ibrahim, *Handbook of Structural Life Assessment* (John Wiley, London, U.K., 2017)
85. R.A. Ibrahim, I.M. Grace, Modeling of ship roll dynamics and its coupling with heave and pitch. Math. Prob. Eng. **2010**, 934714, 32 (2010)
86. A.S. Iglesias, L.P. Rojas, R.Z. Rodriguez, Simulation of anti-roll tanks and sloshing type problems with smoothed particle hydrodynamics. Ocean Eng. **31**(8–9), 1169–1192 (2004)
87. S.C. Jiang, B. Ting, W. Bai, Y. Gou, Numerical simulation of coupling effect between ship motion and liquid sloshing under wave action. Ocean Eng. **108**, 140–154 (2015)
88. H.Z. Jin, H.H. Zhang, C.H. Ben, Improved dual tank anti-rolling system for ships (in Chinese). J. Harbin Eng. Univ. **29**(3), 242–246, 250 (2008)
89. J.M.J. Journée, Liquid cargo and its effect on ship motions, in *Proceedings of 6th International Conference on Stability of Ships and Ocean Structures (Stab'97)* (Varna, Bulgaria, 1997), pp. 22–27
90. G. Kempf, Die Stabilität Beanspruchung der Schiffe Durch Wellen und Schwingungen (The stability stress of the ships by waves and vibrations). Werft Reederei Hafen **19**, 200–202 (1938)
91. M. Kerkvliet, G. Vaz, N. Carette, M. Gunsing, Analysis of U-type anti-roll tank using RANS, sensitivity and validation, in *Proceedings of ASME 33rd International Conference on Ocean, Offshore and Artic Engineering*, OMAE2014-23483 (San Francisco, CA, 2014), p. 10
92. M. Kerkvliet, N. Carette, O. Van Straten, Analysis of free surface anti-roll tank using URANS, verification and validation, in *Proceedings of 13th International Symposium on PRActical Design of Ships and Other Floating Structures* (Copenhagen, Denmark, 2016), Paper ID055

93. J.E. Kerwin, Notes on rolling in longitudinal waves. Int. Shipbuild. Prog. **2**(16), 597–614 (1955)
94. K.S. Kim, B.H. Lee, M.H. Kim, J.C. Park, H.S. Choi, A study of anti-rolling tank on floating vessel, in *Proceedings of 35th ASME International Conference on Offshore Mechanics and Arctic Engineering*, vol. 7 (Busan, Korea, 2016), p. 6
95. Y. Kim, A numerical study on sloshing flows coupled with ship motion: the anti-rolling tank problem. J. Ship Res. **46**(1), 56–62 (2002)
96. Y. Kim, B.W. Nam, D.W. Kim, Y.S. Kim, Study on coupling effects of ship motion and sloshing. Ocean Eng. **34**(16), 2176–2187 (2007)
97. Y.H. Kim, H.G. Sung, S.K. Cho, H.S. Choi, The sloshing effect on the roll motion and 2-DoF motions of a 2D rectangular cylinder. J. Soc. Nav. Archit. Korea **50**(2), 69–78 (2013)
98. W.D. Kinney, *On the Unstable Rolling Motions of Ships Resulting from Nonlinear Coupling with Pitch Including the Effect of Damping in Roll, Series 173, Issue 3* (Institute of Engineering Research, University of California, Berkeley, California, 1961)
99. K.S. Kula, An overview of roll stabilizers and systems for their control. Trans. Nav. Int. J. Mar. Navig. Saf. Sea Transp. **9**(3), 405–414 (2015)
100. B.S. Lee, D. Vassalos, An investigation into the stabilization effects of anti-roll tanks with flow obstructions. Int. Shipbuild. Prog. **43**(433), 70–88 (1996)
101. D.Y. Lee, H.S. Choi, Study on sloshing in cargo tanks including hydroelastic effects. J. Mar. Sci. Technol. **4**, 27–34 (1999)
102. S.J. Lee, M.H. Kim, D.H. Lee, Y.S. Shin, Y.H. Kim, The effects of LNG-tank sloshing on the roll responses of LNG-carriers, in *Proceedings of 16th International Conference on Offshore and Polar Engineering (ISOPE)* (California, San Francisco, 2006), pp. 212–218
103. S.J. Lee, M.H. Kim, D.H. Lee, Y.S. Shin, The effects of tank sloshing on LNG-ship responses, in *Proceedings of 26th ASME International Offshore Mechanical and Arctic Engineering Conference* (San Diego, USA, 2007)
104. S.J. Lee, M.H. Kim, D.H. Lee, J.W. Kim, Y.H. Kim, The effects of LNG-tank sloshing on the global motions of LNG carriers. Ocean Eng. **34**(1), 10–20 (2007)
105. S.J. Lee, M.H. Kim, The Effects of inner-liquid motion on LNG vessel responses. ASME J. Offshore Mech. Arct. Eng. **132**(2), 021101-8 (2010)
106. M.L. Levadou, R. Van't Veer, Parametric roll and ship design, in *Proceedings of 9th International Conference on Stability of Ships and Ocean Vehicles*, vol. 1 (Rio de Janeiro, Brazil, 2006), pp. 191–206
107. J.M. Lew, H. Kim, B.J. Choi, Development of passive and active anti-rolling tanks, in *Proceedings of 5th International Society of Offshore and Polar Engineers, Pacific/Asia Offshore Mechanics Symposium*, ISOPE-P-02-023 (Daejeon, Korea, 2002), p. 6
108. G.R.G. Lewison, Optimum design of passive roll stabilizer tanks, RINA Trans and Annual Report (1976), pp. 31–45
109. Y. Li, Computional fluid dynamics(CFD) study on free surface anti-roll tank and experimental validation. Master Thesis, Aalesund University College, Norway, 2015
110. Y. Li, K.H. Halse, J.F. Xu, Sloshing flows in a free surface anti-roll tank—Numerical simulations and experimental validation, in *Proceedings of 13th International Symposium on PRActical Design of Ships and Other Floating Structures* (Denmark, Copenhagen, 2016), p. 8
111. A.R.J.M. Lloyd, *Sea Keeping-Ship Behavior in Rough Weather* (Ellis Horwood Limited, Chichester, U.K., 1989)
112. A.P. Lui, Y.K. Lou, Dynamic coupling of a liquid tank system under transient excitations. Ocean Eng. **17**(3), 263–277 (1990)
113. H.R. Luth, R.P. Dallinga, Prediction of excessive rolling of cruise vessels in head and following waves, in *Proceedings of 7th International Symposium on Practical Design of Ships and other Floating Structures Conference*, vol. 11 (The Hague, 1999), pp. 625–632
114. Ŝ. Malenica, M. Zalar, X.B. Chen, Dynamic coupling of seakeeping and sloshing, in *Proceedings of 13th International Offshore and Polar Engineering Conference* (Hawaii, 2003), p. 7

115. O.A. Marzouk, A.H. Nayfeh, Mitigation of ship motion using passive and active anti-roll tanks, in *Proceedings of ASME International Design Engineering Technical Conference and Computers and Information in Engineering Conference*, DETC2007-35571, vol. 1 (Las Vegas, Nevada, 2007), pp. 215–229
116. O.A. Marzouk, A.H. Nayfeh, Control of ship roll using passive and active anti-roll tanks. Ocean Eng. **36**, 661–671 (2009)
117. N.W. McLachlan, *Theory and Applications of Mathieu Functions* (Oxford University Press, New York, 1947)
118. J.J. McMullen, Ship stabilization: The growing demand and the economic case for flume stabilization, in *The Motor Ship* (1967), pp. 541–542
119. N.E. Mikelis, J.M.J. Journee, Experimental and numerical simulations of sloshing behavior in liquid cargo tanks and its effect on ship motions, in *Proceedings of National Conference on Numerical Methods for Transient and Coupled Problems* (Venice, Italy, 1984), pp. 9–13
120. N. Minorsky, Problems of anti-rolling stabilization of ships by the activated tank method. Am. Soc. Nav. Eng. **47**, 87 (1935)
121. S. Mitra, C.Z. Wang, J.N. Reddy, B.C. Khoo, A 3D fully coupled analysis of nonlinear sloshing and ship motion. Ocean Eng. **39**, 1–13 (2011)
122. S. Mitra, L.V. Hai, L. Jing, B.C. Khoo, A fully coupled ship motion and sloshing analysis in various container geometries. J. Mar. Sci. Technol. **17**(2), 139–153 (2012)
123. R. Moaleji, Adaptive control for ship roll stabilization using anti-roll tanks. Ph.D. Thesis, University College London, Dept Mech Eng, London, UK, 2006
124. R. Moaleji, A.R. Greig, Inverse control for roll stabilization of ships using active tanks, in *Proceedings of 7th IFAC Conference on Manoeuvring and Control of Marine Craft* (Lisbon, 2006)
125. R. Moaleji, A.R. Greig, Roll reduction of ships using anti-roll n-tanks, in *Proceedings of World Maritime Conference* (London, 2006)
126. R. Moaleji, A.R. Greig, On the development of anti-roll tanks. Ocean Eng. **34**, 103–121 (2007)
127. B. Molin, F. Remy, S. Rigaud, Ch. de Jouette, LNG FPSO's: frequency domain, coupled analysis of support and liquid cargo motion, in *Proceedings of 10th International Maritime Association of the Mediterranean Conference* (Rethymnon, Greece, 2002), p. 8
128. D.T. Mook, L.R. Marshall, A.H. Nayfeh, Subharmonic and superharmonic resonances in the pitch and roll modes of ship motions. J. Hydronaut. **8**(1), 32–40 (1974)
129. B.W. Nam, Y. Kim, Effect of sloshing on the motion response of LNG—FPSO in waves, in *Proceedings of 22nd Workshop on Water Waves and Floating Bodies* (Plitviz, Croatia, 2007), p. 4
130. B.W. Nam, Y. Kim, D.W. Kim, Y.S. Kim, Experimental and numerical studies on ship motion responses coupled with sloshing in waves. J. Ship Res. **53**(2), 68–82 (2009)
131. T. Nasar, S.A. Sannasiraj, V. Sundar, Experimental study of liquid sloshing dynamics in a barge carrying tank. Fluid Dyn. Res. **40**, 427–458 (2008)
132. T. Nasar, S.A. Sannasiraj, V. Sundar, Sloshing pressure variation in a barge carrying tank. Ships Offshore Struct. **3**(3), 185–203 (2008)
133. T. Nasar, S.A. Sannasiraj, V. Sundar, Wave induced sloshing pressure in a liquid tank under irregular waves. Part M J. Eng. Marit. Environ. **223**(2), 145–161 (2008)
134. T. Nasar, S. Sannasiraj, V. Sundar, Motion responses of barge carrying liquid tank. Ocean Eng. **37**, 935–946 (2010)
135. T. Nasar, S. Sannasiraj, V. Sundar, Liquid sloshing dynamics in a barge carrying container subjected to random wave excitation. J. Nav. Archit. Mar. Eng. **9**, 43–65 (2012)
136. A.H. Nayfeh, On the undesirable roll characteristics of ships in regular seas. J. Ship Res. **32**(2), 92–100 (1988)
137. A.H. Nayfeh, D.T. Mook, L.R. Marchall, Nonlinear coupling of pitch and roll modes in ship motions. J. Hydronaut. **7**(4), 145–152 (1973)
138. A.H. Nayfeh, D.T. Mook, L.R. Marshall, Perturbation energy approach for the development of the nonlinear equations of ship motion. J. Hydronaut. **8**(4), 130–136 (1974)

139. M.A.S. Neves, N. Pérez, O. Lorca, Experimental analysis on parametric resonance for two fishing vessels in head seas, in *Proceedings of 6th International Ship Stability Workshop* (Webb Institute, NY, USA, 2002)
140. M.A.S. Neves, C.A. Rodriguez, On unstable ship motions resulting from strong non-linear coupling. Ocean Eng. **33**(14–15), 1853–1883 (2006)
141. M.A.S. Neves, C.A. Rodriguez, Influence of nonlinearities on the limits of stability of ships rolling in head seas. Ocean Eng. **34**(11–12), 1618–1630 (2007)
142. M.A.S. Neves, C.A. Rodriguez, An investigation on roll parametric resonance in regular waves. Int. Shipbuild. Prog. **54**(4), 207–225 (2007)
143. M.A.S. Neves, C.A. Rodriguez, Nonlinear aspects of coupled parametric rolling in head seas, in *Proceedings of 10th International Symposium on Practical Design of Ships and Other Floating Structures*, vol. 2 (Houston, Texas, 2007), pp. 699–706
144. M.A.S. Neves, C.A. Rodriguez, A coupled nonlinear mathematical model of parametric resonance of ships in head seas. Appl. Math. Model. **33**(6), 2630–2645 (2009)
145. M.A.S. Neves, J.A. Merino, C.A. Rodriguez, A nonlinear model of parametric rolling stabilization by anti-roll tanks. Ocean Eng. **36**(14), 1048–1059 (2009)
146. J.N. Newman, Wave effects on vessels with internal tanks, in *Proceedings of 20th Workshop on Water Waves and Floating Bodies* (Spitsbergen, Norway, 2005), p. 4
147. C.S. Nielsen, U.D. Nielsen, Reducing roll motion by passive free surface tanks, in *Proceedings of 33rd ASME International Conference on Ocean, Offshore and Arctic Engineering*, OMAE2014-23299, vol. 7 (San Francisco, California, 2014), p. 12
148. I.G. Oh, A.H. Nayfeh, D.T. Mook, Theoretical and experimental study of the nonlinearity coupled heave, pitch, and roll motions of a ship in longitudinal waves, in *Proceedings of 19th Symposium on Naval Hydrodynamics* (Seoul, Korea, 1992), pp. 93–111
149. I.G. Oh, A.H. Nayfeh, D.T. Mook, A theoretical and experimental investigation of indirectly excited roll motion in ships. The nonlinear dynamics of ships. Phil. Trans. Math. Phys. Eng. Sci. **358**(1771), 1853–1881 (2000)
150. M. Palmquist, C. Nygren, Recording of head-sea parametric rolling on a PCTC, Technical report, (International Maritime Organization, 2004), Annex in IMO SLF 47/INF.5.2004
151. R. Pan, H. Davies, Responses of a non-linearly coupled pitch-roll ship model under harmonic excitation. Nonlinear Dyn. **9**(4), 349–368 (1996)
152. J.R. Paulling, The transverse stability of a ship in a longitudinal seaway. J. Ship Res. **4**(4), 37–49 (1961)
153. J.R. Paulling, R.M. Rosenberg, On unstable ship motions resulting from nonlinear coupling. J. Ship Res. **3**(1), 36–46 (1959)
154. M. Peric, T. Zorn, O. Moctar, T.E. Schellin, Y.S. Kim, Simulation of sloshing in LNG-tanks. ASME J. Offshore Mech. Arct. Eng. **131**(3), 031101, 11 (2009)
155. E. Peşman, H. Ölmez, M. Taylan, On the roll motion of a ship with passive anti-roll tank in regular longitudinal waves, in *Proceedings of 2nd International Symposium on Naval Architecture and Maritime*, pp. 531–554
156. T. Phairoh, J.K. Huang, Modeling and analysis of ship roll tank stimulator. Ocean Eng. **32**(8–9), 1037–1053 (2005)
157. T. Phairoh, J.K. Huang, Adaptive ship roll mitigation by using a U-tube tank. Ocean Eng. **34**(3–4), 403–415 (2007)
158. W.J. Pierson, L. Moscowitz, A proposed spectral form for fully developed wind seas based on the similarity theory of S A Kitaigorodskii. J. Geophys. Res. **69**(24), 5181–5190 (1964)
159. W.S. Plank, G.F. Beardsley Jr., W.V. Burt, Experimental evaluation of a passive anti-roll tank system. Ocean Eng. **2**(3), 131–139 (1972)
160. W.G. Price, R.E.D. Bishop, *Probability Theory of Ship Dynamics* (Chapman and Hall, London, U.K., 1974)
161. A.V. Ramana Reddy, V.A. Subramanian, A.S. Ramesh, Performance analysis of U-tube tank for roll stabilization. Int. J. Innov. Res. Dev. **1**(10), 288–299 (2012)
162. F.E. Reed, Dynamic vibration absorbers and auxiliary mass dampers, chapter 6, in *Shock and Vibration Handbook*, ed. by C.M. Harris, C.E. Crede, vol. 1 (McGraw-Hill, NY, 1961)

163. G.N. Roberts, T.L. Barboza, Analysis of warship roll stabilization by controlled anti-roll tanks with the aid of digital simulation, in *Proceedings of International Conference on CONTROL*, Publ. No. 285, vol. 88 (Oxford, U.K., 1988), pp. 672–676
164. O.F. Rognebakke, O.M. Faltinsen, Coupling of sloshing and ship motions. J. Ship Res. **47**(3), 208–221 (2003)
165. J.R. Saripilli, D. Sen, Numerical studies of coupling effect of sloshing on 3D ship motions. Int. J. Offshore Polar Eng. **27**(1), 27–35 (2017)
166. J.R. Saripilli, D. Sen, Numerical studies on sloshing loads using sloshing coupled ship motion algorithm, in *Proceedings of 27th International Ocean and Polar Engineering (ISOPE) Conference* (California, San Francisco, 2017), pp. 1093–1102
167. J.R. Saripilli, D. Sen, Numerical studies on effects of slosh coupling on ship motions and derived slosh loads. Appl. Ocean Res. **76**, 71–87 (2018)
168. D. Sen, J.R. Saripilli, Numerical studies on slosh-induced loads using coupled algorithm for sloshing and 3D ship motions, in *Proceedings of ASME 36th International Conference on Ocean, Offshore and Arctic Engineering* (Trondheim, Norway, 2017), pp. 1–9
169. Y.S. Shin, V.I. Belenky, J.R. Paulling, K.M. Weems, W.M. Lin, Criteria for parametric roll of large containerships in longitudinal seas, in *Trans Joint Ship Production Symposium and Society of Naval Architects and Marine Engineers*, vol. 112 (Washington, D.C., 2005), pp. 117–147
170. A. Shinkai, S. Monaka, M. Mano, M. Fuji, Numerical analysis of sloshing problems for the middle sized double hull tanker. J. Soc. Nav. Archit. Jpn. **176**, 387–396 (1994)
171. A. Shinkai, S. Tamia, Sloshing impact pressure induced on cargo oil tank walls on the middle-sized double hull tanker. Trans. Soc. Nav. Archit. West Jpn. **90**, 91–98 (1995)
172. S.R. Silva, A. Turk, C.G. Soares, J. Prpić-Oršić, On the parametric rolling of container vessels. Brodo Gradnja **61**(4), 347–358 (2010)
173. S.R. Silva, G. Vasquez, C.G. Soares, A. Maron, The stabilizing effect of U-tanks as passive anti-rolling devices, in *Proceedings of ASME 30th International Conference on Ocean, Offshore and Arctic Engineering* (Rio de Janeiro, Brazil, 2012), Paper No. OMAE2012-83501, pp. 479–490, 12
174. C. Stigter, The performance of U-tanks as a passive anti-rolling device, the royal institution of naval architects. Int. Shipbuild. Prog. ISP **13**(144), 249–275 (1966)
175. K.M. Taggart, *Modelling of Sloshing in Free Surface Tanks for ShipMo3D Ship Motion Predictions*, DRDC Atlantic ECR 2011-084, Defense, Research and Development Canada—Atlantic (2012), p. 64
176. K.M. Taggart, Modelling of U-tube tanks for ShipMo3D ship motion predictions, Canadian Coast Guard Major Crown Projects Directorate, External Client Report, DRDC Atlantic ECR 2011-300 (Ottawa, 2012), p. 40
177. H. Taguchi, H. Sawada, K. Tanizawa, A study on the complicated roll motion of a ship equipped with an anti-rolling tank, in *Proceedings of 8th International Conference on Stability of Ships and Ocean Vehicles*, Escuela Técnica Superior de Ingenieros Navales (Madrid, 2003), pp. 611–612
178. H. Takemoto, T. Ando, K. Abe, S. Oka, M. Komiya, S. Naito, Experimental study on sloshing impact loads of middle sized tankers with double hull. J. Soc. Nav. Archit. Jpn. **176**, 399–410 (1994)
179. B.U. Taskar, D. Dasgupta, V. Nagarajan, S. Chakraborty, A. Chattejee, O.P. Sha, CFD aided modelling of anti-rolling tanks towards more accurate ship dynamics. Ocean Eng. **92**, 296–303 (2014)
180. W. Thanyamanta, D. Molyneux, Prediction of stabilizing moments and effects of U-tube anti-roll tank geometry using CFD, in *Proceedings of 31st ASME International Conference on Offshore Mechanics and Arctic Engineering*, vol. 5 (Rio de Janeiro, Brazil, 2012), pp. 503–512
181. N. Themelis, K.J. Spyrou, Probabilistic assessment of resonant instability, in *Proceedings of 9th International Stability of Ships and Ocean Vehicles* (2006), pp. 37–48
182. K.K. Tikka, J.R. Paulling, Prediction of critical wave conditions for extreme vessel response in random seas, in *Proceedings of 4th International Conference on Stability of Ships and Ocean Vehicles* (Naples, Italy, 1990)

183. T.W. Treakle, A time domain numerical study of passive and active anti-roll tanks to reduce ship motion. MS Thesis, Department of Aerospace and Ocean Engineering, Virginia Polytechnic Institute and State University, 1998
184. N. Umeda, Probabilistic study on surf-riding of a ship in irregular following seas, in *Proceedings of 4th International Conference on Stability of Ships and Ocean Vehicles*, vol. 1 (Naples, Italy, 1990), pp. 336–343
185. N. Umeda, Y. Yamakoshi, Probability of ship capsizing due to pure loss of stability in irregular quartering seas. Nav. Archit. Ocean Eng. **30**, 73–85 (1992) Soc. Nav. Arch. Jpn
186. N. Umeda, M. Hamamoto, Y. Takashi, Y. Chiba, A. Matsuda, W. Sera, S. Suzuki, K. Spyrou, K. Watanabe, Model experiments of ship capsize in astern seas. J. Soc. Nav. Archit. Jpn. **177**, 207–218 (1995)
187. N. Umeda, H. Hashimoto, D. Vassalos, S. Urano, K. Okou, Nonlinear dynamics on parametric roll resonance with realistic numerical modelling. Int. Shipbuild. Prog. **51**, 205–220 (2004)
188. N. Umeda, H. Hashimoto, S. Minegaki, A. Matsuda, An investigation of different methods for the prevention of parametric rolling. J Mar. Technol. Soc. **13**, 16–23 (2008)
189. E.F.G. Van Daalen, A.G. Van Doeveren, P.C.M. Driessen, C. Visser, Two-dimensional free surface anti-roll tank simulations with a volume of fluid based Navier-Stokes solver, Report No. 15306-1-OE (Maritime Research Institute, Netherlands, 1999)
190. E.F.G. Van Daalen, K.M.T. Kleefsman, J. Gerrits, H.R. Luth, A.E.P. Veldman, Anti-roll tank simulations with a volume of fluid (VOF) based Navier-Stokes solver, University of Groningen, Johann Bernoulli Institute for Mathematics and Computer Science (2001), p. 117
191. E.F.G. Van Daalen, M. Gunsing, J. Grasman, J. Remmert, Roll dynamics of a ship sailing in large amplitude head waves. J. Eng. Math. **89**(1), 137–146 (2014)
192. J. Vasta, A.J. Giddings, A. Taplin, J.J. Stilwell, Roll stabilization by means of passive tanks. Trans. Soc. Nav. Archit. Mar. Eng. **69**, 411–460 (1961)
193. J.H.G. Verhagen, L. van Wijngaarden, Non-linear oscillations of fluid in a container. J. Fluid Mech. **22**, 737–751 (1965)
194. J.H. Vugts, A comparative study on four different passive roll damping tanks—part II. Int. Shipbuild. Prog. **16**, 212–223 (1969)
195. Y. Watanabe, On the dynamic properties of the transverse instability of a ship due to pitching. J. Soc. Nav. Archit. Jpn. **53**, 51–70 (1934)
196. P. Watts, On a method of reducing the rolling of ships at sea. Trans. Inst. Nav. Archit. **24**, 165–191 (1883)
197. P. Watts, The use of water chambers for reducing the rolling of ships at sea. Trans. Inst. Nav. Archit. **26**, 30 (1885)
198. W.S. Webster, Analysis of the control of activated antiroll tanks, in *Proceedings of Annual Meeting of the Society of Naval Architects and Marine Engineering* (New York, 1967), pp. 296–325
199. A.I. Xiaoyong, G. Li, H. Zhang, L. Liang, Natural period measurement of U-shape anti-roll tank using model experiment, in *Proceedings of International Conference on Intelligent Mechatronics and Automation* (Chengdu, China, 2004), pp. 704–707
200. A.I. Xiaoyong, L.I. Guobin, H. Zhang, L. Liang, Model experiment of anti-roll tank based on oscillation platform, in *Proceedings of Society of Instrument and Control Engineers (SICE) Annual Conf*, Article number: FPI-11-1 (Sapporo, Japan, 2004), pp. 2493–2498
201. S. Yamaguchi, A. Shinkai, An advanced adaptive control system for activated anti-rolling tank. ISPOE Int. J. Offshore Polar Eng. **5**, 17–22 (1995)
202. S. Yamamoto, F. Kataoka, S. Shioda, Y. Ashitani, Study on impact pressure due to sloshing in midsized LNG carrier. Int. J. Offshore Polar Eng. **5**(1), 10–16 (1995)
203. K.S. Youssef, S.A. Ragab, A.H. Nayfeh, D.T. Mook, Design of passive antiroll tanks for roll stabilization in the nonlinear range. Ocean Eng. **29**, 177–192 (2002)
204. K.S. Youssef, D.T. Mook, A.H. Nayfeh, S.S. Ragab, Roll stabilization by passive anti-roll tanks using an improved model of the tank-liquid motion. J. Vib. Control **9**(7), 839–862 (2003)
205. M. Zalar, Operating guidance for membrane type LNG carrier in partial filling condition, in *SNAME Maritime Technology Conference* (Houston, Texas, USA, 2005)

206. M. Zalar, P. Cambos, P. Besse, B. Le Gallo, Partial filling of membrane type LNG carriers, Bureau Veritas, Marine Division, 92077, Paris—La Défense Cedex, France (2005), p. 22
207. M. Zalar, Š. Malenica, L. Diebold, *Selected hydrodynamic issues in design of large LNG carriers* (Bureau Veritas, France, 2006), p. 8
208. D. Zhao, Z. Hu, G. Chen, X. Chen, X. Feng, Coupling analysis between vessel motion and internal nonlinear sloshing for FLNG applications. J. Fluids Struct. **76**, 431–453 (2018)
209. W. Zhao, J. Yang, Z. Hu, L. Xiao, L. Tao, Coupling between roll motions of an FLNG vessel and internal sloshing. ASME J. Offshore Mech. Arct. Eng. **136**(2), 10 (2014)
210. W. Zhao, J. Yang, Z. Hu, L. Xiao, L. Tao, Hydrodynamics of a 2D vessel including internal sloshing flows. Ocean Eng. **84**, 45–53 (2014)
211. Z. Zhong, J.M. Falzarano, R.M. Fithen, Numerical study of U-tube passive anti-rolling tanks, in *Proceedings of 8th International Offshore and Polar Engineering Conference*, vol. 3 (Montreal, Canada, 1998), pp. 504–512
212. P.E. Ziegler, Anti-rolling tank design. MS Thesis, MIT, Cambridge, MA, 1975
213. K. Zou, J. Xu, A method determining ship motion with anti-roll tanks in time domain (in Chinese). Ship Build. China **57**(1), 31–37 (2016)

Chapter 2
Dynamics Analysis and Control of the Malkus-Lorenz Waterwheel with Parametric Errors

Angelo M. Tusset, Jose M. Balthazar, Mauricio A. Ribeiro, Wagner B. Lenz, Thiago C. L. Marsola and Mateus F. V. Pereira

Abstract This work presents a dynamical analysis for the Malkus-Lorenz waterwheel, a physical system that behaves following the Lorenz equations. With this, two types of controllers were designed to control the system presenting chaotic behavior. The first controller is the time-delay feedback control (TDFC), and the second one is the State-Dependent Riccati Equation control (SDRE). The control strategy for the SDRE control involves the application of two signals: a nonlinear feedforward signal to maintain the controlled system in a periodic orbit, and a feedback signal, to take the system trajectory into the desired periodic orbit. Numerical simulations demonstrated the effectiveness of the control strategy in taking the system presenting chaotic behavior into a desired periodic orbit. In addition, the SDRE control robustness is investigated analyzing parametric errors in control loop.

2.1 Introduction

According to [1, 2] the original waterwheel models were developed by Malkus, Howard and Krishnamurti, considering that the waterwheel has leaking cups hanging from its rim, with pouring water only at the top cup. Therefore, in these particular conditions, the proposed mathematical model follows the classical Lorenz equations.

Complementing the mathematical model, the work proposed in [3] add two components of the wheel that characterizes its deceleration, and the analysis is simplified by treating only a combination of them. In [2, 4, 5], other mathematical models are proposed, but not including this wheel deceleration due to the input of water stream.

In this work, it is considered the model proposed by [3], presenting chaotic behavior. In order to eliminate this condition, it is proposed an application of the Time Delay Feedback Controller (TDFC) with the State-Dependent Riccati Equation (SDRE) control.

A. M. Tusset (✉) · J. M. Balthazar · M. A. Ribeiro · W. B. Lenz · T. C. L. Marsola · M. F. V. Pereira
Federal University of Technology—Paraná, Ponta Grossa, PR, Brazil
e-mail: tusset@utfpr.edu.br

M. Belhaq (ed.), *Topics in Nonlinear Mechanics and Physics*,
Springer Proceedings in Physics 228, https://doi.org/10.1007/978-981-13-9463-8_2

The TDFC was originally proposed by Pyragas [6] considering a continuous control input U, which stabilized a chaotic oscillation given by the difference between the current output and the past one [6].

The SDRE nonlinear regulator produces a closed-loop solution, which is locally asymptotically stable. The procedure to drive the top position to the desired point or trajectory, via SDRE technique, considers successive optimal solutions for static equations, stabilizing the system through feedback loop [7, 8].

2.2 Mathematical Model

In Fig. 2.1 is possible to see that water is dropped at a constant rate from the top. If the drop rate is too slow, the superior cup never fills, and the wheel never starts spinning. For a faster inflow, the cups from the top start filled with water, overcoming friction. Then, the waterwheel settles into a steady rotation given the initial conditions.

In order to understand better the waterwheel dynamics, the coordinates, variables and parameters for the wheel's motion are described: θ is the angle of rotation in the lab frame; $\omega(t)$ is angular velocity of the wheel, increasing in the counterclockwise direction, and $m(\theta, t)$ is mass distribution of water around the rim of the wheel. The total mass of water between any two points, θ_1 and θ_2, is given by $\int_{\theta_1}^{\theta_2} m(\theta, t)d\theta$, the total mass of inflow water from the pump is characterized by $\int_{\theta_1}^{\theta_2} Qd\theta$, and the mass of water that leaks from the system is described by $\left[-\int_{\theta_1}^{\theta_2} kmd\theta\right]\Delta t$. The parameter m characterizes the rate at which water flows out of a region, proportional to the mass contained within, and also ensures that water will never flow from a region with no enclosed mass. The mass carried out by the rotational wheel is given by $m\theta_1\omega\Delta t$, where $m\theta_1$ is the mass per unit angle and $\omega\Delta t$ is the angular width. The mass that rotates out follows the equation $-m\theta_2\omega\Delta t$. Considering the integral of these terms yields in rotational terms, dividing all by Δt and taking the limit as $\Delta t \to 0$, the result is:

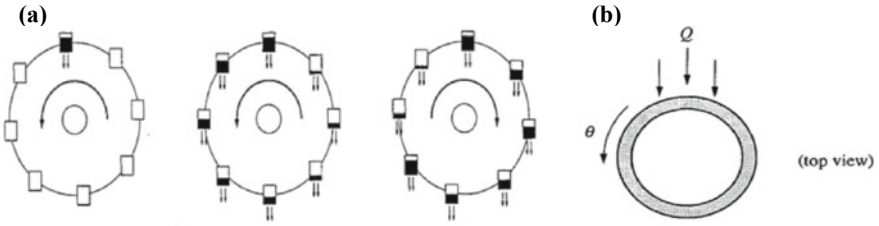

Fig. 2.1 **a** Illustration of the waterwheel system [1]. **b** Dynamic of the waterwheel system [3]

$$\frac{\partial m}{\partial t} = Q - km - \omega \frac{\partial m}{\partial Q} \tag{2.1}$$

There are two sources of rotational damping in the waterwheel. The first one is the brake, which can be adjusted by the user, the second one is the introduction of water at $\omega_0 = 0$, which must gain momentum until it reaches the system's velocity at $\omega_f = \omega$. These terms are proportional to the angular velocity. For an infinitesimal angle $d\theta$, there is a gravitational torque on the system given by $d\tau = mgr \sin\theta d\theta$, and the damping torque is given by $-\nu\omega$ for $\nu > 0$.

Integrating (2.1) over the total mass and combining with the damping torque term, the equation governing the angular velocity is given by:

$$\tau = I\dot{\omega} = -\nu\omega + gr \int_0^{2\pi} \mathrm{m}(\theta, t) \sin\theta d\theta \tag{2.2}$$

where Q is the rate at which water is pumped into the top, r is radius of the wheel, g the acceleration of gravity, which can be changed by increasing or decreasing the tilt of the waterwheel, ν is the rotational damping rate, which can be altered by increasing or decreasing the friction in the brake, I is the moment of inertia of the wheel and τ is the torque applied to the waterwheel.

Since the mass is 2π periodic in θ, it is possible to rewrite (2.1) in terms of a Fourier series:

$$m(\theta, t) = \sum_{n=0}^{\infty} [a_n(t) \sin\, n\theta + b_n(t) \cos n\theta] \tag{2.3}$$

The transformation of the (2.1) and (2.2) in (2.3) yields differential equations for a_n and b_n, known as amplitude equations, described as:

$$Q(\theta) = \sum_{n=0}^{\infty} q_n(t) \cos n\theta \tag{2.4}$$

where the sin term is neglected since the inflow is assumed to be symmetric about $\theta = 0$ (the top of the waterwheel). Substituting the series representations for m and Q into (2.1) and collecting sin $n\theta$ and cos $n\theta$ terms, the differential equation for the Fourier coefficient a_n is given by:

$$\dot{a}_n = n\omega b_n - k a_n \dot{b}_n = -n\omega a_n - k b_n + q_n \tag{2.5}$$

Thus, the equation governing ω in terms of Fourier series can be described as:

$$I\dot{\omega} = \nu\omega + gr\int_0^{2\pi}\sum_{n=0}^{\infty}[a_n(t)\sin n\theta + b_n(t)\cos n\theta]\sin\theta d\theta =$$

$$= -\nu\omega + gr\int_0^{2\pi} a_1\sin^2\theta d\theta = -\nu\omega + \pi gra_1 \tag{2.6}$$

where all the other terms have integrated to zero by orthogonality. Thus a_1, b_1, and ω form a closed system, decoupled from all higher order modes.

Finally, the governing equations for the waterwheel are [3]:

$$\begin{aligned}\dot{x}_1 &= -\alpha x_1 + \beta x_2\\ \dot{x}_2 &= x_1x_3 - kx_2\\ \dot{x}_3 &= -x_1x_2 - kx_3 + q_1\end{aligned} \tag{2.7}$$

where k is the leakage rate [kg/s], q_1 is the amplitude coefficients in Fourier series of inflow [kg/s], with $\alpha = \frac{n}{I}$ and $\beta = \frac{\pi gr}{I}$.

2.3 Numerical Results

In order to perform numerical simulations, the following parameters values are: $n = 40$, $q_1 = 12126.10$, $\beta = [2 : 50]$, $\alpha = [20 : 70]$ and $k = [0 : 20]$. In Fig. 2.2, it is possible to observe the bifurcation diagram behavior of the system (2.4).

As can be seen in Fig. 2.2, for certain variations of the parameters (β, α and k) the system may have a chaotic or periodic behavior. Figure 2.3 shows the variation of the largest Lyapunov exponent for the same variations of the parameters ($\beta = [2 : 50]$, $\alpha = [20 : 70]$ and $k = [0 : 20]$).

Additionally, in Fig. 2.3 is also possible to observe that for (a) $\beta = 6.5973$, $n = 40$, $q_1 = 12126.10$, $\alpha = 40$ and $k = 10$ the system's equations described in (2.7) present chaotic behavior. In Fig. 2.4, the dynamic behavior of the system for these parameters are shown.

2.4 Time Delayed Feedback Control

As originally suggested by the author of [6], continuous control input stabilizing a chaotic oscillation is given by the difference between the current output and the past output, as follows [6]:

$$U_i = K_{t_i}\{g[x_i(t-T), \dot{x}_i(t-T)] - g[x_i(t), \dot{x}_i(t)]\} \tag{2.8}$$

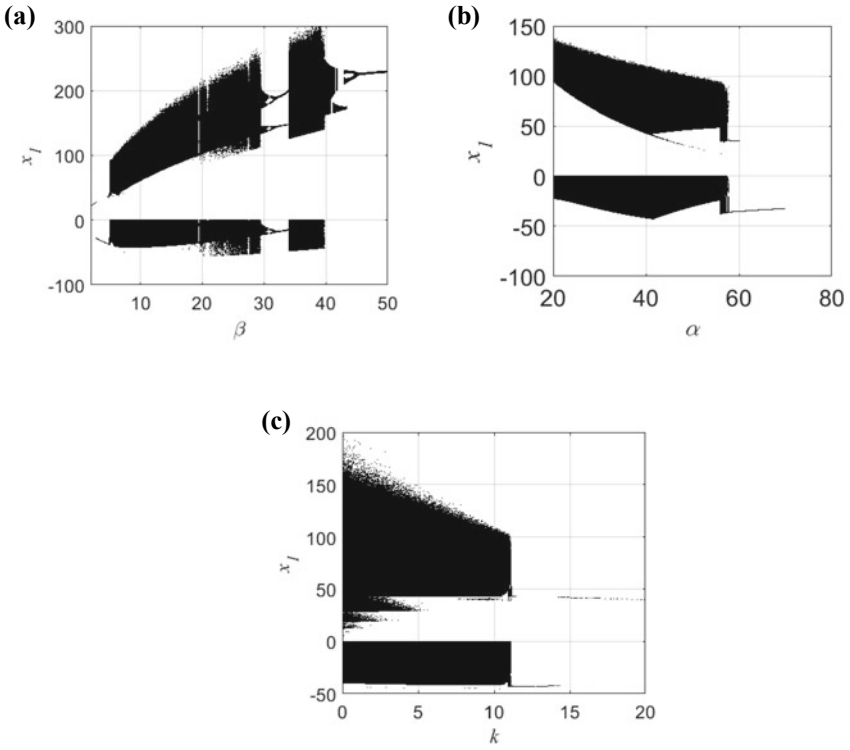

Fig. 2.2 Bifurcation diagram. **a** $\beta = [2 : 50]$, $n = 40$, $q_1 = 12126.10$, $\alpha = 40$ and $k = 10$. **b** $\alpha = [20 : 70]$, $n = 40$, $q_1 = 12126.10$, $\beta = 6.5973$ and $k = 10$. **c** $k = [0 : 20]$, $n = 40$, $q_1 = 12126.10$, $\alpha = 40$ and $\beta = 6.5973$

where T is the time delay coefficient and K_{t_i} the feedback gain, with i varying from 1 to 3. Assuming that the velocity of oscillation $\dot{x}_i$ is measured as the output of the nonlinear system in (2.7), the Time Delayed Feedback Control (TDF control) signal U_i is given by:

$$U_i = K_{t_i}[\dot{x}_i(t - T) - \dot{x}_i(t)] \tag{2.9}$$

where $T = \frac{2\pi}{\varpi}$ is the time delay, K_{t_i} the feedback gain, and ϖ is the frequency with period T.

In Fig. 2.5 is possible to see the diagram representative for time-delay control.

The system (2.7) with the control (2.9) can be represented by:

$$\begin{aligned}
\dot{x}_1 &= -\alpha x_1 + \beta x_2 + K_{t_1}[x_1(t - T) - x_1(t)] \\
\dot{x}_2 &= x_1 x_3 - k x_2 + K_{t_2}[x_2(t - T) - x_2(t)] \\
\dot{x}_3 &= -x_1 x_2 - k x_3 + q_1 + K_{t_3}[x_3(t - T) - x_3(t)]
\end{aligned} \tag{2.10}$$

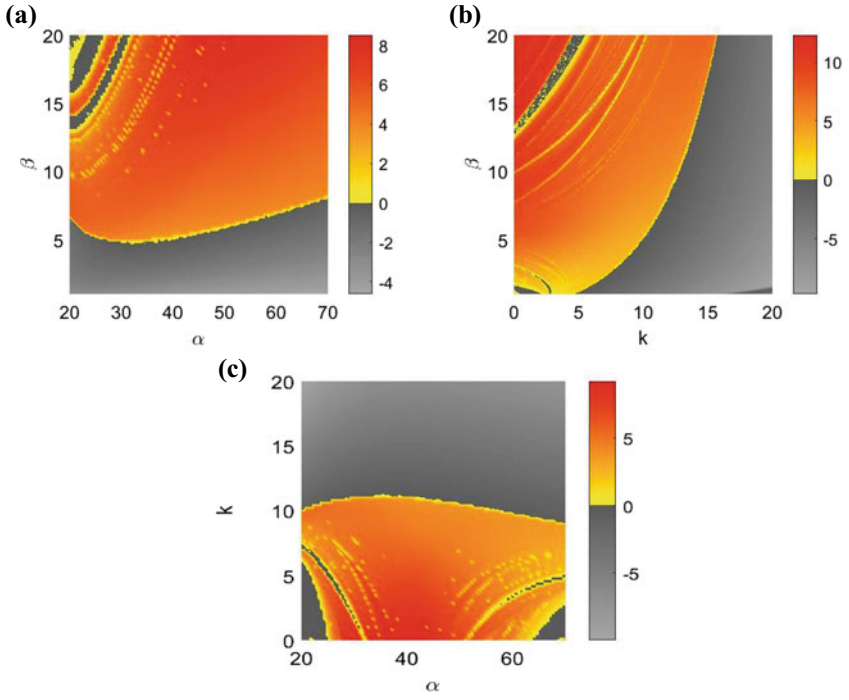

Fig. 2.3 Largest Lyapunov exponent. **a** $\beta = [2 : 50]$ versus $\alpha = [20 : 70]$. **b** $\beta = [2 : 50]$ versus $k = [0 : 20]$. **c** $\alpha = [20 : 70]$ versus $k = [0 : 20]$

In Fig. 2.6, the Time Delayed Feedback controllers of (2.9) for the (2.7) with parameters $K_{t_1} = 3.5$, $K_{t_2} = 3.5$, $K_{t_3} = 3.5$ and $\varpi = 1$ are described. Also, it is possible to see the combinations of the control signals U_1, U_2, and U_3.

In Fig. 2.7 the state x_1 with time delay control is described. Figures 2.8 and 2.9 follows the same representation, but now for states x_2 and x_3, respectively.

As can be seen in Figs. 2.7, 2.8 and 2.9, using only a control signal or with the combination of two control signals it is possible to bring the system from a chaotic behavior to a without chaotic behavior.

In Fig. 2.10 the system is considering the use of the three control signals, with $K_{t_1} = 1.5$, $K_{t_2} = 1.5$, $K_{t_3} = 1.5$ and $\varpi = 1$.

Therefore, the system described by (2.7) with the three control signals have left its chaotic behavior to a periodic behavior with the action of smaller control signals (Fig. 2.10b) than those used with only one control signal or with two control signals (Fig. 2.6).

Applying Fourier series in the data of Fig. 2.10a, the periodic behavior of the system given by (2.10) of Fig. 2.10a can be approximated by the following equations:

$$x_1 = -41.9595 - 0.91937\cos(49.78833t) + 14.16747\sin(49.78833t)$$
$$x_2 = -254.617 + 29.56434\cos(49.78833t) + 133.4926\sin(49.78833t)$$

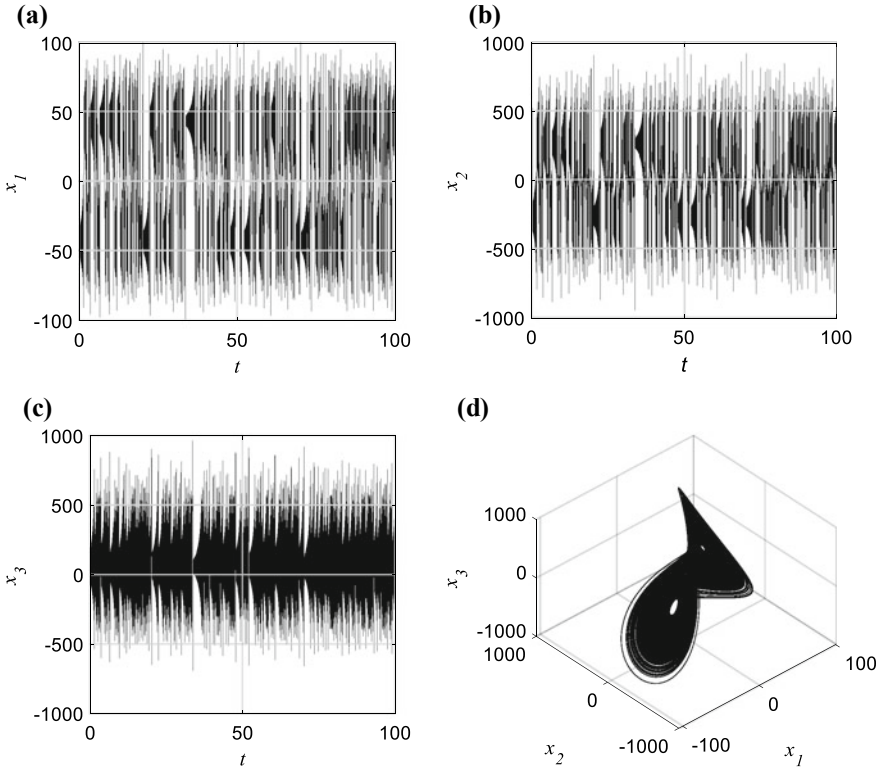

Fig. 2.4 **a** Displacement in time x_1. **b** Displacement in time x_2. **c** Displacement in time x_3. **d** Phase Diagram (x_1 vs. x_2 vs. x_3)

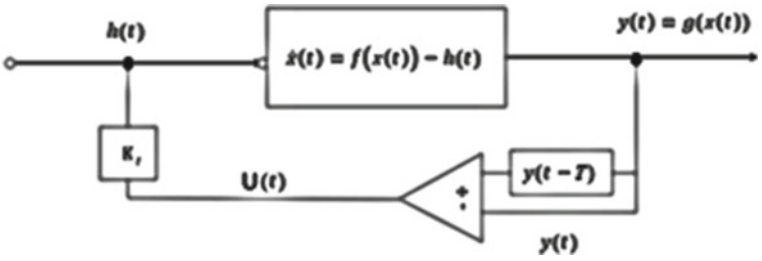

Fig. 2.5 Diagram representative for time-delay control

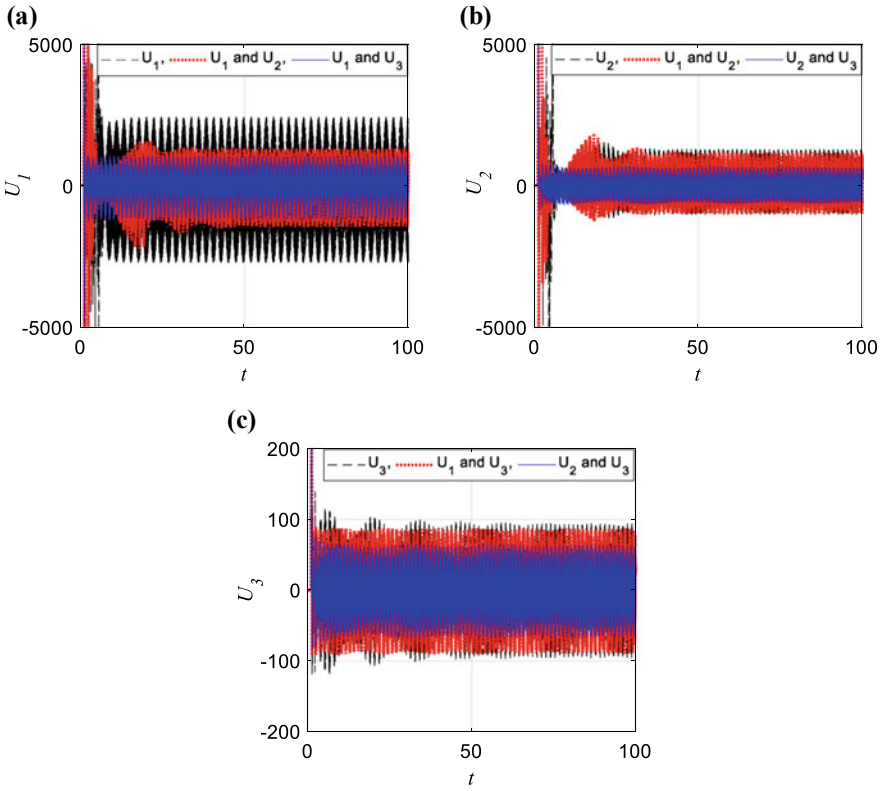

Fig. 2.6 Signal of the control. **a** Signal of the control U_1 and combination with the U_2 and U_3 controls. **b** Signal of the control U_2 and combination with the U_1 and U_3 controls. **c** Signal of the control U_3 and combination with the U_1 and U_2 controls

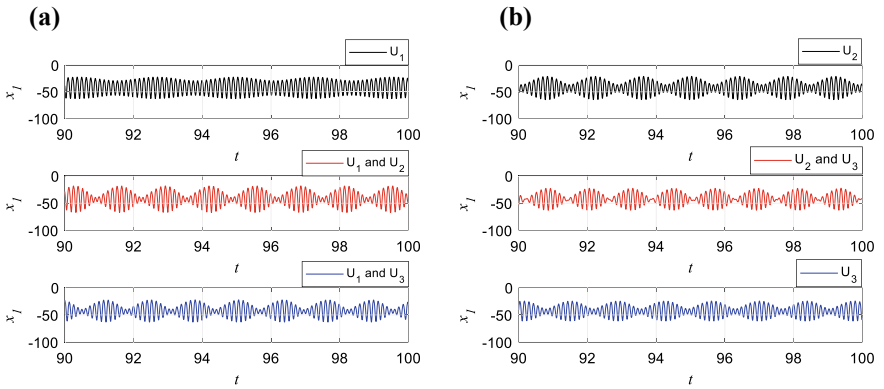

Fig. 2.7 Displacement in time x_1. **a** Using the control U_1 and combination with the U_2 and U_3 controls. **b** Using only combination the U_2 and U_3 controls

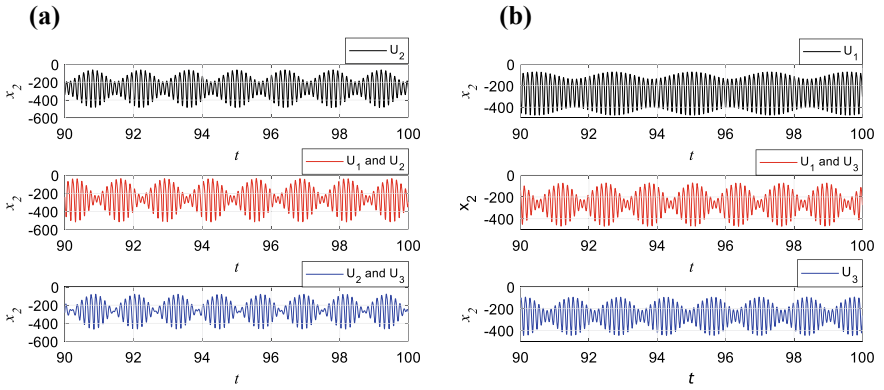

Fig. 2.8 Displacement in time x_2. **a** Using the control U_2 and combination with the U_1 and U_3 controls. **b** Using only combination the U_1 and U_3 controls

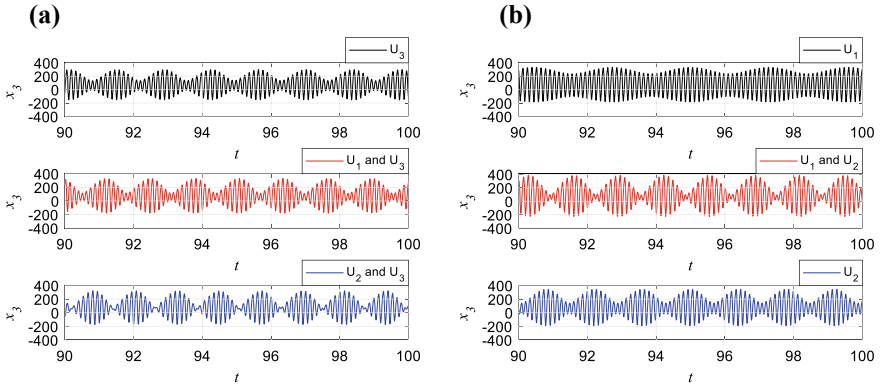

Fig. 2.9 Displacement in time x_3. **a** Using the control U_3 and combination with the U_1 and U_2 controls. **b** Using only combination the U_1 and U_2 controls

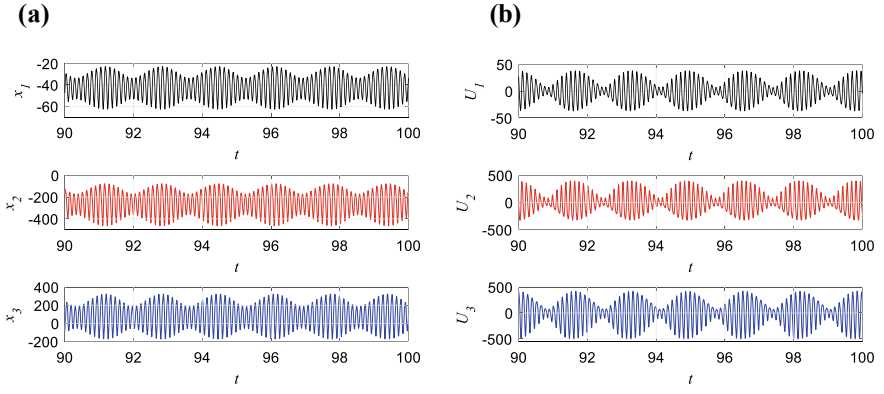

Fig. 2.10 **a** Displacement in time (x_1,x_2 and x_3). **a** Signal of the control (U_1, U_2 and U_3)

$$x_2 = 82.92315 - 79.0167\cos(49.78833t) + 157.6064\sin(49.78833t) \quad (2.11)$$

2.5 Suppression of Chaotic Behavior Using SDRE Control

As can be seen in the previous results, the time delay control was efficient in taking the system from the chaotic behavior to the periodical one. However, this behavior is determined by the control, not having the possibility of imposing a periodic orbit. For the cases in which it is desired to determine a specific state to the system, the SDRE control is one of the possible efficient alternatives [9].

Consider a nonlinear system represented in a matrix form:

$$\dot{\mathbf{X}} = A(X)X + BU \quad (2.12)$$

The desired trajectory errors are defined as:

$$\begin{bmatrix} e_1 \\ e_2 \\ e_3 \end{bmatrix} = \begin{bmatrix} x_1 - \tilde{x}_1 \\ x_2 - \tilde{x}_2 \\ x_3 - \tilde{x}_3 \end{bmatrix} \quad (2.13)$$

where $\tilde{x}$ is the desired trajectory.

Substituting (2.13) in the controlled (2.12), the result is:

$$\dot{\mathbf{e}} = \mathbf{A}(\mathbf{e})\mathbf{e} + \mathbf{Bu} \quad (2.14)$$

where $\mathbf{U}$ is the feedback control, obtained from:

$$\mathbf{u} = -\mathbf{R}^{-1}\mathbf{B}^{\mathbf{T}}\mathbf{P}(\mathbf{e})\mathbf{e} \quad (2.15)$$

Then, control $\mathbf{u}$ is suboptimal and transfers the (2.14) from any initial state to final state $\mathbf{e}(\infty) = 0$, minimizing the cost function:

$$J = \int_0^\infty (\mathbf{e}^T\mathbf{Q}\mathbf{e} + \mathbf{u}^T\mathbf{R}\,\mathbf{u})dt \quad (2.16)$$

where $\mathbf{Q}$ is a matrix positive definite or semidefinite, and $\mathbf{R}$ is a matrix positive definite. The State-Dependent Riccati equation is solved to obtain $\mathbf{P}(\mathbf{e})$, given by:

$$\mathbf{A}^T(\mathbf{e})\mathbf{P}(\mathbf{e}) + \mathbf{P}(\mathbf{e})\mathbf{A}(\mathbf{e}) - \mathbf{P}(\mathbf{e})\mathbf{B}\mathbf{R}^{-1}\mathbf{B}^T\mathbf{P}(\mathbf{e}) + \mathbf{Q} = 0 \quad (2.17)$$

The controllability equation $\left[\mathbf{B}\vdots\mathbf{A}^n\mathbf{B}\right]$ is applied for the static problem $\dot{\mathbf{e}} = \mathbf{A}(\mathbf{e})\mathbf{e} + \mathbf{Bu}$, where the SDRE method considers a solution for this static point wise problem, for a small time interval, in this neighborhood.

With this, the SDRE technique is used to obtain a suboptimal solution for dynamic control problem, having the following procedure [9]:

Step 1. Define the space-state model for the dynamic equations with the state-dependent coefficient form as described in (2.14);
Step 2. Measure the state of the system $\mathbf{e}(t)$, i.e. define $\mathbf{e}(0) = \mathbf{e}_0$, and choose the coefficients of weight matrices $\mathbf{Q}$ and $\mathbf{R}$;
Step 3. Solve the Riccati (2.17) for the state $\mathbf{e}(t)$;
Step 4. Calculate the input signal from (2.15);
Step 5. Integrate the system (2.14) and update the state of the system $\mathbf{e}(t)$ with these results. Go to step 3 until the error reaches an acceptable predeterminate value.

2.5.1 Application of SDRE Control

The objective is to find the control such that $\mathbf{X}$ stay in a asymptotically stable periodic orbit (2.11), with frequency and amplitude similar to that obtained with the TDF control.

Now, (2.12) can be represented in deviation as:

$$\dot{\mathbf{e}} = \mathbf{A}(\mathbf{e})\mathbf{e} + \mathbf{\Gamma} + \mathbf{BU} \tag{2.18}$$

with

$$\mathbf{e} = \begin{bmatrix} e_1 \\ e_2 \\ e_3 \end{bmatrix}, \mathbf{A}(\mathbf{e}) = \begin{bmatrix} -\alpha & \beta & 0 \\ (e_3 + \tilde{x}_3) & -k & n\tilde{x}_1 \\ -(e_2 + \tilde{x}_2) & -n\tilde{x}_1 & -k \end{bmatrix}, \Gamma = \begin{bmatrix} \beta\tilde{x}_2 - \dot{\tilde{x}}_1 - \alpha\tilde{x}_1 \\ -k\tilde{x}_2 - \dot{\tilde{x}}_2 + \tilde{x}_1\tilde{x}_3 \\ -\tilde{x}_1\tilde{x}_2 - k\tilde{x}_3 + q_1 - \dot{\tilde{x}}_3 \end{bmatrix} \text{and}$$

$$\mathbf{B} = \begin{bmatrix} 1\,0\,0 \\ 0\,1\,0 \\ 0\,0\,1 \end{bmatrix}.$$

Considering that $\mathbf{U} = \mathbf{u} + \tilde{\mathbf{u}}$, where $\mathbf{u}$ is the state feedback control, the feedforward control $\tilde{\mathbf{u}}$ can be described as:

$$\tilde{\mathbf{u}} = -\mathbf{\Gamma} \tag{2.19}$$

Substituting (2.19) in (2.18), the result is:

$$\dot{\mathbf{e}} = \mathbf{A}(\mathbf{e})\mathbf{e} + \mathbf{Bu} \tag{2.20}$$

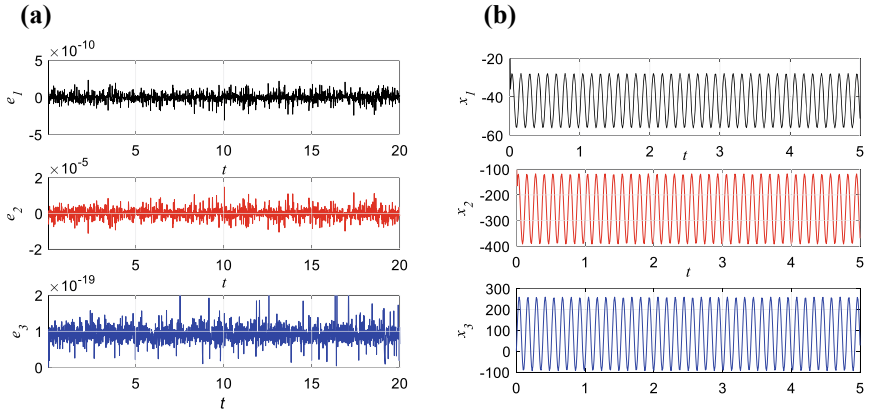

Fig. 2.11 **a** Desired trajectory error. **b** Desired trajectory

Now, making $\mathbf{Q} = 10^3 \begin{bmatrix} 1 & 0 & 0 \\ 0 & 10^5 & 0 \\ 0 & 0 & 1 \end{bmatrix}$ and $\mathbf{R} = 10^{-3} \begin{bmatrix} 1 & 0 & 0 \\ 0 & 1 & 0 \\ 0 & 0 & 1 \end{bmatrix}$, in Fig. 2.11 is possible to observe the system given by (2.20) with the application of SDRE control.

2.5.2 *Effect of Parameter Uncertainties in SDRE Control*

With the purpose of considering the effects of parameter uncertainties on the performance of the controller, the parameters used in the control will be considered to have a random error of [9–11]. Thus, the parameters taking into account uncertainties are described as: $\hat{\beta} = \beta(0.8 + 0.4r(t))$, $\hat{\alpha} = \alpha(0.8 + 0.4r(t))$ and $\hat{k} = k(0.8 + 0.4r(t))$, where $r(t)$ are normally distributed random functions.

Since the TDFC control does not depend on the system parameters, in this section only the parametric sensitivity of the SDRE control will be considered.

In Fig. 2.12a, the robustness of the feedback can be observed, and in Fig. 2.12b the robustness of the feedforward can be viewed as well.

As can be seen in Fig. 2.12a, the feedback control $\mathbf{u}$ is robust to parametric uncertainties, but as can be seen in Fig. 2.12b the feedforward control $\tilde{\mathbf{u}}$ is sensitive to parametric uncertainties. Behavior also observed by the authors [9–11].

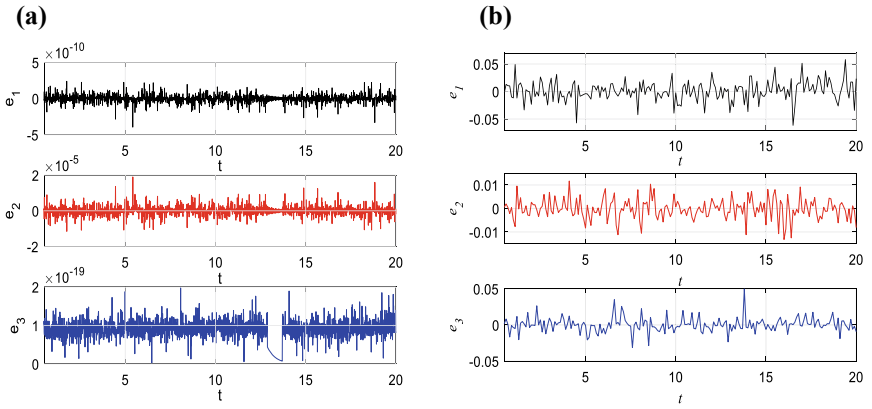

Fig. 2.12 **a** Desired trajectory error (uncertainties in feedback control **u**). **b** Desired trajectory error (uncertainties in feedforward control $\tilde{\mathbf{u}}$)

2.6 Conclusions

In order to control the chaotic behavior presented in the Malkus-Lorenz waterwheel system, the time-delay feedback control (TDFC) was designed and applied. The results were demonstrated through numerical simulations in order to inhibit this chaotic behavior of the system, proven to be efficient in maintaining the amplitude of the systems in periodic orbit. Moreover, with the association of a feedforward and feedback signals given by the State-Dependent Riccati Equation control (SDRE), it is possible to control the oscillations in the periodic orbits with a control signal close to that obtained with the TDFC controller. Also, it can be seen that the feedback control u is robust to parametric uncertainties while the feedforward control ($\tilde{\mathbf{u}}$) is sensitive to parametric uncertainties.

References

1. L.E. Matson, The Malkus-Lorenz water wheel revisited. Am. J. Phys. **75**(12), 1114–1122 (2007)
2. C. Sparrow, *The Lorenz Equations: Bifurcations, Chaos, and Strange Attractors* (Springer, New York, 1982), Chapter 1 and Appendix B
3. S.H. Strogatz, *Nonlinear Dynamics and Chaos Perseus Books* (Cambridge, MA, 1994)
4. J.L. Tylee, Chaos in a real system. Simulation **64**(3), 176–183 (1995)
5. F. Gassmann, Noise-induced chaos-order transitions. Phys. Rev. E **55**, 2215–2221 (1997)
6. K. Pyragas, Continuous control of chaos by self-controlling feedback. Phys. Lett. A **170**, 421–428 (1992)
7. P.C. Mracek, J.R. Cloutier, Control designs for the nonlinear benchmark problem via the state-dependent Riccati equation method. Int. J. Robust Nonlinear Control, 401–433 (1998)
8. H.T. Banks, B.M. Lewis, H.T. Tran, Nonlinear feedback controllers and compensators: a state-dependent Riccati equation approach. Comput. Optim. Appl. 177–218 (2007)

9. A.M. Tusset, V. Piccirillo, A.M. Bueno, J.M. Balthazar, D. Sado, J.L.P. Felix, R.M.L.R.F. Brasil, Chaos control and sensitivity analysis of a double pendulum arm excited by an RLC circuit based nonlinear shaker. J. Vib. Control (22), 3621–3637 (2016)
10. A.M. Tusset, F.C. Janzen, R.T. Rocha, J.M. Balthazar, On an optimal control applied in MEMS oscillator with chaotic behavior including fractional order. Complexity 1–12 (2018)
11. N.J. Peruzzi, F.R. Chavarette, J.M. Balthazar, A.M. Tusset, A.L.P.M. Perticarrari, R.M.F.L. Brasil, The dynamic behavior of a parametrically excited time-periodic MEMS taking into account parametric errors. J. Vib. Control **22**, 4101–4110 (2016)

Chapter 3
Nonlinear Characterization of a Bistable Energy Harvester Dynamical System

Vinicius G. Lopes, João Victor L. L. Peterson and Americo Cunha Jr.

Abstract This chapter explores the nonlinear dynamics of a bistable piezo-magneto-elastic energy harvester with the objective of determining the influence of external force parameters on the system response. Time series, phase space trajectories, Poincaré maps and bifurcation diagrams are employed in order to reveal system dynamics complexity and nonlinear effects, such as chaos incidence and hysteresis.

3.1 Introduction

Technological advances of the last decades have brought a wide variety of new portable electronic devices (smart phones, remote and micro sensors, smart medical implants, etc) and, at the same time bring great facilities to everyday life, created a huge demand for autonomous sources of energy. In this context, the energy harvesting technologies have been seeing as a potential solution in scenarios where conventional power supplying may not be practical or even available.

Energy harvesting technologies are based on physical-chemical properties of special (energy harvesting) materials, which provides electrical potential in response to an external stimulus, such as light (photoelectric), heat (pyroelectric) or mechanical vibration (piezoelectric), among others. A popular and comprehensible example of application may be found in solar energy generation, where the photovoltaic panels, gathering the minor units called cells which contains the silicon-based photoelectric material, when exposed to the sunlight incidence, performs its conversion into the electrical output power.

V. G. Lopes · J. V. L. L. Peterson · A. Cunha Jr. (✉)
Universidade do Estado do Rio de Janeiro, Rio de Janeiro, Brazil
e-mail: americo@ime.uerj.br

V. G. Lopes
e-mail: vinicius.g.lopes@uerj.br

J. V. L. L. Peterson
e-mail: joao.peterson@uerj.br

M. Belhaq (ed.), *Topics in Nonlinear Mechanics and Physics*,
Springer Proceedings in Physics 228, https://doi.org/10.1007/978-981-13-9463-8_3

The piezoelectric energy harvesting systems have been widely discussed on recent works. An interesting aspect concerns into the shape versatility of such materials making them suitable for many design applications, as shown by [37], also contributing to diversify its application possibilities—a review on it is addressed in [43]. Among the most promising ones, some examples can be found in different knowledge areas, as in medicine for powering pacemakers [23], the electrical engineering and telecommunications, for industrial facilities [14] and Internet of Things (IoF) wireless devices power supplying [19]; in mechanics, as way for power recovering from friction losses on vehicle suspensions [1] or from skyscrapers oscillations [44] or even for damping structural vibrations [13, 40].

The first vibration energy harvesting systems proposed were based on linear configurations, as the cantilever beam layout shown on Fig. 3.1. The relative simplicity of this system motivates new analysis and layouts, for example, as seen in [30]. Although, as shown by Cottone et al. [7] and, in more recent papers [20, 21, 41, 42], nonlinear configurations, such as the bistable inverse pendulum depicted in Fig. 3.2, may present better power recovering performances, when compared to the linear counterparts.

The richness of such devices dynamics, combined with the new available improvements in numerical simulation tools and computing resources, have been propelling a wide variety of analysis considering different devices layouts, as seen in [10, 18, 34, 39] for composite and cantilever vibrating beams, or in [11, 15, 25, 26] for inverse pendulum layouts and new designs as those discussed in [5, 8, 16, 33, 45].

The external forcing influence over harvesters energetic performance and dynamic characteristics have also been widely investigated in [4, 29, 31, 35], which consider mixed harmonic and random noise forcing, and also in [3, 12], that explore the possibility of energy scavenging in a quasi-periodic regime from a delayed dynamics. The multidisciplinary character of the theme also motivates the extension of the discussion to the coupled electrical circuits, as seen on [2, 6, 24, 38].

The same nonlinearities responsible to improve the devices energetic performance, on the other hand, contributes to raise the systems dynamics complexity, even leading to chaotic and unstable responses for some operational configurations. In [27, 28, 36] the authors demonstrates the presence of hysteresis effects on the nonlinear dynamical response of a piezo-magneto-elastic energy harvesting system, that is associated to the co-existence of multiple solutions, for the same operational conditions depending on the external forcing parameters values. Such phenomena highlight the importance of a detailed investigation of the nonlinear dynamics of devices in order to improve the comprehension of its behavior and limitations.

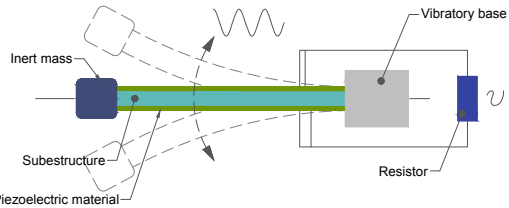

Fig. 3.1 Illustration of a linear vibration energy harvester

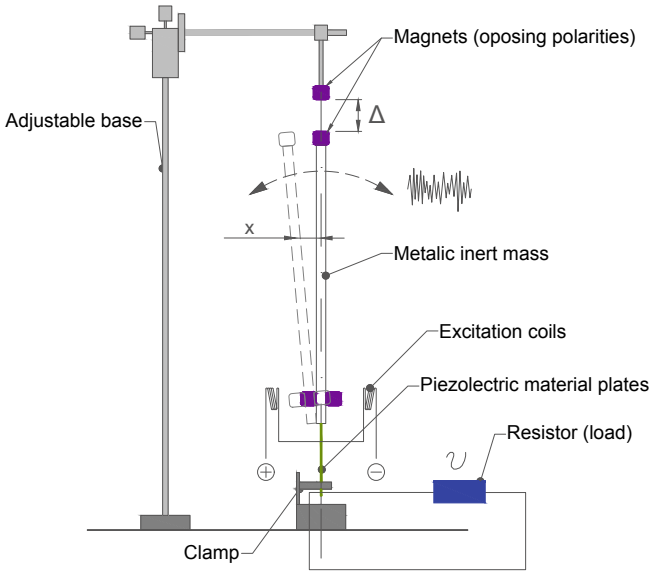

Fig. 3.2 Illustration of a nonlinear vibration energy harvester

In this sense, this chapter presents an analysis of the dynamics of a nonlinear bistable piezo-magneto-elastic energy harvesting system, aiming to investigate the influence of different harmonic forcing parameters on system output voltage. Numerical simulations reveals the effects of the amplitude and frequency excitation conditions on the chaos and regularity incidence on system electrical response. The bifurcation diagrams analysis allows to clearly identify the hysteresis phenomena and map those dynamics regions susceptible to chaos incidence. The voltage time series results sampled from such diagrams deepens the analysis of chaotic dynamics effects on the electrical output.

The rest of this chapter is organized as follows. The second section presents the energy harvesting system and its mathematical modeling. Next, in Sects. 3.3 and 3.4, the dynamical system is analyzed by time series and bifurcation diagrams, respectively. Final remarks close the text in the Sect. 3.5.

3.2 Bistable Energy Harvester

3.2.1 Physical System

The physical system of interest in this work is the piezo-magneto-elastic energy harvesting device depicted in Fig. 3.3. This electromechanical system consists of an elastic beam in vertical configuration, made of ferromagnetic material, with the

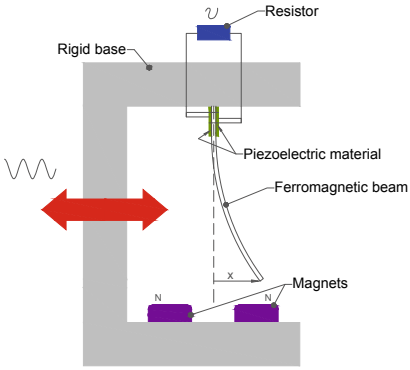

Fig. 3.3 Illustration of the piezo-magneto-elastic energy harvester

upper extreme clamped into a rigid base, and the bottom end moves freely. A pair of magnets is placed at the rigid base lower part. Two piezoelectric laminae are placed on beam's highest part, being also connected to a resistive circuit. The rigid base is periodically excited by an external source, which, together with the magnetic field generated by magnets, induces large amplitude vibrations in the beam. Once this movement is perceived by the piezoelectric laminae, the mechanical energy is converted into electrical power, which is dissipated in the resistor. This energy harvesting dispositive, proposed by Erturk et al. [9], is based on the classical magneto-elastic beam of Moon and Holmes [17, 32].

3.2.2 *Mathematical Model*

If the piezoelectric laminae and the electric circuit are not coupled to the system, the dynamic behavior of the beam is well approximated (for a limited frequency band) by its first mode shape, whose amplitude evolves according to a single degree-of-freedom Duffing oscillator [22]. However, once the piezoelectric transducer is attached to the beam, it starts to influence the system dynamic behavior so that piezoelectric interaction effect must be taken into account [9].

In this sense, [9] shows that the harvesting device dynamics can described by the following initial value problem

$$\ddot{x}(t) + 2\,\xi\,\dot{x}(t) - \frac{1}{2}x(t)\left(1 - x^2(t)\right) - \chi\,v(t) = f\,\cos\left(\Omega\,t\right), \tag{3.1}$$

$$\dot{v}(t) + \lambda\,v(t) + \kappa\,\dot{x}(t) = 0, \tag{3.2}$$

$$x(0) = x_0,\ \dot{x}(0) = \dot{x}_0,\ v(0) = v_0, \tag{3.3}$$

where t denotes time; x is the beam tip amplitude of oscillation; v is the voltage in the resistor; ξ is the damping ratio; f is the amplitude of the external force induced by the rigid base oscillation; Ω is the external excitation frequency; λ is a reciprocal time constant; the piezoelectric coupling terms are represented by χ, in the mechanical equation, and by κ in the electrical one; x_0 represents the beam edge initial position; $\dot{x}_0$ is the beam edge initial velocity; and v_0 denotes the initial voltage over the resistor. The upper dot is an abbreviation for time derivative. All parameters described above are dimensionless.

For all the simulations reported below, unless something is said on the contrary, the following dimensionless parameters are used: $\xi = 0.01$, $\kappa = 0.5$, $\chi = 0.05$, $\lambda = 0.05$, $\Omega = 0.8$. The standard initial conditions is $(x_0, \dot{x}_0, v_0) = (1, 0, 0)$. Different values of f are used, being indicated below. The dynamic is investigated for a temporal window defined by the interval $0 \leq t \leq 5000$.

3.3 Time Series Analysis

3.3.1 Effects of Excitation Amplitude

The voltage time series, analyzed for $0.019 \leq f \leq 0.275$, with amplitude increments of 0.032, are shown in Fig. 3.4. The steady state behavior is shown in the red window and, when pertinent, the transient behavior is depicted in a yellow box.

Figure 3.4a show the response of the system for excitation amplitude $f = 0.019$. The energy generated with such small excitation amplitude is minimal, and the response present regular behavior throughout the analyzed range. In Fig. 3.4b, as the forcing amplitude increases, the response assumes a larger amplitude. With $f = 0.083$ the response assumes a chaotic behavior, as can be seen in the yellow and red boxes. The voltage generated by the system increases. In Fig. 3.4d the dynamic presents regular steady state response starting from approximately 1000 time units, whereas it transient response is still chaotic. The amplitude of voltage output rises, to approximately 1 nondimensional volt, now that the energy input is considerably higher. The subsequent images Fig. (3.4e, f, g, h and i) present more or less the same response. All of them have wide amplitude range, between -1 and 1, and regular response at steady state, with little transient response.

In Fig. 3.5 it is possible to see a comparison between the chaotic attractor for $f = 0.083$, and the regular one, for $f = 0.115$. This figure also show the respective projections in the planes of displacement versus velocity, displacement versus voltage and velocity versus voltage, and corresponding Poincaré sections depicted by red dots. One can notice that a minimum change of the order of 0.032, that corresponds to 3.2% of the characteristic displacement used in the nondimensionalization, in the value of excitation amplitude can resolve in a totally different response. For $f = 0.083$, the dynamic presents chaotic behavior, trapped in the chaotic strange attractor, whereas for $f = 0.115$ the system resolve in a regular attractor. Once for the

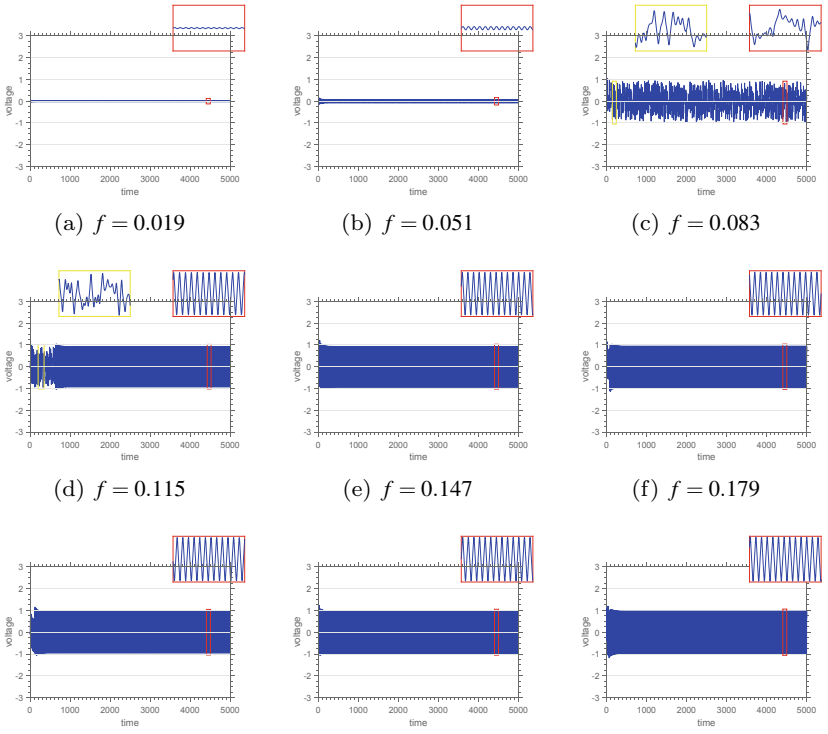

(a) $f = 0.019$ (b) $f = 0.051$ (c) $f = 0.083$

(d) $f = 0.115$ (e) $f = 0.147$ (f) $f = 0.179$

(g) $f = 0.211$ (h) $f = 0.243$ (i) $f = 0.275$

Fig. 3.4 Time series of voltage for $0.019 \leq f \leq 0.275$

chaotic configuration the system response presents non periodic pattern, its Poincaré section is represented by a large number of red dots not organized according to an invariant topological structure. The regular behavior has only one frequency, and thus, its Poincaré section has only one dot. The projections show that the regular attractor has higher energy output, characterized by its large amplitude in displacement.

A wide overview of the dynamics is best carried out by mapping the various attractors of the dynamical system. For this purpose the dynamics is integrated, for an excitation frequency $\Omega = 0.8$ and a total of 1200 different initial conditions, uniformly spaced in the region $-3 \leq x_0 \leq 3$, $-3 \leq \dot{x}_0 \leq 3$ and $v_0 = 0$, and the attractors corresponding to the steady-state of each case are identified. Projections of the identified attractors are shown in Fig. 3.6.

The attractors projections for forcing amplitude $f = 0.019$ are depicted on Fig. 3.6a. They are four in number, all with single period, being those depicted on magenta and cyan colors the more energetic orbits. For $f = 0.051$, which results are depicted on Fig. 3.6b, similar magenta and cyan basins are observed, as an expressive enlargement of blue and red basins shapes. Three regular orbits, depicted on brown, golden and green colors appears around those ones, reveling more energetic orbits which may be associated to the forcing amplitude increase. For $f = 0.083$,

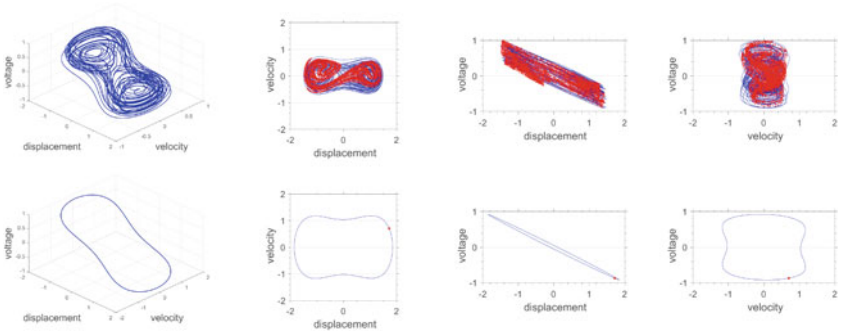

Fig. 3.5 Attractors in phase space for $f = 0.083$ (top) and $f = 0.115$ (bottom), phase space trajectories projections and corresponding Poincaré sections

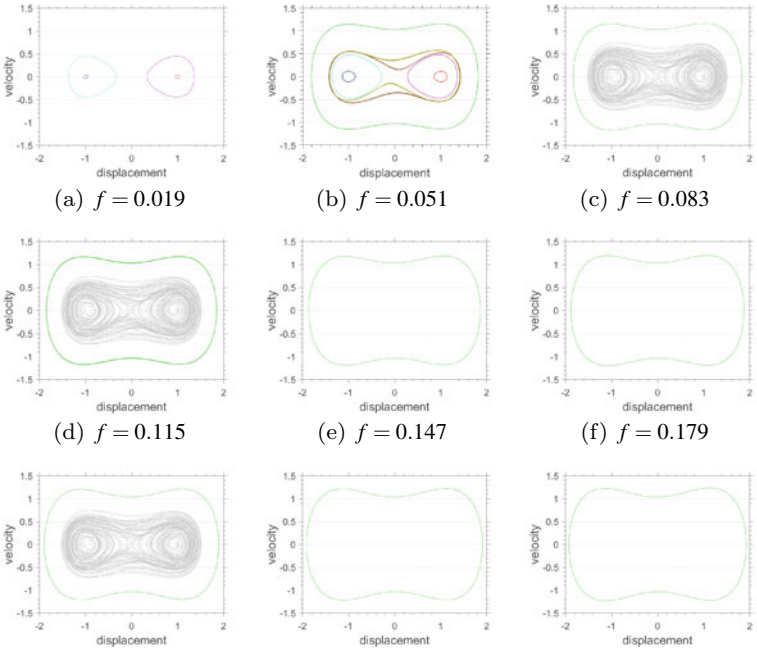

(a) $f = 0.019$ (b) $f = 0.051$ (c) $f = 0.083$

(d) $f = 0.115$ (e) $f = 0.147$ (f) $f = 0.179$

(g) $f = 0.211$ (h) $f = 0.243$ (i) $f = 0.275$

Fig. 3.6 Phase space trajectories projections for $0.019 \leq f \leq 0.275$ and $\Omega = 0.8$

on Fig. 3.6c, instead, the green orbit remains while the others disappears. A chaotic dynamics orbit, depicted on gray color, emerges corroborating the results observed on the phase attractor in Fig. 3.5, for the same model parameters. Similar results can be observed for $f = 0.211$, on Fig. 3.6g. For $f = 0.147$, $f = 0.179$, $f = 0.243$ and $f = 0.275$, which results are depicted, respectively, on Fig. 3.6e, f, h and i, a

single period orbit is observed, what reveals that, for such configurations, the system dynamics is regular.

3.3.2 *Effects of Excitation Frequency*

Now the effects of the excitation frequency over the system dynamics is explored trough attractors projections, calculated in a similar way as in the previous section, for $f = 0.083$, $f = 0.115$ and $0.1 \leq \Omega \leq 0.9$, and shown in Figs. 3.7 and 3.8, respectively.

The Fig. 3.7a, for $\Omega = 0.1$, reveals two low energy regular attractors with low amplitude orbits for beam displacement and velocity. Similar results can be observed for $f = 0.115$, on Fig. 3.8a, but with a chaotic attractor, on gray color. For $\Omega = 0.2$, on Fig. 3.7b, a clear narrowing of the basins shape is observed, as the chaos incidence, depicted on gray color, corresponding to larger amplitudes. The analysis of the attractors reveals a larger velocity range in regular response if compared with the previous case. Despite of the presence of a green regular attractor, no expressive changes are observed for $f = 0.115$ results, on Fig. 3.8b, in comparison with those for $f = 0.083$. For $\Omega = 0.3$, on Fig. 3.7c, the red basin prevails over the blue one;

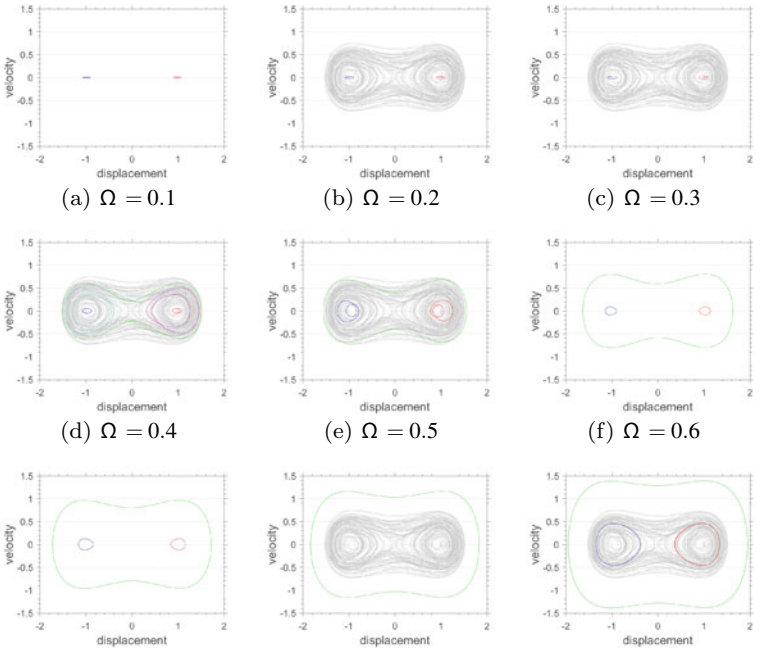

(a) $\Omega = 0.1$ (b) $\Omega = 0.2$ (c) $\Omega = 0.3$

(d) $\Omega = 0.4$ (e) $\Omega = 0.5$ (f) $\Omega = 0.6$

(g) $\Omega = 0.7$ (h) $\Omega = 0.8$ (i) $\Omega = 0.9$

Fig. 3.7 Phase space trajectories projections for $0.1 \leq \Omega \leq 0.9$ and $f = 0.083$

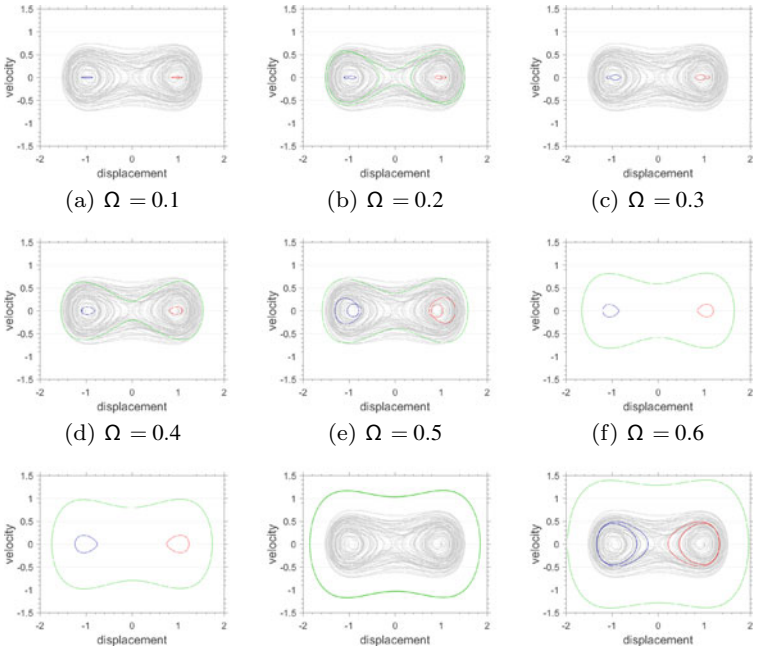

(a) $\Omega = 0.1$ (b) $\Omega = 0.2$ (c) $\Omega = 0.3$

(d) $\Omega = 0.4$ (e) $\Omega = 0.5$ (f) $\Omega = 0.6$

(g) $\Omega = 0.7$ (h) $\Omega = 0.8$ (i) $\Omega = 0.9$

Fig. 3.8 Phase space trajectories projections for $0.1 \leq \Omega \leq 0.9$ and $f = 0.115$

furthermore, the tendency of narrowing as the system moves away from the unforced system equilibrium points (presents in $(-1, 0)$ and $(1, 0)$) continues. The chaos still remains, as the attractors keep to increase in amplitude. A similar behavior is observed by considering $f = 0.115$, as show on Fig. 3.8c. For $\Omega = 0.4$, on Fig. 3.7d, one can note the predominance of the blue basin, although the red and blue basins are even more mixed. An expressive incidence of chaos is noted, despite of the presence of a new basin, depicted on green color, is noteworthy. The attractors show that such basin is more energetic due to a greater amplitude both in displacement and velocity. In addition, it is observed the emergency of two other basins, depicted on cyan and magenta colors, both with more energy than others, presenting two periods. For $f = 0.115$, on Fig. 3.8d, similar results can be observed except for the double period basins, which have disappeared. For $\Omega = 0.5$, in Fig. 3.7e, an expressive growth of the green basin occurs, along with the greater mix of peripheral regions, as the system gets closer to the resonance frequency. The attractors show the expansion of the green, blue and red basins and the inexistence of cyan and magenta ones. Also noteworthy is the transformation of the blue and red basins, now with two periods. No differences can be noted for $f = 0.115$ results, on Fig. 3.8e. The Fig. 3.7f, for $\Omega = 0.6$, shows the predominance of the green basin with blue and red islands. The attractors present a continuous growth of the green orbit, alongside with small growth of the blue and red orbits, which returned to present a single period and, in

counterpart with the previous case, there is absence of chaotic responses. Similar results are observed for $f = 0.115$, on Fig. 3.8f. For $\Omega = 0.7$, in Fig. 3.7g, a growth of the blue and red islands, as an increasing relevance of the green basin can be observed. The attractors continue to have more energetic orbits. Similar results can be observed for $f = 0.115$, depicted on Fig. 3.8g. In the system resonance frequency of $\Omega = 0.8$, depicted on Fig. 3.7h, the chaotic responses predominates along with the most energetic orbit, on green color. The attractors show that such orbit is the only regular one. Similar results are observed for $f = 0.115$, on Fig. 3.8h. Finally, for $\Omega = 0.9$, which results are depicted on Fig. 3.7i, the blue and red basins return subtly, still with presence of chaos. The attractors show the most energetic orbits. For $f = 0.115$, on Fig. 3.8i, despite of the similarities, the red and blue basins present double period orbits.

3.4 Bifurcation Analysis

The system bifurcation diagrams are built by sampling 1200 values for external excitation parameters from regularly spaced observation interval. Results are referred as forward and backward for an ascending and descending values sampling ordering, respectively. For each sampled amplitude, the dynamical system is integrated for a constant frequency. The first 90% of system response time series is neglected, as a way to avoid the transient response. From displacement, velocity and voltage results, the amplitude forward and backward bifurcation diagrams are obtained, according the chosen sampling ordering. A similar process can be carried out for frequency values, with constant amplitudes, leading to frequency forward and backward bifurcation diagrams. For ongoing results, typically, cool colors are reserved for forward results, while the warm colors scale depict the backward ones.

3.4.1 Influence of Excitation Amplitude

Regarding amplitude analysis, both forward and backward bifurcation diagrams are built for nine Ω values regularly sampled from $0.1 \leq \Omega \leq 0.9$, considering the amplitude sampling interval as $0.1 \leq f \leq 1.4$. The output voltage results are shown on Fig. 3.9.

The blurred regions depict chaotic dynamic on system response, for those on that output voltage may assume a wide range of different values. An overview of both, forward and backward bifurcation diagrams, points that the system is strongly sensitive to non-regular dynamics for the highest amplitude and lowest frequency values analysed. Some similar phenomena can be seen on the first portion of amplitude control interval on highest frequencies. From $\Omega = 0.5$ and higher frequency values, some expressive discrepancies are observed on voltage output by comparison

of forward and backward sampling orderings. This concerns to the nonlinear effects introduced by the pair of magnets on harvester, which are also responsible for the bistable configuration. For $\Omega = 0.6$ and 0.7, the system voltage response keeps regular for all tested amplitudes on the interval. A multiple period region appears for the last forcing amplitude values, after some slim band of chaotic dynamics. Similar formations are observed between the chaotic regions on the two highest frequencies analysed.

The Fig. 3.10 presents both forward and backward bifurcation diagrams for $\Omega = 0.2$ and 0.8 extracted from frequencies observation window overview in Fig. 3.9. In both cases, for $\Omega = 0.2$, the system presents chaotic dynamics about $0.260 \leq f \leq 0.270$. A pitchfork bifurcation revealed on forward diagram near $f = 0.23$ is hidden by system dynamics on backward, and reappears about $f = 0.27$, which highlights the system response dependence from the problem initial conditions. Discontinuous regions are also observed on the last portion of amplitudes interval, suggesting a

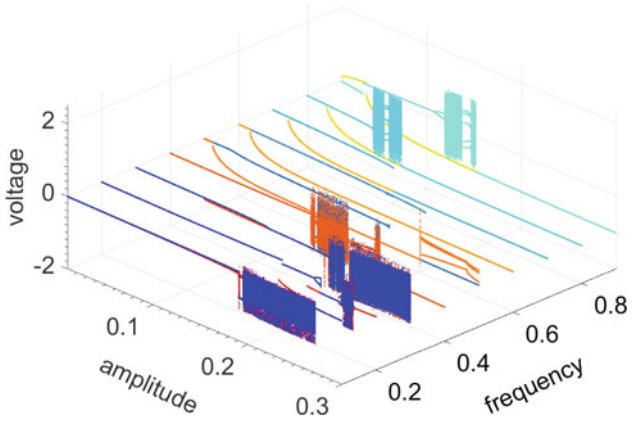

Fig. 3.9 Bifurcation diagram of voltage as function of excitation amplitude f, for several values of excitation frequency Ω

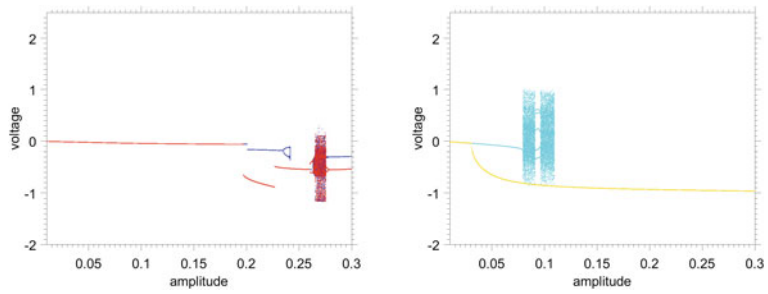

Fig. 3.10 Bifurcation diagrams for $\Omega = 0.2$ (left) and $\Omega = 0.8$ (right). Forward diagrams on blue colors and backward, on red and yellow

voltage behavior more independent of initial conditions, thus, reliable for the early amplitudes on this frequency. It is important to take account that such conclusions are true only for the model parameters defined. A similar analysis can be carried out for the amplitude bifurcation diagram for $\Omega = 0.8$. A pair of chaotic voltage

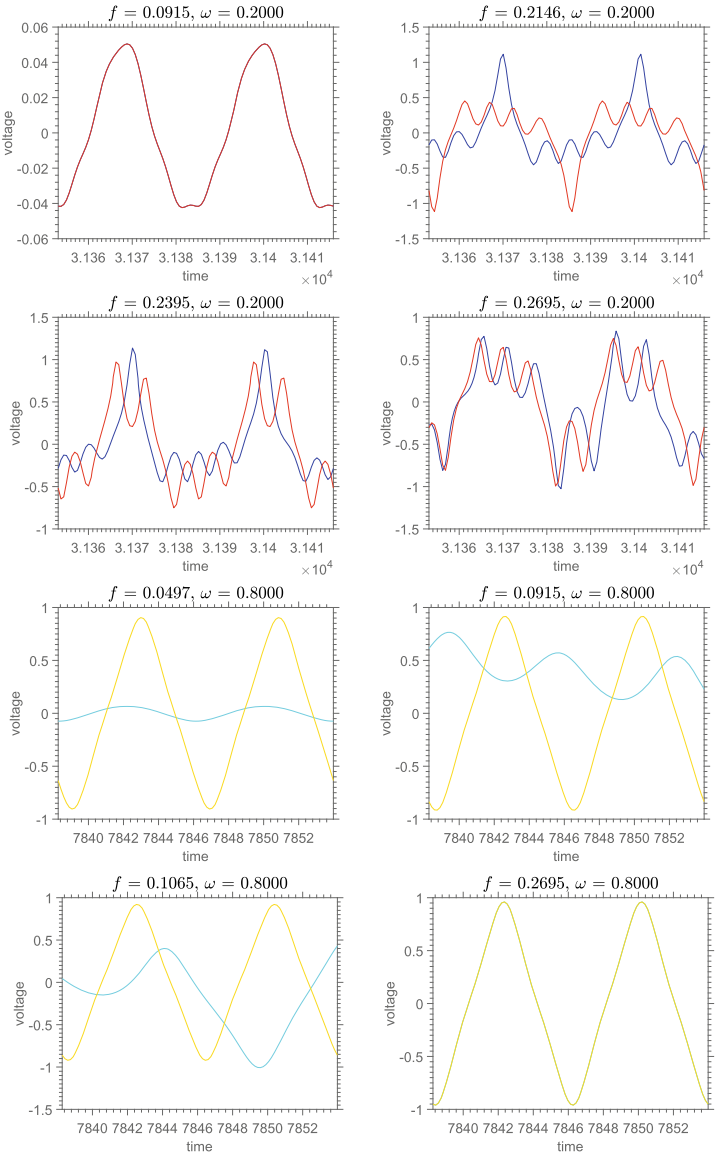

Fig. 3.11 Voltage time series for $\Omega = 0.2/\Omega = 0.8$ and several values of f. Forward diagrams on blue colors and backward, on red

bands can be seen on forward diagram for $0.07 \leq f \leq 0.08$ and $0.09 \leq f \leq 1.00$ filled by a richer multiple region. Now, instead, a strong regular dynamics region fills the middle and the last portions of the amplitude intervals both for forward and backward results.

Extending the previous discussion, Fig. 3.11 shows the voltage waveforms, obtained by sampling the system dynamics for specific forcing amplitude values taken from Fig. 3.10. For example, for $\Omega = 0.2$ and $f = 0.2146$, the harvester output voltage is regular, both on forward and backward diagrams, as seen before, besides the signal waveforms are quite distorted. For $f = 0.2695$ and the same excitation frequency, although both forward and backward waveforms have no period defined due to the chaotic motion.

3.4.2 *Influence of Excitation Frequency*

For the frequency analysis, the forward and backward diagrams are built for nine amplitude regularly sampled values from $0.019 \leq f \leq 0.275$, for $0.01 \leq \Omega \leq 1.4$ set as the frequency sampling interval. The Fig. 3.12 presents the harvester output voltage results.

For both forward and backward cases, the system reveals itself more susceptible to the chaos occurrence, when compared with those for amplitude analysis, depicted in Fig. 3.9. Despite of it, all diagrams present a common regular behavior in the middle portion of frequencies interval. The blurred regions became more evident for the last amplitude values in the observation windows, for which both low and high frequencies leads the system to chaos condition. Particularly, for $f \geq 0.179$, voltage results present multiple chaotic regions on backward diagrams, what emphasizes

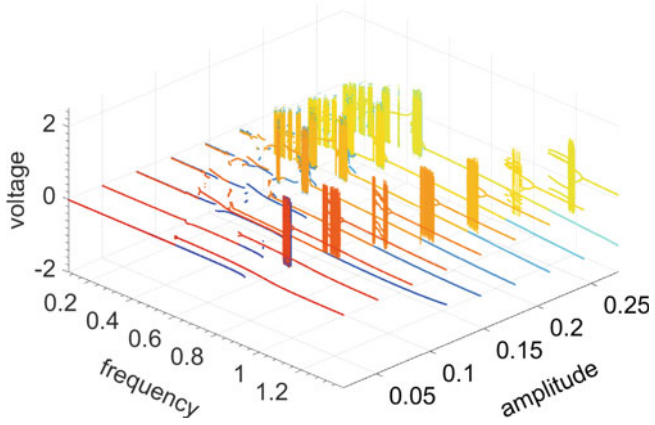

Fig. 3.12 Bifurcation diagram of voltage as function of excitation frequency Ω, for several values of excitation amplitude f

the influence of sampling ordering on explicit IPV solution. For higher amplitudes, multiple period regions and pitchfork bifurcations appear close to the chaotic regions, although it still means regular dynamics. A similar phenomena occurs on the early portion of frequencies interval $0.083 \leq f \leq 0.147$, where some discontinuities are also observed, both on forward and backward cases. By comparison with the same regions on higher amplitudes diagrams, the discontinuities, thus, may be inferred as a way to predict the chaos occurrence. For the lowest amplitude, system voltage results remains regular for all investigated frequencies. A small pitchfork bifurcation can still be noted on backward results about $f = 0.6$. This indicates that for different operation frequencies, a small forcing amplitude value may be interesting once it prevents chaotic dynamics.

The Fig. 3.13 presents the forward and backward diagrams for $f = 0.083$ and $f = 0.179$, sampled from amplitude observation window overview in Fig. 3.12. For $f = 0.083$, forward and backward methods reveals a similar dynamics profile regarding the chaos and regularity. The exception is confined to the region between $0.4 \leq f \leq 0.6$, where a pitchfork bifurcation on backward case gives rise to a discontinuity on forward one. The chaotic dynamics region about $\Omega = 0.8$ is small if compared with those observed for higher amplitude values, both on forward and backward results. For $f = 0.179$, as an overview of Fig. 3.12 suggestsc that the system presents a rich dynamics related to chaos occurrence. A strongly nonlinear region can be observed on the first middle of the frequencies interval, filled with large discontinuities region on its early portion. The system susceptibility to initial conditions for higher amplitudes, inducted by the sampling ordering, becomes more evident when forward and backward results are compared. A massive chaotic region rises around of $\Omega = 1.0$ on backward case, in contrast with regular dynamics on forward diagram on same region.

The system results investigation may be improved by sampling amplitude and frequency values from diagrams in Fig. 3.13, as shown by the voltage time series presented in Fig. 3.14. The voltage time series for $f = 0.179$ and $\Omega = 0.3786$, for example, highlights the importance of a deep investigation. System voltage waveforms presents a regular pattern, both on forward and backward diagrams. Although, the multiple period region distortion is more evident on backward case, once forward voltage waveform seems to preserve some characteristics of the harmonic forcing.

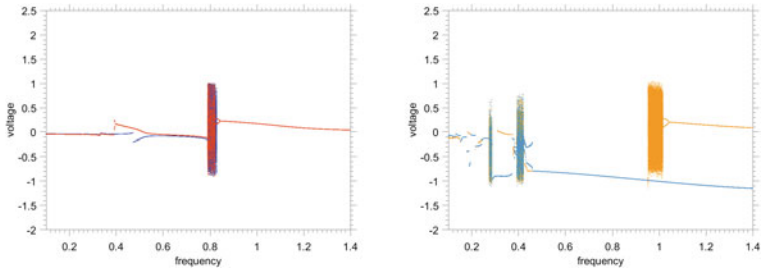

Fig. 3.13 Bifurcation diagrams for $f = 0.083$ (left) and $f = 0.179$ (right). Forward diagrams on blue colors and backward, on red

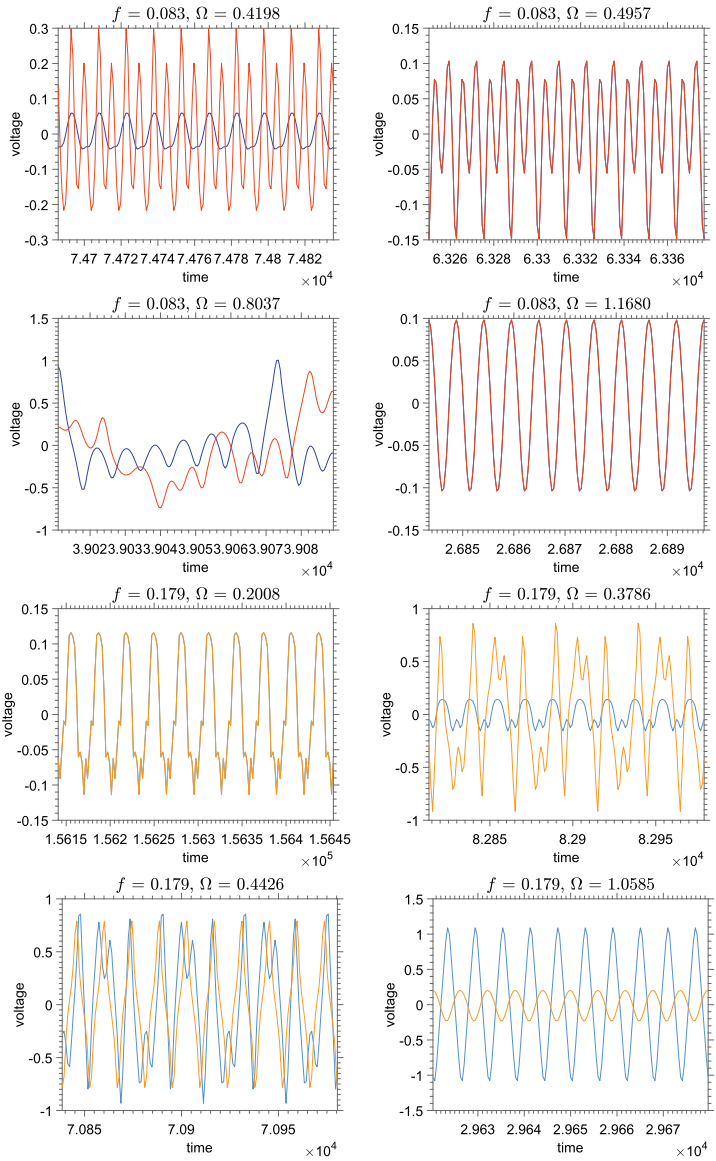

Fig. 3.14 Voltage time series for $f = 0.083/f = 0.179$ and several values of Ω. Forward diagrams on blue colors and backward, on red

In this sense, best results are observed for $f = 0.179$ with $\Omega = 1.0585$, where forward amplitudes overcomes backward one. The chaotic dynamics consequences is observed better for $f = 0.083$ with $\Omega = 0.8037$, in Fig. 3.14. A periodic behavior is not clearly seen on voltage waveforms, neither on forward or backward cases.

3.5 Concluding Remarks

This chapter presents a nonlinear dynamic analysis of a piezo-magneto-elastic energy harvesting system. Its nonlinear behavior is explored by time series, Poincaré maps, phase space trajectories and bifurcation diagrams. The voltage output time series and the phase attractors analysis allow to relate the length of the transient dynamics response to the external forcing frequency and amplitude parameters values. The same graphs also provide a way to link the magnitude of the harmonic forcing and the amount of output power. The bifurcation diagrams analysis reveals a hysteresis effects on the system dynamics which may be associated to the model nonlinearities, introduced by the pair of magnets placed on the rigid structure lower part, also responsible to the bistable configuration. The voltage time series sampled from such diagrams provides a detailed overview of the chaos incidence distortions on system output voltage waveforms.

Acknowledgements The authors acknowledge the support given to this research by the funding agencies Carlos Chagas Filho Research Foundation of Rio de Janeiro State (FAPERJ) under grants E-26/010.002.178/2015 and E-26/010.000.805/2018, and Coordenação de Aperfeiçoamento de Pessoal de Nível Superior–Brasil (CAPES)–Finance Code 001.

References

1. M.A.A. Abdelkareem, L. Xu, M.K.A. Ali, A. Elagouz, J. Mi, S. Guo, Y. Liu, L. Zuo, Vibration energy harvesting in automotive suspension system: a detailed review. Appl. Energy **229**, 672–699 (2018)
2. C.H.C.C. Basqueroto, F.R. Chavarette, S. da Silva, Analysis of bistable and chaotic piezoelectric energy harvesting device coupled with diode bridge rectifier. Int. J. Pure Appl. Math. **98**, 275–289 (2015)
3. M. Belhaq, M. Hamdi, Energy harvesting from quasi-periodic vibrations. Nonlinear Dyn. **86**, 2193–2205 (2016)
4. M. Borowiec, Energy harvesting of cantilever beam system with linear and nonlinear piezoelectric model. Eur. Phys. J. Spec. Top. **224**(14), 2771–2785 (2015)
5. S. Bradai, S. Naifar, C. Viehweger, O. Kanoun, G. Litak, Nonlinear analysis of an electrodynamic broadband energy harvester. Eur. Phys. J. Spec. Top. **224**(14), 2919–2927 (2015)
6. M.A. Clementino, R. Reginatto, S. da Silva, Modeling of piezoeletric energy harvesting considering the dependence of the rectifier circuit. J. Intell. Mater. Syst. Struct. **36**, 283–292 (2014)
7. F. Cottone, H. Vocca, L. Gammaitoni, Nonlinear energy harvesting. Phys. Rev. Lett. **102**, 080601 (2009)
8. H.L. Dai, Y.W. Yang, A. Abdelkefi, L. Wang, Nonlinear analysis and characteristics of inductive galloping energy harvesters. Commun. Nonlinear Sci. Numer. Simul. **59**, 580–591 (2018)
9. A. Erturk, J. Hoffmann, D.J. Inman, A piezomagnetoelastic structure for broadband vibration energy harvesting. Appl. Phys. Lett. **94**, 254102 (2009)
10. F.M. Foong, C.K. Thein, D. Yurchenko, On mechanical damping of cantilever beam-based electromagnetic resonators. Mech. Syst. Signal Process. **119**, 120–137 (2019)
11. M.I. Friswell, S.F. Ali, O. Bilgen, S. Adhikari, A.W. Lees, G. Litak, Non-linear piezoelectric vibration energy harvesting from a vertical cantilever beam with tip mass. J. Intell. Mater. Syst. Struct. **23**(13), 1505–1521 (2012)

12. Z. Ghouli, M. Hamdi, F. Lakrad, M. Belhaq, Quasiperiodic energy harvesting in a forced and delayed Duffing harvester device. J. Sound Vib. **407**, 271–285 (2017)
13. J.A.B. Gripp, L.C.S. Góes, O. Heuss, F. Scinocca, An adaptive piezoelectric vibration absorber enhanced by a negative capacitance applied to a shell structure. Smart Mater. Struct. **24**(12), 125017 (2015)
14. Z. Hadas, L. Janak, J. Smilek, Virtual prototypes of energy harvesting systems for industrial applications. Mech. Syst. Signal Process. **110**, 152–164 (2018)
15. E. Halvorsen, G. Litak, Statistics of a noise-driven elastic inverted pendulum. Eur. Phys. J. Appl. Phys. **70**(1), 10901 (2015)
16. P. Harris, G. Litak, J. Iwaniec, C.R. Bowen, Recurrence plot and recurrence quantification of the dynamic properties of cross-shaped laminated energy harvester. Appl. Mech. Mater. **849**, 95–105 (2016)
17. P. Holmes, A nonlinear oscillator with a strange attractor. Philos. Trans. R. Soc. A **292**, 429–448 (1979)
18. S. Ju, C. Ji, Impact-based piezoelectric vibration energy harvester. Appl. Energy **214**, 139–151 (2018)
19. P. Kamalinejad, C. Mahapatra, Z. Sheng, S. Mirabbasi, V.C.M. Leung, Y.L. Guan, Wireless energy harvesting for the internet of things. IEEE Commun. Mag. **53**, 102–108 (2015)
20. S. Kato, S. Ushiki, A. Masuda, A broadband energy harvester using leaf springs and stoppers with response stabilization control. J. Phys. Conf. Ser. **1052**, 012083 (2018)
21. J.M. Kluger, T.P. Sapsis, A.H. Slocum, Robust energy harvesting from walking vibrations by means of nonlinear cantilever beams. J. Sound Vib. **341**, 174–194 (2015)
22. I. Kovacic, M. Brennan, *The Duffing Equation: Nonlinear Oscillators and their Behavior* (Wiley, 2011)
23. A. Kumar, R. Kiran, V.S. Chauhan, R. Kumar, R. Vaish, Piezoelectric energy harvester for pacemaker application: a comparative study. Mater. Res. Express **5**, 075701 (2018)
24. Y. Liao, J. Liang, Unified modeling, analysis and comparison of piezoelectric vibration energy harvesters. Mech. Syst. Signal Process. **123**, 403–425 (2019)
25. G. Litak, M.I. Friswell, S. Adhikari, Regular and chaotic vibration in a piezoelectric energy harvester. Meccanica **51**(5), 1017–1025 (2016)
26. G. Litak, A. Rysak, M. Borowiec, M. Scheffler, J. Gier, Vertical beam modal response in a broadband energy harvester. Proc. Inst. Mech. Eng. Part K J. Multi-Body Dyn. 230 (2016)
27. V.G. Lopes, J.V.L.L. Peterson, A. Cunha Jr., Numerical study of parameters influence over the dynamics of a piezo-magneto-elastic energy harvesting device (In XXXVII Congresso Nacional de Matemática Aplicada e Computacional, São José dos Campos, Brazil, 2017)
28. V.G. Lopes, J.V.L.L. Peterson, A. Cunha Jr, On the nonlinear dynamics of a bi-stable piezoelectric energy harvesting device, in *24th ABCM International Congress of Mechanical Engineering (COBEM 2017)* (Curitiba, Brazil, 2017)
29. V.G. Lopes, J.V.L.L. Peterson, A. Cunha Jr, Analysis of the nonlinear dynamics of a bistable energy harvesting system with colored noise disturbances, in *Conference of Computational Interdisciplinary Science (CCIS 2019)* (2019)
30. Q. Lu, L. Liu, F. Scarpa, J. Leng, Y. Liu, A novel composite multi-layer piezoelectric energy harvester. Compos. Struct. **201**, 121–130 (2018)
31. W. Martens, U. von Wagner, G. Litak, Stationary response of nonlinear magneto-piezoelectric energy harvester systems under stochastic excitation. Eur. Phys. J. Spec. Top. **222**(7), 1665–1673 (2013)
32. F.C. Moon, P.J. Holmes, A magnetoelastic strange attractor. J. Sound Vib. **65**, 275–296 (1979)
33. R. Naseer, H.L. Dai, A. Abdelkefi, L. Wang, Piezomagnetoelastic energy harvesting from vortex-induced vibrations using monostable characteristics. Appl. Energy **203**, 142–153 (2017)
34. D. Pan, F. Dai, Design and analysis of a broadband vibratory energy harvester using bi-stable piezoelectric composite laminate. Energy Convers. Manag. **169**, 149–160 (2018)
35. T. Pereira, A. Paula, A. Fabro, M. Savi. Random effects in a nonlinear vibration-based piezoelectric energy harvesting system. Int. J. Bifurc. Chaos, (in press) (2019)

36. J.V.L.L. Peterson, V.G. Lopes, A. Cunha Jr., Dynamic analysis and characterization of a nonlinear bi-stable piezo-magneto-elastic energy harvester, in MATEC Web of Conferences vol. 241 (2018), p. 01001
37. D. Puspitarini, A. Suzianti, H. Al Rasyid, Designing a sustainable energy-harvesting stairway: determining product specifications using triz method. Procedia Soc. Behav. Sci. **216**, 938–947, in *Urban Planning and Architectural Design for Sustainable Development (UPADSD)* (2016)
38. T.M.P. Silva, M.A. Clementino, A. Erturk, C. de Marqui Jr., Equivalent electrical circuit framework for nonlinear and high quality factor piezoelectric structures. Mechatronics **54**, 133–143 (2018)
39. S. Stoykov, G. Litak, E. Manoach, Vibration energy harvesting by a timoshenko beam model and piezoelectric transducer. Eur. Phys. J. Spec. Top. **224**(14), 2755–2770 (2015)
40. M.A. Trindade, C.C. Pagani, L.P.R. Oliveira, Semi-modal active vibration control of plates using discrete piezoelectric modal filters. J. Sound Vib. **351**, 17–28 (2015)
41. K. Vijayan, M.I. Friswell, H. Haddad Khodaparast, S. Adhikari, Non-linear energy harvesting from coupled impacting beams. Int. J. Mech. Sci. **96**-**97**, 101–109 (2015)
42. C. Wang, Q. Zhang, W. Wang, J. Feng, A low-frequency, wideband quad-stable energy harvester using combined nonlinearity and frequency up-conversion by cantilever-surface contact. Mech. Syst. Signal Process. **112**, 305–318 (2018)
43. C. Wei, X. Jing, A comprehensive review on vibration energy harvesting: modelling and realization. Renew. Sustain. Energy Rev. **74**, 1–18 (2017)
44. X.D. Xie, Q. Wang, S.J. Wang, Energy harvesting from high-rise buildings by a piezoelectric harvester device. Energy **93**, 1345–1352 (2015)
45. Z. Zhou, W. Qin, W. Du, P. Zhu, Q. Liu, Improving energy harvesting from random excitation by nonlinear flexible bi-stable energy harvester with a variable potential energy function. Mech. Syst. Signal Process. **115**, 162–172 (2019)

Chapter 4
The Delayed van der Pol Oscillator and Energy Harvesting

Zakaria Ghouli, Mustapha Hamdi and Mohamed Belhaq

Abstract In the first part of the chapter, we present some results on quasi-periodic (QP) vibration-based energy harvesting (EH) in a delayed van der Pol oscillator with modulated delay amplitude. Two examples are considered which include a delayed van der Pol harvester coupled either to a delayed or undelayed electromagnetic subsystem. The influence of delay parameters on the performance of the harvester has been examined. It is shown that a maximum amplitude of the response does not induce necessarily a maximum output power. In the second part, we investigate QP vibration-based EH in the case where the van der Pol oscillator is subjected to external harmonic excitation and coupled to a delayed piezoelectric component. Perturbation method is applied near a resonance to obtain approximation of the periodic and QP responses as well as the amplitude of the harvested powers. To guarantee the robustness of the QP vibration during energy extraction operation, a stability analysis is performed and the QP stability chart is determined. Results show that in the presence of time delay in the electrical circuit of the excited van der Pol oscillator, it is possible to harvest energy from QP vibrations with a good performance over a broadband of system parameters away from the resonance. Numerical simulations are conducted to support the analytical predictions.

4.1 Introduction

One of the major goals of using quasi-periodic (QP) vibrations to scavenge energy, usually made away from the resonance, is to improve the stability range and robustness of the energy harvester device which is not always secured when operating in

Z. Ghouli · M. Belhaq (✉)
Faculty of Sciences Ain Chock, University Hassan II Casablanca, Casablanca, Morocco
e-mail: mbelhaq@yahoo.fr

Z. Ghouli
e-mail: ghoulizakaria@gmail.com

M. Hamdi
University Mohammed I Oujda, FST-Al Hoceima, Al-Hoceima, Morocco
e-mail: hamustapha2000@yahoo.fr

M. Belhaq (ed.), *Topics in Nonlinear Mechanics and Physics*,
Springer Proceedings in Physics 228, https://doi.org/10.1007/978-981-13-9463-8_4

the vicinity of the considered resonance. Indeed, when the harvester is operating in the linear regime, its best performance is achieved traditionally at the resonance peak with large-amplitude oscillations. However, such large-amplitude oscillations are obtained only in a narrow region located around the peak, thus limiting considerably the performance of the harvester device; see for instance [1–4]. In the nonlinear regime, on the other hand, energy harvesting (EH) capability can be improved by extending the bandwidth of the harvester over broadband of the excitation frequency. A major inconvenient is that the instability phenomenon induced in the nonlinear frequency response can reduce substantially the system performance when the response is attracted to the low-amplitude motions or when it suffers jump phenomena, as shown in [5]. Thus, the idea emerged from such a limitation is to use the possibility of harvesting energy from vibrations away from the resonance thereby circumventing instabilities. Under certain conditions, QP regime with large amplitude when present away from the resonance may constitute a good candidate.

A simple way to harvest energy in the QP regime away from the resonance is to consider self-induced vibrations represented by limit-cycle (LC) oscillations. Under certain conditions (for instance the presence of additional frequency in the system), the steady-state LC oscillations may lose stability via a secondary Hopf bifurcation producing QP vibrations. However, it is known that the amplitude of such QP vibrations occurring away from the resonance is smaller compared to that of the periodic ones; see for instance [6, 7]. In this case the harvester suffers a substantial reduction in the harvested power indicating that the QP regime should be avoided. For instance, in energy harvester systems subjected to combined aerodynamic and base excitations, it was observed that beyond the flutter speed, the QP response of the harvester leads to a substantial drop of the output power [8, 9]. However, in a recent work by Hamdi and Belhaq [10] it was reported analytically and using numerical simulations that in the delayed van der Pol oscillator with modulated delay amplitude, large-amplitude QP vibrations (larger than the periodic ones) performing in broader range of parameters can take place. This analytical finding has been first exploited by Belhaq and Hamdi [11] to demonstrate the possibility to scavenge energy directly from QP vibrations over a broadband of modulation frequency away from the resonance with a good performance. Later, Ghouli et al. [12] investigated QP vibration-based EH in a forced and delayed Duffing harvester device considering an electromagnetic coupling with time delay [13]. More recently, the problem of QP vibration-based EH in a Mathieu-van der Pol-Duffing MEMS device using time delay was studied in [14]. Other variants on the topic have been examined in [15, 16]. The conclusion emerged from these previous works was that for appropriate values of delay parameters, QP vibration-based EH can be used to extract energy over a broadband of excitation frequencies away from the resonance with good performance, thereby circumventing bistability and jump phenomena near the resonance.

The objective of this work is to provide, in a first part, a review on the main results obtained on the QP vibration-based EH in a van der Pol harvester and then investigate, in a second part, EH in a van der Pol oscillator subject to harmonic excitation and coupled to a delayed piezoelectric mechanism.

The chapter is organized as follows: In Sect. 4.2 we present a review on the recent results on QP vibration-based EH in a van der Pol oscillator with time-periodic delay amplitude coupled either to undelayed electromagnetic component or to delayed electromagnetic one. Section 4.3 investigates QP vibration-based EH in a forced van der Pol oscillator coupled to a delayed piezoelectric element. Approximations of the periodic response and the amplitude of the output power near the primary resonance are given using the multiple scales method. Section 4.4 provides approximation of the QP response and the corresponding harvested power applying the second-step multiple scales method. The influence of time delay parameters in the electrical circuit on the EH performance is analyzed. A summary of the results is given in the concluding section.

4.2 The van der Pol Oscillator and Energy Harvesting

The concept of harvesting energy from QP vibrations is demonstrated in this section through two examples. Namely, a delayed van der Pol oscillator coupled to undelayed or delayed electromagnetic component. First, consider a delayed pure van der Pol oscillator with time-periodic delay amplitude studied by Hamdi and Belhaq [10]. The authors analyzed the influence of the modulated time-delay amplitude on the response of the following van der Pol oscillator with time delay in the position and velocity

$$\ddot{x} + x - \varepsilon(\alpha - \beta x^2)\dot{x} - \varepsilon\lambda(t)x(t-\tau) - \varepsilon\lambda_3\dot{x}(t-\tau) = 0 \tag{4.1}$$

where ε is a small positive parameter, α, β are damping coefficients, $\lambda(t)$, λ_3 are delay amplitudes in the position and velocity, respectively, and τ is the time delay. An overdot denotes differentiation with respect to time t. Equation (4.1) can model ambient sustained self-excited vibrations under a delayed feedback control. Examples includes, for instance, controlled vibration produced by high speed rotating machines or regenerative effects in cutting processes [17–19]. To generate a resonant condition and guarantee the occurrence of QP vibrations, it was assumed that the delay amplitude in the position $\lambda(t)$ is time-periodic around a nominal value λ_1, such that

$$\lambda(t) = \lambda_1 + \lambda_2 \cos\,\omega t \tag{4.2}$$

where λ_2 and ω are the amplitude and the frequency of the modulation. The nominal value λ_1 being the unmodulated delay amplitude. The case of *delay parametric resonance* for which the frequency ω of the modulation is near twice the natural frequency of the oscillator was considered. This resonance imposes the condition $1 = (\frac{\omega}{2})^2 + \varepsilon\sigma$ where σ is the detuning parameter.

The periodic response near this *delay parametric resonance* is approximated using the averaging method [20] and the amplitudes of the QP vibrations are obtained applying the second-step multiple scales method [22].

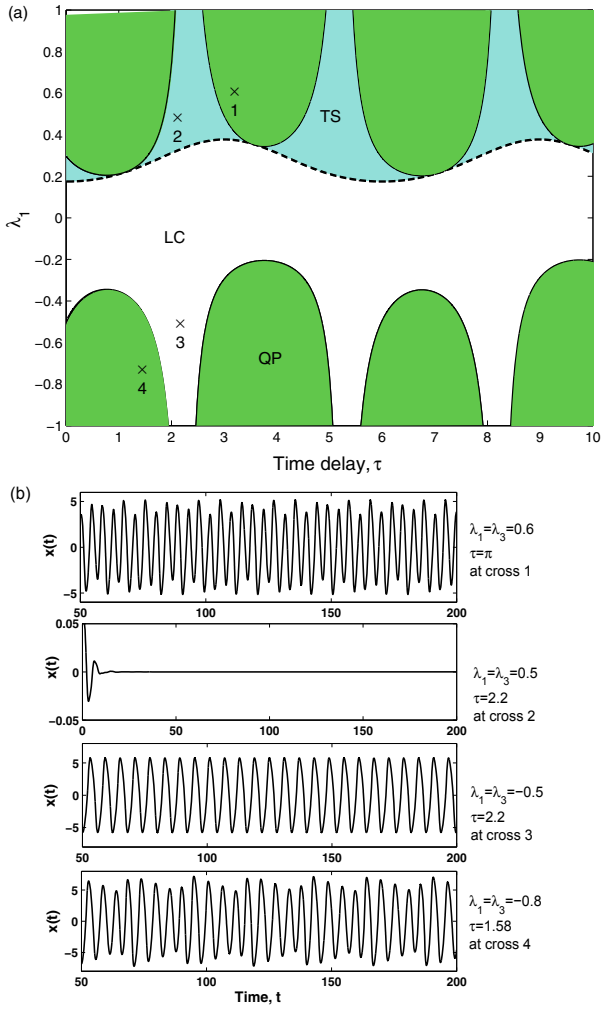

Fig. 4.1 **a** Stability chart of the QP response in the parameter plane (λ_1, τ); $\omega = 2.1$ and $\lambda_2 = 0.8$, LC: Limit cycle, TS: trivial solution, **b** time histories corresponding to different regions [10]

Figure 4.1a provides the stability chart of the QP vibrations in the parameter plane (λ_1, τ) and Fig. 4.1b shows time histories corresponding to different regions of Fig. 4.1a. The transitions of solutions are shown by moving between the crosses 1, 2, 3 and 4 in Fig. 4.1a. For instance, between cross 2 and cross 1 the response of the system undergoes a transition between no oscillation and QP vibration which is a bifurcation of a trivial stable equilibrium point to a stable QP solution. From cross 2 to 3 Hopf bifurcation takes place leading to periodic response and from cross 3 to 4 the solution bifurcates from periodic to QP oscillation, and from cross 3 to 1 similar bifurcation occurs via a secondary Hopf bifurcation.

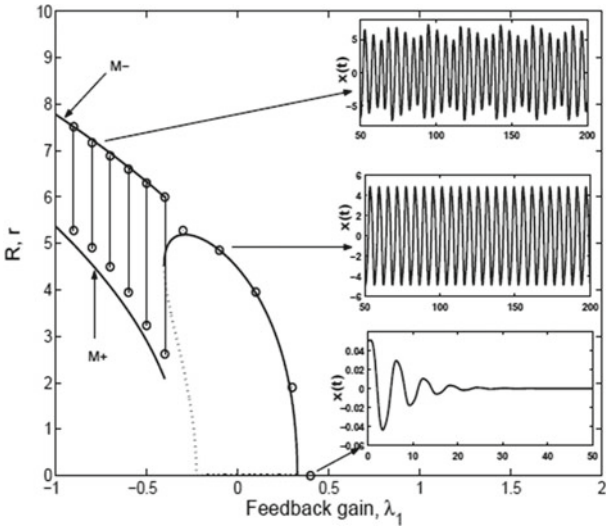

Fig. 4.2 Variation of periodic and QP responses versus λ_1 [10]

In Fig. 4.2 is shown the variation of periodic and QP repones versus λ_1 for $\lambda_3 = \lambda_1$, $\lambda_2 = 0.8$ and $\tau = 1.58$. The QP modulation envelope obtained by numerical simulation (circles) are compared to the analytical prediction (solid lines) for validation. Time series correspond to different regimes are also provided. The main result indicates that the modulation of the delay amplitude in the position gives birth to QP vibrations with large-amplitude performing away from the resonance in the region of negative λ_1.

Taking advantage of this previous finding, its first application to EH has been addressed in Belhaq and Hamdi [11]. They have considered a harvester device consisting in a delayed van der Pol oscillator coupled to an electromagnetic coupling in the form

$$\ddot{x} + x - \varepsilon(\alpha - \beta x^2)\dot{x} = \varepsilon\lambda(t)x(t-\tau) + \varepsilon\gamma_1 i \tag{4.3}$$

$$\frac{di}{dt} + \gamma_2 i = -\dot{z} \tag{4.4}$$

where ε is a small positive parameter, α, β are damping coefficients, $\lambda(t)$ is the delay amplitude, τ is the time delay and γ_1 is the electromagnetic coupling coefficient. The delay amplitude $\lambda(t)$ is assumed to be modulated harmonically as $\lambda(t) = \lambda_1 + \lambda_2 \cos \omega t$, where λ_1 is the unmodulated delay amplitude and λ_2, ω are, respectively, the amplitude and the frequency of the modulation, while i and $\frac{di}{dt}$ have been substituted for electric charge coordinate q ($i = \dot{q}$). The coefficient γ_2 is the reciprocal of the time constant of the electrical circuit. It is worthy to point out that the delay in the mechanical part is not considered as an input power. It should be considered as inherently present in the harvester system as in milling and

turning operations [17–19]. The system response was investigated near the *delay parametric resonance* assumig the resonance condition $1 = (\frac{\omega}{2})^2 + \varepsilon\sigma$ where σ is a detuning parameter. Averaging method was used to approximate the amplitude and the output power of the periodic vibrations and the second-step perturbation method was applied to approximate the amplitude of the QP vibrations and the corresponding output power of the harvester device. For validation, the analytical prediction

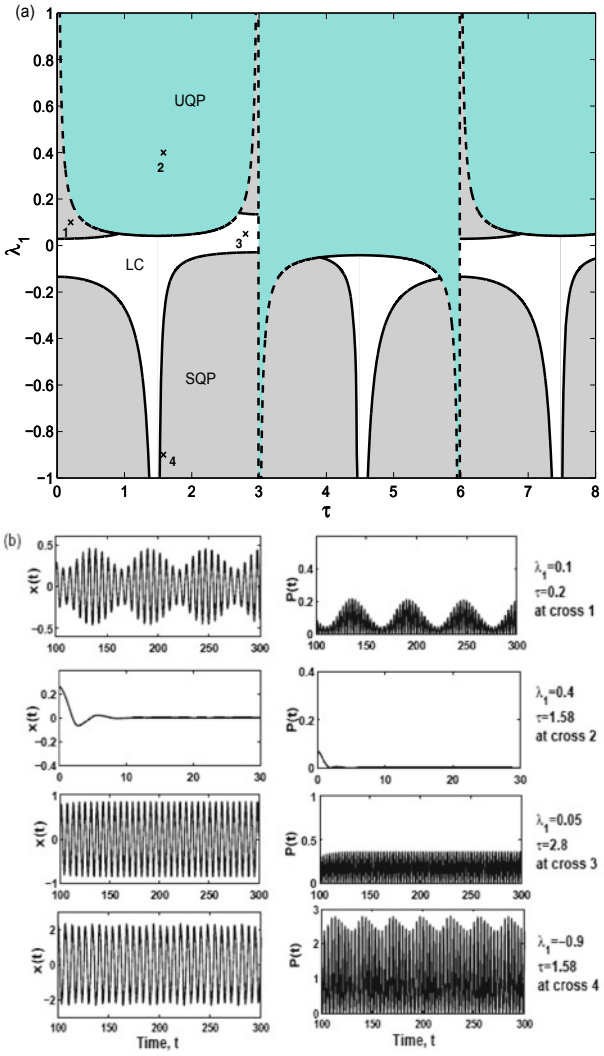

Fig. 4.3 **a** Stability chart of QP solutions in the parameter plane (λ_1, τ), **b** time histories corresponding to different regions; $\lambda_2 = 0.2$, $\omega = 2.1$ and $\gamma_2 = 1.33$. UQP: unstable QP, SQP: stable QP, LC: limit cycle [11]

(solid lines) are compared to numerical simulation (circles) obtained using dde23 algorithm [21].

In Fig. 4.3a is presented the stability chart of the QP vibrations in the parameter plane (λ_1, τ). Regions of stable and unstable QP vibrations are indicated, respectively, by UQP (aqua regions) and SQP (grey regions). Within the white region periodic oscillations indicated by LC occur. Time histories of responses and powers corresponding to different regions of Fig. 4.3a are shown in Fig. 4.3b. Bifurcation of solutions are obtained by moving between regions in Fig. 4.3a. For instance, from cross 2 to 3 Hopf bifurcation occurs giving rise to LC oscillations. The system behavior changes from LC to SQP oscillation with a slight modulation when moving from

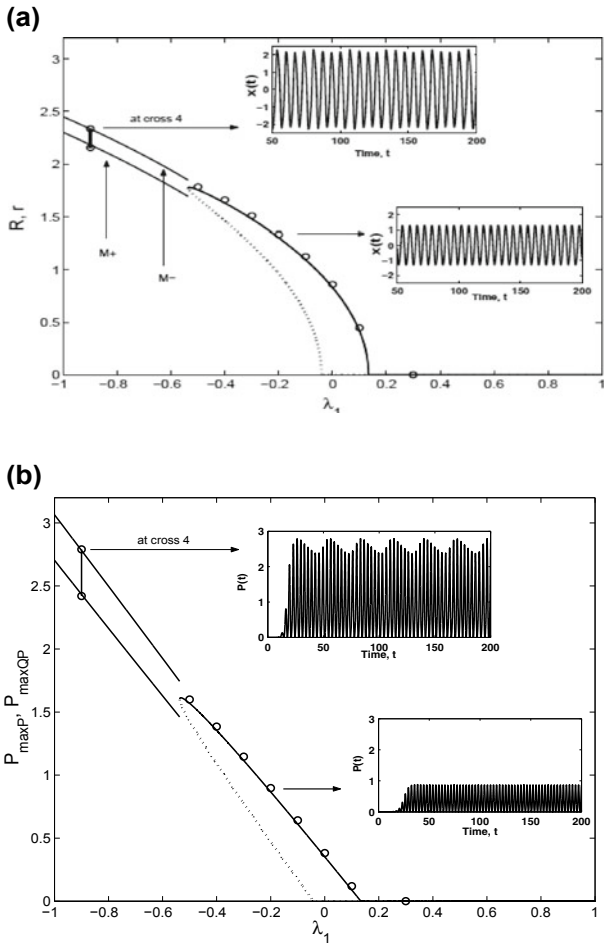

Fig. 4.4 Vibration (**a**) and power (**b**) amplitudes versus λ_1 for $\tau = 1.58$, $\omega = 2.1$ and $\gamma_2 = 1.33$; analytical (solid lines) and numerical (circles) approximations [11]

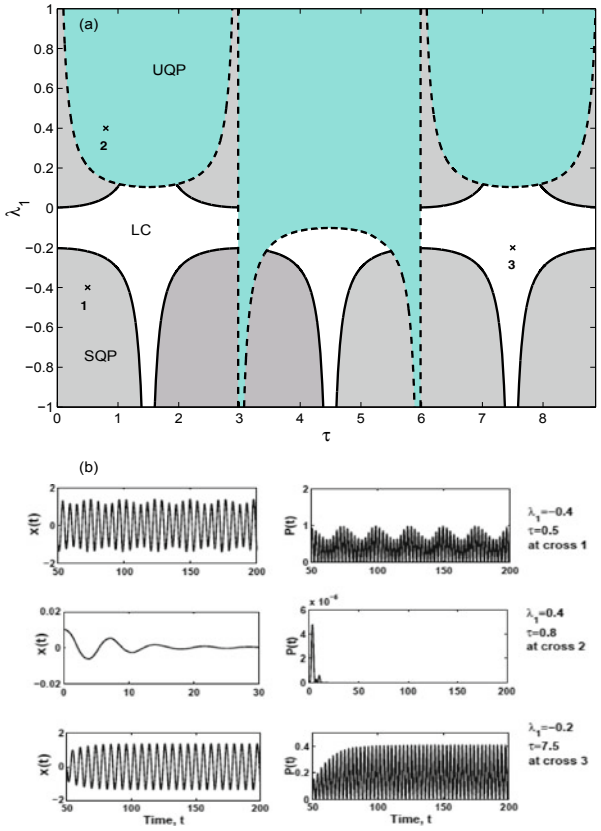

Fig. 4.5 **a** Stability chart of QP solutions in the plane (λ_1, τ), **b** time histories corresponding to different regions; $\lambda_2 = 0.2$, $\omega = 2.1$ and $K = \gamma_2 = 1.33$. UQP: unstable QP, SQP: stable QP, LC: limit cycle [13]

cross 3 to 4. It is worthy mentioning that cross 4 has been carefully chosen close to the bifurcation curve to demonstrate the accuracy of the analytical prediction of the stability chart. This is illustrated by comparison to time series corresponding to cross 4 in Fig. 4.3a (see Fig. 4.3b bottom).

Figure 4.4 depicts the variation of vibration and power amplitudes versus λ_1. One can clearly observe from Fig. 4.4a that for negative values of λ_1 the amplitude of the QP modulation is larger comparing to the amplitude of the periodic response. Accordingly, the corresponding power amplitudes shown in Fig. 4.4b demonstrate clearly that the performance of the extracted power in the QP region is better than the performance of the output power in the periodic region.

Another case has been considered by Ghouli et al. [13] for which the time delay is introduced in both mechanical and electrical components. In this case, the EH system consists of a delayed van der Pol oscillator coupled to a delayed electromagnetic

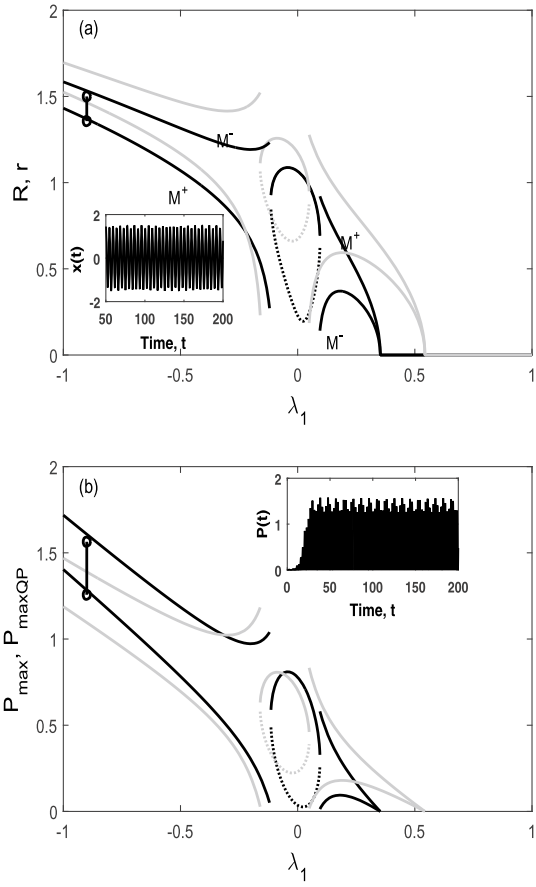

Fig. 4.6 Vibration (**a**) and power (**b**) amplitudes versus λ_1 for $\tau = 0.3$, $\lambda_2 = 0.2$, $\omega = 2.1$ and $\gamma_2 = 1.33$; analytical (solid lines) and numerical (circles) approximations. Black line for delayed circuit $K = \gamma_2$, grey line for undelayed circuit $K = 0$. Solid line for stable and doted line for unstable [13]

element. The governing equations are written as

$$\ddot{x} + x - \varepsilon(\alpha - \beta x^2)\dot{x} = \varepsilon\lambda(t)x(t-\tau) + \varepsilon\gamma_1 i \tag{4.5}$$

$$\frac{di}{dt} + \gamma_2 i = Ki(t-\tau) - \dot{z} \tag{4.6}$$

where K is the delay amplitude in the electric circuit and τ is the time delay. The other parameters are defined as before.

As in the previous case (4.3), (4.4), the response of the system was investigated near the *delay parametric resonance* using a similar perturbation analysis.

Figure 4.5a presents the stability chart of the QP vibrations in the parameter plane (λ_1, τ). The dashed lines delimit domains of unstable QP vibrations and the solid lines determine the domains where the QP vibrations are stable. Similarly, UQP (*aqua* regions) means unstable QP while SQP (*grey* regions) means stable QP. The

periodic oscillations exist in the *white* regions and are indicated by LC. Time histories and the corresponding output power responses are shown in Fig. 4.5b. The transitions of solutions are obtained by moving between the crosses 1, 2 and 3 in Fig. 4.5a.

Figure 4.6 shows the variation of vibration and power amplitudes versus λ_1 for $K = 0$ (undelayed circuit, *grey* lines) and $K = \gamma_2$ (delayed circuit, *black* lines). It can be seen that negative values of λ_1 decreases the amplitude of the QP modulation (Fig. 4.6a, *black* envelope), but on the contrary, increases the harvested power (Fig. 4.6b, *black* envelope). In other words, in the delayed van der Pol harvester in which the delay is also introduced in the electrical circuit the maximum output power extracted from QP vibration does not necessarily correspond to the maximum amplitude of QP oscillations.

4.3 The Excited van der Pol Oscillator and Energy Harvesting

In this part we study QP vibration-based EH in an excited van der Pol oscillator coupled to a delayed piezoelectric device. The main purpose here is to examine the influence of the time delay in the electrical circuit on the energy extracted from QP vibrations. The corresponding schematic of the harvester is presented in Fig. 4.7 and the governing equations can be written in the dimensionless form as

$$\ddot{x}(t) + x(t) - [\alpha - \beta x(t)^2]\dot{x}(t) - \chi v(t) = f\cos(\omega t) \tag{4.7}$$

$$\dot{v}(t) + \lambda[v(t) - v(t-\tau)] + \kappa\dot{x}(t) = 0 \tag{4.8}$$

where $x(t)$ is the relative displacement of the rigid mass m, α and β are the mechanical damping coefficients, f, ω are, respectively, the amplitude and the frequency of the harmonic excitation, $v(t)$ is the voltage across the load resistance, χ is the piezoelectric coupling term in the mechanical attachment, κ is the piezoelectric coupling term, λ is the reciprocal of the time constant of the electrical circuit and τ is the time delay.

The objective is to investigate periodic and QP responses as well as the corresponding output powers of the harvester device (4.7), (4.8). We perform perturbation method near the principal resonance by introducing the resonance condition $1 = \omega^2 + \sigma$ where σ is a detuning parameter. The first-step multiple scales method is implemented by introducing a bookkeeping parameter ε and scaling parameters such as (4.7) and (4.8) take the form

$$\ddot{x}(t) + \omega^2 x(t) = \varepsilon[(\alpha - \beta x(t)^2)\dot{x}(t) + \chi v(t) + f\cos(\omega t) - \sigma x(t)] \tag{4.9}$$

$$\dot{v}(t) + \lambda[v(t) - v(t-\tau)] + \kappa\dot{x}(t) = 0 \tag{4.10}$$

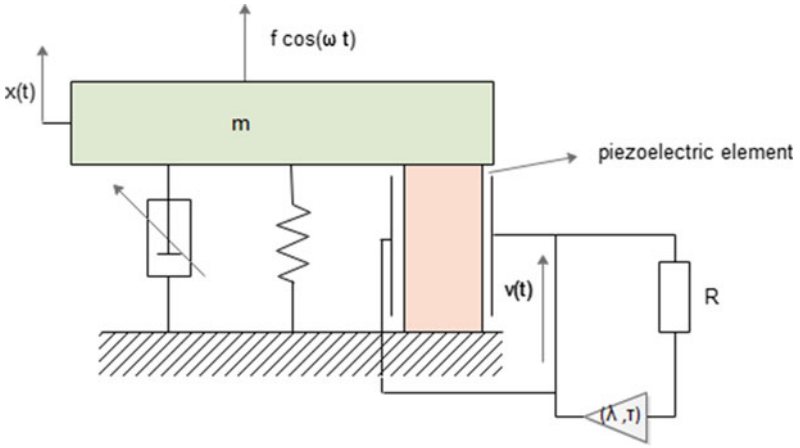

Fig. 4.7 Schematic description of the EH system

A solution to (4.9) and (4.10) can be sought in the form

$$x(t) = x_0(T_0, T_1) + \varepsilon x_1(T_0, T_1) + O(\varepsilon^2) \tag{4.11}$$

$$v(t) = v_0(T_0, T_1) + \varepsilon v_1(T_0, T_1) + O(\varepsilon^2) \tag{4.12}$$

where $T_0 = t$ and $T_1 = \varepsilon t$. The time derivatives become $\frac{d}{dt} = D_0 + \varepsilon D_1 + O(\varepsilon^2)$ and $\frac{d^2}{dt^2} = D_0^2 + \varepsilon^2 D_1^2 + 2\varepsilon D_0 D_1 + O(\varepsilon^2)$ where $D_i^j = \frac{\partial^j}{\partial^j T_i}$. Substituting (4.11) and (4.12) into (4.9) and (4.10) and equating coefficient of like powers of ε, we obtain up to the second order the following hierarchy of problems:

At the first order:

$$D_0^2 x_0 + \omega^2 x_0 = 0 \tag{4.13}$$

$$D_0 v_0 + \lambda[v_0 - v_{0\tau}] + \kappa D_0 x_0 = 0 \tag{4.14}$$

and at the second order:

$$D_0^2 x_1 + \omega^2 x_1 = -2D_0 D_1 x_0 + (\alpha - \beta x_0^2) D_0 x_0 - \sigma x_0 + \chi v_0 + f\cos(\omega t) \tag{4.15}$$

$$D_0 v_1 + \lambda[v_1 - v_{1\tau}] = -D_1 v_0 - \kappa D_0 x_1 - \kappa D_1 x_0 \tag{4.16}$$

Up to the first order the solution is given by

$$x_0(T_0, T_1) = A(T_1)e^{i\omega T_0} + \bar{A}(T_1)e^{-i\omega T_0} \tag{4.17}$$

$$v_0(T_0, T_1) = \frac{-\kappa i\omega A(T_1)}{\lambda + i\omega - \lambda e^{-i\omega\tau}} e^{i\omega T_0} + \frac{\kappa i\omega \bar{A}(T_1)}{\lambda - i\omega - \lambda e^{i\omega\tau}} e^{-i\omega T_0} \tag{4.18}$$

where $A(T_1)$ and $\bar{A}(T_1)$ are unknown complex conjugate functions. Substituting (4.17) and (4.18) into (4.15) and (4.16) and eliminating the secular terms, one obtains

$$-2i\omega(D_1 A) + i\alpha\omega A - i\beta\omega A^2\bar{A} - \sigma A - \frac{\kappa i\omega\chi A}{\lambda + i\omega - \lambda e^{-i\omega\tau}} + \frac{f}{2} = 0 \quad (4.19)$$

Expressing $A = \frac{1}{2}ae^{i\theta}$ where a and θ are the amplitude and the phase, we obtain up to the first order the modulation equations

$$\begin{cases} \dfrac{da}{dt} = S_1 a + S_2 a^3 + S_3 \sin(\theta) \\ a\dfrac{d\theta}{dt} = S_4 a + S_3 \cos(\theta) \end{cases} \quad (4.20)$$

where $S_i (i = 1, ..., 4)$ are given by

$$S_1 = \frac{\alpha}{2} - \frac{\kappa\chi(\lambda - \lambda\cos(\omega\tau))}{2(\lambda - \lambda\cos(\omega\tau))^2 + 2(\omega + \lambda\sin(\omega\tau))^2}$$

$$S_2 = \frac{-\beta}{8} \qquad S_3 = -\frac{f}{2\omega}$$

$$S_4 = \frac{\sigma}{2\omega} + \frac{\kappa\chi(\omega + \lambda\sin(\omega\tau))}{2(\lambda - \lambda\cos(\omega\tau))^2 + 2(\omega + \lambda\sin(\omega\tau))^2}$$

The solution up to the first order given by (4.17) and (4.18) can be expressed as

$$\begin{cases} x_0(T_0, T_1) = a\cos(\omega t + \theta) \\ v_0(T_0, T_1) = V\cos(\omega t + \theta + \arctan\dfrac{\lambda - \lambda\cos(\omega\tau)}{\omega + \lambda\sin(\omega\tau)}) \end{cases} \quad (4.21)$$

such that the condition $\omega + \lambda\sin(\omega\tau) \neq 0$ must be satisfied. Moreover, the voltage amplitude V is given by

$$V = \frac{\kappa\omega}{\sqrt{(\lambda - \lambda\cos(\omega\tau))^2 + (\omega + \lambda\sin(\omega\tau))^2}}a \quad (4.22)$$

The steady-state response of system (4.20), corresponding to periodic solutions of (4.9) and (4.10), are determined by setting $\frac{da}{dt} = \frac{d\theta}{dt} = 0$. Eliminating the phase, we obtain the following algebraic equation in a

$$S_2^2 a^6 + 2S_1 S_2 a^4 + (S_1^2 + S_4^2)a^2 - S_3^2 = 0 \quad (4.23)$$

An expression for the average power is obtained by integrating the dimensionless form of the instantaneous power $P(t) = \lambda v(t)^2$ over a period T. This leads to

$$P_{av} = \frac{1}{T}\int_0^T \lambda v^2 dt \tag{4.24}$$

where $T = \frac{2\pi}{\omega}$. Then, the average power expressed by $P_{av} = \frac{\lambda V^2}{2}$ reads

$$P_{av} = \frac{1}{2}\left(\frac{\lambda\kappa^2\omega^2}{(\lambda - \lambda\cos(\omega\tau))^2 + (\omega + \lambda\sin(\omega\tau))^2}\right)a^2 \tag{4.25}$$

where the amplitude a is obtained from (4.23). Using the maximization procedure, the maximum power response is given by

$$P_{max} = \frac{\lambda\kappa^2\omega^2 a^2}{(\lambda - \lambda\cos(\omega\tau))^2 + (\omega + \lambda\sin(\omega\tau))^2} \tag{4.26}$$

Equations (4.23) and (4.26) are used to examine the influence of different system parameters on the periodic response and on the corresponding maximum output power of the harvester.

To approximate the QP response of the original system, we apply the second-step perturbation method [22] on the modulation equations (4.20). To this end, it is convenient to transform the modulation equations (4.20) from the polar form to the following Cartesian system using the variable change $u = a\cos\theta$ and $w = -a\sin\theta$

$$\begin{cases} \dfrac{du}{dt} = S_4 w + \mu\{S_1 u + S_2 u(u^2 + w^2)\} \\ \dfrac{dw}{dt} = -S_4 u - S_3 + \mu\{S_1 w + S_2 w(u^2 + w^2)\} \end{cases} \tag{4.27}$$

where μ is a new bookkeeping parameter introduced to perform the second-step multiple scales method. A periodic solution of the slow flow (4.27) corresponding to the QP response of the original system (4.9), (4.10) can be expressed in the forme

$$u(t) = u_0(T_0, T_1) + \mu u_1(T_0, T_1) + O(\mu^2) \tag{4.28}$$

$$w(t) = w_0(T_0, T_1) + \mu w_1(T_0, T_1) + O(\mu^2) \tag{4.29}$$

where $T_0 = t$ and $T_1 = \mu t$. The time derivatives become $\frac{d}{dt} = D_0 + \mu D_1 + O(\mu^2)$ where $D_i^j = \frac{\partial^j}{\partial^j T_i}$. Substituting (4.28) and (4.29) into (4.27), and equating coefficient of like powers of μ, we obtain at the first order

$$D_0^2 u_0 + S_4^2 u_0 = -S_3 S_4 \tag{4.30}$$

$$S_4 w_0 = D_0 u_0 \tag{4.31}$$

and at the second order we have

$$\begin{aligned} D_0^2 u_1 + S_4^2 u_1 = &-D_0 D_1 u_0 + S_1 D_0 u_0 + S_2 D_0 u_0 (u_0^2 + w_0^2) \\ &-S_4 D_1 w_0 + S_2 u_0 D_0 (u_0^2 + w_0^2) + S_4 S_1 w_0 + S_4 S_2 w_0 (u_0^2 + w_0^2) \end{aligned} \tag{4.32}$$

$$S_4 w_1 = D_0 u_1 + D_1 u_0 - S_1 u_0 - S_2 u_0 (u_0^2 + w_0^2) \tag{4.33}$$

where S_4 is the frequency of the QP modulation. The solution up to the first order is written as

$$u_0(T_0, T_1) = R(T_1) \cos(S_4 T_0 + \psi(T_1)) - \alpha_2 \tag{4.34}$$

$$w_0(T_0, T_1) = -R \sin(S_4 T_0 + \psi(T_1)) \tag{4.35}$$

where R and ψ are, respectively, the amplitude and the phase of the QP modulation and $\alpha_2 = \frac{S_3}{S_4}$. Substituting (4.34) and (4.35) into (4.32) and removing secular terms gives the following *slow-modulation* equations

$$\begin{cases} \dfrac{dR}{dt} = (S_1 + 2S_2\alpha_2^2)R + S_2 R^3 \\ R\dfrac{d\psi}{dt} = 0 \end{cases} \tag{4.36}$$

The equilibria of this *slow-modulation* system determine the periodic solutions of the modulation equations (4.36), corresponding to the QP solutions of the original system (4.9), (4.10). The nontrivial equilibrium obtained by setting $\frac{dR}{dt} = 0$ is given by

$$R = \sqrt{-\frac{S_1 + 2S_2\alpha_2^2}{S_2}} \tag{4.37}$$

Consequently, the approximate periodic solution of the slow flow (4.27) is given by

$$u(t) = R cos(\theta t) - \alpha_2 \tag{4.38}$$

$$w(t) = -R sin(\theta t) \tag{4.39}$$

The approximate amplitude $a(t)$ of the QP response reads

$$a(t) = \sqrt{R^2 + \alpha_2^2 - 2\alpha_2 R \cos(\theta t)} \tag{4.40}$$

and the QP modulation envelope is delimited by a_{min} and a_{max} given by

$$a_{min} = min\{\sqrt{R^2 + \alpha_2^2 \pm 2\alpha_2 R}\} \tag{4.41}$$

$$a_{max} = max\{\sqrt{R^2 + \alpha_2^2 \pm 2\alpha_2 R}\} \tag{4.42}$$

The explicit expression of the QP response of the original equation (4.9) is then written as

$$x(t) = u(t)\cos(\omega t) + w(t)\sin(\omega t) \tag{4.43}$$

On the other hand, the QP solution of the voltage $v(t)$, obtained by inserting (4.43) into (4.8), can be extracted via a convolution integral with the boundary condition $v(0) = v(T)$ where $T = \frac{2\pi}{\nu}$. This leads to

$$v(t) = -\kappa e^{(\lambda e^{\lambda\tau} - \lambda)t} \int_0^t \dot{x}(t') e^{(\lambda - \lambda e^{\lambda\tau})t'} dt' \tag{4.44}$$

Consequently, the power, the average and the maximum output powers in the QP regime are given, respectively, by

$$P_{QP}(t) = \lambda(-\kappa e^{(\lambda e^{\lambda\tau} - \lambda)t} \int_0^t \dot{x}(t') e^{(\lambda - \lambda e^{\lambda\tau})t'} dt')^2 \tag{4.45}$$

$$P_{avQP} = \frac{\lambda\kappa^2\nu^2}{2[(\lambda - \lambda\cos(\omega\tau))^2 + (\nu + \lambda\sin(\omega\tau))^2]} a^2 \tag{4.46}$$

$$P_{maxQP} = \frac{\lambda\kappa^2\nu^2}{[(\lambda - \lambda\cos(\omega\tau))^2 + (\nu + \lambda\sin(\omega\tau))^2]} a^2 \tag{4.47}$$

where $\nu = S_4$ is the frequency of the QP modulation and a is now derived from (4.41) and (4.42).

Figure 4.8a, b show the frequency response of periodic and QP solutions and the corresponding output power amplitudes (P_{max}, P_{maxQP}) versus the frequency ω, respectively, in the case of the undelayed electrical circuit of the harvester ($\tau = 0$). The periodic response is given by (4.23) and the boundaries of the QP modulation envelope are obtained from (4.41) and (4.42). Similarly, the maximum powers for periodic and QP vibrations are given, respectively, by (4.26) and (4.47). For validation, the analytical prediction (solid lines for stable and dashed line for unstable) are compared to numerical simulation (circles) obtained using Runge Kutta of order 4. The plots in Fig. 4.8b show that in the absence of time delay, periodic vibration-based EH can be achieved, but in a very narrow region located around the resonance peak. Instead, QP vibration-based EH can be obtained over a broadband of frequency

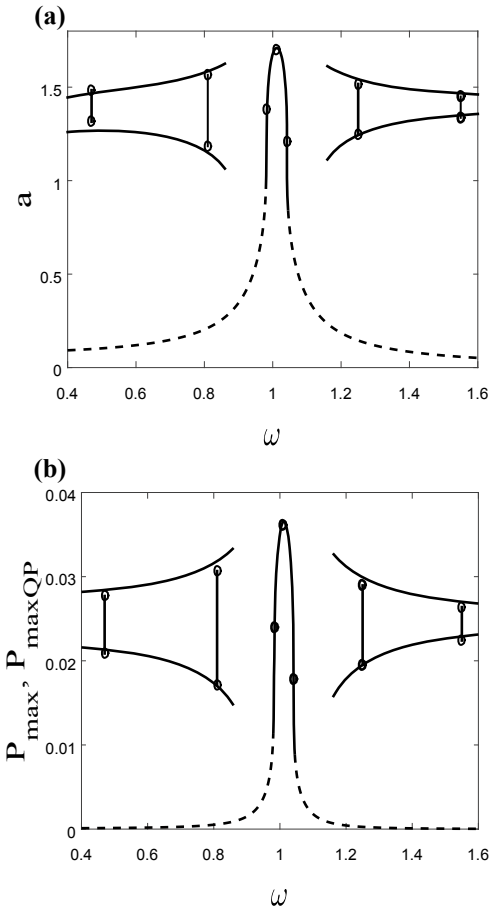

Fig. 4.8 Vibration and power amplitudes versus ω for $\alpha = 0.1$, $\beta = 0.2$, $\chi = 0.05$, $\lambda = 0.05$, $\kappa = 0.5$, $f = 0.08$ and $\tau = 0$. Analytical prediction (solid lines for stable and dashed line for unstable) and numerical simulation (circles)

away from the resonance with a performance comparable to that provided by periodic vibrations.

In Fig. 4.9 is shown the influence of time delay in the electrical component on the EH performance of the system. The curves given by the *black* lines correspond to the delayed case ($\tau = 6.2$). For comparison, we plot in *grey* the case where the delay is absent ($\tau = 0$). It can be observed that the presence of the delay in the electrical circuit increases the QP output power over a certain range of the frequency ω located away from the resonance (Fig. 4.9b). This QP output power can achieve a better performance comparing to the periodic output power, as illustrated in the vicinity of $\omega = 0.8$ and $\omega = 1.2$ (Fig. 4.9b).

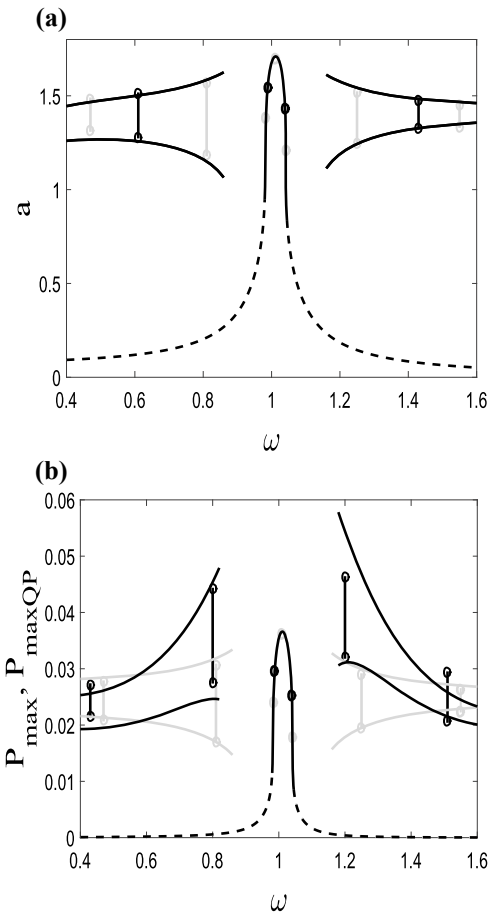

Fig. 4.9 Vibration and power amplitudes versus ω for $\alpha = 0.1$, $\beta = 0.2$, $\chi = 0.05$, $\lambda = 0.05$, $\kappa = 0.5$ and $f = 0.08$. Analytical prediction (solid lines for stable and dashed line for unstable) and numerical simulation (circles). *black* lines for delayed electric circuit ($\tau = 6.2$) and *grey* lines for undelayed circuit ($\tau = 0$, Fig. 4.8)

To ensure the stability of the QP vibrations during energy extraction operation, it is important to determine the stability chart of the response. This can be done by considering the stability of the nontrivial solution of the slow-slow flow (4.36) obtained by calculating the eigenvalues of the corresponding Jacobian matrix $\mathbf{J}$. The curves delimiting the regions of existence of the QP oscillations and their domains of stability are given by the conditions ($Tr(\mathbf{J}) = -2S_1 - 4S_2\alpha_2^2 < 0$ and $Det(\mathbf{J}) = 0$).

Figure 4.10a shows this stability chart in the parameter plane (f, ω) for $\tau = 6.2$ indicating the *grey* regions where stable QP (SQP) solutions take place and the *white* region corresponding to stable periodic (SP) solutions. In Fig. 4.10b are shown time histories and the corresponding output power responses related to crosses labelled 1, 2, 3 in Fig. 4.10a. From cross 1 to cross 2 or 3 the response bifurcates from SP to SQP oscillations via secondary Hopf bifurcation producing a slight modulation of the amplitude response and a significant performance of the output power at cross 3.

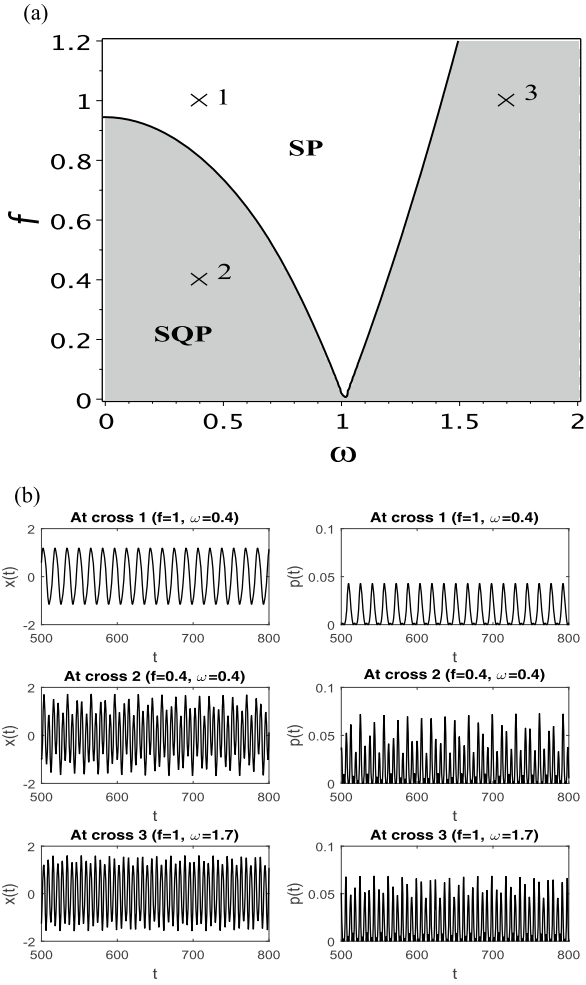

Fig. 4.10 **a** Stability chart in the plane (f, ω), **b** time and power histories corresponding to different regions picked from (**a**). SP: stable periodic, SQP: stable QP; $\alpha = 0.1, \beta = 0.2, \chi = 0.05, \lambda = 0.05, \alpha = 0.1, \kappa = 0.5$, and $\tau = 6.2$

Finally, we show in Fig. 4.11 the variation of vibration and maximum power amplitudes χ versus the piezoelectric coupling coefficient χ. It can be seen that a good performance of QP vibration-based EH can be achieved in certain range of negative χ located slightly at the right of the periodic region near $\chi = -0.5$ (Fig. 4.11b).

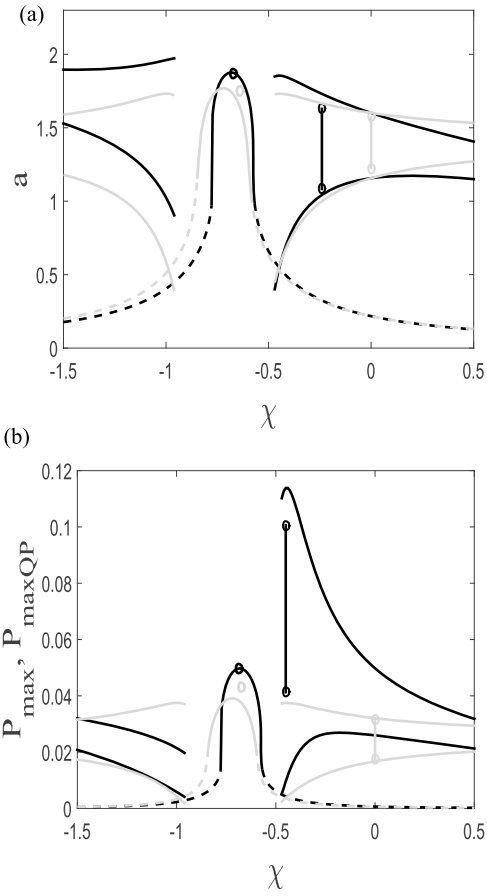

Fig. 4.11 Vibration and power amplitudes versus χ for $\alpha = 0.1$, $\beta = 0.2$, $\omega = 0.8$, $\lambda = 0.05$, $\alpha = 0.1$, $\kappa = 0.5$ and $f = 0.08$. Analytical prediction (solid lines for stable and dashed line for unstable) and numerical simulation (circles). *black* lines for delayed circuit ($\tau = 6.2$) and *grey* lines for undelayed circuit ($\tau = 0$)

4.4 Conclusions

We have provided in a first part of the chapter recent results in QP vibration-based EH for some variants of delayed van der Pol harvesters for which the delay amplitude is modulated with certain amplitude and frequency around a nominal value. These variants include the delayed van der Pol harvester coupled either to delayed or undelayed electromagnetic subsystem. The influence of delay parameters on the performance of the harvester has been examined. In particular, it was shown that when the delay is introduced in both the mechanical oscillator and the electrical circuit the maximum output power extracted from QP vibrations does not necessarily correspond to the maximum amplitude of QP oscillations.

In a second part of the chapter we have investigated QP vibration-based EH in the case where the van der Pol oscillator is subjected to external harmonic excitation and coupled to a delayed piezoelectric component. The second-step multiple scales

method was applied near the primary resonance to obtain approximation of the QP responses as well as the amplitude of the harvested power. Results showed that in the presence of time delay in the electrical circuit of the harvester, it is possible to harvest energy from the induced QP vibrations with a good performance over a broadband of system parameters away from the resonance. Such a performance is comparable to the one provided by the periodic vibrations, except that the energy extracted from periodic vibrations can be achieved only in a narrow region located around the resonance peak, while energy extracted from QP vibrations can be attained over a broadband of frequency away from the resonance. To guarantee the robustness of the QP vibration during energy extraction operation, a stability analysis was performed and the QP stability chart was determined. Numerical simulations have been conducted to confirm the analytical predictions. This study provides an interesting alternative to harvest energy in nonlinear harvesters away from the resonance, as instabilities and jump phenomena present often difficulty in maintaining energy harvesting operations in a stable and robust regime near the resonance.

References

1. N.G. Stephen, On energy harvesting from ambient vibration. J. Sound Vib. **293**, 409–425 (2006)
2. G.A. Lesieutre, G.K. Ottman, H.F. Hofmann, Damping as a result of piezoelectric energy harvesting. J. Sound Vib. **269**, 991–1001 (2004)
3. H.A. Sodano, D.J. Inman, G. Park, Generation and storage of electricity from power harvesting devices. J. Intell. Mater. Syst. **16**, 67–75 (2005)
4. H.A. Sodano, D.J. Inman, G. Park, Comparison of piezoelectric energy harvesting devices for recharging batteries. J. Intell. Mater. Syst. **16**, 799–807 (2005)
5. D.D. Quinn, A.L. Triplett, A.F. Vakakis, L.A. Bergman, Energy harvesting from impulsive loads using intestinal essential nonlinearities. J. Vib. Acoust. **133**, 011004 (2011)
6. A. Abdelkefi, A.H. Nayfeh, M.R. Hajj, Modeling and analysis of piezoaeroelastic energy harvesters. Nonlinear Dyn. **67**, 925–939 (2011)
7. A. Abdelkefi, A.H. Nayfeh, M.R. Hajj, Design of piezoaeroelastic energy harvesters. Nonlinear Dyn. **68**, 519–530 (2012)
8. B.P. Mann, N.D. Sims, Energy harvesting from the nonlinear oscillations of magnetic levitation. J. Sound Vib. **319**, 515–530 (2009)
9. A. Bibo, M.F. Daqaq, Energy harvesting under combined aerodynamic and base excitations. J. Sound Vib. **332**, 5086–5102 (2013)
10. M. Hamdi, M. Belhaq, Quasi-periodic vibrations in a delayed van der Pol oscillator with time-periodic delay amplitude. J. Vib. Control (2015). https://doi.org/10.1177/1077546315597821
11. M. Belhaq, M. Hamdi, Energy harversting from quasi-periodic vibrations. Nonlinear Dyn. **86**, 2193–2205 (2016)
12. Z. Ghouli, M. Hamdi, F. Lakrad, M. Belhaq, Quasiperiodic energy harvesting in a forced and delayed Duffing harvester device. J. Sound Vib. **407**, 271–285 (2017)
13. Z. Ghouli, M. Hamdi, M. Belhaq, Energy harvesting from quasi-periodic vibrations using electromagnetic coupling with delay. Nonlinear Dyn. **89**, 1625–1636 (2017)
14. M. Belhaq, Z. Ghouli, M. Hamdi, Energy harvesting in a Mathieu-van der Pol-Duffing MEMS device using time delay. Nonlinear Dyn. **94**, 2537–2546 (2018)
15. Z. Ghouli, M. Hamdi, M. Belhaq, Improving energy harvesting in excited Duffing harvester device using a delayed piezoelectric coupling, in *MATEC Web of Conferences*, vol. 241 (2018), pp. 01010

16. I. Kirrou, A. Bichri, M. Belhaq, Energy harvesting in a delayed Rayleigh harvester device, in *MATEC Web of Conferences*, vol. 241 (2018), pp. 01026
17. G. Stepan, T. Kalmr-Nagy, Nonlinear regenerative machine tool vibrations, in *Proceedings of the 1997 ASME Design Engineering Technical Conferences, 16th ASME Biennial Conference on Mechanical Vibration and Noise (Sacramento, 1997)*, DETC97/VIB-4021 (1997), pp. 1–11
18. T. Kalmr-Nagy, G. Stepan, F.C. Moon, Subcritical Hopf bifurcation in the delay equation model for machine tool vibrations. Nonlinear Dyn. **26**, 121–142 (2001)
19. R. Rusinek, A. Weremczuk, J. Warminski, Regenerative model of cutting process with nonlinear Duffing oscillator. Mech. Mech. Eng. **15**, 129–143 (2011)
20. A.H. Nayfeh, D.T. Mook, *Nonlinear Oscillations* (Wiley, New York, 1979)
21. L.E. Shampine, S. Thompson, Solving delay differential equations with dde23 (2000). http://www.radford.edu/~thompson/webddes/tutorial.pdf
22. M. Belhaq, M. Houssni, Quasi-periodic oscillations, chaos and suppression of chaos in a nonlinear oscillator driven by parametric and external excitations. Nonlinear Dyn. **18**, 1–24 (1999)

Chapter 5
Reference Dynamics Based Motion Planning for Robotic Systems with Flexible Components

Elżbieta Jarzębowska, Krzysztof Augustynek and Andrzej Urbaś

Abstract Analysis of robot dynamics based motion planning is presented in the chapter. Motion of a robot is task based and is formulated upon work dedicated to it. The focus of motion planning is positioning and velocity of the robot end-effector, which are programmed by position and kinematic constraint equations. The constraints are incorporated into the system dynamics, referred to as reference dynamics, whose outputs deliver position and velocity time histories of the end-effector and joints. A special computational procedure for the constrained dynamics generation enables development of the reference dynamics for rigid and flexible system models such that vibration, allowable velocity profiles for robot joints and other programmed motion kinematic properties can be analyzed. This analysis enables planning feasible tasks for robots and design controllers for vibration compensation.

5.1 Introduction

Analysis of robot motion planning, which is task based and dedicated to work and services delivery is presented in the chapter. The focus of motion planning is positioning and velocity of the robot end-effector, which are programmed by position and kinematic constraint equations. The constraints are incorporated into the system dynamics, referred to as reference dynamics, whose outputs deliver position and velocity time histories of the end-effector and joints. The key contribution of the paper is in three aspects of the analysis. The first one is the possibility of kinematic constraints incorporation into the system dynamics, the second one is the special computational procedure for the constrained dynamics generation, which

E. Jarzębowska (✉)
Warsaw University of Technology, Nowowiejska 24, 00-665 Warsaw, Poland
e-mail: elajarz@meil.pw.edu.pl

K. Augustynek · A. Urbaś
University of Bielsko-Biala, Willowa 2, 43-309 Bielsko-Biala, Poland
e-mail: Kaugustynek@ath.bielsko.pl

A. Urbaś
e-mail: aurbas@ath.bielsko.pl

M. Belhaq (ed.), *Topics in Nonlinear Mechanics and Physics*,
Springer Proceedings in Physics 228, https://doi.org/10.1007/978-981-13-9463-8_5

provides reference dynamic models satisfying all constraints upon them. The third contribution, comparing to the results reported in the literature, see e.g. [1, 2], is in modelling flexibility of the system parts and supports. The constraints put on a system are referred to as programmed and they are imposed as control goals on system performance or service task requirements. The procedure of generating reference dynamics offers automated derivation of equations and it was successfully developed and implemented to rigid system models [5, 6]. The advantage of this procedure is that it serves both reference and control oriented dynamics derivation and the final dynamic models are obtained in the reduced state form, i.e. constraint reaction forces are eliminated. The procedure is extended on flexible subsystems of lightweight and fast machine parts and servicing equipment, which are prone to vibration in some work regimes. Vibrations may significantly affect system performance and disable effective controller designs. Flexibility of links is modelled using the rigid finite element method [3, 9, 10], which advantage relies in its ability of application of the rigid body approach to modelling flexible link elements. The novelty of the presented method is its ability to analyze any system reference motion, including flexible link vibration, in the presence of kinematic task-based constraints. The results of this analysis may contribute to verification of a system behavior when it is subjected to given kinematic constraints, help to specify desired task-based constraints properly, e.g. put tighter velocity limits, to exclude some work regimes or to design controllers correctly. The possibility of reference motion analysis, e.g. desired positions of the robot end-effector [7], in these aspects enables simulation of various work regimes for system models and selection of required and safe task based motion parameters, accordingly. The special interest of this chapter is paid to plan a robot end-effector desired velocity. Usually, the robot velocity is controlled through the joint velocities at the kinematics or dynamic levels, see e.g. [8] and references there. In [8], traditional velocity control of robot manipulators in joint space, assuming Lagrangian non-linear dynamics, by three control schemes resulting as extensions of proportional-integral velocity regulators of direct current motors is examined. In this chapter a method of desired position and velocity specification through the programmed constraints is provided. It is followed by subsequent derivation of the reference dynamics for the constrained motion and its analysis. The outcomes of the reference dynamics can be used for motion controller design. The theoretical development presented in the chapter is illustrated by simulation studies of an example of a flexible link and support manipulator model, whose service tasks are predefined by the programmed constraints, specifically its end-effector is to move according to some velocity profile. Special interest of this study is to analyze flexible link vibrations when the manipulator performs the desired tasks.

The chapter is organized as follows. After introduction, Sect. 5.2 reports the generalized programmed motion equations derivation procedure briefly. Section 5.3 presents formulation of the programmed constraints for the manipulator end-effector. In Sect. 5.4 the GPME (generalized programmed motion equations) for the manipulator are derived and simulation studies demonstrating programmed motion executions are presented in Sect. 5.5. The chapter closes with conclusions and the list of references.

5.2 Reference Dynamics Model of a Flexible Supported Manipulator

A model of the flexible supported manipulator is presented in Fig. 5.1. The manipulator is driven by a driving torque $\mathbf{t}_{dr}^{(2)}$. It is assumed that the third link of the manipulator can be treated as rigid or flexible. If the flexibility of this link is taken into account, the rigid finite element method is used for discretization.

A vector of generalized coordinates (joint coordinates) which describes motion of the manipulator has the following form:

$$\mathbf{q} = (q_i)_{i=1,\ldots,n_{dof}} = \left[\tilde{\mathbf{q}}^{(1)^T} \ \tilde{\mathbf{q}}^{(2)^T} \ \tilde{\mathbf{q}}^{(3)^T} \ \tilde{\mathbf{q}}^{(4)^T} \right]^T, \tag{5.1}$$

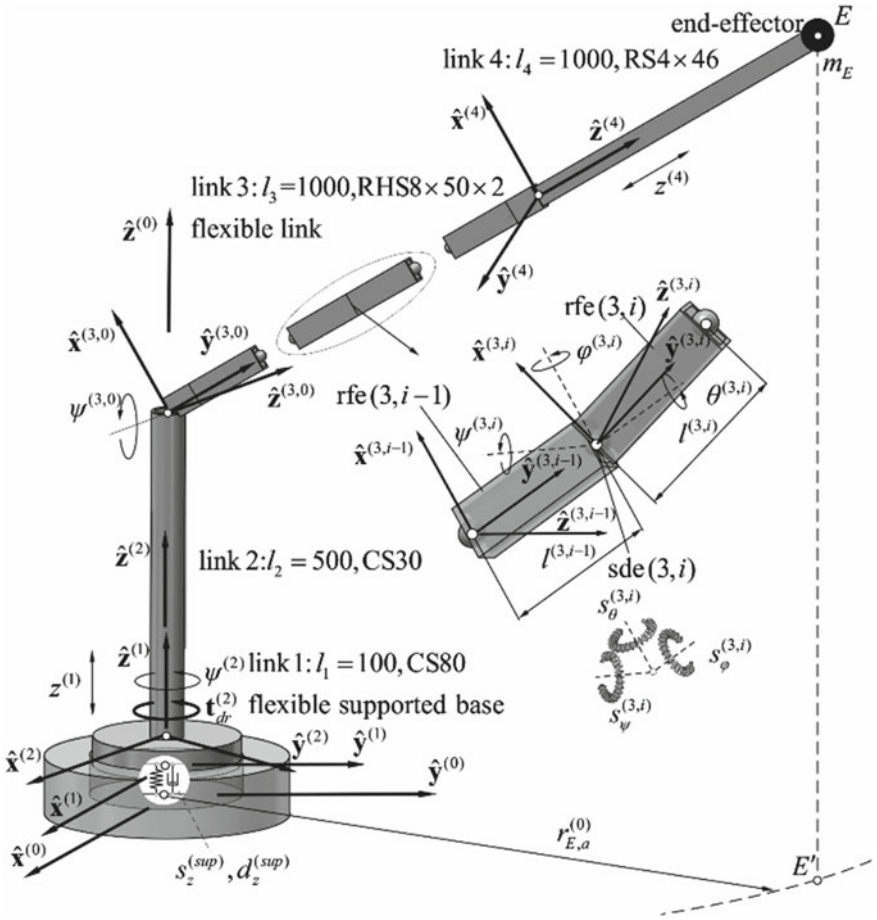

Fig. 5.1 Model of a manipulator

where: $\tilde{\mathbf{q}}^{(1)} = \left[z^{(1)}\right]$, $\tilde{\mathbf{q}}^{(2)} = \left[\psi^{(2)}\right]$, $\tilde{\mathbf{q}}^{(3)} = \left[\begin{array}{cc} \tilde{\mathbf{q}}^{(3,0)^T} & \tilde{\mathbf{q}}_f^{(3)^T} \end{array}\right]^T$

$$\tilde{\mathbf{q}}_f^{(3)} = \begin{cases} \varnothing & - \text{ rigid link} \\ \left[\begin{array}{ccccc} \tilde{\mathbf{q}}^{(3,1)^T} & \cdots & \tilde{\mathbf{q}}^{(3,r)^T} & \cdots & \tilde{\mathbf{q}}^{(3,n_{rfe}^{(3)}-1)^T} \end{array}\right]^T & - \text{ flexible link} \end{cases}$$

$$\tilde{\mathbf{q}}^{(3,0)} = \left[\psi^{(3,0)}\right], \tilde{\mathbf{q}}^{(3,r)} = \left[\begin{array}{ccc} \psi^{(3,r)} & \theta^{(3,r)} & \varphi^{(3,r)} \end{array}\right]^T, \tilde{\mathbf{q}}^{(4)} = \left[z^{(4)}\right].$$

The generalized coordinates describing motion of the link l with respect to the global reference frame can be presented in the following form:

$$\mathbf{q}^{(l)}\big|_{l=1,\ldots,n_l} = \left(q_i^{(l)}\right)_{i=1,\ldots,n_{dof}^{(l)}} = \left[\begin{array}{cc} \mathbf{q}^{(l-1)^T} & \tilde{\mathbf{q}}^{(l)^T} \end{array}\right]^T, \tag{5.2}$$

where $\mathbf{q}^{(0)} = \varnothing$, $\mathbf{q}^{(l-1)}\big|_{l=4} = \begin{cases} \mathbf{q}^{(3,0)} & -\text{rigid link} \\ \mathbf{q}^{(3,n_{rfe}^{(3)}-1)} & -\text{flexible link} \end{cases}$.

In further considerations the generalized coordinates vector $\mathbf{q}$ is divided into independent and dependent coordinates as follows:

$$\mathbf{q} = \begin{bmatrix} \mathbf{q}_{i_c} \\ \mathbf{q}_{d_c} \end{bmatrix}, \tag{5.3}$$

where $\mathbf{q}_{i_c} = \left(q_j\right)_{j \in i_{i_c}}$, $\mathbf{q}_{d_c} = \left(q_j\right)_{j \in i_{d_c}}$, and i_{i_c} and i_{d_c} stand for subscripts for describing dependent and independent coordinates. For the analyzed robotic system the following division into dependent and independent coordinates is assumed:

$$i_{d_c} \in \left\{3, n_{dof}\right\}, \tag{5.4.1}$$

$$i_{i_c} \in \left\{1, 2, \ldots, n_{dof}\right\} - i_{d_c}, \tag{5.4.2}$$

The generalized programmed motions equations (GPME) with first order programmed constraints are derived according to the procedure described in [5, 6]. This procedure requires formulation of some function R_1 which components depend on the kinetic and potential energy of the system, i.e.

$$R_1 = \sum_{l=1}^{n_l} \dot{E}_k^{(l)} + \sum_{l=1}^{n_l} \sum_{i=1}^{n_{dof}^{(l)}} \left(\frac{\partial E_{p,g}^{(l)}}{\partial q_i^{(l)}} \dot{q}_i^{(l)} - 2 \frac{\partial E_k^{(l)}}{\partial q_i^{(l)}} \dot{q}_i^{(l)} \right) + \sum_{r=1}^{n_{rfe}^{(3)}-1} \sum_{i=1}^{n_{dof}^{(3,r)}} \frac{\partial E_{p,f_l}^{(3,r)}}{\partial q_i^{(3,r)}} \dot{q}_i^{(3,r)}$$
$$+ \frac{\partial R_{sup}^{(1)}}{\partial \dot{q}_1^{(1)}} \dot{q}_1^{(1)} + \frac{\partial E_{p,sup}^{(1)}}{\partial q_1^{(1)}} \dot{q}_1^{(1)} - \sum_{i=1}^{n_{dof}^{(2)}} t_i \dot{q}_i^{(2)}, \tag{5.5}$$

where:

$$E_k^{(l)} = \begin{cases} \frac{1}{2}\mathrm{tr}\left\{\dot{\mathbf{T}}^{(l)}\mathbf{H}^{(l)}\left(\dot{\mathbf{T}}^{(l)}\right)^T\right\}, & l \neq 3 \\ \frac{1}{2}\sum\limits_{r=0}^{n_{rfe}^{(l)}-1}\mathrm{tr}\left\{\dot{\mathbf{T}}^{(l,r)}\mathbf{H}^{(l,r)}\left(\dot{\mathbf{T}}^{(l,r)}\right)^T\right\}, & l = 3 \end{cases}$$ – the kinetic energy of the link l,

$$E_{p,g}^{(l)} = \begin{cases} m^{(l)}g\mathbf{J}_3\mathbf{T}^{(l)}\mathbf{r}_{C^{(l)}}^{(l)}, & l \neq 3 \\ \sum\limits_{r=0}^{n_{rfe}^{(l)}-1} m^{(l,r)}g\mathbf{J}_3\mathbf{T}^{(l,r)}\mathbf{r}_{C^{(l,r)}}^{(l,r)}, & l \neq 3 \end{cases}$$ – the potential energy of gravity forces of the link l,

$$\mathbf{J} = \begin{bmatrix} \mathbf{J}_1 \\ \mathbf{J}_2 \\ \mathbf{J}_3 \end{bmatrix} = \begin{bmatrix} 1\,0\,0\,0 \\ 0\,1\,0\,0 \\ 0\,0\,1\,0 \end{bmatrix},$$

$E_{p,sup}^{(1)} = \frac{1}{2}s_z^{(sup)}\left(z^{(1)}\right)^2$, $R_{sup}^{(1)} = \frac{1}{2}d_z^{(sup)}\left(\dot{z}^{(1)}\right)^2$—the spring deformation energy and the Rayleigh dissipation function of the flexible supported base,

$E_{p,f_l}^{(3,r)} = \frac{1}{2}\left(\tilde{\mathbf{q}}^{(3,r)}\right)^T\mathbf{S}^{(3,r)}\tilde{\mathbf{q}}^{(3,r)}$, $\mathbf{S}^{(3,r)} = \mathrm{diag}\left\{s_\psi^{(3,r)}, s_\theta^{(3,r)}, s_\varphi^{(3,r)}\right\}$—the spring deformation energy of the flexible link,

$\mathbf{t} = \left[0\ t_{dr}^{(2)} - t_{res}^{(2)}\right]^T$—vector containing the driving torques.

Finally, the GPME dynamic equations of motion of the robotic system subjected to programmed constraints can be obtained as:

$$\left.\frac{\partial R_1}{\partial \dot{q}_i}\right|_{i\in i_{i_c}} + \sum_{j\in i_{d_c}}\frac{\partial R_1}{\partial \dot{q}_j}\frac{\partial \dot{q}_j}{\partial \dot{q}_i} = 0, \tag{5.6}$$

Notice, that the number of dynamic equations of motion (5.6) is equal to the number of the independent coordinates n_{i_c}. Therefore, the resulting equations have to be supplemented by the programmed constraints equations, in this case of the first order.

5.3 Programmed Constraint Equations Formulation

A programmed motion of the manipulator is defined as follows: the end-effector moves along an elliptical trajectory designed in a plane parallel to the $\hat{\mathbf{x}}^{(0)}\hat{\mathbf{y}}^{(0)}$ plane and the velocity of the end-effector in $z^{(0)}$ direction has to change according to time-dependent function $\dot{z}_{E,a}^{(0)}(t)$ shown in Fig. 5.2.

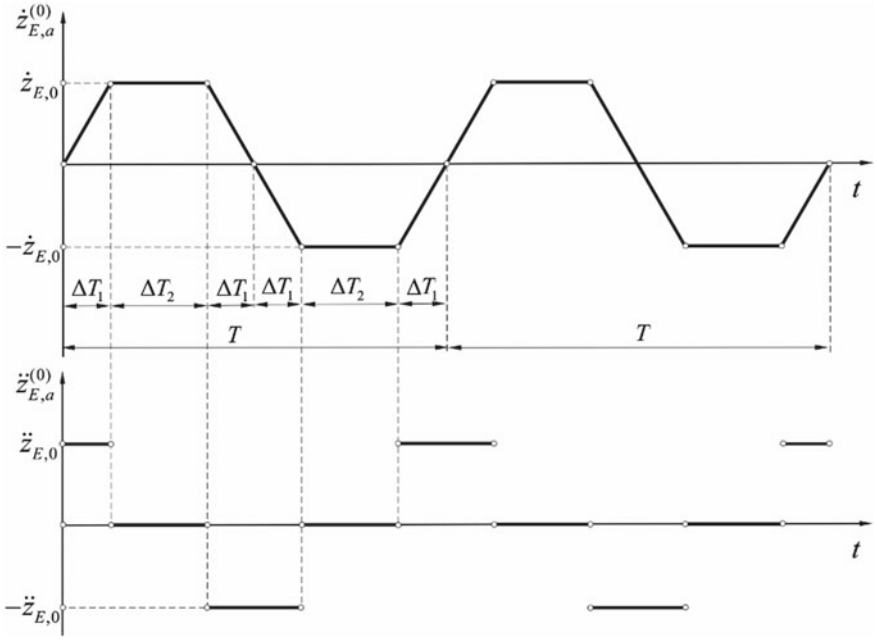

Fig. 5.2 Assumed time courses of the velocity and acceleration of the end-effector

The constraint equations corresponding to the proposed programmed motion can be presented as:

$$\Phi_1 \equiv 0 \Rightarrow \left(\frac{x_E^{(0)}}{a_{E,a}^{(0)}}\right)^2 + \left(\frac{y_E^{(0)}}{b_{E,a}^{(0)}}\right)^2 - 1 = 0 \tag{5.7.1}$$

$$\dot{\Phi}_2 \equiv 0 \Rightarrow \dot{z}_E^{(0)} - \dot{z}_{E,a}^{(0)}(t) = 0 \tag{5.7.2}$$

where $x_E^{(0)} = \mathbf{J}_1\mathbf{T}^{(4)}\mathbf{r}_E^{(4)}$, $y_E^{(0)} = \mathbf{J}_2\mathbf{T}^{(4)}\mathbf{r}_E^{(4)}$, $z_E^{(0)} = \mathbf{J}_3\mathbf{T}^{(4)}\mathbf{r}_E^{(4)}$. It can be noticed that the first constraint equation is defined at the position level and the second one is kinematic, i.e. formulated at the velocity level.

The GPME algorithm [5] requires the constraint equations in differentiated form which can be calculated as follows:

$$\dot{\Phi}_1 \equiv 0 \Rightarrow \mathbf{u}\dot{\mathbf{q}} = \mathbf{0}, \tag{5.8.1}$$

$$\dot{\Phi}_2 \equiv 0 \Rightarrow \mathbf{C}_3\dot{\mathbf{q}} - \dot{z}^{(0)}_{E,a}(t) = 0, \tag{5.8.2}$$

$$\ddot{\Phi}_1 \equiv 0 \Rightarrow \mathbf{u}\ddot{\mathbf{q}} + v = 0, \tag{5.8.3}$$

$$\ddot{\Phi}_2 \equiv 0 \Rightarrow \mathbf{C}_3\ddot{\mathbf{q}} + d_3 - \ddot{z}^{(0)}_{E,a}(t) = 0, \tag{5.8.4}$$

with:

$$\mathbf{C} = \begin{bmatrix} \mathbf{C}_1 \\ \mathbf{C}_2 \\ \mathbf{C}_3 \end{bmatrix} = \left(c_{ij}\right)_{\substack{i=1,2,3 \\ j=1,\ldots,4}} = \mathbf{J}\left[\, \mathbf{T}^{(4)}_1\mathbf{r}^{(4)}_E \;\cdots\; \mathbf{T}^{(4)}_4\mathbf{r}^{(4)}_E \,\right],$$

$$\mathbf{d} = (d_i)_{i=1,\ldots,3} = \mathbf{J}\left(\left(\sum_{i=1}^{n_{dof}}\sum_{j=1}^{n_{dof}} \mathbf{T}^{(4)}_{ij}\dot{q}_i\dot{q}_j\right)\mathbf{r}^{(4)}_E\right),$$

$$\mathbf{u} = \left(u_j\right)_{j=1,\ldots,4} = \frac{1}{\left(a^{(0)}_{E,a}\right)^2}\mathbf{J}_1\mathbf{T}^{(4)}\mathbf{r}^{(4)}_E\mathbf{C}_1 + \frac{1}{\left(b^{(0)}_{E,a}\right)^2}\mathbf{J}_2\mathbf{T}^{(4)}\mathbf{r}^{(4)}_E\mathbf{C}_2,$$

$$v = \frac{1}{\left(a^{(0)}_{E,a}\right)^2}\left((\mathbf{C}_1\dot{\mathbf{q}})^2 + \mathbf{J}_1\mathbf{T}^{(4)}\mathbf{r}^{(4)}_E d_1\right) + \frac{1}{\left(b^{(0)}_{E,a}\right)^2}\left((\mathbf{C}_2\dot{\mathbf{q}})^2 + \mathbf{J}_2\mathbf{T}^{(4)}\mathbf{r}^{(4)}_E d_2\right),$$

$a^{(0)}_{E,a}$, $b^{(0)}_{E,a}$ are elliptical trajectory semi-major and semi-minor axes, respectively.

Relations between dependent and independent velocities can be found by proper transformations of (5.8). As the result, these relations can be written as follows:

$$\dot{\mathbf{q}}_{d_c} = -\mathbf{K}^{-1}_{d_c}\mathbf{K}_{i_c}\dot{\mathbf{q}}_{i_c}, \tag{5.9}$$

where:

$$\mathbf{K}_{d_c} = \begin{bmatrix} u_2 & u_4 \\ c_{12} & c_{14} \end{bmatrix}, \mathbf{K}_{i_c} = \begin{bmatrix} u_1 & u_3 \\ c_{11} & c_{13} \end{bmatrix}.$$

5.4 The GPME Generation for the Constrained Manipulator Model

The GPME (6) supplemented by the equations of the programmed constraints (5.8.3) and (5.8.4) in the stabilized form can be written as follows:

$$\begin{bmatrix} \mathbf{M}_{1\cdot} + \sum\limits_{j\in i_{d_c}} \mathbf{M}_{j\cdot} \frac{\partial \dot{q}_j}{\partial \dot{q}_1} \\ \vdots \\ \mathbf{M}_{n_{i_c}\cdot} + \sum\limits_{j\in i_{d_c}} \mathbf{M}_{j\cdot} \frac{\partial \dot{q}_j}{\partial \dot{q}_{n_{i_c}}} \\ \mathbf{u} \\ \mathbf{C}_3 \end{bmatrix} \ddot{\mathbf{q}}$$

$$= \begin{bmatrix} h_1 + Q_1 + \sum\limits_{j=1}^{n_{dof}} \dot{q}_j \frac{\partial Q_j}{\partial \dot{q}_1} + \sum\limits_{k\in i_{d_c}} \left(h_k + Q_k + \sum\limits_{j=1}^{n_{dof}} \dot{q}_j \frac{\partial Q_j}{\partial \dot{q}_k} \right) \frac{\partial \dot{q}_k}{\partial \dot{q}_1} \\ \vdots \\ h_{n_{i_c}} + Q_{n_{i_c}} + \sum\limits_{j=1}^{n_{dof}} \dot{q}_j \frac{\partial Q_j}{\partial \dot{q}_{n_{i_c}}} + \sum\limits_{k\in i_{d_c}} \left(h_k + Q_k + \sum\limits_{j=1}^{n_{dof}} \dot{q}_j \frac{\partial Q_j}{\partial \dot{q}_k} \right) \frac{\partial \dot{q}_k}{\partial \dot{q}_{n_{i_c}}} \\ -v - 2\alpha\, \dot{\Phi}_1 - \beta^2\, \Phi_1 \\ -d_3 + \ddot{z}^{(0)}_{E,a}(t) - 2\alpha\, \dot{\Phi}_2 \end{bmatrix}, \quad (5.10)$$

where:

$$\mathbf{M} = \sum_{\substack{l=1 \\ l\neq 3}}^{n_l} \mathbf{M}^{(l)} + \sum_{r=0}^{n^{(3)}_{rfe}-1} \mathbf{M}^{(3,r)}, \mathbf{M}^{(\bullet)} = \left(m^{(\bullet)}_{ij} \right)_{i,j=1,\ldots,n^{(\bullet)}_{dof}}, m^{(\bullet)}_{ij} = \mathrm{tr}\left\{ \mathbf{T}^{(\bullet)}_i \mathbf{H}^{(\bullet)} \left(\mathbf{T}^{(\bullet)}_j \right)^T \right\},$$

$$\mathbf{M}_{i\cdot}|_{i\in i_{i_c}} = \mathrm{row}_i(\mathbf{M}),\ \mathbf{M}_{j\cdot}\big|_{j\in i_{d_c}} = \mathrm{row}_j(\mathbf{M}),$$

$$\mathbf{h} = \sum_{\substack{l=1 \\ l\neq 3}}^{n_l} \mathbf{h}^{(l)} + \sum_{r=0}^{n^{(3)}_{rfe}-1} \mathbf{h}^{(3,r)}, \mathbf{h}^{(\bullet)} = \left(h^{(\bullet)}_i \right)_{i=1,\ldots,n^{(\bullet)}_{dof}},$$

$$h^{(\bullet)}_i = \sum_{m=1}^{n^{(\bullet)}_{dof}} \sum_{n=1}^{n^{(\bullet)}_{dof}} \mathrm{tr}\left\{ \mathbf{T}^{(\bullet)}_m \mathbf{H}^{(\bullet)} \left(\mathbf{T}^{(\bullet)}_{m,n} \right)^T \right\} \dot{q}^{(\bullet)}_m \dot{q}^{(\bullet)}_n + 2 \sum_{m=1}^{n^{(\bullet)}_{dof}} \sum_{n=1}^{n^{(\bullet)}_{dof}} \mathrm{tr}\left\{ \mathbf{T}^{(\bullet)}_m \mathbf{H}^{(\bullet)} \left(\mathbf{T}^{(\bullet)}_{i,n} \right)^T \right\} \dot{q}^{(\bullet)}_m \dot{q}^{(\bullet)}_n,$$

$$\mathbf{T}^{(\bullet)}_i = \frac{\partial \mathbf{T}^{(\bullet)}}{\partial q^{(\bullet)}_i}, \mathbf{T}^{(\bullet)}_{i,j} = \frac{\partial^2 \mathbf{T}^{(\bullet)}}{\partial q^{(\bullet)}_i \partial q^{(\bullet)}_j},$$

$$\mathbf{Q} = -\left(\mathbf{g} + \mathbf{d}_{sup} + \mathbf{f}_{sup} + \mathbf{f}_{fl} \right) + \mathbf{t}_{dr},$$

$$\mathbf{g} = \sum_{\substack{l=1 \\ l\neq 3}}^{n_l} \mathbf{g}^{(l)} + \sum_{r=0}^{n^{(1)}_{rfe}-1} \mathbf{g}^{(3,r)}, \mathbf{g}^{(\bullet)} = \left(g^{(\bullet)}_i \right)_{i=1,\ldots,n^{(\bullet)}_{dof}}, g^{(\bullet)}_i = m^{(\bullet)} g \mathbf{J}_3 \mathbf{T}^{(\bullet)}_i \mathbf{r}^{(\bullet)}_{C^{(\bullet)}},$$

$$\mathbf{f}_{sup} = \left(f_{sup,i} \right)_{i=1,\ldots,n_{dof}} = \left[s^{(sup)}_z z^{(1)}\ \mathbf{0} \right]^T, \mathbf{d}_{sup} = \left(d_{sup,i} \right)_{i=1,\ldots,n_{dof}} = \left[d^{(sup)}_z \dot{z}^{(1)}\ \mathbf{0} \right]^T,$$

$$\mathbf{f}_{fl} = \left(f_{fl,i} \right)_{i=1,\ldots,n_{dof}} = \left[\mathbf{0}\ \mathbf{S}^{(3,1)} \tilde{\mathbf{q}}^{(3,1)}\ \ldots\ \mathbf{S}^{(3,n^{(3)}_{rfe}-1)} \tilde{\mathbf{q}}^{(3,n^{(3)}_{rfe}-1)} \right],$$

$$\mathbf{t}_{dr} = \left(t_{dr,i}\right)_{i=1,\ldots,n_{dof}} = \left[\mathbf{t}^T \ \mathbf{0}\right]^T,$$

in which $\mathbf{H}$ is the pseudo-inertia matrix, g is the acceleration of gravity, and α, β are coefficients for the Baumgarte method.

For simulations, the Baumgarte stabilization method [4] is applied to eliminate constraint violation at position and velocity levels. The Baumgarte method is simple in implementations and provides satisfactory stabilization results to constrained motion equations solutions. Unfortunately, the parameters α, β have to be selected by the trial and error method. However, the method returns good adjustment of the parameters, such which secure the solution convergence, after a couple of simulation runs.

Finally, the dynamic equations of motion (5.10) form $(n_{dof} - 2)$ ordinary differential equations, which need to be supplemented by 2 equations corresponding to the programmed constraints (5.8.3) and (5.8.4). Notice that the GPME derivation procedure eliminates the constraint reaction forces from the equations. Thus (5.10) are the smallest set of motion equations.

5.5 Numerical Simulation Studies—End-Effector Programmed Motion

The procedure of generation of reference dynamics (5.10) enables simulations of the programmed motion of the flexible supported three link manipulator. Parameters of the analyzed robotic system applied in simulations are gathered in Table 5.1.

Table 5.1 Parameters of the manipulator

Parameters	Value
Stiffness coefficient of the support $s_z^{(sup)}$	10^4 Nm^{-1}
Damping coefficient of the support $d_z^{(sup)}$	2.5 N s m^{-1}
Young modulus E	$2.1 \cdot 10^5$ MPa
Poisson ratio v	0.3
Density ρ	7801 kg m^3
Mass of the end-effector m_E	2 kg
Number of rigid finite elements $n_{rfe}^{(3)}$	4
Semi-major radius of the ellipse-shaped trajectory $a_{E,a}^{(0)}$	0.875 m
Semi-minor radius of the ellipse-shaped trajectory $b_{E,a}^{(0)}$	1.75 m
The Baumgarte coefficient α	10^3
The Baumgarte coefficient β	10^2

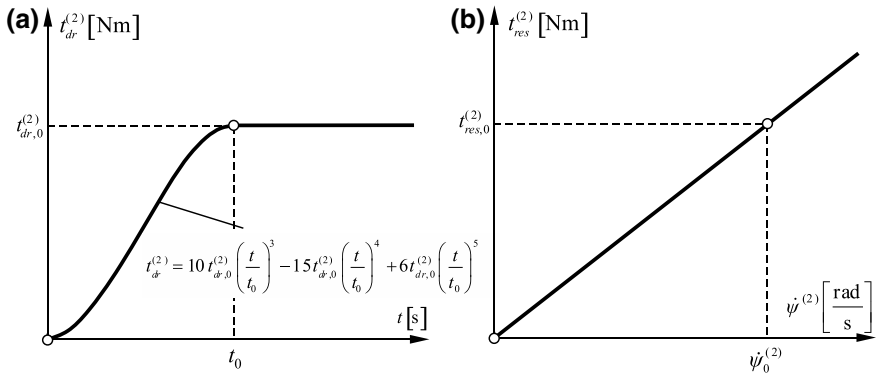

Fig. 5.3 Courses of the driving and resistance torques

Motion of the manipulator is forced by the driving torque together with the resistance torque applied to column (2) whose courses are presented Fig. 5.3.

The following is assumed: $t_{dr,0}^{(2)} = 2\,\text{Nm}$, $t_0 = 10$ and $\psi_0^{(2)} = 9\,\text{Nm}$.

At the initial configuration the flexible link is inclined to the plane $\hat{\mathbf{x}}^{(0)}\hat{\mathbf{y}}^{(0)}$ at the angle 45°. The generalized coordinates vector at time $t = 0\,\text{s}$ can be presented as follows:

$$q_i|_{\substack{t=0\text{s} \\ i=1,\ldots,n_{dof}}} = \begin{cases} 0, & i \neq 3 \\ 45°, & i = 3 \end{cases} \tag{5.11.1}$$

$$\dot{q}_i|_{\substack{t=0\text{s} \\ i=1,\ldots,n_{dof}}} = 0 \tag{5.11.2}$$

At the first step of the simulation, static analysis of the manipulator is performed. Initially, the position of the end-effector with respect to the inertial frame was $\mathbf{r}_E^{(0)} = \begin{bmatrix} 1.4142 & 0 & 2.5142 & 1 \end{bmatrix}^T$. After applying the gravity forces, the position of the end-effector changed to $\mathbf{r}_E^{(0)} = \begin{bmatrix} 1.5065 & 0 & 2.3813 & 1 \end{bmatrix}^T$. The dynamic equations of motion are integrated using 4th order Runge-Kutta scheme with the constant step size $h = 10^{-3}$ s, when all links of the manipulator are treated as rigid, and $h = 10^{-5}$ s if link's flexibility is taken into account. Time courses of values of displacements of the base and joints are shown in Fig. 5.4.

It can be noticed that flexibility of link (3) has a significant effect on dynamics of the manipulator. Vibrations due to link's flexibility are compensated by an appropriate selection of the drive function acting in joint (3, 0). The influence of link's (3) flexibility on other links and the flexible supported base motion is also clearly visible.

Programmed trajectories of the end-effector projected on planes $\hat{\mathbf{x}}^{(0)}\hat{\mathbf{y}}^{(0)}$ and $\hat{\mathbf{x}}^{(0)}\hat{\mathbf{z}}^{(0)}$ are presented in Fig. 5.5. Time courses of the end-effector vertical displacement and velocity are shown in Fig. 5.6.

Analyzing the obtained results, it can be stated that the programmed constraints resulting from the assumed elliptical trajectory and the end-effector vertical veloc-

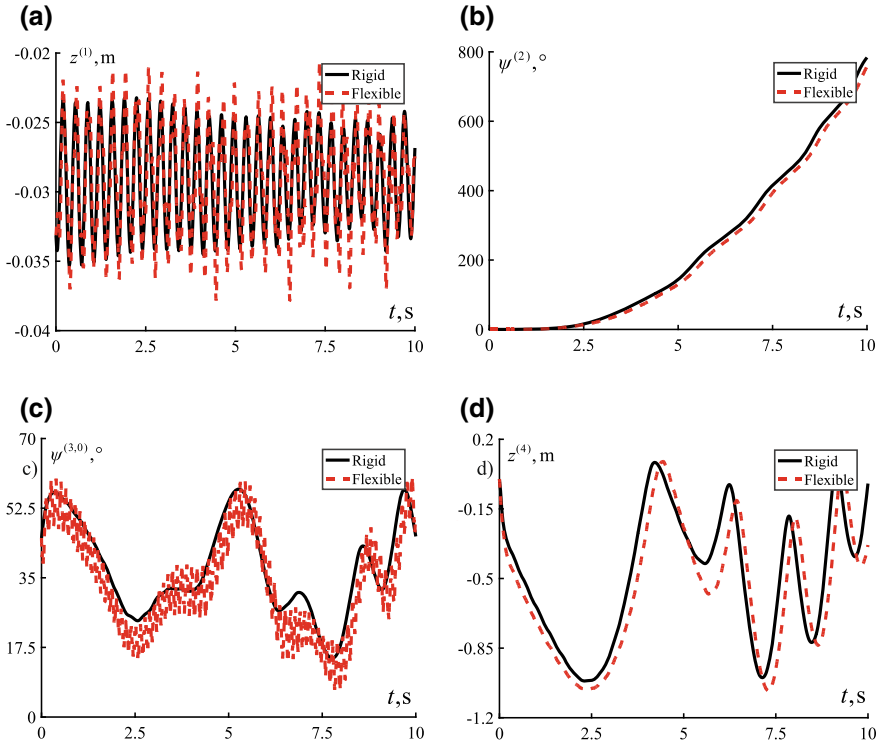

Fig. 5.4 Time course of the joint coordinates

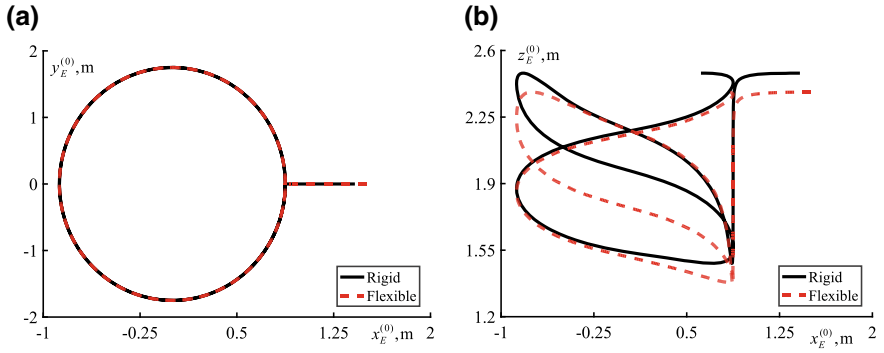

Fig. 5.5 A trajectory of the end-effector

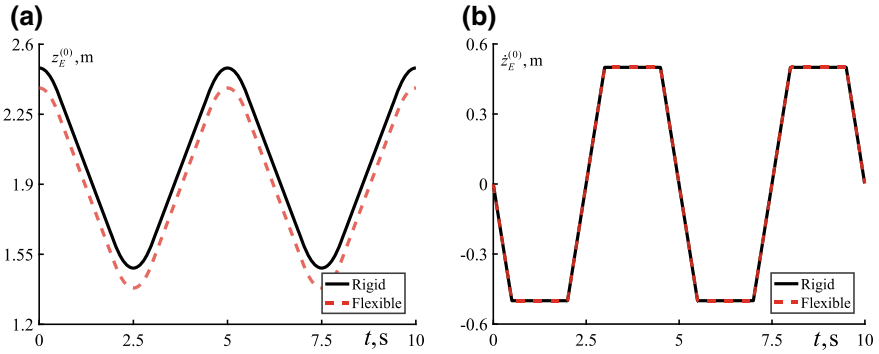

Fig. 5.6 Z-component of the end-effector displacement and the velocity vector

ity are satisfied. Thus, the reference dynamics provides motion samples along the specified program. This motion can be analyzed with respect to the manipulator capabilities and vibrations of its links. For the model with the flexible link, it can be seen that the trajectory of the end-effector in the plane $\hat{\mathbf{x}}^{(0)}\hat{\mathbf{z}}^{(0)}$ is also well executed comparing to the trajectory obtained for the model with rigid links. Moreover, this offset results from the initial deformation of the flexible link (3) due to the effects of gravity. This is also noticeable in time courses of the end-effector displacement $z_E^{(0)}$.

5.6 Conclusions

In the chapter a mathematical model of the example of a robotic system with a flexible link is analyzed. Its motion is subjected to the programmed constraints resulting from task oriented motion planning. An automated numerical procedure based on the GMPE algorithm was applied to generate dynamic equations of a multi-link robotic system subjected to programmed constraints. It enables calculating time histories of joint positions and their derivatives in the programmed motion. Joint coordinates and homogeneous transformation matrices were applied to describe kinematics of the manipulator. Links flexibility was modelled using the rigid finite element method. The presented approach can be easily generalized for robotic systems with any number of rigid or flexible links subjected to other kinematic constraint equations. The reference dynamics and the results of the programmed motion analysis can be used directly for a motion controller design what is the next step of the research plan.

References

1. A.A. Ata, H. Johar, Dynamic simulation of task constrained of a rigid-flexible manipulator. Int. J. Adv. Robot. Syst. **1**(2), 61–66 (2004)
2. A.A. Ata, W.F. Faresb, M.Y. Sadeh, Dynamic analysis of a two-link flexible manipulator subject to different sets of conditions. Procedia Eng. **41**, 1253–1260 (2012)
3. K. Augustynek, A. Urbaś, Two approaches of the rigid finite element method to modelling the flexibility of spatial linkage links, in *Proceedings of the ECCOMAS Thematic Conference on Multibody Dynamics, Prague, 19–22 June 2017*
4. J.W. Baumgarte, Stabilization of constraints and integrals of motion in dynamical systems. Comput. Methods Appl. Mech. Eng. **1**(1), 1–16 (1972)
5. E. Jarzębowska, K. Augustynek, A. Urbaś, Automated generation of reference dynamical models for constrained robotic systems in the presence of friction and damping effects, in *Concurrency and Computation: Practice and Experience* (2018). https://doi.org/10.1002/cpe.4452.25
6. E. Jarzębowska, K. Augustynek, A. Urbaś, Computational reference dynamical model of a multibody system with first order constraints, in *Proceedings ASME Design Engineering Technical Conference*, No. UNSP V006T10A016 (2017)
7. E. Jarzębowska, K. Augustynek, A. Urbaś, Programmed task based motion analysis of robotic systems equipped with flexible links and supports, in *MATEC Web of Conferences*, vol. 241, No. 01008, 1–4 (2018). https://doi.org/10.1051/matecconf/201824101008
8. J. Moreno, R. Kelly, Velocity control of robot manipulators: analysis and experiments. Int. J. Control **76**(14), 1420–1427 (2003)
9. A. Urbaś, Computational implementation of the rigid finite element method in the statics and dynamics analysis of forest cranes. Appl. Math. Model. **46**, 750–762 (2017). https://doi.org/10.1016/j.apm.2016.08.006
10. E. Wittbrodt, M. Szczotka, A. Maczyński, S. Wojciech, *Rigid Finite Element Method in Analysis of Dynamics of Offshore Structures* (Ocean Engineering & Oceanography. Springer, Berlin, Heidelberg, 2013)

Chapter 6
Suppression of Time-Delayed Induced Vibrations Through the Dynamic Vibration Absorber: Application to the Inverted Pendulum

Giuseppe Habib

Abstract A tuned mass damper (TMD) is implemented for the suppression of delay-induced vibrations. An inverted pendulum subject to proportional-derivative feedback control is considered as primary system. A TMD is then attached to it, in order to enlarge the stable region in the space of the control gains and mitigate vibrations induced by time delay in the feedback loop. Stability and bifurcation analysis enable us to evaluate the performance of the absorber both in terms of linear stability and of robustness against external perturbations. Results illustrate that, although the TMD is able to enlarge the stable region and suppress vibrations, in order to be efficient it requires a fine tuning and the knowledge of the system parameters, including time delay. Bifurcation analysis showed that the implementation of the TMD does not significantly improve the behavior of the system in terms of robustness of the system equilibrium because of the existence of subcritical bifurcations.

6.1 Introduction

Time delay in control is a major cause of instability, which is relevant for many engineering systems [19]. Micro- and nano-electromechanical systems can experience instabilities even when time delay seems negligible because of their very high natural frequency [17]. Complex control algorithms require non-negligible computational time, causing instabilities in industrial robots [10]. Human-controlled systems are subject to time delay related to human reflex time, this causes, for instance, the failure of high-precision haptic interfaces [6], dangerous speed wobble in bicycles and motorbikes [1, 20] and it is also responsible of balancing problems in elderly people [2, 12].

The tuned mass damper (TMD) is an established solution for passively mitigating undesired vibrations and improve stability in otherwise unstable systems. It is

G. Habib (✉)
Department of Applied Mechanics, MTA-BME Lendület Human Balancing Research Group, Budapest University of Technology and Economics, Műegyetem rkp. 3, Budapest 1111, Hungary
e-mail: habib@mm.me.hu

M. Belhaq (ed.), *Topics in Nonlinear Mechanics and Physics*,
Springer Proceedings in Physics 228, https://doi.org/10.1007/978-981-13-9463-8_6

successfully adopted for the stabilization of many engineering systems, such as slender structures subject to wind induced vibrations [3] or to seismic excitation [18], machine tools undergoing regenerative chatter vibrations [21] or friction-induced vibrations in braking systems [4].

In this study, we consider a primary system consisting of an inverted pendulum subject to proportional-differential (PD) position control with feedback delay. The objective of the controller is to stabilize the upright position of the pendulum, otherwise unstable. Because of time delay in the feedback loop, the stable region in the space of the control gains is bounded, which might cause instability if the control gains are not properly tuned. A TMD is attached to this primary system with the objective of enlarging the stable region. In the first part of the paper, the stability analysis of the primary system with and without TMD is analytically accomplished. Based on stability analysis, an optimization of the absorber parameter is performed. In the second part of the paper, the bifurcation behavior of the system at the loss of stability is analytically studied, exploiting the method of multiple scales [16]. The analysis is carried out for the primary system with and without absorber. The bifurcation analysis allows to evaluate the robustness of the system to perturbations within the stable region, an aspect practically relevant, completely overlooked by a linear stability analysis.

With respect to the engineering relevance of the system considered, it should be pointed out that employing a control algorithm more sophisticated than a simple PD controller is possible to achieve better performance than attaching a TMD. For instance, periodic or predictive controllers are effective for compensating time delay in feedback loop [11, 13, 15]. In this respect, the approach proposed in this study refers to those systems whose control algorithm is practically inaccessible, such as, for instance, human controlled systems.

6.2 Primary System Definition

We consider as primary system a simple planar pendulum, which is subject to a PD position control aiming at stabilizing the vertical upright position. The controller reads the position and velocity of the system and computes the force to be applied proportionally to those values. However, it requires a certain finite amount of time to react to the input, which causes time delay in the feedback loop. The dynamics of the system in nondimensional form is described by the following delay differential equation

$$\ddot{\varphi}_1 - \sin(\varphi_1) = -p\varphi_1(t-\tau) - d\dot{\varphi}_1(t-\tau) \tag{6.1}$$

where p and d are the dimensionless proportional and differential gains, respectively.

6.3 Stability Analysis

Although the stability of the trivial solution of the system in (6.1) has been extensively studied in the literature [14], for the sake of clarity we briefly repeat the analysis, applying the D-subdivision method [19].

After linearizing the equation of motion around $\varphi_1 = 0$, we introduce the tentative solution $\varphi_1 = \xi_1 e^{\lambda t}$, obtaining

$$\lambda^2 \xi_1 e^{\lambda t} - \xi_1 e^{\lambda t} + p\xi_1 e^{\lambda t - \lambda\tau} + d\lambda\xi_1 e^{\lambda t - \lambda\tau} = 0, \tag{6.2}$$

from which we attain the characteristic polynomial

$$\lambda^2 - 1 + d\lambda e^{-\lambda\tau} + p e^{-\lambda\tau} = 0. \tag{6.3}$$

The system is asymptotically stable if and only if all the infinite solutions of (6.3) have negative real part. Imposing the condition $\lambda = i\omega$, where ω is a real number, we can identify borders separating regions with the same number of eigenvalues having positive real part [14, 19]. Separating then real and imaginary part, we obtain

$$\begin{aligned} d\omega \sin(\omega\tau) + p\cos(\omega\tau) &= \omega^2 + 1 \\ d\omega \cos(\omega\tau) - p\sin(\omega\tau) &= 0, \end{aligned} \tag{6.4}$$

whose solution is

$$\begin{aligned} p &= \left(\omega^2 + 1\right)\cos(\omega\tau) \\ d &= \frac{\omega^2 + 1}{\omega}\sin(\omega\tau). \end{aligned} \tag{6.5}$$

We notice that for $\omega = 0$ we have $p = 1$, which corresponds to the minimum allowed value of p to avoid instabilities. Considering (6.5) and analyzing the transversality condition [14, 19], stability region can be identified in the p, d space. This is depicted in Fig. 6.1a for various values of τ.

We notice that the shape of the stable region resembles a capital letter D. The left vertical border corresponds to a static loss of stability, therefore it is not related to the time delay, and it causes the system to diverge monotonically from the zero position. The right curved border corresponds to Andronov-Hopf bifurcations, therefore to the generation of limit cycle oscillations (LCOs) having frequency ω. Increasing the value of the time delay τ the stable region shrinks, until it eventually disappears for $\tau = \sqrt{2}$ [19]. For $\tau \leq \sqrt{2}$ the system is always stable for any control gain value. On the contrary, for $\tau \to 0$ (no time delay), the stable region is unbounded and the system is stable if $p > 1$ and $d > 0$.

Figure 6.1b depicts the values of the vibration frequency ω occurring at the loss of stability. We notice that the frequency range of interest is wide and it is largely affected by the value of τ. As it will be shown later, this aspect is critical for the design of a proper tuned mass damper for vibration mitigation.

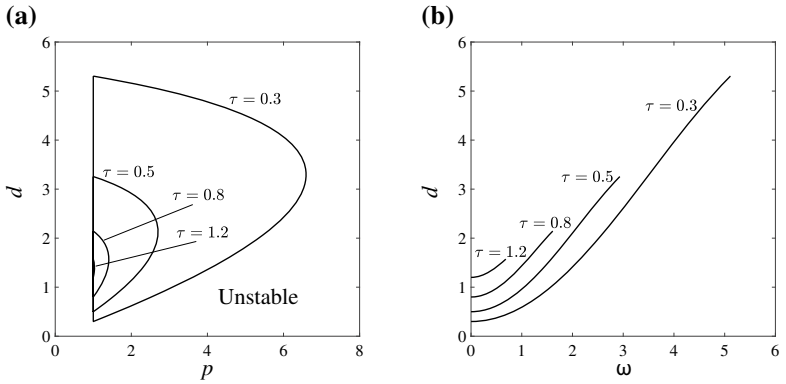

Fig. 6.1 **a** Stability chart in the space of the control gains p, d; the system is stable inside the D-shaped curve; **b** vibration frequencies at the loss of stability

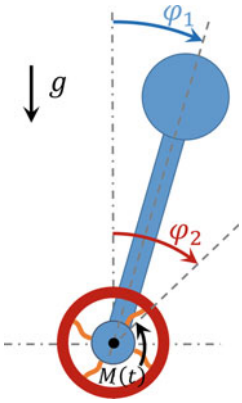

Fig. 6.2 Schematic representation of the inverted pendulum with attached TMD

6.3.1 Inverted Pendulum with Attached TMD

With the objective of improving the stability properties of the system, we attach to it a TMD, consisting of a small mass connected to the primary system through a linear viscoelastic element. A schematic representation of the mechanical system is provided in Fig. 6.2. The equations of motion of the augmented system in dimensionless form are

$$\begin{aligned} &\ddot{\varphi} - \sin(\varphi_1) + 2\zeta_2\mu\gamma\left(\dot{\varphi}_1 - \dot{\varphi}_2\right) + \mu\gamma^2\left(\varphi_1 - \varphi_2\right) + p\varphi_1\left(t-\tau\right) + d\dot{\varphi}_1\left(t-\tau\right) = 0 \\ &\mu\left(\ddot{\varphi}_2 + 2\zeta_2\gamma\left(\dot{\varphi}_2 - \dot{\varphi}_1\right) + \gamma^2\left(\varphi_2 - \varphi_1\right)\right) = 0, \end{aligned} \tag{6.6}$$

where μ is ratio between the mass moment of inertia of the absorber and of the primary system, γ is the natural frequency ratio and ζ_2 is the relative damping of the absorber.

After linearizing the system, we perform the same analysis as done for the single-DoF case, obtaining the characteristic polynomial

$$\begin{aligned}&\left(-\left(\gamma^2+2\gamma\lambda\zeta_2+\lambda^2\right)+\lambda^2\left(\gamma^2(\mu+1)+2\gamma\lambda\zeta_2(\mu+1)+\lambda^2\right)\right)\\&\quad+e^{-\lambda\tau}\left(d\lambda\left(\gamma^2+2\gamma\lambda\zeta_2+\lambda^2\right)+p\left(\gamma^2+2\gamma\lambda\zeta_2+\lambda^2\right)\right)=0.\end{aligned}\tag{6.7}$$

Imposing the condition $\lambda = i\omega$, separating real and imaginary parts and finally solving the resultant equations for p and d, we obtain

$$\begin{aligned}p=&\left(\cos(\tau\omega)\left(\gamma^4\left(\omega^2(\mu+1)+1\right)+\gamma^2\omega^2\left(4\zeta_2^2\left(\omega^2(\mu+1)+1\right)-\omega^2(\mu+2)-2\right)\right.\right.\\&\left.\left.+\omega^6+\omega^4\right)+2\gamma\zeta_2\omega^5\mu\sin(\tau\omega)\right)\Big/\left(\gamma^4+2\gamma^2\left(2\zeta_2^2-1\right)\omega^2+\omega^4\right)\\d=&\left(\sin(\tau\omega)\left(\gamma^4\left(\omega^2(\mu+1)+1\right)+\gamma^2\omega^2\left(4\zeta_2^2\left(\omega^2(\mu+1)+1\right)-\omega^2(\mu+2)-2\right)\right.\right.\\&\left.\left.+\omega^6+\omega^4\right)-2\gamma\zeta_2\omega^5\mu\cos(\tau\omega)\right)\Big/\left(\omega\left(\gamma^4+2\gamma^2\left(2\zeta_2^2-1\right)\omega^2+\omega^4\right)\right),\end{aligned}\tag{6.8}$$

which mark the separations between regions having the same number of eigenvalues with positive real part.

Fixing parameter values and varying ω, (6.8) provide the stability boundary of the system in the p, d space, which is reported in Fig. 6.3. In the figure, the red dashed line marks stability boundary for the pendulum without TMD, while the solid lines indicate stability for the system with an attached TMD for various values of γ. τ is fixed to 0.5, while mass ratio $\mu = 0.1$ and damping ratio $\zeta_2 = 0.15$.

The different stability charts show that the TMD is able to improve stability, however it is effective only in a specific region of the chart. Considering that the TMD works only around its natural frequency, this result is not surprising. The

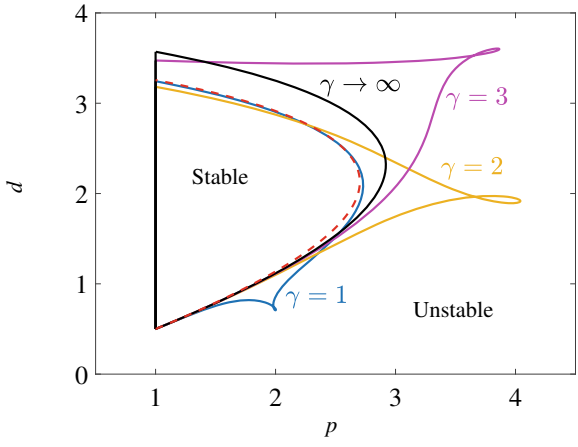

Fig. 6.3 Stability chart for the inverted pendulum with attached TMD. $\tau = 0.5$, $\mu = 0.1$ and $\zeta_2 = 0.15$. Red dashed lines refer to the pendulum without absorber

phenomenon can be better understood comparing Figs. 6.3 and 6.1b. For instance, for $\gamma = 1$ the TMD is effective for $d \approx 1$, while Fig. 6.1b shows that for $d \approx 1$ and $\tau = 0.5$, vibration frequency at the loss of stability is indeed close to 1. Analogous observations can be done for $\gamma = 2$ and $\gamma = 3$. The consequence of this result is that the TMD can be used only for specific parameter ranges and it requires a knowledge of the time delay τ in order to be properly tuned. We notice that the area inside the small loop formed by the stability boundary is unstable.

The black line in Fig. 6.3 indicates the case of an infinitely rigid absorber. In this case the TMD simply increases the inertia of the system. As it can be seen in the figure, this has a positive effect on the stability, since the increased inertia reduces the effective relative time delay (although here equations were provided directly in dimensionless form, dimensionless time delay τ is given by the dimensional time delay multiplied by the natural frequency of the pendulum). For this reason, we believe that a fair assessment of the performance of the TMD should consist in its comparison with a rigid TMD.

Figure 6.4a and b illustrate the effect on the stability of variations of the damping ζ_2 and of the mass ratio μ, respectively. Figure 6.4a illustrates the effect of variations of the damping ζ_2 on the stability of the system. From the figure it can be recognized that a relatively large damping ratio of the TMD is required to obtain good performance. However, an optimum value exists and excessive damping can also reduce performance. Figure 6.4b shows the effect of variations of the mass ratio on the system stability. In this case, increases of the mass ratio tend to generally improve stability. However, in most of engineering applications, limits on the entity of an additional mass are driven by practical considerations. Conclusions drawn here regarding the effect of mass and damping ratios on stability are analogous to those obtained for other applications of the TMD [5, 8].

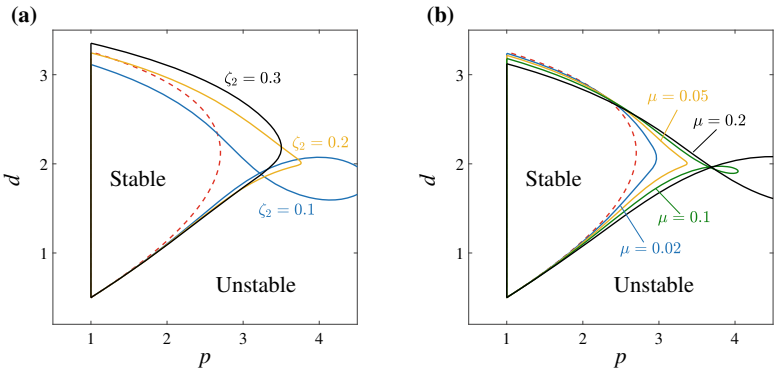

Fig. 6.4 Stability charts for the inverted pendulum with attached TMD, $\tau = 0.5$ and $\gamma = 2$. **a** $\mu = 0.1$; **b** $\zeta_2 = 0.15$. Red dashed lines refer to the pendulum without absorber

6.3.2 Absorber Optimization

The previous analysis suggests that γ and ζ_2 parameters must be correctly tuned in order to obtain an efficient absorber, it is therefore useful to identify the optimal parameter values for a specific purpose. We consider three different objectives related to the shape of the stability chart. Namely, maximize either p or d control gains which give stability and maximize the stable region in the p, d space. For the optimization, time delay and mass ratio are assumed fixed at $\tau = 0.5$ and $\mu = 0.1$.

Optimization is performed adopting the semi-discretization method [14], which consists in discretizing the time, in order to transform the delay differential equation describing the dynamics of the system into a discrete map. For more details on the procedure, we address the interested reader to [14]. The time is discretized in intervals $\Delta t = \tau/m$, the larger is m, the more precise is the computation. To give an idea of the approximation obtained, Fig. 6.5 illustrates the approximated stability chart for $m = 5$, 15 and 50. The black line in the figure indicates the exact solution. The advantage of the semi-discretization method over analytical computation, for this specific case, is that it provides an easy way to determine the maximum value of p and d of the stable region and its area. As a compromise between precision and computational time, we adopted $m = 15$ for the system optimization.

The optimization provided the parameter values indicated in Table 6.1. Corresponding stability charts are plotted in Fig. 6.6. We notice that, although optimization was performed through the semi-discretization method, the stability charts in Fig. 6.6 are the exact ones.

Comparing the optimized stability charts in Fig. 6.6 with the case of only inertial contribution of the absorber (infinitely rigid, dashed line in the figure), it can be noticed that the improvement is significant. Exact values of the obtained improvement are indicated in Table 6.1. Nevertheless, we remark that in order to obtain this optimized value it is necessary to have a good knowledge of the system delay and mass ratio.

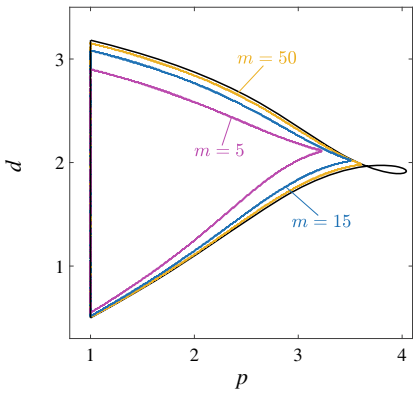

Fig. 6.5 Stability chart for the inverted pendulum with attached TMD. $\tau = 0.5$, $\mu = 0.1$, $\zeta_2 = 0.15$ and $\gamma = 2$. Black line: exact solution, colored lines: semi-dscretization method

Table 6.1 Absorber parameters required to maximize either the maximal p or d of the stable region, or its area in the p, d space. Last column indicate improvement with respect to an absorber with infinite stiffness ($\gamma \to \infty$)

	γ	ζ_2	Improv. (%)
Max p	2.3	0.174	+ 42.6
Max d	3.55	0.126	+ 21.6
Max Area	3.3	0.126	+ 36

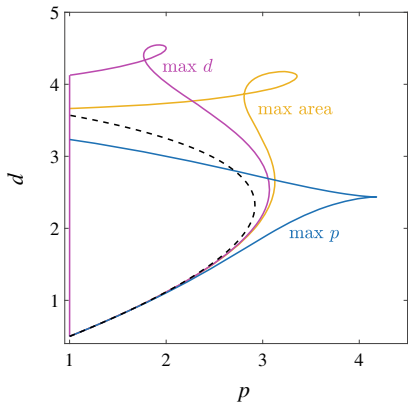

Fig. 6.6 Stability chart for the inverted pendulum with attached TMD. $\tau = 0.5$ and $\mu = 0.1$. Blue line: p maximized, magenta line: d maximized, orange line: area maximized, dashed black line: infinitely rigid absorber

6.4 Bifurcation Analysis

Referring to the inverted pendulum without TMD, we already noticed that, while the stability boundary is related to a static loss of stability ($\omega = 0$), the right border corresponds to the occurrence of Andronov-Hopf bifurcations. In order to investigate the behavior of the system after the loss of stability a bifurcation analysis is therefore performed. The method of multiple scales for time delayed systems is adopted [9, 16]. The procedure is first illustrated for the pendulum without TMD and then extended to the case of the coupled system. The same analysis for a very similar system is performed in [22].

6.4.1 Inverted Pendulum Without Absorber

First, we expand the equation of motion in (6.1) in Taylor series around $\varphi = 0$ and transform it into first-order form, i.e.

$$\dot{\mathbf{x}} = \mathbf{L}\mathbf{x} - \left(p\mathbf{R}_p + \mathbf{R}_d\right)\mathbf{x}_\tau + \mathbf{f}, \tag{6.9}$$

where

$$\mathbf{x} = \begin{bmatrix} \varphi_1 \\ \dot{\varphi}_1 \end{bmatrix}, \ \mathbf{x}_\tau = \mathbf{x}(t-\tau), \ \mathbf{L} = \begin{bmatrix} 0 & 1 \\ 1 & 0 \end{bmatrix}, \ \mathbf{R}_p = \begin{bmatrix} 0 & 0 \\ 1 & 0 \end{bmatrix}, \ \mathbf{R}_p = \begin{bmatrix} 0 & 0 \\ 0 & d \end{bmatrix}, \ \mathbf{f} = \begin{bmatrix} 0 \\ -\frac{\varphi_1^3}{6} \end{bmatrix}, \tag{6.10}$$

p is the bifurcation parameter adopted.

Next, we expand the solution of (6.9) as

$$\mathbf{x}(t;\varepsilon) = \varepsilon^{1/2}\mathbf{x}_1(T_0, T_1) + \varepsilon^{3/2}\mathbf{x}_2(T_0, T_1) + \cdots \tag{6.11}$$

where $T_0 = t$, $T_1 = \varepsilon t$ and ε is a small bookkeeping parameter. The derivative with respect to t is transformed into

$$\frac{\mathrm{d}}{\mathrm{d}t} = \frac{\partial}{\partial T_0} + \varepsilon\frac{\partial}{\partial T_1} + \cdots = D_0 + \varepsilon D_1 + \cdots \tag{6.12}$$

while delayed terms are expressed as

$$\mathbf{x}(t-\tau;\varepsilon) = \varepsilon^{1/2}\mathbf{x}(T_0 - \tau, T_1) + \varepsilon^{3/2}\mathbf{x}_2(T_0 - \tau, T_1) - \varepsilon^{3/2}\tau D_1\mathbf{x}_1(T_0 - \tau, T_1) + \cdots \tag{6.13}$$

The bifurcation parameter p is rewritten as $p = p_{cr} + \varepsilon\delta$, where p_{cr} corresponds to the p value at the loss of stability. For a clearer explanation of the formalism adopted, we address the interested reader to [16].

Substituting (6.11)–(6.13) into (6.9) and equating terms of equal order of ε we have

$$\varepsilon^{1/2}: \ D_0\mathbf{x}_1 - \mathbf{L}\mathbf{x}_1 + \left(p_{cr}\mathbf{R}_p + \mathbf{R}_d\right)\mathbf{x}_{1\tau} = \mathbf{0} \tag{6.14}$$

$$\varepsilon^{3/2}: \ D_0\mathbf{x}_2 - \mathbf{L}\mathbf{x}_2 + \left(p_{cr}\mathbf{R}_p + \mathbf{R}_d\right)\mathbf{x}_{2\tau} = -\delta\mathbf{R}_p\mathbf{x}_{1\tau} - D_1\mathbf{x}_1 + \left(p_{cr}\mathbf{R}_p + \mathbf{R}_d\right)\tau D_1\mathbf{x}_{1\tau} + \mathbf{f}(\mathbf{x}_1) \tag{6.15}$$

6.4.1.1 Order $\varepsilon^{1/2}$

The general steady state solution of (6.14) is

$$\mathbf{x}_1(T_0, T_1) = A(T_1)\mathbf{c}e^{i\omega_c T_0} + \bar{A}(T_1)\mathbf{c}e^{-i\omega_c T_0}, \tag{6.16}$$

where the overbar indicates complex conjugate and ω_c is given by (6.5) for $p = p_{cr}$. $\mathbf{c} = [1 \quad c_2]^{\mathrm{T}}$ is obtained by the linear homogeneous system of equation

$$\left(i\omega_c\mathbf{I} - \mathbf{L} + \left(p_{cr}\mathbf{R}_p + \mathbf{R}_d\right)e^{-i\omega_c\tau}\right)\mathbf{c} = \mathbf{0}, \tag{6.17}$$

which gives $c_2 = i\omega_c$.

6.4.1.2 Order $\varepsilon^{3/2}$

Substituting (6.16) into (6.15) we obtain

$$D_0\mathbf{x}_2 - \mathbf{L}\mathbf{x}_2 + \left(p_{cr}\mathbf{R}_p + \mathbf{R}_d\right)\mathbf{x}_{2\tau} = -\left[\mathbf{I} - \left(p_{cr}\mathbf{R}_p + \mathbf{R}_d\right)e^{-i\omega_c\tau}\right]\mathbf{c}A'e^{i\omega_c T_0} - \delta\mathbf{R}_p A\mathbf{c}e^{i\omega_c T_0}e^{-i\omega_c\tau} + A^2\bar{A}\tilde{\mathbf{f}}e^{i\omega_c T_0} + \text{c.c.} + \text{n.s.t.} \tag{6.18}$$

where $\tilde{\mathbf{f}} = [0 \quad -1/2]^{\mathrm{T}}$, prime ($'$) stands for derivation with respect to T_0, c.c. and n.s.t. stand for "complex conjugate" and for "non secular terms", respectively.

Because the homogeneous part of (6.18) has nontrivial solutions, the nonhomogeneous equation has a solution only if a solvability condition is satisfied. To determine this solvability condition, we set a particular solution of the form

$$\mathbf{x}_2(T_0, T_1) = \phi(T_1)e^{i\omega_c T_0} \tag{6.19}$$

and obtain

$$\left[\mathbf{L} - \left(p_{cr}\mathbf{R}_p + \mathbf{R}_d\right)e^{-i\omega_c\tau} - i\omega_c\mathbf{I}\right]\phi = \left[\mathbf{I} - \left(p_{cr}\mathbf{R}_p + \mathbf{R}_d\right)e^{-i\omega_c\tau}\right]\mathbf{c}A' + \delta\mathbf{R}_p A\mathbf{c}e^{-i\omega_c\tau} - A^2\bar{A}\tilde{\mathbf{f}}. \tag{6.20}$$

The solvability condition demands that the right-hand side of (6.20) is orthogonal to every solution of the adjoint homogeneous problem. The adjoint problem is governed by

$$\left[\mathbf{L}^{\mathrm{H}} - \left(p_{cr}\mathbf{R}_p^{\mathrm{H}} + \mathbf{R}_d^{\mathrm{H}}\right)e^{i\omega_c\tau} + i\omega_c\mathbf{I}\right]\mathbf{b} = \mathbf{0}, \tag{6.21}$$

where $^{\mathrm{H}}$ indicates the conjugate transpose. To make $\mathbf{b}$ unique we impose the condition

$$\mathbf{b}^{\mathrm{H}}\mathbf{c} = 1 \tag{6.22}$$

and obtain

$$\mathbf{b} = \begin{bmatrix} 1 \\ -\frac{i\omega_c}{e^{i\omega_c}p_{cr}-1} \end{bmatrix}. \tag{6.23}$$

We take the inner product of $\mathbf{b}^{\mathrm{H}}$ with the right-hand side of (6.20), i.e.

$$\mathbf{b}^{\mathrm{H}}\left(\left[\mathbf{I} - \left(p_{cr}\mathbf{R}_p + \mathbf{R}_d\right)e^{-i\omega_c\tau}\right]\mathbf{c}A' + \delta\mathbf{R}_p A\mathbf{c}e^{-i\omega_c\tau} - A^2\bar{A}\tilde{\mathbf{f}}\right) = 0, \tag{6.24}$$

from which we get the expression

$$A' = \Lambda_1\delta A + \Lambda_2 A^2\bar{A}. \tag{6.25}$$

6.4.1.3 Normal Form

We then introduce the polar form

$$A = \frac{1}{2} a e^{i\beta}, \tag{6.26}$$

where a and β are real functions of T_1. Substituting (6.26) into (6.25) and separating real and imaginary parts we have

$$\text{Re:} \quad a' = \delta \Lambda_{1R} a + \frac{1}{4} a^3 \Lambda_{2R} \tag{6.27}$$

$$\text{Im:} \quad a\beta' = \delta \Lambda_{1I} a + \frac{1}{4} a^3 \Lambda_{2I}, \tag{6.28}$$

where Λ_{1R}, Λ_{2R}, Λ_{1I} and Λ_{2I} are the real and imaginary parts of Λ_1 and Λ_2, respectively.

Equation (6.27) provides information about the oscillation amplitude of the system in the vicinity of the bifurcation. In order to identify periodic solutions, we impose $a' = 0$ and obtain the solutions

$$a_0 = 0 \quad \text{and} \quad a_1 = 2\sqrt{-\frac{\delta}{\Delta}}, \tag{6.29}$$

where

$$\Delta = \Lambda_{2R}/\Lambda_{1R} = \frac{\left(\omega_c^2 + 1\right)\left(2\tau\omega_c - \sin(2\tau\omega_c)\right)}{4\left(\left(\omega_c^2 - 1\right)\sin(\tau\omega_c) + \tau\omega_c\left(\omega_c^2 + 1\right)\cos(\tau\omega_c)\right)}. \tag{6.30}$$

Recalling (6.11), (6.16), (6.26), (6.29) and that $p = p_{cr} + \varepsilon\delta$, we have that the amplitude of the LCOs in the vicinity of the bifurcation is approximated by

$$\varphi_1 = \varphi_0 \cos(\omega_c t + \beta), \quad \varphi_0 = 2\sqrt{\frac{p_{cr} - p}{\Delta}}. \tag{6.31}$$

Since δ represents small variations of p with respect to its critical value p_{cr}, a_1 is real for $\delta > 0\ (< 0)$ if $\Delta < 0\ (> 0)$. With respect to the Andronov-Hopf bifurcation occurring at the loss of stability, the bifurcation is therefore supercritical if $\Delta < 0$ and subcritical if $\Delta > 0$.

It can be verified that for values of ω_c and τ compatible with points of the stability boundary Δ is always positive, therefore the bifurcation is always subcritical.

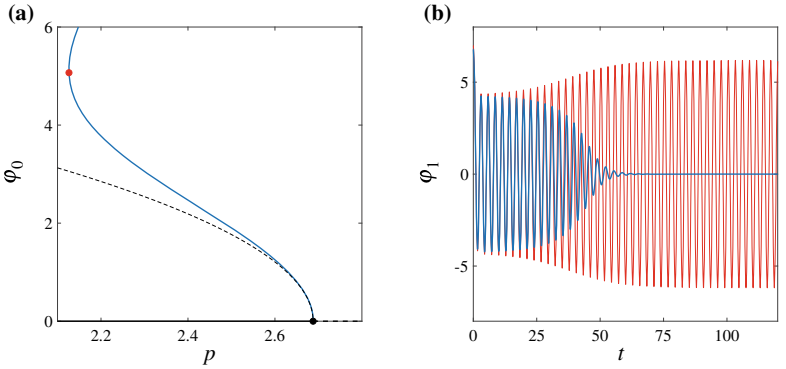

Fig. 6.7 **a** Bifurcation diagram for $\tau = 0.5$ and $d = 2$; dashed black line: analytical, solid blue line: numerical, black dot: Andronov-Hopf bifurcation, red dot: fold; **b** time series for $p = 2.15$, initial conditions: thin red line $(\varphi(s), \dot{\varphi}(s)) = (6.9, 0)$, thick blue line $(\varphi(s), \dot{\varphi}(s)) = (6.8, 0)$, with $s \in [-\tau, 0]$

6.4.1.4 Bifurcation Diagrams

Figure 6.7a provides a comparison between the bifurcation diagram predicted analytically (dashed black line) and calculated numerically (solid blue line). It can be noticed that the two curves are very close to each other for small amplitude, which confirms the validity of the analytical procedure. For increasing amplitude, the numerical curve diverges from the analytical one, exhibiting a fold point. This feature cannot be captured by the analytical procedure, which is valid only in the vicinity of the bifurcation. The numerical bifurcation branch was obtained through the Matlab based continuation software DDE-Biftool [7].

The subcritical characteristic of the bifurcation limits the basin of attraction of the stable trivial solution. This is verified through direct numerical integration in Fig. 6.7b, where the red and blue curves refer to time series obtained with the same parameter values $\tau = 0.5$, $d = 2$ and $p = 2.15$, but with different initial conditions $(\varphi(s), \dot{\varphi}(s)) = (6.9, 0)$ and $(\varphi(s), \dot{\varphi}(s)) = (6.8, 0)$, with $s \in [-\tau, 0]$, respectively. While the red curve results in a periodic solution, the blue one converges to 0. We notice that the initial cycles of both curves have amplitude $\varphi_0 \approx 4.4$, in excellent agreement with the amplitude of the branch of unstable periodic solutions in Fig. 6.7a for $p = 2.15$. Similar bifurcation diagrams can be plotted for different values of control gains p and d and time delay τ.

6.4.2 Inverted Pendulum with Absorber

The analysis already performed for the simple pendulum is repeated including the vibration absorber in the system, as it is in (6.6). The system is reduced to the same form as in (6.9), where

$$\mathbf{x} = \begin{bmatrix} \varphi_1 \\ \dot{\varphi}_1 \\ \varphi_2 \\ \dot{\varphi}_2 \end{bmatrix}, \ \mathbf{x}_\tau = \mathbf{x}(t-\tau), \ \mathbf{L} = \begin{bmatrix} 0 & 1 & 0 & 0 \\ 1-\gamma^2\mu & -2\gamma\zeta_2\mu & \gamma^2\mu & 2\gamma\zeta_2\mu \\ 0 & 0 & 0 & 1 \\ \gamma^2 & 2\gamma\zeta_2 & -\gamma^2 & -2\gamma\zeta_2 \end{bmatrix},$$
$$\mathbf{R}_p = \begin{bmatrix} 0\,0\,0\,0 \\ 1\,0\,0\,0 \\ 0\,0\,0\,0 \\ 0\,0\,0\,0 \end{bmatrix}, \ \mathbf{R}_p = \begin{bmatrix} 0\,0\,0\,0 \\ 0\,d\,0\,0 \\ 0\,0\,0\,0 \\ 0\,0\,0\,0 \end{bmatrix}, \ \mathbf{f} = \begin{bmatrix} 0 \\ -\frac{\varphi_1^3}{6} \\ 0 \\ 0 \end{bmatrix}. \tag{6.32}$$

Then, exactly the same steps performed in the previous section are repeated (from 6.11 to 6.30). Finally, we approximate the system response by

$$\varphi_1 = \varphi_0 \cos(\omega_c t + \beta), \quad \varphi_0 = 2\sqrt{\frac{p_{cr} - p}{\Delta_{TMD}}}, \tag{6.33}$$

where Δ_{TMD} has a much lengthier form than Δ found in the previous section. Because of this, its explicit formulation is omitted here. Instead, the value of Δ_{TMD} is exploited to characterize the bifurcation in some specific cases.

We consider the system with a TMD optimized for maximizing the proportional gain p, as indicated in the first line of Table 6.1. The bifurcation analysis indicates that the Andronov-Hopf bifurcations are subcritical on most of the stability boundary, while only on a small portion it is supercritical, as represented in Fig. 6.8. This result is validated numerically by plotting bifurcation diagrams.

Figure 6.9a represents a subcritical bifurcation and dashed and solid lines indicate analytical and numerical results, respectively. Also in this case, the two curves are in good agreement for low oscillation amplitudes, while they diverge as amplitude increases. The numerically obtained curve shows that at $p = 1.26$ a fold point is reached. This scenario is analogous to the one depicted in Fig. 6.7. Time series obtained through direct numerical simulations are illustrated in Fig. 6.9b for $p = 2$,

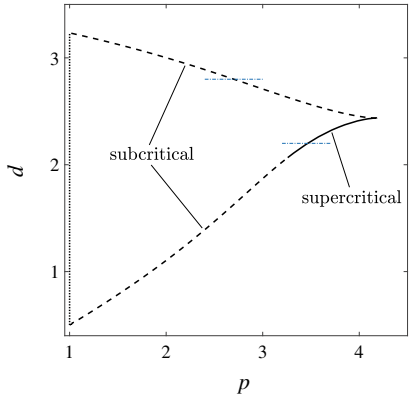

Fig. 6.8 Bifurcation characterization for the inverted pendulum with attached TMD. $\tau = 0.5$, $\mu = 0.1$, $\gamma = 2.3$ and $\zeta_2 = 0.174$. Dashed lines: subcritical bifurcations, solid line: supercritical bifurcations. Blue dash-dotted lines indicate bifurcation diagrams plotted in Figs. 6.9–6.10

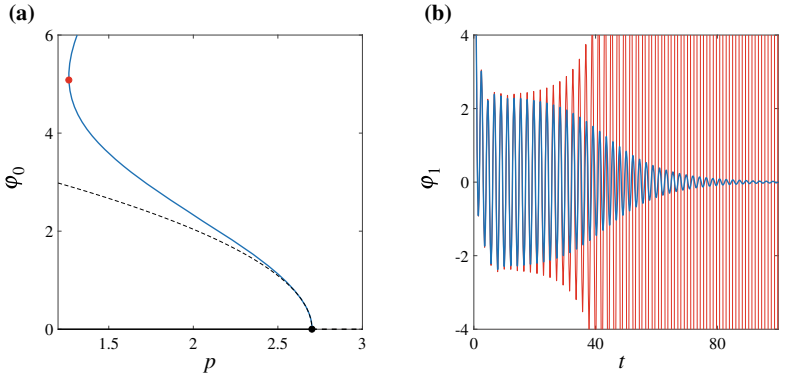

Fig. 6.9 **a** Bifurcation diagram for $\tau = 0.5$, $d = 2.8$, $\gamma = 2.3$ and $\zeta_2 = 0.174$; dashed black line: analytical, solid blue line: numerical, black dot: Andronov-Hopf bifurcation, red dot: fold; **b** time series for $p = 2$, initial conditions: thin red line $(\varphi_1(s), \dot{\varphi}_1(s), \varphi_2(s), \dot{\varphi}_2(s)) = (9.2, 0, 9.2, 0)$, thick blue line $(\varphi_1(s), \dot{\varphi}_1(s), \varphi_2(s), \dot{\varphi}_2(s)) = (9.1, 0, 9.1, 0)$, with $s \in [-\tau, 0]$

i.e. within the stable region. Although the blue and red curves in the figure have very close initial conditions, one asymptotically converges to the trivial solution, while the other one grows unboundedly. This clearly prove the limited extent of the basin of attraction of the stable trivial solution also for the pendulum with attached TMD. Both the time series allow to grasp the shape of the unstable solution limiting the basin of attraction, which is in good agreement with the result obtained numerically at $\varphi_0 \approx 2$ for $p = 2$.

Figure 6.10a illustrates a bifurcation diagram for $d = 2.2$. According to the analytical calculation, $\Delta < 0$, therefore the bifurcation is supercritical. This is confirmed by the numerical simulation. Besides the good matching between analytical and numerical results at low amplitude, an interesting feature, is exhibited by the numerical results, unpredicted by the analytical investigation. The branch of stable periodic solution emerging at the Andronov-Hopf bifurcation turns back for $p = 3.9$ and reaches values of p within the stable region. Eventually, at $p = 3$ another fold occurs. This double fold has an important implication with respect to the system dynamics. First of all, although the bifurcation is supercritical, as correctly predicted by the analytical development, the basin of attraction in the vicinity of the bifurcation is not unbounded. Which means that from a practical point of view the two scenarios in Figs. 6.9 and 6.10 are not very different. Secondly, in the unstable region there exist a stable periodic attractor only for p smaller than the value of p at the fold ($p = 3.9$ in this case). For $p > 3.9$ the response of the system grows unboundedly and for p between the Andronov-Hopf bifurcation and the right fold ($p \in (3.47, 3.9)$ in this case) the system can either converge to a periodic solution or diverge, as clearly illustrated in Fig. 6.10c. We notice that, for this system, in most of cases presenting subcritical bifurcations, for any p value outside the stable region the system response diverges unboundedly.

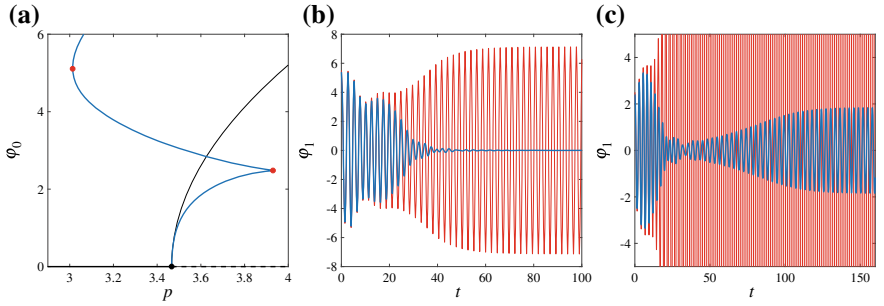

Fig. 6.10 **a** Bifurcation diagram for $\tau = 0.5, d = 2.2, \gamma = 2.3$ and $\zeta_2 = 0.174$; black line: analytical, blue line: numerical, black dot: Andronov-Hopf bifurcation, red dot: fold; **b** time series for $p = 3.2$, initial conditions: thin red line $(\varphi_1(s), \dot{\varphi}_1(s), \varphi_2(s), \dot{\varphi}_2(s)) = (5.5, 0, 5.5, 0)$, thick blue line $(\varphi_1(s), \dot{\varphi}_1(s), \varphi_2(s), \dot{\varphi}_2(s)) = (5.4, 0, 5.4, 0)$; **c** time series for $p = 3.6$, initial conditions: thin red line $(\varphi_1(s), \dot{\varphi}_1(s), \varphi_2(s), \dot{\varphi}_2(s)) = (2.5, 0, 2.5, 0)$, thick blue line $(\varphi_1(s), \dot{\varphi}_1(s), \varphi_2(s), \dot{\varphi}_2(s)) = (2.4, 0, 2.4, 0)$; $s \in [-\tau, 0]$

6.5 Conclusions

In this work, the application of a TMD for the suppression of delay-induced vibrations was investigated. Results illustrate that the TMD can significantly improve stability properties of the system. However, the optimal tuning of the natural frequency of the absorber critically depends on the control delay. This suggests that, in order to implement it in a real engineering application, an accurate knowledge of the time delay (and of the primary system natural frequency) is required. This limit might be overcome either employing a self-tuning mechanism for the absorber parameters or adopting multiple TMD in order to enlarge the frequency bandwidth of operation. These two further developments will be the objective of future studies.

The bifurcation analysis of the system illustrates that significant problems related to the system robustness within the stable region exist. The application of the TMD does not seem to improve the system robustness. Possible alternatives to improve the robustness of the equilibrium with respect to perturbations might be given by the introduction of nonlinear terms either in the active controller (for example considering a progressive saturation) or introducing nonlinearities in the absorber. These aspects will also be studied in future works.

Acknowledgements The author would like to acknowledge the financial support of the European Union, H2020 Marie Skłodoska-Curie Individual Fellowship, Grant Agreement 704133 (PIEZOMACH) and of the Higher Education Excellence Program of the Ministry of Human Capacities in the frame of Biotechnology research area of Budapest University of Technology and Economics (BME FIKP-BIO).

References

1. S. Beregi, D. Takács, Analysis of the tyre–road interaction with a non-smooth delayed contact model. Multibody Syst. Dyn. 1–17 (2017)
2. J.L. Cabrera, J.G. Milton, On-off intermittency in a human balancing task. Phys. Rev. Lett. **89**(15), 158, 702 (2002)
3. A. Casalotti, A. Arena, W. Lacarbonara, Mitigation of post-flutter oscillations in suspension bridges by hysteretic tuned mass dampers. Eng. Struct. **69**, 62–71 (2014)
4. S. Chatterjee, On the design criteria of dynamic vibration absorbers for controlling friction-induced oscillations. J. Vib. Control. **14**(3), 397–415 (2008)
5. J.P. Den Hartog, Mechanical vibrations (Courier Corporation, 1985)
6. N. Enayati, E. De Momi, G. Ferrigno, Haptics in robot-assisted surgery: challenges and benefits. IEEE Rev. Biomed. Eng. **9**, 49–65 (2016)
7. K. Engelborghs, T. Luzyanina, D. Roose, Numerical bifurcation analysis of delay differential equations using dde-biftool. ACM Trans. Math. Softw. (TOMS) **28**(1), 1–21 (2002)
8. G. Habib, G. Kerschen, Suppression of limit cycle oscillations using the nonlinear tuned vibration absorber. Proc. R. Soc. A **471**(2176), 20140,976 (2015)
9. G. Habib, G. Kerschen, G. Stépán, Chatter mitigation using the nonlinear tuned vibration absorber. Int. J. Non-Linear Mech. **91**, 103–112 (2017)
10. G. Habib, G. Rega, G. Stépán, Stability analysis of a two-degree-of-freedom mechanical system subject to proportional-derivative digital position control. J. Vib. Control. **21**(8), 1539–1555 (2015)
11. G. Habib, G. Rega, G. Stépán, Delayed digital position control of a single-dof system and the nonlinear behavior of the act-and-wait controller. J. Vib. Control. **22**(2), 481–495 (2016)
12. T. Insperger, J. Milton, G. Stépán, Acceleration feedback improves balancing against reflex delay. J. R. Soc. Interface**10**(79), 20120,763 (2013)
13. T. Insperger, G. Stépán, Act-and-wait control concept for discrete-time systems with feedback delay. IET Control. Theory Appl. **1**(3), 553–557 (2007)
14. T. Insperger, G. Stépán, Semi-discretization for time-delay systems: stability and engineering applications, vol. 178 (Springer Science & Business Media, 2011)
15. W. Michiels, S.I. Niculescu, On the delay sensitivity of smith predictors. Int. J. Syst. Sci. **34**(8–9), 543–551 (2003)
16. A.H. Nayfeh, Order reduction of retarded nonlinear systems-the method of multiple scales versus center-manifold reduction. Nonlinear Dyn. **51**(4), 483–500 (2008)
17. P. Nwagoum Tuwa, P. Woafo, Analysis of an electrostatically actuated micro-plate subject to proportional-derivative controllers. J. Vib. Control. **24**(10), 2020–2029 (2018)
18. F. Sadek, B. Mohraz, A.W. Taylor, R.M. Chung, A method of estimating the parameters of tuned mass dampers for seismic applications. Earthq. Eng. Struct. Dyn. **26**(6), 617–635 (1997)
19. G. Stépán, Retarded dynamical systems: stability and characteristic functions (Longman Scientific & Technical, 1989)
20. B. Varszegi, D. Takacs, G. Stépán, S.J. Hogan, Stabilizing skateboard speed-wobble with reflex delay. J. R. Soc. Interface **13**(121), 20160,345 (2016)
21. Y. Yang, J. Munoa, Y. Altintas, Optimization of multiple tuned mass dampers to suppress machine tool chatter. Int. J. Mach. Tools Manuf. **50**(9), 834–842 (2010)
22. L. Zhang, G. Stépán, Hopf bifurcation analysis of scalar implicit neutral delay differential equation. Electron. J. Qual. Theory Differ. Equations **2018**(62), 1–9 (2018)

Chapter 7
Modal Analysis Investigation of Mechanical Kerr Frequency Combs

Samer Houri, Daiki Hatanaka, Yaroslav M. Blanter and Hiroshi Yamaguchi

Abstract The aim of this work is to theoretically investigate the possibility of Kerr frequency combs in mechanical systems. In particular, whether microelectromechanical devices (MEMS) can be used to generate frequency combs in a manner that is analogous to the optical frequency combs generated in optical microresonators with Kerr-type nonlinearity. The analysis assumes a beam-like micromechanical structure, and starting from the Euler-Bernoulli beam equation derives the necessary conditions in parameter space for the comb generation. The chapter equally presents potential means for the physical implementation of mechanical Kerr combs.

7.1 Introduction

Optical frequency combs,[1] as their name suggests, produce an output that has equidistant frequency components within a relatively wide spectral range. The time domain corollary of this discrete and equidistant multispectral structure is that the output takes the form of a periodic train of narrow pulses ([24]). The highly periodic signal output and equidistant spectral components have made optical frequency combs an invaluable tool for timing and spectroscopy applications [15, 17, 45, 63].

Several means exist for the generation of optical frequency combs, in one approach mode-locked cavities such as Ti: Sapphire laser cavities that can support a large number of longitudinal modes is used to provide the equidistant components of

S. Houri (✉) · D. Hatanaka · H. Yamaguchi
NTT Basic Research Laboratories, NTT Corporation, 3-1 Morinosato-Wakamiya, Atsugi-Shi, Kanagawa 243-0198, Japan
e-mail: Houri.Samer@lab.ntt.co.jp; samer.houri.dg@hco.ntt.co.jp

Y. M. Blanter
Kavli Institute of Nanoscience, Delft University of Technology, Lorentzweg 1, 2628 CJ, Delft, The Netherlands

[1] **Optical frequency comb** is a laser source whose spectrum consists of a series of discrete, equally spaced frequency lines. Frequency combs can be generated by a number of mechanisms, including periodic modulation (in amplitude and/or phase) of a continuous-wave laser, four-wave mixing in nonlinear media, or stabilization of the pulse train generated by a mode-locked laser.

M. Belhaq (ed.), *Topics in Nonlinear Mechanics and Physics*,
Springer Proceedings in Physics 228, https://doi.org/10.1007/978-981-13-9463-8_7

the optical comb [13, 59]. In a slightly different implementation, known as the Q-switched cavity, a phase relation is established between the different cavity modes using a saturable absorber [29].

More recently a very promising approach for the generation of optical frequency combs making use of Kerr nonlinear optical resonators has been demonstrated. The basic principle behind the operation of such Kerr frequency combs consists of applying a laser pump that is nearly resonant with one of the cavity's many modes, the laser pump is thus confined to micrometric dimensions inside the resonator resulting in very large electric fields. The intra-cavity fields are large enough to undergo nonlinear degenerate four-wave mixing (FWM) which produces photons with slightly different frequencies that excite nearby cavity modes. These newly excited modes in their turn undergo a process of either degenerate or non-degenerate FWM to produce more sidebands that correspond to other cavity modes, and so on in a cascade process [16, 37].

The introduction of Kerr frequency combs has sparked great interest that is motivated by fundamental as well as practical questions. On a more technological end a significant appeal of Kerr frequency combs is their use of microscale optical resonators thus promising to reduce both footprint and power consumption considerably compared to the more classical mode-locked lasers approach [38, 41, 60, 61]. Whereas the generation of solitons [2, 22, 30 49, 55], rogue waves [1, 11], emerging patterns [43], and chaotic behavior [10, 52, 56] are all issues of importance from a more fundamental point of view.

Seen the great progress and interest in photonic frequency combs, it is not surprising that phononic, i.e. mechanical or acoustic, frequency combs should also be investigated. This is especially true since micromechanical systems (MEMS) offer strongly nonlinear behavior [42] that is promising for frequency comb implementation. Indeed several approaches have been undertaken to demonstrate frequency combs, the first approach relies on mixing two drive tones using the nonlinearity of the MEMS device [18, 27, 33–35]. A second approach relies on inducing instabilities in a highly nonlinear M/NEMS device, such instabilities usually originates from the nonlinear interaction between different oscillating modes or devices [4, 14, 19, 20, 32–34, 36, 47, 48, 58].

Despite such progress in demonstrating mechanical frequency combs, these demonstrations remain limited to combs generated within the envelope of a single nonlinearly oscillating mode, while a true multimodal mechanical frequency comb with a large number of cavity modes excited simultaneously, in a manner analogous to optical frequency combs remains to be demonstrated. Indeed even the questions regarding the possibility and properties of a Kerr mechanical frequency comb have not been addressed in a satisfactorily fashion.

Therefore, it is the aim of this work to explore the possibility of producing a multimodal mechanical frequency comb that functions according to the same principals of that of optical Kerr combs. The theoretical investigation will further explore the conditions in parameter space that are necessary for the onset of such combs, in the aim of guiding future experimental effort. Thereafter, the chapter proposes experimental means for the generation of mechanical combs.

7.2 Analytical Formulation

In addition to numerous experimental investigations, optical Kerr combs have equally benefited from a detailed and extensive mathematical analysis of their properties, formation conditions, and dynamics [7, 21, 51], whereas such analytical basis is still lacking for the case of mechanical Kerr combs.

This section will provides mathematical foundation that establishes a relation between beam mechanics and the dynamics of FWM Kerr comb generation. Once a mechanical analogue to the optical governing equations is established, attention is given to the physical interpretation of these equations and their corresponding parameter space. Equally important this section investigates the impact of some MEMS-specific properties such as internal stresses that are often encountered in MEMS devices but have no analogue in optics. This work assumes a beam-like geometry that is compatible with the Euler-Bernoulli beam equation.

7.2.1 Euler-Bernoulli Modal Expansion

We start our investigation by considering the beam equation to describe the dynamics of MEMS beam structures. We then decompose the mechanical vibrations of the beam into a set of normal modes in a manner that is analogous to the modal decomposition of optical microresonators [6]. The beam equation used in this work is the Euler-Bernoulli equation which along with the boundary conditions for a clamped-clamped beam, reads [9]:

$$\begin{cases} EI\frac{\partial^4 y}{\partial x^4} + \gamma\frac{\partial y}{\partial t} + \rho A\frac{\partial^2 y}{\partial t^2} - \frac{EA}{2L}\int_0^L \left(\frac{\partial y}{\partial x'}\right)^2 dx' \frac{\partial^2 y}{\partial x^2} = F(x,t) \\ y(0,t) = y(L,t) = y'(0,t) = y'(L,t) \end{cases} \tag{7.1}$$

where x and $y(x,t)$ are the longitudinal coordinate and the beam's displacement respectively, E is the Young's modulus, I is the second area moment of inertia of the beam section, γ is the viscous damping term, ρ is the density of the beam, A is the beam's cross-sectional area, L is the beam's length, $F(x,t)$ is the driving force applied to the structure, x' is also a longitudinal coordinate used only within the integral and the last term on the left hand side is the nonlinear term originating from beam stretching [9].

In order to make this description scale free, the above equation is changed into a dimensionless version by resorting to the following set of parameter transformation:

$$\bar{x} = \frac{x}{L},\ \bar{y} = \frac{y}{h},\ \bar{\gamma} = \frac{\gamma L^4}{EIT},\ \bar{F} = \frac{FL^4}{EIh},\ \bar{t} = \frac{t}{T},\ T = \sqrt{\frac{\rho A L^4}{EI}} \tag{7.2}$$

where the bar indicates a dimensionless quantity.

The dimensionless Euler-Bernoulli equation now reads (dropping the bars for convenience):

$$\frac{\partial^4 y}{\partial x^4} + \gamma \frac{\partial y}{\partial t} + \frac{\partial^2 y}{\partial t^2} - 6 \int_0^1 \left(\frac{\partial y}{\partial x'} \right)^2 dx' \frac{\partial^2 y}{\partial x^2} = F(x,t) \tag{7.3}$$

At this point we resort to a modal decomposition where the motion of the vibrating beam is projected on a set of harmonic basis functions, i.e. $y(x,t) = \sum_i \psi_i(x)\xi_i(t)$. These latter are simply the natural modes of vibration of a linear beam, and can equally be obtained as the homogenous solution of the Euler-Bernoulli equation, written as (the same boundary conditions apply):

$$\frac{d^4\psi(x)}{dx^4} = \omega^2 \psi(x) \tag{7.4}$$

Whose solution, i.e., mode shapes for a clamped-clamped beam are:

$$\psi_n(x) = a_n\left(\cos\left(\omega_n^{1/2}x\right) - \cosh\left(\omega_n^{1/2}x\right)\right) + b_n\left(\sin\left(\omega_n^{1/2}x\right) - \sinh\left(\omega_n^{1/2}x\right)\right) \tag{7.5}$$

And the normal mode frequencies are obtained from numerically solving the following transcendental function:

$$\cos\left(\omega_n^{1/2}x\right)\cosh\left(\omega_n^{1/2}x\right) = 1. \tag{7.6}$$

Inserting the harmonic summation into the partial differential equation (7.3), the latter now reads:

$$\sum_k \left(\xi_k \frac{d^4\psi}{dx^4} + \gamma_k \psi_k \dot{\xi}_k + \psi_k \ddot{\xi}_k - 6 \int_0^1 \left(\sum_l \sum_m \psi_l' \psi_m' \right) dx' \psi_k'' \xi_k \xi_l \xi_m \right) = F(x,t) \tag{7.7}$$

where $(\bullet)$ indicates time derivative, and $(')$ indicates spatial derivative. The orthonormality of the mode shapes imply the following identities:

$$\int_0^1 \psi_n \psi_m dx' = 0; \int_0^1 \psi_n \psi_n dx' = 1. \tag{7.8}$$

Multiplying (7.7) by $\psi_n(x)$ and integrating from 0 to 1, we obtain the following modal equation:

$$\ddot{\xi}_n + \gamma_n \dot{\xi}_n + \omega_n^2 \xi_n + 6 \sum_k \sum_l \sum_m \int_0^1 \left(\psi_k' \psi_l'\right) dx' \int_0^1 \left(\psi_m' \psi_n'\right) dx' \xi_k \xi_l \xi_m = F_n(t) \tag{7.9}$$

where γ_n is the modal damping, F_n is the modal forcing given as $F_n(t) = \int_0^1 F(x,t)\psi_n dx$, and we have modified the nonlinear term using the identity $\int_0^1 \left(\psi'_m \psi'_n\right) dx' = -\int_0^1 \left(\psi_m \psi''_n\right) dx'$.

We define the following equality, $\Lambda_{mn} = \int_0^1 \left(\psi'_m \psi'_n\right) dx'$, thus using these identities the partial differential (7.3) can finally be written as the following set of ordinary differential equations:

$$\ddot{\xi}_n + \gamma_n \dot{\xi}_n + \omega_n^2 \xi_n + 6 \sum_{klm} \Lambda_{mn} \Lambda_{kl} \xi_k \xi_l \xi_m = F_n(t) \tag{7.10}$$

Note that the obtained equation, reduces to a classical Duffing equation if the number of modes are reduced to one, and reduces to a mode-coupling equation [44, 50 65, 66] if only two modes are allowed.

To proceed, a rotating frame approximation [23] is applied whereby the motion of the structure's modes is expressed as:

$$\xi_j = \frac{1}{2}\left(A_j e^{i\omega_j t} + A_J^* e^{-i\omega_j t}\right); \text{ and } F_n(t) = \frac{F_n}{2}\left(e^{i\omega t} + e^{-i\omega t}\right) \tag{7.11}$$

where A_j is a slowly varying complex envelope that will capture the main dynamics of the jth mode, F_n and ω are the amplitude and frequency of the driving force respectively, with ω being very close to ω_n.

Note that since we define the amplitude envelope to be slowly varying, that implies that our rotating frame can only account for effects that take place on time scales that are $\gg 1/\omega$, a subtlety that will have important implications later on.

Furthermore, we define $\omega = \omega_n(1+\delta)$, where δ is detuning parameter. Substituting (7.11) into (7.10), and drop all second order terms of δ, e.g. δ^2 and $\delta\gamma$, keeping only the first order time derivative of the complex amplitude envelope, and removing all frequency terms that are not on the order ~ω (i.e., dropping all terms that are of the order 2ω, 3ω …) we obtain the following:

$$i\omega_n \dot{A}_n - \delta\omega_n^2 A_n + \frac{i}{2}\gamma_n \omega_n A_n + \frac{3}{4}\sum_{k,l,m} \Lambda_{kl}\Lambda_{mn} A_k A_l^* A_m e^{-i\Delta\omega_{klmn} t} = \frac{F_n e^{i(\omega-\omega_n)t}}{2} \tag{7.12}$$

where $\Delta\omega_{klmn} = \omega_k - \omega_l + \omega_m - \omega_n$. Note that for the rotating frame approximation to apply we must have $\Delta\omega_{klmn} \ll \omega$, i.e., separation between the relevant modes must be small compared to the frequency of the modes themselves.

Equation (7.12) is identical to that describing optical frequency combs [6]. Thus modal analysis of the Euler-Bernoulli equation demonstrates a close parallel with optics concerning the governing dynamics of Kerr combs.

7.2.2 Stability Analysis for Mechanical Comb Generation

The task ahead is to determine the parameter space necessary for such comb generation. The below stability and comb threshold analysis follows the same logic presented for optical frequency combs [6, 7, 21, 51] while accounting for the specificity of mechanical systems.

It is possible to define the comb generation threshold as the minimum necessary amplitude and detuning for a given driven mode to undergo auto-parametric conversion and generates sidebands that are (nearly) resonant with adjacent modes.

From the above definition, we base our threshold analysis on only three modes, a driven mode (denoted as mode "0"), and two adjacent modes (denoted as "−"and "+" respectively) as shown schematically in Fig. 7.1a, knowing that by adjacent we mean nearby and not necessarily nearest. We further define:

$$\begin{cases} \Lambda_{00} \cong \Lambda_{++} \cong \Lambda_{--} \equiv \Lambda \\ \Lambda_{-0} = \Lambda_{0-} \cong \Lambda_{0+} = \Lambda_{+0} \equiv \Gamma \\ \Lambda_{+-} = \Lambda_{-+} \equiv \Pi \end{cases} \tag{7.13}$$

Since only mode "0" is driven, the right hand side of (7.12) is equated to zero for modes "+" and "−".

The summation corresponding to the nonlinear terms can be further simplified by dropping all second order terms in A_+ or A_-, (7.12) now reads for the "+" and "−" modes respectively:

$$\begin{cases} \dot{A}_+ = \frac{-\gamma}{2} A_+ + i \frac{6}{8\omega_+} \left(2\left(\Lambda^2 + 2\Gamma^2\right)|A_0|^2 A_+ + \left(\Pi\,\Lambda + 2\Gamma^2\right) A_0 A_-^* A_0 e^{i\Delta t}\right) \\ \dot{A}_- = \frac{-\gamma}{2} A_- + i \frac{6}{8\omega_-} \left(2\left(\Lambda^2 + 2\Gamma^2\right)|A_0|^2 A_- + \left(\Pi\,\Lambda + 2\Gamma^2\right) A_0 A_+^* A_0 e^{i\Delta t}\right) \end{cases} \tag{7.14}$$

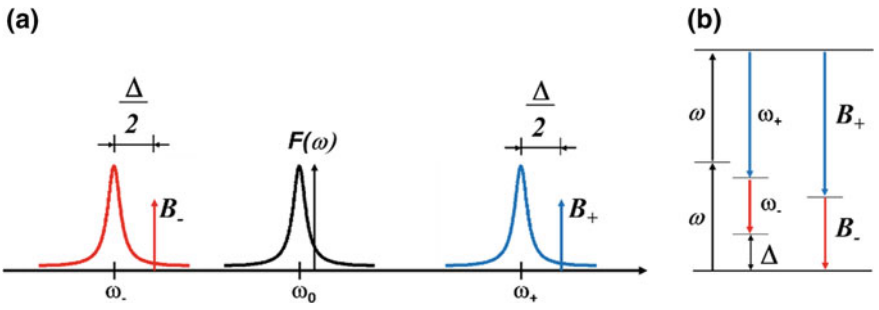

Fig. 7.1 Schematic representing the envelope of the driven mode "0", the detuned drive force "*F(ω)*", the envelopes of the adjacent modes "+" and "−", and the effect of dispersion Δ on the generated sidebands $B_\pm$ (**a**). And in (**b**) schematic representation showing the necessity of introducing the modified rotating frame $B_\pm$ to adjust the phonon energy

where $\Delta = 2\omega - \omega_+ - \omega_- = 2\omega_0 + 2\delta\omega_0 - \omega_+ - \omega_- = \Delta_0 + 2\delta\omega_0$, and Δ_0 is a measure of dispersion, i.e., non-uniform spacing of adjacent modes, whereas $\delta\omega_0$ denotes detuning.

In the above equation, the modal damping coefficients are assumed to take the same value for all modes, a very reasonable assumption for nearby mechanical modes. Since A_0 is directly driven, and below the autoparametric threshold the amplitudes A_+ and A_- are negligibly small, thus A_0 can simply be determined by solving the classical Duffing equation [9]:

$$-\delta\omega_0^2 B_0 + \frac{i}{2}\omega_0\gamma B_0 + \frac{3}{8}6\Lambda^2|B_0|^2 B_0 = \frac{F_0}{2} \tag{7.15}$$

where $B_0 = A_0 e^{i(\omega_0-\omega)t}$, and $|B_0| = |A_0|$ is a rotating frame transformation used to remove the time dependence in the right hand side of (7.12).

At this point one more rotating reference frame transformation is undertaken whereby the complex amplitudes $B_\pm$ are defined as $B_\pm = A_\pm e^{i\frac{\Delta}{2}t}$. Thus (7.14) now reduces to:

$$\begin{cases} \dot{B}_+ = -i\frac{\Delta}{2}B_+ - \frac{\gamma}{2}B_+ + i\frac{6}{8\omega_+}\left(2\left(\Lambda^2+2\Gamma^2\right)|B_0|^2 B_+ + \left(\Pi\,\Lambda + 2\Gamma^2\right)B_0 B_-^* B_0\right) \\ \dot{B}_-^* = i\frac{\Delta}{2}B_-^* - \frac{\gamma}{2}B_-^* - i\frac{6}{8\omega_-}\left(2\left(\Lambda^2+2\Gamma^2\right)|B_0|^2 B_-^* + \left(\Pi\,\Lambda + 2\Gamma^2\right)B_0^* B_+ B_0^*\right) \end{cases} \tag{7.16}$$

The introduction of the $B_\pm$ coordinates has for objective to eliminate any frequency (energy) mismatch between the pump mode (phonons) and the sideband modes (phonons) as shown schematically in Fig. 7.1b. Equation (7.16) represents an autonomous system that is fully defined by the system parameters, the Jacobian matrix of which is:

$$\boldsymbol{J} = \begin{bmatrix} -i\frac{\Delta}{2} - \frac{\gamma}{2} + \frac{i6}{4\omega_+}\left(\Lambda^2+2\Gamma^2\right)|B_0|^2 & \frac{i6}{8\omega_+}\left(\Pi\,\Lambda + 2\Gamma^2\right)B_0^2 \\ \frac{-i6}{8\omega_-}\left(\Pi\,\Lambda + 2\Gamma^2\right)B_0^{*2} & i\frac{\Delta}{2} - \frac{\gamma}{2} - \frac{i6}{4\omega_-}\left(\Lambda^2+2\Gamma^2\right)|B_0|^2 \end{bmatrix} \tag{7.17}$$

The mechanical Kerr comb generation requires that the eigenvalues (λ) of the Jacobian matrix $\boldsymbol{J}$ have a positive real part, i.e. $Re(\lambda) > 0$. The threshold of instability, i.e. comb generation, is $Re(\lambda) = 0$ which can be explicitly written as (note that in the denominator we apply the approximation $\omega_0 \cong \omega_+ \cong \omega_-$):

$$\left[-\left(-\Delta + \frac{3}{\omega_0}\left(\Lambda^2+2\Gamma^2\right)|B_0|^2\right)^2 + \frac{9}{4\omega_0^2}\left(\Lambda\,\Pi + 2\Gamma^2\right)^2|B_0|^4\right] > \gamma^2 \tag{7.18}$$

7.2.3 Exploring Parameter Space

To determine where in the parameter space it is most promising to look for mechanical frequency combs, it is first necessary to determine the main trends of how the nonlinear terms Λ, Γ, and Π scale with modal number and mode spacing.

Since for the above rotating frame analysis to be valid we need $\omega \gg \Delta$, we consider only large mode numbers, particularly even modes from 50 to 150, so that the spacing between consecutive modes would be much smaller than the mode frequencies.

The coupling terms are calculated by numerically integrating the spatial derivatives of the mode shapes, as explained in Sect. 7.2.1, the interaction matrix of which is shown in Fig. 7.2a. Note that the diagonal terms of the figure represent Λ, whereas off-diagonal terms represent Γ. It is clear that self- terms are much larger than cross-terms, furthermore cross-interaction terms change very slowly with mode number as can be seen for example from the line plot for the 100th mode shown in Fig. 7.2b.

Based on the result of these simulations we can approximate $\Gamma \sim \Pi$, and knowing that $\Lambda \gg \Gamma$, therefore it is possible to simplify expression (7.18) into:

$$\left[-\left(-\Delta + \frac{3}{\omega_0}\Lambda^2|B_0|^2\right)^2 + \frac{9}{4\omega_0^2}(\Lambda\,\Pi)^2|B_0|^4 - \gamma^2\right] > 0 \tag{7.19}$$

Equation (7.19) indicates that for comb generation to take place, the nonlinear (Duffing) detuning has to cancel the dispersion, i.e. $\omega_0\Delta = 3\Lambda^2|B_0|^2$, and at the same time the cross-Kerr term has to overcome damping, i.e. $3\Lambda\,\Pi|B_0|^2 = 2\gamma^2$. The threshold values for the amplitude of the pump mode A_0 necessary to induce FWM is determined by setting (7.19) to zero, resulting in the following quadratic equation:

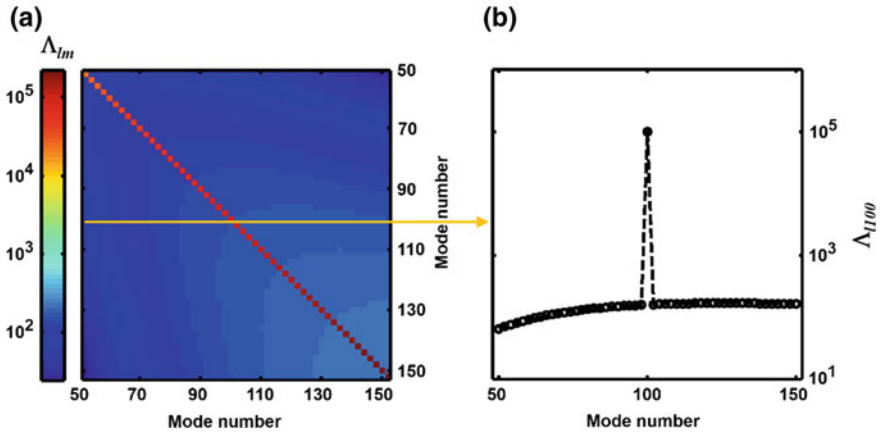

Fig. 7.2 Calculation of Λ_{lm} showing a strong self-interaction term compared to cross-interaction for modes ranging from 50 to 100 (**a**). A plot of Λ_{1100} for mode number 100 showing 3 orders of magnitude difference between self- and cross- Kerr terms (**b**)

$$\frac{9}{\omega_0^2}\Lambda^2\left(\frac{\Pi^2}{4}-\Lambda^2\right)|B_0|^4+\frac{6}{\omega_0}\Delta\,\Lambda^2|B_0|^2-\left(\Delta^2+\gamma^2\right)=0 \tag{7.20}$$

Thus the necessary amplitude for comb generation can be given as function of the system parameters as:

$$|B_0|^2=\frac{2\omega_0\left(2\Delta\,\Lambda\pm\sqrt{\Delta^2\Pi^2+\gamma^2\Pi^2-4\gamma^2\Lambda^2}\right)}{3\Lambda\left(4\Lambda^2-\Pi^2\right)} \tag{7.21}$$

The boundary of the comb generation area is limited by $\gamma=0$, thus the pump amplitude will need to always be contained between:

$$|B_0|^2=\frac{4\omega_0\Delta(\Lambda\pm\Pi/2)}{3\Lambda\left(4\Lambda^2-\Pi^2\right)}\cong\frac{\omega_0\Delta}{3\Lambda^2}(1\pm\Pi/2\Lambda) \tag{7.22}$$

Because $\Pi/\Lambda\approx10^{-3}$, (7.22) imposes stringent conditions on the pump amplitude, since it needs to be within a very narrow range given by $\sim\frac{\omega_0\Delta}{3\Lambda^2}\left(10^{-3}\right)$.

Furthermore, the necessary oscillation amplitude of the pump mode should not fall within the unstable boundaries of the Duffing equation calculated from (7.15). Now we express the boundaries of the region of instability of (7.15) as:

$$|B_0|^2=\frac{8\delta\omega_0^2}{27\Lambda^2}(1\pm1/2) \tag{7.23}$$

And rewrite (7.22) as:

$$|B_0|^2=\frac{\omega_0\Delta_0+2\delta\omega_0^2}{3\Lambda^2}(1\pm\Pi/2\Lambda) \tag{7.24}$$

Equations (7.23) and (7.24) define the necessary amplitude-detuning space for comb generation area and for the unstable amplitude solution, respectively. Several important distinctions between the optics and mechanics cases are readily visible. For one, in the optics case if $\Delta_0=0$ then comb generation does not take place because the slope of the comb generation area is identical to that of the Duffing unstable solution [6]. This is not the case in mechanics, since for $\Pi/\Lambda\ll1$ the slope of the comb generation space is quite different than that of the Duffing unstable regime.

A further important distinction between optical and mechanical frequency combs, is that for the latter the calculated Duffing nonlinearity always takes on positive values, i.e. $\Lambda^2>0$. This does not change the anomalous dispersion case, i.e. $\Delta_0<0$, being the more promising case to achieve frequency comb generation as can be seen in Fig. 7.3.

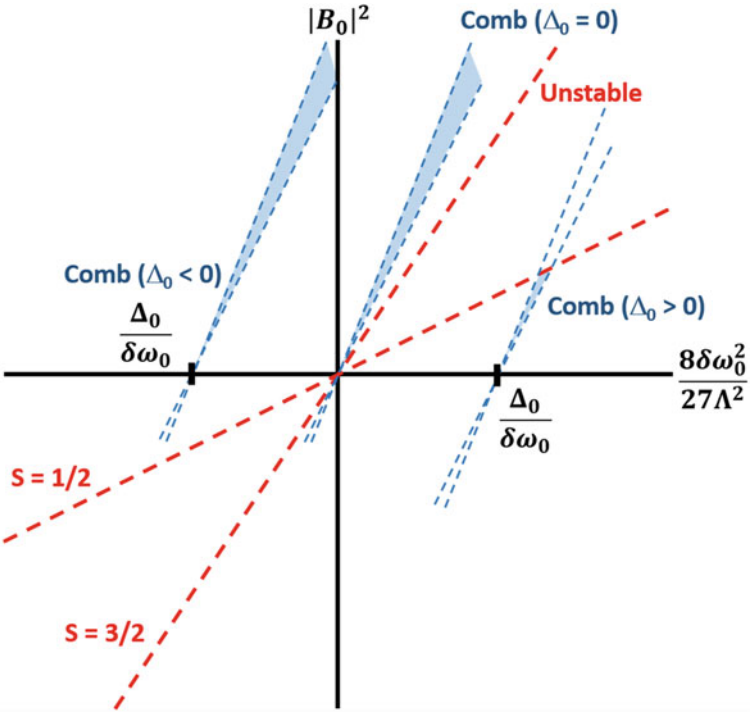

Fig. 7.3 Comb generation zone in amplitude-detuning parameter space shown in light blue shading, the border of the unstable amplitude solution area is shown with the dashed red lines. Unlike optics, comb generation can still take place if no dispersion exists, i.e. $\Delta_0 = 0$, but requires frequency detuning, i.e. $\delta\omega_0 \neq 0$. Comb generation also takes place if dispersion is introduced, i.e. $\Delta_0 \neq 0$, but the situation with $\Delta_0 < 0$ is more promising. Π/Λ is taken to be 0.2 to make the parameter space more visible, in reality Π/Λ is smaller than that

7.2.4 Effect of Internal Stresses on Comb Generation

When fabricating micro- and nanomechanical devices, a great deal of internal structural stresses are encountered that usually originate from the deposition techniques used to produce the fine layering of M/NEMS devices [40, 46]. Such internal stresses can change drastically the behavior of a MEMS device by shifting its resonance frequencies, and changing the mode shapes [31].

To account for such possibility we introduce an initial stress term in the dimensionless Euler-Bernoulli equation (7.3) that now reads:

$$\frac{\partial^4 y}{\partial x^4} + \gamma\frac{\partial y}{\partial t} + \frac{\partial^2 y}{\partial t^2} - \left(12\bar{N} + 6\int_0^1 \left(\frac{\partial y}{\partial x}\right)^2 dx\right)\frac{\partial^2 y}{\partial x^2} = F \tag{7.25}$$

where $\bar{N}$ is the normalized internal stress given as: $\bar{N} = \frac{NL^2}{EAh^2}$, where N is the absolute stress, note that for tensile stresses N is positive, and compressive stresses appear as negative N. As done previously from hereon we drop the bars for convenience.

Here again the normal modes can be obtained from the homogenous Euler-Bernoulli equation by solving:

$$\frac{d^4\psi(x)}{dx^4} - 12N\frac{d^2\psi(x)}{dx^2} = \omega^2\psi(x) \tag{7.26}$$

Whose mode shapes are expressed as [3, 62]:

$$\psi_n(x) = \cos(\lambda_n x) - \cosh(\mu_n x) + \frac{\cos(\lambda_n) - \cosh(\mu_n)}{-\sin(\lambda_n) + \frac{\lambda_n}{\mu_n}\sinh(\mu_n)}(\sin(\lambda_n x) - \sinh(\mu_n x)) \tag{7.27}$$

Where:

$$\begin{cases} \mu_n = \left[6N + \sqrt{37N^2 + \omega_n^2}\right]^{1/2} \\ \lambda_n = \left[-6N + \sqrt{37N^2 + \omega_n^2}\right]^{1/2} \\ \cos(\lambda_n)\cosh(\mu_n) - 0.5\left(\frac{\mu_n}{\lambda_n} - \frac{\lambda_n}{\mu_n}\right)\sinh(\mu_n)\sin(\lambda_n) - 1 = 0 \end{cases} \tag{7.28}$$

Whereas the modal analysis procedure itself is not altered significantly by the introduction of the initial tension term, the change to the modal shapes has a considerable impact on the cross-Kerr coefficients.

This impact can be conceptually understood by considering that beam structures under very high tensile stresses can be described as strings [64] where the fourth order spatial derivative is dropped, and for such second order differential equation the cross-Kerr terms are zero. Thus the more the structure is subjected to tensile stresses the more the mode shapes resembles pure sinusoids, and the smaller the cross-Kerr terms are. The impact of internal stress is demonstrated in Fig. 7.4 where the terms Λ_{33}, and Π_{35} are shown as a function of normalized tension.

Thus, internal stresses (tension in particular) suppress the formation of frequency combs, and inhomogeneous stresses most likely make it impossible.

7.3 Experimental Validation

The modal analysis performed so far has relied on the approximation that the frequency spacing between the modes is much smaller than the frequency of the modes themselves. If one desires such a condition to be true for simple Euler-Bernoulli clamped-clamped beams, then the range of validity is restricted to high mode numbers.

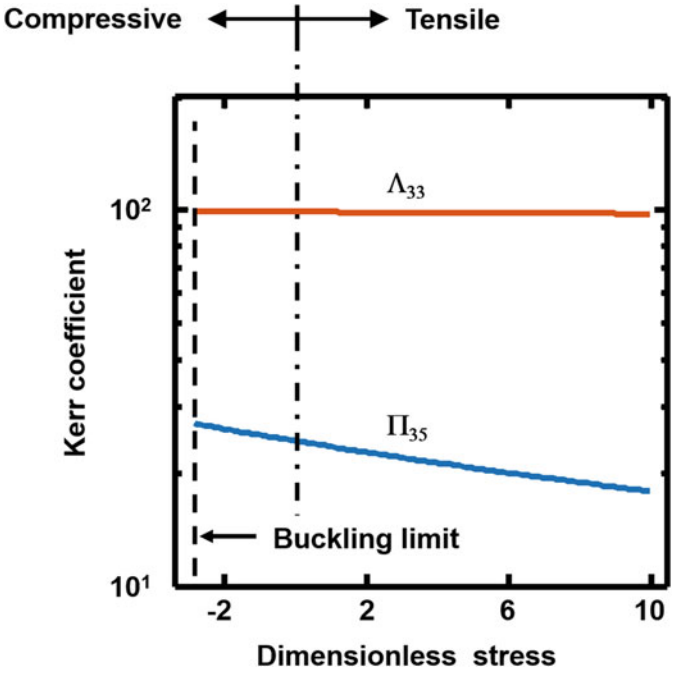

Fig. 7.4 Effect of internal stress on the coupling parameters Π_{35} and Λ_{33}, showing that the cross-Kerr term drops quickly as the normalized stress is increased. Note that for the small mode numbers used here (modes 3 and 5) the ratio $\Pi/\Lambda \sim 10^{-1}$ which is 2 orders of magnitude larger than for large mode numbers

Nevertheless, high mode numbers come with their own problems, most notably the $\Pi/\Lambda \sim 10^{-3}$ ratio calculated in Sect. 7.2.3 for mode numbers from 50 to 150, are particularly small, making the area for comb generation within parameter space miniscule and difficult to achieve experimentally. Furthermore, very large mode numbers are experimentally difficult to excite in an efficient manner.

This leads to a seemingly contradictory conclusion where to obtain a large Π/Λ ratio a low mode number is required whereas to maintain the approximation of $\Delta \ll \omega$ a high mode number is required.

A promising workaround consists in using mechanical Fabry-Perot like structures [5, 25, 26, 28, 39]. These structures are in fact rectangular suspended plates, as shown schematically in Fig. 7.5a, where one of the plate dimensions is much smaller than the other, say *length* $\gg$ *width*. Despite the plate equation being more cumbersome, the nonlinear vibrations of a plate can be reduced to an equation similar to (7.10) that governs the multimode nonlinear response of Euler-Bernoulli beams [8, 12, 53, 54, 57].

Unlike beams, plate geometry induces a cutoff frequency set by the smaller of the two geometrical dimensions. The larger the length-to-width ratio of the mechanical cavity is, the higher the cavity cutoff frequency and the closer the modes are to

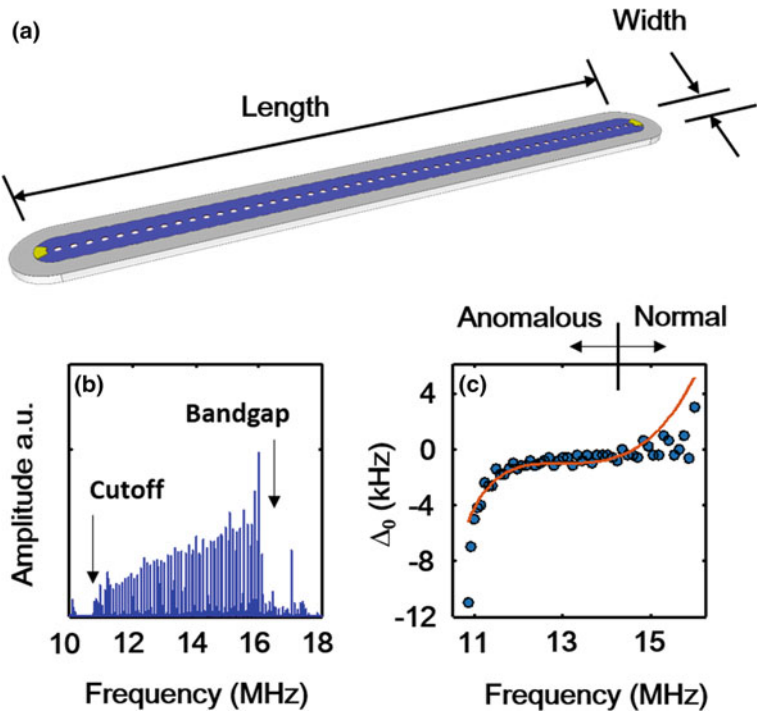

Fig. 7.5 Schematic representation of a mechanical Fabry-Perot cavity with *length* $\gg$ *width,* showing the suspended portion (in blue) and the periodically located etch holes (**a**). The measured frequency response of a mechanical cavity having width $= 20\ \mu$m, and length $= 1$ mm (**b**) clearly showing the cutoff and bandgap. From the resonance frequencies shown in (**b**) it is possible to extract the dispersion Δ_0 of the structure, which despite the scatter shows a negative value, corresponding to anomalous dispersion, after the cutoff and positive values, corresponding to normal dispersion, nearing the bandgap (**c**)

each other. This is shown in the experimentally measured frequency response of a piezoelectric AlGaAs/GaAs mechanical Fabry-Perot cavity with a width of 20 μm and a length of 1 mm, Fig. 7.5b. Thus for a Fabry-Perot type mechanical cavity it is possible to satisfy both the condition $\Delta \ll \omega$ and the condition of a small modal number simultaneously. In addition nonlinear response was demonstrated for such structures [27], in the form of non-degenerate FWM under the effect of dual tone drive.

Note that the microfabrication process necessitates to have periodically located etch holes in the structures. These are simply small circular openings that allow the chemical etching of the underlying material and thus the release and suspension of the plate structure. The presence of such periodic lattice of holes induces bandgaps in the frequency response of the cavity. The effects of the latter is to change the dispersion relation as the bandgap is approached, whereas the system exhibits anomalous

dispersion after the cutoff, i.e. $\Delta_0 < 0$, the sign of dispersion changes as we approach the bandgap. An effect that is visible in Fig. 7.5c for the experimentally obtained values of Δ_0.

7.4 Conclusions

In summary this work demonstrated that starting from a generic description of a beamlike mechanical MEMS structure, it is possible to derive through a modal analysis approach a governing equation that is qualitatively identical to that governing optical frequency combs. Thereafter the possibility of generating mechanical frequency combs was investigated in depth to determine the necessary experimental conditions. The analysis performed led to a seemingly contradictory set of conditions where on the one hand it required a large modal number for the approximations made to hold, while on the other hand a large modal number gives an impractically small area for comb generation.

A workaround was suggested to employ rectangular plate structures with a high width to length ratio, these structures preserve the dynamics to a large extent while alleviating the conditions on frequency separation. In addition the presence of a periodic lattice in the suspended membrane induces bandgaps that also provide means for dispersion engineering.

Despite these early encouraging results, their remain several open question regarding the scaling of nonlinear Kerr coefficients in a plate-like structure, and the experimental difficulties in exciting sufficiently large amplitudes for multimodal mechanical comb generation to take place.

Acknowledgements This work is partly supported by a MEXT Grant-in-Aid for Scientific Research on Innovative Areas “Science of hybrid quantum systems” (Grant No. JP15H05869 and JP15K21727).

References

1. N. Akhmediev, J.M. Dudley, D.R. Solli, S.K. Turitsyn, Recent progress in investigating optical rogue waves. J. Opt. **15**(6), 060201 (2013)
2. C. Bao, Y. Xuan, D.E. Leaird, S. Wabnitz, M. Qi, A.M. Weiner, Spatial mode-interaction induced single soliton generation in microresonators. Optica **4**(9), 1011–1015 (2017)
3. R.D. Blevins, R. Plunkett, Formulas for natural frequency and mode shape. J. Appl. Mech. **47**, 461 (1980)
4. L.S. Cao, D.X. Qi, R.W. Peng, M. Wang, P. Schmelcher, Phononic frequency combs through nonlinear resonances. Phys. Rev. Lett. **112**(7), 075505 (2014)
5. J. Cha, C. Daraio, Electrical tuning of elastic wave propagation in nanomechanical lattices at MHz frequencies. Nat. Nanotechnol. **13**(11), 1016 (2018)
6. Y.K. Chembo, N. Yu, Modal expansion approach to optical-frequency-comb generation with monolithic whispering-gallery-mode resonators. Phys. Rev. A **82**(3), 033801 (2010)

7. Y.K. Chembo, C.R. Menyuk, Spatiotemporal Lugiato-Lefever formalism for Kerr-comb generation in whispering-gallery-mode resonators. Phys. Rev. A **87**(5), 053852 (2013)
8. Chia, C.Y., 1980. Nonlinear analysis of plates. McGraw-Hill International Book Company
9. N.A. Cleland, *Foundations of Nanomechanics: From Solid-State Theory to Device Applications* (Springer, New York, 2003), pp. 312–319
10. A. Coillet, Y.K. Chembo, Routes to spatiotemporal chaos in Kerr optical frequency combs. Chaos: Interdiscip. J. Nonlinear Sci. **24**(1), 013113 (2014)
11. A. Coillet, J. Dudley, G. Genty, L. Larger, Y.K. Chembo, Optical rogue waves in whispering-gallery-mode resonators. Phys. Rev. A **89**(1), 013835 (2014)
12. J. Crawford, S. Atluri, Non-linear vibrations of a flat plate with initial stresses. J. Sound Vib. **43**(1), 117–129 (1975)
13. S.T. Cundiff, J. Ye, J.L. Hall, Optical frequency synthesis based on mode-locked lasers. Rev. Sci. Instrum. **72**(10), 3749–3771 (2001)
14. D.A. Czaplewski, C. Chen, D. Lopez, O. Shoshani, A.M. Eriksson, S. Strachan, S.W. Shaw, Bifurcation generated mechanical frequency comb. Phys. Rev. Lett. **121**(24), 244302 (2018)
15. S.A. Diddams, D.J. Jones, J. Ye, S.T. Cundiff, J.L. Hall, J.K. Ranka, R.S. Windeler, R. Holzwarth, T. Udem, T.W. Hänsch, Direct link between microwave and optical frequencies with a 300 THz femtosecond laser comb. Phys. Rev. Lett. **84**(22), 5102 (2000)
16. P. Del'Haye, A. Schliesser, O. Arcizet, T. Wilken, R. Holzwarth, T.J. Kippenberg, Optical frequency comb generation from a monolithic microresonator. Nature **450**(7173), 1214 (2007)
17. J.N. Eckstein, A.I. Ferguson, T.W. Hänsch, High-resolution two-photon spectroscopy with picosecond light pulses. Phys. Rev. Lett. **40**(13), 847 (1978)
18. A. Erbe, H. Krömmer, A. Kraus, R.H. Blick, G. Corso, K. Richter, Mechanical mixing in nonlinear nanomechanical resonators. Appl. Phys. Lett. **77**(19), 3102–3104 (2000)
19. A. Ganesan, C. Do, A. Seshia, Phononic frequency comb via intrinsic three-wave mixing. Phys. Rev. Lett. **118**(3), 033903 (2017)
20. A. Ganesan, C. Do, A. Seshia, Phononic frequency comb via three-mode parametric resonance. Appl. Phys. Lett. **112**(2), 021906 (2018)
21. C. Godey, I.V. Balakireva, A. Coillet, Y.K. Chembo, Stability analysis of the spatiotemporal Lugiato-Lefever model for Kerr optical frequency combs in the anomalous and normal dispersion regimes. Phys. Rev. A **89**(6), 063814 (2014)
22. P. Grelu, N. Akhmediev, Dissipative solitons for mode-locked lasers. Nat. Photonics **6**(2), 84 (2012)
23. D.S. Greywall, B. Yurke, P.A. Busch, A.N. Pargellis, R.L. Willett, Evading amplifier noise in nonlinear oscillators. Phys. Rev. Lett. **72**(19), 2992 (1994)
24. J.L. Hall, Nobel lecture: defining and measuring optical frequencies. Rev. Mod. Phys. **78**(4), 1279 (2006)
25. D. Hatanaka, I. Mahboob, K. Onomitsu, H. Yamaguchi, Phonon waveguides for electromechanical circuits. Nat. Nanotechnol. **9**(7), 520 (2014)
26. D. Hatanaka, A. Dodel, I. Mahboob, K. Onomitsu, H. Yamaguchi, Phonon propagation dynamics in band-engineered one-dimensional phononic crystal waveguides. New J. Phys. **17**(11), 113032 (2015)
27. D. Hatanaka, T. Darras, I. Mahboob, K. Onomitsu, H. Yamaguchi, Broadband reconfigurable logic gates in phonon waveguides. Sci. Rep. **7**(1), 12745 (2017)
28. D. Hatanaka, A. Bachtold, H. Yamaguchi, Electrostatically induced phononic crystal. Phys. Rev. Appl. **11**(2), 024024 (2019)
29. H. Haus, Parameter ranges for CW passive mode locking. IEEE J. Quantum Electron. **12**(3), 169–176 (1976)
30. T. Herr, V. Brasch, J.D. Jost, C.Y. Wang, N.M. Kondratiev, M.L. Gorodetsky, T.J. Kippenberg, Temporal solitons in optical microresonators. Nat. Photonics **8**(2), 145 (2014)
31. S. Houri, U. Bhaskar, B. Gallacher, L. Francis, T. Pardoen, J.P. Raskin, Dynamic analysis of multi-beam MEMS structures for the extraction of the stress-strain response of thin films. Exp. Mech. **53**(3), 441–453 (2013)

32. S. Houri, S.J. Cartamil-Bueno, M. Poot, P.G. Steeneken, H.S.J. van der Zant, W.J. Venstra, Direct and parametric synchronization of a graphene self-oscillator. Appl. Phys. Lett. **110**(7), 073103 (2017)
33. S. Houri, R. Ohta, M. Asano, Y.M. Blanter, H. Yamaguchi, Pulse-width modulated oscillations in a nonlinear resonator under two-tone driving as a means for MEMS sensor readout. Jpn. J. Appl. Phys., **58**(SB), SBBI05 (2019)
34. S.Houri, D. Hatanaka, M. Asano, R. Ohta, H. Yamaguchi, Limit cycles and bifurcations in a nonlinear MEMS resonator with a 1: 3 internal resonance. Appl. Phys. Lett., **114**(10), 103103 (2019)
35. N. Jaber, A. Ramini, M.I. Younis, Multifrequency excitation of a clamped–clamped microbeam: analytical and experimental investigation. Microsystems & Nanoeng. **2**, 16002 (2016)
36. R.B. Karabalin, M.C. Cross, M.L. Roukes, Nonlinear dynamics and chaos in two coupled nanomechanical resonators. Phys. Rev. B **79**(16), 165309 (2009)
37. T.J. Kippenberg, S.M. Spillane, K.J. Vahala, Kerr-nonlinearity optical parametric oscillation in an ultrahigh-Q toroid microcavity. Phys. Rev. Lett. **93**(8), 083904 (2004)
38. T.J. Kippenberg, R. Holzwarth, S.A. Diddams, Microresonator-based optical frequency combs. Science **332**(6029), 555–559 (2011)
39. M. Kurosu, D. Hatanaka, K. Onomitsu, H. Yamaguchi, On-chip temporal focusing of elastic waves in a phononic crystal waveguide. Nat. Commun. **9**(1), 1331 (2018)
40. J. Laconte, D. Flandre, J.P. Raskin, *Micromachined Thin-Film Sensors for SOI-CMOS Co-integration* (Springer Science & Business Media, 2006)
41. J.S. Levy, A. Gondarenko, M.A. Foster, A.C. Turner-Foster, A.L. Gaeta, M. Lipson, CMOS-compatible multiple-wavelength oscillator for on-chip optical interconnects. Nat. Photonics **4**(1), 37 (2010)
42. R. Lifshitz, M.C. Cross, Nonlinear dynamics of nanomechanical and micromechanical resonators. Rev. Nonlinear Dyn. Complex. **1**, 1–52 (2008)
43. L.A. Lugiato, R. Lefever, Spatial dissipative structures in passive optical systems. Phys. Rev. Lett. **58**(21), 2209 (1987)
44. K.J. Lulla, R.B. Cousins, A. Venkatesan, M.J. Patton, A.D. Armour, C.J. Mellor, J.R. Owers-Bradley, Nonlinear modal coupling in a high-stress doubly-clamped nanomechanical resonator. New J. Phys. **14**(11), 113040 (2012)
45. L.-S. Ma, Z. Bi, A. Bartels, L. Robertsson, M. Zucco, R.S. Windeler, G. Wilpers, C. Oates, L. Hollberg, S.A. Diddams, Optical frequency synthesis and comparison with uncertainty at the 10–19 level. Science **303**(5665), 1843–1845 (2004)
46. M.J. Madou, Manufacturing Techniques for Microfabrication and Nanotechnology, vol. 2 (CRC press, 2011)
47. I. Mahboob, Q. Wilmart, K. Nishiguchi, A. Fujiwara, H. Yamaguchi, Tuneable electromechanical comb generation. Appl. Phys. Lett. **100**(11), 113109 (2012)
48. I. Mahboob, R. Dupuy, K. Nishiguchi, A. Fujiwara, H. Yamaguchi, Hopf and period-doubling bifurcations in an electromechanical resonator. Appl. Phys. Lett. **109**(7), 073101 (2016)
49. P. Marin-Palomo, J.N. Kemal, M. Karpov, A. Kordts, J. Pfeifle, M.H. Pfeiffer, P. Trocha et al., Microresonator-based solitons for massively parallel coherent optical communications. Nature **546**(7657), 274 (2017)
50. M.H. Matheny, L.G. Villanueva, R.B. Karabalin, J.E. Sader, M.L. Roukes, Nonlinear mode-coupling in nanomechanical systems. Nano Lett., **13**(4), 1622–1626 (2013)
51. A.B. Matsko, A.A. Savchenkov, D. Strekalov, V.S. Ilchenko, L. Maleki, Optical hyperparametric oscillations in a whispering-gallery-mode resonator: threshold and phase diffusion. Phys. Rev. A **71**(3), 033804 (2005)
52. A.B. Matsko, W. Liang, A.A. Savchenkov, L. Maleki, Chaotic dynamics of frequency combs generated with continuously pumped nonlinear microresonators. Opt. Lett. **38**(4), 525–527 (2013)
53. A.H. Nayfeh, D.T. Mook, *Nonlinear Oscillations* (Willey, New York, 1979)
54. A.H. Nayfeh, R.A. Ibrahim, Nonlinear interactions: analytical, computational, and experimental methods. Appl. Mech. Rev., **54**, B60 (2001)

55. E. Obrzud, S. Lecomte, T. Herr, Temporal solitons in microresonators driven by optical pulses. Nat. Photonics **11**(9), 600 (2017)
56. K. Panajotov, M.G. Clerc, M. Tlidi, Spatiotemporal chaos and two-dimensional dissipative rogue waves in Lugiato-Lefever model. Eur. Phys. J. D **71**(7), 176 (2017)
57. M. Sathyamoorthy, *Nonlinear Analysis of Structures* (1997) (CRC Press 2017)
58. M.J. Seitner, M. Abdi, A. Ridolfo, M.J. Hartmann, E.M. Weig, Parametric oscillation, frequency mixing, and injection locking of strongly coupled nanomechanical resonator modes. Phys. Rev. Lett. **118**(25), 254301 (2017)
59. D.E. Spence, P.N. Kean, W. Sibbett, 60-fsec pulse generation from a self-mode-locked Ti: sapphire laser. Opt. Lett. **16**(1), 42–44 (1991)
60. D.T. Spencer, T. Drake, T.C. Briles, J. Stone, L.C. Sinclair, C. Fredrick, Q. Li, et al., An optical-frequency synthesizer using integrated photonics. Nature **557**(7703), 81–85 (2018)
61. B. Stern, X. Ji, Y. Okawachi, A.L. Gaeta, M. Lipson, Battery-operated integrated frequency comb generator. Nature **562**(7727), 401 (2018)
62. H.A. Tilmans, M. Elwenspoek, J.H. Fluitman, Micro resonant force gauges. Sens. Actuators, A **30**(1–2), 35–53 (1992)
63. T. Udem, J. Reichert, R. Holzwarth, T.W. Hänsch, Absolute optical frequency measurement of the cesium D 1 line with a mode-locked laser. Phys. Rev. Lett. **82**(18), 3568 (1999)
64. S.S. Verbridge, J.M. Parpia, R.B. Reichenbach, L.M. Bellan, H.G. Craighead, High quality factor resonance at room temperature with nanostrings under high tensile stress. J. Appl. Phys. **99**(12), 124304 (2006)
65. H.J.R. Westra, M. Poot, H.S.J. Van Der Zant, W.J. Venstra, Nonlinear modal interactions in clamped-clamped mechanical resonators. Phys. Rev. Lett. **105**(11), 117205 (2010)
66. H. Yamaguchi, I. Mahboob, Parametric mode mixing in asymmetric doubly clamped beam resonators. New J. Phys. **15**(1), 015023 (2013)

Chapter 8
Characterization of Rolling Element Bearing Data Using the Gottwald and Melbourne's 0-1 Test and the Hugichi Fractal Dimension

C. A. Kitio Kwuimy, T. Haj Mohamad and C. Nataraj

Abstract The paper considers the characterization of the data extracted from an experimental model of rotor supported on rolling elements. A description of the method is provided as well as an illustration using a standard dynamic map. The 0-1 test for chaos and the Higuchi dimension are shown to be effective tool in the identification of chaotic behavior of the system bearing with and without faults.

8.1 Introduction

Time series analysis is generally referred to as the transformation of observed dynamic data into insight for making better decisions [1]. The data extracted from the behavior of dynamic systems can be non-periodic and eventually stochastic. For specific applications these data need to be characterized and analyzed in order to extract information about the system. Several methods have been used in various branches of science including engineering, epidemiology, biology and finance [2–7]. Traditional methods for time series in these domains include statistical analysis and dynamic method which include methods in the time domain, methods in the state space domain and methods in the frequency domain.

The most used frequency analysis method is the Fast Fourier Transform (FFT), which is in fact a linear method based on the analysis of the spectrum of the frequencies contained in the response of the system. For instance, a periodic system will be completely described by its FFT while for a non-periodic or stochastic system, the

C. A. K. Kwuimy (✉)
Department of Engineering Education, College of Engineering and Applied Science, University of Cincinnati, Cincinnati, OH 45221, USA
e-mail: cedrick.kwuimy@uc.edu

T. . Haj Mohamad · C. Nataraj
Villanova Center for Analytics of Dynamic Systems (VCADS), Villanova University, Villanova, PA 19085, USA
e-mail: thajmoha@villanova.edu

C. Nataraj
e-mail: c.nataraj@villanova.edu

M. Belhaq (ed.), *Topics in Nonlinear Mechanics and Physics*,
Springer Proceedings in Physics 228, https://doi.org/10.1007/978-981-13-9463-8_8

broad-banded FFT will give limited information [5]. State space methods include all methods developed in the state space of the system. These methods involve all state variables of the system dynamics. The key point here is the necessity of the state space, which in general (when one cannot obtain the measurement of the dynamics variables of the system) needs to be reconstructed from one of the available measurement. From a mathematical model, the state variable can be clearly identified (by writing the flow) [3, 5–9]. State space methods include methods developed using the state variables of the system. This includes the Lyapunov exponent, traditional fractal dimensions such as the correlation dimension, and the method of recurrence analysis. Although these methods have been widely used [2, 3, 5], the pitfall here is that they require excessive computing in terms of reconstruction of the state space and some of these methods (Lyapunov exponent for example) are very sensitive to noise and require a certain level of advanced expertise from the user [3, 5, 10–12]. The time domain methods which consist of a simple plot of the data as function of time. Such plot provides preliminaries information about the nature (periodic, stochastic, chaotic) of the data. Additionally, statistical measurement and fractal measurement of the time response have been shown to provide reliable and efficient information about the nonlinear nature of the system.

The latter is considered in this paper. We consider a machine fault simulator and collect data for three conditions of the system (healthy, slightly defective and strongly defective). The objective is to provide additional insight in the system response. In fact, in previous contribution, we used statistical methods and methods of the state space, namely the method of recurrence analysis for similar investigations [13–15]. Extension was made to the detection and classification of faults. This paper is focused on identification of chaotic response. The 0-1 test for chaos and the Higuchi's fractal dimension are used to analyze the time series. The methods have been previously used in various branches of science, including finance, engineering and biology [10–12, 15–20].

The paper is organized as follows. In Sect. 8.2, the description of the methods is summarized and illustrations are given using the logistic map. In Sect. 8.3, data from healthy and defective experimental systems are analyzed, periodic and chaotic responses are considered. The last section is the conclusion.

8.2 Methods and Illustrations

8.2.1 The 0-1 Test for Chaos

The 0-1 test for chaos was developed by Gottwald and Melbourne [10–12] to distinguish between regular and chaotic dynamics in deterministic dynamical systems. Rather than requiring phase space reconstruction which is necessary to apply standard chaotic indicators such as the Lyapunov exponent, the test works directly with the

time series and does not involve any preprocessing of the data. Since its development, the test has found applications in a wide range of fields [10–12, 21–23].

The method is based on the estimation of a statistical parameter K which is used to conclude on the periodic ($K \to 0$) and chaotic ($K \to 1$) nature of the a time signal. To compute K from a time series

$$X = x(1), x(2), \ldots x(N) \tag{8.1}$$

where N is the total number of data collected, the time series is projected into a plane (p, q) defined as

$$\begin{aligned} p(n, c) &= \sum_{j=1}^{n} x(j) \cos jc \\ q(n, c) &= \sum_{j=1}^{n} x(j) \sin jc \end{aligned} \tag{8.2}$$

where $n = 1, 2, .., N$ and $c \in (0, 2\pi)$ is an arbitrary constant. The diffusive and non-diffusive behavior of $p(n, c)$ and $q(n, c)$ are used to estimate K. For this end, the adjusted mean-square displacement is estimated. It is given by [10–12]

$$D(n, c) = M(n, c) - \Phi^2 \frac{1 - \cos nc}{1 - \cos c} \tag{8.3}$$

where

$$M(n, c) = \frac{1}{N} \sum_{j=1}^{N} \left[\Delta_1^2 + \Delta_2^2\right] \tag{8.4}$$

$$\Delta_1 = p(n + j, c) - p(j, c), \;\; \Delta_2 = q(n + j, c) - q(j, c) \tag{8.5}$$

and

$$\Phi = \frac{\lim}{N \to \infty} \frac{1}{N} \sum_{j=1}^{N} \phi(j) \tag{8.6}$$

To ensure the limit $N \to \infty$, in general the limit $n \leq N_0$ with $N_0 \ll N$ [10–12] ($N_0 = N/20$ in this paper) is considered. The second term in (8.3) is added to minimize eventual fluctuation in $M(n, c)$. For each values of c, the parameter K_c is estimated as

$$K_c = \frac{\text{cov}\,(\zeta, \delta)}{\sqrt{\text{var}(\zeta)\text{var}(\delta)}} \tag{8.7}$$

where $\zeta = 1, 2, .., N_0$ and $\delta = D(c, 1), D(c, 2), ..D(c, N_0)$. The final value of K is estimated as the median of all $K_c = f(c)$. The use of the median instead of the

average value is justified by the fact that, it avoid large drift caused by possible resonance in a specific value of c. See [10–12] for illustrations.

8.2.1.1 Higuchi Fractal Dimension

The Higuchi's fractal dimension is a powerful fractal measurement of the structure of data [16–18]. The specificity here is that, unless other fractal dimensions which are estimated in the (reconstructed) state space, the Huguichi's fractal dimension can be computed from a single time series.

From the time series in (8.1), one can extract different short time series as

$$X_k^m = x(m), x(m+k), ...x\left(m + \left\lceil \frac{n-m}{k} \right\rceil k\right) \tag{8.8}$$

where $\lceil . \rceil$ is the ceiling function. The length of the curve associated to each new time series X_k^m is then computed as the sum of algebraic distances between consecutive elements of the new time series, that is

$$L_m(k) = \sum_{i=1}^{\left\lceil \frac{n-m}{k} \right\rceil} (x(m+ik) - x(m-(i-1)k)) \tag{8.9}$$

The dimension is computed using the following scaling relation

$$< L(k) > \propto k^{-D} \tag{8.10}$$

where $< L(k) >$ is the average lengths of the segment used to measure the total length of the time series at scale k, and $L(k)$ is the normalized length defined as

$$L_m = \frac{N-1}{\left\lceil \frac{n-m}{k} \right\rceil k} \sum_{i=1}^{\left\lceil \frac{n-m}{k} \right\rceil} (x(m+ik) - x(m-(i-1)k)) \tag{8.11}$$

The Higuchi fractal dimension is then estimated as the slope of the least square linear fit of $\langle \mathrm{Ln}\,(L(k)) \rangle = \mathrm{Ln}\,(1/k)$.

8.2.2 *Illustrations: The Logistic Map*

We consider the well-known logistic map $x_{n+1} = cx_n(1-x_n), (c > 0)$ as illustration of the affectivity of the 0-1 test and the Higuchi fractal dimension as tool to detect chaos in dynamic systems. The logistic map shows a periodic behavior for $c = 3.55$ and a chaotic behavior for $c = 3.99$ as illustrated in Fig. 8.1. The signals x_n extracted

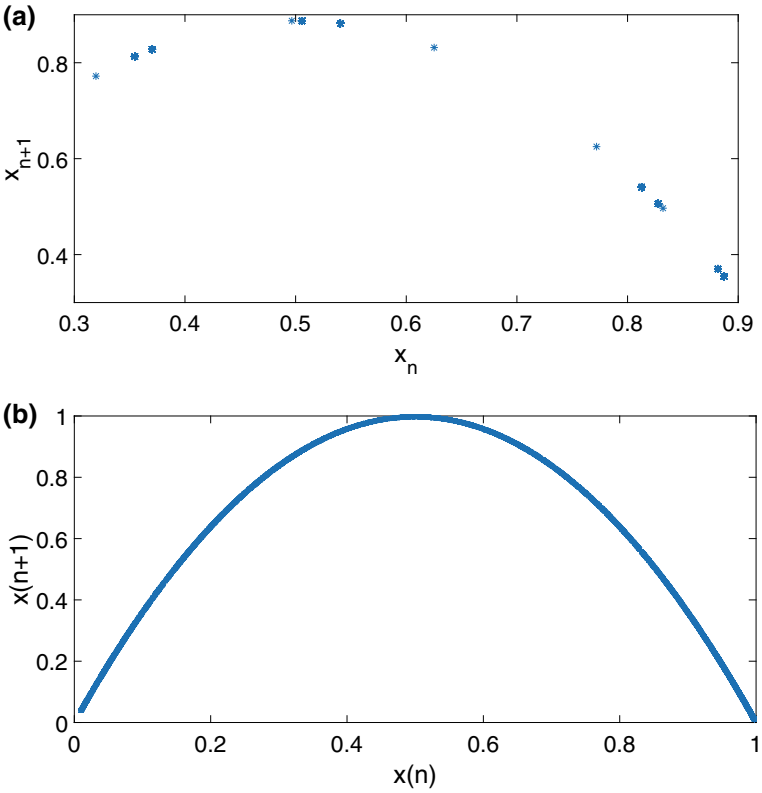

Fig. 8.1 State diagram of the logistic map. **a** Periodic response $c = 3.55$. **b** Chaotic response $c = 3.99$

from the logistic map are analyzed using the 0-1 test and the Higuchi fractal dimension. The Higuchi fractal dimension can reveal interesting information about the periodic and chaotic nature of the system. Looking at Fig. 8.2a, one notices the presence of down peaks. The appearance of these peaks are directly connected to the periodicity of the response. In fact, the appearance of peaks is connected to the definition of the subsets X_c^k. For a periodic signal of the form $y(i) = \sum_{r=1}^{r_{max}} \sin(r\omega_r \Delta t)$ where Δt is the sampling time and $\omega_r = 2\pi/T$ the frequency, a peak (resonance) in the value of L_m will be obtained for specific values of k since $x(m + ik) - x(m - (i - 1)k)$ are small (see 8.9). The Higuchi fractal dimension is for this reason used to detect periodic components in time series [16–18].

For this example, one observes several families of peaks. The appearance of multiple peaks is due to the fact that the system has a multiple periodic response. In order to estimate the dimension H from the graph $\langle \mathrm{Ln}\,(L(k))\rangle = \mathrm{Ln}\,(1/k)$, we interpolate the different sets of lower peaks (or upper peaks) and find the slope of the corresponding lines (which are parallel). The slope is obtained as $H = 2.03$. It

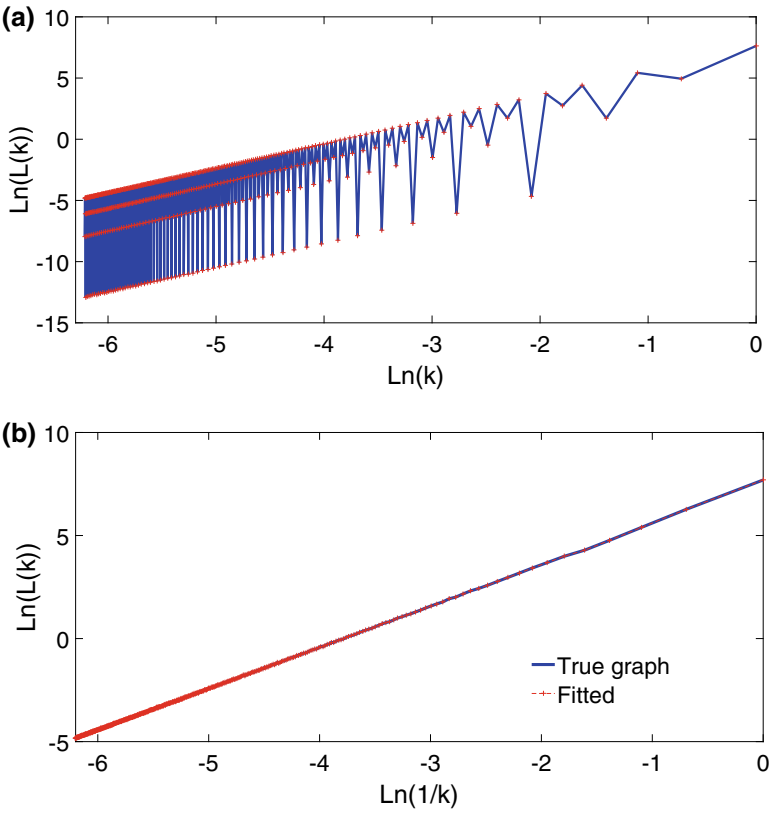

Fig. 8.2 Estimation of the Higuchi fractal dimension. **a** $c = 3.55$, $H = 2.03$. **b** $c = 3.99$, $H = 2.002$

is interesting to notice that the number of peaks can implies information about the number of period in the response. By connecting the peaks of each family, one will form a set of parallel straight lines which are parallel to the least square estimate of the data. Thus the slope can be computed from either line. Repeating the same observations for the Fig. 8.2b, one will find that chaotic response will correspond to $r_{max} \to \infty$. That is an infinite number of "resonance" leading to a "straight" line. The slope (Higuchi dimension) is then obtained as $H = 2.002$. Thus, on a graphical point of view, the Higuchi dimension can be used to discriminate between periodic and chaotic responses. However, as reported in literature for experimental data, the Higuchi fractal dimension can be affected by noise. Thus to complement the analysis, we also use the 0-1 test (known to be more robust) to discriminate between the dynamic responses of the system.

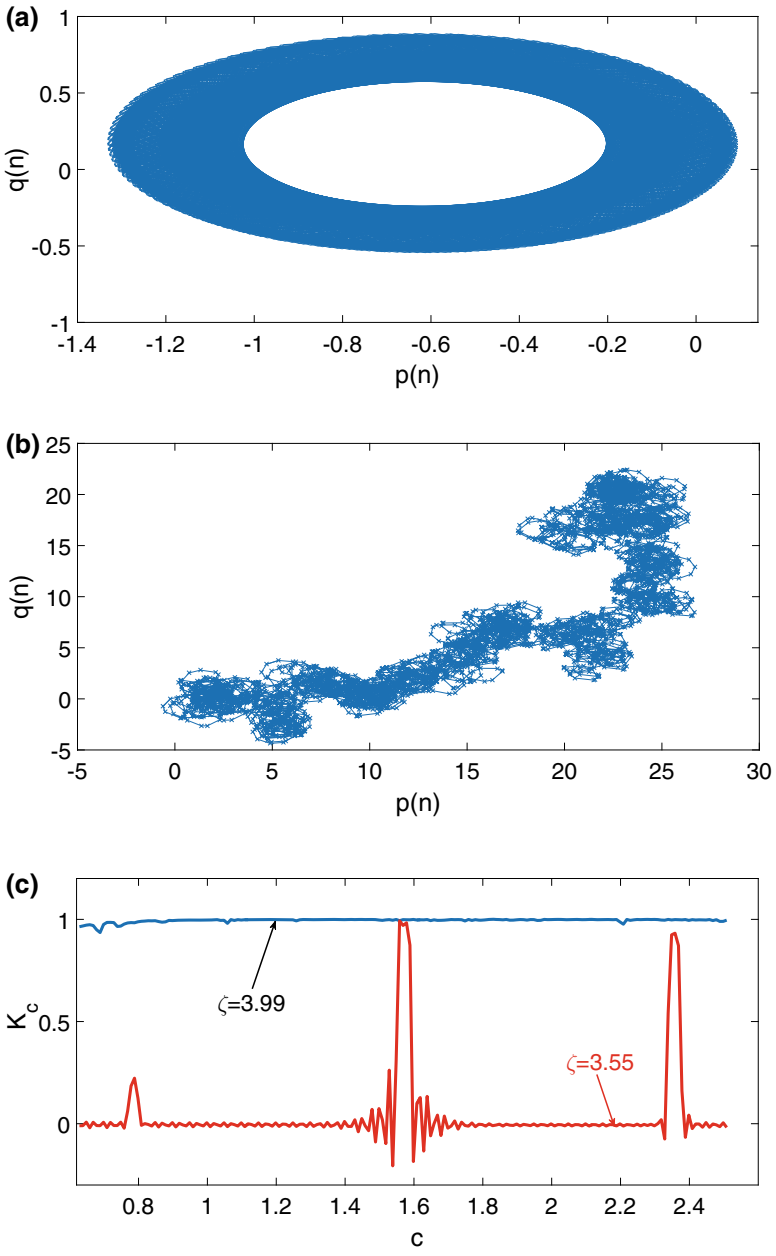

Fig. 8.3 0-1 test for the logistic equation. **a** State response in the $(p(n, \pi/5)$ and $(q(n, \pi/5)$ space for $c = 3.55$. **b** State response in the $(p(n, \pi/5)$ and $(q(n, \pi/5)$ space for $c = 3.99$. **c** Estimation of K for the periodic and chaotic responses

To compute the 0-1 test parameter k, 100 values of c are selected in the interval $[0, 2\pi]$. The auxiliary parameters $p(c, n)$ and $q(c, n)$ are then computed for each value of c. Sample of such parameters are shown in Fig. 8.3a–b for $c = \pi/5$, and the graph of $K_c = f(c)$ is shown in Fig. 8.3c for both chaotic and periodic responses of the logistic map. The plots in Fig. 8.3a–b are typical for periodic and chaotic responses [10–12]. In Fig. 8.3, for the chaotic response, the median value is about $K_c = 0.96$ and for periodic response it is about $K_c = 0.01$. However, one observes resonance peaks for some values of c. The presence of these resonances can be explained as in the previous section for the Higuchi dimension.

8.3 Detection of Chaotic Behavior in Bearings

8.3.1 The Experimental Setup and Data Collection

The machine fault simulator used as experimental setup is shown in Fig. 8.4. It consists of a motor with a closed loop speed control connected to a shaft supported on rolling element bearings. The span of the shaft is fixed but shafts of various diameters can be used. The bearings are placed in the bearing casing and can be easily replaced. The system can be loaded using a mass and balancing disks. A load mass of 5 kg is used in this research. The balancing disk has two rows of screw holes drilled near the edge into which different masses can be inserted to balance the shaft. The whole system is supported on a solid base with dampers so that ambient vibrations affecting the system are minimized. To provide more support, the setup is placed on heavy cement blocks. The speed of the system is set using a computer attached to the motor controller.

Figure 8.5 shows the bearings with outer race defects. The value of the parameters of the various components used in the experimental setup are listed in Table 8.1. Data are captured with three different bearings. Two of these bearings have an outer race defect with different defect severity and one bearing does not have any defect. The signals from the experimental setup are collected with a proximity probe placed at the selected bearing.

8.3.2 Data Analysis and Evidence of Chaos

8.3.2.1 Periodic Response

By adjusting the rotor speed, the dynamics of the system is affected. As illustration, the signal response of the Fig. 8.6a is obtained for a speed 40 rpm for the healthy system. The horizontal axis represents the time while the vertical axis represent the measured vibration of the system. The response of the system plotted in the space

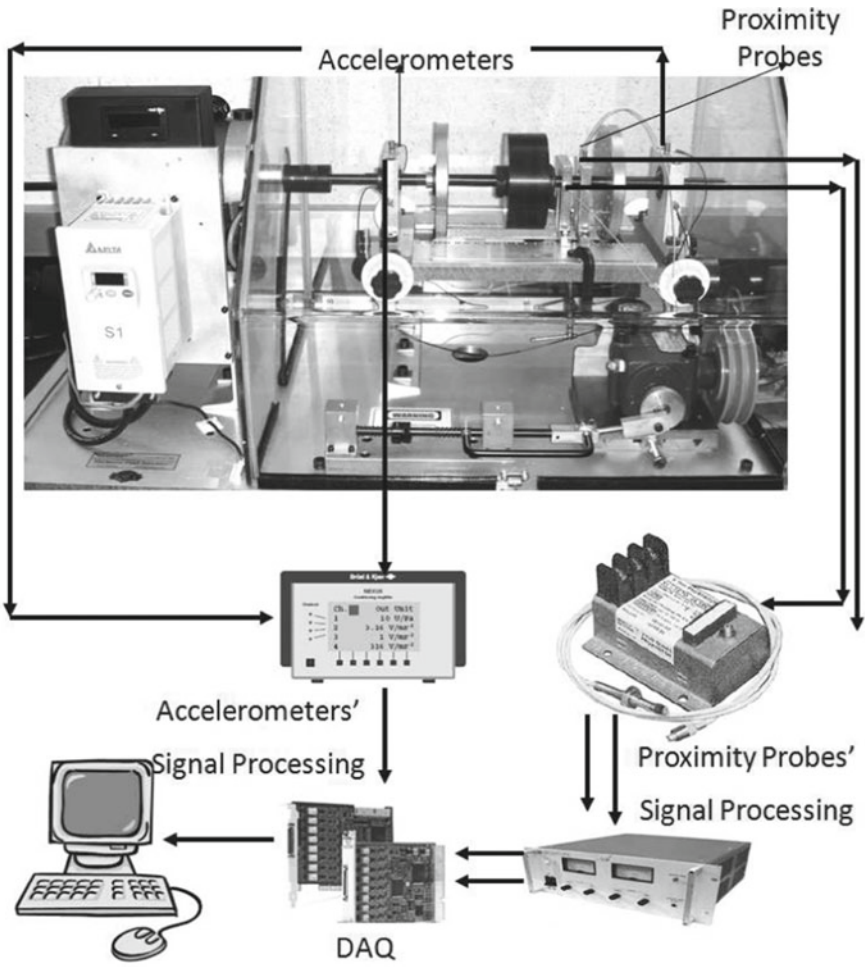

Fig. 8.4 Experimental setup

$(p(n, c)q(n, c))$ (with $c = 1.2$) as shown in Fig. 8.6b. The obtained structure is typical for periodic behavior. For $c \in (1, 5)$, the values of $K(c)$ are computed as described in the previous section and plotted in Fig. 8.6c and the estimated median is deduced as $K = 0.0034$. Thus, based on the 0-1 test for chaos, the system has a periodic response. Repeating the procedure for the estimation of the Higuchi dimension, one obtains the plot of Fig. 8.6d, showing a single down peak, signature of single periodicity in the system response. The fractal dimension is obtained as $H = 1.96$. The dashed line was obtained using standard linear curve fitting and the continued line was used to connect the down peaks.

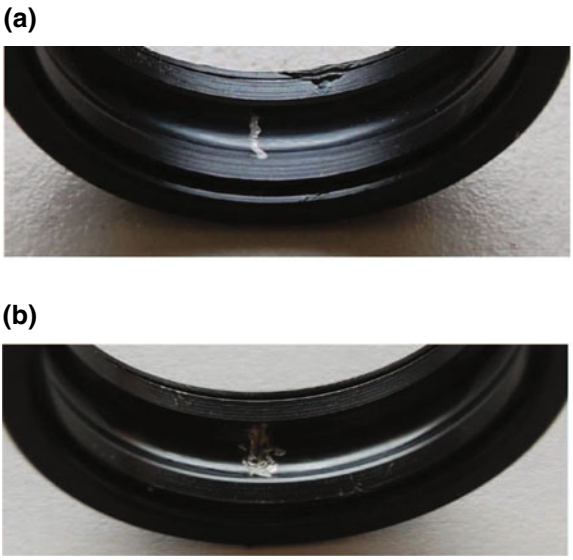

Fig. 8.5 Outer race defects. **a** Small defect. **b** Large defect

Table 8.1 Parameters in the experimental setup

Parameters	Values	Parameters	Values
Mass (shaft)	0.831 kg	Mass (disk)	0.66 kg
Diameter (shaft)	0.016 m	Diameter (disk)	0.152 m
Length (shaft)	0.35 m	Length (disk)	0.016 m
I (shaft)	3.1179×10^{-9} m^4	I_D (disk)	0.0019 kgm^2
I_p (shaft)	1.5588×10^{-9} m^4	I_p (disk)	1.3101×10^{-5} m^4
E (shaft)	200 N/m^2	Diameter (rotation element)	0.079 m
k (shaft)	6.616×10^5 N/m	Mean diameter	0.335 m
Load mass	5 kg	Contact angle	0°
n (bearing constant)	1.5	Elasticity constant	1.8315×10^9 N/m
Inner race osculation	0.52	Outer race osculation	0.52

8.3.2.2 Chaotic Response

In this section, data are collected at speed 30 rpm for the healthy and defective conditions. A sample of the data captured from the experimental setup is shown in Fig. 8.7. In this figure, the first subplot is the vibration signal from a defect-free system, the second subplot is the signal from a system with the smaller outer race

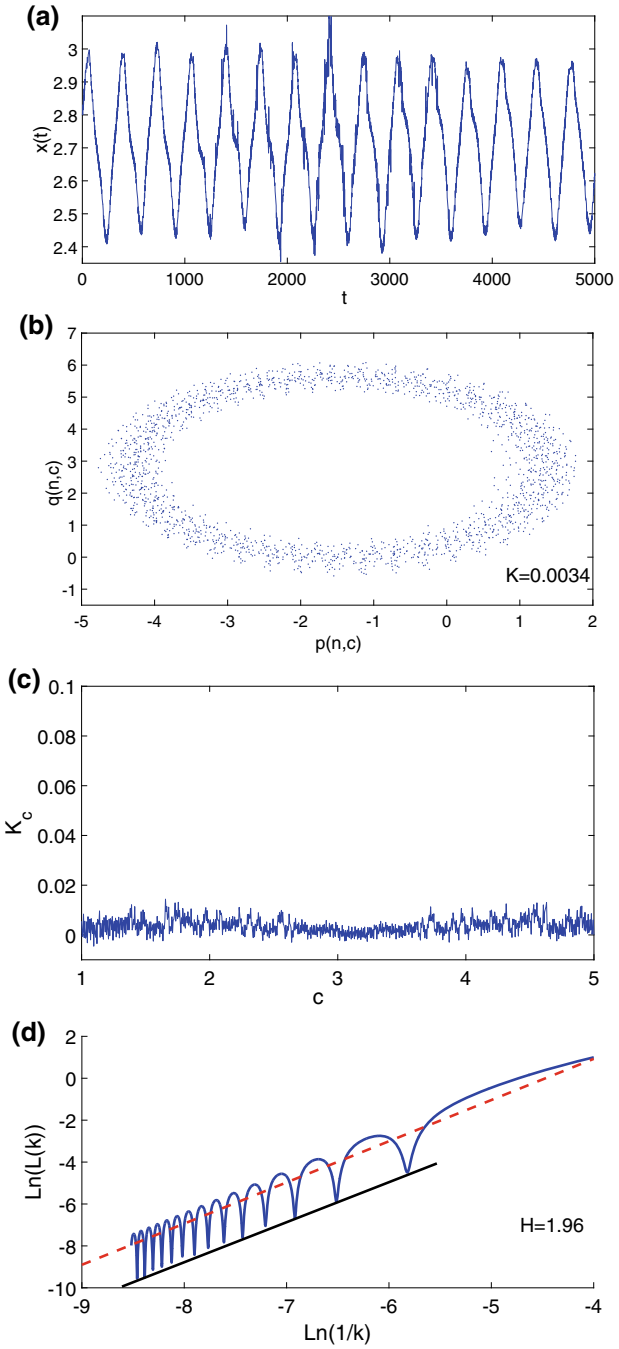

Fig. 8.6 Characterization of a periodic response for healthy system. **a** Time response. **b** Response in the $(p(n, 1.2)$ and $(q(n, 1.2)$ space. **c** Estimation of the 0-1 test. **d** Estimation of the Higuchi fractal dimension

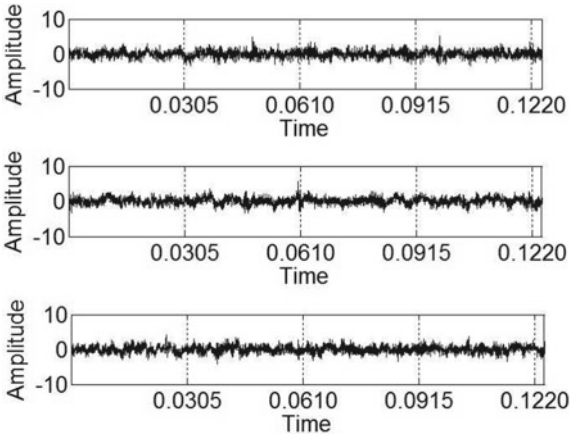

Fig. 8.7 Sample response of the system at 40 rpm.: The first subplot corresponds to signal from a defect-free system, the second subplot correspond to signal from a system with the smaller outer race defect and the third subplot is the signal from a system with the larger outer race defect

defect and the third subplot is the signal from a system with the larger outer race defect. Bearings with outer race defects have impulses excited by the rolling element entering the defect.

The $(p(n,c), q(n,c))$ projection of the data are shown in Fig. 8.7 respectively for the healthy system and the system with small and large defects. The diffusive structure of the plot is clearly a signature of a non-periodic dynamics. For different values of c, the global behavior of Fig. 8.8 is obtained and for this specific set of parameters, the corresponding median is quite identical ($K = 0.99$) for the three states of the system as shown in the figures (Fig. 8.9).

The graphs of Fig. 8.10 are obtained using the procedure described above for the Higuchi dimension. The slopes are obtained respectively as $H = 1.96$ for the healthy system, $H = 1.81$ and $H = 1.95$ for the system with small and large defects. The figure also shows an extension of the procedure for different set of data corresponding to rotor speed 50 and 10 rpm. The results are structurally characteristic of a non-periodic response.

As studied in previous contributions [14], the structure of the time response of the bearing can be quite complex. This complexity was initially captured through the structure of the recurrence plots matrix and quantified using the so-called recurrence quantification parameters. The results obtained in this paper, provide a more "simplistic" identification of chaos. The Higuchi dimension can be seen here as a graphical tool (from which a quantification can be deduced) and it is complement with the 0-1 test.

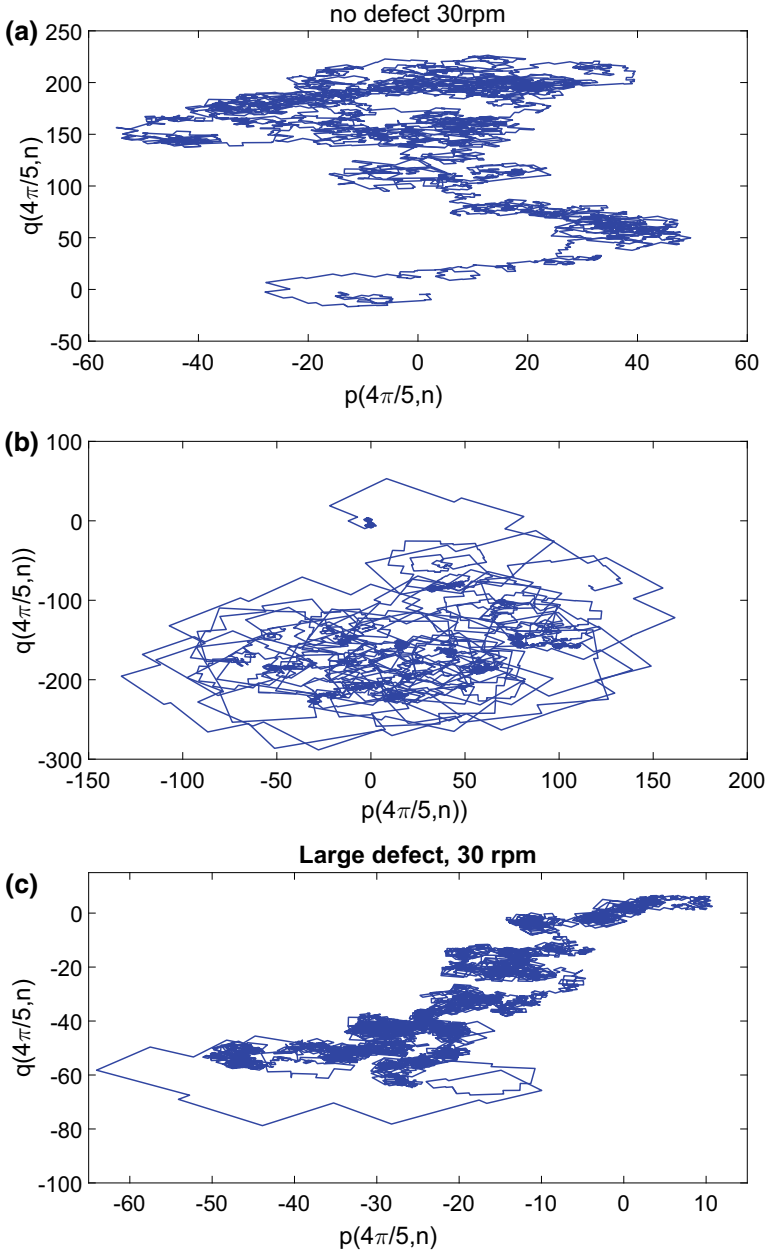

Fig. 8.8 State response in the $(p(n, \pi/5)$ and $(q(n, \pi/5)$ space **a** Healthy system. **b** System with small defect. **c** System with large defect

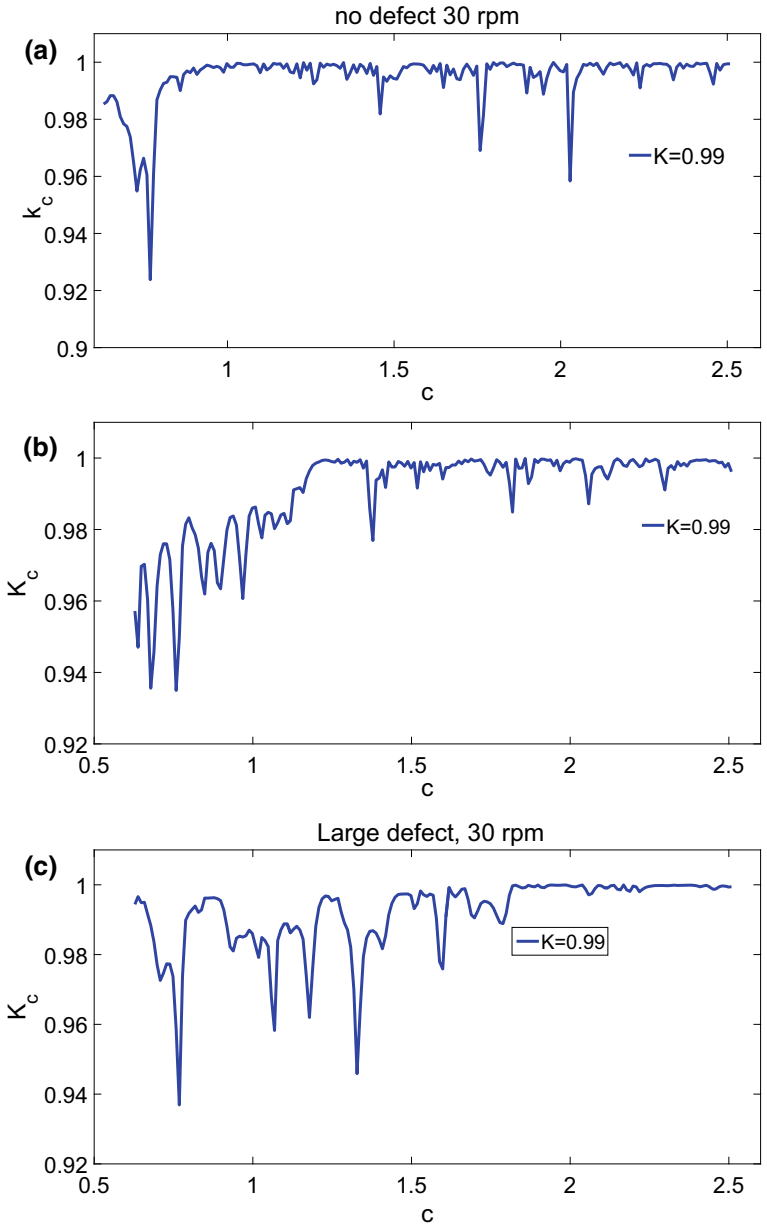

Fig. 8.9 Estimation of the 0-1 test parameter of the bearing system. **a** Healthy system. **b** System with small defect. **c** System with large defect

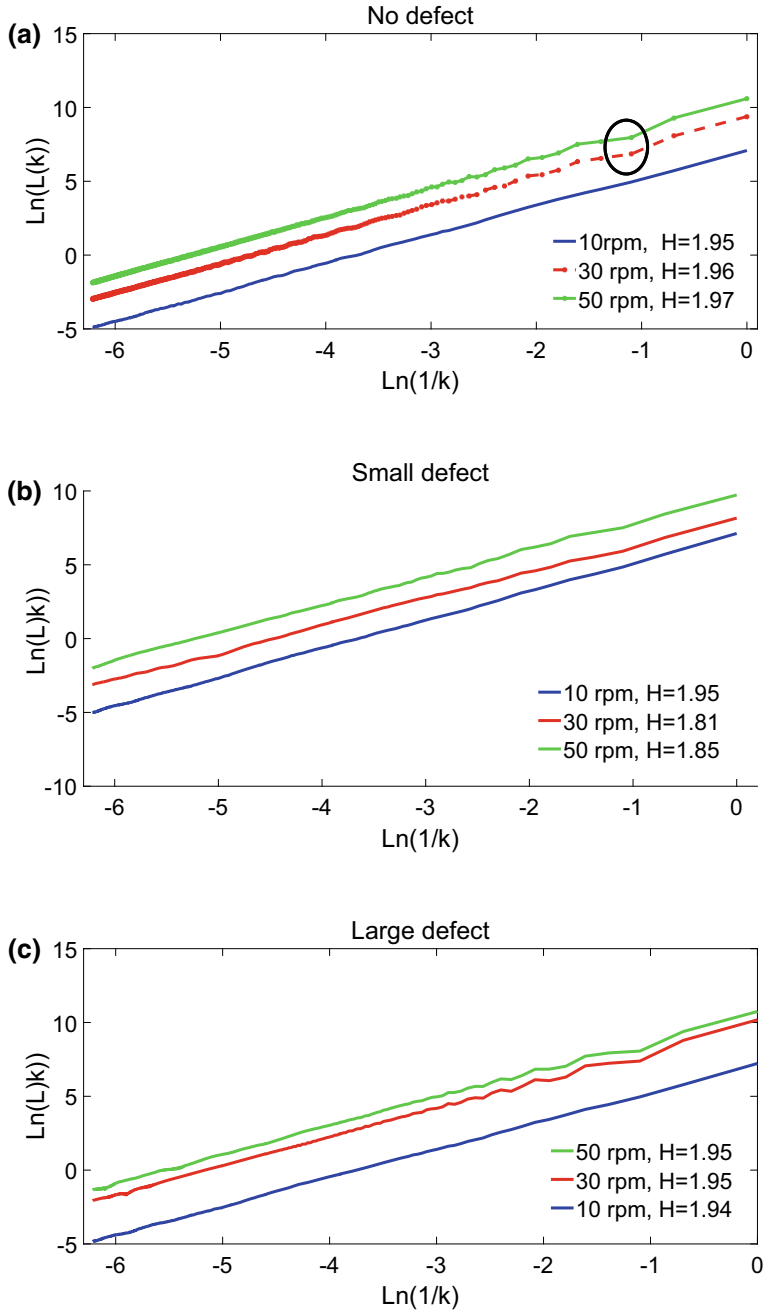

Fig. 8.10 Estimation of the Higuchi fractal dimension. **a** Healthy system. **b** System with small defect. **c** System with large defect

8.4 Conclusion

The main objective of this work was to identify chaotic response of bearing system with and without defects. Two methods were used. The 0-1 test for chaos and the Higuchi fractal dimension. The first task was to describe the method and provide an illustration using a well-known system, namely the discrete logistic equation. Then, the second task was focussed on the applicability of the method in analyzing experimental data extracted from a laboratory model of fault simulator. The collected data were analyzed and the methods have been shown to be an effective tool for the identification of chaotic behavior.

The results obtained in this paper are extensions of results obtained in other applications, where the 0-1 test and the Higuchi dimension were used either separably to analyze experimental data. One key relevance of this work is the relative simplicity of the methods and their robustness. Thus, it appears that these methods can be further explored for the characterization of experimental data as well as fault analysis. In fact, in these two applications, simpler and robust methods are always advantageous (computational cost and robustness). Current investigations are carried out to analyze the effects of noise and the dynamics of the system under various parameter configurations.

Acknowledgements Part of this work was done during the Postdoctoral fellow of C.A.K. Kwuimy at the VCADS. He would like to thank Dr. C. Nataraj and the US Office of Naval Research for the financial support (grant N00014-13-1-0485).

References

1. E.A. Boyd, Analytics **7**, 6 (2012)
2. A. Galka, *Topics in Nonlinear Time Series Analysis* (World Scienti, 2000)
3. H. Kantz, T. Schreiber, *Nonlinear Time Series Analysis* (University Press-Cambridge, 2004)
4. D. Kateris, D. Moshou, X.E. Pantazi, I. Gravalos, N. Sawalhi, S. Loutridis, J. Mech. Sci. Technol. **28**, 1 (2014)
5. H.D.I. Abarbanel, *Analysis of Observed Chaotic Data* (Springer, New York, 1996)
6. C.A.K. Kwuimy, C. Nataraj, *Structural Nonlinear Dynamics & Control and Diagnosis* (Springer, 2015), pp. 97–123
7. C.A.K. Kwuimy, G. Litak, C. Nataraj, Nonlinear Dyn. **80**, 491 (2015)
8. N. Marwan, M.C. Romano, M. Thiel, J. Kurths, Phys. Rep. **438**(5–6), 237 (2007)
9. N. Marwan, J. Kurths, P. Saparin, Phys. Lett. A **360**, 545–551 (2007)
10. A.G. Gottwald, I. Melbourne, SIAM J. Appl. Dyn. Syst. **8**, 129 (2009)
11. G.A. Gottwald, I. Melbourne, Physics D pp. 100–110 (2005)
12. G.A. Gottwald, I. Melbourne, Proceeding R. Soc. A 603–611 (2004)
13. C.A.K. Kwuimy, M. Samadani, P. Kankar, C. Nataraj, ASME J. Comput. Nonlinear Dyn. (2014)
14. C.A.K. Kwuimy, M. Samadani, K. Kappaganthu, C. Nataraj, in *International Conference on Vibration Engineering and Technology of Machinery* (2014)
15. T.H. Mohamad, M. Samadani, C. Nataraj, J. Vib. Acoust. **140**(6), 061009 (2018)
16. T. Higuchi, Physica **23**, 277 (1988)
17. B. Raghavendra, D. Dutt, Computers in biology and medicine, pp. 1006–1012 (2009)

18. J.A. Balderas Lopez, J.L.del Rio Correa, G. Galvez Coyt, A. Munoz Diosdado, F.A. Brown, Revista Mexicana de Fisica 1–6 (2009)
19. G. Litak, A. Syta, M. Wiercigroch, Chaos Solitons Fractals **40**(5), 2095 (2009)
20. S. Chatterton, P. Pennacchi, A. Vania, P.V. Dang, F. Cangioli, in *ASME 2015 International Design Engineering Technical Conferences and Computers and Information in Engineering Conference*, vol. 8 (2015), pp. 46609
21. L. Zachilas, I.N. Psarianos, J. Appl. Math. 681296 (2012)
22. F. Leon, Neurocomputing 173–186 (2014)
23. G. Litak, J.T. Sawick, ZAMM–J. Appl. Math. Mech./Zeitschrift für Angewandte Mathematik und Mechanik **89**(7), 587–592 (2009)

Chapter 9
Dynamical Response of a Planetary Gear System with Faults Using Recurrence Statistics

B. Ambrożkiewicz, Y. Guo, G. Litak and P. Wolszczak

Abstract Recurrence plots and recurrence plots quantification analysis were applied to the planetary gears system to identify faults in the system. In this chapter the recurrence rate parameter adopted in the gear fault detection is presented. It is indicated in terms of recurrence statistics that the response of the gears system with faults is more periodic. This is caused by selected harmonics which are more pronounced in system with faults. Usefulness of other recurrence parameters is also discussed.

9.1 Introduction

Planetary gear systems are frequently used in modern machines torque and momentum transfer [7]. Generally, due to the backlash phenomenon in gears boxes these systems are highly nonlinear [1, 4, 8]. Dynamics of gear boxes with faults was investigated in many simulations and experiments [7]. The main evidence of faults appeared to be related to increase of nonlinearities through the meshing stiffness of tooth deformations [5, 6, 8].

Planetary gear boxes show unique behaviors comparing to fixed-axis gear boxes which significantly influence possible fault diagnosis methods. Here, the vibration transmission path is time-varying causing difficulties to detect localized gear faults of planetary gear boxes. Damages in a planet or a sun gear often cause catastrophic

B. Ambrożkiewicz · G. Litak · P. Wolszczak (✉)
Faculty of Mechanical Engineering, Department of Automation, Lublin University of Technology, Nadbystrzycka 36 p.727, 20-618 Lublin, Poland
e-mail: p.wolszczak@pollub.pl

B. Ambrożkiewicz
e-mail: b.ambrozkiewicz@pollub.pl

G. Litak
e-mail: g.litak@pollub.pl

Y. Guo
Faculty of Mechanical and Electrical Engineering, Kunming University of Science and Technology, Kunming City, Yunnan Province, China
e-mail: kmgary@163.com

M. Belhaq (ed.), *Topics in Nonlinear Mechanics and Physics*,
Springer Proceedings in Physics 228, https://doi.org/10.1007/978-981-13-9463-8_9

failures to the composite rotating machinery [2]. However, the epicyclic motion of planet gears and multi-meshing make gear faults detection of planetary gear sets more difficult. In the present chapter, the recurrence approach to distinguish dynamics of healthy and failure gearbox is applied [3, 9, 10].

9.2 Experimental Setup and Measurement Procedure

A planetary transmission typically consists of a sun gear, a ring gear, a planet carrier and several planet gears. Starting from a ring gear fixed planetary transmission, the sun gear rotates around its center. Planet gears rotate around their own center, and also revolve around the sun gear and held together by the carrier. All planetary gears are meshed with the sun gear and the ring gear at the same time. For condition monitoring, an accelerometer is mounted on the ring gear. Generally, vibration transmission paths to the transducer are multiplied. However, all the paths are time-varying due to the epicyclic motion of planet gears. In addition, the localized gear faults related vibration are usually too weak to expose the corresponding characteristic frequency lines by performing vibration analysis directly. This is because the picked up vibrations are rich in strong components from multi-meshing sources in the planetary gearbox. The test rig photo of our system is presented in Fig. 9.1.

Supposing a planet gear fault as a carrier single tooth crack, the local vibration signal is propagated during revolution of the carrier. Namely, different teeth on the planet gear mesh with teeth of the ring gear in a specific sequence. The Fig. 9.2 shows the representative time series for healthy and fault gear box responses. In that figure one can distinguish a characteristic modulation (envelop) in the faulty gear box response (Fig. 9.2b), while the time series of the healthy gear box is more uniform where the existing modulations are weaker and unpredictable.

This more periodic tendency in cracked gear system is also visible in Fig. 9.3a and b where the Fourier spectra are plotted for healthy and faulty gear box responses, respectively. In Fig. 9.3b many additional harmonics (sub and super-harmonics) are showed transparently. This effect is generally related to the increasing role of

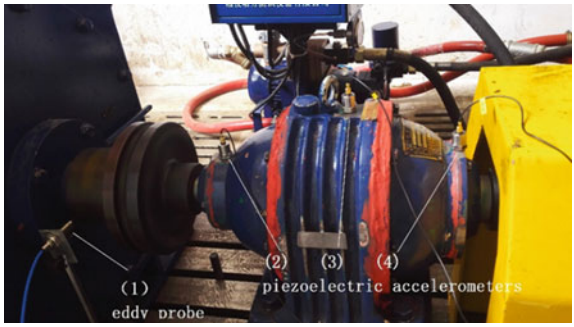

Fig. 9.1 Experimental setup: the single-stage planetary gearbox transmission (type: 2K–H). The consecutive numbers indicates, eddy probe (1), piezoelectric accelerometers (2–4)

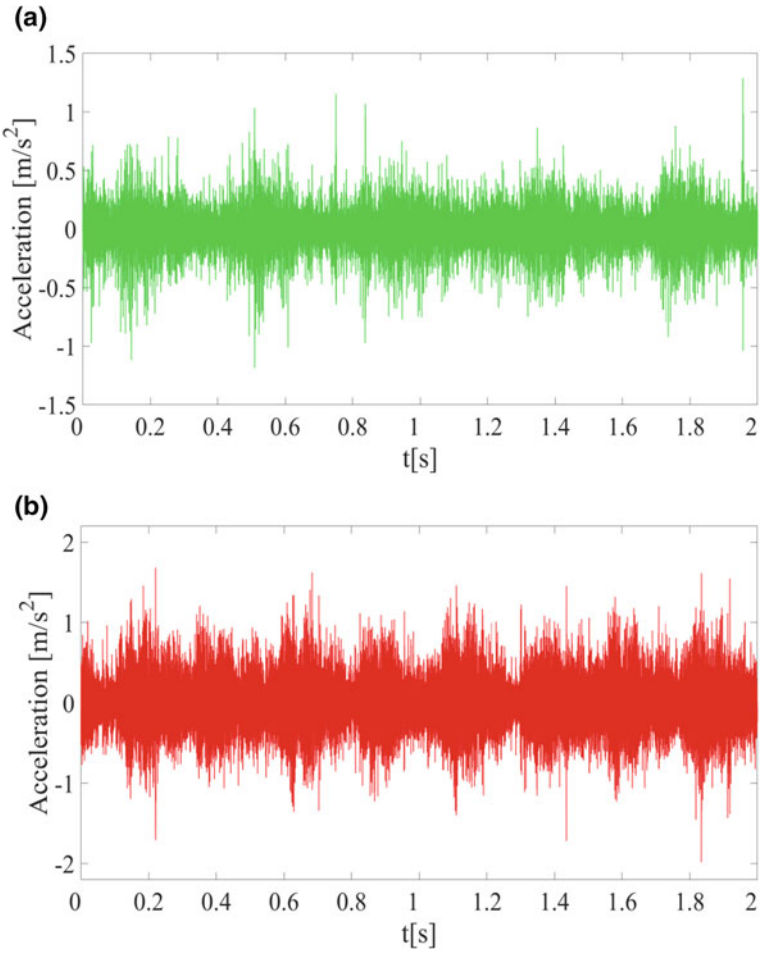

Fig. 9.2 Experimental time series for healthy (**a**) and fault (**b**) gears responses. The characteristic standard deviations $\sigma = 0.1584$ for the healthy gearbox and $\sigma = 2924$ for the faulty one

nonlinearities in the faulty system dynamical responses. Overall, the system seems to behave more periodically. Consequently, the phases of consecutive harmonics are correlated. As the Fourier transform does not take into account the corresponding phases of above mentioned harmonics we propose the method of recurrence plots which is sensitive to them in the next section.

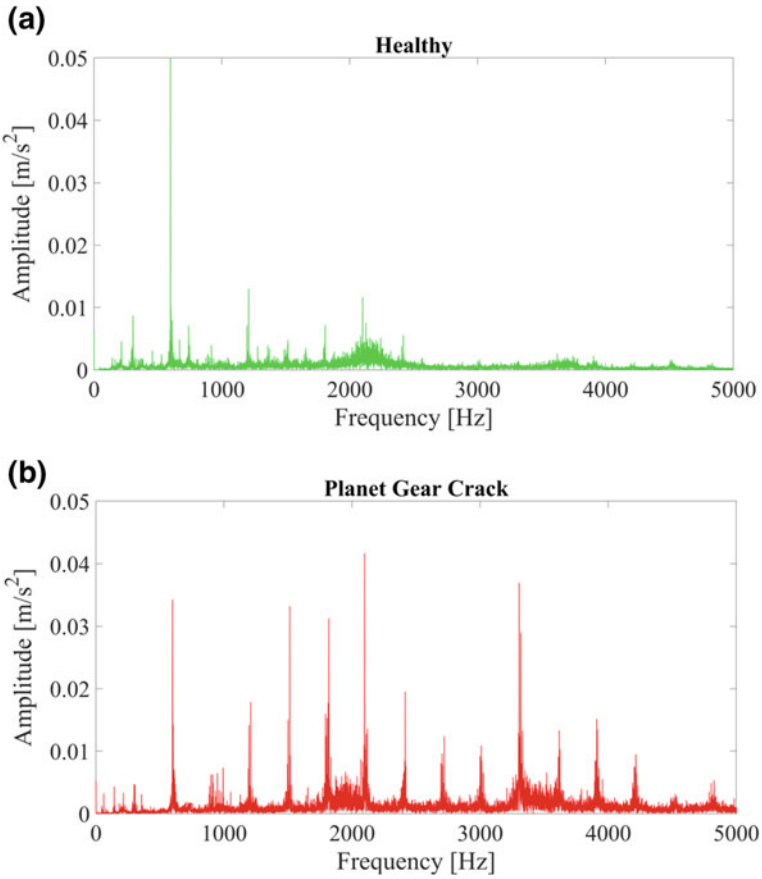

Fig. 9.3 Fourier spectra for healthy (**a**) and fault (**b**) gears responses (respective to Fig. 9.2)

9.3 Recurrence Analysis

One of promising methods used for diagnostics of dynamical systems is the application of recurrence plots and its statistical extension on recurrence quantifications [11, 12]. This has been already used to rotary systems by Litak et al. [3, 9]. Simulation or experimental output data of acceleration from nonlinear dynamical system can be studied by analysis of its phase space trajectories. Typically, the dynamical state of each considered system can be described by the discrete time delay vector

$$y_i = \left[y_i, y_{i-\Delta}, y_{i-2\Delta}, \ldots, y_{i-(M-1)\Delta}\right], \tag{9.1}$$

where M denotes embedding dimension and Δ corresponds to time delay in the signal sampling (the sampling frequency for acceleration signal was 51.2 kHz). To obtain such values, Cross Recurrence Toolbox introduced by Marwan [13] was used.

For analysis of healthy and damaged planetary gear system, signals consisted of 500 samples were taken for consideration. Then the time delay Δi was determined for both states as 2, basing on first minimum in the average mutual information. To obtain embedding dimension M, time delay number was used and determined value of M for both states was equal to 3. For this false nearest neighbours (FNN) approach was applied.

Next, recurrence plot is reconstructed from the distance matrix R with its element R_{ij} calculated as follows (see [12])

$$R_{ij} = H\left(\varepsilon - \left\|x_i - x_j\right\|\right), \tag{9.2}$$

where ε is the threshold value and H is the Heaviside step function. Obtained distance matrix consists of zeros and ones corresponding to the state of the system (1—recurrence, 0—no recurrence).

The next step of system analysis was application of several main recurrence quantity tools such as recurrence rate (RR), determinism (DET) and the length of the longest diagonal (L).

First of the above mentioned quantificators, RR is expressing the ratio between recurrence points and all other points appearing on the graph:

$$RR = \frac{1}{N^2} \sum_{i,j=1}^{N} R_{i,j} \text{ for } |i - j| \geq 1 \tag{9.3}$$

It also determines the fraction of recurrences in a recurrence plot and is the probability that the system will recur.

Another important recurrence quantification is determinism (DET) related with the predictability of the dynamical system. A quantity of determinism is calculated as follows:

$$DET = \frac{\sum_{l=l_{\min}}^{n} l P(l)}{\sum_{l=1}^{n} l P(l)} \tag{9.4}$$

where $P(l)$ is a histogram of diagonal lines of the length l and the minimum length of lines is defined by $l_{min} = 2$. Large number of determinism denotes that the system is more predictable with diagonal lines in recurrence plot. Any another parallel line to the main diagonal in recurrence plot can be considered as a recurrence of two different states of the system for the time equal to the length of the line. System analysis was started with the above recurrence quantificators. All results are shown in standard deviation units for considered signal fragments in Fig. 9.4, 9.5, 9.6 for RR, DET, and lengths of next longest diagonal to main one, respectively. The above mentioned recurrence parameters are plotted against ε. Interestingly, in all the cases the cracked case was characterized by higher value. On recurrence rate plot it is clearly visible

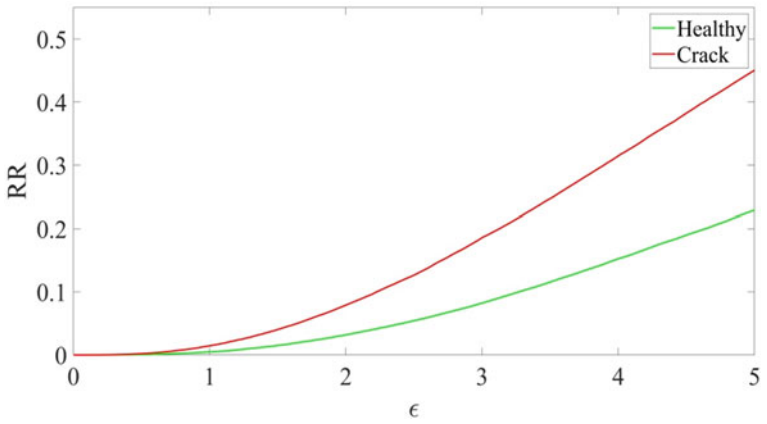

Fig. 9.4 The recurrence rate (RR) versus ε for planetary gear system states

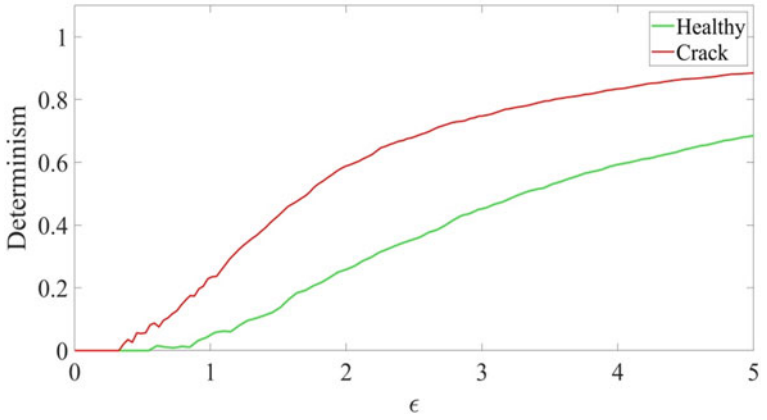

Fig. 9.5 The determinism (DET) versus ε for planetary gear system states

that obtained lines for both states of planetary gear systems are separating from ε = 0.5. Choosing ε for recurrence plot is crucial for showing the difference between states on recurrence plots on an equal footing.

To illustrate the differences between particular dynamical responses we provide the corresponding recurrence plots for the signals. They are presented for selected values of ε, (a) ε = 0.22 and (b) ε = 0.42 where there was the maximum separation of RR lines divided by standard deviation of each signal and (c) and (d) with respect to the universal value of ε = 1.

Here, the fragments of the dynamic system trajectories embedded in recovered space run back to the same area providing a recurrence point represented by a black point on the recurrence plot (Fig. 9.7). Such points are located in 2D space spanned on the discretized time. In Fig. 9.7a and b areas with long diagonal lines character-

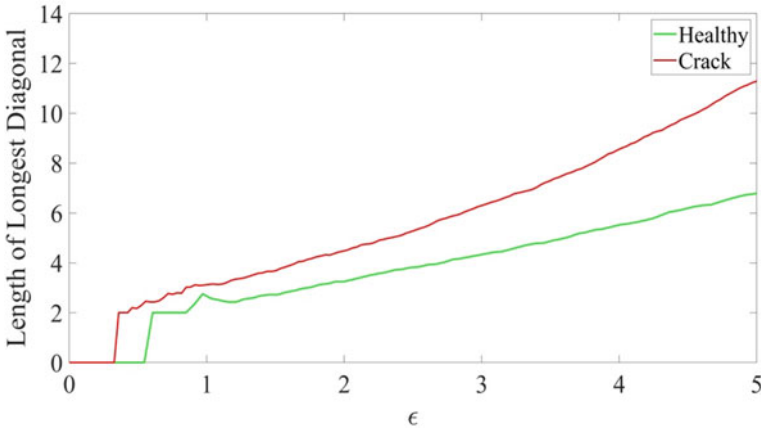

Fig. 9.6 The length of the longest diagonal (L) versus ε for planetary gear system states

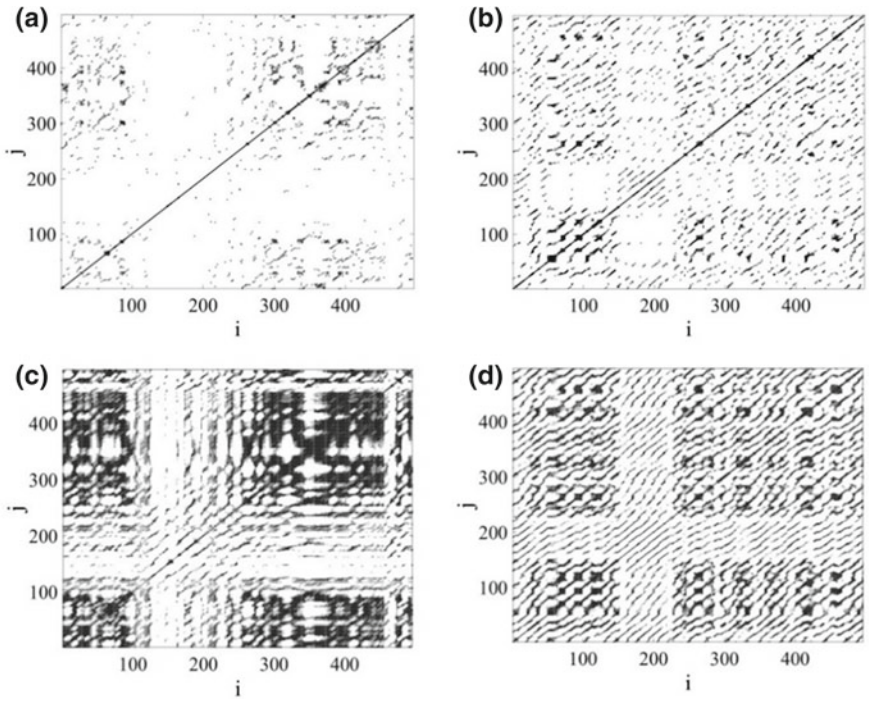

Fig. 9.7 Recurrence plots for considered signals will be presented for different values of ε, **a**, **b** ε = 0.22 and **c**, **d** ε = 0.42. **a**, **c** correspond to healthy while **b**, **d** to cracled systems

istic of stationary and periodic dynamical systems are not clearly visible. Whereas, isolated small areas can be seen. They are caused by non-periodic behaviour of the system. Additional vertical or/and horizontal modulation indicate presence of intermittences. While in the Fig. 9.7a–c, fairly small structures are present. In Fig. 9.7d larger diagonal structures are emerging as lines. Lines occurrence signal automatically increasing periodicity in observed phenomenon. Distances between diagonal structures in Fig. 9.7d undergo small fluctuations, which means a quasi- or multi-periodicity. Their presence explain the damage to the tooth, which increases nonlinearity and consequently causes the occurrence of periodicity in the measured signal. This periodicity is also visible in the FFT (Fig. 9.3b). Finally, Fig. 9.7d shows that the pattern has a more regular character indicating the presence of damage.

9.4 Conclusion

The study concerned the problem of gear fault detection. The vibration signal of the gear is time-varying causing difficulties to detect gear faults of planetary gear boxes. The signal of cracked gears contains many additional harmonics (sub and super-harmonics) and seems to behave more periodically comparing to the case of gear without tooth crack. As the Fourier transform does not take into account the corresponding phases of harmonics the method of recurrence plots is proposed. The recurrence rate parameter is adopted in the analysis of the response of the gears system with faults. Other parameter as determinism and longest diagonal line also provide useful information. Basing on the recurrence parameters cracked and healthy systems were distinguished. Here, due to the backlash phenomenon the gears boxes system becomes more nonlinear which make the system more predictable with more clear structure of diagonal lines in the recurrence plot.

References

1. F. Chaari, T. Fakhfakh, M. Haddar, Dynamic analysis of a planetary gear failure caused by tooth pitting and cracking. J. Fail. Anal. Prev. **6**, 73–78 (2006)
2. Z. Cheng, N. Hu. Quantitative Damage Detection for Planetary Gear Sets Based on Physical Models. Chin. J. Mech. Eng. **25**(1), 190–196 (2012)
3. M.I. Friswell, G. Litak, J.T. Sawicki, Crack identification in rotating machines with active bearings, in *Proceedings of ISMA* (Leuven, Belgium, 20–22 September, 2010), pp. 2843–2855
4. Y.C. Guo, R.G. Parker, Analytical determination of mesh phase relations in general compound planetary gears. Mech. Mach. Theory **46**, 1869–1887 (2011)
5. C. Hu, W.A. Smith, R.B. Randall, Z. Peng, Development of a gear vibration indicator and its application in gear wear monitoring. Mech. Syst. Signal Process. **76–77**, 319–336 (2016). https://doi.org/10.1016/j.ymssp.2016.01.018
6. Y.G. Lei, M.J. Zuo, Z.J. He et al., A multidimensional hybrid intelligent method for gear fault diagnosis. Expert Syst. Appl. **37**, 1419–1430 (2010)
7. Y.G. Lei, J. Lin, M.J. Zuo, Z. He, Condition monitoring and fault diagnosis of planetary gear boxes: a review. Measurement **48**, 292–305 (2014)

8. G. Litak, M.I. Friswell, Dynamics of a gear system with faults in meshing stiffness. Nonlinear Dyn. **41**, 415–421 (2005). https://doi.org/10.1007/s11071-005-1398-y
9. G. Litak, J.T. Sawicki, R. Kasperek, Cracked rotor detection by recurrence plots. Nondestruct. Test. Eval. **24**(4), 347–351 (2009)
10. G. Litak, M. Wiercigroch, B.W. Horton, X. Xu, Transient chaotic behaviour versus periodic motion of a parametric pendulum by recurrence plots. ZAMM-Zeitschrift für Angewandte Mathematik und Mechanik **90**(1), 33–41 (2010)
11. N. Marwan, J. Kurths, Nonlinear analysis of bivariate data withcross recurrence plots. Phys. Lett. A **302**, 299–307 (2002)
12. N. Marwan, M.C. Romano, M. Thiel, Recurrence plots for the analysis of complex systems. Phys. Rep. **438**, 237–329 (2007)
13. N. Marwan, CRP Toolbox for MATLAB v.5.19, Potsdam Institute for Climate Impact Research (PIK) (2016). http://tocsy.pik-potsdam.de/crp.php

Chapter 10
Analytical Approach to a Two-Module Vibro-Impact System

Pawel Fritzkowski, Roman Starosta and Jan Awrejcewicz

Abstract A mechanical system composed of two weakly coupled vibro-impact modules under harmonic excitation is considered. The mathematical model of the system is presented in a non-dimensional form. The analytical approach based on the combination of the multiple scales method and the saw-tooth function is employed. The periodic responses of the system with two impacts per cycle near 1:1 resonance are studied. The results have semi-analytical character. Stability of the periodic motions is evaluated. In the unstable case, occurrence of a different response regime is shown: the strongly modulated response. The analytical predictions are compared with purely numerical results.

10.1 Introduction

Vibro-impact processes arise in many areas of physical science and engineering. Computational analysis and understanding of the mechanical systems in which systematic collisions occur requires specific approaches and tools. From the theoretical point of view, the vibro-impact systems, even the simplest ones, are strongly nonlinear. Their non-smooth dynamics and complex behaviours make it practically impossible to formulate general analytical solutions or strategies.

Many approximate analytical methods suitable for nonlinear dynamical systems have evolved from the classical perturbation approach. Therefore, their applicability is usually limited to weakly nonlinear problems [1, 2]. However, over past decades,

P. Fritzkowski (✉) · R. Starosta
Institute of Applied Mechanics, Poznan University of Technology,
ul. Jana Pawła II 24, 60-965 Poznań, Poland
e-mail: pawel.fritzkowski@put.poznan.pl

J. Awrejcewicz
Department of Automatics and Biomechanics, Technical University of Łódź,
ul. Stefanowskiego 1/15, 90-924 Łódź, Poland

M. Belhaq (ed.), *Topics in Nonlinear Mechanics and Physics*,
Springer Proceedings in Physics 228, https://doi.org/10.1007/978-981-13-9463-8_10

a number of analytical techniques have been developed to cope with vibro-impact models, e.g. the power-law phenomenological modeling [3], the Ivanov non-smooth coordinate transformation [3], the non-smooth temporal transformation (NSTT) [3–5], the concept of impact modes [6].

In particular, a combination of the multiple scales method with a saw-tooth function has been recently applied to the systems including vibro-impact nonlinear energy sink (VI NES) [7–12]. Such problems are strictly connected with the increasingly extensive studies on targeted energy transfer (TET) and energy harvesting [13]. However, this analytical approach has been used to relatively simple systems (two degrees of freedom: one primary oscillator and one impacting particle).

In what follows, a more complicated mechanical system is considered. It consists of two weakly coupled vibro-impact modules under harmonic forces. The main aim of this chapter is to present the applicability of the abovementioned method to the four-degree-of-freedom system. The response of the system in the case of 1:1 resonance is studied, and the effect of selected model parameters on the dynamics is analyzed.

10.2 Mechanical System and Mathematical Model

Consider a two-module system schematically illustrated in Fig. 10.1. Each module consists of two interacting parts: a primary body (box) of mass M, and a particle of mass m, moving freely in a straight cavity. Basically, the boxes themselves are linear oscillators (LO) with viscous damping and harmonic excitation. The stiffness constants of linear springs and the damping coefficients are denoted by k_i and c_i, respectively ($i = 1, 2$). The external forces, in turn, take the form $F_i(t) = F_{i0}\sin(\omega_i t)$. The modules are interconnected by a linear spring and damper (k_{12} and c_{12}).

Mass of the balls is assumed to be relatively small ($M \ll m$). Impacts between the particles and the boxes are characterized by the restitution coefficient, κ. We focus on the case of imperfectly elastic collisions ($0 < \kappa < 1$). Moreover, the coupling between the two modules is supposed to be weak ($k_{12} \ll k_1,\ k_2$ and $c_{12} \ll c_1,\ c_2$). Friction and any other resistance forces in the system are neglected.

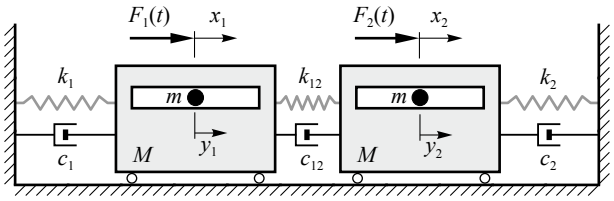

Fig. 10.1 The vibro-impact system to be considered

A single-module system of this type was analyzed by Gendelman [7] as well as Gendelman and Alloni [8]. The analytical approach proposed in these papers has been adpoted and used in our studies.

In recent years, different configurations of primary structures and NESs have been investigated analytically, numerically as well experimentally, and the researches are not of a purely theoretical nature. Particularly, VI NESs are simple in construction and have been found to be very efficient devices with the capacity for rapid energy absorption. Thus, they can be used to suppress shock effects, e.g. in structures under seismic vibrations or in vehicles during collisions [13]. The presented studies, focused on various response regimes and stability of analytical solutions, are the first step, and can be followed by optimization of the VI NES to obtain the most efficient response regime.

Let x_i and y_i denote the absolute displacements of the primary bodies and the balls ($-L \leqslant y_i \leqslant L$, see Fig. 10.2). Using these variables as the generalized coordinates, we can write the equations of motion of the four-degree-of-freedom system between impacts (for $|x_i - y_i| < L$) as:

$$\begin{aligned} &M\ddot{x}_1 + c_1\dot{x}_1 + k_1x_1 - c_{12}(\dot{x}_2 - \dot{x}_1) - k_{12}(x_2 - x_1) = F_{10}\sin(\omega_1 t) \\ &m\ddot{y}_1 = 0 \\ &M\ddot{x}_2 + c_2\dot{x}_2 + k_2x_2 + c_{12}(\dot{x}_2 - \dot{x}_1) + k_{12}(x_2 - x_1) = F_{20}\sin(\omega_2 t) \\ &m\ddot{y}_2 = 0 \end{aligned} \tag{10.1}$$

We assume that the duration of the box-ball collision is very short, and the classical approach can be applied: the simplest impact law (Newton's restitution rule) together with the law of conservation of linear momentum [14, 15].

Let us introduce the dimensionless time and displacements:

$$\tau = \omega_{10}t, \qquad \omega_{10}^2 = \frac{k_1}{M}, \qquad X_i = \frac{x_i}{L}, \qquad Y_i = \frac{y_i}{L}$$

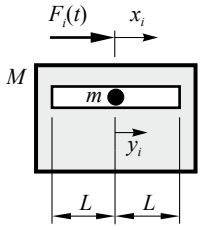

Fig. 10.2 A single module of the system and the characteristic dimension

Taking into account the mentioned standard description of impacts, equations of motion (10.1) can be reformulated and written in the non-dimensional form:

$$\begin{aligned}
&\ddot{X}_1 + \gamma_1 \dot{X}_1 + X_1 - \gamma_{12}(\dot{X}_2 - \dot{X}_1) - \alpha_{12}(X_2 - X_1) = \\
&\qquad = -\varepsilon \frac{1+\kappa}{1+\varepsilon} \sum_j (\dot{X}_1^- - \dot{Y}_1^-)\delta(\tau - \tau_j) + f_{10}\sin(\Omega_1 \tau) \\
&\qquad \varepsilon \ddot{Y}_1 = \varepsilon \frac{1+\kappa}{1+\varepsilon} \sum_j (\dot{X}_1^- - \dot{Y}_1^-)\delta(\tau - \tau_j) \\
&\ddot{X}_2 + \gamma_2 \dot{X}_2 + \Omega_{20}^2 X_2 + \gamma_{12}(\dot{X}_2 - \dot{X}_1) + \alpha_{12}(X_2 - X_1) = \\
&\qquad = -\varepsilon \frac{1+\kappa}{1+\varepsilon} \sum_j (\dot{X}_2^- - \dot{Y}_2^-)\delta(\tau - \tau_j) + f_{20}\sin(\Omega_2 \tau) \\
&\qquad \varepsilon \ddot{Y}_2 = \varepsilon \frac{1+\kappa}{1+\varepsilon} \sum_j (\dot{X}_2^- - \dot{Y}_2^-)\delta(\tau - \tau_j)
\end{aligned} \tag{10.2}$$

where

$$\varepsilon = \frac{m}{M}, \quad \Omega_{20}^2 = \frac{k_2}{M\omega_{10}^2}, \quad \gamma_1 = \frac{c_1}{M\omega_{10}}, \quad \gamma_2 = \frac{c_2}{M\omega_{10}},$$

$$\alpha_{12} = \frac{k_{12}}{M\omega_{10}^2}, \quad \gamma_{12} = \frac{c_{12}}{M\omega_{10}}, \quad \Omega_i = \frac{\omega_i}{\omega_{10}}, \quad f_{i0} = \frac{F_{i0}}{ML\omega_{10}^2}.$$

Obviously, now the overdots denote differentiation with respect to τ. Moreover, $\delta(\bullet)$ stands for the Dirac delta function, τ_j is the time instance of the jth impact (for $|X_i - Y_i| = 1$), and $\dot{X}_i^-$, $\dot{Y}_i^-$ are the velocities immediately before the impact. The sums on the right-hand sides of (10.2) come just from the simple impact model and correspond to the momenta transferred to/from the primary oscillators in consecutive impacts (e.g. see [7, 8]).

For the convenience of further analytical studies, the following new coordinates are defined:

$$U_i = X_i + \varepsilon Y_i, \qquad W_i = X_i - Y_i \qquad (i = 1, 2)$$

Using these relations in (10.2), we get

$$
\begin{aligned}
&\ddot{U}_1 + \gamma_1 \frac{\dot{U}_1 + \varepsilon\dot{W}_1}{1+\varepsilon} + \frac{U_1 + \varepsilon W_1}{1+\varepsilon} + \gamma_{12}\frac{\dot{U}_1 + \varepsilon\dot{W}_1}{1+\varepsilon} + \alpha_{12}\frac{U_1 + \varepsilon W_1}{1+\varepsilon} + \\
&\quad - \gamma_{12}\frac{\dot{U}_2 + \varepsilon\dot{W}_2}{1+\varepsilon} - \alpha_{12}\frac{U_2 + \varepsilon W_2}{1+\varepsilon} = f_{10}\sin(\Omega_1\tau) \\
&\ddot{W}_1 + \gamma_1 \frac{\dot{U}_1 + \varepsilon\dot{W}_1}{1+\varepsilon} + \frac{U_1 + \varepsilon W_1}{1+\varepsilon} + \gamma_{12}\frac{\dot{U}_1 + \varepsilon\dot{W}_1}{1+\varepsilon} + \alpha_{12}\frac{U_1 + \varepsilon W_1}{1+\varepsilon} + \\
&\quad - \gamma_{12}\frac{\dot{U}_2 + \varepsilon\dot{W}_2}{1+\varepsilon} - \alpha_{12}\frac{U_2 + \varepsilon W_2}{1+\varepsilon} = \\
&\quad = -(1+\kappa)\sum_j \dot{W}_1^-\delta(\tau - \tau_j) + f_{20}\sin(\Omega_2\tau) \\
&\ddot{U}_2 + \gamma_2 \frac{\dot{U}_2 + \varepsilon\dot{W}_2}{1+\varepsilon} + \Omega_{20}^2\frac{U_2 + \varepsilon W_2}{1+\varepsilon} + \gamma_{12}\frac{\dot{U}_2 + \varepsilon\dot{W}_2}{1+\varepsilon} + \alpha_{12}\frac{U_2 + \varepsilon W_2}{1+\varepsilon} + \\
&\quad - \gamma_{12}\frac{\dot{U}_1 + \varepsilon\dot{W}_1}{1+\varepsilon} - \alpha_{12}\frac{U_1 + \varepsilon W_1}{1+\varepsilon} = f_{20}\sin(\Omega_2\tau) \\
&\ddot{W}_2 + \gamma_2 \frac{\dot{U}_2 + \varepsilon\dot{W}_2}{1+\varepsilon} + \Omega_{20}^2\frac{U_2 + \varepsilon W_2}{1+\varepsilon} + \gamma_{12}\frac{\dot{U}_2 + \varepsilon\dot{W}_2}{1+\varepsilon} + \alpha_{12}\frac{U_2 + \varepsilon W_2}{1+\varepsilon} + \\
&\quad - \gamma_{12}\frac{\dot{U}_1 + \varepsilon\dot{W}_1}{1+\varepsilon} - \alpha_{12}\frac{U_1 + \varepsilon W_1}{1+\varepsilon} = \\
&\quad = -(1+\kappa)\sum_j \dot{W}_2^-\delta(\tau - \tau_j) + f_{20}\sin(\Omega_2\tau)
\end{aligned}
\tag{10.3}
$$

As can be seen, the left-hand sides of all the equations are more complicated now. However, the impact-related sums are present only in the differential equations corresponding to variables W_i.

10.3 Analytical Treatment of the Problem

In the approximate analytical approach to the problem, the mass ratio plays a role of the small parameter ($\varepsilon \ll 1$). From the physical viewpoint, some factors within the system are assumed to be weak, and the following parameters are formally introduced:

$$\gamma_i = \varepsilon\hat{\gamma}_i, \quad \alpha_{12} = \varepsilon\hat{\alpha}_{12}, \quad \gamma_{12} = \varepsilon\hat{\gamma}_{12}, \quad f_{i0} = \varepsilon\hat{f}_{i0}. \tag{10.4}$$

Moreover, we focus on the most common type of motion studied in the field of vibro-impact systems, i.e. periodic oscillations with two impacts per cycle, near 1:1 resonance. Let us describe the proximity of Ω_{20} and Ω_1, Ω_2 to the natural frequency (normalized to unity) of the first LO by

$$\Omega_{20}^2 = 1 + \sigma_{20}, \quad \Omega_1 = \Omega_2 = 1 + \sigma_e, \tag{10.5}$$

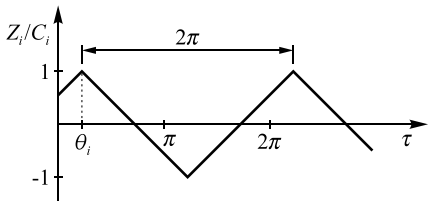

Fig. 10.3 The saw-tooth function used as a part of the solution W_{i0}

where the detuning parameters can be expressed as

$$\sigma_{20} = \varepsilon\hat{\sigma}_{20}, \quad \sigma_e = \varepsilon\hat{\sigma}_e. \tag{10.6}$$

In the following analysis, the method of multiple scales is employed [1, 2]. Two time scales are used:

$$\tau_k = \varepsilon^k \tau, \qquad k = 0,\ 1$$

and the solution of the problem is approximated by

$$U_i = U_{i0}(\tau_0,\ \tau_1) + \varepsilon U_{i1}(\tau_0,\ \tau_1), \qquad W_i = W_{i0}(\tau_0,\ \tau_1) + \varepsilon W_{i1}(\tau_0,\ \tau_1). \tag{10.7}$$

Substituting expansions (10.7), frequencies (10.5) with (10.6), and parameters (10.4) into (10.3), and then equating coefficients of order ε^0, we obtain

$$\begin{aligned} &D_0^2 U_{i0} + U_{i0} = 0, \\ &D_0^2 W_{i0} = -(1+\kappa)\sum_j D_0 W_{i0}^- \delta(\tau_0 - \tau_{0j}) - U_{i0}, \end{aligned} \tag{10.8}$$

where $D_k^n = \partial^n / \partial \tau_k^n$. For the first equation, the solution is simply

$$U_{i0} = B_i(\tau_1)\sin(\tau_0 + \phi_i(\tau_1)). \tag{10.9}$$

In the second case, in turn, we assume that

$$W_{i0} = B_i(\tau_1)\sin(\tau_0 + \phi_i(\tau_1)) + Z_i(\tau_0,\ \tau_1), \tag{10.10}$$

where Z_i is the saw-tooth function

$$Z_i(\tau_0,\ \tau_1) = \frac{2}{\pi} C_i(\tau_1)\arcsin[\cos(\tau_0 - \theta_i(\tau_1))] \tag{10.11}$$

which describes the non-smooth nature of the motion due to impacts that occur at $\tau_{0j} = j\pi + \theta_i$ for $j = 0,\ 1,\ 2,\ \ldots$. This specific part of the solution for constant C_i and θ_i is presented graphically in Fig. 10.3.

In order to determine relations between B_i and C_i, we analyze the impact conditions. Firstly, it is assumed that $W_i = \pm 1$ for $\tau_{0j} = j\pi + \theta_i$. Taking into account (10.10), we get

$$B_i \sin(\theta_i + \phi_i) + C_i = 1 \tag{10.12}$$

Secondly, inserting solution (10.10) to the second equation of (10.8) leads to

$$\frac{\partial^2 Z_i}{\partial \tau_0^2} + (1+\kappa) \sum_j \left[B_i \cos(\tau_0 + \phi_i) + \frac{\partial Z_i^-}{\partial \tau_0} \right] \delta(\tau_0 - \tau_{0j}) = 0. \tag{10.13}$$

After integration of this equation over a small time interval around $\tau_0 = \theta_i$, we obtain:

$$-\frac{4}{\pi} C_i + (1+\kappa) \left[B_i \cos(\theta_i + \phi_i) + \frac{2}{\pi} C_i \right] = 0. \tag{10.14}$$

A combination of (10.12) and (10.14) gives the following relation between the slow-time-scale variables:

$$C_i = \frac{1 \pm \sqrt{(1+\rho^2) B_i^2 - \rho^2}}{1+\rho^2}, \qquad \rho = \frac{2(1-\kappa)}{\pi(1+\kappa)} \tag{10.15}$$

or alternatively

$$B_i^2 = 1 - 2C_i + (1+\rho^2) C_i^2. \tag{10.16}$$

The equations define the so called slow invariant manifold (SIM) of the problem for the case of 1:1 resonance. Furthermore, the phase angles, ϕ_i and θ_i, are specified by the formulas:

$$\sin(\theta_i + \phi_i) = \frac{1 - C_i}{B_i}, \qquad \cos(\theta_i + \phi_i) = \frac{\rho C_i}{B_i}. \tag{10.17}$$

In order to find the fixed points and observe the evolution of the system on the SIM, the equations related to U_i at the higher order of approximation (ε^1) are used (due to their complexity they are not presented in the full form):

$$\begin{aligned} D_0^2 U_{11} + U_{11} &= g_1(\tau_0,\ U_{10},\ W_{10},\ U_{20}), \\ D_0^2 U_{21} + U_{21} &= g_2(\tau_0,\ U_{20},\ W_{20},\ U_{10}). \end{aligned} \tag{10.18}$$

The functions Z_i included on the right hand sides, g_i, can be expanded into a Fourier series (with respect to τ_0):

$$Z_i = \frac{8}{\pi^2} C_i \sum_{n=1,3,5}^{\infty} \frac{1}{n^2} \cos[n(\tau_0 - \theta_i)] \tag{10.19}$$

Next, elimination of secular terms provides the solvability conditions, i.e. the system of differential equations for the amplitudes and phases:

$$\begin{aligned} D_1 B_1 &= h_{B1}(\tau_1,\ B_1,\ \phi_1,\ B_2,\ \phi_2,\ C_1,\ \theta_1),\\ D_1 \phi_1 &= h_{\phi 1}(\tau_1,\ B_1,\ \phi_1,\ B_2,\ \phi_2,\ C_1,\ \theta_1),\\ D_1 B_2 &= h_{B2}(\tau_1,\ B_1,\ \phi_1,\ B_2,\ \phi_2,\ C_2,\ \theta_2),\\ D_1 \phi_2 &= h_{\phi 2}(\tau_1,\ B_1,\ \phi_1,\ B_2,\ \phi_2,\ C_2,\ \theta_2). \end{aligned} \tag{10.20}$$

To transform (10.20) into an autonomous system, we use relations (10.17) and put

$$\psi_1 = \hat{\sigma}_e \tau_1 - \phi_1, \qquad \psi_2 = \hat{\sigma}_e \tau_1 - \phi_2. \tag{10.21}$$

Consequently, we obtain

$$\begin{aligned} D_1 B_1 &= h^*_{B1}(B_1,\ \psi_1,\ B_2,\ \psi_2,\ C_1),\\ D_1 \psi_1 &= h^*_{\psi 1}(B_1,\ \psi_1,\ B_2,\ \psi_2,\ C_1),\\ D_1 B_2 &= h^*_{B2}(B_1,\ \psi_1,\ B_2,\ \psi_2,\ C_2),\\ D_1 \psi_2 &= h^*_{\psi 2}(B_1,\ \psi_1,\ B_2,\ \psi_2,\ C_2). \end{aligned} \tag{10.22}$$

The steady-state motions correspond to the solutions of the algebraic system

$$h^*_{B1} = 0, \qquad h^*_{\psi 1} = 0, \qquad h^*_{B2} = 0, \qquad h^*_{\psi 2} = 0. \tag{10.23}$$

Finally, determining $\sin\psi_i$, $\cos\psi_i$ and $\sin(\psi_2 - \psi_1)$, $\cos(\psi_2 - \psi_1)$ appearing in (10.23), and using elementary trigonometric identities, we can eliminate ψ_i and arrive at the rational equations in which B_i, C_i are the only unknowns:

$$h_1(B_1,\ C_1,\ B_2,\ C_2) = 0, \qquad h_2(B_1,\ C_1,\ B_2,\ C_2) = 0. \tag{10.24}$$

Solving these equations together with (10.16), we can find the fixed points of the slow flow.

The SIM, that is the curve $B_i(C_i)$, is shown in Fig. 10.4. The minimal allowable (real) value of B_i and the corresponding value of C_i are given by

$$B_{\min} = \frac{\rho}{\sqrt{1+\rho^2}}, \qquad C_{\min} = \frac{1}{1+\rho^2} \tag{10.25}$$

A careful analysis of the function $W_{i0}(\tau_0,\ \tau_1)$ leads to the conclusion that non-degenerate solutions, i.e. the ones that do not violate the no-penetration condition ($|W_{i0}| \leqslant 1$ for all τ_0), exist for $C_i \geq 0$.

Moreover, the curve $B_i(C_i)$ can be divided into two branches: one is stable and the other is unstable. Stability of periodic motions can be studied by means of the technique proposed by Masri [16] and adopted, for example, in [17, 18]. The approach

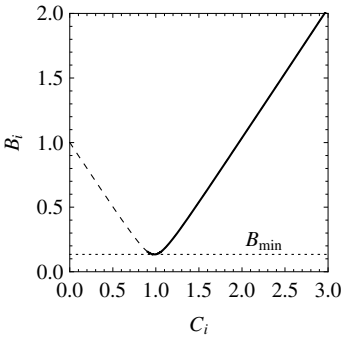

Fig. 10.4 SIM of the system for $\kappa = 0.65$: the stable branch (bold solid) and the unstable branch (dashed); dotted line depicts the $B_{\min}$ level

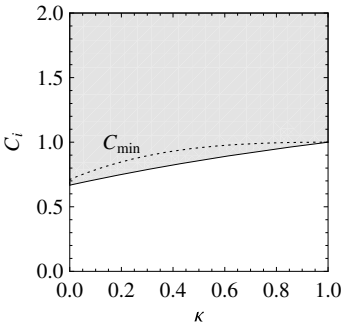

Fig. 10.5 Stable (shaded) and unstable (white) regions for the vibro-impact system; dotted line depicts the $C_{\min}(\kappa)$ curve

allows one to analyze the propagation of small perturbations in the original periodic motion. More precisely, one can evaluate the effect of small variation of the steady-state values (displacement and velocity) just after an impact, $(\Delta_1\theta_i^+,\ \Delta_1\dot{W}_i^+)$, on the instants of subsequent collisions and the resulting variation in the displacement and velocity, i.e. $(\Delta_j\theta_i^+,\ \Delta_j\dot{W}_i^+)$ with $j = 2,\ 3,\ \ldots$. More detailed discussion of the technique goes beyond the scope of this paper. Such an analysis conducted for the considered system leads to the following condition for the existence of asymptotically stable periodic motions:

$$C_i > \frac{4}{4+\pi\rho}. \tag{10.26}$$

The stability region on the plane $(\kappa,\ C_i)$ is presented in Fig. 10.5. As can be seen, the right arm $(C_i > C_{\min})$ of the hyperbola $B_i(C_i)$ belongs entirely to the stable branch, which additionally contains a short piece of the left arm $(C_i < C_{\min})$.

10.4 Analytical-Numerical Results

The results presented below have an analytical-numerical character. Firstly, due to the complexity of the system of algebraic equations (10.16)–(10.24), the fixed points of

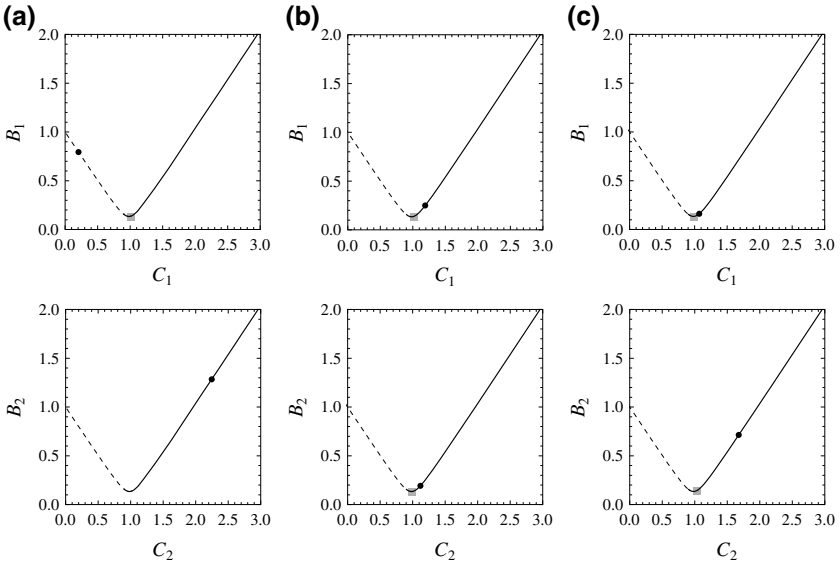

Fig. 10.6 Fixed points of the system: **a** unstable, **b** stable, **c** stable. Results obtained for $\hat{f}_{10} = \hat{f}_{20} = 1$

the slow flow are searched numerically. Secondly, the theoretically predicted steady-state responses of the system are compared to the purely numerical solutions, i.e. the results obtained by a direct numerical integration of (10.1). All the numerical experiments are performed for the following set of dimensionless parameters:

$$\varepsilon = 0.1, \qquad \kappa = 0.65, \qquad \hat{\alpha}_{12} = 1,$$
$$\hat{\gamma}_1 = \hat{\gamma}_2 = \hat{\gamma}_{12} = 0.2, \qquad \hat{\sigma}_{20} = 0.5, \qquad \hat{\sigma}_e = 0.2.$$

Values of the excitation amplitudes will be altered.

Let us start with identical amplitudes of two forces: $\hat{f}_{10} = \hat{f}_{20} = 1$. Three fixed points existing in this case are illustrated in Fig. 10.6. More precisely, the projection of the fixed points on the $(C_i,\ B_i)$ planes are represented by black circles. The projection on the $(C_1,\ B_1)$ plane located on the left arm of the SIM (see Fig. 10.6a) indicates that the corresponding fixed point is unstable; the next two ones are stable.

The theoretically predicted steady-state response of the system (two impacts per cycle) for the stable fixed point (c) is presented in Fig. 10.7. The absolute displacements of the primary oscillators and the coordinates U_i are marked in grey while the absolute and relative displacements of the particles are shown in black lines. Similar results can be obtained numerically. Needless to say, in a dynamic simulation, a long-term behaviour of the system must be analyzed to omit any transient motion. As an example, the purely numerical solutions W_2 and X_2 are given in Fig. 10.8.

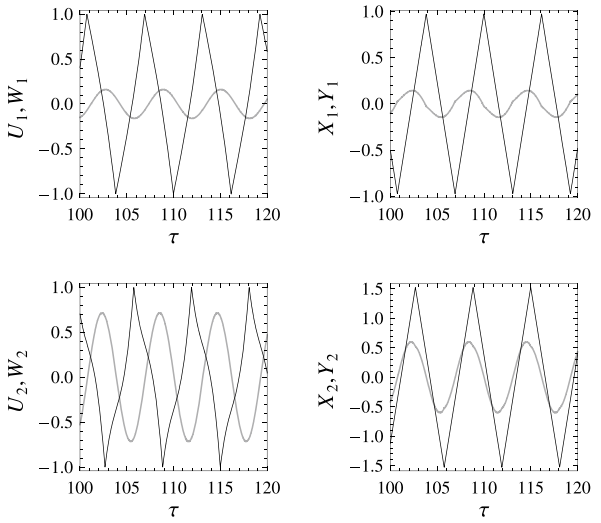

Fig. 10.7 Steady-state response of the system – fixed point (c): U_i, X_i (grey) and W_i, Y_i (black). Results obtained for $\hat{f}_{10} = \hat{f}_{20} = 1$

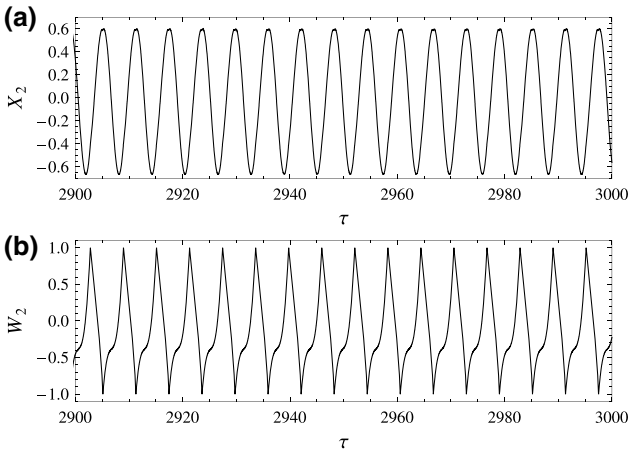

Fig. 10.8 Steady-state response of the system: **a** displacement of the second box, **b** relative displacement of the particle. Numerical solution obtained for $\hat{f}_{10} = \hat{f}_{20} = 1$

The grey squares appearing in Fig. 10.6 are related to singular points. Let $P_1 = (C_1^*,\ B_1^*)$ and $P_2 = (C_2^*,\ B_2^*)$ be the projections of a fixed point onto $(C_1,\ B_1)$ and $(C_2,\ B_2)$ planes, respectively. By S_1 we denote a point on $(C_1,\ B_1)$ corresponding to a singularity of h_1 and h_2 in (10.24) at $C_2 = C_2^*$ and $B_2 = B_2^*$. Analogously, S_2 on the $(C_2,\ B_2)$ plane comes from a singularity of h_1 and h_2 when $C_1 = C_1^*$ and $B_1 = B_1^*$. Obviously, locations of P_1, P_2 and S_1, S_2 on the SIM projections change

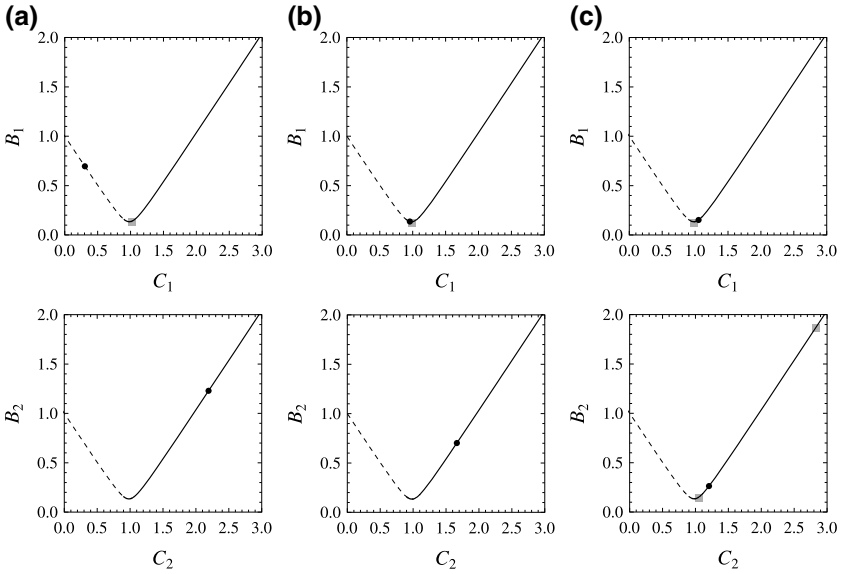

Fig. 10.9 Fixed points of the system: **a** unstable, **b** unstable, **c** stable. Results obtained for $\hat{f}_{10} = 1$, $\hat{f}_{20} = 0.89$

with varying values of some parameters. However, if P_i gets closer to S_i, the fixed point becomes a singular point, potentially associated to a bifurcation.

Now, let us decrease one of the excitation amplitudes. For $\hat{f}_{20} = 0.89$, there are still three fixed points (see Fig. 10.9), but only one of them turns out to be stable. As can be seen from a comparison of all cases in Figs. 10.6 and 10.9, the projections P_1 and P_2 move along the SIM-related curves from right to left. Particularly, projections of the stable fixed points move down the right branch of the SIM.

As the last example, let us consider the case when both the excitation amplitudes are decreased up to 0.5. In such a case only one fixed point exists. Its projections on the $(C_i,\ B_i)$ planes as well as the corresponding steady-state response are presented in Fig. 10.10. However, since P_1 and P_2 are located on the left branch of the SIM, the fixed point is unstable. The only possible behaviour for the system is the so called strongly modulated response (SMR). Thus, the analytical periodic solution has no practical importance. The actual motion of the system can be observed by means of numerical simulations. As can be seen from Fig. 10.11, in the relative displacement of a particle we can distinguish intervals of resonant motion divided by relatively short, irregular non-resonant behaviour. The primary oscillators, in turn, undergoe the characteristic beating-like motion, i.e. large modulations of the vibration amplitudes.

To sum up, when treating the forces amplitudes as the control parameters, we can observe a series of changes in the location of fixed points on the SIM and their stability. By decreasing the amplitudes, we can lead to the case when no stable fixed points exist, and the mechanical system exhibits strongly modulated response that

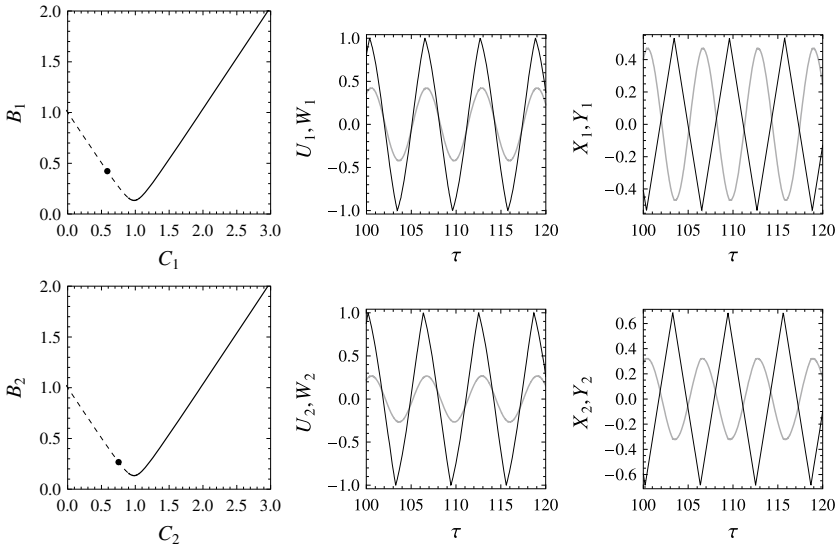

Fig. 10.10 Fixed point (unstable) and the theoretical response of the system: U_i, X_i (grey) and W_i, Y_i (black). Results obtained for $\hat{f}_{10} = \hat{f}_{20} = 0.5$

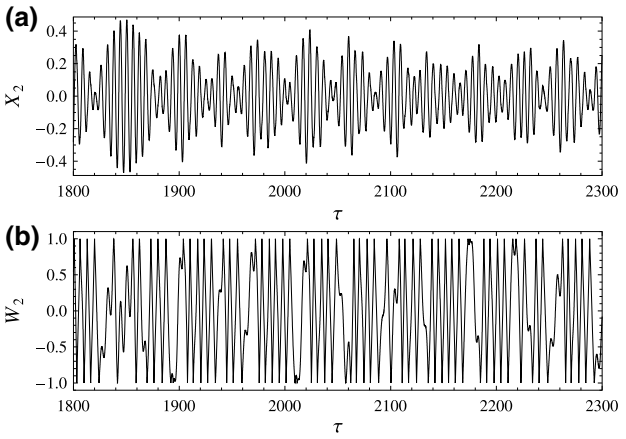

Fig. 10.11 Strongly modulated response of the system: **a** displacement of the second box, **b** relative displacement of the particle. Numerical solution obtained for $\hat{f}_{10} = \hat{f}_{20} = 0.5$

may be advantageous for potential energy harvesting applications [8, 13]. Analysis of the interplay between various model parameters goes beyond the scope of this paper.

10.5 Conclusions

The four-degree-of-freedom system composed of two weakly coupled vibro-impact modules under harmonic forces has been considered. The analytical approach based on the multiple scales method combined with the saw-tooth impact modelling has been adopted and used. The response of the system with two impacts per cycle near 1:1 resonance has been studied.

The applied technique can provide semi-analytical periodic solutions, and is useful in assessing stability of the solutions. It should be noticed that this approach does not require the restitution coefficient to be close to unity. Validity of the analytical predictions has been examined by numerical experiments.

Naturally, such a mechanical system can undergo complex behaviours, and many interesting problems may be studied in detail, e.g. stability of fixed points, singular points and bifurcations, interplay between different model parameters. Apart from that, the applicability of the method to more complex mechanical systems should be verified and extended. Particularly, models including strong and nonlinear couplings, and one-sided impact interactions merit further attention.

References

1. V. Marinca, N. Herisanu, *Nonlinear Dynamical Systems in Engineering: Some Approximate Approaches* (Springer, Heidelberg, 2011)
2. A.H. Nayfeh, D.T. Mook, *Nonlinear Oscillations* (Wiley, New York, 1995)
3. R. Ibrahim, *Vibro-Impact Dynamics: Modeling, Mapping and Applications* (Springer, Berlin, 2009)
4. V. Pilipchuk, Analytical study of vibrating systems with strong non-linearities by employing saw-tooth time transformations. J. Sound Vib. **192**, 43–64 (1996)
5. V. Pilipchuk, A. Vakakis, M. Azeez, Study of a class of subharmonic motions using a non-smooth temporal transformation (NSTT). Phys. D **100**, 145–164 (1997)
6. V. Pilipchuk, Impact modes in discrete vibrating systems with rigid barriers. Int. J. Nonlinear Mech. **36**, 999–1012 (2001)
7. O. Gendelman, Analytic treatment of a system with a vibro-impact nonlinear energy sink. J. Sound. Vib. **331**, 4599–4608 (2012)
8. O. Gendelman, A. Alloni, Forced system with vibro-impact energy sink: chaotic strongly modulated responses. Procedia IUTAM **19**, 53–64 (2016)
9. T. Li, S. Seguy, A. Berlioz, Dynamics of cubic and vibro-impact nonlinear energy sink: analytical, numerical, and experimental analysis. J. Vib. Acoust. **138**, 031010 (2016)
10. T. Li, S. Seguy, A. Berlioz, Optimization mechanism of targeted energy transfer with vibro-impact energy sink under periodic and transient excitation. Nonlinear Dyn. **87**, 2415–2433 (2016)

11. T. Li, S. Seguy, A. Berlioz, On the dynamics around targeted energy transfer for vibro-impact nonlinear energy sink. Nonlinear Dyn. **87**, 1453–1466 (2017)
12. T. Li, D. Qiu, S. Seguy, A. Berlioz, Activation characteristic of a vibro-impact energy sink and its application to chatter control in turning. J. Sound Vib. **405**, 1–18 (2017)
13. A. Vakakis, O. Gendelman, L. Bergman, D. McFarland, G. Kerschen, Y. Lee, *Nonlinear Targeted Energy Transfer in Mechanical and Structural Systems*. Solid Mechanics and Its Applications (Springer, 2009)
14. V. Babitsky, *Theory of Vibro-Impact Systems and Applications* (Springer, Berlin, 1998)
15. S. Thornton, J. Marion, *Classical Dynamics of Particles and Systems* (Brooks/Cole, Belmont, 2004)
16. S. Masri, Analytical and experimental studies of impact dampers. Ph.D. thesis, California Institute of Technology (1965)
17. K. Czolczynski, B. Blazejczyk-Okolewska, A. Okolewski, Analytical and numerical investigations of stable periodic solutions of the impacting oscillator with a moving base. Int. J. Mech. Sci. **115–116**, 325–338 (2016)
18. N. Popplewell, C. Bapat, K. McLachlan, Stable periodic vibroimpacts of an oscillator. J. Sound Vib. **87**, 41–59 (1983)

Chapter 11
Complex Fractional Moments for the Characterization of the Probabilistic Response of Non-linear Systems Subjected to White Noises

Mario Di Paola, Antonina Pirrotta, Gioacchino Alotta, Alberto Di Matteo and Francesco Paolo Pinnola

Abstract In this chapter the solution of Fokker-Planck-Kolmogorov type equations is pursued with the aid of Complex Fractional Moments (CFMs). These quantities are the generalization of the well-known integer-order moments and are obtained as Mellin transform of the Probability Density Function (PDF). From this point of view, the PDF can be seen as inverse Mellin transform of the CFMs, and it can be obtained through a limited number of CFMs. These CFMs' capability allows to solve the Fokker-Planck-Kolmogorov equation governing the evolutionary PDF of non-linear systems forced by white noise with an elegant and efficient strategy. The main difference between this new approach and the other one based on integer moments lies in the fact that CFMs do not require the closure scheme because a limited number of them is sufficient to accurately describe the evolutionary PDF and no hierarchy problem occurs.

M. Di Paola · A. Pirrotta (✉) · G. Alotta · A. Di Matteo
Department of Engineering, University of Palermo, Viale Delle Scienze Ed. 8, 90128 Palermo, Italy
e-mail: antonina.pirrotta@unipa.it

M. Di Paola
e-mail: mario.dipaola@unipa.it

G. Alotta
e-mail: gioacchino.alotta@unipa.it

A. Di Matteo
e-mail: alberto.dimatteo@unipa.it

F. P. Pinnola
Department of Structures for Engineering and Architecture (DIST), University of Naples "Federico II", Via Claudio 21, Ed. 6, 80125 Naples, Italy
e-mail: francescopaolo.pinnola@unina.it

M. Belhaq (ed.), *Topics in Nonlinear Mechanics and Physics*,
Springer Proceedings in Physics 228, https://doi.org/10.1007/978-981-13-9463-8_11

11.1 Introduction

The dawns of stochastic differential calculus is dated back to the last century. Thanks to the pioneering papers of Itô, Wong and Zakaj, Kolmogorov and other authors new horizons were opened giving rise to the modern stochastic mechanics [5, 17, 23, 31]. In this context, a relevant problem is represented by the study of nonlinear system forced by normal white noise. Excitations such as ground motion, wind turbulence, sea waves, surface roughness, blasts and impacts loads being stochastic processes induce that structural responses are stochastic processes too. Thus, the analysis is concerned with the problem of the response statistical characterization. An approach to describe this kind of problems, that is typical of several physical applications [16], is based on the study of the Fokker-Planck equation (FPK) which represents a partial differential equation that describes the evolution of the response conditional probability density function (PDF).

Nowadays, the resolution of FPK equation or its generalized form for different kind of forced white noise (Poissonian, α-stable, etc.) still represents an open problem. Indeed, the FPK equation admits analytical solution in very few cases, for this reason we resort to numerical methods. A possible way to treat such partial differential equation problem is related to the evaluation of the moments of the PDF. This method consists in writing differential equations for the response statistical moments of any order. However, when dealing with nonlinear systems, a serious problem arises in the Moment Equation (ME) approach, the entire system is hierarchic in the sense that the equations for the moments of a fixed order, say K, contain moments of order higher than K. In this way, the ME form an infinite hierarchy. Then, due to the hierarchical nature of the forcing processes, this approach needs a truncation of the involved higher-orders moments in the solution.

Although other strategies, based upon the Hermite polynomials, and cumulants, provide some solutions for a certain few cases, these approaches show some particular limits [13, 16, 25, 26, 34]. Certainly, a meaningful limit of such classical methods is the inability to well describe the tails of the PDF that leads to serious problem in reliability analysis.

Other more complex approaches are available in literature but they are not discussed here for sake of brevity [11, 14, 20, 22, 24, 27, 29, 32, 35, 37]. Instead, in this chapter we focus on a recent development in the resolution of the FPK based on the moment approach [1, 12, 14]. Such recent improvement is obtained thanks to the introduction of the complex-order moments. It has been shown that these complex quantities, known as Complex Fractional Moments (CFMs), are related to the Mellin transform and to the Riesz integral at the origin of the PDF [30, 33]. Moreover, the link between CFMs, Mellin transform and Riesz integrals has provided several important relations and properties [7, 9, 15]. Undoubtedly, one of important properties of CFMs is the capability to reconstruct both PDF and characteristic function. Therefore, the knowledge of the CFMs represents another way to characterize random variables. As will be shown later, this property is fundamental for the resolution of FPK by this

new approach. Further information on the applications of these complex quantities can be found in [2, 8, 11, 21, 28, 36].

11.2 Basic Concepts on Mellin Transform Operator

The Mellin transform operator is a very interesting tool of fractional calculus. It proves to be very useful in solving some problems of engineering interest [1, 2, 4, 7–12, 14, 15, 18, 28, 36]. Let $f(x)$ be any real function defined in $0 \leq x < \infty$. The Mellin transform, labeled as $M_f(\gamma - 1)$, is defined as

$$\mathcal{M}\{f(x); \gamma\} = M_f(\gamma - 1) = \int_0^\infty f(x) x^{\gamma - 1} dx; \quad \gamma = \rho + i\,\eta \tag{11.1}$$

where $i = \sqrt{-1}$ and $\rho, \eta \in \mathbb{R}$.

If the Mellin transform exists, then the function $f(x)$ may be rewritten in the form

$$f(x) = \mathcal{M}^{-1}\{M_f(\gamma - 1); x\} = \frac{1}{2\pi} \int_{\eta=-\infty}^{\infty} M_f(\gamma - 1) x^{-\gamma} d\eta\,; x > 0 \tag{11.2}$$

It is noted that the integration is performed along the imaginary axis and the value of ρ remains fixed. The condition for the existence of the Mellin transform is that $-p < \rho < -q$, being p and q the order of zero at $x = 0$ and $x = \infty$, respectively. Namely

$$\lim_{x \to 0} f(x) = O(x^p); \quad \lim_{x \to \infty} f(x) = O(x^q) \tag{11.3}$$

where $O(\cdot)$ stands for the order of the term in parenthesis.

For example, let us assume that $f(x) = (1 + x)^{-1}$, since $\lim_{x \to 0} f(x) = 1\big[O(x^0)\big]$ then $p = 0$, and $\lim_{x \to \infty} f(x) = x^{-1}\big[O(x^0)\big]$, then $q = -1$; it follows that in this case the existence condition of the Mellin transform is $0 < \rho < 1$.. The strip in the complex plane such that $-p < \rho < -q$ is commonly known as *Fundamental Strip* (FS) of the Mellin transform. If $-q$ is lesser than $-p$ the Mellin transform and its inverse do not exist.

Equation (11.2) may be used in a discretized form as

$$f(x) \cong \frac{\Delta\eta}{2\pi} \sum_{k=-m}^{m} M_f(\gamma_k - 1) x^{-\gamma_k} \quad ; \quad \gamma_k = \rho + i\,k\,\Delta\eta \tag{11.4}$$

where $\Delta\eta$ is the discretization step along to the imaginary axis, $m\Delta\eta = \overline{\eta}$ is a cut-off value chosen in such a way that the contribution of terms of higher order than m do not produce sensible variations on $f(x)$. It is to be remarked that $M_f(\gamma - 1)$ is analytic

onto the fundamental strip, and is such that

$$M_f(\rho + i\,\eta - 1) = M_f^*(\rho - i\,\eta - 1) \tag{11.5}$$

where the star means complex conjugate. It follows that with simple manipulations the summation in (11.4) may be rewritten in a summation from 0 to m.

The Riesz fractional integral of a certain function $f(x)$ that is zero for $x < 0$, denoted as $(I^\gamma f)(x)$, is defined as

$$(I^\gamma f)(x) = \frac{1}{2v_c(\gamma)} \int_0^\infty f(\xi)|x - \xi|^{\gamma-1} d\xi; \quad \rho > 0, \rho \neq 1, 3, .. \tag{11.6}$$

where $v_c(\gamma) = \Gamma(\gamma)\cos\left(\gamma \frac{\pi}{2}\right)$ and $\Gamma(\cdot)$ is the Euler Gamma function. By comparing (11.1) and (11.6) it may be stated that the Mellin transform is related to Riesz fractional integral in $x = 0$, that is

$$2v_c(\gamma)(I^\gamma f)(0) = M_f(\gamma - 1) \tag{11.7}$$

Under this perspective the representation in (11.4) looks like a Taylor expansion because it involves an operator in zero and a (complex) power series on x; for more details see [33]. The main difference is that when a truncation on the classical Taylor series is performed, always the Taylor series diverges as x diverges, while no divergence problem occur using (11.4) since summation is performed along the imaginary axis and ρ remains fixed. Moreover, unless $f(x)$ belongs to the class C_∞ in zero, the various derivatives in zero may be divergent quantities and the Taylor expansion in such cases is meaningless. On the contrary the series expressed in (11.4) never diverges provided ρ belongs to the FS of the Mellin transform and then $f(x)$ is reproduced in the whole domain with the exception of the value in zero. With these simple information we can now solve the FPK equation by using Mellin transform theorem.

11.2.1 Use of CFMs to Construct Probability Density Functions

In the ensuing derivations, for simplicity sake's, we suppose that the PDF of a stochastic process $X(t)$, in the following denoted as $p_X(x, t)$, is symmetric, namely $p_X(x, t) = p_X(-x, t)$.

The Mellin transform of $p_X(x, t)$, denoted as $M_{p_X}(\gamma - 1)$, is given in the form

$$M_{p_X}(\gamma - 1, t) = \int_0^\infty p_X(x, t)x^{\gamma-1} dx = \frac{1}{2}E\left[|X(t)|^{\gamma-1}\right] \tag{11.8}$$

where $E[\cdot]$ means ensemble average. From this equation it may be stated that the Mellin transform of the PDF is strictly related to moments of the type $E\left[|X(t)|^{\gamma-1}\right]$.

According to (11.4) the discretized version of the inverse Mellin Transform is written for $x > 0$ in the equivalent forms

$$p_X(x,t) = \frac{1}{4b}\sum_{k=-m}^{m} E\left[|X(t)|^{\gamma_k-1}\right]x^{-\gamma_k} = \frac{1}{2b}x^{-\rho}\sum_{k=-m}^{m} M_{p_X}(\gamma_k-1,t)x^{-i\frac{k\pi}{b}};$$
$$\gamma_k = \rho + i\frac{k\pi}{b} \tag{11.9}$$

where $b = \pi/\Delta\eta$ and ρ belongs to the FS of $p_X(x,t)$. Since $p_X(x,t) \geq 0$ and the area of the PDF in $0 \div \infty$ is 1/2 then $\lim_{x\to\infty} p_X(x,t) = 0$. It follows that the fundamental strip of $p_X(x,t)$ always exists and, for $p_X(0,t) \neq 0$, it is $0 < \rho < u$. The value of u depends of the order of zero of the PDF at $x = \infty$. As an example for α-stable random variable the moments $E[|X|^{\beta}](\beta \in \Re)$ do not diverge only in the range $-1 < \beta < \alpha$ [33]. Then for such random variable the FS is $0 < \rho < \alpha + 1$. In general if for a given stochastic process the integer moments diverge starting from a certain value, say r, then the strictest FS is $0 < \rho < r + 1$.

An important issue of this representation of the PDF is the discretization of the inverse Mellin transform, more specifically the number m that define the number of CFMs to be used in order to efficiently represent the PDF. In order to properly define the parameter m, some considerations are necessary: (i) the choice of m strictly depends of $\Delta\eta$ since $m\Delta\eta = \bar{\eta}$ is the truncation of $M_p(\gamma-1)$ that in turns depends of the value of ρ selected; (ii) higher value of ρ, at a parity of the PDF at hands produces oscillations in $M_p(\gamma-1)$ as shown in Fig. 11.1 in which CFM are reported for different values of ρ ($\rho = 0.5$; $\rho = 10$). It follows that in order to properly discretize the inverse Mellin transform it is necessary of a smaller value of $\Delta\eta$ as ρ increase.

In the case of α-stable Lévy white noise the selection of ρ is obligated by the limitations of the FS of the Mellin transform and on the non-linearity. So because m and consequently $\Delta\eta$ depends on many parameters we can proceed with trial and error (two or three attempts are enough) or if we have a crude estimation on the

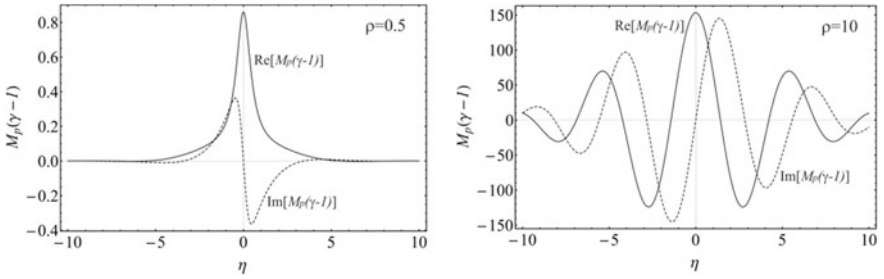

Fig. 11.1 CFMs of a Gaussian distribution with unitary variance and different values of ρ

PDF of the response at steady state by using approximate techniques (like stochastic linearization) then a preliminary choice of m may be readily performed. In quiescent systems, since in t = 0 all CFMs are zero and the tails of the PDF increase then the worst situation will remain the PDF at the steady state or when the scale attains the maximum value. It follows that as the PDF is well reproduced for the steady state or in correspondence of the maximum scale (or of the variance if it exists) then all the parameters (m and $\bar{\eta}$) may be used also in the transient zone.

11.3 Applications of CFMs for the Solution of FPK-Type Equation

In this section we will show how to solve the equations ruling the evolution of the PDF describing the motion of a spring-dashpot system (first-order differential equation) subjected to a Gaussian white noise (Fokker-Planck equation), to a-stable white noise (Fractional Fokker-Planck equation) and to Poissonian white noise (Kolomogorov-Feller equation). For all the three cases some numerical applications are also presented in order to show the accuracy of this approach.

11.3.1 Fokker-Planck Equation (Gaussian White Noise)

Let us suppose that the equation of motion of a (mass-less) non-linear system is given in the form

$$\begin{cases} \dot{X} = f(X,t) + W(t) \\ X(0) = X_0 \end{cases} \tag{11.10}$$

$W(t)$ is a normal zero mean white noise, formal derivative of the Brownian motion $B(t)$, $(dB(t)/dt = W(t))$ characterized by $E\left[dB^2(t)\right] = q\,dt$, being q the intensity of the white noise. In (11.10) it is assumed that $f(X,t) = -f(-X,t)$ is a deterministic non-linear function of the stochastic output process $X(t)$. X_0 is a random variable with assigned distribution $(p_X(x,0) = p_X(-x,0))$. Under these assumptions the output stochastic process has a symmetric distribution $p_X(x,t)$.

The Fokker-Planck equation, ruling the transition probability of $X(t)$, is written in the form

$$\begin{cases} \frac{\partial p_X(x,t)}{\partial t} = -\frac{\partial}{\partial x}(f(x,t)p_X(x,t)) + \frac{q}{2}\frac{\partial^2 p_X(x,t)}{\partial x^2} \\ p_X(x,0) = \overline{p_X}(x) \end{cases} \tag{11.11}$$

where the overbar means assigned PDF in $t = 0$.

The differential equations of integer moments may be obtained multiplying (11.11) by $x^k dx (k = 0, 1, \ldots, n)$, and integrating over $-\infty \div \infty$. The solution of the FPK equation in terms of integer moments cannot be obtained, unless $f(X,t) = cX$, since the set of differential equations is hierarchical. That is, the moment equation of an assigned order, say s, involves moments of higher order than s. Since fractional moments are able to return the PDF in the whole range (excluding the value in zero), one may wonder what happens when CFM are used instead of integer moments. In order to answer this question, we multiply (11.11) by $x^{\gamma-1}dx$ and integrating over the range $0 \div \infty$ yields

$$\frac{\partial M_{p_X}(\gamma-1,t)}{\partial t} = -\left[f(x,t)x^{\gamma-1}p_X(x,t)\right]_0^\infty + (\gamma-1)\int_0^\infty x^{\gamma-2}f(x,t)p_X(x,t)dx + \frac{q}{2}\left[\frac{\partial p_X(x,t)}{\partial x}x^{\gamma-1}\right]_0^\infty + -\frac{q}{2}(\gamma-1)\left[x^{\gamma-2}p_X(x,t)\right]_0^\infty + \frac{q}{2}(\gamma-1)(\gamma-2)\int_0^\infty x^{\gamma-3}p_X(x,t)dx \quad (11.12)$$

where the first, third and fourth term at the right-hand side of (11.12) come out from integration by parts.

Under the hypothesis that $X(t)$ is stable in distribution and moments up to the m-order are stable, by properly selecting $\rho > 2$, it may be easily demonstrated that the first, the third and the fourth term in (11.12) vanish. For more details see [14].

Next, let us suppose that $f(X,t) = -\sum_{j=1}^{n} c_j |X(t)|^{\beta_j} sgn(X(t)) \left(c_j > 0, \beta_j > 0\right)$, then the equation in terms of fractional moments is written as

$$\begin{cases} \frac{\partial M_{p_X}(\gamma-1,t)}{\partial t} = -(\gamma-1)\sum_{j=1}^{n} c_j M_{p_X}(\gamma+\beta_j-2,t) + \\ \qquad \frac{q}{2}(\gamma-1)(\gamma-2)M_{p_X}(\gamma-3,t); \quad \rho > 2 \\ M_{p_X}(\gamma-1,0) = \int_0^\infty x^{\gamma-1}\overline{p}_X(x)dx \quad \text{assigned} \end{cases} \quad (11.13)$$

This equation may be discretized for $\gamma_k = \rho + i\,k\frac{\pi}{b}$ so obtaining a set of $(2m+1)$ ordinary (linear) differential equations, being m the truncation of the discretized inverse Mellin transform of the PDF.

The main difficulty in solving such a set of differential equations is that the fractional moments are evaluated for different values of ρ. This problem is the analogue of the infinite hierarchy problem. Then at first glance it seems that the use of complex fractional moments does not open new breaks for the solution of the FPK equation. However, to overcome this drawback the following strategy can be adopted.

Since (11.9) remains valid for every value of ρ, provided it belongs to the FS, we equate (11.9) for two different values of ρ say $\rho_1 = \rho$ and $\rho_2 = \rho + \Delta\rho$, denoting as $M_{p_X}(\gamma_k^{(1)} - 1, t)$ and $M_{p_X}(\gamma_k^{(2)} - 1, t)$ the CFM evaluated in $\gamma_k^{(j)} = \rho_j + i\,k\Delta\eta$ $(j = 1, 2)$. Then multiplying such equation for $x^{-1/2}$ gives

$$x^{-1/2}\sum_{k=-m}^{m} M_{p_X}(\gamma_k^{(1)}-1,t)e^{-ik\frac{\pi}{b}\ln x} = x^{-(\Delta\rho+1/2)}\sum_{k=-m}^{m} M_{p_X}(\gamma_k^{(2)}-1,t)e^{-ik\frac{\pi}{b}\ln x};$$
$$x>0 \qquad (11.14)$$

It is to be emphasized that equality in (11.14) strictly holds for $x>0$, since zero singularities appear. Now it is assumed that $M_{p_X}(\gamma_k^{(2)}-1,t)$ are already known and thus it is possible to evaluate $M_{p_X}(\gamma_k^{(1)}-1,t)$, i.e., to evaluate $M_{p_X}(\gamma-1,t)$ for different values of ρ. Because (11.9) is an approximation then (11.14) is to be satisfied in a weak sense in the interval $x_1>0, x_2 \gg x_1$, i.e.,

$$\int_{x_1}^{x_2}\frac{1}{x}\left\{\left[\sum_{k=-m}^{m} M_{p_X}(\gamma_k^{(1)}-1,t)e^{-ik\frac{\pi}{b}\ln x} - x^{-\Delta\rho}\sum_{k=-m}^{m} M_{p_X}(\gamma_k^{(2)}-1,t)e^{-ik\frac{\pi}{b}\ln x}\right]\times\right.$$
$$\left.\times\left[\sum_{k=-m}^{m} M^*_{p_X}(\gamma_k^{(1)}-1,t)e^{ik\frac{\pi}{b}\ln x} - x^{-\Delta\rho}\sum_{k=-m}^{m} M^*_{p_X}(\gamma_k^{(2)}-1,t)e^{ik\frac{\pi}{b}\ln x}\right]\right\}dx =$$
$$= min(M_{p_X}(\gamma_k^{(1)}-1,t)) \qquad (11.15)$$

Now performing the following change of variable

$$\xi=\ln x,\quad d\xi=\frac{dx}{x};\ \xi_j=\ln x_j,\quad j=1,2 \qquad (11.16)$$

In order to find $M_{p_X}(\gamma_s^{(1)}-1,t)$ as a linear combination of $M_{p_X}(\gamma_k^{(2)}-1,t)$ we perform variations and instead of putting $x_1=0, x_2=\infty$, we put $x_1=e^{-b}$ and $x_2=e^b$: In this way three goals are achieved: (i) the interval $e^{-b}\div e^b$ is very large since $b=\pi/\Delta\eta$ and $\Delta\eta$ is of order $0.3\div 0.5$ then the interval $e^{-b}\div e^b$ is of order $e^{-10}\div e^{10}$ (for $\Delta\eta=0.314$) or $e^{-6.28}\div e^{6.28}$ (for $\Delta\eta=0.5$); (ii) the value $x_1=0$ is excluded, that is the main problem to perform variations in (11.15) since in zero a divergence occurs; and (iii) with the choice $e^{-b}\div e^b$ the integral (11.15), taking into account the position of (11.16), is in the range $-b\div b$.

It follows that with the choice of the interval $e^{-b}\div e^b$, (11.15), with the positions in (11.16), is written as

$$\int_{-b}^{b}\left\{\left[\sum_{k=-m}^{m} M_{p_X}(\gamma_k^{(1)}-1,t)e^{-ik\frac{\pi}{b}\xi} - e^{-\Delta\rho\xi}\sum_{k=-m}^{m} M_{p_X}(\gamma_k^{(2)}-1,t)e^{-ik\frac{\pi}{b}\xi}\right]\times\right.$$
$$\left.\left[\sum_{k=-m}^{m} M^*_{p_X}(\gamma_k^{(1)}-1,t)e^{ik\frac{\pi}{b}\xi} - e^{-\Delta\rho\xi}\sum_{k=-m}^{m} M^*_{p_X}(\gamma_k^{(2)}-1,t)e^{ik\frac{\pi}{b}\xi}\right]\right\}d\xi =$$
$$= min(M_{p_X}(\gamma_k^{(1)}-1,t)) \qquad (11.17)$$

with the orthogonality condition of $e^{ik\frac{\pi}{b}\xi}$ and after minimization we get

$$2bM_{p_X}(\gamma_s^{(1)}-1,t)=\sum_{k=-m}^{m}M_{p_X}(\gamma_k^{(2)}-1,t)a_{ks}(\Delta\rho) \tag{11.18}$$

where

$$a_{ks}(\Delta\rho)=\int_{-b}^{b}e^{-\Delta\rho\xi}e^{-i(k-s)\frac{\pi}{b}\xi}d\xi=\frac{2b\sin[\pi(k-s)-ib\Delta\rho]}{\pi(k-s)-ib\Delta\rho} \tag{11.19}$$

From (11.18) we recognize that $M_{p_X}(\gamma_s^{(1)}-1,t)$ may be obtained as a linear combination of $M_{p_X}(\gamma_k^{(2)}-1,t)$, i.e., it is possible to solve FPK equation by using Mellin transform.

Since in (11.13) we have $M_{p_X}(\gamma_s-1,t)$, $M_{p_X}(\gamma_s+\beta-2,t)$, and $M_{p_X}(\gamma_s-3,t)$, then we select the initial value of $\rho>2$. In this manner we are sure that $Re(\gamma_s-2)>0$ is inside the FS. Thus, taking into account (11.13) and (11.18), yields

$$\begin{aligned}M_{p_X}(\gamma_s+\beta-2,t)&=\frac{1}{2b}\sum_{k=-m}^{m}M_{p_X}(\gamma_k-1,t)a_{ks}(1-\beta)\\M_{p_X}(\gamma_s-3,t)&=\frac{1}{2b}\sum_{k=-m}^{m}M_{p_X}(\gamma_k-1,t)a_{ks}(2)\end{aligned} \tag{11.20}$$

By inserting these equations in (11.13) for $\gamma=\gamma_s$ $(s=-m,..,0,..m)$ we get a set of complex ordinary differential equations in the unknowns $M_{p_X}(\gamma_s-1,t)$.

If the system of differential equations is directly implemented using a computer program the solution is not correct because we need of another information, i.e., the area of the PDF into the interval $e^{-b}\div e^{b}$ will be 1/2. This constraint may be enforced very easily. Taking into account (11.9), we get

$$\frac{1}{2b}\sum_{k=-m}^{m}M_{p_X}(\gamma_k-1,t)\int_{e^{-b}}^{e^{b}}x^{-\gamma_k}dx=\frac{1}{2} \tag{11.21}$$

This equation gives the following information in the Mellin transform domain

$$M_{p_X}(\gamma_0-1,t)=\frac{1-\rho}{e_0}\left[b-\sum_{\substack{k=-m\\k\neq0}}^{m}\left(\frac{e_k}{1-\gamma_k}\right)M_{p_X}(\gamma_k-1,t)\right] \tag{11.22}$$

where

$$e_0=\left(e^{b}\right)^{1-\rho}-\left(e^{-b}\right)^{1-\rho} \tag{11.23}$$

and

$$e_k = \left(e^{b}\right)^{1-\gamma_k} - \left(e^{-b}\right)^{1-\gamma_k} \tag{11.24}$$

In this manner, a set of 2 m linear (complex) differential equations is obtained, which involves only CFMs evaluated in the same value of ρ ruling the evolution of the CFMs. The *s-th* equation is

$$\begin{aligned}\frac{\partial M_{p_X}(\gamma_s-1,t)}{\partial t} = -(\gamma_s-1)\sum_{j=1}^{n} c_j \Bigg[\sum_{\substack{k=-m \\ k\neq 0}}^{m} M_{p_X}(\gamma_k-1,t)a_{ks}(1-\beta_j) + \\ + \frac{1-\rho}{e_0} a_{0s}(1-\beta_j)\left(b - \sum_{\substack{k=-m \\ k\neq 0}}^{m} M_{p_X}(\gamma_k-1,t)\frac{e_k}{1-\gamma_k}\right)\Bigg] + \\ + \frac{q}{2}(\gamma_s-1)(\gamma_s-2)\Bigg[\sum_{\substack{k=-m \\ k\neq 0}}^{m} M_{p_X}(\gamma_k-1,t)a_{ks}(2) + \\ + \frac{1-\rho}{e_0} a_{0s}(2)\left(b - \sum_{\substack{k=-m \\ k\neq 0}}^{m} M_{p_X}(\gamma_k-1,t)\frac{e_k}{1-\gamma_k}\right)\Bigg] \qquad s=-m,\ldots,-1,1,\ldots,m\end{aligned} \tag{11.25}$$

Equation (11.25) constitute a set of linear coupled ordinary differential equations in the unknown $M_{p_X}(\gamma_s - 1, t)$ that may be easily solved by inserting the initial conditions given in (11.13). Moreover $M_{p_X}(\gamma_0 - 1, t)$ in (11.25) is given in (11.22). Thus (11.25) is not homogeneous and the steady state solution may be readily found. If the system is quiescent at $t = 0$, that is $\bar{p}_X(x) = \delta(x)$, then all $M_{p_X}(\gamma_s - 1, 0)$ are zeros.

System of (11.25) may be reduced to only m equations by taking into account that $M_p(\gamma_s - 1, t) = M_p^*(\gamma_{-s} - 1, t)$.

In order to show the capability of the method, we suppose that the nonlinear function in (11.10) is $f(X, t) = -c|X|^{\beta}\mathrm{sgn}(X)$, with $c > 0$ and $\beta \geq 0$. Moreover, let us suppose that $\bar{p}_X(x) = \delta(x)$, that is the system is quiescent at $t = 0$. For this system for the case $\beta = 1$ (linear system) the transient response is already known and is given in the form

$$p_X(x,t) = \frac{1}{\sqrt{2\pi}\sigma(t)} exp\left(-\frac{x^2}{2\sigma^2(t)}\right) \tag{11.26}$$

where

$$\sigma^2(t) = \frac{q}{2c}(1 - e^{-2ct}) \tag{11.27}$$

while if $\beta \neq 1$ the stationary solution is known in analytical form and it reads

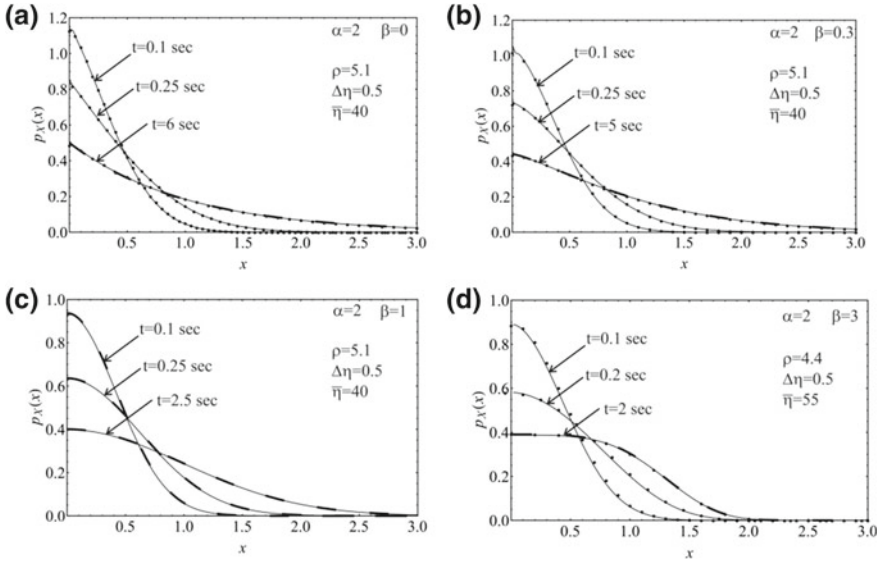

Fig. 11.2 Probability density function for different values of β; continuous line solution in terms of CFM, dotted line Monte Carlo simulation; dashed line exact solution

$$p_X(x, \infty) = \nu \exp\left(-\frac{2c|x|^{\beta+1}}{(\beta+1)q}\right) \tag{11.28}$$

where ν is a normalization constant such that $\int_0^\infty p_X(x, \infty)dx = 1/2$.

In Fig. 11.2 the PDF of the nonlinear system given by the procedure outlined above is contrasted with the solution obtained by the Monte Carlo simulation with 10^6 samples, for different values of β ($\beta = 0,\ \beta = 0.3,\ \beta = 1,\ \beta = 3$). In particular for $\beta = 1$ also the exact solution given in (11.26) is plotted (dashed line) at various time instants. Further in Fig. 11.2a, b and d also the steady state solution is plotted in dashed line and contrasted with the results obtained by CFMs. During the transitory phase the comparison is made with the PDF obtained by Monte Carlo simulation. The value of c selected for these applications is $c = 1$ and $q = 2$. The various parameters ($\rho,\ \Delta\eta,\ \bar{\eta}$) are given in the figures.

11.3.2 Fractional Fokker-Planck Equation (α-Stable White Noise)

Let us now suppose that the same mechanical system of the previous section (spring-dashpot system) is subjected to an α-stable white noise $W_\alpha(t)$. Without loss of generality we assume that $W_\alpha(t)$, formal derivative of the Lévy α-stable process $L_\alpha(t)$, is a symmetric α-stable ($S_\alpha S$) process.

The corresponding non-linear Langevin equation may be written as follows

$$\begin{cases} \dot{X} = f(X,t) + W_\alpha(t) \\ X(0) = X_0 \end{cases} \tag{11.29}$$

The Itô equation associated to (11.29) may be written in the form

$$dX(t) = f(X,t)dt + dL_\alpha(t) \tag{11.30}$$

where the characteristic function (CF) of $dL_\alpha(t)$ is in the form

$$\phi_{dL_\alpha}(t) = \exp(-dt\sigma|\theta|^\alpha) \tag{11.31}$$

where σ is the scale factor (not the standard deviation) and α is the stability index. The equation ruling the evolution of the PDF of the output process is known as Fractional Fokker-Planck (FPP) equation and is given in the form

$$\begin{cases} \frac{\partial p_X(x,t)}{\partial t} = -\frac{\partial}{\partial x}(f(x,t)p_X(x,t)) + \sigma^\alpha D_X^\alpha(p_X(x,t)) \\ p_X(x,0) = \overline{p_X}(x) \end{cases} \tag{11.32}$$

where the symbol $D_X^\alpha(\cdot)$ denotes the Riesz fractional derivative defined as

$$D_x^\alpha(u(x,t)) = \begin{cases} -\frac{1}{2\cos(\pi\alpha/2)}\left[D_{x^+}^\alpha(u(x,t)) + D_{x^-}^\alpha(u(x,t))\right]; & \alpha \neq 1 \\ -\frac{d}{dx}\mathcal{H}[u(x,t)]; & \alpha = 1 \end{cases} \tag{11.33}$$

In (11.33) $D_{x^+}^\alpha$ and $D_{x^-}^\alpha$ are the left and right Riemann-Liouville fractional derivatives that may be written in the form

$$\begin{aligned} D_{x^+}^\alpha(u(x,t)) &= \frac{1}{\Gamma(n-\alpha)}\frac{d^n}{dx^n}\int_{-\infty}^{x}\frac{u(\xi,t)}{(x-\xi)^{\alpha-n+1}}d\xi \\ D_{x^-}^\alpha(u(x,t)) &= \frac{1}{\Gamma(n-\alpha)}\left(-\frac{d}{dx}\right)^n\int_{x}^{\infty}\frac{u(\xi,t)}{(\xi-x)^{\alpha-n+1}}d\xi \end{aligned} \tag{11.34}$$

where $n = [\alpha] + 1$ and $[\alpha]$ is the integer part of α and $\mathcal{H}[\cdot]$ is the Hilbert transform operator defined as

$$\mathcal{H}[u(x,t)] = \frac{1}{\pi}\mathcal{P}\int_{-\infty}^{\infty}\frac{u(\xi,t)}{|x-\xi|}d\xi \tag{11.35}$$

being $\mathcal{P}$ the Cauchy principal value.

In order to solve the FFP equation the same approach of the previous section is adopted. We suppose that $f(X,t) = -\sum_{j=1}^{r} c_j |X(t)|^{\beta_j} sgn(X(t))$ $(c_j > 0,\ \beta_j > 0)$ and we perform Mellin transform of (11.32):

$$\begin{aligned}\frac{\partial M_p(\gamma-1,t)}{\partial t} &= \sum_{j=1}^{r} c_j \left[x^{\gamma-1+\beta_j} p_X(x,t)\right]_0^{\infty} - (\gamma-1)\sum_{j=1}^{r} c_j M_p(\gamma-2+\beta_j,t) + \\ &- \sum_{k=0}^{n-1} \frac{\Gamma(\gamma-1+k)}{\Gamma(\gamma-1)} \left[\frac{d^{n-k-1}}{dx^{n-k-1}} \left(\int_{-\infty}^{x} \frac{p_X(\xi,t)}{(x-\xi)^{\alpha-n+1}} d\xi + \right.\right. \\ &\left.\left. +(-1)^n \int_{x}^{\infty} \frac{p_X(\xi,t)}{(\xi-x)^{\alpha-n+1}} d\xi \right) x^{\gamma-k-1} \right]_0^{\infty} - \sigma^{\alpha} \frac{v_c(\gamma)}{v_c(\gamma-\alpha)} M_p(\gamma-1-\alpha,t) \end{aligned} \tag{11.36}$$

The terms in square brackets, coming from integration by parts, vanish by properly selecting the value of ρ and (11.36) reduces to

$$\frac{\partial M_p(\gamma-1,t)}{\partial t} = -(\gamma-1)\sum_{j=1}^{r} c_j M_p(\gamma-2+\beta_j,t) - \sigma^{\alpha} \frac{v_c(\gamma)}{v_c(\gamma-\alpha)} M_p(\gamma-1-\alpha,t) \tag{11.37}$$

By evaluating (11.36) for different values in $2m+1$ values $\gamma_k = \rho + ik\Delta\eta$, a set of ordinary linear differential equations is obtained. In order to solve this system, it is necessary to write all CFMs in terms of CFMs of one order. Then, following the results of the previous section, we may write:

$$M_{p_X}(\gamma_s+\beta_j-2,t) = \frac{1}{2b}\sum_{k=-m}^{m} M_{p_X}(\gamma_k-1,t) a_{ks}(1-\beta_j) \tag{11.38}$$

$$M_{p_X}(\gamma_s-1-\alpha,t) = \frac{1}{2b}\sum_{k=-m}^{m} M_{p_X}(\gamma_k-1,t) a_{ks}(\alpha) \tag{11.39}$$

By inserting (11.38) and (11.39) into (11.37) and enforcing the normalization condition (11.21)–(11.22) a solvable set of 2 m linear differential equations ruling the time evolution of CFMs is obtained. The *s-th* equation is written as

$$\begin{aligned}\frac{\partial M_p(\gamma_s-1,t)}{\partial t} &= -(\gamma-1)\sum_{j=1}^{r} c_j \left(\sum_{\substack{k=-m \\ k\neq m}}^{m} M_p(\gamma_k-1,t)\, a_{ks}(1-\beta_j) + \right. \\ &\left. + \frac{1-\rho}{e_0} a_{0s}(1-\beta_j) \left(b - \sum_{\substack{k=-m \\ k\neq 0}}^{m} M_{p_X}(\gamma_k-1,t) \frac{e_k}{1-\gamma_k} \right) \right) + \\ &- \sigma^{\alpha} \frac{v_c(\gamma)}{v_c(\gamma-\alpha)} \left(\sum_{\substack{k=-m \\ k\neq m}}^{m} M_p(\gamma_k-1,t) a_{ks}(\alpha) + \frac{1-\rho}{e_0} a_{0s}(\alpha) \left(b - \sum_{\substack{k=-m \\ k\neq 0}}^{m} M_{p_X}(\gamma_k-1,t) \frac{e_k}{1-\gamma_k} \right) \right) \end{aligned} \tag{11.40}$$

The solution of FFP in terms of CFMs has been tested with different values of the stability index α and with different order of non-linearity β. The case $\alpha = 2$ corresponds to the case of Gaussian white noise that has been treated in the previous section, hence for the sake of brevity it is not repeated in the following. The solution in terms of CFMs have been contrasted with analytical solutions, when available, and with results of Monte Carlo simulations with 10^6 samples.

Consider

- $\alpha = 1.5$

This value of α has been investigated as a general case in the range $1 \div 2$. When stability index is less than 2 the fundamental strip depends on the values of α and β, because of the decay of the PDF for $x \to \infty$. In particular, it has been demonstrated by Chechkin et al. [6] that for α-stable input, the tails of the PDF of the output decay as a power law x^{-u}, being $u = \alpha + 1$ for the linear dashpot-system ($\beta = 1$) and $u = \alpha + 3$ for the quartic system ($\beta = 3$), so in both cases $u = \alpha + \beta$. This allows us to do some considerations on the FS that is unknown. These considerations resulted in the choice of ρ in the range $0 \div 1 + \alpha$. From this descends that, since in the Mellin transform of FFP equation there are CFMs evaluated for different value of ρ, we cannot solve the system with some values of $\beta > 1.7$ because CFMs from the drift term and from diffusive term are evaluated in value of ρ outside the FS, for more details see [1]. In the following, results for $\alpha = 1.5$ are reported in Fig. 11.3.

- $\alpha = 1$

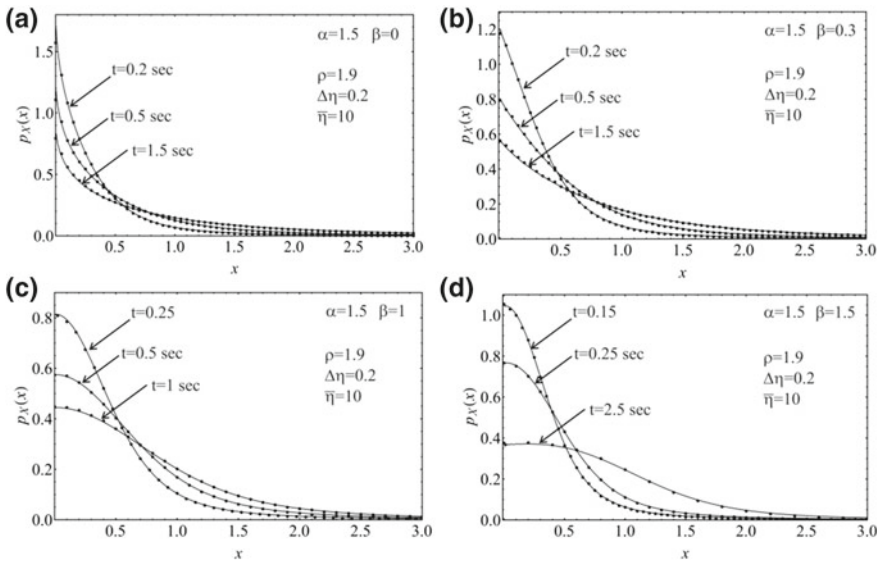

Fig. 11.3 Probability density function for different values of β; continuous line solution in terms of CFM, dotted line Monte Carlo simulation

This is the case when the input is a Cauchy process. In this case the steady state solution for $\beta = 1$ is known as

$$p_X(x, \infty) = \frac{\sigma c}{\pi(\sigma^2 + c^2 x^2)} \tag{11.41}$$

Figure 11.4 shows the response pdf for various value for β at different time instant.

- $\alpha = 0.8$

This case is taken as general case in the range $0 \leq \alpha \leq 1$. In the following result for various values for β at different instants are shown in Fig. 11.5.

- $\alpha = 0.5$

In this case the input is a symmetric Lévy process. For this value of α we are actually able to solve only the linear case for which the steady state solution may be obtained in the following form

$$p_X(x, \infty) = \sqrt{\frac{\bar{\sigma}}{2\pi|x|^3}}\left(\cos\left(\frac{\bar{\sigma}}{4x}\right)\left(\frac{1}{2} - F_c\left(\sqrt{\frac{\bar{\sigma}}{2\pi|x|}}\right)\right) + \right.$$
$$\left. + \sin\left(\frac{\bar{\sigma}}{4x}\right)\left(\frac{1}{2} - F_s\left(\sqrt{\frac{\bar{\sigma}}{2\pi|x|}}\right)\right)\right) \tag{11.42}$$

where $F_c(\cdot)$ and $F_s(\cdot)$ are the Fresnel integrals defined as follow

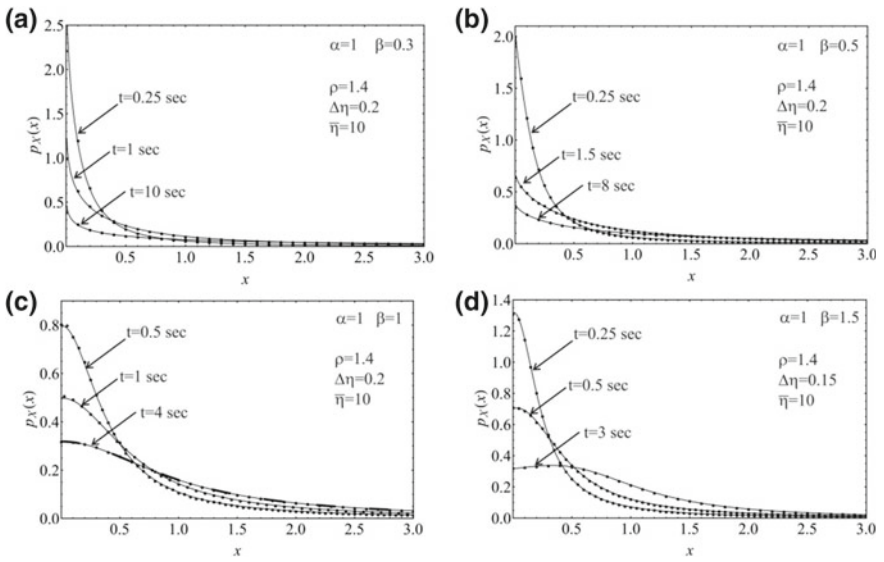

Fig. 11.4 Probability density function for different values of β; continuous line solution in terms of CFM, dotted line Monte Carlo simulation, dashed line exact solution

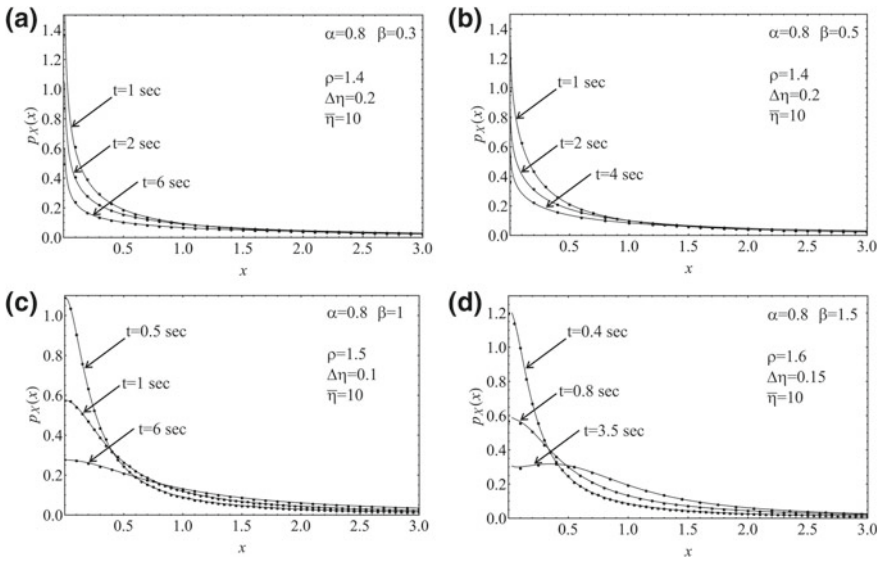

Fig. 11.5 Probability density function for different values of β; continuous line solution in terms of CFM, dotted line Monte Carlo simulation

$$F_c(x) = \int_0^x \cos\left(\frac{\pi t^2}{2}\right) dt$$
$$F_s(x) = \int_0^x \sin\left(\frac{\pi t^2}{2}\right) dt \tag{11.43}$$

and $\bar{\sigma}$ is the scale factor of the output defined as

$$\bar{\sigma} = \sigma\left(\frac{c}{2}\right)^{-2} \tag{11.44}$$

The following Fig. 11.6 shows the results for $\beta = 1$.

- Trend of the PDF at ∞

Figure 11.7a, b show logarithmic plots of the stationary solution of the FFP equation for the linear case ($\beta = 1$) and for two different values of α 1 and 0.5, respectively, for which the stationary solution is known in analytical form. From these figures it is possible to observe that the solution provided by the proposed method coalesces with the exact one also for large values of x. This fact is very important because other methods of solution fail in the description of the long tails of the PDF.

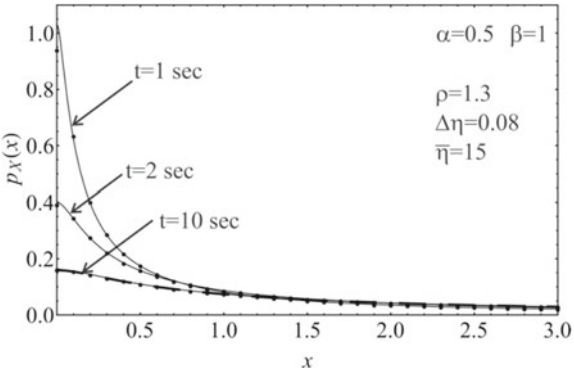

Fig. 11.6 Probability density function for $\beta = 1$ and $\alpha = 0.5$; continuous line solution in terms of CFM, dotted line Monte Carlo simulation, dashed line exact stationary solution

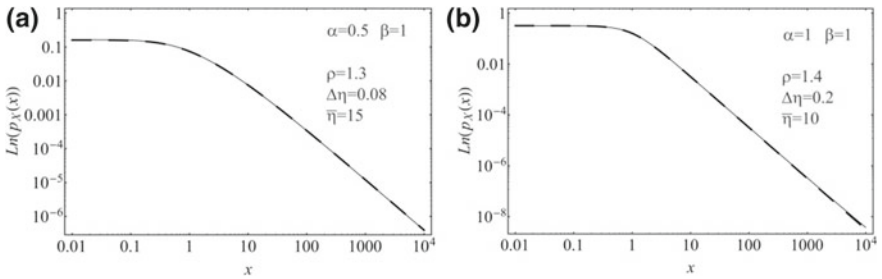

Fig. 11.7 Log-Log plot of the stationary solution for $\beta = 1$ and $\alpha = 0.5, 1$ contrasted with exact steady state solution

11.3.3 Kolmogorov-Feller Equation (Poissonian White Noise)

Let us now consider the case of a non-linear system, as in (11.10), in which, however, $W(t)$ is now a Poisson white noise process. This process can be assumed as constituted by a train of impulses of random amplitude Y, with assigned PDF $p_Y(y, t)$. The impulse occurrence is distributed in time according to a Poisson law. Thus, each impulse Y_k occurs at a time instant T_k, with random independent distribution T. Under these assumptions the Poisson white noise $W(t)$ is given by

$$W(t) = \sum_{k=1}^{N(t)} Y_k \, \delta(t - T_k) \tag{11.45}$$

where $\delta(\cdot)$ is the Dirac's delta and $N(t)$ is a Poisson counting process giving the number of impulses in $0 \div t$.

In this case, the equation governing the evolution of the transition probability of $X(t)$ is the so-called Kolmogorv-Feller (KF) equation, which can be written as

$$\begin{cases} \dfrac{\partial p_X(x,t)}{\partial t} = -\dfrac{\partial}{\partial x}(f(x,t)p_X(x,t)) - \lambda(t)p_X(x,t) + \lambda(t)\displaystyle\int_{-\infty}^{\infty} p_Y(\xi)\; p_X(x-\xi,t)d\xi \\ p_X(x,0) = \overline{p_X}(x) \end{cases} \tag{11.46}$$

Note that, the drift term in (11.46) is identical to the corresponding one in the case of normal white noise input (FPK equation) in (11.11). On the other hand, the diffusive expression (second and third term at the right-hand side of (11.46)) contains a convolution integral instead of the second derivative of the PDF.

Next, assuming that also $p_Y(y)$ has a symmetric distribution, i.e., the response PDF is symmetric, and taking into account (11.4) the discretized version of the Mellin Transform of $p_X(x-\xi,t)$ is

$$p_X(x-\xi,t) \cong \frac{1}{2b}\sum_{k=-m}^{m} \mathcal{M}_{p_X}(\gamma_k - 1, t)\,|x-\xi|^{-\gamma_k}; \quad \gamma_k = \rho + i\frac{k\pi}{b} \tag{11.47}$$

Further, following the procedure described in Sect. 11.3.1, and after some algebra, yields the equation evaluated for $\gamma_s = \rho + i\,s\,\Delta\eta$ as

$$\begin{aligned} \frac{\partial M_{p_X}(\gamma_s - 1, t)}{\partial t} &= -\Big[f(x,t)p_X(x,t)x^{\gamma_s - 1}\Big]_0^{\infty} + (\gamma_s - 1)\int_0^{\infty} f(x,t)p_X(x,t)x^{\gamma_s - 2}dx + \\ &- \lambda M_{p_X}(\gamma_s - 1, t) + \frac{\lambda}{b}\sum_{k=-m}^{m} M_{p_X}(\gamma_k - 1, t)\,\nu_c(1-\gamma_k)\mu_{ks}(t);\; s = -m, \ldots, 0, \ldots, m \end{aligned} \tag{11.48}$$

where

$$\mu_{ks}(t) = \int_0^{\infty} \big(\mathrm{I}^{1-\gamma_k} p_Y(y,t)\big)x^{\gamma_s - 1}dx \tag{11.49}$$

which represents the Mellin transform of the Riesz fractional integral of the function $p_Y(y,t)$, defined as

$$(\mathrm{I}^{\gamma} p_Y)(y,t) = \frac{1}{2\nu_c(\gamma)}\int_{-\infty}^{\infty} \frac{p_Y(\xi,t)}{|y-\xi|^{1-\gamma}}d\xi; \quad \rho \neq 1, 3, \ldots \tag{11.50}$$

Now consider again the nonlinear function of the form

$$f(X,t) = -c|X|^{\beta} sgn(X),\;\; \beta \geq 0,\;\; c > 0,$$

then if $\beta + \rho - 1 > 0$ (that is $\rho > 1 - \beta$), the first term at the right hand side of (11.48) vanishes leading to the equation of CFMs in the form

$$\frac{\partial M_{p_X}(\gamma_s - 1, t)}{\partial t} = -c(\gamma_s - 1) M_{p_X}(\gamma_s + \beta - 2, t) - \lambda M_{p_X}(\gamma_s - 1, t) + \\ + \frac{\lambda}{b} \sum_{k=-m}^{m} M_{p_X}(\gamma_k - 1, t)\, v_c(1 - \gamma_k) \mu_{ks}(t); \quad s = -m, \ldots, 0, \ldots, m \tag{11.51}$$

Further, taking into account the condition in (11.22), yields

$$\frac{\partial M_{p_X}(\gamma_s - 1, t)}{\partial t} = -c(\gamma_s - 1) \sum_{\substack{k=-m \\ k \neq 0}}^{m} M_{p_X}(\gamma_k - 1, t)\, a_{ks}(1 - \beta) - \lambda M_{p_X}(\gamma_s - 1, t) + \\ + \frac{\lambda}{b} \sum_{\substack{k=-m \\ k \neq 0}}^{m} M_{p_X}(\gamma_k - 1, t)\, v_c(1 - \gamma_k) \mu_{ks}(t) - c(\gamma_s - 1) \frac{1 - \rho}{e_0} a_{0s} \times \\ \times \left(b - \sum_{\substack{k=-m \\ k \neq 0}}^{m} M_{p_X}(\gamma_k - 1, t) \frac{e_k}{1 - \gamma_k} \right) + \\ + \frac{\lambda}{b} \frac{1 - \rho}{e_0} v_c(1 - \gamma_0) \mu_{0s}(t) \left(b - \sum_{\substack{k=-m \\ k \neq 0}}^{m} M_{p_X}(\gamma_k - 1, t) \frac{e_k}{1 - \gamma_k} \right); \quad s = -m \div m\,;\ s \neq 0 \tag{11.52}$$

In this manner, a set of $2\,m$ linear (complex) differential equations is obtained, which involves only CFMs evaluated in the same value of ρ.

In order to show the accuracy of the method, consider the non-linear system with $c = 0.2$ and $\beta = 0.6$. Further, let the assigned PDF at the initial time instant be given as

$$\bar{p}_X(x) = \frac{1}{\sqrt{2\pi}\sigma_0} \exp\left(-\frac{x^2}{2\sigma_0^2} \right) \tag{11.53}$$

and the PDF of the impulse amplitude be

$$p_Y(y) = \frac{1}{\sqrt{2\pi}\sigma_y} \exp\left(-\frac{y^2}{2\sigma_y^2} \right) \tag{11.54}$$

with $\lambda(t) = \lambda = 1$, $\sigma_0 = 1$ and $\sigma_y = 0.5$.

Figure 11.8 shows the evolution of the response PDF of the system. Specifically, the system in (11.52) is solved assuming $\rho = 0.95$, $\Delta\eta = 0.5$ and a cut-off value $\bar{\eta} = 50$ (thus $m = 100$). Solution obtained by the proposed procedure is compared with MCS data, using 40000 samples.

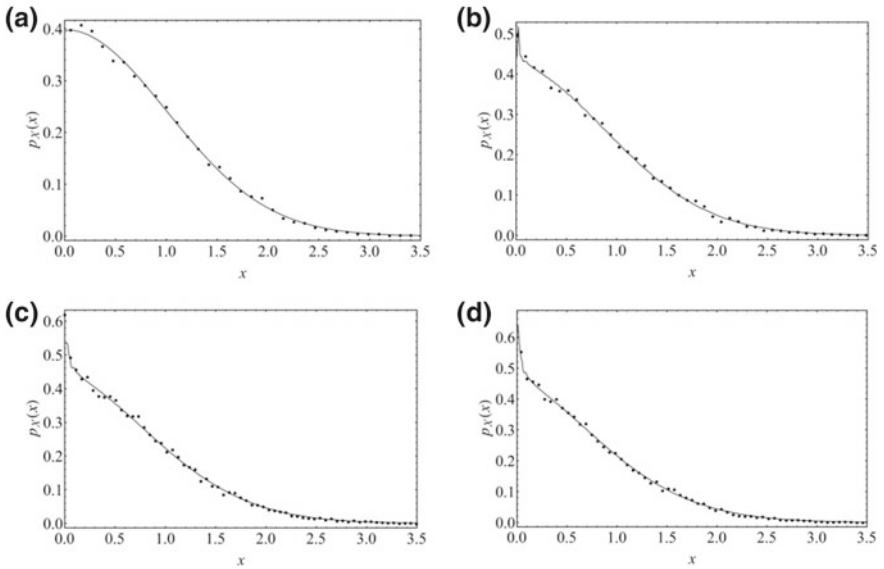

Fig. 11.8 Probability density function at various time instant; continuous line solution in terms of CFM, dots Monte Carlo simulation: **a** t = 0 s; **b** t = 0.5 s; **c** t = 1 s; **d** t = 1.5 s

11.4 PDF Representation Through CFMS Versus Integer Moments

In this section an emphasis is given to the comparison between the capability of integer order moments and CFMs to efficiently describe PDF and to solve FP-type equations. The expression of PDF in terms of CFMs reminds that one in terms of cumulants of integer order j K_j in the form at steady state condition as [19]

$$p_x(x) \cong \frac{1}{\sqrt{2\pi}\sigma} \exp\left[-\frac{(x-\mu)^2}{2\sigma^2}\right]\left(1+\sum_{j=3}^{m}\frac{K_j(-1)^j}{j!\sigma^j}H_j\left(\frac{x-\mu}{\sigma^2}\right)\right) \quad (11.55)$$

being σ the standard deviation, μ the mean, $H_j(x)$ the probabilistic Hermite polynomials and K_j the cumulants of order j which are related to the integer moments through the following relation

$$E[X^j] = K_j + \sum_{r=1}^{j-1}\frac{(j-1)!}{r!(j-1-r)!}K_{j-r}E[X^r] \quad (11.56)$$

With the above expression the PDF of the system response is approximated with the Gram-Charlier series. However, as it is well known, such a series can be inconsis-

tent with probability theory, e.g., negative probabilities may result. Moreover another problem related to this expression is the *jth*-order hierarchy truncation method.

In fact, the cumulants K_j are written once all integer moments $E\left[X(t)^j\right]$ are known solving the following system of differential equation

$$\dot{E}\left[X(t)^j\right] = (j)\int_0^\infty x^{k-1} f(x,t) p_X(x,t) dx + \frac{q}{2}(j)(j-1)E\left[X(t)^{j-2}\right] \quad (11.57)$$

Such a strategy belongs to the moment equation (ME) approach, proposed in 1978 [3] as an alternative method to Monte Carlo approach. If on one hand the ME method requires much less computation involving the solution of a system of coupled deterministic ordinary differential equations, on the other hand the disadvantage of the ME is that, unless for linear systems or special case of nonlinear ones, the differential equations for moments of a given order will contain terms involving higher-order moments leading to an infinite hierarchy of coupled equations requiring a closure scheme-procedure. Then, the *jth*-order hierarchy truncation will require approximations for the *(j + 1)th*- and *(j + 2)th*-order moments.

At this point, some important remarks come out:

(i) Although the system (11.57) is very similar to system (11.13) (setting $(\gamma - 1) =$ j) the hierarchy problem does not in the latter case.
(ii) At first glance the required evaluation of CFMs in different values of ρ may mislead. However, if one thinks that the same requirement occurs for linear systems, it will be clear that this is not a closure scheme procedure.

11.4.1 Numerical Applications

Let the nonlinear function $f(X,t)$ in (11.10) be given in the form $f(X,t) = -c_1 X - c_2|X|^\beta \text{sgn}(X)$ with $\beta > 0$. Further let the assigned PDF in zero be $\bar{p}(x) = \delta(x)$, that is the system is quiescent in $t = 0$. In order to compare the accuracies of the proposed and integer moments approach, the case of a bimodal PDF is considered. Thus, let $c_1 < 0$, $c_2 > 0$ and $\beta = 3$ (quartic system). Note that in this case the steady state PDF is known in closed form as

$$p_X(x,\infty) = \nu \exp\left[\frac{1}{2q}\left(x^2 - \frac{x^4}{2}\right)\right] \quad (11.58)$$

in which ν is a normalization constant such that $\int_0^\infty p_X(x,\infty)\, dx = 1/2$.

As far as the Gram-Charlier series expansion in (11.55) is concerned, the equation of integers moments for the steady state case can be particularized as

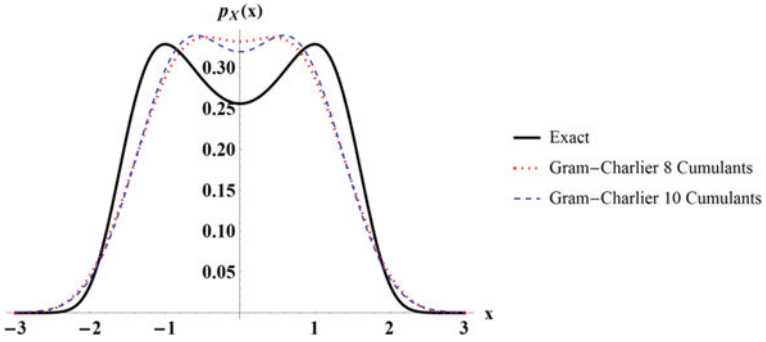

Fig. 11.9 Comparison among the Exact steady state PDF (black line) and Gram-Charlier series expansion with 8 cumulants (red dotted line) and 10 cumulants (blue dashed line)

$$-kc_1 E[X^k] - kc_2 E[X^{k-1+\beta}] + \frac{q}{2}k(k-1)E[X^{k-2}] = 0 \tag{11.59}$$

Note that this equation cannot be solved since an infinite order hierarchy problem appears. However, the aforementioned issue can be circumvented by expressing integer moments in terms of cumulants through (11.56) and considering equal to zero cumulants of order $n > \tilde{m}$ with $\tilde{m}$ arbitrary.

Figure 11.9 shows a comparison among the exact steady state PDF and the PDF obtained through (11.55), for the case $c_1 = -0.5$ and $c_2 = 0.5$, considering two different values of $\tilde{m}$.

As it can be observed from this figure, as the number of cumulants increases, the Gram-Charlier expansion does not lead to the exact solution and even considering 10 cumulants the approximated PDF is rather different from the exact steady state solution $p_X(x, \infty)$.

On the other hand, as far as the series form of the PDF through CFMs is concerned, for the system under consideration the equation ruling the evolution of the CFMs is explicitly given as

$$\begin{aligned}\dot{\mathrm{M}}_{p_X}(\gamma-1,t) = &-c_1(\gamma-1)\mathrm{M}_{p_X}(\gamma-1,t) - c_2(\gamma-1)\mathrm{M}_{p_X}(\gamma+\beta-2,t)+\\ &+\frac{q}{2}(\gamma-1)(\gamma-2)\mathrm{M}_{p_X}(\gamma-3,t)\end{aligned} \tag{11.60}$$

in which CFMs $\mathcal{M}_{p_X}(\gamma+\beta-2,t)$ and $\mathcal{M}_{p_X}(\gamma-3,t)$ can be easily evaluated through the following relations

$$\mathcal{M}_{p_X}(\gamma+\beta-2,t) = \sum_{k=-m}^{m} \mathcal{M}_p(\gamma_k-1)a_{ks}(1-\beta) \tag{11.61}$$

$$\mathcal{M}_{p_X}(\gamma-3,t) = \sum_{k=-m}^{m} \mathcal{M}_p(\gamma_k-1)a_{ks}(2) \tag{11.62}$$

Following the approach extensively discussed in Sect. 11.3 the system in (11.60) may be reduced to a set of 2 m coupled ordinary differential equations which solutions in terms of CFMs is easily found.

Figure 11.10 shows the evolution of the system response PDF for various time instants vis-à-vis the exact steady state solution. In this case the values of $\Delta\eta = 0.5$ and $m = 140$ have been chosen for solution in terms of CFMs. Note that, even if the value m of CFMs is greater than the number of cumulants chosen $\tilde{m}$, computational time is comparable for the two approaches.

Finally, in order to show the accuracy of the proposed approach with respect to the closure method, Fig. 11.11 shows the solution obtained through CFMs is contrasted with the Gram-Charlier expansion for the steady state case in (11.58).

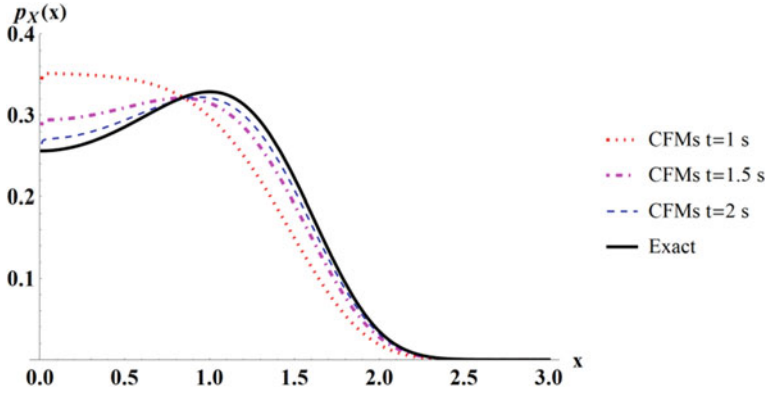

Fig. 11.10 Evolution of the response PDF

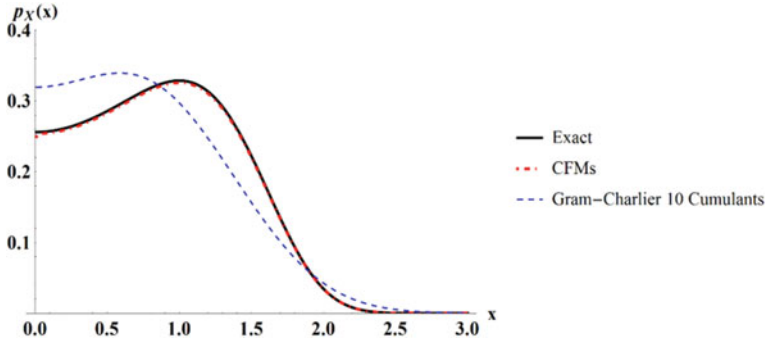

Fig. 11.11 Comparison among Exact steady state solution (Black line), CFMs (Red dashed line) and Gram-Charlier Expansion for 10 cumulants (Blue dashed line)

11.5 Conclusions

This chapter presented an efficient method to analyse the stochastic response of non-linear systems in terms of fractional moments. Instead of using moments of integer order, the FPK equation is written in terms of complex fractional order obtained as Mellin transform of the PDF. The main advantage in using CFMs instead of classical integer order ones is that thanks to the properties of Mellin transform operator the PDF may be reconstructed accurately with a limited number of terms. Moreover, CFMs of a given order may be written in terms of CFMs of a different order, thus eliminating the infinite hierarchy problem that affects the integer order moment approach. Numerical applications have extensively shown that the method is very accurate not only in describing the steady-state PDF but also its evolution for a range of non-linear systems forced by Gaussian, Lévy and Poissonian white noises.

References

1. G. Alotta, M. Di Paola, Probabilistic characterization of nonlinear systems under α-stable white noise via complex fractional moments. Phys. A **420**, 265–276 (2015)
2. G. Alotta, M. Di Paola, F.P. Pinnola, Cross-correlation and cross-power spectral density representation by complex spectral moments. Int. J. Non-Linear Mech. **94**, 20–27 (2017)
3. D.C.C. Bover, Moment equation methods for nonlinear stochastic system. J. Math. Anal. Appl. **65**, 306–320 (1978)
4. S. Butera, M. Di Paola, Fractional differential equations solved by using Mellin transform. Comm. Nonlinear Sci. Num. Simul. **19**(7), 2220–2227 (2014)
5. G.Q. Cai, Y.K. Lin, Exact and approximate solutions for randomly excited non-linear systems. Int. J. Nonlinear Mech. **31**, 647–655 (1996)
6. A. Chechkin, V. Gonchar, J. Klafter, R. Metzler, L. Tanatarov, Stationary state of non-linear oscillator driven by Lévy noise. Chem. Phys. **284**, 233–251 (2002)
7. G. Cottone, M. Di Paola, On the use of fractional calculus for the probabilistic characterization of random variable. Probab. Eng. Mech. **24**, 321–330 (2009)
8. G. Cottone, M. Di Paola, A new representation of power spectral density and correlation function by means of fractional spectral moments. Probab. Eng. Mech. **25**(3), 348–353 (2010)
9. G. Cottone, M. Di Paola, R. Metzler, Fractional calculus approach to the statistical characterization of random variables and vectors. Phys. A **389**, 909–920 (2010)
10. H. Dai, Z. Ma, L. Li, An improved complex fractional moment-based approach for the probabilistic characterization of random variables. Probab. Eng. Mech. **53**, 52–58 (2018)
11. A. Di Matteo, M. Di Paola, A. Pirrotta, Probabilistic characterization of nonlinear systems under Poisson white noise via complex fractional moments. Nonlinear Dyn. **77**(3), 729–738 (2014)
12. A. Di Matteo, M. Di Paola, A. Pirrotta, Poisson white noise parametric input and response by using complex fractional moments. Probab. Eng. Mech. **38**, 119–126 (2014)
13. M. Di Paola, G. Ricciardi, M. Vasta, A method for the probabilistic analysis of nonlinear systems. Probab. Eng. Mech. **10**, 1–10 (1995)
14. M. Di Paola, Fokker Planck equation solved in terms of complex fractional moments. Probab. Eng. Mech. **38**, 70–76 (2014)
15. M. Di Paola, F.P. Pinnola, Riesz fractional integrals and complex fractional moments for the probabilistic characterization of random variables. Probab. Eng. Mech. **29**, 149–156 (2012)

16. G.K. Er, Exponential closure methods for some randomly excited nonlinear systems. Int. J. Nonlinear Mech. **35**, 69–78 (2000)
17. C.W. Gardiner, *Handbook of Stochastic Methods for Physics Chemistry and The Natural Science* (Springer, Berlin, 1983)
18. R. Hilfer, *Application of Fractional Calculus in Physics* (World Scientific, Singapore, 2000)
19. R.A. Ibrahim, *Parametric Random Vibrations* (Wiley, New York, 1985)
20. R. Iwankiewicz, S.R.K. Nielsen, Solution techniques for pulse problems in non-linear stochastic dynamics Original Research Article. Probab. Eng. Mech. **15**, 25–36 (2000)
21. X. Jin, Y. Wang, Z. Huang, M. Di Paola, Constructing transient response probability density of non-linear system through complex fractional moments. Int. J. Non-Linear Mech. **65**, 253–259 (2014)
22. I.A. Kougioumtzoglou, P.D. Spanos, An analytical Wiener path integral technique for non-stationary response determination of nonlinear oscillators. Probab. Eng. Mech. **28**, 125–131 (2012)
23. Y.K. Lin, *Probabilistic Theory of Structural Dynamics* (McGraw Hill, New York, 1967)
24. E. Mamontov, A. Naess, An analytical-numerical method for fast evaluation of probability densities for transient solutions of nonlinear Itô's stochastic differential equations. Int. J. Eng. Sci. **47**, 116–130 (2009)
25. G. Muscolino, G. Ricciardi, M. Vasta, Stationary and non-stationary probability density function for nonlinear oscillator. Int. J. Nonlinear Mech. **32**, 1051–1064 (1997)
26. G. Muscolino, G. Ricciardi, Probability density function of MDOF systems under non-normal delta-correlated inputs. Comput. Methods Appl. Mech. Eng. **168**, 121–133 (1999)
27. A. Naess, V. Moe, Efficient path integration methods for nonlinear dynamic systems. Probab. Eng. Mech. **15**, 221–231 (2000)
28. F.P. Pinnola, Statistical correlation of fractional oscillator response by complex spectral moments and state variable expansion. Commun. Nonlinear Sci. Numer. Simul. **39**, 343–359 (2016)
29. A. Pirrotta, R. Santoro, Probabilistic response of nonlinear systems under combined normal and Poisson white noise via path integral method. Probab. Eng. Mech. **25**, 25–32 (2011)
30. I. Podlubny, *Fractional Differential Equations* (Academic Press, San Diego, 1999)
31. H. Risken, *The Fokker-Planck Equation. Methods of Solution and Applications* (Springer, Berlin, 1989)
32. J.B. Roberts, P.D. Spanos, Stochastic averaging: an approximate method of solving random vibration problems Review Article. Int. J. Non-Linear Mech. **21**, 111–134 (1986)
33. G.S. Samko, A.A. Kilbas, O.I. Marichev, *Fractional Integrals and Derivatives: Theory and Applications* (Gordon and Breach Science Publishers, 1993)
34. P.D. Spanos, A. Sofi, M. Di Paola, Nonstationary response envelope probability densities of nonlinear oscillators. J. Appl. Mech. Trans. ASME **74**(2), 315–324 (2007)
35. B.F. Spencer, L.A. Bergman, On the numerical solution of the Fokker-Planck equation for nonlinear stochastic systems. Nonlinear Dyn. **4**, 357–372 (1993)
36. A. Vriza, A. Kargioti, P.J. Papakanellos, G. Fikioris, Analytical evaluation of certain integrals occurring in studies of wireless communications systems using the Mellin-transform method. Phys. Comm. **31**, 133–140 (2018)
37. W.Q. Zhu, Stochastic averaging method in random vibration. Appl. Mech. Rev. **41**, 189–199 (1988)

Chapter 12
Oscillations Under Hysteretic Conditions: From Simple Oscillator to Discrete Sine-Gordon Model

Mikhail E. Semenov, Olga O. Reshetova, Akim V. Tolkachev, Andrey M. Solovyov and Peter A. Meleshenko

Abstract In this paper we study the resonance properties of oscillating system in the case when the energy pumping is made by external source of hysteretic nature. We investigate the unbounded solutions of autonomous oscillating system with hysteretic block with a negative spin. The influence of a hysteretic block on an oscillator in the presence of Coulomb and viscous friction is also investigated. Namely, we establish the appearance of self-oscillating regimes for both kinds of friction. A separate part of this work is devoted to synchronization of periodic self-oscillations by a harmonic external force. Using the small parameter approach it is shown that the width of "trapping" band depends on the intensity (amplitude) of the external impact. Also in this work we introduce the novel class of hysteretic operators with random parameters. We consider the definition of these operators in terms of the "input-output" relations, namely: for all permissible continuous inputs corresponds the output in the form of stochastic Markovian process. The properties of such operators are also considered and discussed on the example of a non-ideal relay with random param-

M. E. Semenov (✉)
Geophysical Survey of Russia Academy of Sciences, Lenina av. 189, 249035 Obninsk, Russia
e-mail: mkl150@mail.ru

Meteorology Department, Zhukovsky–Gagarin Air Force Academy,
Starykh Bolshevikov st. 54 "A", 394064 Voronezh, Russia

Digital Technologies Department, Voronezh State University, Universitetskaya sq. 1,
394006 Voronezh, Russia

Mathematics Department, Voronezh State University of Architecture and Civil Engineering,
XX-letiya Oktyabrya st. 84, 394006 Voronezh, Russia

O. O. Reshetova · A. M. Solovyov
Digital Technologies Department, Voronezh State University, Universitetskaya sq. 1,
394006 Voronezh, Russia

A. V. Tolkachev
Zhukovsky–Gagarin Air Force Academy, Starykh Bolshevikov st. 54 "A", 394064 Voronezh,
Russia

P. A. Meleshenko
Communication Department, Zhukovsky–Gagarin Air Force Academy,
Starykh Bolshevikov st. 54 "A", 394064 Voronezh, Russia
e-mail: melechp@yandex.ru

M. Belhaq (ed.), *Topics in Nonlinear Mechanics and Physics*,
Springer Proceedings in Physics 228, https://doi.org/10.1007/978-981-13-9463-8_12

eters. Application of hysteretic operator with stochastic parameters is demonstrated on the example of simple oscillating system and the results of numerical simulations are presented. We consider also a nonlinear dynamical system which is a set of nonlinear oscillators coupled by springs with hysteretic blocks (modified sine-Gordon system or hysteretic sine-Gordon model where the hysteretic nonlinearity is simulated by the Bouc-Wen model). We investigate the wave processes (namely, the solitonic solutions) in such a system taking into account the hysteretic nonlinearity in the coupling.

12.1 Introduction

Oscillatory processes are widely used in various fields of both fundamental and applied science. The theory of oscillations, which studies oscillations occurring in various systems, is an intensively developing field of modern mathematics and physics [11, 20, 22, 26]. The main models of the theory of oscillations are the linear and nonlinear oscillators, rotators, RLC circuit, etc. These are used in modeling of physical processes in various real-life systems. New features of oscillatory processes appear in the cases when there is a large number of interacting subsystems. The standard model of wave processes is a finite and infinite chain of coupled (interacting) oscillators. Such chains are often used in radio engineering as filters that allocate or suppress signals with frequencies lying in a certain band. From the fundamental point of view, chains of oscillators are used as models of solid media with oscillations and waves with various properties [3, 16, 27]. The oscillatory processes of a large number of such elements are called waves. Wave phenomena are widespread in nature: waves on the surface of a fluid, sound waves in a gas, compression-expansion waves in a solid, vibrations of a string and membrane, electromagnetic waves, etc.

Note that, in addition to nonlinear oscillations, there are also nonlinear waves described by nonlinear partial differential equations. Within the framework of the theory of nonlinear waves there exist the standard models, similar to the reference models in the theory of oscillations, namely, simple waves, shock waves, as well as the solitary waves (solitons), that play significant roles in the theory of nonlinear processes. One of the basic models for studying the nonlinear processes is the sine-Gordon model (a chain of nonlinear oscillators connected by coil springs) [17].

Another example of a strong nonlinear system playing a significant role in modern research is hysteresis (see [4, 9, 14, 18, 19, 28] and related references). Hysteretic behavior is typical both for the characteristics of substances (ferroelectrics, ferromagnetics, piezoelectrics, etc.), and for the dynamics of many mechanical systems (backlash, stop, etc.). In the mechanical systems hysteretic nonlinearities arise due to an aging of the material and must be taken into account at the modeling level for the corresponding mechanical systems. The hysteresis in such systems leads to the problem of investigation of nonlinear operator-differential equations, which is an extremely complex problem.

Such an interest to hysteretic phenomena is caused by high incidence of these phenomena in a various technical systems (such as robotic, mechanical, electromechanical systems, management systems for tracking of aircrafts, etc.) Also, these phenomena determine some unusual elasto-plastic properties of modern nanomaterials (such a properties are served as a base for construction of modern self-healing materials) on the basis of fullerene films. Moreover, the hysteretic phenomena are widely known in biology, chemistry, economics, etc. It should be noted that the hysteretic behavior of such systems is caused by either their internal structure, or the presence of separate blocks with hysteretic characteristics. Of course, when modeling the dynamics of such systems, it is necessary to use an adequate mathematical apparatus.

Currently used models of hysteretic phenomena both constructive (such as non-ideal relay, Preisach and Ishlinskii-Prandtl models, etc. [21]), and phenomenological (Bouc-Wen model, Duhem model, etc. [6]) assume a priori the stability of the parameters that identify the hysteretic properties of the corresponding operators. However, the stability of parameters in real-life engineering systems (e.g., in the systems modelled by the coupled inverted pendula [20]) does not always take place. In this way, such operators are the natural model in the situation when the parameters of hysteresis carrier are under influence of stochastic, uncontrollable affections. For example, it is difficult to control the switching numbers of non-ideal relay, which is a part of control systems of the corresponding devices, when the various external factors take place (in this case the switching numbers may be subjected to random changes). These circumstances make it necessary to develop the extended models of hysteretic effects, taking into account the stochastic changes in the parameters of the corresponding hysteretic operators. We note that the equations with random parameters (principally such equations are linear) were considered in [13, 30, 31]. The strongly nonlinear differential equations containing the operator nonlinearity with random properties have not been considered in the literature. Thus, construction and investigation of the properties of hysteretic operators with random parameters seems novel and promising problem.

An important problem is the study of resonance phenomena in systems with hysteresis [9]. In this way we note a well-known fact: in the presence of viscous friction the harmonic resonance is not realized (for details see, e.g., [8]). In particular, in [8] it is considered the dynamics of the oscillator with strong nonlinearity (authors studied its phase portrait and the trajectory). It is proved that the form of periodic solutions depends on the "origin" of strong nonlinearity. The main result of [8] is that for a class of equations, which describe the harmonic oscillations with resonance external force and hysteretic operator in the right part of equation, the presence or absence of unbounded solutions depend on the amplitude of the external excitation.

In this chapter we study the resonance properties of systems in which the energy pumping is realized due to the presence of external source with hysteretic nature. Examples of such systems are the oscillations of the ferromagnetic ball in a magnetic field, oscillations of the system of coupled oscillators when the "connection force" has a hysteretic nature [18], etc. Moreover, we introduce the new class of hysteretic operators with random parameters. We consider the definition of these operators in

terms of the "input-output" relations. The properties of such operators are also considered and discussed for the example of a non-ideal relay with random parameters. Application of hysteretic operator with stochastic parameters is demonstrated for the example of simple oscillating system and the results of numerical simulations are presented. Also, the dynamics of nonlinear oscillatory system (discrete mechanical sine-Gordon system) is investigated taking into account the hysteretic coupling conditions between individual links of such a system. We consider the sine-Gordon model in the case when the links between pendulums contain hysteresis nonlinearities (modified sine-Gordon model). On the basis of numerical modeling, the dynamics of soliton-like solutions in such a system is studied and filtering properties of hysteretic links are established.

12.2 Oscillator Under Hysteretic Force

12.2.1 Unbounded Solutions to Autonomous Systems with Hysteretic Blocks with Negative Spin

Let us consider a system whose dynamics is described by the following equation with the corresponding initial conditions:

$$\begin{gathered} \ddot{x} + \omega^2 x = R[\alpha, \beta, \omega_0]x, \\ x(0) = x_0, \ \ \dot{x}(0) = x_1. \end{gathered} \tag{12.1}$$

where $R[\alpha, \beta, \omega_r]$ is a non-ideal relay operator with the negative spin, and ω_0 is an initial state of this operator. A more detailed description of the properties of such an operator can be found in [9].

Theorem. Let the initial value satisfies the condition $x_0 \notin [\alpha, \beta]$. Then, the corresponding solutions are unbounded.

Proof: For simplicity we consider the case where $\alpha = -1$, $\beta = 1$. Let us assume that the initial conditions obey the following inequality $x_0 < -1$, then at a certain initial period of time ($t \geq 0$) the solution to (12.1) will have the form $x_0 = A_1 \cos(t + \varphi_0) + 1$, $0 \leq t \leq t_0$, where t_1 is the time at which the equality $x(t_1) = 1$ is satisfied. It is clear that this moment exists. The solution to (12.1) at interval $[t_1, t_2]$ will be determined by the relation $x_1(t) = A_1 \cos(t + \varphi_1)$. Here t_2 is the moment at which the equality $x_1(t_2) = -1$ is satisfied. It is also clearly that such a moment exists ($A_1 \geq 1$ because $x_1(t_1) = 1$), etc.

Thus, in the absence of switching the solution to (12.1) is composed of the functions defined by following relations for even n:

$$x_n(t) = A_n \cos(t + \varphi_n) + 1,$$

and for odd n:

$$x_{n+1}(t) = A_{n+1}\cos(t + \varphi_{n+1}).$$

Using the continuity conditions for solution and its derivative at the point t_n (the moment when the right switching number is achieved) we obtain the following equality:

$$\begin{cases} A_n\cos(\varphi_n) + 1 = A_{n+1}\cos(\varphi_{n+1}), \\ -A_n\sin(\varphi_n) = -A_{n+1}\sin(\varphi_{n+1}), \\ A_n\cos(\varphi_n) + 1 = 1. \end{cases} \tag{12.2}$$

Squaring and summing the first two equalities in (12.2) we obtain:

$$\begin{cases} A_n^2\cos^2(\varphi_n) + 2A_n\cos(\varphi_n) + 1 = A_{n+1}^2\cos^2(\varphi_{n+1}), \\ A_n^2\sin^2(\varphi_n) = A_{n+1}^2\sin^2(\varphi_{n+1}), \\ A_n\cos(\varphi_n) = 0, \end{cases} \tag{12.3}$$

or

$$\begin{cases} A_n^2 + 2A_n\cos(\varphi_n) + 1 = A_{n+1}^2, \\ A_n\cos(\varphi_n) = 0. \end{cases} \tag{12.4}$$

Finally we obtain:

$$A_n^2 + 1 = A_{n+1}^2 \tag{12.5}$$

Similarly, for the next interval, at the point at which the solution has the value -1, we have:

$$\begin{cases} A_{n+1}\cos(\varphi_{n+2}) = A_{n+2}\cos(\varphi_{n+3}) + 1, \\ -A_{n+1}\sin(\varphi_{n+2}) = -A_{n+2}\sin(\varphi_{n+3}), \\ A_{n+1}\cos(\varphi_{n+2}) = -1. \end{cases} \tag{12.6}$$

Squaring the first two equalities:

$$\begin{cases} A_{n+1}^2\cos^2(\varphi_{n+2}) - 2A_{n+1}\cos(\varphi_{n+2}) + 1 = A_{n+2}^2\cos^2(\varphi_{n+3}), \\ A_{n+1}^2\sin^2(\varphi_{n+2}) = A_{n+2}^2\sin^2(\varphi_{n+3}), \\ A_{n+1}\cos(\varphi_{n+2}) = -1. \end{cases} \tag{12.7}$$

Then, summation of them leads to

$$\begin{cases} A_{n+1}^2 - 2A_{n+1}\cos(\varphi_{n+2}) + 1 = A_{n+2}^2, \\ A_n\cos(\varphi_n) = -1. \end{cases} \tag{12.8}$$

Finally we get:

$$A_{n+2}^2 = A_{n+1}^2 + 3 \tag{12.9}$$

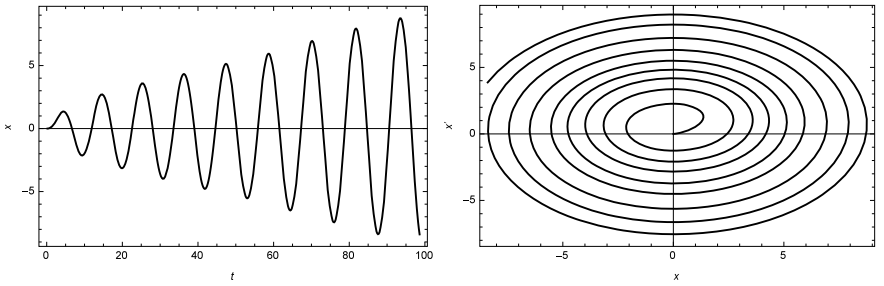

Fig. 12.1 Solution (left panel) and phase portrait (right panel) to (12.1) with given initial conditions

Then, from (12.8) and (12.9) it follows:

$$A_{n+2}^2 = A_n^2 + 4$$

In other words, if the initial value is such that the hysteretic element "works", then the corresponding solution is unbounded. Results of numerical simulations are presented in Fig. 12.1.

Note 1. Let us note that the solution oscillates and the rate of growth of amplitude is proportional to $\sqrt{t}$.

Note 2. The theorem remains valid for other types of hysteretic nonlinearities. The main requirement is the positiveness of the loop's area.

12.2.2 Systems with Coulomb and Viscous Friction

"Natural" generalization of the system under consideration is the system with various types of friction (namely, the Coulomb and viscous friction). The dynamics of oscillator with a viscous friction can be described by the equation:

$$\begin{gathered} \ddot{x} + 2b\dot{x} + \omega^2 x = R[\alpha, \beta, \omega_0]x, \\ x(0) = x_0, \;\; \dot{x}(0) = x_1. \end{gathered} \tag{12.10}$$

In the following consideration we assume that switching numbers of a non-ideal relay are symmetric relative to the origin. Considering the dynamics of the solution, it should be noted that once the amplitude of the solution becomes high enough, the work of the friction force balances the energy obtained by the oscillator from the hysteretic element. Let us consider two cases related to the different kind of the roots of characteristic equation of the linear part of the (12.10).

Let us consider (12.10) with a given initial conditions for these two cases:

$$\ddot{x}^+ + 2b\dot{x}^+ + \omega^2 x^+ = 1, \tag{12.11}$$

$$\ddot{x}^- + 2b\dot{x}^- + \omega^2 x^- = -1. \tag{12.12}$$

For the first case a solution to equation has the following form:

$$x^+(t) = \frac{1}{\omega^2} + C_1 \exp\left[t\left(-b - \sqrt{b^2 - \omega^2}\right)\right] + C_2 \exp\left[t\left(-b + \sqrt{b^2 - \omega^2}\right)\right] \tag{12.13}$$

Obviously, the term $\frac{1}{\omega^2}$ is an asymptotic limit for this solution, and therefore, if the inequalities $\alpha < \frac{1}{\omega^2}$, $\beta > -\frac{1}{\omega^2}$ are satisfied for some T, then the inequality $x^+ = -\alpha$ is obeyed too. Further dynamics will be determined by an equation with a value of a non-ideal relay converter equal $-\alpha = -1$. Reasoning in a similar way, it is easy to establish that for some T_1 the solution will take the value α. Taking into account the fact that the equations are autonomous, the solutions obtained in this way will be periodic. A period can be found using the following relations:

$$x^+(t) = C_1 \exp(t\lambda_1) + C_2 \exp(t\lambda_2), \tag{12.14}$$

$$x^-(t) = C_3 \exp(t\lambda_3) + C_4 \exp(t\lambda_4), \tag{12.15}$$

where

$$C_1 = \frac{\left(1+\omega^2\right)\left(-b + \sqrt{b^2 - \omega^2}\right)}{2\omega^2\sqrt{b^2 - \omega^2}},$$

$$C_2 = \frac{\left(1+\omega^2\right)\left(b + \sqrt{b^2 - \omega^2}\right)}{2\omega^2\sqrt{b^2 - \omega^2}},$$

$$C_3 = -\frac{\left(-1+\omega^2\right)\left(-b + \sqrt{b^2 - \omega^2}\right)}{2\omega^2\sqrt{b^2 - \omega^2}}, \tag{12.16}$$

$$C_4 = -\frac{\left(1+\omega^2\right)\left(b + \sqrt{b^2 - \omega^2}\right)}{2\omega^2\sqrt{b^2 - \omega^2}},$$

$$\lambda_1 = \lambda_3 = -b - \sqrt{b^2 - \omega^2},$$
$$\lambda_2 = \lambda_4 = -b + \sqrt{b^2 - \omega^2},$$

and the period of oscillations is determined by

$$T = \frac{\pi}{\sqrt{b^2 - \omega^2}}. \tag{12.17}$$

Let us consider the second case when the roots of the characteristic equation to the linear part of (12.10) are complex conjugate. Then, the solution to the equation with initial conditions can be written as follows:

$$x(t) = \exp(-bt)\left[B\cos(\omega t) + C\sin(\omega t)\right] - \frac{1}{\omega_0^2}, \tag{12.18}$$

where $\omega = \sqrt{b^2 - \omega_0^2}$.

Taking into account the initial conditions, we get:

$$-\frac{1}{\omega_0^2} + \frac{1+\omega_0^2}{\omega_0^2}\sqrt{1+\left(\frac{b}{\omega}\right)^2}\exp(-bt)\sin\left[\omega t + \arcsin\left(\frac{1}{\sqrt{1+\left(\frac{b}{t}\right)^2}}\right)\right] = 1. \tag{12.19}$$

A half period can be defined as a solution to a transcendental equation (12.19). A solution and phase portrait are shown in the following Fig. 12.2.

Note that for a given value of the parameter $b = 1$, a bifurcation occurs. Such a bifurcation corresponds to a change in the period (see Fig. 12.3).

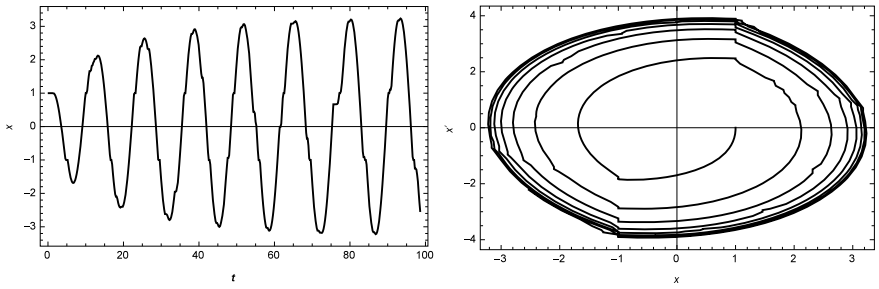

Fig. 12.2 Solution (left panel) and phase portrait (right panel) to (12.10) with given initial conditions

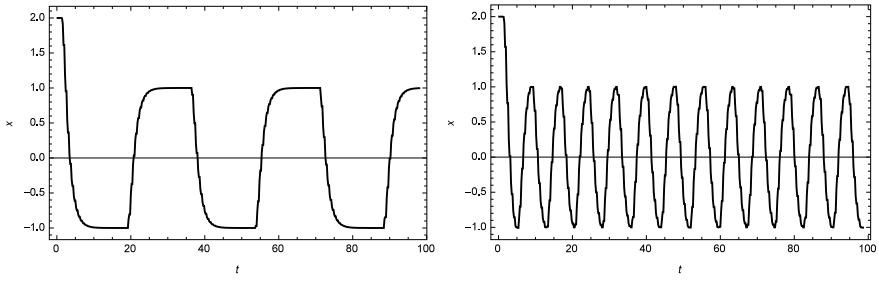

Fig. 12.3 Oscillations in the system (12.10) at $b = 0.9$ (left panel) and $b = 1.1$ (right panel)

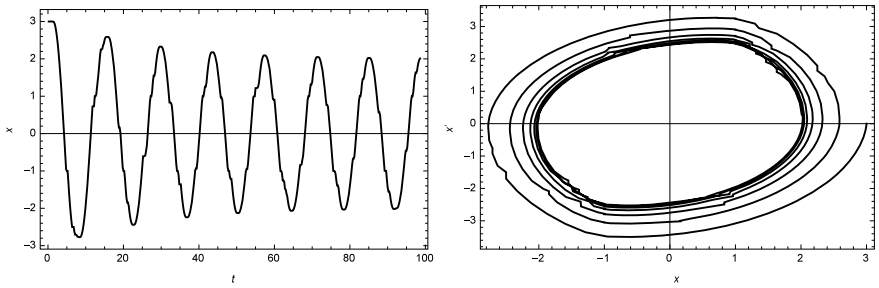

Fig. 12.4 Solution (left panel) and phase portrait (right panel) to the system (12.20) at $\eta = 0.5$

The dynamics of the oscillator with the Coulomb friction under external hysteretic affection is described by the equation:

$$\ddot{x} + \eta \text{sign}(\dot{x}) + x = R[\alpha, \beta, \omega_0]x \tag{12.20}$$

Multiplying both sides of (12.21) by $\dot{x}$, and integrating over the period T we obtain:

$$\int_0^T \frac{1}{2}\frac{d}{dt}(\dot{x}^2 + x^2)\mathrm{d}t = -\int_0^T \eta \text{sign}(\dot{x})\dot{x}\mathrm{d}t + \int_0^T \dot{x}R[\alpha, \beta, \omega_0]x\mathrm{d}t, \tag{12.21}$$

$$\Delta E = -\eta \int_0^T |\dot{x}|\mathrm{d}t + S_p. \tag{12.22}$$

From the (12.22) it follows that the energy gain ΔE will be positive if the work of friction forces will be smaller than the loop's area S_p (otherwise it will be negative). Thus, the considered system can be treated as a system with the negative feedback. Let us note that at steady-state regime the condition $2(x_{\max} - x_{\min})\eta = S_p$ is satisfied. This means that the amplitude of the oscillation is such that the work of frictional forces on the period is equal to the loop's area. These results are illustrated in Fig. 12.4.

As it can be seen from the presented results, a harmonic oscillator with Coulomb and viscous friction under hysteretic external force significantly differs from the "classical" model of a harmonic oscillator, where, regardless to initial conditions, the damped oscillations in the vicinity of equilibrium point take place.

12.2.3 Frequency "trapping" in the System with Relay Nonlinearity: The Small Parameter Method

Synchronization of periodic self-oscillations by a harmonic external force has been a long-studied phenomenon, which can be formulated as follows. As soon as the frequency of the external excitation becomes close to the frequency of free self-oscillations, synchronization ("trapping") of the frequency occurs. Let us consider a self-oscillating system with one degree of freedom, which is under periodic external force with a frequency ω (we consider the case where this frequency is close to the frequency of free self-oscillations).

$$\ddot{x} + 2b\dot{x} + \omega_0^2 x = R[\alpha, \beta, \omega_r]x + B_1 \sin \omega t. \tag{12.23}$$

To analyze the dynamic features of such a system, the small parameter method is used [10], which allows to make an identification of the process of frequency "trapping" (the frequency of external harmonic force) by an autonomous system with hysteresis. To do this, we rewrite the original (12.23) in the form:

$$\ddot{x} + \omega_0^2 x = \varepsilon \left(-2b\dot{x} + R[\alpha, \beta, \omega_r]x + B_1 \sin \omega t\right), \tag{12.24}$$

where ε is a small parameter. The solution to this equation can be written in the following standard form:

$$x = A \cos \psi + \varepsilon u_1 (A, \psi) + \cdots, \tag{12.25}$$

where $\psi = \omega t + \varphi(t)$, and $u_1 (A, \psi)$ are unknown functions which do not contain resonance frequencies; A and φ are the amplitude and phase, respectively, which satisfy the following equations:

$$\dot{A} = \varepsilon f_1 (A, \varphi) + \ldots; \; \dot{\varphi} = -\Delta + \varepsilon F_1 (A, \varphi) + \cdots, \tag{12.26}$$

and $\Delta = \omega - \omega_0$ is the frequency difference. F_1, f_1 are unknown functions that are to be determined from the condition of the absence of resonant terms in the function u_1. Substituting the general form of the solution into the original equation, taking into account the equations for the amplitude and phase and using the described definitions we obtain for $\dot{x}$ and $\ddot{x}$:

$$\dot{x} = \dot{A} \cos \psi - A \sin \psi \dot{\psi} + \varepsilon \dot{u}_1 \omega; \tag{12.27}$$

$$\ddot{x} = \ddot{A} \cos \psi - 2\dot{A} \sin \psi \dot{\psi} - A \cos \psi \dot{\psi}^2 - A \sin \psi \ddot{\psi} + \varepsilon \ddot{u}_1 \omega^2. \tag{12.28}$$

Substituting the obtained expressions in the left side of the (12.24), and using (12.25) and (12.26) we get:

$$\ddot{x} + \omega_0^2 x = \ddot{A}\cos\psi - 2\dot{A}\sin\psi\dot{\psi} - A\cos\psi\dot{\psi}^2 - A\sin\psi\ddot{\psi} + \varepsilon\ddot{u}_1\omega^2 +$$

$$+ \omega_0^2 A\cos\psi + \omega_0^2\varepsilon u_1 = \varepsilon\ddot{u}_1\omega^2 + \omega_0^2\varepsilon u_1 - \left(2\dot{A}\dot{\psi} + A\ddot{\psi}\right)\sin\psi +$$

$$+ \left(\ddot{A} - A\dot{\psi}^2 + \omega_0^2 A\right)\cos\psi = \tag{12.29}$$

$$= \varepsilon\ddot{u}_1\omega^2 + \omega_0^2\varepsilon u_1 - \left(2\varepsilon f_1\left(-\Delta + \varepsilon F_1\right) + A\varepsilon\dot{F}_1\right)\sin\psi +$$

$$+ \left(\varepsilon\dot{f}_1 - A(-\Delta + \varepsilon F_1)^2 + \omega_0^2 A\right)\cos\psi.$$

For the right side of the (12.24) we obtain in the same manner:

$$\varepsilon\left(-2b\dot{x} + R[\alpha, \beta, \omega_r]x + f(t)\right) =$$

$$= \varepsilon\left(R[\alpha, \beta, \omega_r]x - 2b\left(\dot{A}\cos\psi - A\sin\psi\dot{\psi} + \varepsilon u_1\omega)\right) + f(t)\right) =$$

$$= \varepsilon\left(R[\alpha, \beta, \omega_r]x - 2b\varepsilon f_1\cos\psi + 2bA\left(-\Delta + \varepsilon F_1\right)\sin\psi + \varepsilon u_1\omega + f(t)\right). \tag{12.30}$$

Equating the terms of the same order of smallness in the right and left parts, we obtain the equation for determining the unknown function u_1:

$$\omega^2\frac{\partial^2 u_1}{\partial\psi^2} + \omega_0^2 u_1 = \left(2\omega_0 f_1 - A\frac{\partial F_1}{\partial\varphi}\Delta\right)\sin\psi + \left(2\omega_0 A F_1 - A\frac{\partial f_1}{\partial\varphi}\Delta\right)\cos\psi -$$

$$- AR[\alpha, \beta, \omega_r]x\cos\psi + f(t). \tag{12.31}$$

From the condition of the absence of resonant terms in the function $u_1(A, \psi)$ (factors at harmonic functions are equal to zero) we obtain the following equations for the unknown functions F_1 and f_1:

$$2f_1 - A\frac{\Delta}{\omega_0}\frac{\partial F_1}{\partial\varphi} = -2bA - \frac{B_1}{\omega}\sin\varphi;\ \ 2AF_1 + \frac{\Delta}{\omega_0}\frac{\partial f_1}{\partial\varphi} = AR[\alpha, \beta, \omega_r]x - \frac{B_1}{\omega}\cos\varphi. \tag{12.32}$$

The particular solution to this system is:

$$f_1 = -bA - \frac{B_1\sin\varphi}{\omega + \omega_0};\ \ F_1 = \frac{R[\alpha, \beta, \omega_r]x}{2} - \frac{B_1\cos\varphi}{A(\omega + \omega_0)}. \tag{12.33}$$

In the first approximation in ε from (12.33) and (12.26), taking into account the condition $u_1(A, \psi) = 0$ we get:

$$\dot{A} = -bA - \frac{B_1\sin\varphi}{\omega + \omega_0}, \dot{\varphi} = -\Delta + \frac{R[\alpha, \beta, \omega_r]x}{2} - \frac{B_1\cos\varphi}{A(\omega + \omega_0)}. \tag{12.34}$$

The numerical values of the amplitude and phase are presented in Fig. 12.5. In Fig. 12.6 we present the amplitude-phase portrait as well. The amplitude-phase

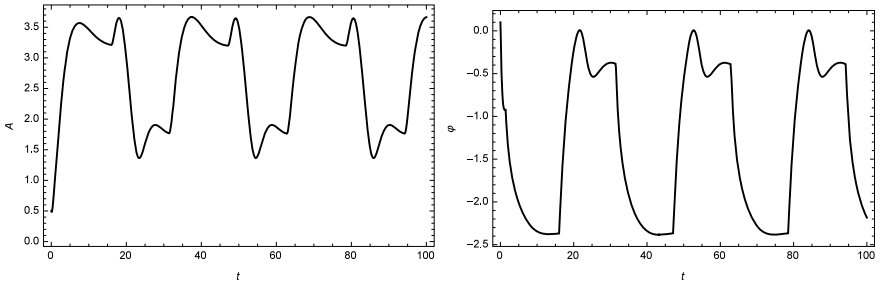

Fig. 12.5 Aplitude (left panel) and phase (right panel) versus time for the following parameters: $b = 0.5$, $B_1 = 1$, $\omega_0 = 1$, $\omega = 1.2$, $\alpha = -\beta = 1$, $\omega_r = 1$

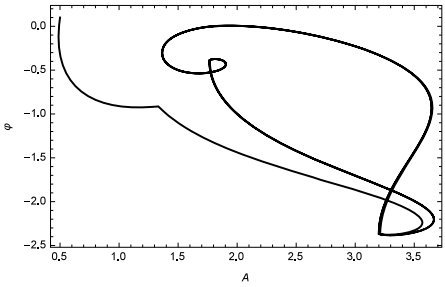

Fig. 12.6 Aplitude-phase portrait for the system under consideration with the parameters as in Fig. 12.5

portrait of the system (12.34) is characterized by complex behavior, with many self-intersections.

In Fig. 12.7 we present the numerical solution to the system (12.23) together with the time dependence of the disturbing force, as well as the behavior of the system without external excitation.

As follows from the presented numerical results, the solution to the system becomes not-smooth while switching of a non-ideal relay takes place function. Analyzing the obtained solution, it can be noted that it contains harmonics of a smaller amplitude in addition to the main harmonics. Note that the synchronization of the frequency of free self-oscillations with the frequency of external force also takes place for systems containing hysteretic nonlinearity. As the amplitude of the external force

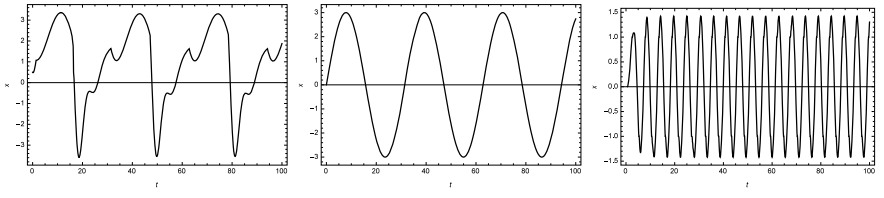

Fig. 12.7 Left panel: numerical solution to the system (12.23); Middle panel: time dependence of the disturbing force; Right panel: system behavior without external force

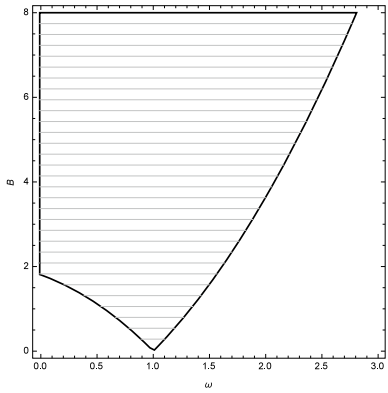

Fig. 12.8 The frequency "trapping" domain

increases, the frequency interval (Δ) increases too (at this interval the frequency "trapping" takes place). Figure 12.8 presents the dependence of the amplitude of the external force on the frequency of the periodic force, at which the frequency "trapping" occurs.

12.3 Oscillator Under Hysteretic Force with Random Parameters

12.3.1 Non-ideal Relay with Random Parameters

Consider a non-ideal relay (a detailed description of this and other hysteretic converters, as well as their properties in the case of deterministic parameters, are given in the classical book of Krasnosel'skii and Pokrovskii [9]), in which the switching numbers are not fixed, but are treated as random variables with absolutely continuous distribution function. Concerning these random variables, we make the following assumption: the probability density of each of the switching numbers will be assumed to be finite with non-intersecting supports. We denote these switching numbers as $\varphi_\alpha(u)$ and $\varphi_\beta(u)$. We will consider the case when the supports of the function $\varphi_\alpha(u)$ and $\varphi_\beta(u)$ are contained in the intervals $[u_\alpha^-, u_\alpha^+]$ and $[u_\beta^-, u_\beta^+]$, respectively.

Following the basic ideas presented in [9] (as well as, following the terminology presented in this book), the dynamics of the input-output relations for the operator of a non-ideal relay with random switching numbers is determined by two relations, namely: "input-state" and "state-output". We assume that all permissible continuous inputs are given on the non-negative semi-axis ($t > 0$) (the input-output relation for this converter R has the form $x(t) = R[t_0, x_0, \alpha, \beta]u(t)$, $(t \geq t_0)$). The space of possible states of such an operator is defined as $\Omega = \Omega(\omega, p, u)$, $(\omega = 0, 1, 0 \leq p \leq 1, -\infty < u < +\infty)$.

The variable state of the converter $R\left[(1;\ p_0);\ x_0;\ \varphi_\alpha(u);\ \varphi_\beta(u)\right]u(t)$ is a random value that takes the value 0 with probability $(1 - p(t))$ and a value of 1 with probability $p(t)$. In other words, it can be presented as a pair $\{1;\ p(t)\}$ (here the second output component corresponds to the probability that at the time t the first component is 1). The output of this converter is a random function $x(t)$ (Markovian process) taking a value of 1 with probability $p(t)$. The rule that determines the value of probability $p(t)$ will be given below.

12.3.1.1 Definition of Input-Output Relation for a Non-ideal Relay with Random Switching Numbers

Following the classical scheme proposed in [9], we give the definition of the input-output relation by means of a three-step construction:

- At the first step we define the input-output relation on the monotonic inputs only;
- At the second step, using the semi-group identity, the input-output relation is defined for all piece-wise monotonic inputs;
- At the third step, using the special limit construction, the corresponding converter will be defined for all monotonic inputs.

We define the operator R on the monotonic inputs. Let us assume that at the initial time point t_0 (to simplify the calculations, we assume that $t_0 = 0$) the operator R is in the state 1; p_0; $u_0 \in \Omega$, $(u(0) = u_0)$. Let the input $u(t)$ be a monotonic increase, then for the time $t > 0$ the output is $x(t) = \{1;\ p(t)\}$ where

$$p(t) = \max\left\{p_0;\ \int\limits_{-\infty}^{u(t)} \varphi_\beta(u)\mathrm{d}u\right\}. \tag{12.35}$$

The semi-group identity for the operator R immediately follows from the definition. Let t_1 be an arbitrary moment of time satisfying the inequality $0 < t_1 < t$, then the semi-group identity for the operator of a non-ideal relay has the form:

$$R\left[t_0;\ p_0;\ u_0;\ \varphi_\alpha;\ \varphi_\beta\right]u(t) = R\left[t_1;\ R\left[t_0;\ p_0;\ u_0;\ \varphi_\alpha;\ \varphi_\beta\right]u(t_1);\ u(t_1);\ \varphi_\alpha;\ \varphi_\beta\right]u(t). \tag{12.36}$$

To define an operator on the piece-wise monotonic inputs (in the case of a finite interval $[0, T]$), we break this interval by points $t_1, t_2, \ldots, t_n$ into intervals of monotonicity. On each of them we define the corresponding operator as an operator on a strictly monotonic input whose initial state will be defined as the state at the instant corresponding to the "last" change in the behavior of the input.

To determine the operator R on continuous inputs, we use the following limit construction. Let $u(t)(t \in [0, T])$ be an arbitrary continuous input. Let us consider an arbitrary sequence of piece-wise monotonic inputs $u_n(t)$, $(n = 1, 2, ...)$ that converges uniformly to each element of this sequence $u(t)$. A single-variable state $p_n(t)$, $(n = 1, 2, ...)$ will form a sequence of state variables $p_n(t)$, $(n = 1, 2, ...)$.

Let us prove that the sequence $p_n(t),\ (n = 1, 2, ...)$ converges uniformly. We estimate the absolute value of the difference:

$$|p_n(t) - p_m(t)| \le \max_t \left| \int_{-\infty}^{u_n(t)} \varphi_\alpha(u)\mathrm{d}u - \int_{-\infty}^{u_m(t)} \varphi_\alpha(u)\mathrm{d}u \right| = \max_t \left| \int_{u_n(t}^{u_m(t)} \varphi_\alpha(u)\mathrm{d}u \right|. \tag{12.37}$$

Since the function $\varphi_\alpha(u)$ is continuous, and because of uniform convergence also

$$\lim_{n,m\to\infty} \max_t |u_n(t) - u_m(t)| = 0,$$

as well as, using the mean value theorem:

$$\max_t \left| \int_{u_n(t}^{u_m(t)} \varphi_\alpha(u)\mathrm{d}u \right| \le \max_t \varphi_\alpha(t)\,[u_n(t) - u_m(t)]$$

the right-hand side of the inequality (12.37) tends to zero. Thus, the sequence of probabilities $p_n(t)$ is fundamental (the continuity is obvious), then there is $\lim_{n\to\infty} p_n(t) = p(t)$, which is comparable to an arbitrary continuous input $u(t)$.

12.3.1.2 Monotonicity of a Non-ideal Relay with Random Parameters

Let us consider the monotonicity property for the constructed converter. We determine the monotonicity with respect to the initial state of the non-ideal relay: if $\{u(t_0, x_0\},\ \{v(t_0, y_0\} \in \Omega(\alpha, \beta),\ x_0 \le y_0$ and $u(t) \le v(t)\ (t \ge t_0)$, then we have:

$$R\,[t_0, x_0, \alpha, \beta]\,u(t) \le R\,[t_0, x_0, \alpha, \beta]\,v(t)\ \ (t \ge t_0).$$

This property can be used as the definition of a non-ideal relay. In order to use it, we define the outputs corresponding to monotonic inputs. Applying a semi-group identity, we define the outputs for piece-wise monotonic inputs. Further, this relation is extended by means of the special limit construction to all monotonic inputs. In this case, this relation will be the exclusive. We can also note a natural monotonicity in the switching numbers. With respect to the modified operator of a non-ideal relay with random parameters, the analogue of monotonicity can be presented in the form of the following theorem.

Theorem 12.1 *Let* $p\{x_{01} = 1\} \ge p\{x_{02} = 1\}$ *and* $x_1(t) \ge x_2(t)$. *Then for any* t: $p\{x_1 = 1\} \ge p\{x_2 = 1\}$.

12.3.2 Dynamics of a System Under Non-ideal Relay with Random Parameters

In order to show the action of the developed operator on the real physical system let us consider the simple oscillating system under hysteretic force with random parameters. Such a simple system is considered in [23, 24] and the external force has the form of a non-ideal relay with inversion of the switching numbers. One of the main results of these studies is the existence of unlimited solutions, namely, if the initial conditions are such that the hysteretic operator is triggered at the first cycle of oscillations, then the corresponding solution is unlimited, while the growth rate of the amplitude is proportional to the square root of time. Let us consider an analogous system with a non-ideal relay with switching numbers distributed according to an even-dimensional law. The equation of motion together with the corresponding initial conditions has the following form:

$$\begin{gathered} \ddot{x}(t) + \omega^2 x(t) = R[t_0;\, p_0;\, u_0;\, \varphi_\alpha;\, \varphi_\beta]x(t), \\ x(0) = x_0,\ \dot{x}(0) = x_1. \end{gathered} \tag{12.38}$$

To implement the numerical solution of the system (12.38), it is necessary to generate a set of random values corresponding to the switching numbers. Let us consider the case when $\varphi_\alpha(u)$ and $\varphi_\beta(u)$ corresponds to the uniform distribution law for α and β. For definiteness, we will assume that these functions correspond to uniform distributions in the intervals $[-1.5, -0.5]$ and $[0.5, 1.5]$, respectively. The solution of the system (12.38) can be obtained by specifying the initial conditions and the values of the switching numbers corresponding to the non-ideal relay. At each period, the switching numbers are selected from the corresponding distributions with the initial conditions for the next realization corresponding to the values of the phase coordinates obtained at the previous step. Using the described algorithm, a solution to the system (12.38) is obtained and the corresponding law of motion together with the phase portrait are shown in Fig. 12.9. Let us note, that non-smooth character of the phase portrait is caused by the hysteretic nature of the external excitation, as well as the random nature of the parameters of a non-ideal relay.

The following theorem characterizes the dynamics of the system (12.38).

Theorem 12.2 *Let us suppose that the supports of the function φ_α and φ_β do not intersect. Then $\overline{\lim_{t\to\infty} x(t)} = \infty$, that is the amplitude tends to infinity with probability equals to* 1.

The proof of this theorem follows from the fact that the area of the minimal hysteretic loop is positive $S_{\min} > 0$, as a consequence, the amplitude value at each cycle satisfies the inequality:

$$A_n^2(t) \geq n S_{\min}.$$

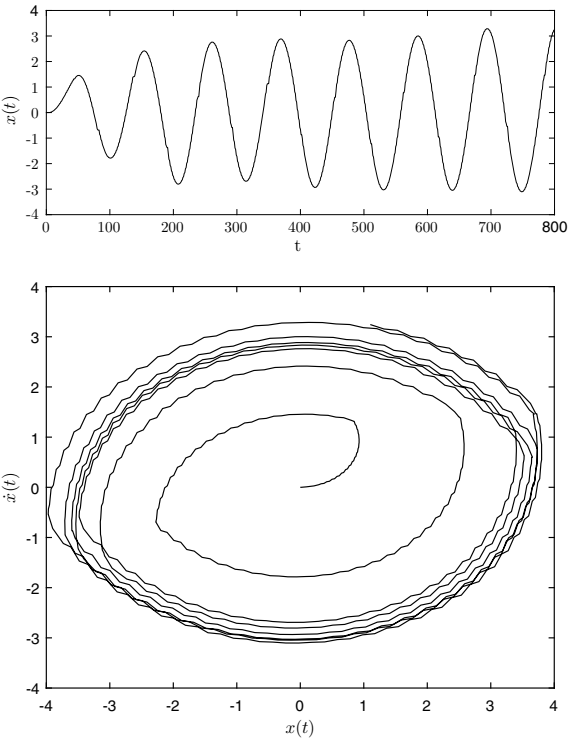

Fig. 12.9 Solution (top panel) and phase portrait (bottom panel) for the system (12.38)

We also note that under the conditions of the theorem, the rate of growth of the amplitude with probability 1 is proportional to the square root of time.

12.4 Hysteresis in Discrete Sine-Gordon Model

12.4.1 Bouc-Wen Model

Dependencies of hysteretic type are determined by input-output correspondences, when the output depends not only on the instantaneous value of the input, but also on its behavior in the preceding moments of time (memory effect). Mathematical models of mechanical properties of many building materials, such as reinforced concrete, steel, wood, as well as the damping materials, usually include a nonlinear hysteresis mechanism that takes into account the restoring properties of these structures.

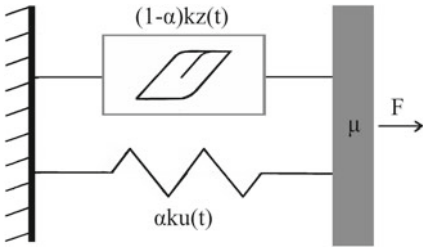

Fig. 12.10 Visualization of the Bouc-Wen model

Mathematical models of hysteresis-type phenomena are rather diverse and include both design models (backlash, stop, non-ideal relay, as well as their continuous analogues, namely the Ishlinskii and Preisach models [9]), and phenomenological models (S-converter, Duhem model, Bouc-Wen model, etc. [1, 5, 7, 14, 29]). In this paper, we focus on the phenomenological approach based on the Bouc-Wen model for describing the hysteresis nonlinearity [2, 7, 23].

Let us consider the equation of motion of a single-degree-of-freedom (Fig. 12.10) system:

$$\mu\ddot{u}(t) + F(u, z) = f(t), \tag{12.39}$$

where μ is the mass, $u(t)$ is the displacement, $F(u, z)$ is the restoring force and $f(t)$ is the excitation force (hereafter the overdot indicates the derivative with respect to time). Following the Bouc-Wen approach the restoring force is presented as (the corresponding function depends on the input and output states)

$$F(u, z) = \alpha k u(t) + (1 - \alpha) k z(t). \tag{12.40}$$

From (12.40) it follows that the restoring force $F(u, z)$ can be divided into elastic and hysteretic parts, where k is the yielding stiffness, α is the ratio of post-yield to pre-yield (elastic) stiffnesses and $z(t)$ is the non-dimensional hysteretic parameter that satisfies the following nonlinear differential equation with zero initial condition ($z(0) = 0$):

$$\dot{z}(t) = \left[A - |z(t)|^n (\beta + \text{sign}\,(z(t)\dot{u}(t))\,\gamma)\right]\dot{u}(t), \tag{12.41}$$

where, A, β, γ and n are non-dimensional parameters controlling the behavior of the model and sign$(\cdot)$ is the standard signum-function. For small values of the positive exponential parameter n the transition from elastic to post-elastic branch is smooth, whereas for large values of this parameter the transition becomes abrupt, approaching that of a bilinear model. Parameters β and γ control the size and shape of the hysteretic loop. Thus, such a multi-parameter model describes wide class of hysteretic systems [2, 7, 23].

12.4.2 Discrete Sine-Gordon Model with Hysteretic Nonlinearity

The most well-known and well-studied equations in mathematical physics are equations describing the propagation of waves in a linear medium. For a nonlinear medium with hysteresis properties, there are no ready-made methods for solution of such equations.

One of the interesting results of the analysis of wave propagation processes in nonlinear media is the existence of soliton solutions—solitary waves behaving like particles. One of the models that has a soliton solution is the sine-Gordon system. This system can be presented as a chain of nonlinear pendulums with elastic torsion-tied links. This model is widely used both in biology and in physics. This system has many applications, including the propagation of crystal defects and domains in ferromagnetic and ferroelectric materials, the propagation of splay waves on biological (lipid) membranes, one-dimensional model of elementary particles and propagation of magnetic flux quanta in the long Josephson junction [17].

In what follows we consider a mechanical system with hysteretic links [12, 25]. The physical model of such a system is shown in Fig. 12.11. It is a chain of identical pendulums strung on a string and connected by springs [15]. Pendulums oscillate transversely to the direction of the chain. The principal feature of the mechanical system under consideration is that the backlash-type hysteretic nonlinearity [24] is included in the connection between two neighboring pendulums. This system is a modification of the classical mechanical sine-Gordon system and can be called hysteretic sine-Gordon system.

Let μ be the mass of the pendulum, μl^2 is the moment of inertia, l is the length, and κ is the torsion constant of the spring. When the deviation of the pendulum with number m from the equilibrium point by an angle θ_m takes place, the gravitational force moment $-\mu g l \sin\theta_m$ acts on the pendulum alongside the torsional moment acting on the side of adjacent springs $-\kappa(\theta_m - \theta_{m-1}) + \kappa(\theta_{m+1} - \theta_m)$. Since the hysteretic nonlinearity is included in the system, the equation of motion can be presented as:

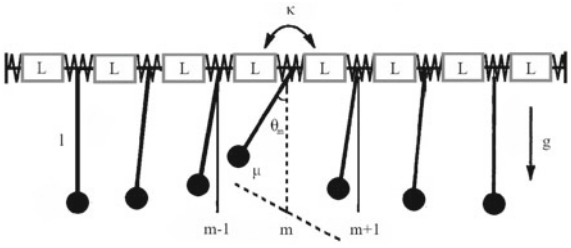

Fig. 12.11 Hysteretic sine-Gordon system model

$$\begin{cases} \mu l^2 \ddot{\theta}_m = -\mu g l \sin\theta_m + \omega_m^l + \omega_m^r, \\ \omega_m^l = L[\omega_m^l(t_0); y_m^l(t_0)] y_m^l(t), \\ y_m^l = -\kappa(\theta_m - \theta_{m-1}), \\ \omega_m^r = L[\omega_m^r(t_0); y_m^r(t_0)] y_m^r(t), \\ y_m^r = \kappa(\theta_{m+1} - \theta_m), \end{cases} \tag{12.42}$$

where the time-dependent outputs ω_m^l, ω_m^r and inputs y_m^l, y_m^r (these inputs are the corresponding moments affecting single pendulum from the left and right sides relative to neighbor pendula, respectively) are the corresponding outputs and inputs for the physically realizable converter $L[\cdot]$ in the frame of Krasnosel'skii and Pokrovskii approach [9], and $\omega_m^{\cdots}(t_0)$, $y_m^{\cdots}(t_0)$ are the corresponding initial states (output and input, respectively) of the converter.

12.4.3 Numerical Results

It is known that the operator interpretation of the hysteretic nonlinearity implies the non-smoothness of the corresponding operator. Therefore, in our numerical simulation we use the approach to hysteresis based on the Bouc-Wen phenomenological model. In this case, the sine-Gordon system with the hysteretic nonlinearity in the links takes the following form:

$$\begin{cases} \mu l^2 \ddot{\theta}_m = -\mu g l \sin\theta_m - \alpha\kappa(\theta_m - \theta_{m-1}) - (1-\alpha)\kappa z_m^l + \\ \qquad\qquad + \alpha\kappa(\theta_{m+1} - \theta_m) + (1-\alpha)\kappa z_m^r, \\ \dot{z}_m^l = \left(A - |z_m^l|^n \left\{\beta + \text{sign}\left[z_m^l(\dot{\theta}_m - \dot{\theta}_{m-1})\right]\right\}\gamma\right)(\dot{\theta}_m - \dot{\theta}_{m-1}), \\ \dot{z}_m^r = \left(A - |z_m^r|^n \left\{\beta + \text{sign}\left[z_m^r(\dot{\theta}_{m+1} - \dot{\theta}_m)\right]\right\}\gamma\right)(\dot{\theta}_{m+1} - \dot{\theta}_m). \end{cases} \tag{12.43}$$

We performed the numerical simulation of the dynamics of the mechanical system described by (12.43). Namely, we obtained the numerical solutions to the Cauchy's problem for (12.43) using the 4-th order Runge-Kutta method (our numerical results obtained using MATLAB® system). For example, for results presented in Fig. 12.12 (right panel) the model time is $t = 200$ and the corresponding time-step is $h = 0.1$. In such a system appearance of soliton-like solutions is expected (in the same manner as for the classical sine-Gordon system). The solitary wave, which is the solution to (12.43), is treated as a dynamical object that retains energy for a long time. The chain has a finite length $m = 100$ (we recall that we consider a discrete system), and its ends are fixed. The initial conditions for pendulums

$$\theta_1(t_0), \dot{\theta}_1(t_0), \theta_2(t_0), \dot{\theta}_2(t_0), \ldots, \theta_{m-1}(t_0), \dot{\theta}_{m-1}(t_0), \theta_m(t_0), \dot{\theta}_m(t_0)$$

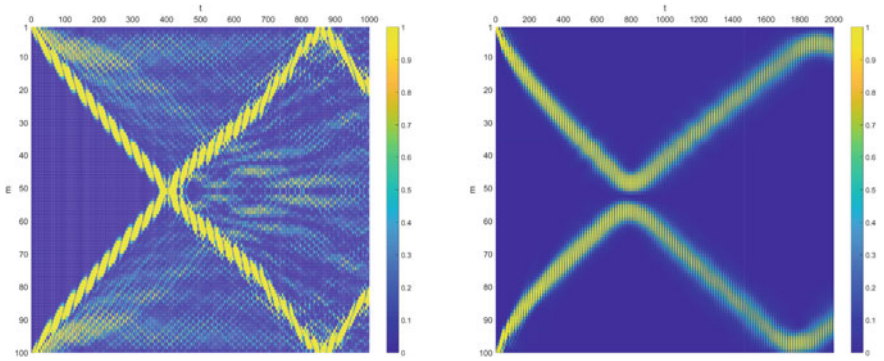

Fig. 12.12 Simulation of the collision of two soliton-like solutions without hysteresis (left panel) and with hysteresis (right panel) in the links

generate a family of solitonic solutions moving with different velocities along the (m, t)-plane with reflection at the ends of the chain ($m = 1, m = 100$). For the parameters of the hysterestic blocks formalized by means of the Bouc-Wen model, $z_m^l(t_0)$, $z_m^r(t_0)$, the initial conditions are zero by default.

Let us have a look on the dynamics of two solitonic solutions launched from opposite ends of the chain, as shown in Fig. 12.12. The corresponding initial conditions

$$\theta_1(t_0) = 2\pi, \dot{\theta}_1(t_0) = 1, \theta_2(t_0) = 0, \ldots, \dot{\theta}_{m-1}(t_0) = 0, \theta_m(t_0) = 2\pi, \dot{\theta}_m(t_0) = 1$$

generate two pulses, moving towards each other. During the simulation, two solitary waves collide in situations without ($\alpha = 1$, left panel) and with ($\alpha = 0.75$, $\beta = 0.1$, $\gamma = 0.9$, right panel) hysteresis in the links. The interaction of two pulses can demonstrate the nature of the colliding formations, since solitons interacting with each other, show special properties (similar to particle behavior). As follows from the numerical results presented in Fig. 12.12 (left panel), the dynamics of solutions demonstrates all the properties of soliton-like objects (they do not change their shape and speed). In the case when there are hysteretic connections between the pendulums (right panel in Fig. 12.12), soliton-like solution changes the speed (as can be seen by breaking the symmetry of the reflection process at the ends of the chain), retaining its shape, as well as the nature of interaction.

In order to study the influence of hysteresis bonds in the system, we consider the case in which the vibrations of 25th ($\theta_{25}(t_0) = 2\pi, \dot{\theta}_{25}(t_0) = 0$) and 75th ($\theta_{75}(t_0) = \pi, \dot{\theta}_{75}(t_0) = 0$) pendulums are excited with the corresponding initial conditions. Under these initial conditions, the oscillations of the corresponding components are excited in the chain (Fig. 12.13 (left panel)). In the case when the hysteresis in the links is taken into account (Fig. 12.13 (right panel)), spatial localization of oscillations is observed.

Let us consider in more detail the evolution of the states of the components of the chain $(\theta(t), \dot{\theta}(t))$ in the neighborhood of 25th and 75th pendulums. Figures 12.14

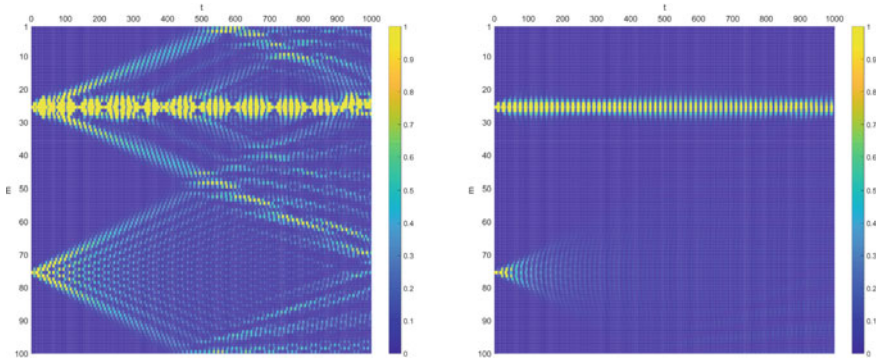

Fig. 12.13 Simulation of the dynamics of localized oscillations of pendulums in a chain without hysteresis (left panel) and with hysteresis (right panel) in the links

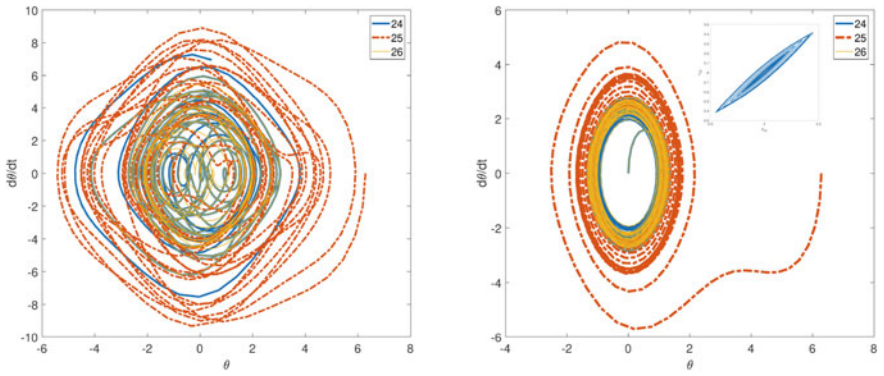

Fig. 12.14 Phase portraits of 24th, 25th, 26s pendulums without hysteresis (left panel) and with hysteresis (right panel) in the links. The input (right panel) shows the corresponding hysteretic loop obtained as a solution to (12.41)

and 12.15 show the phase portraits for 24th, 25th, 26s, 74th, 75th, 76s pendulums, respectively together with corresponding hysteretical loops (such loops are obtained as a numerical solution to (12.41) of the Bouc-Wen model). As follows from these figures, in the absence of hysteretic bonds ($\alpha = 1$) the dynamics of pendulums demonstrates a complex oscillatory structure. However, in the presence of hysteresis in the bonds ($\alpha = 0.5, \beta = 0.1, \gamma = 0.9$), the dynamics in the neighborhood of the 25th pendulum is regularized and the stable limit cycle can be seen. Note a similar behavior for the 75th pendulum (Fig. 12.15).

Also, we investigated the influence of the hysteretic blocks in the connections between pendulums by using the methods of spectral analysis. We performed the Fourier transform for the 25th pendulum in the presence of hysteretic block ($\alpha = 0.5, \beta = 0.1, \gamma = 0.9$) and without ($\alpha = 1$) it. The corresponding results are shown in Fig. 12.16. As it follows from the results presented in this figure, the oscillation

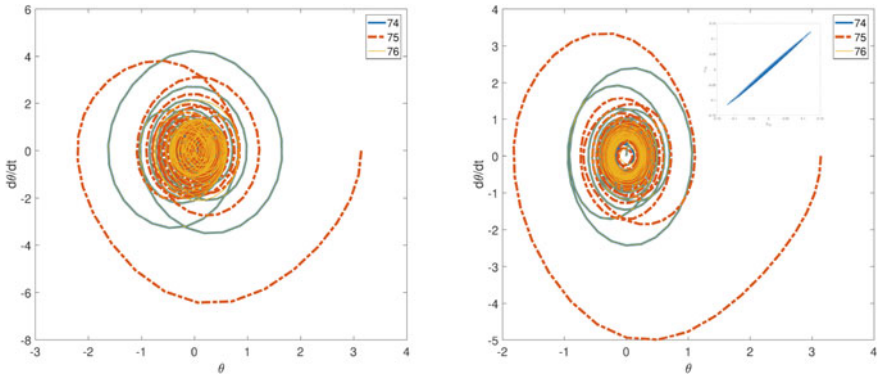

Fig. 12.15 Phase portraits of 74th, 75th, 76s pendulums without hysteresis (left panel) and with hysteresis (right panel) in the links. The input (right panel) shows the corresponding hysteretic loop obtained as a solution to (12.41)

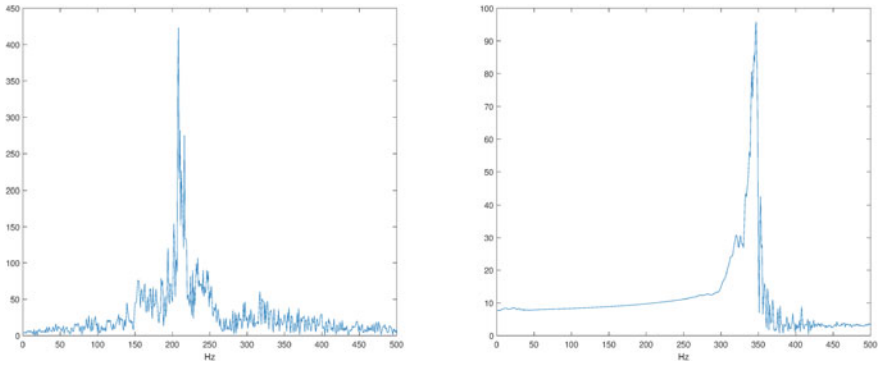

Fig. 12.16 The oscillation spectrum of the 25th pendulum without hysteresis (left panel) and with hysteresis (right panel) in the link

spectrum changes after inclusion of hysteretic bonds. Thus we can conclude that the hysteresis in such a system plays a role of a "filter" that quenches frequencies corresponding to small-amplitude oscillations and releases the main frequency.

12.5 Conclusions

In this chapter we study the resonant properties of autonomous system in which the energy "pumping" takes place due to the presence of a part with hysteretic properties. Unlimited solutions to differential equation corresponding to autonomous system containing hysteretic part with inversion of switching numbers are investigated. The cases of Coulomb and viscous friction for the system being considered

and the occurrence of self-oscillatory regimes is established. We applied also the small parameter approach to the problem of the frequency "trapping" in the system under consideration. It is shown that the "trapping" band is uniquely dependent on the amplitude of the external force.

Also we present a generalization of the classical hysteretic converter in the form of non-ideal relay to the case when its switching numbers are randomly distributed according to a corresponding law. The properties of this converter are established (namely, the definition, together with the monotonicity), as well as the dynamics of the simple mechanical system in the form of oscillator under hysteretic force determined by a non-ideal relay with random parameters is considered.

Special attention was paid to the dynamics of an oscillatory system with many degrees of freedom under conditions of hysteretic blocks in the coupling between the individual parts of the system. This system can be classified as a modified mechanical model of the sine-Gordon system in the case when the connections between the pendulums contain a hysteretic nonlinearity. The hysteretic nonlinearity was formalized by means of the Bouc-Wen model which allows a fairly simple numerical realization. On the basis of numerical simulations, the dynamics of the solitonic solution for this system was studied taking into account the hysteretic nature of the coupling. It was demonstrated that the presence of hysteretic coupling leads to a change in the speed of propagation of the solitary solution while maintaining the character of interaction between various solitary solutions. Also, the results of numerical simulation demonstrate the regularizing role of hysteresis bonds in the character of oscillatory motions. The filtering properties of hysteretic bonds are inferred from the spectral analysis of the oscillatory motions of individual components of the system under consideration.

Acknowledgements The works of authors (Introduction, Oscillator under hysteretic force and Oscillator under force with random parameters (Sects. 12.1–12.3)) was supported by the RFBR (Grants 17-01-00251-a, 18-08-00053-a, and 19-08-00158-a). The work of M.E. Semenov and P.A. Meleshenko (Hysteresis in discrete sine-Gordon model (Sect. 12.4)) was supported by the RSF grant No. 19-11-0197.

References

1. R. Bouc, Modèle mathématique d'hystérésis: application aux systèmes à un degré de liberté. Acustica **24**, 16–25 (1971)
2. A.E. Charalampakis, The response and dissipated energy of Bouc-Wen hysteretic model revisited. Arch. Appl. Mech. **85**(9), 1209–1223 (2015)
3. H. Haken, *Quantum Field Theory of Solids: An Introduction* (North-Holland, 1976)
4. V. Hassani, T. Tjahjowidodo, T. Nho Do, A survey on hysteresis modeling, identification and control. Mech. Syst. Signal Process. **49**(1–2), 209–233 (2014). https://doi.org/10.1016/j.ymssp.2014.04.012
5. F. Ikhouane, J.E. Hurtado, J. Rodellar, Variation of the hysteresis loop with the Bouc-Wen model parameters. Nonlinear Dyn. **48**(4), 361–380 (2007)
6. F. Ikhouane, V. Mañosa, J. Rodellar, Dynamic properties of the hysteretic Bouc-Wen model. Syst. Control. Lett. **56**(3), 197–205 (2007)

7. F. Ikhouane, J. Rodellar, On the hysteretic Bouc-Wen model. Nonlinear Dyn. **42**(1), 63–78 (2005)
8. A. Krasnosel'skii, A. Pokrovskii, Dissipativity of a nonresonant pendulum with ferromagnetic friction. Autom. Remote. Control. **67**, 221–232 (2006)
9. M.A. Krasnosel'skii, A.V. Pokrovskii, *Systems with Hysteresis* (Springer, Berlin, 1989)
10. L.D. Landau, E.M. Lifshitz, *Course of Theoretical Physics*, vol. 1, Mechanics (Pergamon Press, 1960)
11. A.J. Lichtenberg, R. Livi, M. Pettini, S. Ruffo, *Dynamics of Oscillator Chains* (Springer, Berlin, 2007), pp. 21–121
12. P.A. Meleshenko, A.V. Tolkachev, M.E. Semenov, A.V. Perova, A.I. Barsukov, A.F. Klinskikh, Discrete hysteretic sine-Gordon model: soliton versus hysteresis, in *MATEC Web of Conferences*, vol. 241 (2018), p. 01027. https://doi.org/10.1051/matecconf/201824101027
13. B. Øksendal, *Stochastic Differential Equations. An Introduction with Applications* (Springer, Berlin, 2003)
14. Y. Rochdi, F. Giri, F. Ikhouane, F.Z. Chaoui, J. Rodellar, Parametric identification of nonlinear hysteretic systems. Nonlinear Dyn. **58**(1), 393–404 (2009). https://doi.org/10.1007/s11071-009-9487-y
15. A. Scott, A nonlinear Klein-Gordon equation. Am. J. Phys. **37**(1), 52–61 (1969)
16. A.C. Scott, *Active and Nonlinear Wave Propagation in Electronics* (Wiley-Interscience, New-York, 1970)
17. A.C. Scott, *Nonlinear Science. Emergence and Dynamics of Coherent Structures* (Oxford University Press, 1999)
18. M.E. Semenov, P.A. Meleshenko, A.M. Solovyov, A.M. Semenov, *Hysteretic Nonlinearity in Inverted Pendulum Problem* (Springer International Publishing, 2015), pp. 463–506
19. M.E. Semenov, A.M. Solovyov, P.A. Meleshenko, Elastic inverted pendulum with backlash in suspension: stabilization problem. Nonlinear Dyn. **82**(1), 677–688 (2015). https://doi.org/10.1007/s11071-015-2186-y
20. M.E. Semenov, A.M. Solovyov, M.A. Popov, P.A. Meleshenko, Coupled inverted pendulums: stabilization problem. Arch. Appl. Mech. **88**(4), 517–524 (2018)
21. M.E. Semenov, A.M. Solovyov, A.G. Rukavitsyn, V.A. Gorlov, P.A. Meleshenko, Hysteretic damper based on the Ishlinsky–Prandtl model, in *MATEC Web of Conferences*, vol. 83 (2016), p. 01008
22. J. Sieber, T. Kalmár-Nagy, Stability of a chain of phase oscillators. Phys. Rev. E **84**, 016227 (2011)
23. A. Solovyov, M. Semenov, P. Meleshenko, A. Barsukov, Bouc-Wen model of hysteretic damping. Procedia Eng. **201**, 549–555 (2017)
24. A.M. Solovyov, M.E. Semenov, P.A. Meleshenko, O.O. Reshetova, M.A. Popov, E.G. Kabulova, Hysteretic nonlinearity and unbounded solutions in oscillating systems. Procedia Eng. **201**, 578–583 (2017)
25. A. Tolkachev, M. Semenov, P. Meleshenko, O. Reshetova, A. Klinskikh, E. Karpov, Sine-Gordon system with hysteretic links. J. Phys. Conf. Ser. **1096**, 012072 (2018). https://doi.org/10.1088/1742-6596/1096/1/012072
26. C.G. Torre, *Foundations of Wave Phenomena* (Utah State University, 2015)
27. D.I. Trubetskov, A.G. Rozhnev, *Lineynyye kolebaniya i volny* (Fizmatlit, Moscow, 2001). (in Russian)
28. J.Y. Tu, P.Y. Lin, T.Y. Cheng, Continuous hysteresis model using Duffing-like equation. Nonlinear Dyn. **80**(1), 1039–1049 (2015). https://doi.org/10.1007/s11071-015-1926-3
29. Y.K. Wen, Method for random vibration of hysteretic systems. J. Eng. Mech. **102**(2), 249–263 (1976)
30. V.G. Zadorozhniy, Linear chaotic resonance in vortex motion. Comput. Math. Math. Phys. **53**(4), 486–502 (2013)
31. V.G. Zadorozhniy, S.S. Khrebtova, First moment functions of the solution to the heat equation with random coefficients. Comput. Math. Math. Phys. **49**(11), 1853 (2009)

Chapter 13
Drops and Bubbles as Controlled Traveling Reactors and/or Carriers Including Microfluidics Aspects

Manuel G. Velarde, Yuri S. Ryazantsev, Ramon G. Rubio, Eduardo Guzman, Francisco Ortega and Antonio Fernandez-Barbero

Abstract Provided here is a succinct survey of significant features of theory and experiments dealing with drops or bubbles which may act as traveling reactors or mere carriers of appropriate payloads in microfluidic flows and devices. The units could be the seat of inner or surface reactions, internal heat generation, phase transformations or the like that provoke interfacial tension inhomogeneity and eventually controlled, directed or self-propelled motion (Marangoni effect).

13.1 Introduction

Research on capillary phenomena and, in particular, the study and applications of statics and dynamics of drops, bubbles and other systems like liquid bridges, had a high momentum in the second half of the XXth century due to the availability of space exploration related facilities. It was the time of so-called microgravity research, or better said research motivated by the availability of low effective gravity facilities (in principle down to $10^{-6} g_{\text{Earth}}$: drop tubes and towers, sounding rockets, aircraft for parabolic flights, and the various space labs including the one in the Space station). Then at the end of the century, a golden period came for the same fluid physics subfield with the availability of microelectronics and microelectromechanical (MEMS) devices, surely also fostered by the needs of space exploration. These technologies have been indispensable for the extraordinary development of microfluidics.

Microfluidics deals with processing and manipulating small amounts of fluid (subnanoliters/picoliters/subfemtoliters: 10^{-9} to 10^{-18} L), using channels with dimensions 10–100 m, manipulating small groups of molecules in space and time, using fluids together with powders or the like (in the range 10 nm–10 μm or a bit bigger).

M. G. Velarde (✉) · Y. S. Ryazantsev · R. G. Rubio · E. Guzman · F. Ortega
Instituto Pluridisciplinar, UCM, Paseo Juan XXIII, 1, 28040 Madrid, Spain
e-mail: mgvelarde@pluri.ucm.es

R. G. Rubio · E. Guzman · F. Ortega
Departamento de Quimica Fisica, UCM, Ciudad Universitaria, s/n, 28040 Madrid, Spain

A. Fernandez-Barbero
Departamento de Quimica y Fisica, Universidad de Almeria, 04120 Almeria, Spain

M. Belhaq (ed.), *Topics in Nonlinear Mechanics and Physics*,
Springer Proceedings in Physics 228, https://doi.org/10.1007/978-981-13-9463-8_13

Encapsulation (the simplest case is a gas bubble coated with a liquid film; more complex and interesting for its functional applicability are items like chemical or pharmacological payloads) and manipulation, chemical and otherwise, of bacteria (like *Escherichia colli*, encapsulated in, e.g., a water-in-oil drop), single cells (e.g., mammalian cells), individual subcellular organelles or single molecules, hence drops acting as "reactors", subsequently permitting controlled release of "active" agents (the encaged payloads) and thus used as traveling delivery carriers for nutrients, fragrances, drugs, etc., moving in another inert carrier fluid are of current technology in the food processing, cosmetics industry, detergent and pharmaceutical industries and medical care sectors [2, 5, 10, 14, 17, 19, 30, 35–37, 40]. Mixing of encaged reagents in a drop permits reaction kinetic studies.[1]

High surface-to-volume ratios are key in defining fluid and flow characteristics at the microscale. Of equal importance is the effect of those ratios on diffusion-assisted heat and mass transfer in reactive processes for both homogeneous and heterogeneous chemistry like gas-liquid-solid reactions in micro channels. Other ratios of forces/stresses defining significant dimensionless groups are the ratio of interfacial to viscous forces (capillary number) and the ratio of interfacial to inertial forces/hydrodynamic pressure (Weber number). Specific definitions are provided below when strictly necessary. Suffices to say now that for drops or bubbles both such two ratios account for the possible role of deformability (due to motion) and eventual breakage. Here to limit the length of our contribution to a reasonable size, we shall disregard deformability indicating that –presumably due to lack of interest on drops before microfluidics became fashionable– it has taken over two decades to extend to deformable drops the work done, back in 1994, on undeformable drops by two of the present authors [20, 23, 26–29, 34, 44, 45, 47, 49]. Yet another quantity of interest is the capillary length (think about the size of drops or bubbles) which in the presence of gravity, or some other body force (electric, magnetic, etc.), is the root square of the ratio of interfacial tension to the body force. The aspect ratio drop's size/channel scale (say height) is also expected to be significant.

At micro level, long range correlations/influences are of utmost importance. No human body or the like swimming in a pool expects to be affected by another swimmer separated by a distance of, say, 30 lengths of a typical body (say 50 m). It is the opposite what matters in microfluidics where a "strong" correlation/influence tends to exist between swimmers and with nearby boundaries/walls. Typical cases already well documented are oil drop based systems composed of water, oil and surface active agents (in short, surfactants). Oils are generally lighter than water and of higher shear/dynamic viscosity η (generally $\eta_{oil} > \eta_{water} = 10^3$ Ns/m^2; dilatational

[1] Micro $= 10^{-6}$, nano $= 10^{-9}$, pico $= 10^{-12}$, femto $= 10^{-15}$; microfluidic drops/picoliter volumes with sizes up to 100 μm, velocities in the range 1–10 μm/s (or higher). The molecular volume of a "hard" sphere is about 11.25 Angstroms, a water molecule is about 30 Angstroms (1 Å $= 10^{-10}$ m $= 0.1$ nm, 1 nl $= (10^2\ \mu\text{m})^3$), a typical colloidal particle radius is 0.1 m having 10^{12} times the mass of a water molecule, a typical pollen grain radius is 10^{-5} m with a density 1 g/cm^3. Warning: for sizes below 1 μm, Brownian motion becomes significant eventually dominating the evolution (a further comment on this below). There is also nanofluidics coming in with fluids moving along, e.g., 10^2 nm and lower scale channels handling items in the range 1 Å–10^2 nm.

viscosity is here neglected, more on this will be discussed later). Adding surfactants may help preventing drop coalescence thus ensuring stability of single drops, when the surfactant itself does not interact or exchange with the chemicals inside a drop. However, drops are seldom completely sealed and molecules can traverse in and out in their surface, particularly if this is a bilayer. Further, the surfactant concentration can be used to tune the swimming behavior.[2] The surface of the drop is here assumed "infinitesimally" thin considering that its radius is much bigger than the "surface width". Experiments can last for hours with the possibility of creating a large number of "identical" drops or bubbles. One possible design of a traveling carrier (swimmer) is an "active" drop chemically reacting or phase transforming at its surface or internally, with inhomogeneous in/out flux of surfactants, dissolving with spontaneous motion at its surface or eventually splitting into smaller drops, immersed in a solution of a reactive surfactant or illuminated leading to interfacial tension inhomogeneity, change of pH, etc.

As a side remark, it seems worth mentioning that the permeability of soft particles is of special interest for their use as microfluidic devices (such as valves in narrow capillaries) as molecular carriers and local releasers, or as adjustable micro reactors. For instance, polymer-gel micro particles are excellent systems as experimental checkers, due to their ability to change their softness as a response to external triggering signals. For charged Brownian particles, a simple electrophoretic mobility experiment in which particle velocity is recorded after the application of an electrical drag pulling force becomes very useful to access the permeability effects. As a first approximation, a limit final velocity is reached after forces equilibration. However, this very visual frame becomes more interesting when a redistribution of ions by shielding and Donnan effects (around and inside the polymer network) is applied. Experiments using charged polymer particles have shown a dramatic influence of the polymer-network charge on the permeability and consequently, on the particles dynamics. On the other hand, temperature-sensitive polymers (usually Isopropylacrylamide-based polymers) allow a fine swelling control by acting directly on the polymer solubility (temperature control). Additionally, the copolymerization with acrylic acid allows the control of the network charge thought the bulk pH. The effective charge (hydrodynamically manifested) depends on the activation of acid groups responsible for the charge bared on the mesh, shielded by the counter ions migrating from the polyelectrolyte surrounding bath. Those dragged counter ions have proven to provoke additional mechanical propulsion of the fluid inside the polymer mesh. The polymer network will thus act as a valve activated by the external electric field, mediated by the counter ions migration. Neutral swollen polymer particles show non-permeable behavior, with mobility decreasing as size rises. However, for ionic (charged) swollen polymer particles, their mobility rises as size makes larger, as a consequence of the counter ions migration. Though interesting

[2]Warnings: when drops approach each other in the hundred nanometer and lower separation range, the carrier liquid may also prevent coalescence and rather foster aggregation of drops (ruling out or just counteracting Ostwald ripening) if surface forces (Derjaguin-Casimir pressure, DLVO theory, see, e.g., [38, 39] play a significant role (aggregation leading to a solid-like behavior of the compound seems to physicochemically underly ALS and Alzheimer diseases).

enough, we shall not dwell further on these questions which are peripheral to the main subject of this contribution.

It thus seems of clear need understanding the specific features of "swimming" at the microscale, either directed/guided or self-propelled motions, for developing microfluidic devices. At micro level, flow behavior is controlled by viscous rather than inertial forces. Reynolds numbers, characterizing the ratio of inertial to viscous forces, are quite low in microfluidics, $Re = UL/\nu$ where U, L are typical scales of the system and ν is the kinematic viscosity or vorticity diffusivity; $\nu = \eta/\rho$ with ρ denotes density (when dealing with a drop or a bubble the usual length scale would be the radius, say "a"). Flows can be initiated and developed by pressure gradients, electric, osmotic/electroosmotic, magnetic, capillary forces, etc.[3] If it is the space scale that is small, like with the motion of a tiny drop or a micro swimmer, it seems acceptable to consider it too small a size to affect the main carrier flow. Thus microfluidics deals with creeping flows and/or motions of tiny objects, drops or bubbles.[4]

Note also that, generally, when dealing with drops or just liquids in macroscopic flows, as incompressibility is assumed, only the shear viscosity is introduced, hence disregarding the dilatational viscosity. The latter is a measure of the viscous forces which arise when a volume of fluid is compressed or dilated without change of shape. In reality, the compressibility of liquids is not zero and the incompressibility may not be a valid assumption for microfluidics. Indeed, the fractional change in volume per unit increase in a pressure unit is such that for water at 25 °C is 46.4 ppm (parts per million) or otherwise 46×10^{-6}/atm; for ethyl alcohol is 110×10^{-6}/atm, for glycerin is 21×10^{-6}/atm and for mercury is 4×10^{-6}/atm.

In view of the above, turbulence is possible at macro level and never at the micro level. This is the reason flow in blood capillaries is strictly laminar. On the other hand, mixing at macro level is mostly a laminar or turbulent convective process whereas at the micro level it is diffusive and hence at much smaller time and/or space scales.

Finally, it is also worth mentioning, as a side remark related to daily life, that creep in any material causes the stress to be redistributed in such a manner that the more highly stressed parts creep most. Creep in textiles and leather is one reason why our clothes go out of shape and the knees of trousers get baggy. This is why used shoes are more comfortable than the new ones. Therefore, the possible relevance of creeping when dealing with flows in channels of elastic, plastic or other deformable material, like when using polydimethylsiloxane (PDMS), in microfluidic chips, particularly with curved regions.

---

[3]Warning: though low Reynolds number means that viscous drag is paramount this is compatible with the carrier fluid itself being only of small viscosity.

[4]One more warning: please note that, for a given fluid, the ratio η^2/ρ has units of force and any object acted upon by such force will experience a Reynolds number of unity, independently of its size. A drop or other, moving at low Reynolds number therefore experiences forces smaller than η^2/ρ which for water is about one nN. And yet another warning: continuous curved flows in (particularly rectangular or the like) micro channels where the fluid tends to move outward around the curve, with most of the times secondary flows arising, deserve a specific analysis not done here.

13.2 Illustrative Typical Examples of Drop Creation, Drop Motions and Microfluidic Manipulation

There is a huge diversity of microfluidic devices used in scientific and technological applications, and it seems reasonable to just identify a few of the most common ones. Set-ups can make use of pure mechanical means, or profit from illumination affecting reaction (including phase transformations of, say, surfactants) sensitive to a given color not just heat/infrared [1, 3, 4, 6, 7, 9, 11, 13, 15, 16, 21, 33, 35, 41, 46]. Figures 13.1, 13.2, 13.3, 13.4, 13.5, 13.6 and 13.7 illustrate processes ranging from creation to (directed or self-propelled) transport of drops or bubbles, offering single or multiple emulsions, etc.

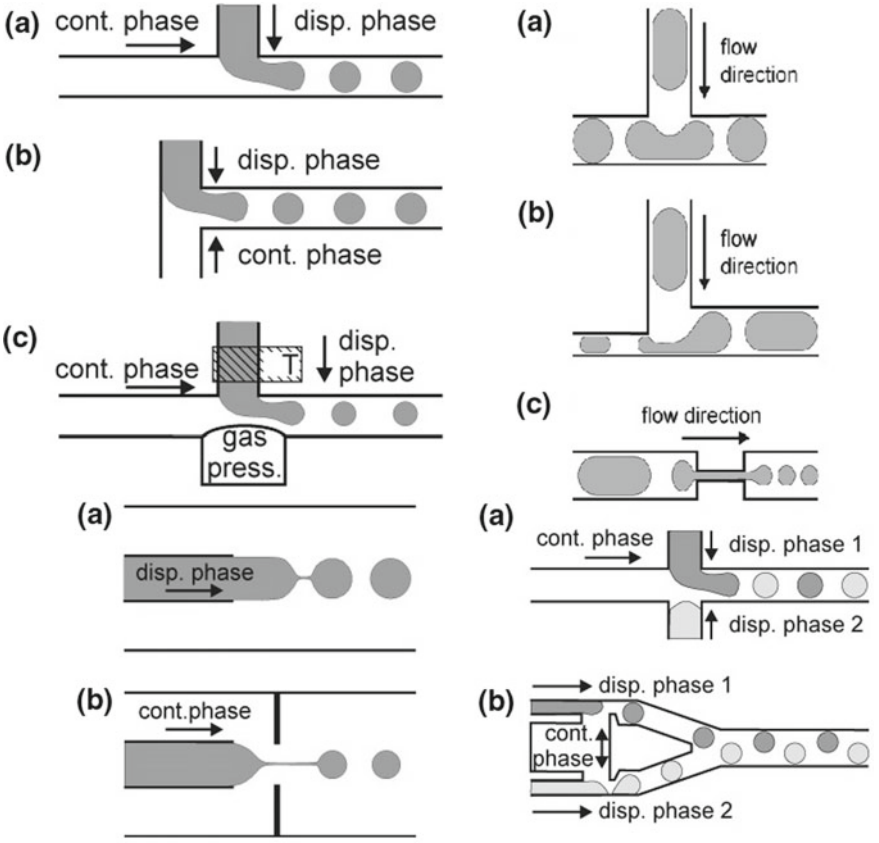

Fig. 13.1 Ways of creating one or more types of drops of different sizes (using one or more fluids to be dispersed) thus providing single or multiple emulsions in typical microfluidic devices with a fluid playing the role of dispersible phase and another that of the carrier fluid as continuous phase: single or double T-junctions with or without the addition of appropriate heating (T), co/crossflow, flow focusing, etc. Adapted from Seeman, et al. [35], with the permission of IOP Publishing

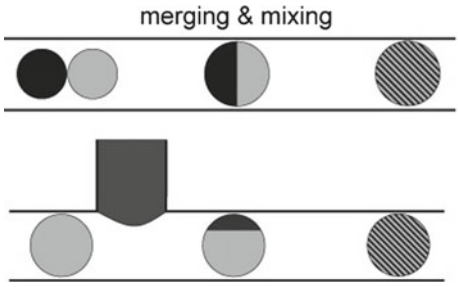

Fig. 13.2 Ways of mixing fluids inside a drop by either previously merging two separate drops (upper panel) or by just appropriately adding a second item on an already traveling drop (lower panel). Adapted from Seeman et al. [35], with the permission of IOP Publishing

Fig. 13.3 Ways of illumination of a drop with alternative consequences (schematic). Light beam crossing a transparent drop midway (left panel) or by the side (lower panel). In the former the drop is pulled towards the light source while in the latter it is the opposite. Reprinted with permission from [33]. Copyright (2004) by the American Physical Society

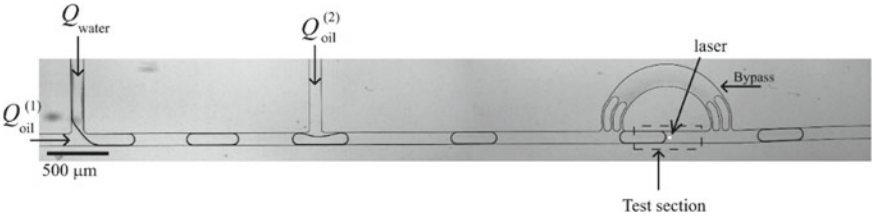

Fig. 13.4 Caging, transporting and arresting a drop in a microfluidic channel with wavelength in the infrared (IR) hence with appropriate heating. Water drops (Q_{water}) are emitted in (hexadecane) oil carrier continuous phase fluid at the extreme left T-junction ($Q_{oil}^{(1)}$). The total flow rate is adjusted downstream by a second oil entry ($Q_{oil}^{(2)}$). The "caged" drop is trapped by the IR laser light (absorbed only by the water) in the dashed rectangular section while oil can flow into the bypass. Estimates of the thermocapillary force needed to block a drop indicate orders of magnitude higher than those generated from electric fields or optical tweezers. Too high Q flows and/or too fast moving drops or too narrow channels may jeopardize the described process whatever the laser light power. Reprinted with permission from [46]. Copyright (2009) American Chemical Society

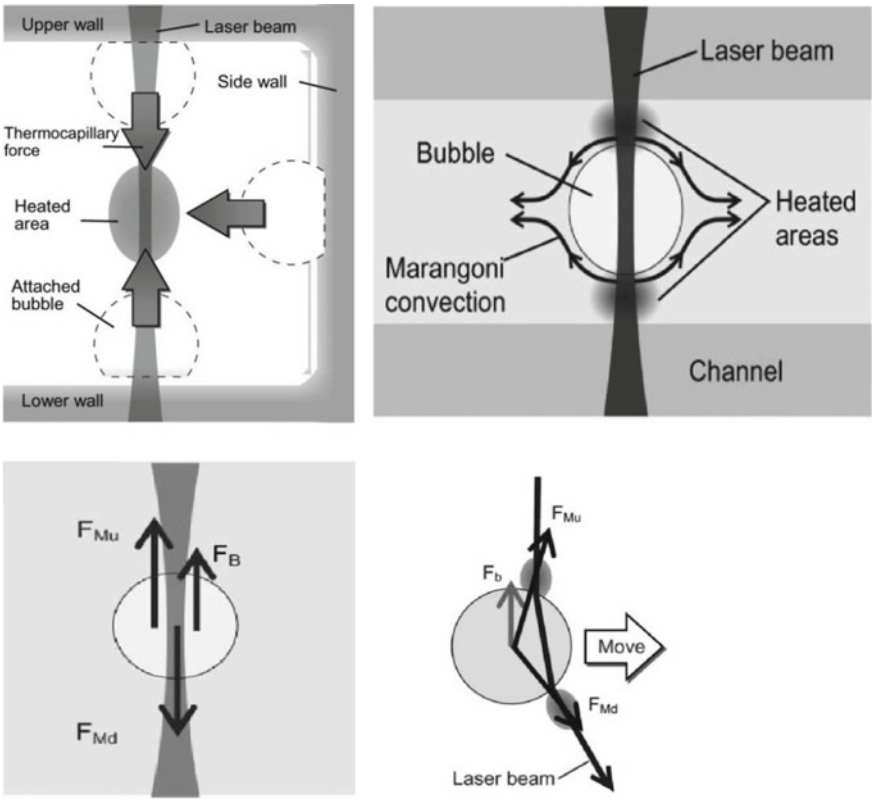

Fig. 13.5 Handling of a bubble with a laser beam and thermocapillarity. Upper panel: The left figure schematizes the creation and detachment of a bubble at a wall. The righ figure illustrates how once the bubble is centered in the space it can be suspended by the combined action of forces in balance. In the lower panel such forces involved appear either straight along the vertical or with inclination thus profiting of refringence across the bubble. Subscripts M_u, M_d and B denote, respectively, up, down and buoyancy (M stands for thermocapillarity, aka Marangoni force). Adapted from Takehuchi, et al. [41] with the permission of Taylor and Francis

Figure 13.5 illustrates how light can be used to detach, move and suspend bubbles, as a variation on one of the pioneering experiments of similar kind [50]. After its creation at a wall (either above, below or on either side of the container) a bubble is forced to detach moving to the center region. Then once it is centered in the space it can be suspended by the combined action of thermocapillarity and buoyancy.

Another device using light beams of appropriately different wavelengths is depicted in Fig. 13.6 [1, 3, 46]. Depending on wavelength there is phase transformation of photosensitive azobenzene (azoTAB) surfactant molecules from *trans* to *cis* configuration or vice versa, with each configuration offering opposite role to the other in interfacial tension alteration. Such *cis–trans* isomerization of azoTAB units has also been used by several authors [7, 15] for moving olive oil droplets along

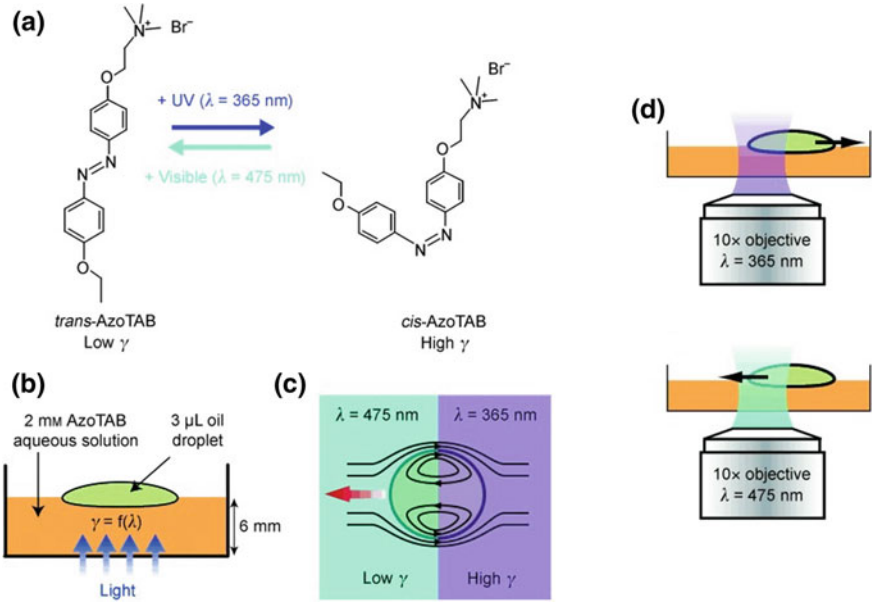

Fig. 13.6 Light beam illuminating an opaque oil drop (greenish) immersed in an aqueous solution (orange-like). **a** phase transformation of photosensitive azoTAB from *trans* (its presence increases interfacial tension on the oil drop) to *cis* configuration (lowers interfacial tension here denoted with γ) and vice versa according to the color used (visible $\lambda = 475$ nm, *UV* $\lambda = 365$ nm), **b** side view of the experimental set-up with an oil drop covered with azoTAB surfactant –black film- floating on an aqueous solution where illumination alters interfacial tension of the former, **c** top view of the set-up depicting expected flows, in the oil drop and in the aqueous solution, due to interfacial tension gradients that depend on light color (so-called chromocapillary effect due to the *trans–cis* transformation), **d** Illustration of the direction of motion according to the light color used and hence according to the role of the concentration of the corresponding surfactant molecule. Adapted from [7]. Copyright (2009), with permission from John Wiley and Sons

the direction parallel to a surface. In this particular case, the change of the surface wettability of the calix[4]resorcinarene derivative having photochromic azoTAB units attached to the substrate leads to the required gradient for liquid motion. Further, similar effect was obtained using a chemical gradient induced by photo degradation of the surface [16].

Yet another device using light of appropriate color thus leading to interfacial tension gradient-driven controlled, directed motion is shown in Fig. 13.7. It is denoted as chromocapillarity or photochemopropulsion related to pH conditions [4, 9]. A microliter drop of dichloromethane (DCM), with a suitable mixture of 2-hexyldecanoic acid (HDA) and chromo-ionophore (CI), is motionless, floating in a channel of yellow protonated merocyanine (MCH^+–SO_3^- solution) under the initial pH condition (pH = 5). Upon irradiation with white light, in kind of photo-modulation of pH, MCH^+–SO_3^- reverts to SP–SO_3^- (radical from water soluble spiropyran sulfonic acid), releasing free H^+ (pH = 3.4). Under this acidic condition, the (conjugated acid,

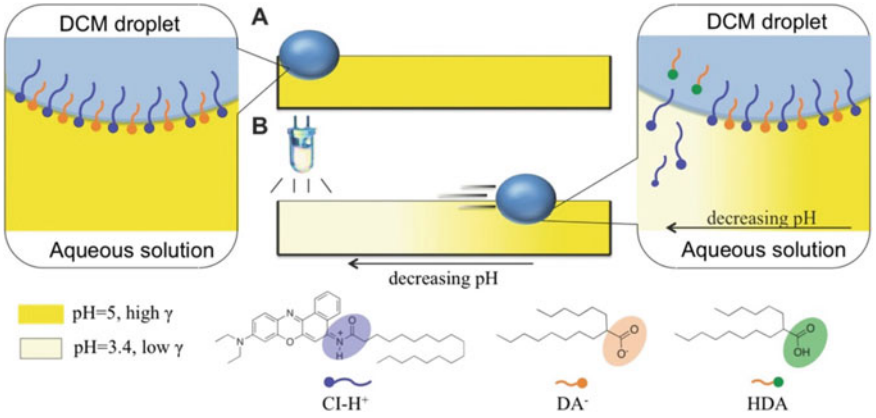

Fig. 13.7 Schematic representation of the role of illumination, change in pH leading to Marangoni-driven directed motion and arrest of a drop. **a** A microliter drop of DCM, with a suitable mixture of HDA and CI [volumen1:1, molar excess HDA: CI about 170:1], is motionless, floating in a channel (l, w, h: 5.5 cm, 2 mm, 1 mm) of MCH^+–SO_3^- solution under the initial pH = 5. **b** Upon irradiation with white light, MCH^+–SO_3^- reverts to SP–SO_3^- releasing free H^+ (pH = 3.4). Under this acidic condition, the CI–H^+ ion migrates into the aqueous phase and the drop moves directed away from the light source, hence from the low pH to the high pH regions (pH = 5). Then the drop stops there. Reprinted from [9]. Copyright (2014), with permission from John Wiley and Sons

lipophilic cationic surfactant; charged head and lyophilic tail) CI–H^+ ion migrates into the aqueous phase, generating a drastic local increase in interfacial tension, and the drop moves spontaneously away from the light source, hence from low pH to high pH regions (recall initially pH = 5). Then the drop stops in the region of high interfacial tension at the extreme right of the channel, at which it re-encounters the pH of initial condition of the extreme left of the channel.

Finally, another worth mentioning device is one where four intersecting channels forming a microfluidic network have three of them ended at platinum (Pt) gauze electrodes that protruded the surface of a solution [11]. The fourth channel ended at a reference electrode (saturated calomel electrode) and a Pt counter electrode submerged beneath the surface of the solution. The authors were able to pump drops of a nematic liquid (used to visualize motions with crossed polarizers due to their birefringence). The application of oxidizing and reducing potentials, respectively, to any two of the three Pt electrodes permitted pumping drops between them with velocities in accordance with the applied voltage.

13.3 Spontaneous Broken Symmetry Due to Competing Forces and the Role of Surfactants

For standard liquids, flow motion proceeds from the hot (low surface tension) to the cold (high surface tension) region. This also occurs when there is a surfactant concentration gradient. Added to earlier figures where this phenomenon has been depicted, Figs. 13.8, 13.9 and 13.10 provides further illustration of possibilities. The flow away from the front of the drop brings surfactant molecules to the rear where they tend to accumulate. This tendency is counteracted to some extent by diffusion, though a rather slow process, that tends toward a uniform surfactant distribution. The interfacial tension gradient tends to restore the interface to its uniform equilibrium state and this engenders flow in the proximity to the interface. This is called Marangoni flow or otherwise Marangoni effect. Surfactants also play a significant eventually

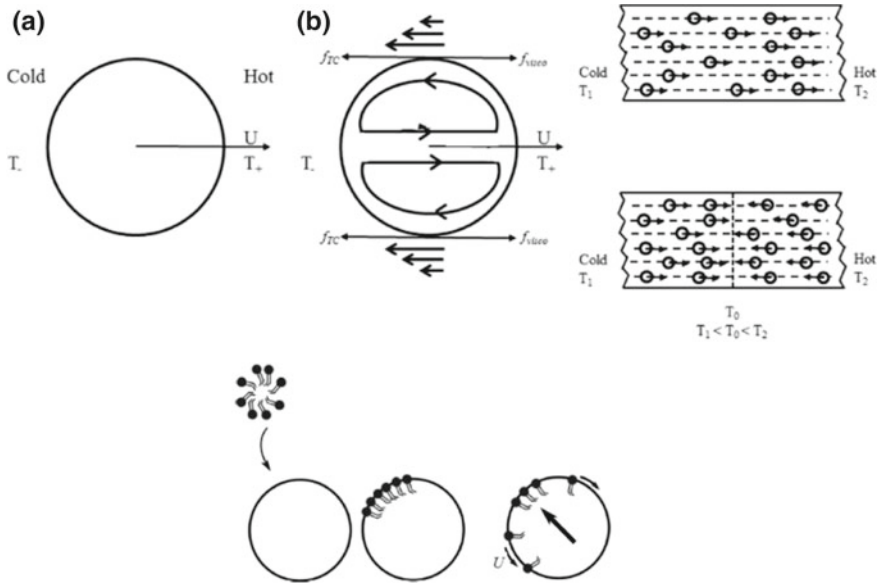

Fig. 13.8 Drop motions and flows in the presence of a temperature gradient or a surfactant concentration gradient. Left two panels: **a** oversimplified view of the expected motion with velocity U, **b** surface tension (f_{TC}) and drag forces (f_{visco}) in competition determine flow fields outside and inside the drop. Center panels: drop motions for two temperature dependences of the surface tension $\sigma = \sigma_0 + (d\sigma/dT)\left(T - T_{ref}\right)$ and $\sigma = \sigma_0 + (1/2)\left(d^2\sigma/dT^2\right)\left(T - T_{ref}\right)^2$ [12], above and below respectively (T_{ref} is a reference temperature but to make life easy T_+, T, T_1, T_2 are used; for standard liquids $(d\sigma/dT)$ could be in the range 1 mN/mK–1 nM/mK and thermocapillary force (a.k.a. Marangoni force) could be in the range 0.1 μN). Reprinted from [31], Copyright (2017), with permission from Elsevier. Extreme right panel: role of the adsorption of a micelle (a spherical aggregate of surfactant molecules) in creating, U, that spreads the surfactant molecules over the drop's surface thus propelling the drop in the direction toward the adsorption site. Adapted from [34], with the permission of AIP Publishing

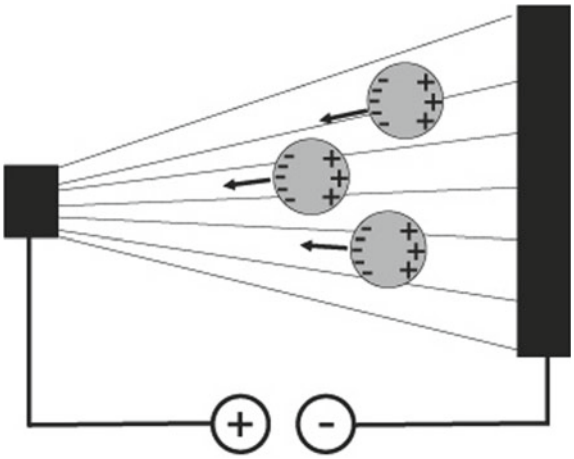

Fig. 13.9 Dielectrophoretic induced motion of drops. Adapted from Seeman, et al. [35], with the permission of IOP Publishing

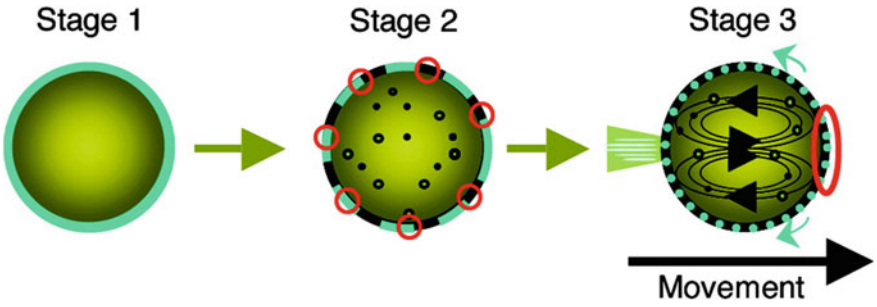

Fig. 13.10 Direct role of pH gradient. Stage 1: an oil drop (yellow) coated with a surfactant film (blue) immersed in an aqueous solution (grey). Stage 2: surfactant molecules start entering the oil and at opening sites hydrolysis occurs (red circles) thus allowing water to also enter the drop. Stage 3: spontaneous broken symmetry occurs and flow motions (arrows inside and outside of the drop). Surfactant molecules move along the surface of the drop and hydrolysis is further enhanced. There is also surfactant leaving the surface and accumulating at the rear pole of the drop thus creating a low pH region (green). Reprinted with permission from [13]. Copyright (2007) American Chemical Society

dominating role in quite many situations thus creating flow motions and for drops or bubbles controlled, directed motions and even autonomous self-propulsion. Indeed, surfactants introduce additional stresses other than stress contributed by a constant

surface tension. As mentioned in the preceding section, surfactant molecules generated at one electrode and consumed at another opposite one can create a gradient in surface pressure to direct drops through a microfluidic channel.[5]

Clearly, if a chemical reaction inducing self-propulsion occurs all over the surface of too small a drop (micrometer size) it may be hard or impossible to identify the point where the reaction starts. As motion develops quickly it may proceed in an uncontrolled direction. Note also that the chemical reaction-flow overall process can be considered as a chemomechanical (Marangoni-driven) transduction triggered by the no uniform surfactant distribution over the drop.[6]

13.4 Succinct Theoretical Analysis. Controlled Directed Motions and Self-propulsion

Consider that there are one or more external forces, like the thermocapillary one (F_{TC}) and some other body force ($F_{external}$), acting upon the drop also subject to viscous drag (F_{visco}) as in Fig. 13.11. Noteworthy is that capillary forces may be several orders of magnitude larger than those generated from electric fields or optical tweezers. When the resultant force is in the direction of the drop's motion (drop velocity and force vectors are parallel, hence having the same sign) we have a resistance force. In the opposite case (antiparallel vectors, hence opposite signs) the force gives thrust due to, e.g., thermocapillarity (F_{TC}).

Figure 13.12 shows that when acting with, e.g., a laser beam in the presence of a body force like buoyancy, or the like, the drop as it is heated tends to move up and down hence oscillations along the transverse direction of the illumination are observed [25, 31].

[5] Warnings: when using surfactants acting on drops it must be taking into account that size matters. As a drop reduces its size the surfactant concentration tends also to diminish with the scale imposed by the ratio of surface to volume and there would be less and less surfactant molecules at its surface so that their role may become negligible. Also to be noted is that when a drop moves, in a gas or air, evaporation may occur. If this is the case its radius evolves with a rate as the inverse square (a^{-2}) so that evaporation tends to proceed faster as size diminishes.

[6] Warning: for a sessile drop or a drop sliding on another liquid or on a solid substrate (disregard now spreading) the wettability conditions like wettability gradient/difference in contact angles, using magnetic fields or other agents as well as degree of hydrophilicity (wettability or hydrophobicity/no wettability) [8, 24] and not solely surface tension difference is of utmost importance and hence the inhomogeneity (chemical, mechanical) of the substrate becomes significant. To the above we must add the dominant role that the mentioned Derjaguin-Casimir forces (DLVO theory) can play.

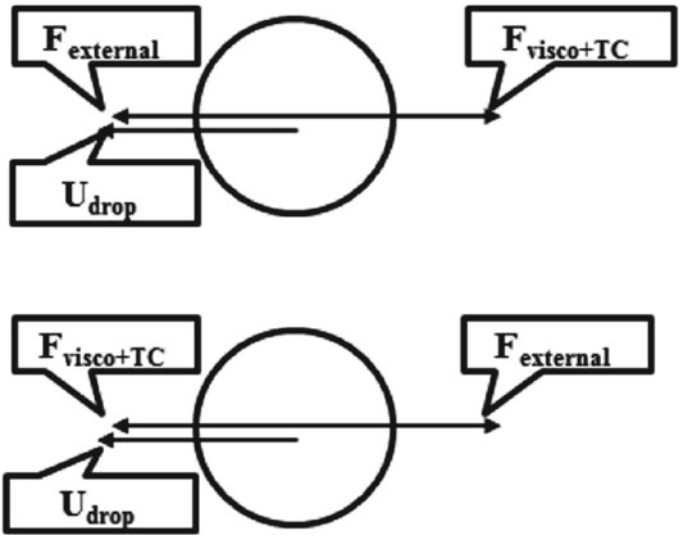

Fig. 13.11 Cooperation or competition between forces (external/$F_{external}$, thermocapillarity/F_{TC}, drag/F_{visco}) acting on a drop or a bubble. Reprinted from [31], Copyright (2017), with permission from Elsevier

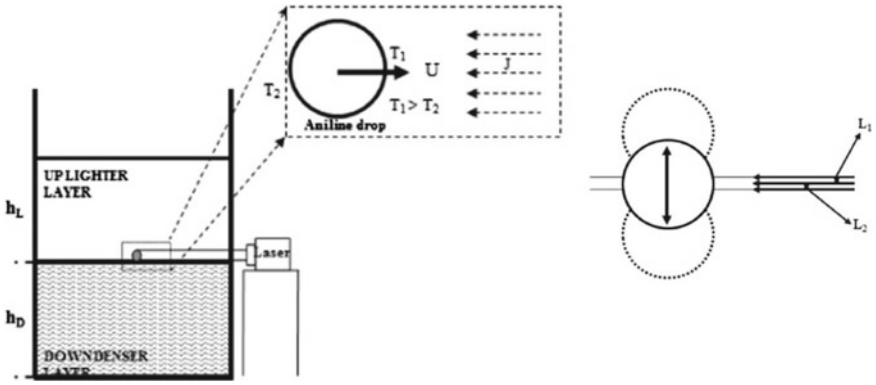

Fig. 13.12 Laser beam heating a drop and the possible oscillatory (up and down) behavior of the latter due to buoyancy leading to transitory misalignment of beam direction and drop's radius. In general, the drag force of flow on a drop scales with the squared radius (a^2) thus implying that the laser power necessary to balance drag goes down with the size of the drop. Left panel: schema of the set-up. Right panel: possible loss of collinearity (L_1, L_2) between laser beam and diameter of the drop as the former heats it. Reprinted from [31], Copyright (2017), with permission from Elsevier

13.4.1 Forces and Stresses Acting Upon a Drop or a Bubble

Let $i = 1, 2$ denote, respectively, fluid out and inside the drop. If we consider $\mathrm{Re_i} = 0$ this approximation defines the so-called Stokes flow. We have kinematic reversibility. The pattern of motion is the same, whether slow or fast, whether forward or backward in time. Any periodic motion of an object with one degree of freedom, such as a scallop, is reciprocal, and hence cannot propel itself in such a case. Yet the same system is thermodynamically irreversible due to (viscous) dissipation. Furthermore, the Stokes flow field satisfying the corresponding boundary conditions and incompressibility is the one producing the flow with minimal dissipation (or otherwise said the minimum entropy production). Note that though $\mathrm{Re_i} = 0$ the velocity remains in the hydrodynamic equations and it allows describing the flows.

For axially symmetric flows the components of the stress tensor acting upon a drop are $\sigma_{rr} = -P_1 + 2\eta_1(\partial V_{r_1}/\partial r$ and $\sigma_{r\theta} = \eta_1\left[\left(\partial V_{\theta_1}/\partial r\right) - \left(V_{\theta_1}/r\right)\right]$ where P, U, r and θ denote, respectively, pressure, velocity, radius/radial and angular direction. Hence the boundary conditions for stresses at the surface can be written as follows: $(P_2 - P_1)/2 = \eta_2\left(\partial V_{r_2}/\partial r\right) - \eta_1\left(\partial V_{r_1}/\partial r\right) + H_n$, and $\eta_1\left[\left(\partial V_{\theta_1}/\partial r\right) - \left(V_{\theta_1}/r\right)\right] - \eta_2\left[\left(\partial V_{\theta_2}/\partial r\right) - \left(V_{\theta_2}/r\right)\right] + H_t = 0$. Here H_n and H_t denote, respectively, non-hydrodynamic normal and tangential stresses (thermo- or solutocapillary stresses or other). These factors influence on the drop's behavior. The pure flow problem corresponds to $H_n = \sigma/a$ (Laplace pressure) and $H_\mathrm{t} = 0$. Recall that with $Re = 0$ as inertial terms disappear from the equations then a drop or a bubble remains spherical irrespective of the value of the (constant) interfacial tension. If the latter depends on temperature we have $H_n = \sigma(T)/a$ (as addition to σ_{rr}) and $H_\mathrm{t} = (1/a)(d\sigma/dT) = (1/a)\sigma_T(dT/d\theta)$ (as addition to $\sigma_{r\theta}$; $\sigma_T = d\sigma/dT$). The latter is the mentioned thermocapillary (Marangoni) force acting at the drop surface. A similar expression holds for surfactant concentration. The actual expressions of the factors H_n and H_t depend on the specific features of physico-chemical phenomena involved and demands the analysis of the corresponding reaction, heat and/or mass transfer or other.

The force acting on each elementary portion of the surface of a drop with the normal directed along the radius ($\vec{\mathrm{n}} = \overrightarrow{\mathrm{i_r}}$) is $\sigma_{\mathrm{rr}}\,\overrightarrow{\mathrm{i_r}} + \sigma_{\mathrm{r\theta}}\,\overrightarrow{\mathrm{i_{r\theta}}}$. Integrating the projection of elementary forces on the velocity direction over the entire drop surface the full force is obtained: $F = -4\pi\eta_1 aAU$. Such expression of the force is universal for Stokes flows irrespective of the details hidden in the "parameter" A [18, 22, 31]. To explicitly find A we need to use the balance of tangential and normal stresses at the surface of the drop (H_n and H_t). For *passive* drops or bubbles the quantity A is a true constant whereas for *active* objects it would account for the specificity of the "activity" (thermo- or solutocapillarity). In the former case if there is an external force the terminal, settling velocity of the drop or bubble in the presence of such external agent can be explicitly determined. The balance of forces from activity and external agents like gravity/buoyancy or other body force (electric, magnetic), permits obtaining the velocity U of self-propelled autonomous motion when the net resultant force is zero.

For simple viscous flow $H_t = 0$ and then $A = (1 + 3\beta/2)/(1 + \beta)$, with $\beta = \eta_2/\eta_1$. The corresponding drag/resistance force experienced by a drop is $F = 4\pi\eta_1 a[(1 + 3\beta/2)/(1 + \beta)$, a result for "clean" bubbles/drops (Rybczynski-Hadamard law). In practice the measured values tend to be lower as surfactants are convected toward the rear stagnation point on the surface. Then the resulting gradient in tension tends to retard the surface flow velocity and thus slows down the motion. For the particular case $\beta = 1$ the value is $F = 5\pi\eta_1 aU$. When $\beta \to \infty$, $A = -3/2$ ($\eta_{solid} \gg \eta_{liquid}$) then $F = 6\pi\eta_1 aU$ which is Stokes law for the drag or viscous resistance force on a solid sphere. The case of a bubble is obtained by setting $\beta \to 0$ ($\eta_{air} \ll \eta_{liquid}$ though $v_{air} \ll v_{liquid}$) and hence $F = 4\pi\eta_1 aU$, just 2/3 the value for a standard solid sphere but the bubble's result also applies to the case of a solid polymeric sphere due to the slippery character of its boundary.[7] If, however, the surface of the bubble adsorbs surfactants present in the surrounding liquid there is the possibility that the bubble behaves like a solid sphere following Stokes drag, as impurities adsorbed endow the surface of a bubble with some measure of rigidity. Noticeable also is that the interfacial tension does not enter and hence merely alters the pressure at an internal point by a constant amount σ/a which is an additive constant that can be eliminated. If a drop is extremely small, then the effect of surface tension is similar to that of rigidity and such tiny drops tend to behave as solid spheres obeying Stokes law. If the motion of the drop is provoked by the action of buoyancy (or any other body force) which is the result of gravity (or the corresponding other field) and difference of density of liquid of drop and surrounding fluid, hence hydrostatic pressure gradient, one has to consider $F_{buoy} = (4/3)\pi a^3 g(\rho_2 - \rho_1)$. When this force is compensated by the viscous drag the net resultant force is zero and then the terminal, settling velocity of the steady motion of the drop is $U = F_{buoy}/4\pi\eta_1 aA$. Falling rain drops or snowflakes or any object end up by having terminal velocity as soon as weight, pulling downward, and drag are exactly equal and opposite, and hence the net resultant force vanishes.

Up to now we have not mentioned surface viscosities, counterpart of bulk-phase viscosities. There are two surface viscosities which characterize, respectively, the resistance of the interface toward flow (surface shear viscosity in the range 10^{-3} kg/s) and deformation under the influence of forces from the adjacent fluid (surface dilatational viscosity in the range of 10^{-7} to 10^{-8} kg/s). They can strongly alter the flow velocity field in the immediate vicinity of the surface of the drop. Long ago surface viscosity had been suggested as responsible for the behavior of drops like rigid spheres but for surfactant-free interfaces it is a negligible effect. If surface shear viscosity dominates over the viscosity in the bulk, along a given length scale, then it could strongly influence the nature of bulk flow near or at the interface depending on the scale involved.

As a side remark note that the neglect of inertial terms, with $\mathrm{Re} = 0$, has some other consequences worth recalling. One is that vorticity obeys Laplace equation (in two

[7]Warning: the case of a highly viscous drop $\eta_2 \gg \eta_1$ moving in a Hele-Shaw channel deserves separate consideration not done here; a typical transverse scale is about 10^2 μm and caged drops can be safely considered as pancaked rather than spherical.

dimensions if pressure is harmonic so is the vorticity). Vorticity is not created in the bulk flow but at boundaries. The flow is due solely to steady molecular diffusion of vorticity to infinity in all directions as the sphere, the drop, is a source of vorticity due to the no slip boundary condition at its surface (clearly this no slip requires inertial terms near the drop to be really small if not negligible). Indeed, the fluid in the immediate contact with the sphere is dragged along at the same speed as the sphere and this leads to the generation of vorticity. Diffusion in all directions away from the sphere as an effective stationary source leads to a flow with fore-and-aft symmetry near the sphere and away from it. Vorticity decreases as $1/r^2$ as originated from a dipolar source that produces for each of its components equal positive and negative quantities at the surface of the sphere. In Hele-Shaw channels vorticity plays no role (the Prandtl number, $Pr = \nu/\kappa$, also vanishes; κ denotes heat diffusivity whereas $\lambda = \rho c \kappa$ denotes heat conductivity with c indicating specific heat). Finally, if a cylindrical drop is a useful approximation for the study of the behavior of a drop in two-dimensions of an otherwise open channel we must have in mind that no steady two-dimensional, creeping flow of an incompressible Newtonian fluid past an infinite circular cylinder, perpendicular to its axis, is possible (Stokes' paradox).

13.4.2 Role of "Activity"

To describe the behavior due to internal heat sources or sinks we must consider the heat or mass equation or both together with the appropriate boundary conditions [31, 32]. The lowest order approximation corresponds to infinitesimally small values of the Reynolds and Peclet numbers such that $\mathrm{Re_i} \approx \mathrm{Pe_{Ti}} \ll 1. Pe = Ua/\kappa$ (or Ua/D for mass diffusion with D denoting mass/surfactant diffusivity). Note that the Peclet number is a heat Reynolds ratio and hence $Pe \ll 1$ implies that heat is dominated by (molecular) diffusion. We can start with the Stokes flow for the purely hydrodynamic part of the problem, but as the temperature field significantly depends on the velocity, and vice versa, we need to go beyond vanishing Peclet number. Indeed, if the latter is set to zero we have diffusion only and there is no influence of the heat upon the drop motion.

When the complete problem is solved [31] the expression of the force is obtained: $F = 4\pi\eta_1 aU[m(3/4 - 3/35\kappa) + 1 + 3\beta/2]/m(1/4 - 2/35\kappa) + 1 + \beta]$ where we have $A = -[m(3/4 - 3/35\kappa) + 1 + 3\beta/2]/m(1/4 - 2/35\kappa) + 1 + \beta]$ with $m = -MPe/9(2 + \delta)$, $M = qa^2\sigma_T/\eta_1\lambda_1 U$, q accounts for an internal heat source or sink and $\delta = \lambda_2/\lambda_1$. Accordingly, if F is an "external" force, like buoyancy, it can balance the thermocapillary and viscous forces thus leading to motion with constant velocity $U = -(1/3)\left[a^2 g(\rho_2 - \rho_1)/\eta_1\right][m(1/4 - 2/35\kappa) + 1 + \beta]/[m(3/4 - 3/35\kappa) + 1 + 3\beta/2]$. A similar expression is expected when buoyancy is replaced by some other body force like electric or magnetic.

It is worth noting that this case does not need the presence of an external temperature gradient or other like illumination and/or heating with a laser beam. Here

the quantity A does not contain the velocity of the drop, as A is a coefficient of proportionality of the "external" force to the velocity and it merely depends on the specific characteristics of the problem involving the parameters of the heat process. Then there are various particular cases of possible drop motion. First of all, we see that without thermal effect ($q = 0$ leading to $M = 0$) thermocapillarity disappears and the motion of the drop will be that corresponding to the Rybczynski-Hadamard case or for a solid sphere the Stokes motion. Also when δ the temperature of the drop's surface becomes constant. Then depending on the characteristics of the drop and the surrounding liquid, and the sign of the thermal effect of the heat process inside the drop, its velocity can be higher or lower than the Rybczynski-Hadamard-Stokes flow velocity. It is for such peculiarity of the drop behavior that we can consider it as "active".

Another case of interest is that of a drop where its surface is the seat of an endo- or exo-thermic chemical reaction thus leading to a no uniform temperature distribution at the surface with corresponding interfacial tension gradient and Marangoni flow (alternatively a reaction inside the drop brings active material to its surface [42, 43]. There also are numerous reports about experiments and/or theory where there is a phase transformation (recall the light-induced *trans–cis* isomerization [48]). To simplify the diffusion regime of the surface reaction is assumed and Stefan flow (convective flow of reactants in direction normal to the surface) is neglected. The main material characteristics of liquid in the drop and outside are supposed to be constant. As in the case of internal heat sources or sinks, at the lowest order approximation the connection between hydrodynamics and heat and surfactant transfer appears in the boundary condition for tangential stresses. Here the novelty is that the temperature field is related to the concentration field and in order to find the thermocapillary force acting on the surface both heat and mass transfer problems must be solved, as earlier noted, at $Pe \neq 0$ (for heat and solute) even if we take the Stokes flow ($Re = 0$). The constant A in the force is determined by solving the combined heat and mass transfer problem because the gradient of temperature depends on reactant inflow at the surface. It appears that [31] $A = (-3/2)(2m - 1 - 2/3\beta)/(m - 1 - 1/\beta)$ with $m = M(1 - L)Pe/12(2 + \delta)\beta$, $L = \kappa_1/D_1$ and $M = QC_\infty D_1\sigma_T/\rho_1 c_1 \eta_1 \kappa_1 U$; Q accounts for the (endo or exothermic) heat effect of reaction. Note that here m contains MPe and hence the velocity scale disappears. Thus A is reduced to a kind of constant of proportionality between the external force and the velocity $F = 6\pi\eta_1 aU(2m - 1 - 2/3\beta)/(m - 1 - 1/\beta)$. In the absence of reaction ($C_\infty = 0$) or the heat effect of reaction vanishes ($Q = 0$), there is no thermocapillarity (M disappears) and we get the Rybczynski-Hadamard result whereas for $\beta \to \infty$ we reobtain the Stokes result, as expected. In the general case, it appears that depending on the numerical value of the parameters involved in the expression of the force acting on the drop it can be negative, positive or equal to zero. It means that the external force which is needed to sustain the drop motion with constant velocity can be greater or less than the Rybczynski-Hadamard force and even equal to zero or to be of thrust type. Clearly, in the case of constant velocity, the force given must be in balance with an external force (buoyancy, electric, magnetic) thus resulting in a net zero resultant force. In such a case there is the possibility of con-

trolled self-propulsion of the drop solely due to the "activity" of the drop. Yet the velocity of such autonomous motion cannot be determined in the frame of the Stokes flow approximation. Further approximations with non-vanishing Peclet numbers are needed to allow the determination of the velocity of the autonomous motion but we shall not dwell on this case here.

To close this section, it seems pertinent to mention that devices exist for on-demand routing of a drop or a sequence of drops. This is achieved using a suitable on-off illumination switch process opposing whatever type of capillary force is used in a microfluidic channel with more than one outlet.

13.5 Typical Flow Patterns in Controlled, Directed Motions or Self-propulsion

The specific value of the parameter A incorporated in the (compact and universal) expression of the (total) force acting on a drop or a bubble determines the form and position of the streamlines as illustrated in Fig. 13.13. With no need of specifying here the physicochemical, electric or magnetic processes involved, suffice to say that when $A - 3/2$ we have the Rybczynski-Hadamard case. As $A = -3/2$ the flow inside the drop disappears and the drop behaves like a Stokes solid sphere. Then as we further decrease its value, $A - 3/2$, the flow circulation inside the drop becomes opposite to that of the Rybczynski-Hadamard case. There is also the appearance of counter flow of the surrounding fluid in the vicinity of the drop leading to a resistance force as super drag, as it is much stronger than the Stokes drag on an equivalent solid sphere.

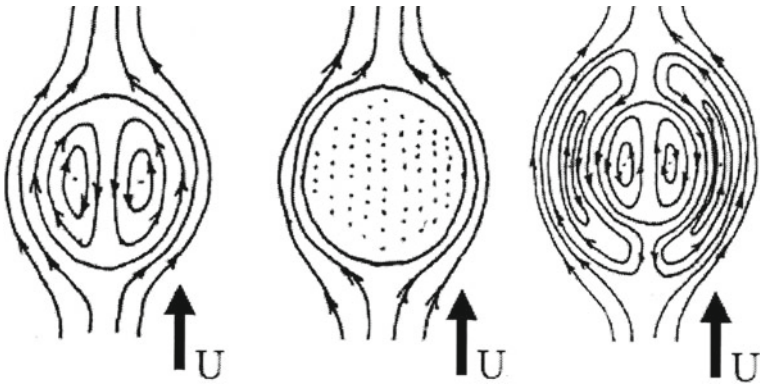

Fig. 13.13 Active drops with Marangoni effect. Flow streamlines outside and inside drop for $-1 > A > -3/2$ (extreme left panel; Rybczynski-Hadamard law), $A = -3/2$ (center panel; dots indicate no motion inside the drop which acts like a solid sphere), and $A < -3/2$ (extreme right panel indicating drag much higher than for an equivalent sphere). Reprinted from [31], Copyright (2017), with permission from Elsevier

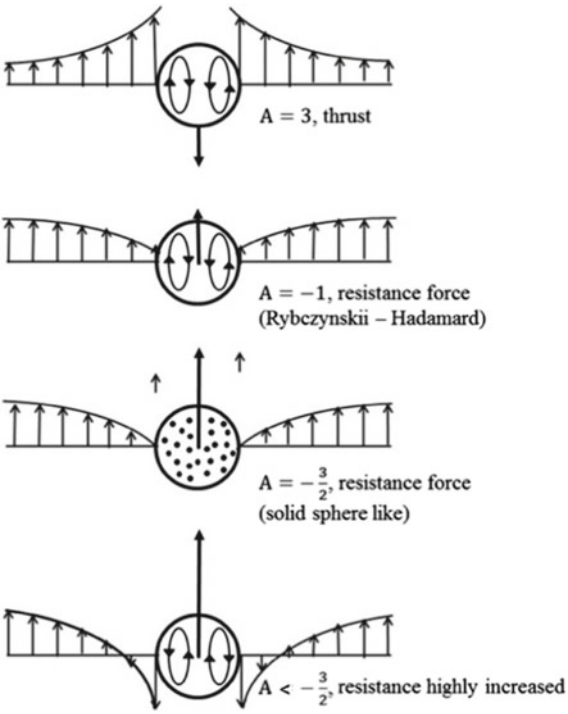

Fig. 13.14 Active drops (companion to preceding Fig. 13.13). Flow velocities at plane $\theta = \pi/2$. Going down in the panel, rom thrust ($A = 3$, $A > 0$) to drag ($A = -1$, $A = -3/2$) and super resistance force ($A < -3/2$). Note that the lowering of resistance force between $A = -1$ and $A = 0$ and the increasing of resistance force for $A < -3/2$ are genuine consequences of the activity of the drop. Reprinted from [31], Copyright (2017), with permission from Elsevier

Companion to Fig. 13.13 is Fig. 13.14 with a sequence illustrating the velocity field outside and inside of the drop as we vary the value of the parameter A from $A = 3$ to $A = -3$. As earlier noted when A is positive the force is antiparallel to U (opposite direction) and we have thrust, whereas with A negative (same direction) both force and velocity are parallel and we have resistance/drag.

13.6 Concluding Remarks

The physicochemical hydrodynamics of drops and bubbles having at its core processes all leading to interfacial tension gradients has recently received great attention by numerous researchers and engineers due to their potential in microfluidics where drops or bubbles can be used either as (static or traveling) reactors or simply as carriers of encapsulated materials in appropriate channels. There is, at present, a huge literature on drops and bubbles in a rather inflationary multiplicity of scientific journals with plenty of redundancy and rediscovery of known results and theories, yet not always giving due credit to earlier contributors to the understanding of just the same problems.

Generally, microfluidics technologies and hence the applied work with drops or bubbles demands using the lowest order hydrodynamic approximation which is the Stokes flow approximation (either creeping flow and/or otherwise flow of tiny objects). At such level the most significant mathematical result is that the force acting on a drop or on a bubble can be expressed in a "universal" formula involving a parameter that accounts for the specificity of the case considered. Such result permits rather easily to ascertain if the net resultant force on a passive or an active drop or bubble leads to resistance or thrust and from that the terminal, settling velocity of the drop or the bubble can be determined when all forces involved are made explicit and in balance. The drop's activity can be due to internal or surface processes leading to heat or surfactant production and/or its transport or chemical reorganization of products with chemical reactions, phase transformations, electric or magnetic related processes, and their combinations. Whatever the process one ends up with a concrete interfacial tension gradient hence a given Marangoni stress, and corresponding Marangoni number, which produces flow motion in and outside the drop. Due to the drop's activity, controlled thrust in the form of self-propulsion is possible as well as a controlled resistance/drag force that could be lower or higher than that predicted for "passive" drops.

Acknowledgements This work was funded in part by EU under Marie Curie ITN CoWet (Grant Number 607861) and by MINECO under grants FIS-2014-62005-EXP and CTQ-2016-78895-R.

References

1. J.-P. Abid, M. Figoli, R. Pansu, J. Szeftel, J. Zyss, C. Larpent, S. Brasselet, Light-driven directed motion of azobenzene-coated polymer nanoparticles in an aqueos medium. Langmuir **27**, 7967–7971 (2011)
2. S.L. Anna, Droplets and bubbles in microfluidic devices. Annu. Rev. Fluid Mech. **48**, 285–309 (2016)
3. D. Baigl, Photo-actuation of liquids for light-driven microfluidics: state of the art and perspectives. Lab Chip **12**, 3637–3653 (2012)
4. T. Ban, T. Yamagami, H. Nakata, Y. Okano, pH-dependent motion of self-propelled droplets due to Marangoni effect at neutral pH. Langmuir **29**, 2554–2561 (2013)
5. M. Björnmalm, Y. Yan, F. Caruso, Engineering and evaluating drug delivery particles in microfluidic devices. J. Controlled Release **190**, 139–149 (2014)
6. R. Chattaraj, N.T. Blum, A. Goodwin, Design and application of stimulus-responsive droplets and bubbles stabilized by phospholipid monolayers, Current Opinion Coll. Interface Sci. **40**, 14–24 (2019)
7. A. Diguet, R.-M. Guillermic, N. Magome, A. Saint-Jalmes, Y. Chen, K. Yoshikawa, D. Baigl, Photomanipulation of a droplet by the chromocapillary effect. Angew. Chem. Int. Ed. **48**, 9281–9284 (2009)
8. A. Egatz-Gomez, S. Melle, A.A. Garcia, S.A. Lindsay, M. Marquez, P. Dominguez-Garcia, M.A. Rubio, S.T. Picraux, J.L. Taraci, T. Clement, D. Yang, M.A. Hayes, D. Gust, Discrete magnetic microfluidics. Appl. Phys. Lett. **89**, 034106 (2006)
9. L. Florea, K. Wagner, P. Wagner, G.G. Wallace, F. Benito-López, D.L. Officer, D. Diamond, Photo-chemopropulsion-Light-stimulated movement of microdroplets. Adv. Mater. **26**, 7339–7345 (2014)

10. F. Fontana, M.P.A. Ferreira, A. Correia, J. Hirvonen, H.A. Santos, Microfluidics as cutting-edge technique for drug delivery. J. Drug Deliv. Sci. Technol. **34**, 76–87 (2016)
11. B.S. Gallardo, V.K. Gupta, F.D. Eagerton, L.I. Jong, V.S. Craig, R.R. Shah, N.L. Abbott, Electrochemical principles for active control of liquids on submillimeter scales. Science **283**, 57–60 (1999)
12. Y.P. Gupalo, A.Y. Rednikov, Y.S. Ryazantsev, Thermocapillary drift of a drop with nonlinear surface tension dependence on temperature. Izv Akad Nauk SSSR Mekh Zhidk Gaza **53**, 433–442 (1989). (in Russian)
13. M.M. Hanczyc, T. Toyota, T. Ikegami, N. Packard, T. Sugawara, Fatty acid chemistry at the oil-water interface: self-propelled oil droplets. J. Am. Chem. Soc. **129**, 9386–9391 (2007)
14. M. He, J.S. Edgar, D.M. Jeffries, R.M. Lorenz, J.P. Shelby, D.T. Chiu, Selective encapsulation of single cells and subcellular organelles into picoliter and femtoliter droplets. Anal. Chem. **77**, 1539–1544 (2005)
15. S.K. Ichimura, M. Nakagawa, Light-driven motion of liquids on a photoresponsive surface. Science **288**, 1624–1626 (2000)
16. Y. Ito, M. Heydari, A. Hashimoto, T. Konno, A. Hirasawa, S. Hori, K. Kurita, A. Nakajima, The movement of a water droplet on a gradient surface prepared by photodegradation. Langmuir **23**, 1845–1850 (2007)
17. S. Koster et al., Drop-based microfluidic devices for encapsulation of single cells. Lab Chip **8**, 1110–1115 (2008)
18. L.G. Leal, *Advanced Transport Phenomena. Fluid Mechanics and Convective Transport Processes* (Cambridge University Press, Cambridge, 2007)
19. C. Maass, C. Krüger, S. Herminghaus, C. Bahr, Swimming droplets. Annu. Rev. Condens. Matter Phys. **7**, 171–193 (2016)
20. M. Morozov, S. Michelin, Self-propulsion near the onset of Marangoni instability of deformable active droplets (2018). arXiv:1810.03983v1[physics.flu-dyn]
21. M. Muto, M. Yamamoto, M. Motosuke, A noncontact picoliter droplet handling by photothermal control of interfacial flow. Anal. Sci. (Japan) **32**, 49–55 (2016)
22. A.A. Nepomnyashchy, M.G. Velarde, P. Colinet, *Interfacial Phenomena and Convection* (Chapman & Hall/CRC, Boca Raton, 2002)
23. T. Ohta, T. Ohkuma, K. Shitara, Deformation of a self-propelled domain in an excitable reaction-diffusion system. Phys. Rev. E **80**, 056203 (2009)
24. L.M. Pismen, U. Thiele, Asymptotic theory for a moving droplet driven by a wettability gradient. Phys. Fluids **18**, 042104 (2006)
25. A.Y. Rednikov, Y.S. Ryanzatsev, Thermocapillary motion of a droplet heated by radiation. Int. J. Heat Mass Transf. **35**, 255–261 (1992)
26. A.Y. Rednikov, Y.S. Ryazantsev, M.G. Velarde, Drop motion with surfactant transfer in a homogeneous surrounding. Phys. Fluids **6**(4), 51–468 (1994)
27. A.Y. Rednikov, Y.S. Ryazantsev, M.G. Velarde, On the development of translational subcritical Marangoni instability for a drop with uniform internal heat generation. J. Colloid Interface Sci. **164**, 168–180 (1994)
28. A.Y. Rednikov, Y.S. Ryazantsev, M.G. Velarde, Active drops and drop motions due to nonequilibrium phenomena. J. Non-Equilib. Thermodyn. **19**, 95–113 (1994)
29. A.Y. Rednikov, V. Kurdyumov, Y.S. Ryanzatsev, M.G. Velarde, The role of time-varying gravity on the motion of a drop induced by Marangoni instability. Phys. Fluids **7**, 2670–2678 (1995)
30. R. Riahi, A. Tamayol, S.A.M. Shaegh, A.M. Ghaemmaghami, M.R. Dokmeci, A. Khademhosseini, Microfluidics for advanced drug delivery systems. Curr. Opin. Chem. Eng. **7**, 101–112 (2015)
31. Y.S Ryazantsev, M.G. Velarde, R.G. Rubio, F. Ortega, P. Lopez, Thermo- and soluto-capillarity: passive and active drops. Adv. Colloid Interface Sci. **247**, 52–80 (2017). (and references therein)
32. Y.S. Ryazantsev, M.G. Velarde, R.G. Rubio, E. Guzman, F. Ortega, J.J. Montoya, On the autonomous motion of active drops or bubbles. J. Coll. Interface Sci. **527**, 180–186 (2018)
33. S. Rybalko, N. Magome, K. Yoshikawa, Forward and backward laser-guided motion of an oil droplet. Phys. Rev. E **70**, 046301 (2004)

34. M. Schmitt, H. Stark, Marangoni flow at droplet interfaces: three-dimensional solution and applications. Phys. Fluids **28**, 012106 (2016)
35. R. Seemann, M. Brinkmann, T. Pfohl, S. Herminghaus, Droplet based microfluidics. Rep. Prog. Phys. **75**, 016601 (2012)
36. L. Shang, Y. Cheng, Y. Zhao, Emerging droplet microfluidics. Chem. Rev. **117**, 7964–8040 (2017)
37. V. Sharma, A. Sundaramurthy, Reusable hollow polymer microreactors incorporated with anisotropic nanoparticles for catalysis application. ACS Omega **4**, 628–636 (2019)
38. V.M. Starov, M.G. Velarde, Surface forces and wetting phenomena. J Phys Cond. Matter **21**, 464121 (2009)
39. V.M. Starov, M.G. Velarde, C.J. Radke, *Wetting and Spreading Dynamics* (CRC Press/Taylor & Francis, Boca Raton, 2007)
40. Y. Sun, T.A. Haglund, A.J. Rogers, A.S. Ghanim, P. Sethu, Microfluidics technologies for blood-based cancer liquid biopsies. Anal. Chim. Acta **1012**, 1–20 (2018)
41. H. Takeuchi, M. Motosuke, S. Honami, Noncontact bubble manipulation in microchannel by using photothermal Marangoni effect. Heat Transfer Engng **333**, 234–244 (2012)
42. T. Toyota, N. Maru, M.M. Hanczyc, T. Ikegami, T. Sugawara, Self-propelled oil droplets consuming "fuel" surfactant. J. Am. Chem. Soc. **131**, 5012–5013 (2009)
43. D. Tsemakh, O.M. Lavrenteva, A. Nir, On the locomotion of a drop, induced by the internal secretion of surfactant. Int. J. Multiph. Flow **30**, 1337–1367 (2004)
44. M.G. Velarde, A.Y. Rednikov, Y.S. Ryazantsev, Drop motions and interfacial instability J Phys: Condens. Matter **8**, 9233–9247 (1996)
45. M.G. Velarde, Drops, liquid layers and the Marangoni effect. Philos. Trans. R. Soc. A **356**, 829–844 (1998)
46. E. Verneuil, M.L. Cordero, F. Gallaire, C.N. Baroud, Laser-induced force on a microfluidic drop: Origin and magnitude. Langmuir **25**, 5127–5134 (2009)
47. S. Yabunaka, T. Ohta, N. Yoshinaga, Self-propelled motion of a fluid droplet under chemical reaction. J. Chem. Phys **136**, 074904 (2012)
48. K.G. Yager, C.J. Barrett, Novel photo-switching using azobenzene functional materials. J. Photochem. Photobiol. A Chem. **182**, 250–261 (2006)
49. N. Yoshinaga, Spotaneous motion and deformation of a self-propelled droplet. Phys. Rev. E **80**, 012913 (2014)
50. N.O. Young, J.S. Goldstein, M.J. Block, The motion of bubbles in a vertical temperature gradient. J. Fluid Mech. **6**, 350–356 (1959)

Chapter 14
Convection in a Horizontal Porous Annulus with Quasi-Periodic Gravitational Modulation

Jabrane Belabid, Karam Allali and Mohamed Belhaq

Abstract This chapter investigates the convective instability in a horizontal porous annulus subjected to quasi-periodic (QP) gravitational modulation having two incommensurate frequencies. The porous matrix is supposed to be filled by an incompressible fluid. The model we consider includes the heat equation and the hydrodynamic equations under Darcy law and Boussinesq approximation. The derived model with the temperature-stream function is solved numerically using the alternate direction implicit method. The main objective is to examine the influence of the QP modulation on the transition from unicellular to bicellular flow regime, corresponding to a substantial change in the thermo-convective regime flow. Numerical simulations are conducted for some values of the amplitudes and frequencies of the modulation and the radius ratio of the annulus. Results showed that the thermo-convective instability in the QP regime is greatly influenced by radius ratio and the amplitudes of the QP gravitational modulation. The effect of the frequencies ratio on the critical Rayleigh number is also examined showing that for certain values of parameters, the maximum critical Rayleigh number is reached when the frequency ratio is equal to $\sqrt{3}$ (QP gravitational modulation) and the minimum is obtained when the frequency ratio is equal to 3 (periodic gravitational modulation).

14.1 Introduction

There has been considerable interest in studying convection in porous annulus because of its wide range of engineering application such as cooling of electronic

J. Belabid (✉) · K. Allali
Faculty of Sciences and Technologies, University Hassan II Casablanca, Mohammedia, Morocco
e-mail: belabide@gmail.com

K. Allali
e-mail: allali@hotmail.com

M. Belhaq
Faculty of Sciences Ain Chock, University Hassan II Casablanca, Casablanca, Morocco
e-mail: mbelhaq@yahoo.fr

M. Belhaq (ed.), *Topics in Nonlinear Mechanics and Physics*,
Springer Proceedings in Physics 228, https://doi.org/10.1007/978-981-13-9463-8_14

equipments, aircraft cabin insulation, geothermal systems, underground transmission lines, storage of nuclear waste materials, solidification of casting to name just a few (see for instance [1, 2] and references therein). The pioneer work by Caltagirone [3] considered the free convection flows in a porous horizontal annulus heated from the inner cylinder. The author observed different flow regimes when the Rayleigh number traverses some critical values. Later, several authors have considered a similar problem of convection in porous annulus. Mota and Saatdjian [4] studied the problem of natural convection in a porous medium bounded by two horizontal isothermal cylinders. It was shown that different flow patterns may appear depending on initial conditions. The authors observed that for very small radius ratio, increasing the Rayleigh number, the flow regime structure changes from two cells to four, to six or to eight cells without exhibiting a hysteresis loop. In the work by Khanafer and Chamkha [5], a numerical study of mixed convection in a horizontal porous annulus has been conducted in the presence of internal heat generation. The outer and inner cylinders are kept at uniform, constant and different temperatures. The outer cylinder rotating at a constant angular velocity induces the forced flow. Attention has been focused on the effect of key parameters on the flow patterns and the heat transfer. It was revealed that the Richardson number plays an important role on the heat transfer characterization within the annulus. The authors observed that an increase in Reynolds number produces a significant effect on the flow regime. Belabid and Cheddadi [6, 7] carried out a numerical study to examine the flow patterns of a fluid inside a porous medium bounded by two horizontal concentric cylinders. They showed that different flow regimes may appear depending on the initial conditions introduced in the computations. The bifurcation phenomena of this problem have been analyzed for gaps of radius ratios between 2 and $2^{\frac{1}{4}}$. The effect of Brinkmann correction has also been highlighted. The obtained results showed that the critical Rayleigh number increases when the Darcy number is increased. Rao et al. [9] studied the problem of two-dimensional bifurcation using the Galerkin method to solve the governing equations. It was demonstrated that the critical Rayleigh numbers obtained numerically are in a good agreement with the experimental tests and with those of Caltagirone [3]. Himasekhar and Bau [10] investigated the same problem of natural convection in a horizontal porous annulus using the regular perturbation expansion for different radii ratio. In a related work, Charrier-Mojtabi et al. [11] used two numerical methods, namely, Fourier-Galerkin and collocation-Chebyshev to solve the physical model. The results of the experimental study match well with the numerical results and indicate the existence of two-dimensional bicellular structures for radius ratio of 2 and for values of Rayleigh number up to 250. In addition, Khanafer et al. [12] used a generalized form of the momentum equation to study the problem of natural convection within a horizontal annulus partially filled with a saturated porous medium. The results revealed the effect of the porous sleeve on the buoyancy induced flow motion under steady-state condition. In a recent work, Belabid and Allali [13] studied the effect of a periodic gravitational modulation on the convective instability in a horizontal porous annulus. They showed that the convective instability is influenced by the amplitude and the frequency of the modulation.

Although the influence of periodic gravitational modulation on convective instability has been widely studied in different applications and configurations, only few

works have considered the effect of quasi-periodic (QP) gravitational modulation on the convective instability. For instance, it was proved that the incommensurate frequencies ratio may have a stabilizing or destabilizing effect on the onset of convection in the problems dealing with reaction front propagation (Allali et al. [14, 15]) and in the pioneer work concerning the Hele-shaw cell performed by Boulal et al. [16, 17]. The purpose of the present paper is to investigate the effect of the QP gravitational modulation on the convective instability in a porous horizontal annulus. In this case, we assume that the annulus is subject to a QP gravitational modulation with two incommensurate frequencies. A part of the results given in the current chapter has been presented in [8]. Note that the present work can be considered as an extension of the results given in [13] in which the gravitational modulation has been taken as periodic.

In Sect. 14.2, the problem description and the mathematical formulation is given. The numerical method is illustrated in Sect. 14.3, followed in Sect. 14.4 by discussing the main numerical results. A summary of the results is provided in the last section.

14.2 Problem Description and Mathematical Formulation

We consider a porous layer bounded by two horizontal concentric cylinders saturated with a Newtonian fluid, as shown in Fig. 14.1. Both inner and outer cylinders are kept at uniform, constant and different temperature T_i and T_o respectively with $T_i > T_o$.

It is taken into account that the flow is two-dimensional, steady and laminar. The porous medium is considered to be homogeneous, isotropic and subjected to a QP gravitational modulation with two incommensurate frequencies. Under the

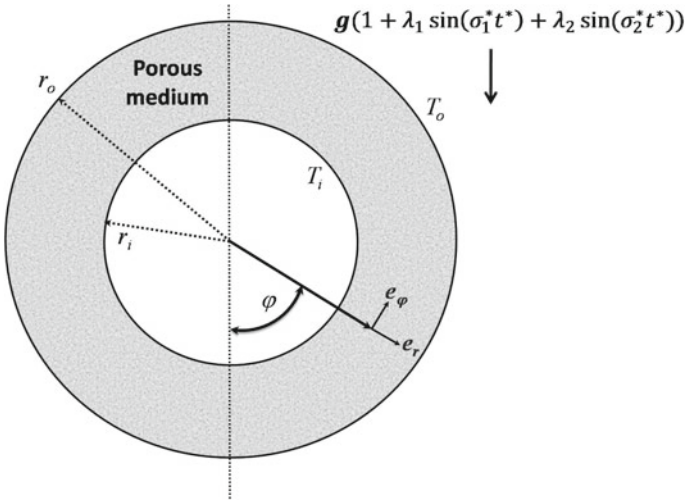

Fig. 14.1 Sketch of the problem

Boussinesq approximation, the basic steady conservation of thermal energy, momentum and mass equations in polar coordinates system can be written as:

$$\frac{\partial T^*}{\partial t^*} + (\mathbf{V}^*.\nabla)T^* = \alpha \nabla^2 T^* \tag{14.1}$$

$$\mathbf{V}^* = -\frac{K}{\mu}(\nabla P^* + \rho_0 \boldsymbol{g}\beta \left(T^* - T_o\right)(1 + \lambda_1 \sin(\sigma_1^* t^*) + \lambda_2 \sin(\sigma_2^* t^*))) \tag{14.2}$$

$$\nabla.\mathbf{V}^* = 0 \tag{14.3}$$

with the boundary conditions:

$$u^* = 0,\ T^* = T_i \text{ on the inner cylinder surface,}$$
$$v^* = 0,\ T^* = T_o \text{ on the outer cylinder surface,}$$

where T^* is the temperature, $\boldsymbol{V}^*$ is the velocity, P^* is the pressure, K the permeability, μ the dynamic viscosity, ρ_0 the reference density, β is the coefficient of thermal expansion, $\boldsymbol{g}$ is the gravitational acceleration, λ_i, σ_i^* $(i = 1, 2)$ stand for the amplitudes and the frequencies of the QP modulation, respectively, and α is the thermal diffusivity.

To obtain the dimensionless model, we introduce the following transformation formula:

$$r = \frac{r^*}{r_i}, \mathbf{V} = \frac{\mathbf{V}^*}{\alpha} r_i, T = \frac{T^* - T_o}{T_i - T_o}, t = \frac{t^*}{r_i^2}\alpha, P = \frac{P^* K}{\alpha \mu}, \sigma_1 = \frac{\sigma_1^* r_i^2}{\alpha} \text{ and } \sigma_2 = \frac{\sigma_2^* r_i^2}{\alpha}.$$

Therefore, the dimensionless governing equations read

$$\frac{\partial T}{\partial t} + (\mathbf{V}.\nabla)T = \nabla^2 T \tag{14.4}$$

$$\mathbf{V} = -\nabla P - RaT\boldsymbol{k}(1 + \lambda_1 \sin(\sigma_1 t) + \lambda_2 \sin(\sigma_2 t)) \tag{14.5}$$

$$\nabla.\mathbf{V} = 0 \tag{14.6}$$

where Ra is the Rayleigh number given by $Ra = \frac{g\beta K \Delta T r_i}{\alpha \nu}$ and $\sigma_2 = \eta\sigma_1$, ν is the kinematic viscosity and $\Delta T = T_i - T_o$. The dimensionless boundary conditions are written as follows:

$$u = 0, T = 1 \text{ on the inner cylinder surface,}$$
$$v = 0, T = 0 \text{ on the outer cylinder surface.}$$

Due to the physical symmetry of the problem the following boundary conditions $\varphi = 0, \pi : v = 0, \dfrac{\partial T}{\partial \varphi} = 0$ are added.

The governing equations for the laminar vibrated natural convection in terms of stream function-temperature formulation can be expressed as follows:

$$\nabla^2\psi = -Ra(\sin\varphi\frac{\partial T}{\partial r} + \frac{\cos\varphi}{r}\frac{\partial T}{\partial \varphi})(1 + \lambda_1\sin(\sigma_1 t) + \lambda_2\sin(\sigma_2 t)) \tag{14.7}$$

$$\frac{\partial T}{\partial t} + \frac{1}{r}\frac{\partial \psi}{\partial \varphi}\frac{\partial T}{\partial r} - \frac{1}{r}\frac{\partial \psi}{\partial r}\frac{\partial T}{\partial \varphi} = \nabla^2 T \tag{14.8}$$

and the corresponding boundary conditions take the following form:

$$\text{for } r = 1 : T = 1 \text{ and } \frac{\partial \psi}{\partial \varphi} = 0,$$
$$\text{for } r = R : T = 0 \text{ and } \frac{\partial \psi}{\partial \varphi} = 0,$$
$$\text{for } \varphi = 0, \pi : \frac{\partial T}{\partial \varphi} = \frac{\partial \psi}{\partial r} = 0.$$

The local Nusselt number along the inner and outer cylinders are estimated as the ratio of convective to conductive heat transfer:

$$Nu_i(r = 1, \varphi) = -\ln R \left.\frac{\partial T}{\partial r}\right|_{r=1} \tag{14.9}$$

$$Nu_o(r = R, \varphi) = -R\ln R \left.\frac{\partial T}{\partial r}\right|_{r=R} \tag{14.10}$$

Then, the average Nusselt numbers evaluated at the inner and outer cylinders can be written as:

$$\overline{Nu} = \frac{1}{\pi}\int_0^\pi Nu_i\, d\varphi = -\frac{1}{\pi}\ln R \int_0^\pi \left.\frac{\partial T}{\partial r}\right|_{r=1} d\varphi \tag{14.11}$$

$$\overline{Nu} = \frac{1}{\pi}\int_0^\pi Nu_o\, d\varphi = -\frac{1}{\pi}\, R\ln R \int_0^\pi \left.\frac{\partial T}{\partial r}\right|_{r=R} d\varphi \tag{14.12}$$

For a sufficient refined mesh, both expressions of the average of the Nusselt number converge to the same value.

14.3 Numerical Methods and Code Validation

The alternate direction implicit finite difference method is used to solve the mathematical problem along with the boundary conditions. The Thomas algorithm in conjunction with iterations is used to solve the resulting matrix systems. It should be

Table 14.1 Nusselt number for $R = 2$ and $\lambda_1 = \lambda_2 = 0$. Comparison with results from literature

	Grid size	$Ra = 50$	$Ra = 100$
Caltagirone [3]	49×49	1.328	1.829
Facas and Farouk [18]	25×25	1.362	1.902
Bau [24]	30×44	1.335	1.844
Rao et al. [9]	10×10	1.341	1.861
Himasekhar and Bau [10]	10×10	1.341	1.861
Facas [19]	50×50	1.342	1.835
Charrier-Mojtabi [20]	30×95	1.344	1.867
Mota et al. [21]	161×101	1.338	1.861
Alfahaid et al. [22]	10×18	1.317	1.865
Alloui and Vasseur [23]	100×240	1.343	1.868
Sheremet and Pop [25]	50×50	1.345	1.875
This study	49×49	1.343	1.851

noted that there is several ways for choosing the initial conditions that can be introduced in the computations. The initial conditions used in this work are the same as those considered in [13]. The convergence of our in-house numerical code has been assessed by a mesh testing procedure. In fact, using various mesh grids, numerical tests were examined for the case without any modulation i.e. $\lambda_i = 0,\ i = 1, 2$; in order to determine the best compromise between the grid independent solutions and the calculation time. The iteration process is terminated when the following criterion is satisfied in each node of the grid:

$$\max \left| \frac{\xi_{i,j}^{n+1} - \xi_{i,j}^{n}}{\xi_{i,j}^{n}} \right| < 10^{-8}$$

where ξ designates T or ψ, the subscripts i and j indices denote grid location in the (r, φ) plane and n refers to the iteration number.

The present code was validated by comparing the obtained result for $Ra = 50$ and $Ra = 100$ with the already published data (see Table 14.1). A good agreement is observed between the obtained streamlines and temperature contour plots and the results by Caltagirone [3], Charrier-Mojtabi [20], Khanafer et al. [12], Rao et al. [9] and Sheremet and Pop [25] for $Ra = 200$ (see Figs. 14.2, 14.3 plotted for different initial conditions). Figure 14.4 shows that we can choose the mesh grid 301×301 for our numerical simulations which ensures the mesh grid independence.

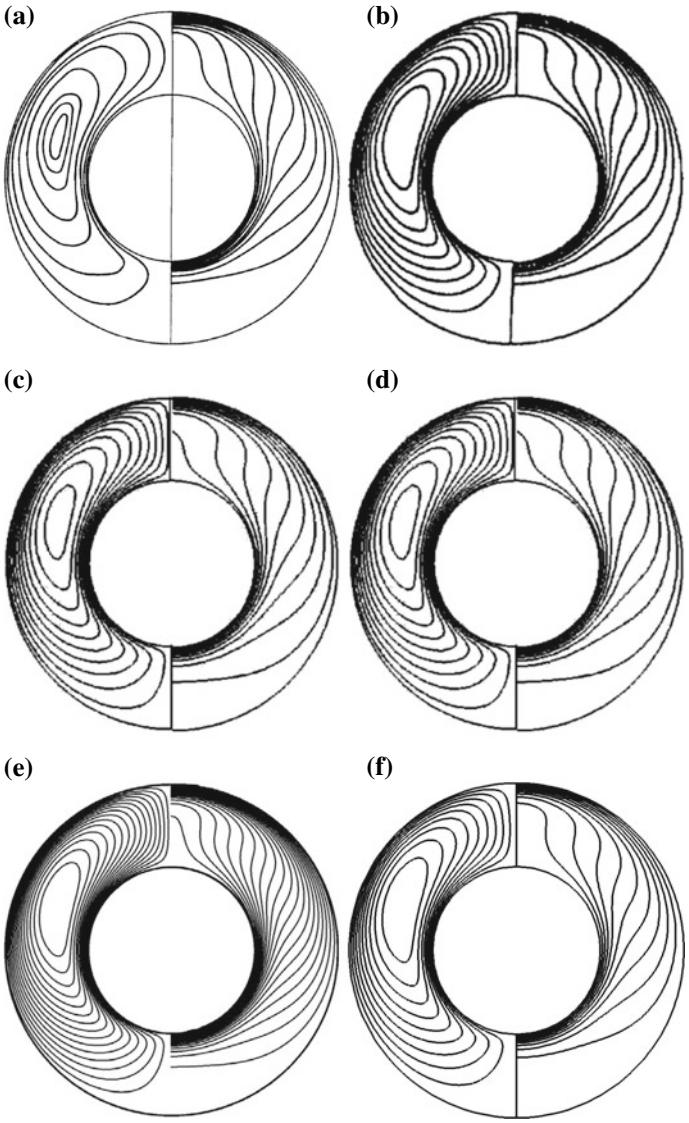

Fig. 14.2 Streamlines (left side of the annulus) and isotherms (right side of the annulus) of unicellular flow regime for $R = 2$, $Ra = 200$ in the absence of modulation. **a** Caltagirone [3], **b** Charrier-Mojtabi [20], **c** Khanafer et al. [12], **d** Rao et al. [9], **e** Sheremet and Pop [25], **f** This study

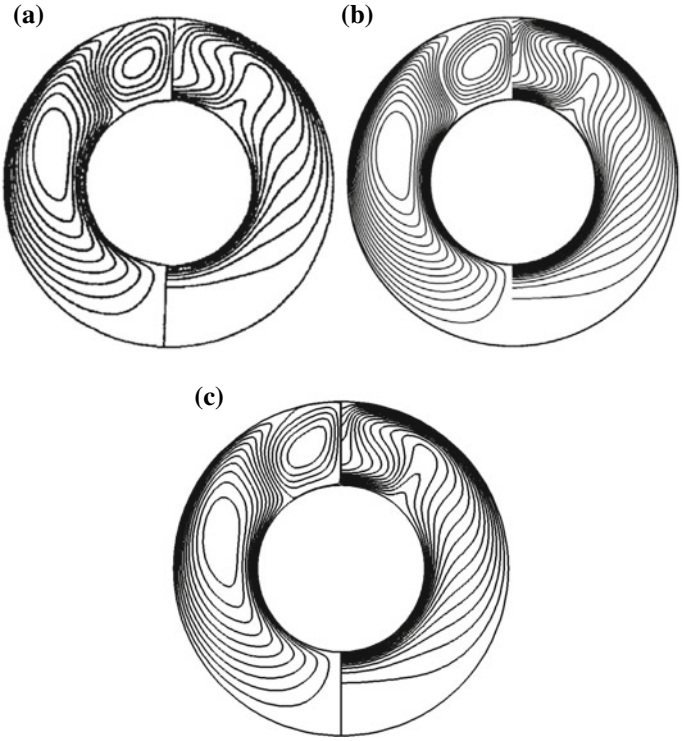

Fig. 14.3 Streamlines (left side of the annulus) and isotherms (right side of the annulus) of bicellular flow regime for $R = 2$, $Ra = 200$ in the absence of modulation for different initial conditions than those used in Fig. 14.2. **a** Charrier-Mojtabi [20], **b** Sheremet and Pop [25], **c** This study

Fig. 14.4 Mesh effect on $\overline{Nu}$ for $\lambda_1 = \lambda_2 = 0$, $R = 2$ and $Ra = 100$

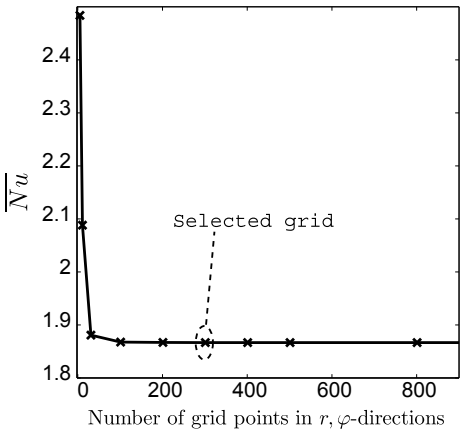

14.4 Main Results

To investigate the effect of QP gravitational modulation on the transition from unicellular to bicellular flow regime (or on the thermal convective instability) in a horizontal porous annulus, numerical simulations are performed for different values of the amplitudes λ_i (i = 1, 2), the frequency σ_1 and the radius ratio R. The frequencies ratio η will be adequately chosen in order to highlight the effect of the QP gravitational modulation on the onset of bicellular convection.

The comparison between the case of the periodic gravitational modulation ($\eta = 0$) and the case of the QP one ($\eta = \sqrt{2}$) is illustrated in Fig. 14.5. For $\eta = 0$ (or $\sigma_2 = 0$) one finds exactly the same results as in [13] in which the behavior of the maximum of stream function (Fig. 14.5, left) and the average Nusselt number (Fig. 14.5, right) is periodic in time (solid lines). In the case where the frequency ratio η is different

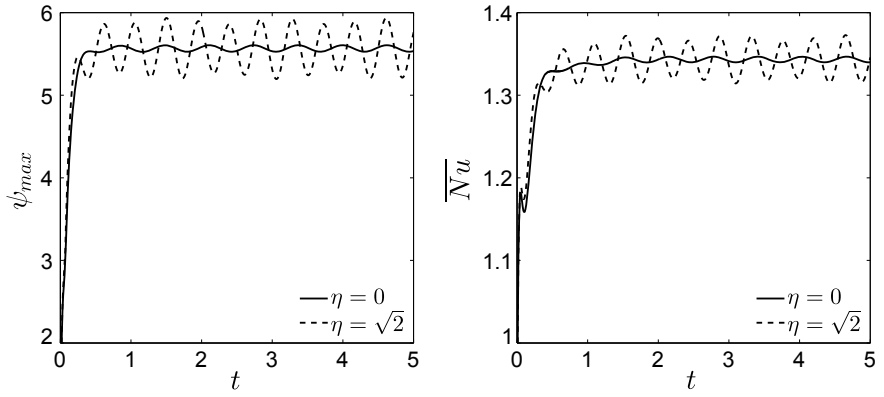

Fig. 14.5 Variation of ψ_{max} (left) and Nusselt number (right) as function of time for $\lambda_1 = \lambda_2 = 0.1$, $\sigma_1 = 10$, $Ra = 50$ and $R = 2$

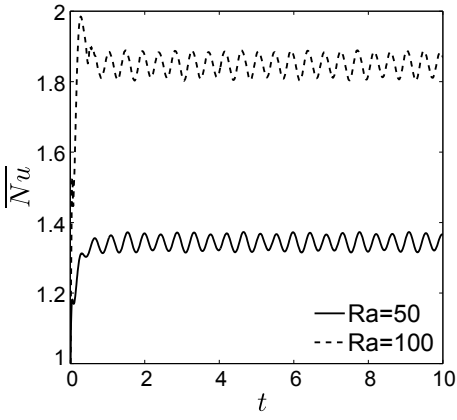

Fig. 14.6 Nusselt number as function of time for $\lambda_1 = \lambda_2 = 0.1$, $\sigma_1 = 10$, $\eta = \sqrt{2}$ and $R = 2$

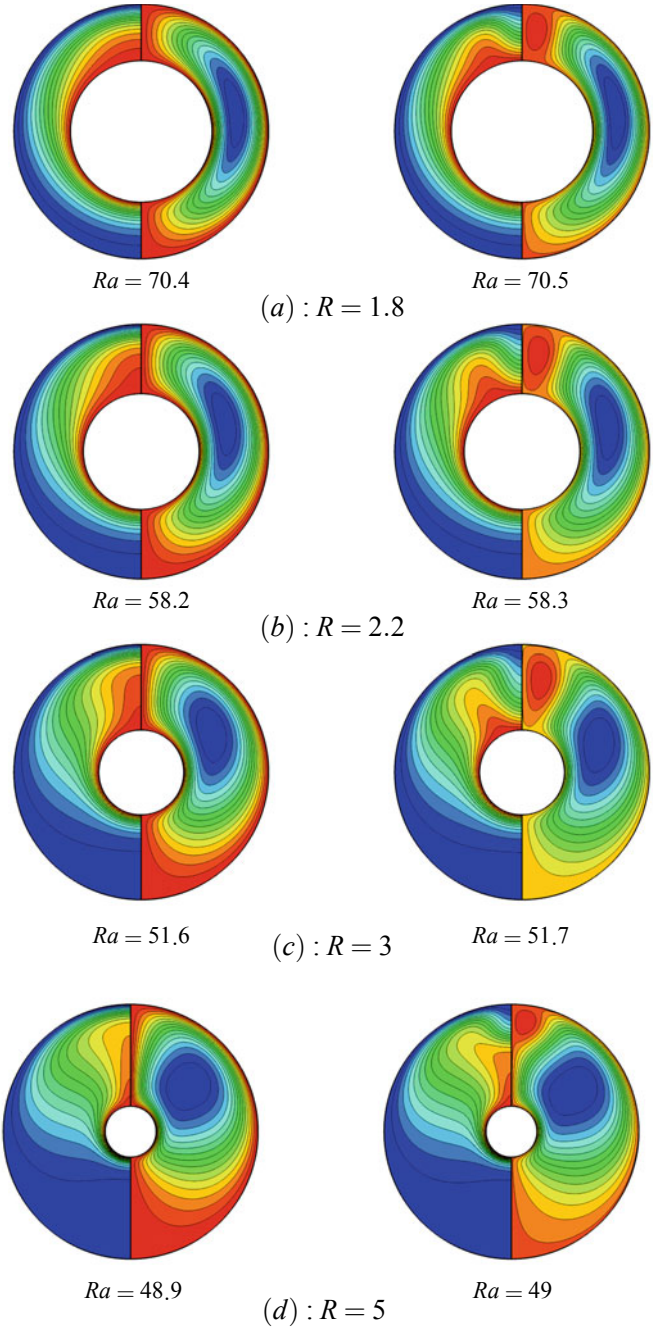

Fig. 14.7 Regime of transition for different value of radius ratio in the absence of modulation

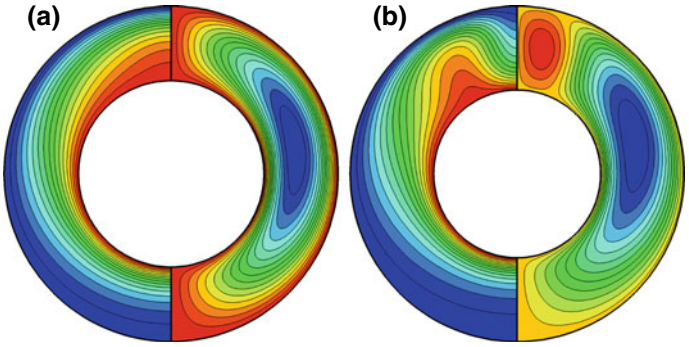

Fig. 14.8 Temperature (left hand side of the annulus) and streamlines (right hand side of the annulus) for $\lambda_1 = \lambda_2 = 0$ and $Ra = 70$. **a** R=1.8, **b** $R = 2$

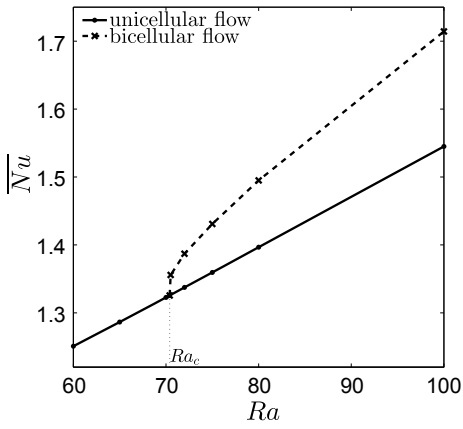

Fig. 14.9 Bifurcation point for $\lambda_1 = \lambda_2 = 0$ and $R = 1.8$

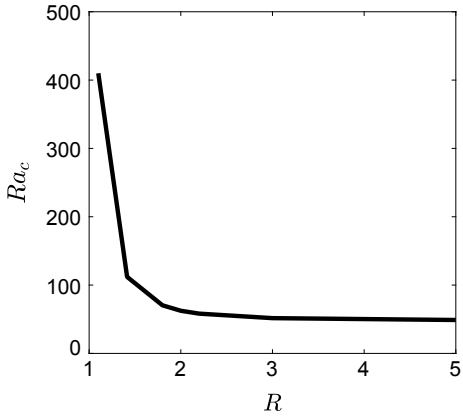

Fig. 14.10 Bifurcation point as function of radius ratio in the absence of modulation

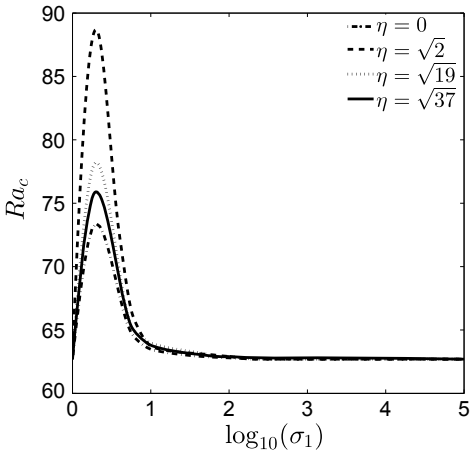

Fig. 14.11 Ra_c as function of $\log_{10}\sigma_1$ for $\lambda_1 = \lambda_2 = 0.2$, $R = 2$ and different η

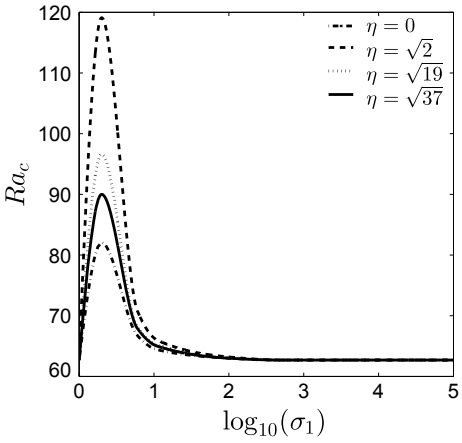

Fig. 14.12 Ra_c as function of $\log_{10}\sigma_1$ for $\lambda_1 = \lambda_2 = 0.3$, $R = 2$ and different η

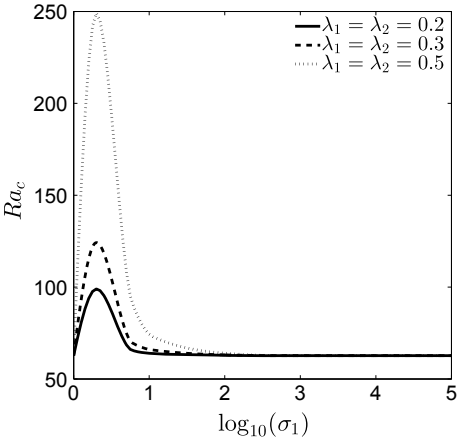

Fig. 14.13 Ra_c as function of $\log_{10}\sigma_1$ for $\eta = \sqrt{3}$, $R = 2$ and different λ

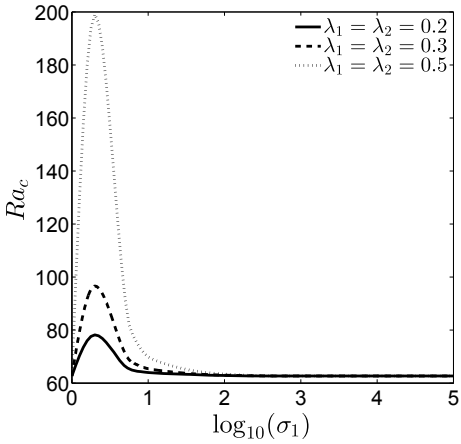

Fig. 14.14 Ra_c as function of $\log_{10}\sigma_1$ for $\eta = \sqrt{19}$, $R = 2$ and different λ

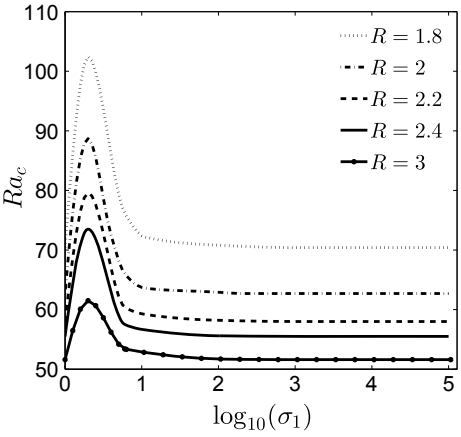

Fig. 14.15 Ra_c as function of $\log_{10}\sigma_1$ for $\lambda_1 = \lambda_2 = 0.2$, $\eta = \sqrt{2}$ and different R

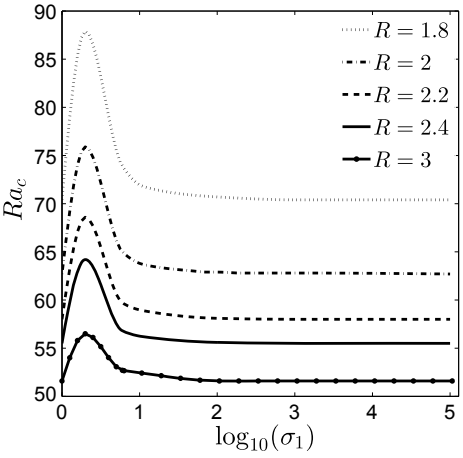

Fig. 14.16 Ra_c as function of $\log_{10}\sigma_1$ for $\lambda_1 = \lambda_2 = 0.2$, $\eta = \sqrt{37}$ and different R

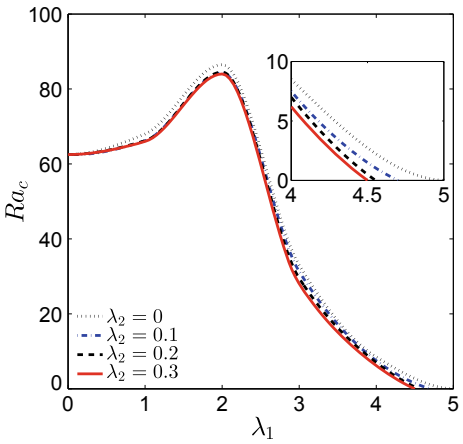

Fig. 14.17 Variation of Ra_c as function of λ_1 for $\sigma_1 = 100$, $\eta = \sqrt{2}$ and different λ_2

from zero ($\eta = \sqrt{2}$), a QP behavior is observed (dashed lines). It can be seen that the amplitude of oscillations in the QP regime is much larger which indicates that a thermo-convective regime flow occurs and thus the heat transfer is enhanced.

Figure 14.6 shows the Nusselt number as function of time for two different values of the Rayleigh number. The plots in the figure reveal that increasing the Rayleigh number causes an increase of the Nusselt number which results in a significant enhancement of the heat transfer. The unicellular, bicellular or multicellular flow patterns may develop for combinations of initial conditions, radius ratio and Rayleigh number. A bifurcation is defined as the transition from steady unicellular flow to multiple branches of solution. This is characterized by the critical value of Rayleigh number Ra_c under which only unicellular flow patterns exist.

Figure 14.7 shows the bifurcation point for different values of the radius ratio R in the case where the gravitational modulation is absent. For instance, when $R = 1.8$ the critical Rayleigh number $Ra_c = 70.4$ (Fig. 14.7a, left) and when $R = 5$, the critical Rayleigh number $Ra_c = 48.9$ (Fig. 14.7d, left). This confirms that a thinner annulus has a stabilizing effect than a wider one.

In Fig. 14.8 is shown the transition to the bicellular flow regime by increasing R. The transition from 2-D unicellular flow to 2-D bicellular flow can also be determined by plotting the average Nusselt number versus Ra (see Fig. 14.9). It can be seen that for $R = 1.8$ we obtain $Ra_c = 70.4$ which confirms the result of Fig. 14.7.

Figure 14.10 depicts the variation of critical Rayleigh number Ra_c as function of the radius ratio R and shows that the critical Rayleigh number decreases with increasing R.

Figures 14.11 and 14.12 show the critical Rayleigh number as function of the frequency σ_1 for fixed values of the radius ratio $R = 2$, different values of the modulation amplitudes λ_1, λ_2 and different values of the frequencies ratio η. All the curves in both figures start from the value $Ra_c = 62.4$ which is the same as in the periodic modulation case [13]. It can also be concluded from these figures that the QP gravitational modulation has a pronounced stabilizing effect than that of the periodic one.

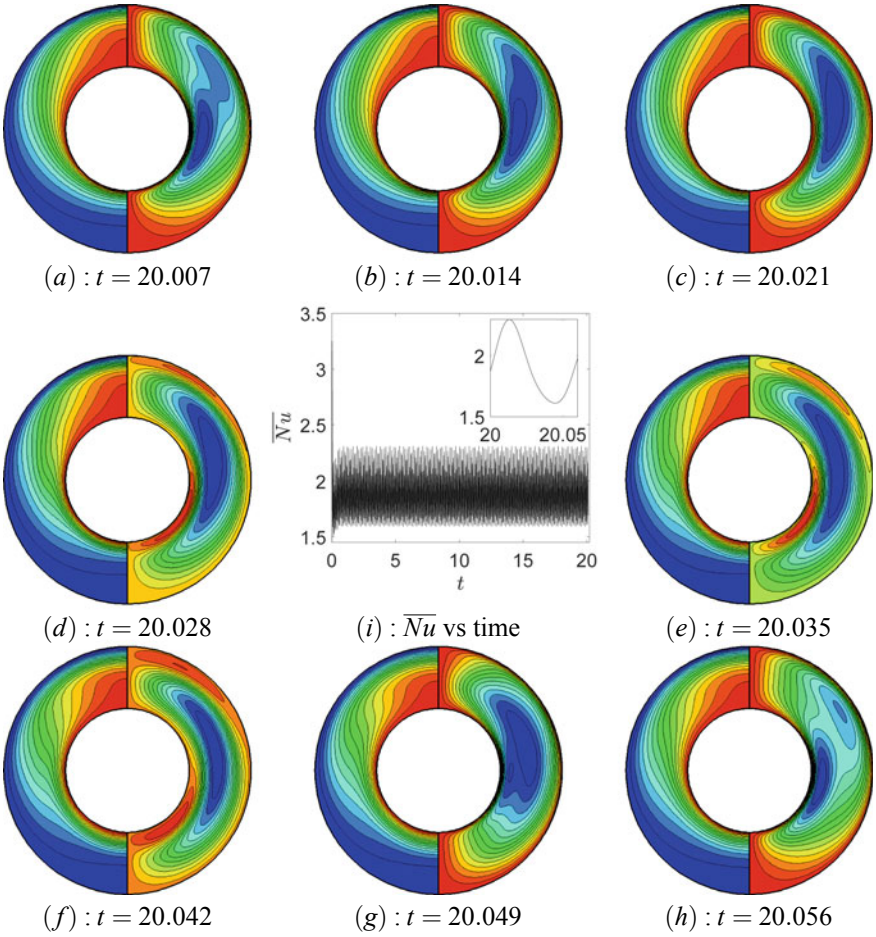

Fig. 14.18 Streamlines and isotherms (**a**–**h**) and average Nusselt number as function of time (**i**) for $\sigma_1 = 100$, $\eta = \sqrt{2}$, $\lambda_1 = 4$, $\lambda_2 = 1$, $R = 2$ and $Ra = 100$

Moreover, increasing the frequencies ratio η causes a stabilizing effect in a certain range of σ_1. These figures also indicate that the critical Rayleigh number increases to reach a certain maximum value for small value of σ_1 and then drops to its starting value $Ra_c = 62.4$ for large values of σ_1.

Figures 14.13 and 14.14 depict the variation of the critical Rayleigh number Ra_c versus σ_1 for fixed R and different values of η and λ_i $(i = 1, 2)$. It can be seen from the figures that when λ_i increases, a stabilizing effect is obtained. For large values of the frequency σ_1, increasing λ_i has no effect on the convective instability.

Figures 14.15 and 14.16 illustrate the variation of the critical Rayleigh number Ra_c as function of σ_1 for fixed value of the modulation amplitudes λ_i and different

values of η and R. The plots reveal that the critical Rayleigh number increases for decreasing values of R. In other words, decreasing the radius ratio causes a stabilizing effect.

Figure 14.17 summarizes the influence of the amplitudes of the QP modulation on the critical Rayleigh number. It is found that the thermo-convective destabilizing effect (unicellular to bicellular transition) in the annulus is more significant over a certain range of the modulation amplitude λ_2 in the vicinity of $\lambda_1 = 2$.

Figure 14.18 presents for large values of λ_1 and λ_2 the streamlines and isotherms as function of time. Various flow regimes with different flow patterns appear. The evolution of the average Nusselt number versus time is also presented in Fig. 14.18i.

Finally, Fig. 14.19a shows the variation of the critical Rayleigh number versus η for the values $R = 2$ and $\sigma_1 = 1$ corresponding to a stable state of the system. It is of interest to compare such a variation for commensurate values of η (harmonic modulation) and incommensurate ones (QP modulation) and examine the contribution of the QP gravitational modulation against the periodic one. The plots clearly show that the critical Rayleigh number Ra_c reaches a maximum value for $\eta = \sqrt{3}$ (QP modulation). At this value, the unicellular flow regime persists for values of the Rayleigh

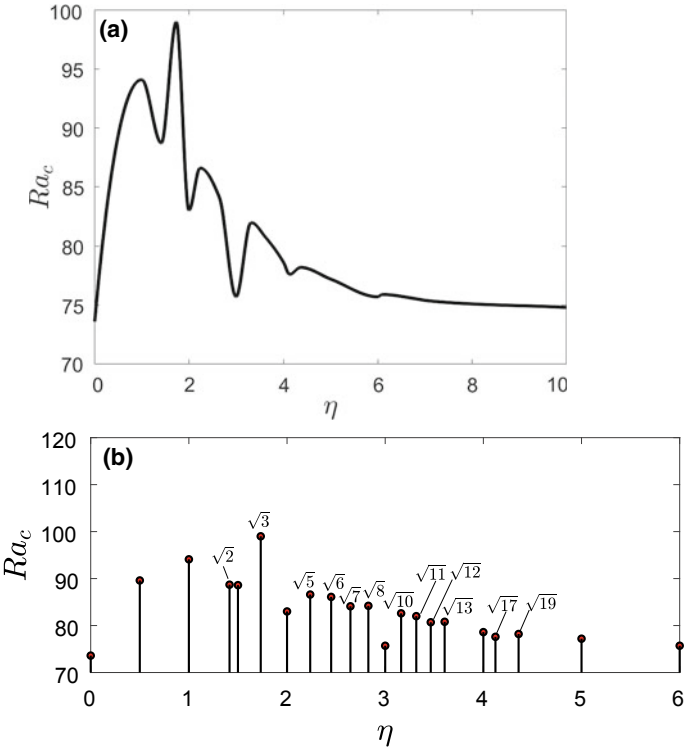

Fig. 14.19 Variation of Ra_c as function of η for $R = 2$, $\lambda_1 = \lambda_2 = 0.2$ and $\sigma_1 = 1$

number up to $Ra_c \approx 100$. Surprisingly, the results indicate that the minimum value of the critical Rayleigh number $Ra_c \approx 76$ is obtained for $\eta = 3$ (harmonic modulation). Figure 14.19a also shows that the QP gravitational modulation has an effect on the thermo-convective instabilities for relatively small values of η. Figure 14.19b illustrates the location of the critical Rayleigh number Ra_c for some specific values of the frequencies ratio η.

14.5 Conclusions

In this chapter, the convective instability in horizontal porous annulus was studied in the case where the annulus is under a QP gravitational modulation. The considered model is formed by the heat equation coupled to the hydrodynamic equations under Darcy law and Boussinesq approximation. The reduced model with the temperature-stream function formulation was solved using the alternate direction implicit method and Thomas algorithm. We have focused on the effect of QP gravitational modulation on the transition from unicellular to bicellular flow regime (corresponding to a substantial change in the heat transfer). Numerical simulations were performed for different values of the modulation amplitudes λ_i (i $= 1, 2$) and the radius ratio R. The frequencies ratio η has been adequately chosen in order to highlight the effect of the QP modulation on the onset of bicellular convection. Results showed that the amplitude of oscillations in the QP regime is larger than that of the periodic one, meaning that the heat transfer can be improved in the QP regime. Examination of the influence of the radius ratio of the annulus R on the critical Rayleigh number Ra_c demonstrates that the critical Rayleigh number decreases with increasing R revealing that a thinner annulus has a stabilizing effect than a wider one. Results also showed that small values of the amplitudes of QP modulation produce a stabilizing effect comparing to the periodic modulation case or the unmodulated one.

Moreover, it was demonstrated that for given values of the radius ratio and the modulation amplitudes, the maximum of the critical Rayleigh number Ra_c is obtained for $\eta = \sqrt{3}$, corresponding to the QP regime, and, surprisingly, the minimum value of Rayleigh number Ra_c is obtained for $\eta = 3$, corresponding to the periodic one.

References

1. K. Vafai, *Handbook of Porous Media* (Crc Press, 2015)
2. D.A. Nield, A. Bejan, *Convection in Porous Media* (Springer, 2017)
3. J.P. Caltagirone, Thermoconvective instabilities in a porous medium bounded by two concentric horizontal cylinders. J. Fluid Mech. **76**(2), 337–362 (1976)
4. J.B. Mota, E. Saatdjian, Natural convection in a porous, horizontal cylindrical annulus. J. Heat Transf. **116**(3), 621–626 (1994)
5. K. Khanafer, A.J. Chamkha, Mixed convection within a porous heat generating horizontal annulus. Int. J. Heat Mass Transf. **46**(10), 1725–1735 (2003)

6. J. Belabid, A. Cheddadi, Comparative numerical simulation of natural convection in a porous horizontal cylindrical annulus. Appl. Mech. Mater. **670**, 613–616 (2014)
7. J. Belabid, A. Cheddadi, Natural convection in an annular porous medium: effect of Brinkman correction on the bifurcation point. Appl. Mech. Mater. **789**, 403–406 (2015)
8. J. Belabid, K. Allali, M. Belhaq, Natural convection in a horizontal porous annulus under quasi-periodic gravitational modulation, in *MATEC Web of Conferences*, vol. 241 (2018), p. 01005
9. Y.F. Rao, K. Fukuda, S. Hasegawa, Steady and transient analyses of natural convection in a horizontal porous annulus with the Galerkin method. J. Heat Transf. **109**, 919–927 (1987)
10. K. Himasekhar, H.H. Bau, Two-dimensional bifurcation phenomena in thermal convection in horizontal, concentric annuli containing saturated porous media. J. Fluid Mech. **187**, 267–300 (1988)
11. M.C. Charrier-Mojtabi, A. Mojtabi, M. Azaiez, G. Labrosse, Numerical and experimental study of multicellular free convection flows in an annular porous layer. Int. J. Heat Mass Transf. **34**, 3061–3074 (1991)
12. K. Khanafer, A. Al-Amiri, I. Pop, Numerical analysis of natural convection heat transfer in a horizontal annulus partially filled with a fluid-saturated porous substrate. Int. J. Heat Mass Transf. **51**, 1613–1627 (2008)
13. J. Belabid, K. Allali, Influence of gravitational modulation on natural convection in a horizontal porous annulus. J. Heat Transf. **139**, 022502 (2017)
14. K. Allali, M. Belhaq, K. El Karouni, Influence of quasi-periodic gravitational modulation on convective instability of reaction fronts in porous media. Commun. Nonlinear Sci. Numer. Simul. **17**, 1588–1596 (2012)
15. K. Allali, S. Assiyad, M. Belhaq, Convection of polymerization front with solid product under quasi-periodic gravitational modulation. Nonlinear Dyn. Syst. Theory **14**, 323–334 (2014)
16. T. Boulal, S. Aniss, M. Belhaq, R. Rand, Effect of quasiperiodic gravitational modulation on the stability of a heated fluid layer. Phys. Rev. E **76**, 056320 (2007)
17. T. Boulal, S. Aniss, M. Belhaq, A. Azouani, Effect of quasi-periodic gravitational modulation on the convective instability in Hele-Shaw cell. Int. J. Non-Linear Mech. **43**, 852–857 (2008)
18. G.N. Facas, B. Farouk, Transient and steady-state natural convection in a porous medium between two concentric cylinders. J. Heat Transf. **105**, 660–663 (1983)
19. G.N. Facas, Natural convection from a buried pipe with external baffles. Numer. Heat Transf. Part A Appl. **27**, 595–609 (1995)
20. M.C. Charrier-Mojtabi, Numerical simulation of two-and threedimensional free convection flows in a horizontal porous annulus using a pressure and temperature formulation. Int. J. Heat Mass Transf. **40**, 1521–1533 (1997)
21. J.P.B. Mota, I.A.A.C. Esteves, C.A.M. Portugal, J.M.S.S. Esperana, E. Saatdjian, Natural convection heat transfer in horizontal eccentric elliptic annuli containing saturated porous media. Int. J. Heat Mass Transf. **43**, 4367–4379 (2000)
22. A.F. Alfahaid, R.Y. Sakr, M.I. Ahmed, Natural Convection Heat Transfer in Concentric Horizontal Annuli Containing a Saturated Porous Medi. IIUM Eng. J. **6** (2005)
23. Z. Alloui, P. Vasseur, Natural convection in a horizontal annular porous cavity saturated by a binary mixture. Comput. Therm. Sci. Int. J. **3** (2011)
24. H.H. Bau, Thermal convection in a horizontal, eccentric annulus containing a saturated porous medium -an extended perturbation expansion. Int. J. Heat Mass Transf. **27**, 2277–2287 (1984)
25. M.A. Sheremet, I. Pop, Free convection in a porous horizontal cylindrical annulus with a nanofluid using Buongiornos model. Comput. Fluids **118**, 182–190 (2015)

Chapter 15
Identification of Non-stationary and Non-linear Drying Processes

Piotr Wolszczak and Waldemar Samociuk

Abstract This chapter discusses a problem of control of a non-stationary and a non-linear drying process of food raw materials, especially yeast. Industrial yeast drying is a non-stationary and a non-linear process with a transport delay. In this work the identification of the yeast drying process was presented. Models for different time intervals of the closed control system were developed. Changes in the model parameters (non-stationarity) caused deterioration in the stability reserve. The developed models will be used to synthesize the control system in the future.

15.1 Introduction

The non-stationary and non-linear processes control is troublesome, especially if there is a transport delay and the process concerns a vivid material. Industrial drying of yeast is such a process. Active dried yeast (ADY) is used in industrial processes; in the craft brewing sector, distilling and baking industries and in wine production [12]. There is supply of warm air to the object during drying, too high temperature has an disadvantageous influence on its fermentation capacity [13]. Dried yeast vitality is influenced not only by the temperature value but also by the rate of its change [9, 19]. During industrial production, various types (strains) of yeast are used which are resistant to temperature to varying degrees [5, 24]. "Skim milk-a widely used protective agent-was used and in all strains, the highest viabilities following air-blast drying were obtained using 10% skim milk" [15]. Drying is continued until the dry weight of the yeast culture is approximately 93–95% dry weight [3] or 92–96% [2].

P. Wolszczak (✉)
Faculty of Mechanical Engineering, Lublin University of Technology, Nadbystrzycka 36, 20-618 Lublin, Poland
e-mail: p.wolszczak@pollub.pl

W. Samociuk
Faculty of Production Engineering, University of Life Sciences in Lublin, 28 Głęboka Street, 20-612 Lublin, Poland
e-mail: waldemar.samociuk@up.lublin.pl

M. Belhaq (ed.), *Topics in Nonlinear Mechanics and Physics*,
Springer Proceedings in Physics 228, https://doi.org/10.1007/978-981-13-9463-8_15

When designing control systems, a compromise between the complexity of the controlled process model and the effort necessary to obtain a reliable mathematical description is inevitable. Finding models from the laws of physics can be troublesome. For this reason, control systems based on the experimental data are designed. The indirect approach uses the collected data to identify the controlled process model, which is then used to synthesize the controller in accordance with the project objectives [1]. This method is based on the system identification tools ([4, 10, 11, 16–18, 25, 27]).

The selection of fixed parameters of the classic control system (PID) for the entire drying cycle can be impossible, therefore it is necessary to use complex control systems (Robust control, Adaptive Control, IMC) [25]. In addition, due to the process safety and high sensitivity of the material to a high temperature (over-regulation), it is advisable to use security systems (locks) at the appropriate SIL level [22, 23].

To enable high quality control it is necessary to know the object properties, saved in the form of an operator transfer function and the range of changes in the process parameters. The aim of the work is to determine the evolution (non-stationarity) of the yeast drying process. The mathematical model of the process (object) is used to determine the structure of the control system (controller type) and the settings of this controller. The basic process properties such as static characteristics, time constant and delay identified using recorded input and output signals or derived from physical laws. The direct approach does not focus on the exact approximation of the process.

During design control systems for processes in which the model parameters change their, it must be taken into account the stability of the control system. For such systems the robust control methodology is recommended [7, 8]. The robust control takes into account the model of object and is designed for correctly operates of the controller in uncertain object parameters conditions. The uncertainty of the model can be caused by: linearization of non-linear objects, inaccurate values of the model parameters, identification errors (disadvantages of the use of measurement data, too low sampling frequency, which impoverishes the characteristics of the object). In the robust control methodology the range of uncertain and the limits of properties variability are defined before mathematical modelling. The operation of robust control system adaptation within these limits and the change of the adopted process control principle is no necessary.

15.2 Food Raw Material Drying Process

Food raw material drying process produces cellular stress as presented in Fig. 15.1 [6]. The drying surface offsets into inside the organic material. The surface of the drying surface changes depends of shape of organic object (round grains, slices, agglomerations, a layer of wet powder or compound and complex shapes). The drying surface area effects the change in speed of moisture transport.

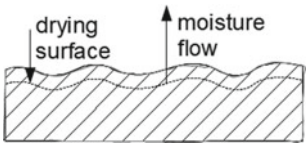

Fig. 15.1 The offset of the drying surface during drying process of organic material [26]

In yeast drying case the temperature value and the rate of temperature change affects the fermentation capacity and lifespan [9, 19]. The level of fermentation capacity degradation depends on the dynamic of the drying process [13].

Different yeast strains used in industrial production distinguishes degrees of resistant to temperature [5, 24]. Moreover to immunize yeast for high temperature some additives like skim milk can by used [15].

The level of yeast degradation depends both on the drying method and on the parameters of the drying process (mainly temperature and its rate of change) [13]. When yeast is dried, the protoplasmic proteins are transformed from hydrosol to hydrogel. This leads to the reversible stop of the vital functions of the systems (anabiosis), depending on the amount of water left [14]. Adverse cellular stress occurs during drying [6]. For example, the optimal temperature of spouted bed is about 40 °C [20].

The drying process is the supply of warm air to the yeast. The yeast loses water during heating. This process is shown schematically in Fig. 15.2.

The drying process control is based on two values: yeast temperature T_Y and air temperature T_A. This is shown on the diagram in Fig. 15.3.

Industrial drying yeast process has non-stationary and non-linear character, therefore the control processes with classical control in this case system are difficult. Due to impossibility of using fixed parameters of the controller of the classical control system for the entire drying cycle, it is recommended to use complex control systems [20].

Process of organic object drying in dryer equipped with one heater located outside the drying chamber is presented in Fig. 15.4. In this schema the drying system

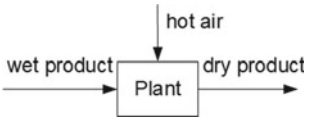

Fig. 15.2 The yeast dehydration process

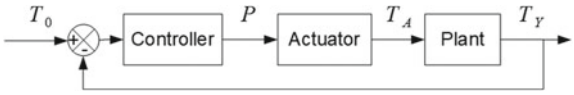

Fig. 15.3 Control of yeast drying, T0—setpoint signal, p—control signal, TA—air temperature, TY—yeast temperature

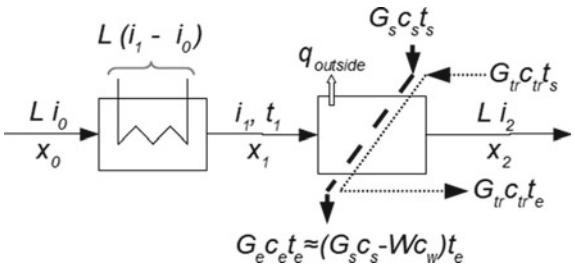

Fig. 15.4 Block diagram of the continuous drying process (normal variant), (a), (b), (c) and (d)—heat streams flowing into the dryer, (e), (f), (g) and (h)—heat streams flowing out of the dryer; heat balance: a + b + c + d = e + f + g + h; left block—preheater, right block—drying chamber. *L*—mass flow of dry air [kg/s], *G*—mass flow of moist material [kg/s], *c*—specific heat [kJ/(kg*K)], *i*—specific enthalpy [KJ/kg] of dry air, *x*—absolute humidity of air [kg of steam/kg of dry air], *t*—temperature [°C], *W*—mass flow of evaporated water from the material [kg/s]; indexes: *s*—initial value (start), *w*—water, *e*—finish value (end), *tr*—transporter, 0—atmospheric air, 1—heated air, 2—humidified air [26]

operates without air recirculation.

Figure 15.5 presents thermodynamic transformations accompanying drying process in the adiabatic process that is different than in the real case. In the schema the heat loss index Q_{loss} and the dry air mass flow L are localized. The difference between enthalpy of humid and atmospheric air is denoted by Δi_{ad} means.

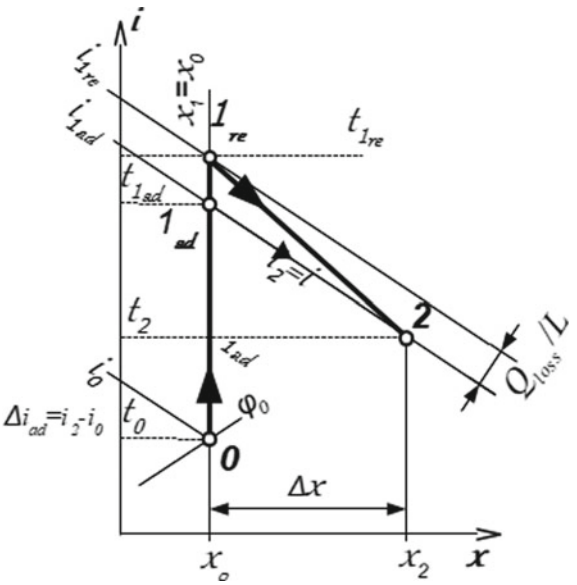

Fig. 15.5 Simplified enthalpy diagram with thermodynamic curves of the drying air in a dryer (normal variant), 0–1_{ad}—heating in the adiabatic process, 0–1_{re}—heating in the real process, 1_{ad}–2—adiabatic dampening, 1_{re}–2—real dampening. *i*—specific enthalpy [KJ/kg] of dry air, *x*—absolute humidity of air [kg of steam/kg of dry air], *t*—temperature [°C] φ_0—relative humidity of atmospheric air; indexes: 0—atmospheric air, 1—heated air, 2—humidified air, *ad*—adiabatic process (theoretic), *re*—real process (with losses) [26]

15.3 Subject of Research

The object of the research was the wet yeast layer dried by heated air flows. The air used for drying is mixed from two air streams: cool and heated air for obtaining right air temperature. The drying cycle takes more than seven hours and the yeast temperature cannot exceed 50°, which would destroy their functions.

The temperature of the yeast is monitored and controlled by air temperature according to the defined drying curve shown in Fig. 15.6. The temperature of the yeast layer is gradually raised during the drying cycle. The described process of the drying surface offsets in the wet organic layer with developed shape causes disruption in the drying control process. Examples of the series of drying cycles are shown in Fig. 15.6. Time series contains: setpoint signal, throttle opening, temperature under the sieve and temperature of the yeast layer. Disruption in the drying control process revealed in the increasing form the value of the error (the difference between the setpoint and wet layer temperature). Changing the sensitivity of the object caused by changes in the physical properties increases the risk of overheating the yeast. The current solution of this problem is step changing the controller's parameters during the process. The control system contains two sets of controller parameters. The controllers' parameters change is made at predefined time. Such a solution involves problems like: mismatching of to the moment of real change of the object's property and its dynamic. The change in properties can be gradual and complex while next parameters set for controller is introduced by step function.

Controlling of the organic product drying process with one PID controller proved to be ineffective. It was prepared a set of the controller parameters, used for a simple switching control model and adapted to changing object properties, as illustrated in

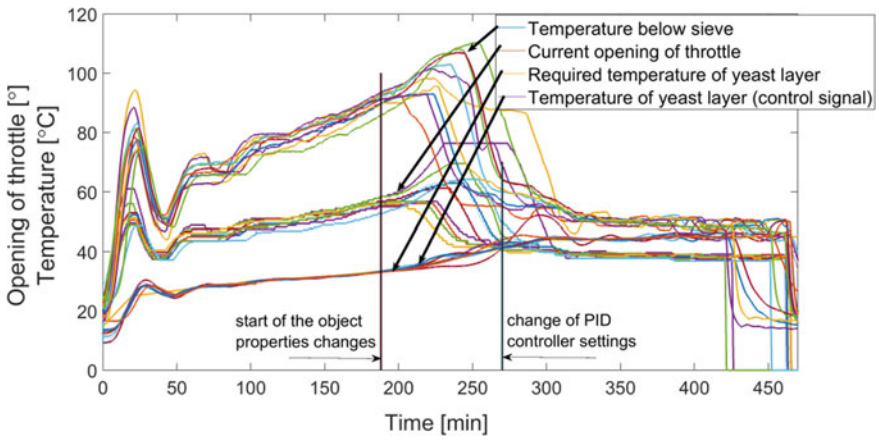

Fig. 15.6 Example sets of signals recorded during drying process. Signals: setpoint trace—required temperature of yeast layer on sieve [°C], control signal—hot air throttle opening [°C], the controlled variables—temperature below sieve and yeast layer temperature [°C] [26]

the Fig. 15.6. The next settings are switched on according to the adopted model of the product temperature curve control.

15.4 Process Identification

There is a transport delay in the analyzed process, but it is difficult to determine because it requires carrying out an experiment that is currently not possible due to ongoing production. Process data is masked by previous states (large inertia of the process)—Fig. 15.7. The main transport delay is caused by the distance between the dried yeast and the heating element. It is possible to determine this delay analytically, but the knowledge of all geometric and technical parameters is needed (they are currently unavailable). At this stage of work, it is planned to identify the process without taking into account the delay. This delay is probably small compared to the inertia of the process (0.7 s—Fig. 15.8). The drying process begins in the 32.5 min of the cycle (beginning of the air temperature T_A increasing). The product's temperature value begins to grow from the 33.2 min recording of results (T_Y). Thus, the transport delay is 0.7 min (42 s). Figure 15.8 shows the time courses of T_Y and T_A temperatures.

The recorded data comes from a closed system that includes an object, a measuring transducer, a controller and an actuator. Intuitively, it can be assumed that it is an inertial object with a delay, but it is uncertain. Yeast is an organic material in which various processes undergo. They have a significant influence on heat transfer. The

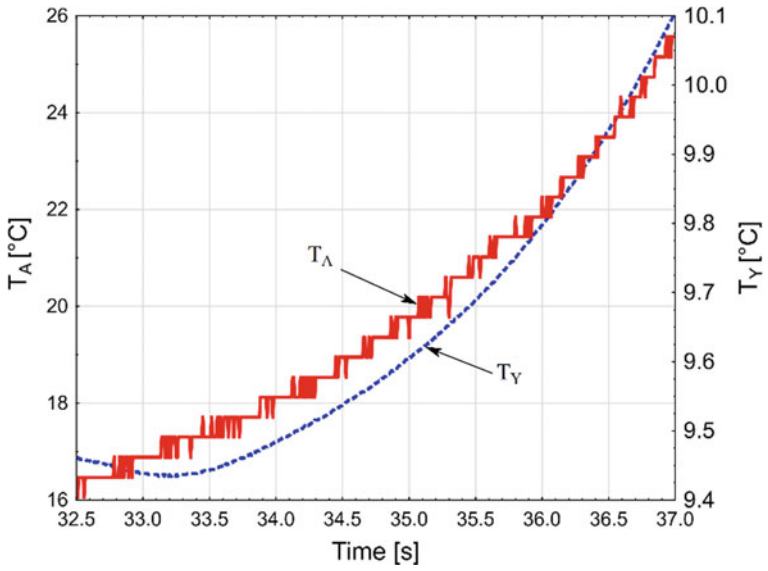

Fig. 15.7 T_A and T_Y temperature in at the beginning of the process

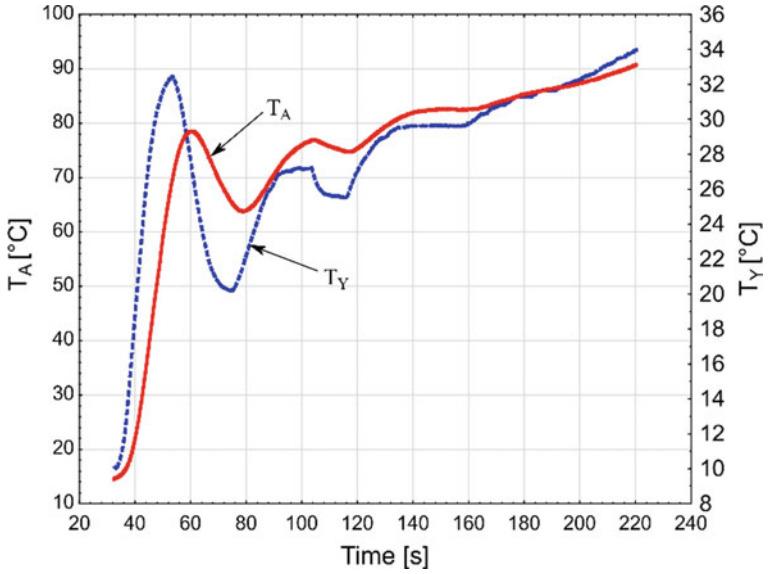

Fig. 15.8 T_A and T_Y temperature in analyzed process

parameters of the object are changing, so the object is nonstationary. The recorded results come from a closed, stable system. Models (discrete operator transmissions) for different time intervals were determined in order to examine whether the system is non-stationary.

Identification of model parameters describing the relationship between air temperature and product temperature.

The model describing the relationship between the discrete value of air temperature and product temperature can be described by a discrete equation (with aggregated parameters) of the form:

$$T_y(k) + a_1 T_y(k-1) - \cdots - a_n T_y(k-n) = b_0 T_A(k-h) + b_1 T_A(k-1-h) + \cdots + b_n T_A(k-n-h) \quad (15.1)$$

where h is a discrete time delay, a_i, b_i are model parameters.

The product temperature values $T_y(k)$ can be determined from the model as follows:

$$\hat{T}_y(k) = b_0 T_A(k-h) + \cdots + b_n T_A(k-n-h) - a_1 T_y(k-1) - \cdots - a_n T_y(k-n) \quad (15.2)$$

Using the reverse operator and substituting:

$$\nabla T_y = T_y(k) - T_y(k-1) = \left(1 - z^{-1}\right) T_y \quad (15.3)$$

$$\nabla T_A = T_A(k) - T_A(k-1) = \left(1 - z^{-1}\right) T_A \tag{15.4}$$

$$A^*(z) = a_1 z^{-1} - a_2 z^{-2} - \cdots - a_n z^{-n} \tag{15.5}$$

$$B(z) = \left(b_0 + b_1 z^{-1} + b_2 z^{-2} + \cdots + b_n z^{-n}\right) z^{-h} \tag{15.6}$$

we obtain

$$\hat{T}_y(k) = B(z) T_A(k) + A^*(z) T_y(k) \tag{15.7}$$

The above model has been supplemented by external disturbances:

$$\hat{T}_y(k) = B(z) T_A(k) + A^*(z) T_y(k) + \eta(k) \tag{15.8}$$

Using the transformation

$$T_y(k) - A^*(z) T_y(k) = B(z) T_A(k) + \eta(k) \tag{15.9}$$

$$A(z) = 1 - A^*(z) \tag{15.10}$$

leads to

$$T_y(k) = \frac{B(z)}{A(z)} T_A(k) + \frac{1}{A(z)} \eta(k) \tag{15.11}$$

The first part of the equation describes the process of heat exchange between the air temperature $T_x(k)$ and the mass of product $T_y(k)$. The second part of the equation takes into account interference effects in this model. The dependency corresponding to the part of the first equation can be written in the form of a discrete transfer function as (with a transport delay):

$$G(z) = \frac{T_y(z)}{T_A(z)} = \frac{B(z)}{A(z)} = \frac{b_0 z^{-1} + b_1 z^{-2} + b_2 z^{-3}}{1 + a_1 z^{-1} + a_2 z^{-2} + a_3 z^{-3}} z^{-h} \tag{15.12}$$

where z^{-1} is the backward difference operator shift ($i = 1, 2, 3, \ldots, n$) and h is the transport delay.

Finally, the heat exchange process is described by third order discrete transmission without delay h as

$$G(z) = \frac{b_0 z^{-1} + b_1 z^{-2} + b_2 z^{-3}}{1 + a_1 z^{-1} + a_2 z^{-2} + a_3 z^{-3}} \tag{15.13}$$

Parameters of identified model are presented in Table 15.1.

Table 15.1 Parameters of identified model

Interval no.	Sample no.	b_0	b_1	b_2	a_1	a_2	a_3
1	0–5000	0.0451	−0.0067	−0.0379	0.3713	0.3191	0.3085
2	3000–8000	0.0595	−0.0153	−0.0437	0.3380	0.3309	0.3300
3	5000–10000	0.0447	−0.0093	−0.0349	0.3523	0.3195	0.3272
4	10000–15000	0.0104	0.0019	−0.0121	0.3466	0.3348	0.3183
5	15000–20000	0.0246	0.0040	−0.0284	0.3269	0.3212	0.3515
6	17500–22500	0.0062	0.0216	−0.0276	0.3355	0.3199	0.3441

Table 15.2 The roots of discrete transmittances

Sample no.	Re1	Im1	Re2	Im2	Re3	Im3
0–5000	−0.3141	0.4583	−0.3141	−0.4583	0.9994	0
5000–10000	−0.3236	0.4718	−0.3236	−0.4718	0.9995	0
10000–15000	−0.3266	0.4601	−0.3266	−0.4601	0.9998	0
15000–20000	−0.3365	0.4882	−0.3365	−0.4882	0.9998	0

The model parameters change with the drying time. The roots of discrete transmittances of the closed system are determined in Table 15.2. The roots (zeros of the characteristic equation) were calculated for the time periods for which discrete transmittances were determined—Table 15.2.

The system is stable if and only if

$$\bigwedge_{i \in 1,k} |z_i| < 1 \tag{15.14}$$

where z_i are the roots of the control system with closed loop (feedback) and k is the number of roots.

Root No. 3 (Re3) is located very close to the unit circle. It means that the system is very close to the stability limit.

The identification concerns separated elements of the system like actuator and object as well as object including a dryer and product. The actuator element that was the throttle can be characterized by the linear transfer function, whereas, the object can be characterized by the non-linear function.

Nonlinear ARX (AutoRegressive with eXogenous inputs) models have structure:

$$y(t) = f(y(t-1), \ldots, y(t-n_a), u(t-n_k), \ldots, u(t-n_k-n_b+1)) \tag{15.15}$$

where u and y are finite numbers of previous inputs and outputs, n_a and n_b are numbers of past output and input terms, which are used to predict the output and n_k is the delay from the input to the output, defined as the number of samples.

In Fig. 15.9 an examples of measured process signals and simulated model outputs

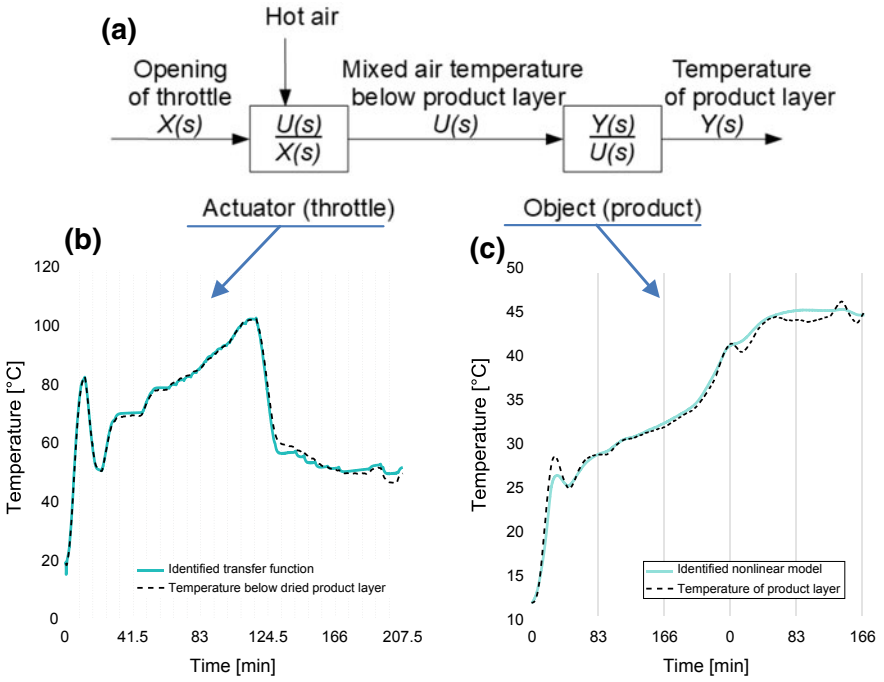

Fig. 15.9 Examples of measured process signals and simulated model output **a** schema of the actuator and object inputs and outputs, **b** actuator output signal (temperature below dried product layer), **c** object output signal (temperature of product)

are presented. The model of actuator was identified by linear transfer function (15.16). Fit to estimation data performs 92.25% (FPE[1] = 1.957, MSE[2] = 1.956).

$$\frac{U(s)}{X(s)} = \frac{-650.4 \cdot s^4 - 199.2 \cdot s^3 + 5 \cdot s^2 + 0.08 \cdot s + 3.2e - 6}{s^5 + 1026 \cdot s^4 + 360.1 \cdot s^3 + 6.8 \cdot s^2 + 0.03 \cdot s + 2e - 6} \tag{15.16}$$

The model of object was estimated by nonlinear ARX model using elements (15.17). Estimation fit to data perform 99.85% (FPE = 0.000159, MSE = 0.000155)

$$y1(t-1),\ y1(t-2),\ u1(t-1),\ u1(t-2) \tag{15.17}$$

Final prediction error (FPE): 0.0001701, Loss function: 0.0001698. Fit to working data: 93.32%

[1]FPE: Final prediction error means percent fit to estimation data.

[2]MSE: Mean-square error.

15.5 Process Simulation

The first stage of the control developing was registration of the signals from the real object. Second stage was identification of the object and estimation of mathematical model of the object. The identification concerns separated elements of the system like actuator and object as well as object including a dryer and product. Similarly, for the estimation there were exposed the complete time series (symbol AB) of the process and parts (symbols A and B) as results of division in the moment of change of controller's set parameters. The third stage was the preparation of the systems for simulation using the classical PID controlled. For ten drying cycle the set of transform functions has been prepared. The functions have different order value of transform functions (characteristic equation). During the identification of the mathematical models, the order of characteristic equation of the objects and function coefficients are adapted. Additionally, the estimation of nonlinear function to identify the model of the object was conducted.

Identification of the mathematical model was conducted separately for the first (A) and second (B) parts of drying cycle. Recorded signals were also used to identify process elements mentioned in Fig. 15.3. Due to the use of a temperature below the sieve signal, it was possible to identify the properties of the yeast layer and process analysis.

For improvement of the currently operating control system the mathematical model was used to optimize the PID controllers' parameters and for optimize moment of switching the PID controller settings. In the Fig. 15.6 can be seen fluctuations in the input and control signals occurs before the switching of the PID controller settings. The control system simulation with identified objects allowed for correction of the time of the controller's settings. The system simulation results after correction of the changeover time of the controller's settings presents Fig. 15.10. The object is

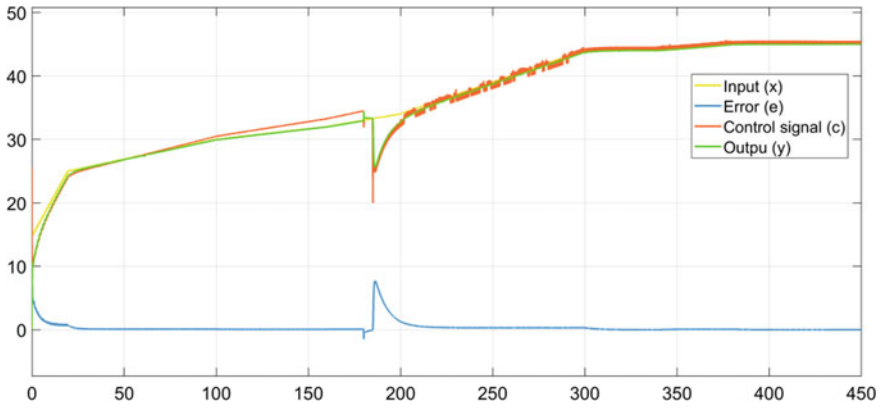

Fig. 15.10 Simulation of drying process characterized by two transfer function G_A, G_B, and two controllers PI ($K_p = 1.7$, $K_i = 0.785$) and PID ($K_p = 1.3$, $K_i = 0.312$, $K_d = 0.758$), with limited output in range from 20 to 80 [°C] switched in 180th time unit of simulation [26]

identified by two transfer function G_A and G_B. The switch time is set in 180th time unit of simulation. The simulation results are presented in Fig. 15.10. Such control system should protect the product from overheating.

$$G_B = \frac{34s^3 + 2.5s^2}{s^4 + 33.4s^3 + 2.5s^2} \tag{15.18}$$

$$G_B = \frac{25s^3}{s^4 + 25.1s^3} \tag{15.19}$$

15.5.1 Robust Uncertainty Principles Application

In order to protect drying product from overheating, the robust method was used. Firstly, signals recorded from the real process were used to identify elements. Secondly, the mathematical model of the object was prepared and applied for the robustness controller. For the characteristic equation coefficients the uncertainty in the range of ± 20% of nominal values was determined. In the Fig. 15.11 a set of the step responses is presented. The set contains response of PI control systems in the first part (A) of the drying cycle, PID controller in the second part (B) of the drying cycle and the robust controller controlling the process in whole cycle. In this case the object transmittance was identified for signals recorded in both parts of the process (parts A and B).

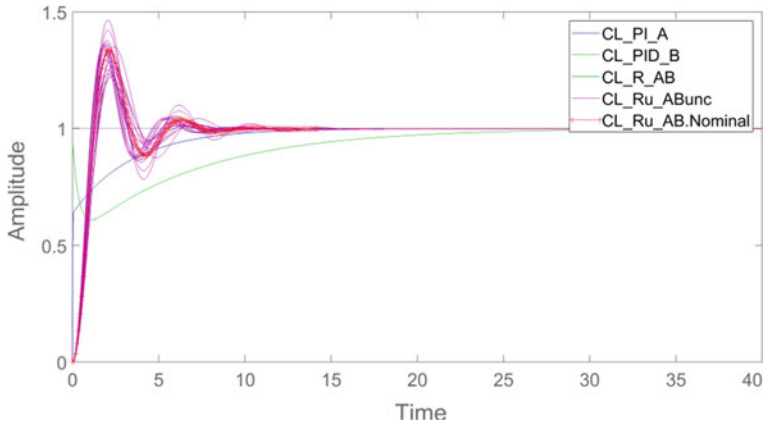

Fig. 15.11 Step response for mathematical models of feedback systems consists of controllers and transfer function of objects: CL_PI_A—PI controller and transfer function of part A, CL_PID_B—PID controller and transfer function of part B, CL_R_AB—Robust controller and transfer function of parts A+B [26]

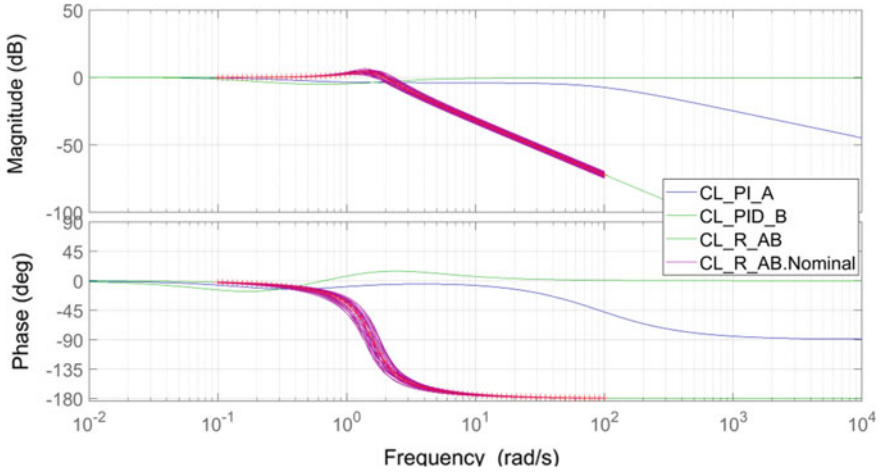

Fig. 15.12 Sensitivity analysis **a** Bode plots for closed-loop systems and **b** Nyquist plot for mathematical models of open-loop systems consists of controllers and transfer function of objects: PI*G_A—PI controller and transfer function of part A, PID*G_B—PID controller and transfer function of part B, C_R*G_AB—Robust controller and transfer function of parts A+B [26]

Simulation with the robustness controller allows controlling the process quality in whole cycle, whilst using of the PI controller during second part (B) and PID controller in the first part (A) causes instability of system in both cases.

Using the inverted model (15.18), the sensitivity of the system was simulated and results are presented in Fig. 15.12.

$$G_S = 1/G_{model} \tag{15.20}$$

Figure 15.11 illustrates the dynamic characteristics of control systems with PI, PID and robustness controllers. The use of a robustness regulator eliminates variation of the product temperature caused by a sudden change of the object's properties.

15.6 Conclusion

Drying of organic products can have a non-linear character caused by the technology used and the change of the physical properties of the object. Changing the physical properties of the object causes an increase in the temperature error value of the object relative to the planned drying curve. This character of the transformation increases the risk of overheating the yeast.

The yeast drying is a non-stationary process, confirmed by changes in transmittance coefficients. Analyzing the position of the poles of the system, it can be state that the reserve of stability is very small and decreases over time. It means that

changes in the properties of the object can lead to the loss of stability of the system (process) that is confirmed by industrial results. Change of the object's properties forces change of the controller's settings during the process. The robust control is known in the literature, but rarely used in practice for non-linear process control. The knowledge about the object's properties will enable selection of the appropriate structure of the control system.

References

1. G. Battistelli, D. Mari, D. Selvi, P. Tesi, Direct control design via controller unfalsification. Int. J. Robust Nonlinear Control **28**(12), 3694–3712 (2017)
2. D. Bayrock, W.M. Ingledew, Mechanism of viability loss during fluidized bed drying of baker's yeast. Food Res. Int. **30**(6), 417–425 (1997). https://doi.org/10.1016/S0963-9969(97)00072-0
3. T. Borowy, Everything about yeast (in Polish). Mistrz branży (2014). http://mistrzbranzy.pl/artykuly/pokaz/Wszystko-o-drozdzach-1721.html
4. R. Cechowicz, P. Staczek, Computer supervision of the group of compressors connected in parallel. Maint. Reliab. **16**(2), 198–202 (2014)
5. K. Charoensopharat, P. Thanonkeo, S. Thanonkeo, M. Yamada, Ethanol production from Jerusalem artichoke tubers at high temperature by newly isolated thermotolerant inulin-utilizing yeast Kluyveromyces marxianus using consolidated bioprocessing. Antonie Leeuwenhoek **108**(1), 173–190 (2015). https://doi.org/10.1007/s10482-015-0476-5
6. E. Gamero-Sandemetrio, L. Payá-Tormo, R. Gómez-Pastor, A. Aranda, E. Matallana, Non-canonical regulation of glutathione and trehalose biosynthesis characterizes non-Saccharomyces wine yeasts with poor performance in active dry yeast production. Microb. Cell **5**(4), 184–197 (2018)
7. C.E. Garcia, M. Morari, Internal model control. A unifying review and some new results. Ind. Eng. Chem. Process. Des. Dev. **21**, 308–323 (1982)
8. C.E. Garcia, M. Morari, Internal model control. 2. Design procedure for multivariable systems. Ind. Eng. Chem. Process. Des. Dev. **24**, 472–484 (1985)
9. P. Gervais, I. Maranon, Effect of the kinetics of temperature variation on Saccharomyces cerevisiae viability and permeability. Biochem. Biophys. Acta **1235**(1), 52–56 (1995)
10. P. Harris, M. Arafa, G. Litak, C.R. Bowen, J. Iwaniec, Output response identification in a multistable system for piezoelectric energy harvesting. Eur. Phys. J. B **90**(1), 1–11 (2017)
11. H. Hjalmarsson, From experiment design to closed-loop control. Automatica **41**, 393–438 (2005)
12. D.M. Jenkins, C.D. Powell, T. Fischborn, K.A. Smart, Rehydration of active dry brewing yeast and its effect on cell viability. J. Inst. Brew. **117**(3), 377–382 (2011)
13. A. Kamińska-Dwórznicka, A. Skoniecka, The influence of drying methods, parameters and the way of storage on the activity of bakery yeasts (in Polish). Zeszyty Problemowe Postępów Nauk Rolniczych **573**, 35–42 (2013)
14. T. Kudra, C. Strumiłło, *Thermal processing of biomaterials. Gordon and Breach Science*. OPA Amsterdam (1998)
15. S.B. Lee, W.S. Choi, H.J. Jo, S.H. Yeo, H.D. Park, Optimization of air-blast drying process for manufacturing Saccharomyces cerevisiae and non-Saccharomyces yeast as industrial wine starters. AMB Express **6**(1), 105 (2016)
16. G. Litak, R. Rusinek, Identification of turning and milling processes by stochastic Langevin equations, in *4th IEEE International Conference on Nonlinear Science and Complexity* (2012), pp. 41–44
17. L. Ljung, *System identification: theory for the user*, 2nd edn. (Prentice Hall PTR, Upper Saddle River, 1999). http://dx.doi.org/10.1002/047134608x.w1046

18. A. Martynenko, Computer vision for real-time control in drying. Food Eng. Rev. **9**(2), 91–111 (2017). https://doi.org/10.1007/s12393-017-9159-5
19. F.I. Mensonides, S. Brul, K.J. Hellingwerf, B.M. Bakker, M.J. Teixeira de Mattos, A kinetic model of catabolic adaptation and protein reprofiling in Saccharomyces cerevisiae during temperature shifts. FEBS J. **281**(3), 825–841 (2014)
20. D. Muhammad, Z. Ahmad, N. Aziz, Implementation of internal model control (IMC) in continuous distillation column, in *Proceedings of the 5th International Symposium on Design, Operation and Control of Chemical Processes* (2010), pp. 812–821
21. M. Pasławska, Influence of the fountain drying temperature on the dewatering kinetics and yeast viability (in Polish). Inżynieria Rolnicza **5**(103), 161–166 (2008)
22. W. Samociuk, Z. Krzysiak, M. Szmigielski, J. Zarajczyk, Z. Stropek, K. Gołacki, G. Bartnik, A. Skic, A. Nieoczym, Modernization of the control system to reduce a risk of severe accidents during non-pressurized ammonia storage (in Polish). Przemysł Chemiczny **95**(5), 1000–1003 (2016). https://doi.org/10.15199/62.2016.5.29
23. W. Samociuk, A. Wyciszkiewicz, K. Gołacki, T. Otto, Risk of catastrophic failure of the reactor for urea synthesis (in Polish). Przemysł Chemiczny **96**(8), 1763–1766 (2017). https://doi.org/10.15199/62.2017.8.32
24. A. Techaparin, P. Thanonkeo, P. Klanrit, High-temperature ethanol production using thermotolerant yeast newly isolated from Greater Mekong Subregion. Braz. J. Microbiol. **48**(3), 461–475 (2017)
25. P. Wolszczak, K. Łygas, G. Litak, Dynamics identification of a piezoelectric vibrational energy harvester by image analysis with a high speed camera. Mech. Syst. Signal Process. **107**, 43–52 (2018)
26. P. Wolszczak, W. Samociuk, The control system of the yeast drying process, in *MATEC Web of Conferences*, vol. 241 (2018), p. 01022. https://doi.org/10.1051/matecconf/201824101022
27. L.-P. Yang, S.-L. Ding, G. Litak, E.-Z. Song, X.-Z. Ma, Identification and quantification analysis of nonlinear dynamics properties of combustion instability in a diesel engine. Chaos **25**, 013105-1–013105-13 (2015)